THE ROLE OF C-O-H FLUIDS IN UPPER MANTLE PROCESSES - A THEORETICAL, EXPERIMENTAL AND SPECTROSCOPIC STUDY.

by

Wayne Robert Taylor [B.Sc.(Hons)]

Submitted in fulfilment of the requirements
for the degree of Doctor of Philosophy.

UNIVERSITY OF TASMANIA
HOBART
1985

This thesis contains no material which has been accepted for the award of any other degree or diploma in any university and to the best of my knowledge and belief, contains no copy or paraphrase of material previously published or written by another person, except where due reference is made in the text of this thesis.

W. R. Taylor
University of Tasmania
June, 1985.

TABLE OF CONTENTS

ABSTRACT

Evidence from natural magmas and mantle xenoliths argues that fluids in the system C-O-H exercise important influences on petrogenetic processes in the Earth's upper mantle. In this thesis, experimental, spectroscopic and theoretical constraints are applied to provide the necessary basis for understanding the nature of mantle melting as a function of oxygen fugacity (fO_2) in the model system "peridotite"-C-O-H.

Until very recently, most petrogenetic models were based on the assumption that fO_2-conditions in magma source-regions of the upper mantle were relatively oxidised, lying near the fO_2 defined by the synthetic assemblage fayalite-magnetite-quartz (FMQ). This was consistent with the petrogenetic role inferred for oxidised CO_2-H_2O volatiles and carbonated peridotite. However, if magma generation involving volatile components takes place in a reduced environment, for example at fO_2's near the synthetic iron-wustite (IW) oxygen buffer - as suggested by intrinsic fO_2 measurements on mantle-derived minerals - then in the model system "peridotite"-C-O-H, volatiles will be dominantly $CH_4 > H_2O > H_2$ mixtures and crystalline carbonates will not be stable relative to diamond or graphite. The nature of mantle melts produced under reduced conditions is expected to be very different from melts originating in an oxidised environment.

To investigate the role of reduced volatiles in upper mantle processes, a two-fold approach has been pursued. Firstly, a thermodynamic model for supercritical C-O-H fluids under elevated P,T conditions was derived. Available volumetric data for the important species: H_2O, CO_2, CO, H_2, CH_4 and C_2H_6 were used to calibrate an MRK-type equation of state. Using fugacity coefficients derived from the MRK-equation, the distribution of C-O-H species as a function of P,T and fO_2 has been determined. Application of this model to fluids incorporated in natural diamond (perhaps the only unequivocal example of upper mantle fluids) suggests that the majority of natural diamonds and coexisting C-O-H fluids were at equilibrium in the mantle under redox conditions near or slightly above fO_2 = IW. A genetic link between methane-bearing fluids and diamond is indicated.

The second approach taken in this study was directed at understanding the nature of mantle melting in the presence of reduced volatile species. Because little is known of the mechanism of reduced volatile interaction with silicate systems, an investigation of the CH_4-H_2-C_2H_6 fluid solubility mechanism in aluminosilicate melts was undertaken. Jadeite and

sodamelilite composition melts were saturated with a C-H fluid at P = 30 kbar and Fourier transform infrared (FTIR) spectra of the resultant high-P quenched glasses were recorded. FTIR spectra distinguish both oxidised and reduced components dissolved in the melt as predicted from theoretical considerations. Low total carbon concentrations (<2000 ppm) in the quenched glasses coupled with FTIR identification of O-H species and a shift in Si-O spectral bands, favour a dissolution mechanism for C-H volatiles that involves formation of O-H groups together with a reduced silicate network component ("silicon monoxide" unit). Dissolution of the latter component results in reduction in overall O:Si stoichiometry of the melt such that O/Si < 2.

The effects of C-O-H fluids on aluminosilicate melt structure are revealed indirectly by movement of liquidus field boundaries, particularly those between enstatite and forsterite. Liquidus phase relations in the system Ne-Fo-Q under conditions of C-H volatile saturation indicate that C-H volatile dissolution increases the activity of non-network aluminium and results in silicate network depolymerisation. This is in agreement with the proposed C-H volatile dissolution mechanism.

Recognising that reduced volatiles such as CH_4 are important primordial components in fluids degassed at mid-ocean ridges and other environments, an hypothesis for redox-reaction induced partial melting of the upper mantle is presented. This hypothesis relates oxidation of methane-rich fluids, precipitation of diamond/graphite and production of incipient H_2O-rich melts as the combined effects of interaction of deep-seated reduced volatiles with oxidised lithosphere.

ACKNOWLEDGEMENTS

This thesis would not have been possible without the assistance and encouragement of those acknowledged below and many others, too numerous to list, who have assisted at various stages.

Above all, I must thank my supervisor, Prof. D.H. Green, whose enthusiasm, guidance and ability to see things in a wider perspective have greatly benefitted this work.

Special thanks go to Keith Harris (Geology) for instruction in the high-pressure laboratory, for tireless hours spent in the preparation of various capsule and assembly parts and for useful discussions - all of which lead to a high experimental success rate despite taking the piston-cylinder apparatus to new extremes of pressure and temperature.

I thank:

Brendon Griffin (University of Adelaide) for spending many hours on the microprobe in search of dissolved reduced carbon in my aluminosilicate glasses.

John Bignell, Noel Davies & Mike Power (Central Science Lab.) for their invaluable technical assistance in FTIR spectroscopy (silicate glasses) and mass spectrometry (capsule gases).

Wieslaw Jablonski (Central Science Lab.) for instruction and assistance with the electron microprobe.

Peter Cornish & Peter Dove (Geology) for many construction and maintenance tasks.

Ron Berry (Geology) for digging out all the theory and checking the tortuous mathematics involved in the fluid inclusion crack propagation model presented in Part 3.

Tony Finney & Ridzuan Nordin (Central Science Lab./Chemistry) for useful discussions on the structural modelling of silicate melts.

David Ellis (Geology, now A.N.U.) for his enthusiasm in experimental petrology and his many ear-bashings on the virtues of a sound background in metamorphic petrology.

Chris Hatton (Geology, now Pretoria) for providing the program FUNFIT and suggesting a way through the thermodynamic maze.

Fellow students and associates in the Geology Dept who proof-read various parts of this thesis and made for a stimulating work environment: J. Adam, A. Crawford, G. Dixon, T. Falloon, S. Foley, R. Ford, A. Gupta, S. Kuehner, K. Mengel, W. Naschwitz, K. Nickel, N. Odling, E. Reid and G. Wheller.

All my bushwalking (Tasmania) and tramping (New Zealand) friends with whom I've spent many happy hours bashing through some of the world's most inpenetrable scrub - a task not unlike writing and producing a thesis except that it doesn't take quite so long.

Lastly, I must thank my typist, June Pongratz, for valiantly battling with the University's MUSE word-processing system and getting this thesis into a readable form despite all those inevitable last minute computer and printer failures.

PERSPECTIVE AND AIMS OF STUDY

Major advances in understanding the role of volatile components in igneous petrogenesis have taken place over the last ten years. Much of this effort has been directed at determining the petrogenetic role of the oxidised volatiles CO_2 and H_2O which are known to have a significant effect on super-solidus phase relations at upper mantle pressures (see review by Holloway, 1981).

Since H_2O and CO_2 are the most abundant species in volcanic gases (e.g. A.T Anderson, 1975), it has been commonly assumed that they will also be the most abundant species at depth in the Earth's upper mantle. If this basic assumption is incorrect, and this will depend to a large extent on the mantle's oxidation state, then the role of volatiles other than H_2O and CO_2 must be considered (Ryabchikov et al., 1981).

Recently, it has been suggested that CH_4, and not CO_2, is the dominant C-bearing volatile species in the Earth's mantle. This idea was formulated as the "deep-Earth-gas hypothesis" by Thomas Gold (Gold, 1979; Gold & Soter, 1981, 1982). Gold's hypothesis is based on the controversial proposal that primordial methane of mantle origin has significantly contributed in the past, and is contributing at present, to crustal hydrocarbon reservoirs and to the global geodynamic cycle of carbon as a whole.

There are two lines of evidence that suggest the mantle may be a major repository for abiogenic methane. Firstly, intrinsic oxygen fugacity measurements on mantle-derived minerals indicate that redox conditions over a significant portion of the upper mantle are such that CH_4 will be a stable volatile species (Arculus & Delano, 1981a). And secondly, Wehlan & Craig (1981, 1983) have shown that primordial CH_4 is a significant component of fluids outgassing at mid-ocean ridge hydrothermal centres. Thus, volatiles in the reduced part of the system C-O-H may be of considerable importance in igneous petrogenesis.

The primary aim of this study is to evaluate the role of C-O-H volatiles in upper mantle processes, placing particular emphasis on the reduced portion of the system. This requires as a basis, an adequate understanding of the thermodynamic properties of C-O-H fluids at elevated pressures and temperatures. The nature of reduced volatile interactions with aluminosilicate melts can then be investigated by experimental and spectroscopic means and the petrogenetic role of CH_4 and other reduced volatiles assessed.

SYMBOLS AND ABBREVIATIONS

Thermodynamic Variables and Quantities

Notation similar to that of Holland (1981); see also explanation to Appendices 1-6.

P	pressure
T	temperature
$H_{P,T}$	enthalpy at pressure (P) and temperature (T)
$S_{P,T}$	entropy at pressure (P) and temperature (T)
$G_{P,T}$	Gibbs free energy at pressure (P) and temperature (T)
C_p	constant pressure heat capacity
ΔX_r	change in property "X" for a reaction r
ΔV_s	change in volume of solid phases for a reaction
x_i	mole fraction of species i
X_C	mole fraction of carbon relative to H_2 (see Frost, 1979)
a_i or a(i)	activity of species i
γ_i	activity coefficient of species i
$f_i (f_i^o)$	fugacity of species i (pure species i in brackets)
fO_2	oxygen fugacity*
$\phi_i (\phi_i^o$ or $\phi_i^{pure})$	fugacity coefficient of species i (pure species i in brackets)
$K_{P,T}$	equilibrium constant at pressure (P) and temperature (T)
V_m	molar volume
$\bar{V}_i$	partial molar volume of species i
V_i^{pure}	molar volume of pure species i
V^{xs}	excess volume of a fluid mixture
V^{mix}	molar volume of a fluid mixture
R	gas constant: 8.3143 $JK^{-1}mol^{-1}$ 83.143 $cm^3 bar\ K^{-1}mol^{-1}$

Common Abbreviations used in the Text

EOS	equation of state
MRK	modified Redlich-Kwong equation
MC	Monte Carlo
MD	molecular dynamics
RDF	radial distribution function
IR	infrared
FTIR	Fourier transform infrared

NMR	nuclear magnetic resonance		
MAS	magic angle spinning		
NBO	non-bridging oxygen		
BO	bridging oxygen		
MORB	mid-ocean ridge basalt		
opx	orthopyroxene	mag	magnesite
olv	olivine	oen	orthoenstatite
qtz	quartz	fo	forsterite
yr	year (10^6.yr = Myr, 10^9.yr = Gyr)		

* See Appendix 9 for a list of reference oxygen buffers and their abbreviations.

Note: unless otherwise stated, reference to a particular oxygen buffer equilibrium in the text does not imply the existence of that fO_2 buffering assemblage but merely provides a convenient **reference position** in P-T-fO_2 space. In some cases the reference position may correspond to an extrapolation of the buffer assemblage to conditions beyond its stability, e.g. when FMQ is used as a reference buffer at mantle pressures.

PART 1

THERMODYNAMIC MODELLING OF C-O-H FLUIDS AT HIGH PRESSURE AND TEMPERATURE

1.1 Introduction

Fluids of mantle and magmatic origin are dominated by C-O-H components that include both oxidised and reduced species. Fluid inclusions in diamond, perhaps the only example of true mantle-derived fluids, typically contain >90 mol% C-O-H species (Melton & Giardini, 1974, 1975, 1981). Volatiles derived from basaltic glass (Byers et al., 1983), amphibole xenoliths (Matson et al., 1984) and magmatic volatiles determined by direct sampling (A.T.Anderson, 1975) all contain a substantial C-O-H content ($\gtrsim$70 mol%). With recent studies indicating a range of mantle redox values extending from oxidised (near the quartz-fayalite-magnetite buffer) to reduced conditions approximated by the synthetic iron-wustite (IW) oxygen buffer (Arculus et al., 1984), the system C-O-H offers a useful model to examine the P-T-fO_2 behaviour of mantle fluids and provides access to the petrogenetically significant volatiles H_2O, CO_2 and CH_4.

The purpose of this section is to calculate the P-V-T relations of C-O-H volatile species under mantle pressures and temperatures ($P < 100$ kbar and $T < 1700$ K) preparatory to a detailed analysis of species distribution as a function of fO_2 and other compositional variables. The procedure follows the outline below:

(i) Equation of State

Selection of a suitable equation of state to reproduce the known P-V-T relations of C-O-H volatiles and provide adequate extrapolation to higher P and T.

(ii) Data Aquisition

Assemble volumetric data for the pure volatile species and derive equation of state parameters using a multiple nonlinear regression procedure.

(iii) Testing the Model

Compare derived volumetric and fugacity coefficient data with that available in experimental and/or calculated data sets from the literature for both pure phases and where available, their mixtures.

To date, no systematic thermodynamic analysis of C-O-H fluid species distribution under upper mantle P,T conditions has been attempted. Current equations of state allow access to mantle conditions for a number of pure species (e.g. H_2O, Halbach & Chatterjee, 1982; CO_2, Bottinga & Richet, 1981) and for mixtures of C-O-H species to lower crustal pressures (H_2O-CO_2, Kerrick & Jacobs, 1981; H_2O-CO_2-CH_4, Jacobs & Kerrick, 1981a). The major aim of this work is to derive an equation of state applicable to upper mantle C-O-H fluid mixtures that includes six major species: H_2O, CO_2, CO, H_2, CH_4 and C_2H_6, with limited consideration (Part 2) of a further two species: CH_3OH and C_2H_4, representative of the alcohols and alkenes found as minor components in fluid inclusions hosted by diamond (Melton & Giardini, 1974, 1975).

1.2 Choice of an equation of state for multicomponent supercritical fluids over a wide P,T range

The volumetric properties of pure fluids and their mixtures may be expressed quantitatively as a function of P and T with an Equation Of State (EOS). Under conditions appropriate to the Earth's upper mantle, a C-O-H fluid phase will exist as a supercritical mixture exhibiting physical and thermodynamic characteristics such as density, viscosity or heat capacity that lie somewhere between those of true liquid and gaseous states. Choice of an EOS able to cover the broad range of P and T conditions applicable to the upper mantle entails a degree of compromise. In general, if a narrow P,T interval is of interest, an EOS can be devised that will fit available volumetric data with a high degree of accuracy. However, for a much larger P,T region there will be a trade-off between accuracy of fit (often requiring a large number of parameters) and ability to extrapolate into regions where experimental data is unavailable (best achieved with simple mathematical functions). For the range of upper mantle conditions, this requirement translates into selection of an EOS having a form suitable for extrapolation while at the same time having sufficient parameters to obtain reasonable accuracy, i.e. reproduces existing experimental data.

Cubic equations of state of the Redlich-Kwong (RK) type have been most successful in this compromise and reproduce well the thermodynamic properties of supercritical fluids (Prausnitz, 1969). The RK EOS is essentially an empirical modification of the van der Waals equation (VDW) which may be written:

VDW

$$P = \frac{RT}{V_m - b} - \frac{a}{V_m^2}$$

or in cubic form

$$0 = V_m^3 - V_m^2 . \left[b + \frac{RT}{P} \right] + V_m . \left[\frac{a.b}{P} \right]$$

where V_m = molar volume
R = gas constant
a,b = adjustable parameters.

The RK equation includes a modified attractive term (Redlich & Kwong, 1949) incorporating an inverse $T^{1/2}$ dependence:

RK

$$P = \frac{RT}{V_m - b} - \frac{a}{T^{1/2} . V_m . (V_m + b)}$$

The VDW equation was derived on the basis of the molecular theory of corresponding states which states ... "if the EOS for any one fluid is written in reduced coordinates (V/V_{crit}, T/T_{crit}, P/P_{crit}) then that equation is also valid for any other fluid" (Prausnitz, 1969, p.70). The parameters "a" and "b" in both equations relate to the existence of finite molecular volumes and attractive forces between molecules. For this reason the "attractive" term on the far right is often known as the "internal or static pressure" and the "repulsive" term on its left the "kinetic pressure" in view of its T proportionality. Solution of the condition $(dP/dV_m) = (d^2P/dV_m^2) = 0$ at the critical point of a fluid yields values of "a" and "b" in terms of the critical constants P_{crit} and T_{crit}; for the RK equation:

$$b/cm^3 mol^{-1} = \frac{0.0867\ RT_{crit}}{P_{crit}}$$

$$a/K^{1/2}cm^6bar\ mol^{-1} = \frac{0.4278\ T_{crit}^{2.5}\ R^2}{P_{crit}}$$

T_{crit} (K), P_{crit} (bar), R = 83.143 $cm^3bar\ K^{-1}mol^{-1}$.
Values for the six C-O-H species are summarized below:

Table 1.2A

	b	$a/10^8$	Source
H_2O	21.16	1.429	1
CO_2	29.73	0.647	1
CO	27.38	0.172	1
H_2	18.45	0.014	1
CH_4	29.87	0.322	2
C_2H_6	45.18	0.989	2

Sources: 1. Mathews (1972)
2. Dzialoszynski et al. (1980)

These constants may be related to the nature of both attractive and repulsive forces operating between molecules and may thus be qualitatively interpreted in terms of measureable physical properties as summarized below in square brackets [ ] (after Prausnitz, 1969, p.53):

(i) Electrostatic interactions: forces between permanent dipoles and quadrupoles [magnitude of dipole or quadrupole moment].

(ii) Induction forces: acting between permanent dipole (or quadrupole) and induced dipoles [average polarisibility and dipole moments].

(iii) Dispersion forces: between instantaneously induced dipoles [average polarisibility and ionisation potential].

(iv) Chemical forces: giving rise to complex formation (mixtures) and/or molecular association (e.g. dimerisation). Hydrogen bonding, important in aqueous fluids, falls into this category [acentric factor, Pitzer et al.(1955)].

Specific values for these measurable molecular properties are indicated in Table 1.2B below:

Table 1.2B

	Dipole Moment μ/D	Quadrupole Moment $Q.10^{-26}$	Average Polarisibility $\bar{\alpha}.10^{-25}/cm^3$	Ionisation Potential I/eV	Acentric Factor w
H_2O	1.85	2	15.9	12.6	0.344
CO_2	0	4.1	26.5	13.7	0.225
CO	0.11	1	19.5	14.1	0.049
H_2	0	0.63	7.9	15.4	-
CH_4	0	0	26.0	13.0	0.013
C_2H_6	0	1.3	44.7	11.8	0.105

From inspection of tables 1.2A and 1.2B good correlation with "a" and "b" parameters is seen for w and $\bar{\alpha}$ respectively with an obvious strong contribution to "a" by the presence of large μ and Q moments. The theoretical basis for the RK EOS in molecular dynamics is thus clearly illustrated.

While the two-parameter RK equation can provide good representation of volumetric properties of many non-polar species and their mixtures to moderate pressures (up to ~2000 bars), the equation is less successful for molecules with large dipole (e.g. H_2O) or quadrupole (e.g. CO_2) moments and the tendency to associate at high pressures (Tarakad et al., 1979). Several multi-parametric modifications of the original two-parameter RK equation (MRKs) have been proposed for supercritical fluids involving polar components. Introduction of a T-dependence to the "a" parameter (de Santis et al., 1974) has produced more satisfactory agreement for polar molecules to at least 1500 bars. This equation was subsequently adopted by Holloway (1977) to provide rough estimates of fugacity coefficients up to ~40 kbar. This success has lead to the development in the geological literature of a number of empirical or semi-empirical MRK equations incorporating P, T or V dependencies (e.g. Kerrick & Jacobs, 1981; Bottinga & Richet, 1981; Chatterjee & Halbach, 1983).

The ten-parameter MRK of Kerrick & Jacobs (1981) (here designated as KJMRK) involves a modified repulsive term of the Carnahan-Starling "hard-sphere" type (Carnahan & Starling, 1969) and appears superior to other MRKs in its handling of supercritical mixtures, particularly those containing H_2O:

KJMRK

$$P = \frac{RT(1+y+y^2-y^3)}{V_m.(1-y)^3} - \frac{a(V,T)}{T^{1/2}.V_m.(V_m+b)}$$

where $y = b/4V$, $a = c+d/V+e/V^2$

and $c = c_1+c_2T+c_3T^2$, $d = d_1+d_2T+d_3T^2$, $e = e_1+e_2T+e_3T^2$.

The equation correctly predicts the limit $(V_m-b) \dashrightarrow 0$ as $P \dashrightarrow \infty$ while equations with the VDW repulsive term yield negative values of (V_m-b) at high pressures (Vera & Prausnitz, 1972). Application of the KJMRK to supercritical mixtures of H_2O, CO_2 and CH_4 at pressures up to 20 kbar using the original RK mixing rules yields good agreement with the known V^{mix} values and activity-composition relations (Kerrick & Jacobs, 1981; Jacobs & Kerrick, 1981a). Beyond about 20 kbar KJMRK derived fugacity coefficients do not predict the position of experimentally determined equilibria with as great an accuracy as a more specifically tailored EOS such as that of Halbach & Chatterjee (1983) for H_2O. Moreover, there are several difficulties in the present KJMRK formulation:

(i) The use of ten-parameters for complete description of volumetric properties may be compared with the far fewer number of parameters used by equally successful (though admittedly pure fluid only) MRKs over greater P,T ranges (e.g. Bottinga & Richet, 1981 for CO_2).

(ii) Difficulties in formulation of the T-dependent "a" term (a three-term polynomial in T) for the KJMRK have led in the case of CO_2 to negative parameter values at $T > 1150^oC$ (Jacobs & Kerrick, 1981b). This is in direct contravention of the RK mixing rule $a_{ij} = (a_i.a_j)^{1/2}$. The inability to determine mixing properties beyond 1150^oC suggests that choice of a complex a(T) function was inappropriate for extrapolation purposes.

(iii) The fitting procedure for determining parameter values from available volumetric data is not straightforward. Several stages of multiple regression are required using sets of isothermal data which for many species are unavailable. Failure to incorporate P and/or T variation in the "b" parameter or regress simultaneously best fit "a" and "b" values has probably necessitated the use of a large number of parameters in the "a" term to obtain an adequate fit.

For the purpose of providing reliable estimates of molar volume and fugacity coefficients over an extensive P,T range (0.5 to ~60 kbar at 400-1700 K) while still retaining the simple RK mixing rules governing species interaction, the general form of the KJMRK has been retained and a number of parameter modifications made. To improve extrapolation ability and to allow simultaneous regression analysis, the number of parameters was halved to five by dropping the explicit T-dependence of "a" and instead incorporating an inverse T-dependence in the "b" term to take into account the effects of increased molecular interpenetration with temperature (Flowers, 1979). These modifications result in no change in thermodynamic self-consistency imposed by Gibbs-Duhem constraints since the standard tests all involve T-independent integrals (Prausnitz, 1969, App.IX). It has already been shown by Kerrick & Jacobs (1981) that equations of the KJMRK type employing RK mixing rules provide internally consistent activity coefficients. The modified five-parameter equation (5PMRK) is outlined below:

5PMRK

$$P = \frac{RT(1+y+y^2-y^3)}{V_m.(1-y)^3} - \frac{a_1+a_2/V+a_3/V^2}{T^{1/2}.V_m.(V_m+b)}$$

where $b = b_1+b_2/T$

and $y = b/4V$

1.3 Derivation of 5PMRK Parameters; Multiple Regression Procedure

Experimental P-V_m-T data for all six C-O-H species were taken from the literature and data sets compiled over the maximum P,T range of available volumetric measurements. For most species the upper pressure limit was ~8-10 kbar and the upper temperature limit ~873 K. Water, however, is an exception with shock-wave studies extending molar volumes to 100 kbar and 1273 K. The ability of the 5PMRK to accurately fit the water volumetric data will thus provide a useful test of the equation's applicability over an extensive pressure range (0.5-100 kbar). The final data sets (plotted on P-T and P-V_m diagrams for each species in Appendices 1 to 6) comprise ~70-100 P-V_m-T data points extending over approximately equal P,T intervals for each species from ~0.3-0.5 kbar to maximum available pressures.

Simultaneous multiple non-linear regression of parameters b_1, b_2, a_1, a_2 and a_3 was performed with the program FUNFIT (Veng-Pedersen, 1977). The program employs the non-derivative simplex method to minimise the residual sum-of-squares value and as such is considerably more reliable and robust than usual gradient methods. By setting appropriate parameter limits, in this case: $b_2 \sim 10^3.b_1$, $a_2 \sim 10^2.a_1$, $a_3 \sim 10^2$-$10^3.a_1$; convergence was achieved in all cases giving multiple regression coefficients (R) exceeding 0.99 (statistical analysis of the fit is given in Appendices 1 to 6 for each species).

Molar volumes, corresponding to the largest cubic root of the 5PMRK equation recast in terms of V_m, and fugacity coefficients were calculated from the equations given by Kerrick & Jacobs (1981) and are presented in Appendices 1 to 6. Parameter values obtained from the fit are listed in Table 1.3 below:

Table 1.3 Parameter values for 5PMRK.

	b_1	b_2	$a_1/10^7$	$a_2/10^9$	$a_3/10^{10}$	b*	$a/10^8$*
H_2O	21.34	5420	13.29	2.541	1.915	24.95	3.934
CO_2	45.53	10730	12.87	1.122	44.43	52.68	8.032
CO	40.11	3769	3.869	0.645	0.8008	42.62	0.808
H_2	15.36	3011	0.4521	0.05734	0.1693	17.37	0.200
CH_4	43.38	7409	6.742	2.893	9.749	48.32	3.331
C_2H_6	76.37	5605	18.26	5.332	14.17	80.11	4.224

* specific values for P = 50 kbar, T = 1500 K.

In general "b" values are ~2 times larger than original RK parameters (depending on T); a similar result was obtained by Kerrick & Jacobs (1981). The empirical nature of MRK equations probably precludes any exact physical significance being attached to these values, however, the relative order of b as $T \dashrightarrow \infty$, i.e. the "hard sphere" part, is close to that of the original RK terms. The corresponding "soft sphere" contribution to "b" can be identified with the b_2 parameter, the magnitude of which determines the degree of molecular interpretation occurring as the kinetic energy of the system increases with temperature. The largest molecules, i.e. CO_2, CH_4 and C_2H_6, also appear to be kinetically the "softest". With the exception of CO_2, perhaps due to its large quadrupole

moment, 5PMRK "a" parameters correlate with those of the RK equation (Table 1.2A).

1.4 Molar Volumes and Fugacity Coefficients from the 5PMRK - a comparison with literature values.

A. Water

Table 1.4A Selected molar volumes at 1273 K.

P/kbar	5PMRK	RW	BHD	HC	SHE	KJ
2.0	54.44	-	54.71	54.52	55.52	54.68
5.0	30.12	29.11	29.51	29.72	30.09	30.11
10.0	22.41	21.42	22.57	21.88	22.48	22.74
20.0	17.91	17.28	-	17.31	18.58	18.57
30.0	16.05	15.96	-	15.37	17.20	16.84
50.0	14.20	14.39	-	13.37	16.47	15.11
100.0	12.31	11.85	-	11.18	15.09	13.31

RW Rice & Walsh (1957)
BHD Burnham, Holloway & Davis (1969b)
HC Halbach & Chaterjee (1983)
SHE Sykes, Holloway & Eichon (1978)
KJ Kerrick & Jacobs (1981)

Reference to Table 1.4A and regression statistics (Appendix 1.3) confirms that the 5PMRK provides a better fit to experimental molar volume data in the region 10-100 kbar, than currently available equations of state. The fit provides a smooth transition between the results of Burnham et al. (1969b) and the shock-wave data of Rice & Walsh (1957) which differ by as much as 5% at 10 kbar, 1273 K. Over the range 30-100 kbar the recently calibrated HCMRK of Halbach & Chaterjee (1983) gives volumes too low by some 4-7% while 5PMRK values are within 0.6-4%. compared with the ten-parameter KJMRK, the 5PMRK fit gives similar molar volumes over the range 0.5-10 kbar and despite the reduction in the number of parameters, a substantial improvement at greater pressures (compare mean percent deviations for the same data set: 5PMRK 4.65% vs KJMRK 6.61%; Appendix 1.3).

Fugacity coefficients (Appendix 1.6) compared at 873 K and 1273 K give values very close to Burnham et al. (1969b) and HCMRK values over the range 0.5-10 kbar and generally plot midway between the KJMRK and HCMRK at P > 20 kbar. The SHEMRK at P > 20 kbar gives fugacity coefficients around twice that of most other estimates (Table 1.4B) leading to fH_2O's inconsistent with the position of high P experimental dehydration equilibria (Holland, 1979; Kerrick & Jacobs, 1981).

Table 1.4B Fugacity coefficients for H_2O at 50 kbar, 873 K.

	5PMRK	KJ	SHE	DH&HK	HC
$\phi^o_{H_2O}$	968	1229	2257	787	745
RT ln $\phi^o_{H_2O}$/kJ	49.9	51.6	56.1	48.4	48.0

The results obtained with the 5PMRK for H_2O give a fit of better accuracy to molar volume data over the range 10-100 kbar and a similar accuracy over 0.5-10 kbar compared with currently available equations of state. This gives confidence in the ability to extrapolate the 5PMRK into P,T conditions beyond the range of experimental measurements for the other C-O-H species.

B. Carbon Dioxide

Regression statistics (Appendix 2.3) for the 5PMRK P-V_m-T data fit (max. P = 8 kbar, max. T = 1273 K) give correlation coefficients and mean deviations very close to that obtained with the ten-parameter KJMRK for the same data set. The fit has more scatter than the KJMRK (compare standard deviation of residuals and percent deviations) but for data points >600°C the fit is equivalent. Selected 5PMRK molar volumes presented in Table 1.4C show a close similarity with the recent compilation of Bottinga & Richet (1981) over the range 5-30 kbar. At upper mantle pressures, the molar volumes derived from the Holloway (1977) and Spera & Bergman (1980) MRKs are from 6% to as much as 25% larger than KJMRK, BRMRK and 5PMRK estimates.

Table 1.4C Selected molar volumes at 1200 K.

P(kbar)	5PMRK	SS	H	SB	KJ	BR
2.0	80.91	80.84	78.06	76.49	81.20	78.36
5.0	50.23	51.14	49.12	48.58	50.59	50.86
10.0	38.60	36.09	39.49	39.28	39.26	39.01
20.0	31.54	-	34.63	34.55	32.44	31.43
30.0	28.61	-	33.00	32.95	29.59	28.46
50.0	25.73	-	32.18	31.66	26.77	-

SS Shmulovich & Shmonov (1975)
H Holloway (1977)
SB Spera & Bergman (1980)
KJ Kerrick & Jacobs (1981)
BR Bottinga & Richet (1981)

A comparison of selected molar volumes at 1000 K is given below:

Table 1.4D

P(kbar)	2	3	4	5	6	7	8	MPD*(%)
SB	68.24	55.50	49.16	45.35	42.80	40.98	39.60	3.0
SS	70.70	57.93	51.26	46.73	43.27	40.49	38.15	0
BR	68.98	56.95	50.86	47.27	43.77	41.18	39.20	1.7
H	69.15	56.07	49.56	45.65	43.03	41.17	39.76	2.5
KJ	70.92	57.50	50.60	46.31	43.35	41.15	39.44	1.2
5P	70.56	57.14	50.19	45.87	42.88	40.65	38.92	1.3

$$*\text{mean percent deviation} = \sum \left[\frac{|V_{SS} - V_{calc}|}{V_{SS}} * 100 \right] \Big/ n$$

n = number of data points

where V_{SS} = Shmulovich & Shmonov (1975) molar volume data.

The temperature of 1000 K used in Table 1.4D is just 19 K higher than the limit of experimental measurements by Shmulovich & Shmonov (1975). Table 1.4D reveals the poor agreement of the SBMRK (MPD = 3%) and illustrates an important point, i.e. to have any confidence in extrapolation an EOS must reproduce accurately known volumetric data as well as providing experimentally consistent integral properties such as fugacity or heat capacity; even though specifically designed for upper mantle pressures the SBMRK does not appear suitable for this purpose.

Bottinga & Richet (1981) have designated $V_m \simeq 27\ cm^3 mol^{-1}$ as the limit for the transition of supercritical fluid CO_2 to the solid phase. The 5PMRK data presented in Appendix 2 suggests this limit will be reached between 40 and 50 kbar at temperatures of 800-1400°C.

A comparison of 5PMRK fugacity coefficients is presented in Appendix 2.6 for 1000 K and 1300 K. Values over the range 0.5-15 kbar are very similar to those derived by Shmulovich & Shmonov (1975) with $\phi^o_{CO_2}$'s lying between the BRMRK and KJMRK derivations. For pressures beyond 15 kbar only the BRMRK gives coefficients close to the 5PMRK, all other equations deviate to much higher values as seen below.

Table 1.4E Selected $\phi^o_{CO_2}$ values.

	5PMRK	KJ	SB	H	BR	OR
$\phi^o_{CO_2}$ (20kb,1000K)	754	862	966	1050	725	1000
$\phi^o_{CO_2}$ (35kb,1300K)	7624	9897	11992	13684	7339	-

OR Ostrovsky & Ryzhenko (1978)

Bottinga & Richet (1981) have presented a full discussion on the applicability of their BRMRK coefficients to calculation of decarbonation equilibria. It was generally concluded that current knowledge of thermochemical functions for the participating phases, particularly the

carbonates, was not adequate to test the validity of their MRK fugacity coefficients. There is little point in specifically tailoring an EOS for CO_2 to reproduce observed decarbonation equilibria since errors in thermodynamic quantities associated with other phases will be incorporated as well. The consistency between BRMRK and 5PMRK derived V_m and $\phi^o_{CO_2}$ values suggest that both equations offer useful extrapolations to pressures of at least 50 kbar.

C. Carbon Monoxide

P-V_m-T data for CO is limited to two literature sources: Robertson & Babb (1970) and Smeeton-Leah (1962) all at T < 673 K but at pressures extending to 10 kbar. The weakly polar, simple diatomic nature of carbon monoxide should make reproduction of CO volumetric properties over a large P-range well within the capability of the 5PMRK. This is borne out by the excellent fit to available P-V_m-T data giving a mean deviation in pressure of 0.97% for all data points and 0.68% for those points >573 K. Selected volumes are compared in Table 1.4F below:

Table 1.4F Selected CO molar volumes at 1273 K.

P/kbar	5PMRK	RK	M
2.0	85.29	78.83	83.37
5.0	50.75	48.00	49.58
10.0	37.37	37.76	36.58
15.0	32.15	34.33	31.54
30.0	25.87	30.88	-

R Redlich & Kwong (1949)
M Mel'nik (1978)

The V_m data of Mel'nik (1978) gives volumes consistently ~2% lower than the 5PMRK while the original two-parameter RK equation shows differences of as much as $\pm$8%.

Table A3.6 (Appendix 3) compares fugacity coefficients. At 673 K there is close agreement between Mel'nik's ϕ^{o}_{CO} values and the 5PMRK while at 1273 K the 5PMRK gives ϕ^{o}_{CO}'s up to 20% higher. The corresponding state approach of Rhyzenko & Volkov (1971) results in a very poor estimates of ϕ^{o}_{CO} beyond 4 kbar with coefficients up to 30% lower than the RK equation and up to 50% lower than the 5PMRK as seen below:

Table 1.4G Selected fugacity coefficients for CO.

	RK	RV	M	5PMRK
ϕ^{o}_{CO} (8kbar,673K)	38.9	21.6	49.5	50.4
ϕ^{o}_{CO} (8kbar,1273K)	7.3	6.4	8.9	10.1

RV Rhyzenko & Volkov (1971)

D. Hydrogen

Volumetric data for H_2 covers a wider P,T range than CO but is limited to 6.5 kbar maximum pressure at 423 K due to experimental difficulties (Tsiklis et al., 1975). The 5PMRK again provides a very good fit to this data set (mean deviation in pressure = 0.66%, Appendix 4.3). Selected molar volumes are compared in Table 1.4H.

Table 1.4H Selected H_2 molar volumes at 1273 K.

P/kbar	5PMRK	CP	SW
2.0	68.26	71.37	68.36
5.0	35.28	39.71	35.39
10.0	23.47	29.17	23.37
15.0	19.16	25.65	-
30.0	14.29	22.13	-
50.0	11.96	-	-

CP Chueh & Prausnitz (1967)

SW Shaw & Wones (1962)

The volumes derived from the CPMRK of Chueh & Prausnitz (1967) are based on the original RK equation but include "effective" critical constants resulting from quantum mechanical rather than classical behaviour of the low molecular weight gases H_2, Ne and He. 5PMRK molar volumes are close to those of Shaw & Wones (1962) and subtantially lower than the CPMRK by some 55% at 1273 K and 30 kbar. The 5PMRK results suggest that H_2 is highly compressible. Comparison with volumetric data for other C-O-H species indicates that 5PMRK derived isothermal compressibility coefficients (β) = $-1/V_T.(\partial V_T/\partial P)$ for H_2 will be larger than all the volatiles including H_2O above ~10 kbar. The low 5PMRK extrapolated H_2 molar volumes ranging from ~9-13 cm^3mol^{-1} over the P,T interval 40-400 kbar, 673-1673 K are consistent with the shock-wave compression experiments of van Thiel & Alder (1966). These authors have obtained a 40 kbar molar volume for fluid H_2 of 10.5 $\pm$0.3 cm^3mol^{-1} at an approximate temperature of 1300 K (Ross, 1974) which is some 20% lower than that predicted by the 5PRMK. The uncertainty in the shock-wave determination is, however, probably much greater than the error brackets indicate (Ross, 1974). According to the pair-potential calculations of Ross (1974), fluid H_2 should undergo a transition to the molecular solid at volumes approaching 2-3 cm^3mol^{-1} corresponding to temperatures of 1000-2000 K at 1-3 Mbar pressure, respectively.

Fugacity coefficient comparisons (Appendix 4.6) at 873 K and 1273 K show that the 5PMRK values lie between those of the CPMRK and Shaw & Wones (1962) polynomials to 3 kbar. At higher pressures the CPMRK deviates markedly to higher $\phi^o_{H_2}$ values. The compilation of Rhyzenko & Volkov (1971) is in excellent agreement with the 5PMRK at 1273 K but at 873 K the coefficients go through a maximum deviation of ~16% at 7 kbar. Coefficients are compared at 3 kbar and 10 kbar, 1273 K below:

Table 1.4I

	5PMRK	RV	CP	SW
$\phi^{o}_{H_2}$ (3kbar,1273K)	1.557	1.559	1.684	1.514
$\phi^{o}_{H_2}$ (10kbar,1273K)	3.861	3.770	5.743	-

Unlike H_2O and CO_2, there are no other currently available estimates of CO and H_2 fugacities to upper mantle pressures; the highly correlated 5PMRK fits for both volatiles gives confidence in extrapolating H_2 and CO volumes and fugacity coefficients to upper mantle conditions.

E. Methane

Surprisingly, methane volumetric data provides the poorest overall fit to the 5PMRK. This is largely due to discontinuities between the various literature data sources particularly at T < 573 K. The extensive set of volumetric data compiled by Angus et al. (1978) gives lower (by ~2-3%) molar volumes than the equivalent data of Tsiklis et al. (1971, 1974). Recent measurements by Francesconi (1984) overlap the lower P-range of the Tsiklis et al. (1971, 1974) data and despite claims that molar volumes are higher by only 0.4% and "within the tolerances given by the authors" they are actually lower by some 4-5%. A comparison is presented in Table 1.4J.

Table 1.4J Comparison of Tsiklis et al. (1971) volumetric data for methane.**

	Tsiklis et al.	Francesconi*
2.0 kbar, 673 K	56.08	53.70
2.0 kbar, 573 K	51.56	49.84
2.0 kbar, 473 K	47.07	44.77
		Angus et al.
5.0 kbar, 473 K	35.89	35.17

** values obtained by linear interpolation of tabulated values.

* derived from equation $P = a+bT+cT^2$ of Francesconi (1984, Table 1).

Methane molar volumes derived from various equations of state are compared in Table 1.4K for 1273 K.

Table 1.4K Selected molar volumes for CH_4 at 1273 K.

P/kbar	5PMRK	KJMRK	M	RK
2.0	85.84	83.94	82.72	80.19
5.0	52.02	50.87	50.43	50.10
10.0	39.04	39.48	37.64	40.10
15.0	33.97	35.24	32.65	36.73
30.0	27.84	30.13		33.33
50.0	24.66	27.40		31.95

M Mel'nik (1978)
RK Redlich & Kwong (1949)

The 5PMRK gives molar volumes ~2% larger than the KJMRK over the range 1.5 to 5 kbar at 1273 K, at 673 K this difference is ~0.6% over the same P-interval. At pressures >5 kbar the 5PMRK reproduces well the volumetric data of Tsiklis et al. (1971, 1974) as seen in Table 1.4L for 673 K:

Table 1.4L Molar volume data at 673 K.

P/kbar	5PMRK	Tsiklis**	KJ
4.0	42.66	42.96	42.70
5.0	39.58	39.88	39.84
6.0	37.39	37.54	37.83
7.0	35.73	35.74	36.30
8.0	34.41	34.30	35.10
MPD (%)*	0.44	0	1.07

* mean percent deviation = $\sum\left[\left|\frac{V_{Tsiklis}-V_{calc}}{V_{Tsiklis}}\right| * 100\right] \Big/ n$
n = no. of data points

** interpolated values

The general improvement of the 5PMRK over the KJMRK in fitting data points at T > 573 K is illustrated above and in Appendix 5.3 for the full data set (compare MPD of 3.25% for 5PMRK vs 4.84% for KJMRK). The discrepancy between molar volume measurements of Tsiklis et al. (1971, 1974) and more recent data (Angus et al., 1978; Francesconi, 1984), showing particularly poor overlap at low P (<2.5 kbar) and low T (<473 K), is likely to be solved only with further experimental work.

Fugacity coefficient comparisons are presented in Appendix 5.6. At 673 K and between 0.5 and 10 kbar 5PRMK coefficients fall close to, although slightly below KJMRK estimates; at >10 kbar 5PMRK and KJMRK values rapidly diverge. Fugacity coefficients derived by Tsiklis et al. and Mel'nik (1978) at 673 K are remarkably coincident, both lying consistently ~5-7% above 5PMRK values to 15 kbar. Compilations of coefficients by Rhyzenko & Volkov (1971) give unacceptably large negative deviations from all other estimates at P < 5 kbar. Extrapolating to 1273 K, 5PMRK $\phi^{o}_{CH_4}$ values are generally larger than other estimates to ~15 kbar and at greater pressures are significantly less. Selected coefficients are compared below:

Table 1.4M Selected $\phi^{o}_{CH_4}$ values.

	5PMRK	KJMRK	RK	TLT	M	RV
8 kbar, 673 K	48.1	49.7	45.8	51.6	51.1	18.7
8 kbar, 1273 K	10.8	9.7	8.2	-	9.2	8.8
30 kbar, 1273 K	2528	3115	3936	-	-	-

TLT Tsiklis et al. (1971, 1974)

A feature of 5PMRK fugacity coefficient estimates at P > 15 kbar for CH_4, CO_2 and H_2O is the consistently lower values compared with KJMRK and de Santis et al. (1972) MRK estimates. These lower values are generally in better accord with other EOS derived coefficient and experimental data (e.g. for H_2O: Halbach & Chatterjee, 1983; Delany & Helgeson, 1978; Holland, 1979). Further P-V_m-T measurements are needed for methane to eliminate discontinuities between presently available data sets.

E. Ethane

P-V_m-T measurements for ethane have been determined to a maximum pressure of 9 kbar by Tsiklis et al. (1972). Data at pressures < 0.7 kbar are available from a number of sources (Appendix 6.3) and generally follows smoothly into the high pressure set resulting in a good fit to the 5PMRK (R = 0.999613 with mean deviation in pressure = 2.53%). Selected molar volumes are summarised below:

Table 1.4N Selected molar volumes for C_2H_6, 673 K.

P/kbar	5PMRK	Tsiklis et al.	RK	RJ
2.0	72.31	70.00	67.53	64.22
5.0	54.45	54.25	54.98	51.59
9.0	46.96	47.05	50.87	47.48
15.0	42.00	-	48.69	45.30
30.0	36.88	-	46.96	43.58
50.0	33.98	-	46.25	42.87

RJ Robinson & Jacoby (1965)

The 5PMRK fit is better than 1% in the volumes for all data at P > 3.5 kbar but differs by up to 3% at lower pressures although the data of Uematsu et al. (1975) at ~300 bars show <1% deviation.

Fugacity coefficient determinations for ethane are limited and comparison has been confined to the original RK equation, the RJMRK of Robinson & Jacoby (1965) and the calculations by Tsiklis et al. (1972) at 673 K (Appendix 6.6). The first two equations were not intended to reproduce fugacity coefficients with any accuracy above ~2 kbar and indeed show widely divergent values at >1 kbar compared with the 5PMRK. Coefficients computed by Tsiklis et al. (1972) over the range 2.5-9.0 kbar are consistently 2x larger than 5PMRK values which possibly indicates a computational error. Selected 5PMRK $\phi^{o}_{C_2H_6}$ values are compared in Table 1.40:

Table 1.40 Selected $\phi^{o}_{C_2H_6}$ values.

	RK	RJ	5PMRK	T
$\phi^{o}_{C_2H_6}$ (9.0kbar,673K)	548	335	617	1333
$\phi^{o}_{C_2H_6}$ (9.0kbar,1273K)	33.1	26.5	59.5	-

T Tsiklis et al. (1972)

For upper mantle conditions, the 5PMRK provides the only available estimates of $V_m(C_2H_6)$ and $\phi^{o}_{C_2H_6}$.

1.5 Volume and Density Relationships for the Pure Fluids and their Mixtures.

Volume and density relationships for all six pure fluids using 5PMRK fugacity coefficients are presented in Figs 1.5A and 1.5B respectively for T = 1400 K. In terms of molar volume variation with pressure, the fluids separate into three groups of similar behaviour:

(i) C_2H_6 highest molar volume and lowest molar density ($1/V_m$);

(ii) CO_2, CO, CH_4 carbon gases group showing intermediate properties; and

(iii) H_2O, H_2 hydrogen gases with lowest molar volume and highest molar density; the curve for H_2 crosses that of H_2O at ~13 kbar where with increasing pressure H_2 becomes the densest fluid on a molar basis.

On a weight basis (Fig. 1.5B) the corresponding densities (ρ) are plotted as a function of pressure. The order of densities are $CO_2 > H_2O > CO > C_2H_6 > CH_4 > H_2$. Changes in density as a result of decompression may be judged from the slope of the ρ vs P curves; at P > 2 kbar the magnitude of $(d\rho/dP)_T$ follows the same order as the densities.

Curves of more relevance to processes involving magmatic volatiles are presented in Fig. 1.5C. In this diagram isothermal (T = 1400 K) decompression is considered from initial pressure (P_i) to an arbitrary final pressure (P_f) of 0.5 kbar. The degree of volume expansion $-(V_i - V_f)/V_i$ is plotted on the y-axis so the curves in effect illustrate the pressure variation in isothermal compressibility coefficients (β_T) of the

Figures 1.5A to 1.5C

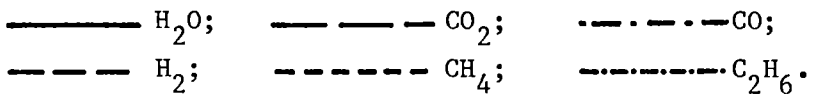

Fig. 1.5A Molar volume versus pressure curves for the pure C-O-H fluids at T = 1400 K.

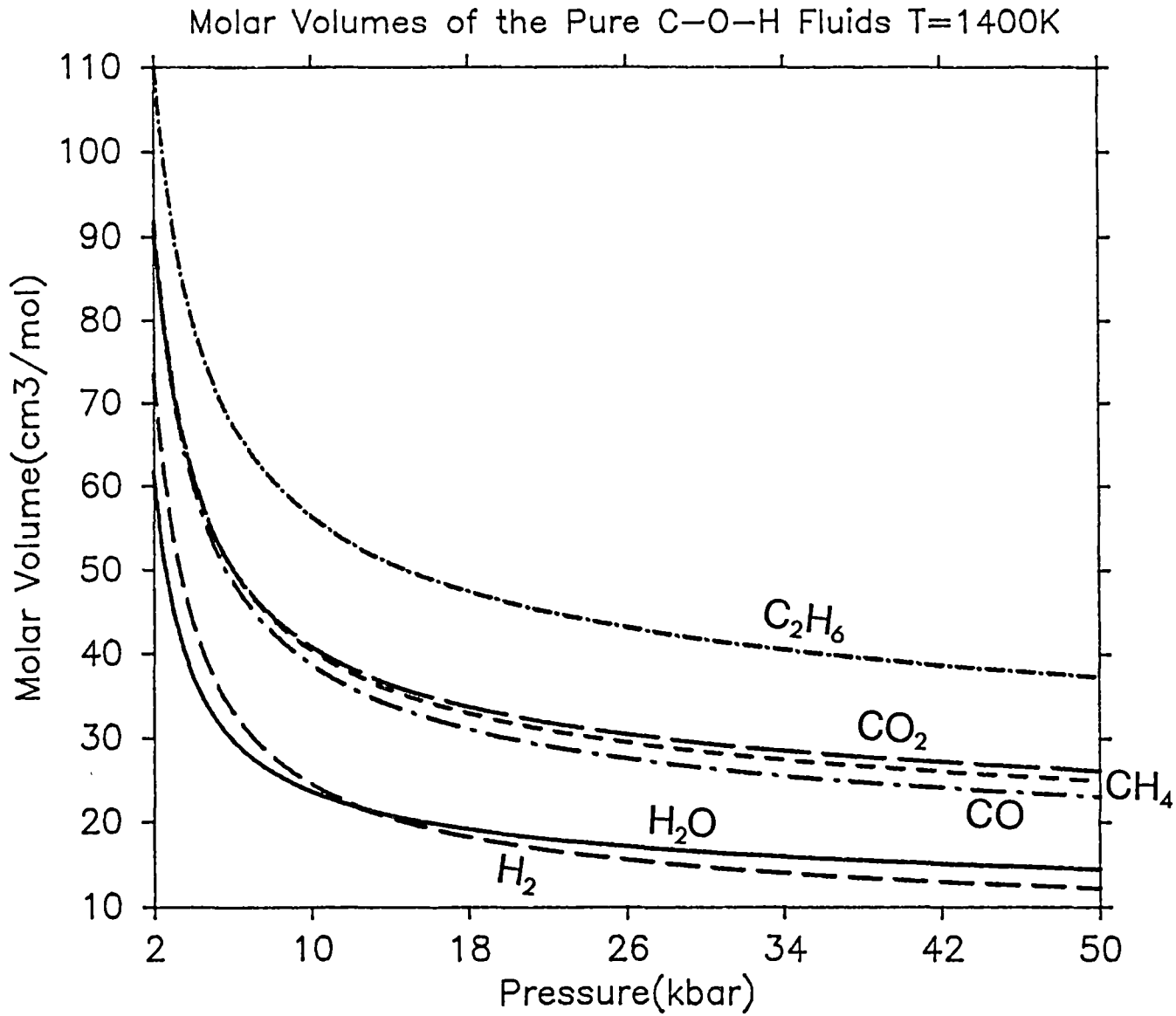
Molar Volumes of the Pure C–O–H Fluids T=1400K
Molar Volume(cm3/mol)
110
100
90
80
70
60
50
40
30
20
10
2
10
18
26
34
42
50
Pressure(kbar)
C_2H_6
CO_2
CH_4
CO
H_2O
H_2

Fig. 1.5B Density versus pressure curves for the pure C-O-H fluids at T = 1400 K.

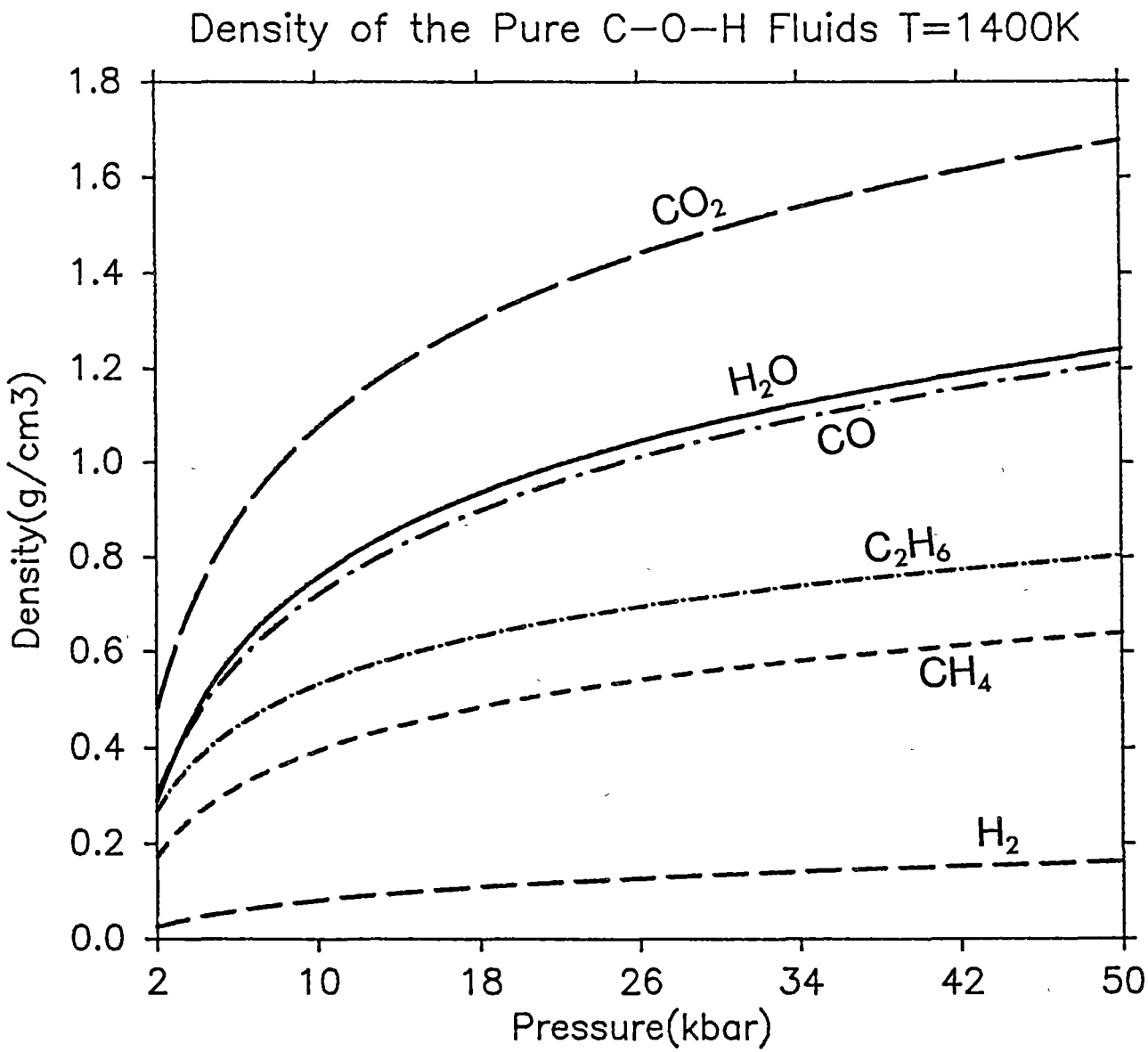
Density of the Pure C–O–H Fluids T=1400K
Density(g/cm3)
1.8
1.6
1.4
1.2
1.0
0.8
0.6
0.4
0.2
0.0
2
10
18
26
34
42
50
Pressure(kbar)
CO2
H2O
CO
C2H6
CH4
H2

Fig. 1.5C Volume expansion curves for isothermal decompression from $P_i = P$ to $P_f = 0.5$ kbar; $\sim \Delta V = (V_i - V_f)$. For example, if a pure H_2 fluid is decompressed from $P_i \simeq 30$ kbar to 0.5 kbar there will be a 16x volume expansion. Up to ~7 kbar H_2O stores the most energy of all the species in compression of the fluid phase.

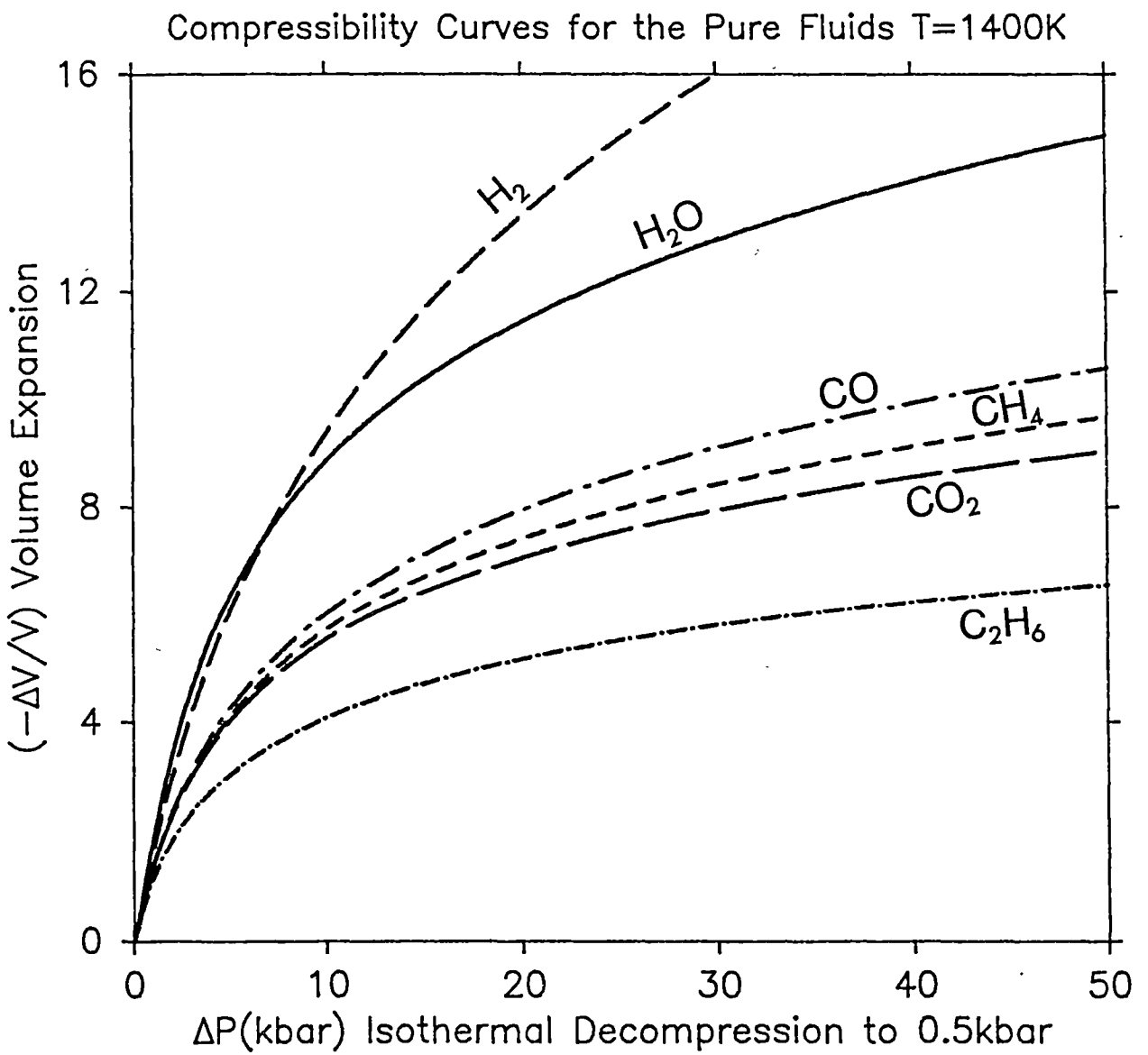
Compressibility Curves for the Pure Fluids T=1400K
16
12
8
4
0
(−ΔV/V) Volume Expansion
H2
H2O
CO
CH4
CO2
C2H6
0
10
20
30
40
50
ΔP(kbar) Isothermal Decompression to 0.5kbar

particular fluid. If a magma becomes saturated with a volatile species at some pressure P_i and is rapidly isothermally decompressed to say P_f = 0.5 kbar, then energy will be released (work done) corresponding to the magnitude of the volume expansion (work done in isothermal irreversible expansion is $w = -P_f \int_{V_i}^{V_f} dV = -P_f.\Delta V$; since $\Delta V = V_f - V_i$ will always be a positive quantity, work will be done by the system on the surroundings as a result of sudden, irreversible decompression). From Fig. 1.5C it is readily seen that on a mole for mole basis the most explosive types of volcanism (highest energy release) will occur in the order of the dominant volatile as $H_2O > H_2 > CO > CH_4 > CO_2 > C_2H_6$ below P_i = 7 kbar and with $H_2 > H_2O$ at higher P_i's. Clearly there are many other factors governing the nature of explosive volcanism particularly the pressure at which volatile saturation occurs for a given species and melt composition. It is worth noting however that an eight-fold volume expansion for H_2O corresponds to P_i = 8 kbar whereas for CO_2, equivalent energy release on a molar basis would require P_i = 30 kbar and for CH_4 P_i = 25 kbar.

It generally follows for Figs 1.5A to 1.5C that the properties of mixed fluids will lie between those of the respective pure endmembers provided excess volumes (V^{xs}) are not too large. Fig. 1.5D plots excess volumes for the binary systems H_2O-CO_2, CH_4-H_2O, CH_4-H_2, C_2H_6-CO and C_2H_6-H_2O at P = 55 kbar and T 1400 K as a percentage of the form:

$$100 * \left[\frac{V^{xs}}{V^{id}}\right] = 100 * \left[\frac{V^{mix}-V^{id}}{V^{id}}\right]$$

where $V^{id} = \sum_i (V_i^{pure}.x_i)$, x_i = mole fraction of species.

In all systems except C_2H_6-H_2O the maximum excess volume does not exceed 1.5% of V^{id} under these conditions. Aqueous hydrocarbon mixtures appear to be the most non-ideal fluids (Section 1.6) due to the incompatibility of intermolecular forces and especially in the case of ethane-water mixtures, the large volume mismatch between species.

Maximum disruption of the H_2O fluid structure in the systems H_2O-CO_2, H_2O-CH_4 and H_2O-C_2H_6 may be linked with the maxima in the V^{xs} vs x_{H_2O} curves (Fig. 1.5D) which occur near x_{H_2O} = 0.7 and correspond approximately

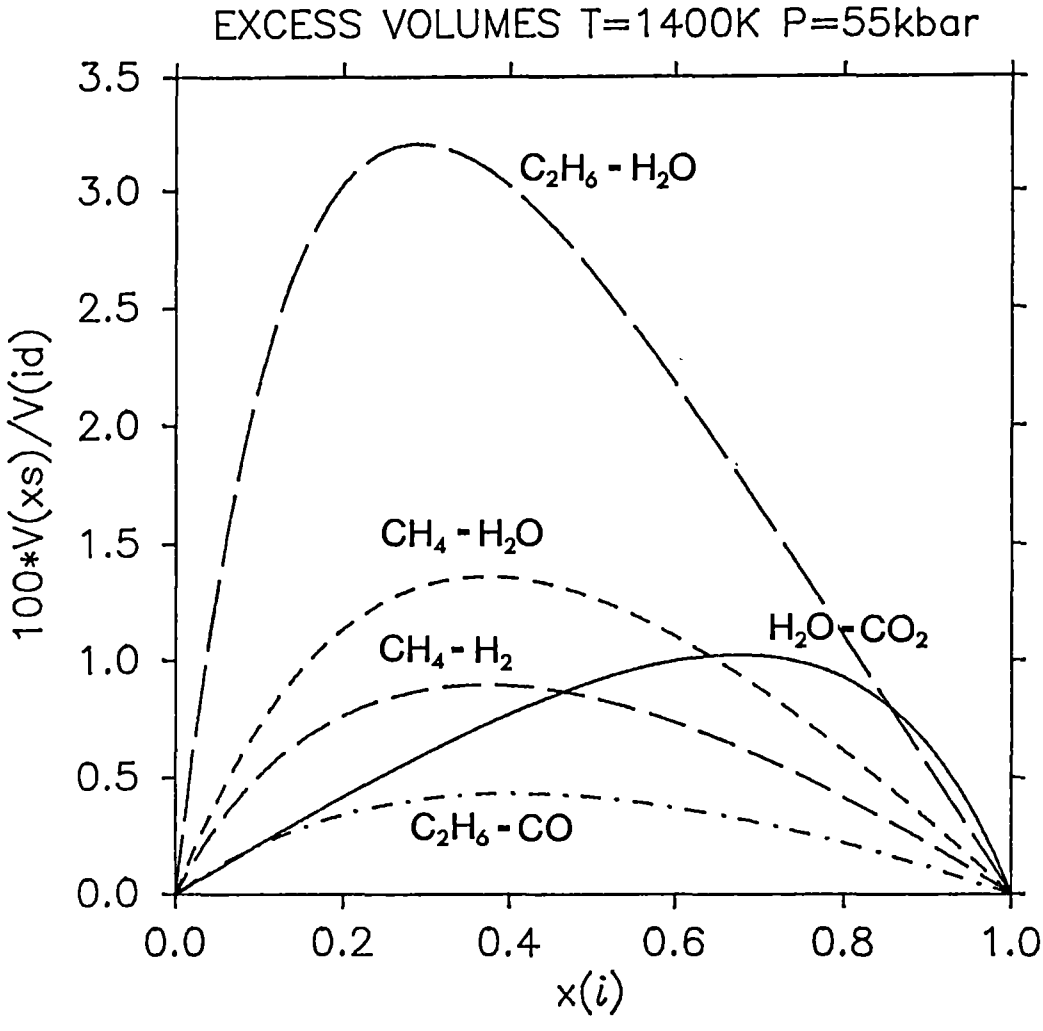

Fig. 1.5D Excess volumes of mixing for various binary C-O-H subsystems represented as a percentage of V^{ideal}:

C_2H_6-H_2O: ——— ——— ——— CH_4-H_2O: — — — — — — — CH_4-H_2: — — — —

C_2H_6-CO: — · — · — · — · H_2O-CO_2: ————————

to compositions containing two-thirds H_2O molecules and one-third other species.

1.6 Activity-Composition Relations in Binary and Pseudo-Binary Systems

A. Activity-Compostion Relations in the System H_2O-CO_2: a comparison with experimental data

The only supercritical fluid mixture to be investigated in sufficient detail to allow comparison with 5PMRK-derived fugacity and activity coefficients is the binary system H_2O-CO_2. Direct P-V_m-T measurements on H_2O-CO_2 mixtures have been made recently by Shmulovich et al. (1982). In combination with volumetric data obtained in earlier studies, the authors were able to derive activity coefficients for H_2O and CO_2 over the range 0.3-5 kbar, 673-873 K. However, no indication of likely uncertainties is given although activity coefficients for H_2O appear to be least well constrained by experimental measurements at low x_{H_2O}. Several other techniques have been used to estimate activities in H_2O-CO_2 fluid mixtures at elevated pressures. These include the hydrogen fugacity sensor method of Chou & Williams (1979) [activity of H_2O determined at 873 K, 2-8 kbar]; the albite-H_2O-CO_2 solidus method of Eggler & Kadik (1979) and Bohlen et al. (1982) [giving Burnham (1979) model-dependent H_2O activities to 20 kbar] and the carbonation/decarbonation equilibria method discussed most reecently by Shmulovich et al. (1982) [an indirect method with larger uncertainties than other techniques].

In Table 1.6A, 5PMRK-derived activity coefficients at P = 5 kbar, T = 873 K are compared with the tabulation of Shmulovich et al. (1982) = SSZ [based on volumetric data] and the results of Chou & Williams (1979) = CW [hydrogen fugacity sensor]. Within experimental uncertainty, activity coefficients in all three cases are greater than or equal to 1.0 at P > 4 kbar (negative CW values at lower pressures are probably in error, see Kerrick & Jacobs, 1981, p.761). 5PMRK γ_{H_2O} values are ~2-15% larger than the equivalent SSZ values and lie between the γ_{H_2O}(SSZ) and γ_{H_2O}(CW) estimates at low x_{H_2O}'s. Agreement between 5PMRK and SSZ CO_2 activity coefficients is excellent at $x_{CO_2} > 0.3$ but 5PMRK values are much larger at low x_{CO_2} where better agreement with CW coefficients is obtained. At low

x_{CO_2}, the P,T position of phase equilibria involving mixed H_2O-CO_2 volatiles is also consistent with γ_{CO_2} values much greater than SSZ estimates (e.g. Zharikov et al., 1977, Fig. 5) suggesting that γ_{CO_2}(SSZ) values may not be appropriate in this region.

Table 1.6A Comparison of activity coefficients in the system H_2O-CO_2 at P = 5 kbar, T = 873 K.*

x_{H_2O}	$\gamma^{5PMRK}_{H_2O}$	$\gamma^{SSZ}_{H_2O}$	$\gamma^{CW}_{H_2O}$	$\gamma^{5PMRK}_{CO_2}$	$\gamma^{SSZ}_{CO_2}$	$\gamma^{CW}_{CO_2}$
1.0	1.00	1.00	1.0**	5.33	1.99	-
0.9	1.03	1.01	1.0	2.62	1.70	2.5
0.8	1.11	1.03	1.0	1.78	1.49	2.1
0.7	1.19	-	1.0	1.41	-	1.8
0.6	1.28	1.12	1.1	1.23	1.22	1.6
0.5	1.38	-	1.2	1.13	-	1.4
0.4	1.47	1.27	1.3	1.07	1.08	1.3
0.3	1.57	-	1.5	1.03	-	1.2
0.2	1.66	1.46	1.9	1.01	1.00	1.1
0.1	1.75	1.58	1.9	1.00	1.00	1.1
0.0	1.84	1.70	-	1.00	1.00	1.0

* SSZ = Shmulovich et al. (1982, Table 1).
CW = Chou & Williams (1979).

** Typical uncertainty in CW coefficients ± 0.05 at high x_{H_2O}; all values read from Fig.1 of Chou & Williams (1979).

In general, however, 5PMRK, SSZ and CW activity coefficients at moderate pressures (~5 kbar) agree to within about 15% over most of the x_{H_2O} range. This contrasts with the much larger values obtained by Eggler & Kadik (1979) = EK and Bohlen et al. (1982) = BBW which predict greater deviations from ideality particularly at low x_{H_2O}. These differences are accentuated at higher pressures as illustrated in Table 1.6B. At 15 kbar and $x_{H_2O} > 0.4$, 5PMRK and BBW coefficients agree within uncertainty limits. At lower water contents, however, γ_{H_2O}(BBW) values are more than twice the 5PMRK estimates with γ_{H_2O}(EK) about 1.5 times 5PMRK estimates. This effect may be a result of the model-based aspects of calculating H_2O activities from the position of the albite-H_2O-CO_2 solidus [i.e. using the Burnham (1979) albite-H_2O model discussed in Appendix 13.5].

Table 1.6B Comparison of H_2O activity coefficients in the system H_2O-CO_2 at P = 15 kbar, T = 900 to 1300 K.*

x_{H_2O}	$\gamma^{5PMRK}_{H_2O}$	$\gamma^{BBW}_{H_2O}$	T/K	$\gamma^{EK}_{H_2O}$	T/K
1.0	1.00	1.0	908		
0.9	1.05-1.02**				
0.8	1.14-1.07	1.1±0.2	988		
0.7	1.26-1.13				
0.6	1.39-1.19				
0.5	1.53-1.25	1.6±0.3	1068		
0.4	1.68-1.32				
0.3	1.82-1.39	2.5±0.4	1118	1.9±0.2	1123
0.2	1.97-1.45	3.3±0.7	1178	2.4±0.4	1223
0.1	2.13-1.52	5.2±1.0	1248	2.8±0.6	1323
0.0	2.28-1.59				

* BBW = Bohlen et al. (1982)
EK = Eggler & Kadik (1979).

** Range quoted is for the interval 900-1300 K.

From a thermodynamic point of view, more reliance should be placed on activity coefficients derived from accurate P-V_m-T measurements of fluid mixtures rather than on phase equilibrium data. The correspondence between 5PMRK and SSZ activity coefficients (except for CO_2 at very low x_{CO_2}) indicates that within experimental uncertainties the original RK mixing rules (employed in both the 5P and KJ MRK's) offers acceptable estimates of activity coefficients in mixtures of polar fluids. For the purposes of calculating phase equilibria in the presence of volatile mixtures, slightly larger activity coefficients compared with SSZ values (such as those derived from the 5PMRK) are likely to give estimates of equilibrium position that more closely agree with experimental determinations (Shmulovich et al. 1982, p.181).

For other binary (and higher order) mixtures, activity-composition data at elevated pressures and temperatures are minimal or non-existent. However, MRK equations incorporating a Carnahan-Starling repulsive term and using the original RK mixing rules, well reproduce experimental molar volumes in polar-nonpolar binary mixtures such as H_2O-CH_4 fluids at pressures up to 1 kbar (Jacobs & Kerrick, 1981a). While the accuracy of

5PMRK-derived activity coefficients is difficult to evaluate in the absence of experimental data at higher pressures, it can at least be demonstrated that a-x relations are consistent with known molecular properties as discussed below.

B. Activity-Compostion Relations using 5PMRK-derived fugacity coefficients: an interpretation using molecular properties

The binary systems (i) H_2O-CO_2, (ii) CH_4-H_2O and (iii) C_2H_6-CO were chosen to illustrate activity composition relations amongst C-O-H fluid mixtures at pressures above available experimental measurements. The significance of this choice will become apparent when the distribution of volatile species in systems containing elemental carbon is considered (Sections 2.7 and 2.9); suffice to say here that systems (i) and (ii) correspond to the major components in equilibrium with graphite or diamond under oxidised and reduced conditions respectively and (iii) corresponds to a simplified metastable fluid where carbon nucleation has been suppressed. In all three systems additional components, arbitrarily fixed at a level of 20 mol%, have also been considered; in certain cases they have a dramatic effect on calculated a-x relations.

Binary (i-j) and pseudo-binary (i-j, x_k=0.2) activity-composition diagrams (where i,j,k are labels for different pure species, and x_k = mol fraction of species k) are presented in Figs. 1.6A to 1.6C for P = 55 kbar and T = 1400 K; a condition within the diamond stability field. Calculations were made with the 5PMRK using the equation:

$$a_i^{55,1400} = \frac{f_i^{mix}}{f_i^{pure}} = \left[\frac{\phi_i^{mix}}{\phi_i^{pure}}\right] x_i = \gamma_i x_i$$

where γ_i = activity coefficient
$x_i = n_i/(n_i+n_j+n_k)$
n_i = mols of species i.

(i) Binary H_2O-CO_2; pseudo-binaries H_2O-CO_2-CH_4 and H_2O-CO_2-H_2

Diagrams are similar in appearance to those of Kerrick & Jacobs (1981). The activity of CO_2 shows strong deviation from ideality at high x_{H_2O} while a_{H_2O} deviates greatly over the full x_{CO_2} range. Weakly polar

Fig. 1.6A-D Activity-composition diagrams for binary and pseudobinary C-O-H subsystems at 55 kbar (system i-j, arrows indicate component k in pseudobinaries).

Fig. 1.6A

Binary: ——— H_2O-CO_2

Pseudobinaries: — — H_2O-CO_2-0.2CH_4;

—·—·— H_2O-CO_2-0.2H_2

Fig. 1.6B

Binary: ——— CH_4-H_2O

Pseudobinaries: — — CH_4-H_2O-0.2H_2;

—·—·— CH_4-H_2O-0.2C_2H_6

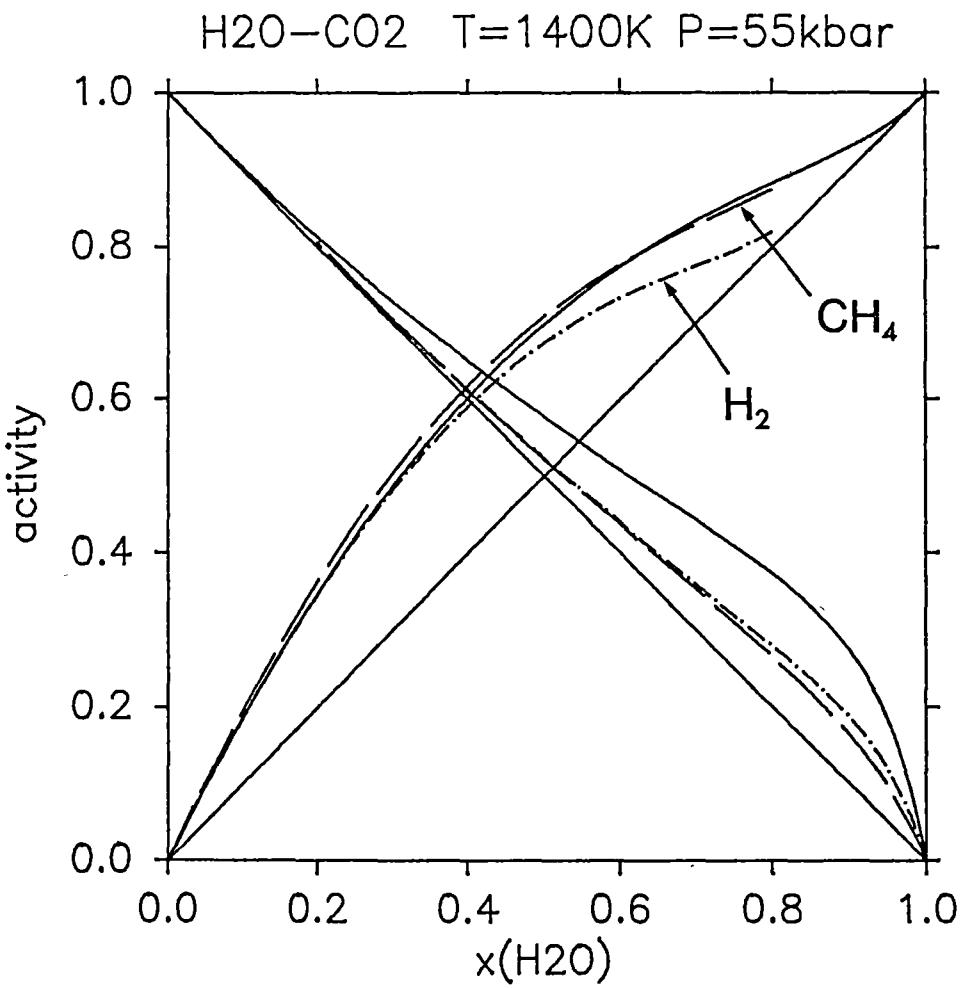
H2O–CO2 T=1400K P=55kbar
activity
x(H2O)
CH4
H2
0.0
0.2
0.4
0.6
0.8
1.0

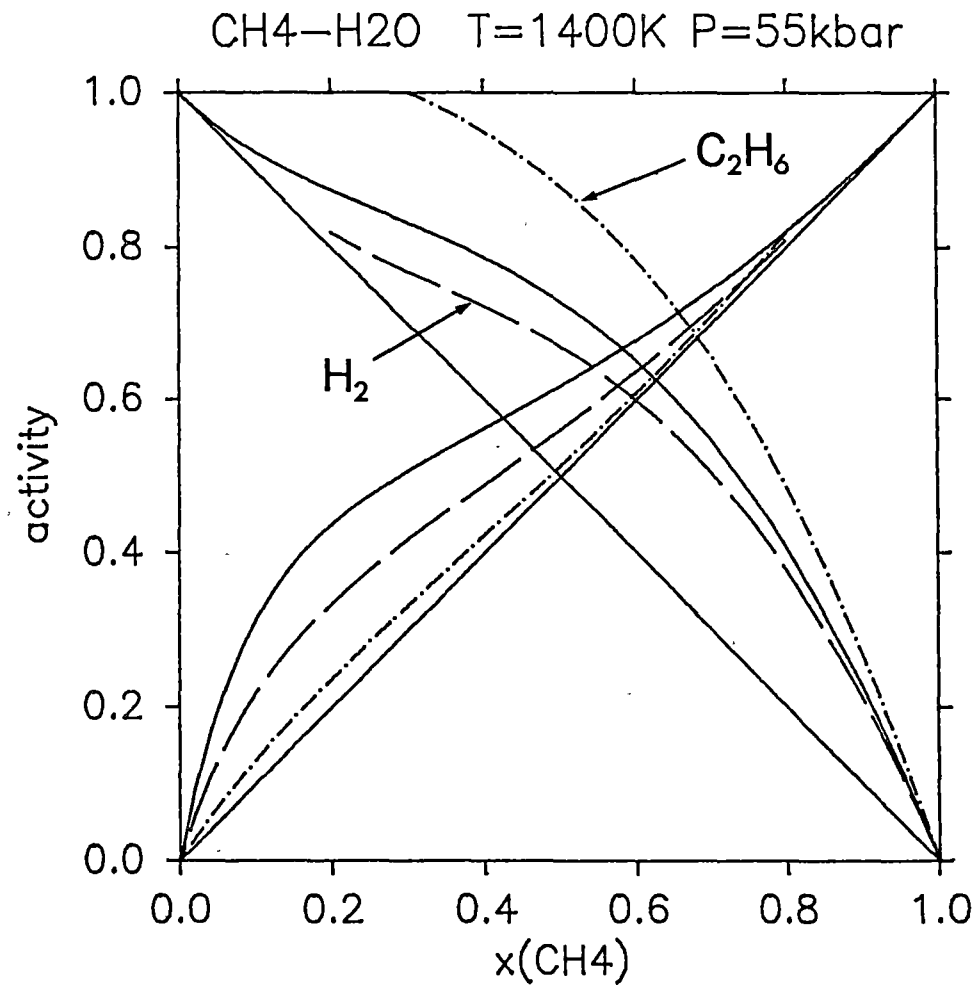
CH4–H2O T=1400K P=55kbar
activity
x(CH4)
C2H6
H2
0.0
0.2
0.4
0.6
0.8
1.0

CO_2 molecules presumably disrupt the tight H-bonded network of supercritical H_2O even when present in small concentrations. The idea of describing activity coefficients in terms of a molecular "discomfort index" (Prausnitz, 1969. p.155) gives an explanation for the non-ideality of CO_2 at high x_{H_2O}: basically CO_2 is much more "uncomfortable" when surrounded by highly polar H_2O molecules (high x_{H_2O}) rather than molecules of its own kind at high x_{CO_2} where $\gamma_{CO_2} \dashrightarrow 1$.

The effect of 20 mol% H_2 and CH_4 is to lower the activity of CO_2 presumably by a dilution effect involving similar weakly polar molecules. CH_4 does not affect a_{H_2O} to any great degree but 20 mol% H_2 lowers a_{H_2O} at high x_{H_2O} suggesting that the relatively small and compressible H_2 molecules disrupt the structure of supercritical H_2O to a much lesser extent than CO_2. Molar volumes of the pure fluids for comparison at 55 kbar, 1400 K are (in cm^3mol^{-1}) H_2O 14.2, H_2 11.9, CO_2 25.7 and CH_4 24.5.

(ii) Binary CH_4-H_2O; pseudo-binaries CH_4-H_2O-H_2 and CH_4-H_2O-C_2H_6.

The CH_4-H_2O diagram (Fig. 1.6B) resembles the H_2O-CO_2 system except that non-ideality is much more pronounced. Similar arguments as those discussed in (i) will apply to this system, however CH_4 is non-polar (no quadrupole or dipole moments) and there is a large volume mismatch between CH_4 and H_2O leading to high excess volumes (Fig. 1.5D). From Table 1.2B it is seen that CH_4 and H_2O are quite dissimilar in their molecular properties and as expected this is reflected in the activity coefficients. Addition of 20 mol% H_2 has a similar effect to that described for the H_2O-CO_2 system, however a 20 mol% C_2H_6 addition results in significant changes. The activity of CH_4 is greatly decreased while that of H_2O increases dramatically, particularly at high x_{H_2O}. These effects may be explained by dilution of the system with hydrocarbon molecules very similar in their properties to CH_4 combined with increased break-up of the H_2O structure caused by ethane's much larger size ($V_{m(C_2H_6)}^{55,1400} = 36.7\ cm^3mol^{-1}$). This volume mismatch effect is probably responsible for the observed dramatic increase in a_{H_2O} at high water contents. The shape of the a-x curves suggest that fluid-fluid immiscibility may take place in the systems CH_4-H_2O and CH_4-H_2O-C_2H_6 at $T < 1400$ K at 55 kbar or at higher pressures. Activity-composition diagrams for the system CH_4-H_2O over a range of T

Fig. 1.6C Binary: ———— C_2H_6-CO

Pseudobinaries: —— —— C_2H_6-CO-0.2H_2O;

—·—·—·— C_2H_6-CO-0.2CO_2

Fig. 1.6D System CH_4-H_2O activity-composition relations at 55 kbar and T =1000, 1200, 1400 K showing appearance of a region of fluid-fluid immiscibility at 1000 K (dashed lines).

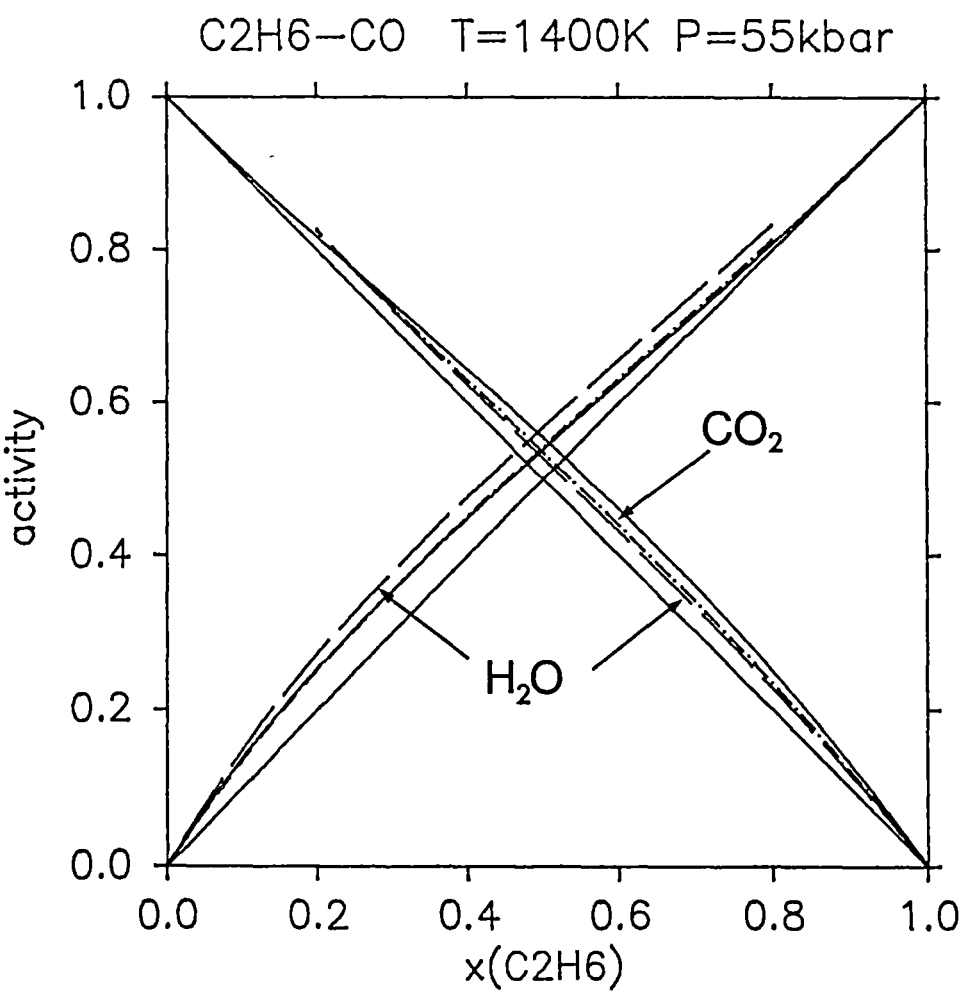
C2H6–CO T=1400K P=55kbar
activity
x(C2H6)
CO2
H2O
0.0
0.2
0.4
0.6
0.8
1.0

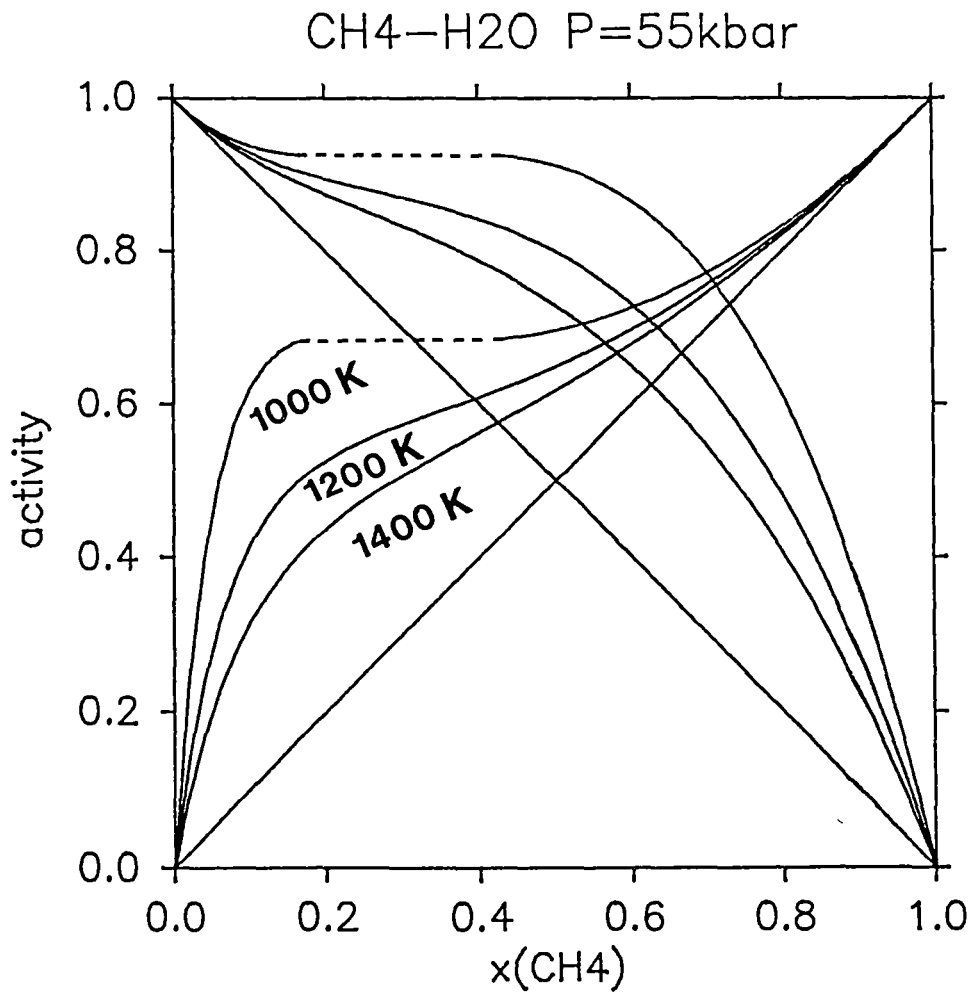
CH4–H2O P=55kbar
activity
x(CH4)
1000 K
1200 K
1400 K
0.0
0.2
0.4
0.6
0.8
1.0

(Fig. 1.6D) indicate the onset of immiscibility between 1000 and 1200 K. A hydrocarbon-rich phase and an aqueous phase corresponding at 1000 K to CH_4 contents of ~45 mol% and ~15 mol% respectively, would be expected to separate. The miscibility gap may be accentuated in natural systems if highly polar components such as dissolved solids (e.g. $NaCl^o$, $Si(OH)_4^o$, $Mg(OH)_2^o$) are also present. These will prefer to be solvated by H_2O molecules thus raising a_{CH_4} and making immiscibility a possibility at much higher temperatures.

(iii) Binary C_2H_6-CO; pseudo-binaries C_2H_6-CO-H_2O and C_2H_6-CO-CO_2

The system C_2H_6-CO (Fig. 1.6C) illustrates behaviour that is close to ideal. This is not surprising in view of the similarity in molecular forces between two weakly polar molecules such as CO and C_2H_6. Addition of 20 mol% CO_2 causes little change in $a_{C_2H_6}$ but results in a lowering of a_{CO} due to a dilution effect by a molecule resembling CO in many of its properties (particularly in dilute solution where association will not be important). Volumetrically, CO and CO_2 are very similar (molar volumes at 55 kbar, 1400 K: CO_2 25.7, CO 22.6) and substitute for one another with little change in activity coefficients of other species. A 20 mol% water addition raises the activity of C_2H_6 for reasons discussed in (ii) while the activity of CO is lowered. This effect is probably associated with the ability of H_2O to contract the volume of the system and hence provide sites favourable to CO; it is expected that H_2 would have a similar effect.

In conclusion to this sub-section, the following points may be noted:

(a) 5PMRK activity coefficients of C-O-H species in binary and pseudo-binary systems are readily explained in terms of known molecular properties.

(b) Activity-composition diagrams constructed with 5PRMK and KJMRK derived activity coefficients are closely similar in form and show the same gross variation on addition of a third component.

(c) Fluid-fluid immiscibility is likely to occur in hydrocarbon-aqueous fluid mixtures under conditions appropriate to the upper mantle.

PART 2

THERMODYNAMIC MODELLING OF SPECIES DISTRIBUTION IN THE SYSTEM C-O-H INCLUDING ELEMENTAL CARBON.

2.1 Introduction

Understanding the behaviour of model mantle C-O-H fluids requires a detailed knowledge of species distribution in P-T-fO_2-x space (where x = other compositional variables). The procedure for calculating species distribution in the presence or absence of a crystalline carbon phase (diamond or graphite) is relatively straight-forward. The method of French (1966), updated to include MRK derived fugacity coefficients (Holloway, 1981) is normally employed for calculations in the presence of elemental carbon if the number of species does not exceed about ten. If calculations involve only a single fluid phase, then additional mass balance constraints need to be applied as in the method of Brown (1977); the complexity of the calculations however rises rapidly as the number of species increases. In this case, methods involving the minimisation of total Gibbs free energy of the system (Smith & Missen, 1982) result in a much more concise treatment.

Despite the seemingly small number of components in the model system, it is not easy to devise a graphical representation to display the maximum amount of information. Clarity is improved by an appropriate choice of compositional variables as discussed below.

2.2 Choice of compositional variables and graphical representation.

The phase rule, $v = c + 2 - p$, may be applied to the system C-O-H $\pm$ graphite or diamond as considered below:

C-O-H fluid + carbon; c = 3, p = 2, v = 3 trivariant.

C-O-H fluid only; c = 3, p = 1, v = 4 tetravariant.

If two phases (fluid + solid) are present then three variables must be specified to fully describe the system. In the fluid-only system four variables are necessary. Since pressure (P) and temperature (T) can be included as two of these, specification of one or two additional compositional variables, for the two-phase and single-phase systems respectively, is required. By fixing P and T at particular values both

systems in effect lose two degrees of freedom; the system C-O-H + carbon may then be described as pseudo-univariant and C-O-H fluid-only as pseudo-divariant (hence represented by a line or a field respectively in compositional diagrams at fixed P,T). In addition, if the nucleation of graphite or diamond is suppressed for any reason, fluid alone may exist where two phases are stable; in this situation the pseudo-divariant field becomes a metastable region containing fluids supersaturated in carbon.

Holloway & Reese (1974) have represented the system C-O-H in terms of an isobaric, isothermal triangular diagram (or portions thereof) with bulk mole fractions of H, C and O plotted at the triangle apices. For any one P,T condition the pseudo-univariant assemblage is represented by a carbon saturation curve. The pseudo-divariant region and metastable region of carbon supersaturation, extending toward the C apex, may be contoured in terms of fO_2, fH_2 or other compositional variables. While the above features are able to display a large amount of information, the diagram as a whole is unsuited to a clear interpretation of species distribution as a function of fO_2 or other variables. Contours in compositional variables, for example, tend to be compressed into the small area of interest approximately bounded by the subsystem CO_2-H_2O-CH_4 and variations along the carbon saturation curve are not delineated. Plotting reference synthetic oxygen buffers or mixed volatile phase equilibria is by no means a straight-forward task as is seen by Fig. 2 of Holloway & Reese (1974). Isobaric diagrams in T-log fO_2 space, as those of Ohmoto & Kerrick (1977) while clearly illustrating devolatilisation equilibria, suffer from the problem that other compositional variables cannot be represented.

More recently, Frost (1979) has developed an isobaric, isothermal diagram plotting log fO_2 vs the compositional variable "X_C" defined as the mole fraction of carbon relative to H_2 in the bulk fluid ($X_C = X_{C/C+H_2}$). This approach clearly distinguishes fluids containing either reduced or oxidised components as is shown by Table 2.2A below [other related variables $X_H = (1-X_C)$ and X_O may be defined similarly]:

Table 2.2A Compositional variables for the pure components.

	$X_C(X^i_{C/C+H_2})$	$X_H(X^i_{H_2/C+H_2})$	$X_O(X^i_{O_2/O_2+H_2})$
CO_2,CO	1	0	1
H_2O	0	1	0.333
H_2	0	1	0
CH_4	0.333	0.667	0
C_2H_6	0.4	0.6	0

For a fluid mixture X_C^{bulk} is simply defined as the sum of X_C^i values for all the pure components times their mole fractions (x_i) in the mixture:

$$X_C^{bulk} = \sum_i (X_C^i \cdot x_i)$$

It must be emphasised that X_C, X_H and X_O all depend upon the nature of the fluid species present so that a fluid having identical H, O and C contents may have very different X_C, X_O or X_H values; consider for example a fluid containing 20 mol% C, 40 mol% H and 40 mol% O which could be any one of the fluids A, B or C below:

Table 2.2B

	H_2O	CO_2	H_2	CO	CH_4	X_C^{bulk}	X_O^{bulk}	X_H^{bulk}
A	-	50	50	-	-	0.5	0.5	0.5
B	50	-	-	50	-	0.5	0.667	0.5
C	33.3	50	-	-	16.7	0.556	0.611	0.444

The chief advantages of the log fO_2-X_C diagram of Frost (1979) are:

(a) clarity of interpreting species distribution as a function of fO_2 along the carbon saturation curve (Section 2.5).

(b) ready visualisation of isopleths (contours of equal composition) in the pseudo-divariant and metastable regions (Section 2.10).

(c) ease of projecting fO_2-dependent or devolatilisation equilibria (Section 2.11).

In the following sections the procedure for calculating the carbon saturation curve, divariant and metastable regions in log fO_2-X_C space is outlined and extensive use is made of the Frost (1979) diagram.

2.3 Calculation procedure for the pseudo-univariant carbon saturation curve in log fO_2-X_C space.

The method employed for calculation of the carbon saturation curve is basically that of French (1966) but modified to incorporate the non-ideality of the fluid phase by specifying $\phi_i(P,T,x)$ values derived from the 5PMRK. Initially eight components were included in the calculation procedure, i.e. H_2O, CO_2, CO, H_2, CH_4, C_2H_6 together with C_2H_4 and CH_3OH as the most likely high pressure representatives of the alkenes and alcohols known from diamond fluid inclusions (Melton & Giardini, 1974). It is likely that members higher in the homologous series of these organic molecules would be of less importance at higher pressures due to the rapid increase of ϕ_i and V_m with molecular size (Tsiklis & Semenova, 1973) since $x_i \propto 1/\phi_i$. In an initial series of calculations with eight species (detailed below), the only large organic molecule found to be of any importance within the pseudo-divariant region was ethane, C_2H_6. Both C_2H_4 and CH_3OH are unimportant species at T < 1000 K (both <0.01 mol%) at pressures to at least 50 kbar. At higher temperatures calculated CH_3OH and C_2H_4 abundances still do not exceed 0.1 mol%, this amount not being particularly sensitive to the choice of fugacity coefficient. Due to the paucity of C_2H_4 and CH_3OH volumetric data available at high pressures, fugacity coefficients were obtained from the 5PMRK using the estimated parameter values given below:

Table 2.3A Estimated 5PMRK parameters for C_2H_4 and CH_3OH.

	b_1	b_2	$a_1/10^8$	$a_2/10^9$	$a_3/10^{10}$
C_2H_4	60	6500	1.3	4	12
CH_3OH	40	5900	1.3	3	7

As a consequence of this treatment only the molecules H_2O, CO_2, CO, H_2, CH_4 and C_2H_6 have been considered in the following discussion. This simplification is justified in the pseudo-divariant region and on the univariant saturation curve and is supported by experimental evidence

(Section 4.2). This, however, has not been tested in the metastable portion of the phase diagram where fluids of high hydrocarbon content are possible (Sections 2.9 and 2.10); in this case the selection of six species to represent species distribution should be regarded as an approximation.

The method of French (1966) requires selection of a set of phase equilibria that completely describes the inter-relation of system components. The choice is largely one of convenience and the equilibrium constants used here are defined below:

K_1	$C + O_2 = CO_2$	$K_{CO_2} = fCO_2/fO_2$
K_2	$CO_2 + C = 2CO$	$K_{CO} = fCO^2/fCO_2$
K_3	$H_2 + 1/2\ O_2 = H_2O$	$K_{H_2O} = fH_2O/fO_2^{1/2}.fH_2$
K_4	$C + 2H_2 = CH_4$	$K_{CH_4} = fCH_4/f_{H_2}^2$
K_5	$2CH_4 = H_2 + C_2H_6$	$K_{C_2H_6} = fC_2H_6.fH_2/fCH_4^2$

Equilibrium constants were determined as a function of P and T from the thermodynamic data of Robie et al. (1978) and Stull et al. (1969). Compressibility (β) and thermal expansion (α) coefficients have been included for graphite and diamond. Where Cp equations were not available to 1700 K, data at lower temperatures were fitted to an equation of the form $Cp = a + bT + cT^{-2} + dT^{-1/2}$ which gives a better extrapolation to higher temperatures (Holland, 1981). $K_{P,T}$'s were then calculated with the standard expression:

$$\left[-\ln K_{P,T}\right] = \left[\frac{\Delta H^o_{r(1,298)}}{RT}\right] - \left[\frac{\Delta S^o_{r(1,298)}}{R}\right] + 1/RT\int_{298}^{T} \Delta Cp.dT - 1/R\int_{298}^{T} \frac{\Delta Cp}{T}.dT + 1/RT\int_{1}^{P} \Delta V_s.dP$$

For any one choice of P,T and fO_2 the fugacities of all other species in equilibrium with elemental carbon may be calculated by combining K_1 to K_5 with a mass balance equation of the form:

$$P_{fluid} = \frac{fH_2O}{\phi_{H_2O}} + \frac{fCO_2}{\phi_{CO_2}} + \frac{fCO}{\phi_{CO}} + \frac{fH_2}{\phi_{H_2}} + \frac{fCH_4}{\phi_{CH_4}}$$

where the terms f_i/ϕ_i correspond to the partial pressures of species i in the mixture. Taking $P_{total} = P_{fluid}$ and rearranging in terms of fH_2O, a cubic equation must be solved. Since $\phi_i = \phi_i(P,T,x_j,x_k...)$ the calculation procedure is repeated a number of times until the mole fractions of species converge (the number of iterations is usually <30 for a convergence criterion of eight decimal places in x_i). Algol programs COH/GRAPHITE6 and COH/DIAMOND6, employing numerical solution methods, have been written specifically for these calculations. Program COH/DIAMOND6 is listed in Appendix 7.

2.4 Method of Calculating Species Distribution in the Pseudo-divariant and Metastable Regions.

Calculation of the species distribution in the absence of elemental carbon requires in addition to P, T and fO_2, the specification of a further compositional variable. Again a set of equilibria, fully describing the inter-relation of system components, are required. The method employed here is basically that of Brown (1977) but modified for non-ideality of fluid species and inclusion of X_C as the compositional variable. Four equilibria are sufficient to relate all species:

K_1 $\quad CO + 1/2\ O_2 = CO_2 \quad K_{CO} = fCO_2/fO_2^{1/2}.fCO$

K_2 $\quad H_2 + 1/2\ O_2 = H_2O \quad K_{H_2O} = fH_2O/fO_2^{1/2}.fH_2$

K_3 $\quad 2H_2 + CO = CH_4 + 1/2\ O_2 \quad K_{CH_4} = fCH_4.fO_2^{1/2}/fH_2^2.fCO$

K_4 $\quad 3H_2 + 2CO = C_2H_6 + O_2 \quad K_{C_2H_6} = fC_2H_6.fO_2/fH_2{}^3.fCO^2$

Noting from Table 2.2A that

$$X_C = x_{CO_2} + x_{CO} + 1/3\ x_{CH_4} + 2/5\ x_{C_2H_6}$$

and

$$X_H = (1-X_C) = x_{H_2O} + x_{H_2} + 2/3\ x_{CH_4} + 3/5\ x_{C_2H_6}$$

the mass balance constraint:

$$1 = x_{CO_2} + x_{CO} + x_{H_2O} + x_{H_2} + x_{CH_4} + x_{C_2H_6}$$

may be used together with $f_i = x_i.\phi_i.P_{total}$ to give the following equations ($P = P_{total} = P_{fluid}$):

$$P = \frac{fCO_2}{\phi_{CO_2}.X_C} + \frac{fCO}{\phi_{CO}.X_C} + \frac{fCH_4}{3\phi_{CH_4}.X_C} + \frac{2fC_2H_6}{5\phi_{C_2H_6}.X_C} \qquad ...(2.4A)$$

and

$$P = \frac{fH_2O}{\phi_{H_2O}(1-X_C)} + \frac{fH_2}{\phi_{H_2}(1-X_C)} + \frac{2fCH_4}{3\phi_{CH_4}(1-X_C)} + \frac{3fC_2H_6}{5\phi_{C_2H_6}(1-X_C)} \quad \ldots(2.4B)$$

substituting into the expressions for K_1 to K_4 we have:

$$P = \left[\frac{K_{CO}.fO_2^{1/2}}{\phi_{CO_2}.X_C} + \frac{1}{\phi_{CO}.X_C}\right].fCO + \left[\frac{K_{CH_4}}{3\phi_{CH_4}.X_C.fO_2^{1/2}}\right].fH_2^2.fCO$$

$$+ \left[\frac{2K_{C_2H_6}}{5\phi_{C_2H_6}.X_C.fO_2}\right].fH_2^3.fCO_2^2 \quad \ldots (2.4C)$$

and

$$P = \left[\frac{K_{H_2O}.fO_2^{1/2}}{\phi_{H_2O}.(1-X_C)} + \frac{1}{\phi_{H_2}.(1-X_C)}\right].fH_2 + \left[\frac{2K_{CH_4}}{3\phi_{CH_4}.(1-X_C).fO_2^{1/2}}\right].fH_2^2.f_{CO}$$

$$+ \left[\frac{3K_{C_2H_6}}{5\phi_{C_2H_4}.(1-X_C).fO_2}\right].fH_2^3.f_{CO}^2 \quad \ldots(2.4D)$$

Solving for fCO in equation (2.4C) by taking the positive root and substituting back into (2.4D) a unique expression for fH_2 is obtained. The final cubic equation in fH_2 is readily solved numerically using an initial estimate of $\left\{P.\phi_{H_2O}.(1-X_C)/(K_{H_2O}.fO_2^{1/2})\right\}$ and hence the other f_i's derived. Since $\phi_i = \phi_i(P,T,x_j,x_k\ldots)$ this procedure must be iterated until all x_i's converge. The program COH/FLUID6, employing 5PMRK fugacity coefficients, has been written to perform these calculations; a listing is presented in Appendix 8.

2.5 Compositional Variations in log fO_2-X_C space: an example at 30 kbar, 1600 K.

Results of the calculations discussed in the two previous sections have been plotted on a log fO_2-X_C diagram for P = 30 kbar and T = 1600 K (Fig. 2.5). Also included is the reference synthetic fO_2 buffer iron-wustite (IW) which plots independently of fluid composition assuming there is no dissolution of volatile components (in this case C, O or H) in the oxide or metallic phases. (Appendix 9 contains a complete list of the reference fO_2 buffers plus literature sources used in this study.) The composition of the fluid phase is indicated at various points on the phase diagram and these are listed in Table 2.5. On the log fO_2-X_C diagram the positions of the pure C-O-H species H_2O, CO_2, CO and H_2 are fixed on the X_C axis but lie at off-scale positions on the fO_2 axis of Fig. 2.5 at points corresponding to the intrinsic fO_2's of the pure species. By "projecting" these points along the fO_2-axis into the fO_2 domain of interest, these species may be located at the diagram's apices: H_2O plots at the top left-hand corner and moving around in clockwise fashion CO_2, CO and H_2 may be placed. As is evident from Table 2.2A, CH_4, C_2H_6 and other hydrocarbons can be similarly plotted along the bottom axis according to their H/C ratio. Elemental carbon (diamond or graphite) will plot off the diagram at the $fO_2 = 0$, $X_C = 1$ extremity. However, in "projecting" along the fO_2-axis carbon and CO will coincide at the lower right-hand apex; a condition valid for all fO_2 ranges under consideration here. The log fO_2-X_C diagram thus neatly divides C-O-H species into four quadrants, i.e.

(a) upper left: dominated by C-poor oxidised volatiles (H_2O-rich)
(b) upper right: dominated by C-rich oxidised volatiles (CO_2-rich)
(c) lower right: dominated by reduced C-rich components either elemental carbon or metastably, CO.
(d) lower left: dominated by C-poor reduced volatiles (H_2-rich).

A fifth region can be identified to include hydrocarbon-rich fluids (CH_4 and C_2H_6) which lie in the reduced part of the diagram between (c) and (d).

Fig. 2.5 shows the pseudo-univariant graphite saturation curve as a function of fO_2. It is divided into oxidised and reduced segments by a large field of graphite that extends to very water-rich fluid compositions (the "nose" of the phase diagram). The horizontal portion of the curve includes dominantly H_2O-CO_2 fluids in equilibrium with graphite. With increasing x_{CO_2} the curve intersects the log fO_2 axis at $X_C = 1$

corresponding to a point on the graphite-CO_2-CO (GCO) fO_2 buffer. At fO_2's less than the water maximum, fluids are $H_2O > CH_4 > H_2$ mixtures progressing to $CH_4 > H_2 > C_2H_6$ mixtures at fO_2's below IW. The reduced extremity of the saturation curve continues beyond the diagram to a point where $fO_2 = 0$; here fluids lie within the subsystem C-H. The pseudo-divariant field (hatched region in Fig. 2.5) is likewise divided into oxidised and reduced regions about the graphite "nose". Fluids lying at fO_2's greater than the carbon saturation curve and above the water maximum are H_2O-CO_2 mixtures. Under reduced conditions the pseudo-divariant region is restricted to X_C values below ~0.3 where fluids are largely H_2-H_2O-CH_4 mixtures. The presence of the graphite "nose" separating oxidised and reduced regions effectively prevents the derivation of oxidised H_2O-CO_2 fluids from those containing CH_4 (or vice versa) without precipitation of elemental carbon. Any fluid evolving along the carbon saturation curve by simultaneous precipitation and removal of carbon from the system will eventually terminate at a fluid composition close to the water maximum (point "c"). If for any reason the nucleation of diamond or graphite is suppressed then fluids will become supersaturated in carbon and move into the metastable region below and to the right of the saturation curve. As can be seen from Table 2.5, fluids in the reduced (fO_2 < IW) part of the metastable region are rich in hydrocarbons and CO while in the oxidised (fO_2 > IW) portion are basically CO_2-H_2O-CH_4 mixtures.

In terms of their relative abundance in the stable portion of the phase diagram the fluid species may be categorised as follows:

major component (>10 mol%): H_2O, CO_2, CH_4,(H_2)

minor component (<10 mol%, >1 mol%): H_2, C_2H_6, CO

The above division as it turns out (Sections 2.9 and 2.10) is maintained over the wide range of P,T conditions appropriate to the upper mantle.

Fig. 2.5 log fO_2-X_C [= mole fraction $C/(C+H_2)$] diagram at 1600 K, 30 kbar showing the graphite saturation curve, stable fluid-only pseudo-divariant region (hatched), metastable pseudo-divariant region (blank) and X_C-independent trace of the IW buffer (dashed line). Arrows indicate the off-scale positions of the six C-O-H volatile species. Filled circles (on the saturation curve) and open circles correspond to the fluid compositions listed in Table 2.5. The maximum mole fraction of H_2O on the graphite saturation curve is reached at point "c".

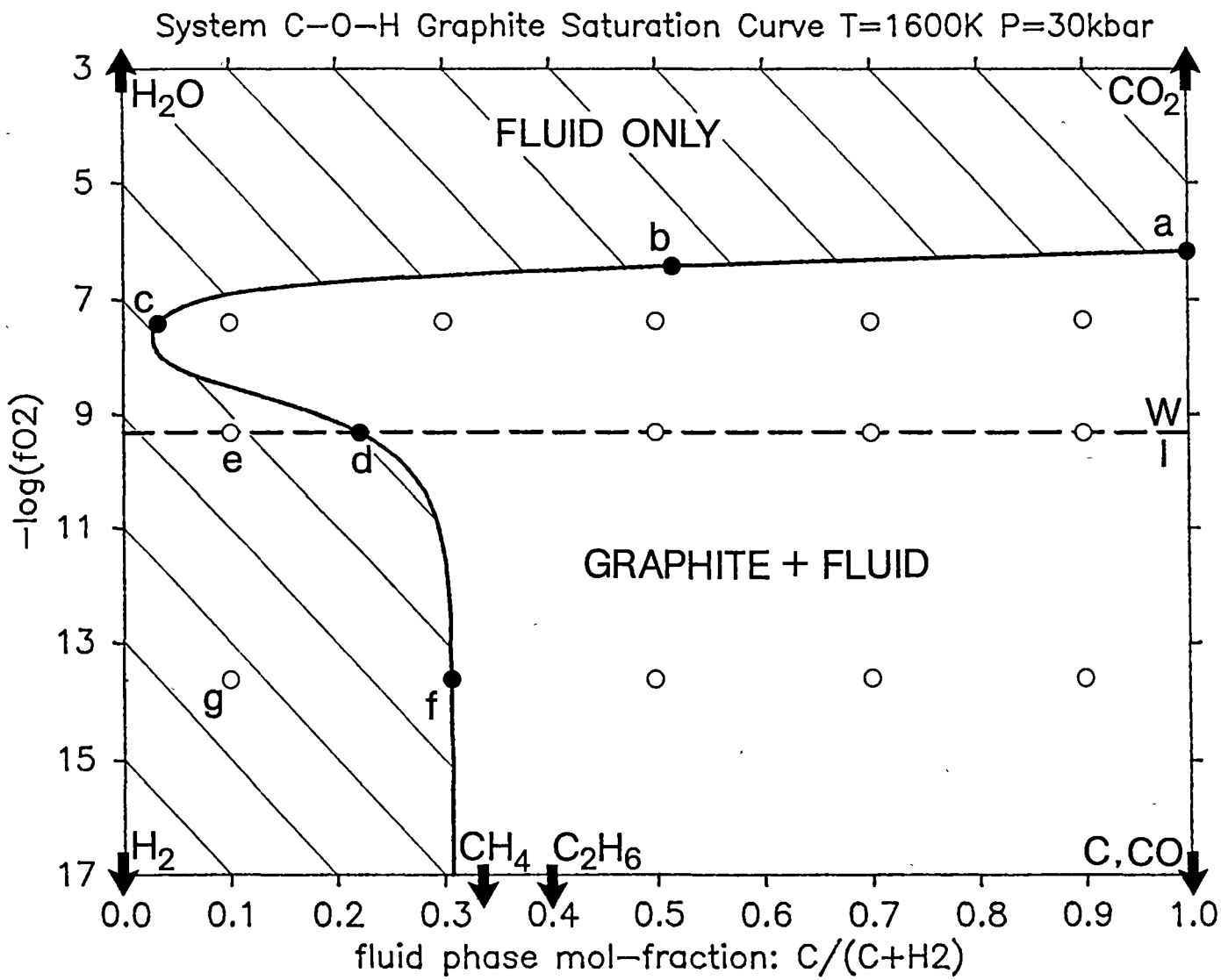
System C–O–H Graphite Saturation Curve T=1600K P=30kbar
FLUID ONLY
GRAPHITE + FLUID
H_2O
CO_2
H_2
CH_4
C_2H_6
C,CO
a
b
c
d
e
f
g
W
I
−log(fO2)
3
5
7
9
11
13
15
17
0.0
0.1
0.2
0.3
0.4
0.5
0.6
0.7
0.8
0.9
1.0
fluid phase mol–fraction: C/(C+H2)

Table 2.5 Fluid compositions at selected points in Fig. 2.5; T = 1600 K, P = 30 kbar.

1. EQUILIBRIUM FLUIDS

				mol% species*						
	$-\log fO_2$	X_C	X_O	H_2O	CO_2	CO	H_2	CH_4	C_2H_6	V^{mix} cm^3 /mol
a[1]	6.15	1.000	1.000	0	97.1	2.9	0	0	0	30.27
b	6.40	0.510	0.671	48.5	49.3	1.6	0.4	0.1	0	24.21
c[2]	7.40	0.032	0.339	94.1	2.3	0.2	1.5	1.9	0	17.90
d[3]	9.30	0.220	0.091	26.9	0.1	0.1	7.8	63.3	1.8	25.60
e[3]	9.30	0.100	0.192	57.4	0	0	12.7	29.7	0.2	21.05
f	13.60	0.306	0.001	0.2	0	0	8.7	87.7	3.4	28.69
g	13.60	0.100	0.004	0.2	0	0	68.8	29.9	0	19.83

1. fO_2 = GCO 2. fO_2 = GW(max.x_{H_2O}) 3. fO_2 = IW

* round-off error = $\pm$ 0.1 mol%

2. METASTABLE FLUIDS (carbon supersaturated)

	(0.10	0.365	84.9	7.4	0.8	1.5	5.3	0	19.18
	(0.30	0.468	61.3	23.7	2.7	1.5	10.7	0.2	22.35
7.40	(0.50	0.601	41.5	41.4	4.9	1.2	10.7	0.3	24.90
	(0.70	0.759	24.7	60.4	7.4	0.8	6.6	0.2	27.01
	(0.90	0.925	8.8	79.5	10.1	0.3	1.3	0	28.97
	(0.50	0.241	1.4	9.0	14.5	0.5	51.2	23.4	32.35
9.30	(0.70	0.542	0.7	21.0	33.0	0.2	30.0	15.1	31.10
	(0.90	0.850	0.4	33.9	50.9	0.1	10.8	3.8	29.37
	(0.50	0.184	0	0.1	18.3	0	15.2	66.4	38.22
13.60	(0.70	0.510	0	0.2	50.8	0	8.5	40.5	34.10
	(0.90	0.837	0	0.3	83.4	0	3.7	12.6	29.60

2.6 Pressure-Temperature Variation of the Graphite/Diamond Saturation Surface

Pressure or temperature variations in the graphite/diamond saturation surface can be investigated by projection of appropriate slices into a log fO_2-X_C plot. Diagrams showing P and T variation are presented in Figs. 2.6A and 2.6B respectively and in general, form a family of similarly shaped curves. The results are discussed in detail below.

(a) Pressure variation: Increasing pressure dramatically expands the field of elemental carbon to higher fO_2's. Concurrently the "nose" portion of the diagram increases both along the X_C and log fO_2 dimensions and the fluids at the water maximum become progressively poorer in carbon. These changes appear to be largely a consequence of the equilibria:

(a) $C + H_2O = CO + H_2$

(b) $2C + 2H_2O = CO_2 + CH_4$

(a) is important at P < 2 kbar and lies well to the right resulting in high X_C fluids at the water maximum at low pressures. With increasing pressure equilibrium (b) becomes more important and there is a general shift to the left providing well defined H_2O-CO_2 and H_2O-CH_4 fluid compositions either side of the water maximum. This eventually leads to very water-rich fluids spanning a large fO_2 range as shown by the 55 kbar curve. This trend is well illustrated by the composition of fluids at the water maximum as a function of pressure (Table 2.6A).

Table 2.6A Composition of fluids at x_{H_2O} = maximum as a function of pressure, T = 1400 K.

P/kbar	H_2O	CO_2	CO	H_2	CH_4	C_2H_6	log fO_2
2	36.4	16.6	16.3	13.1	17.6	0.1	-12.1
5	56.3	15.4	6.3	6.9	15.0	0.1	-11.4
15	88.4	4.8	0.5	1.9	4.4	0	-10.3
30	97.5	1.1	0	0.5	0.8	0	-9.2
55	99.6	0.1	0	0.1	0.1	0	-7.7

(b) Temperature variation: The effect of increasing temperature (Fig. 2.6B) again is to dramatically increase the stability of elemental carbon to much higher fO_2's. However in this case, the effect is accompanied by a decreasing width of the graphite "nose" and a move toward more carbon-rich fluids at the water maximum. Equilibria (a) and (b) move toward the right with increasing temperature as illustrated below:

Fig. 2.6A Pressure variation of the graphite saturation surface for T = 1400 K.

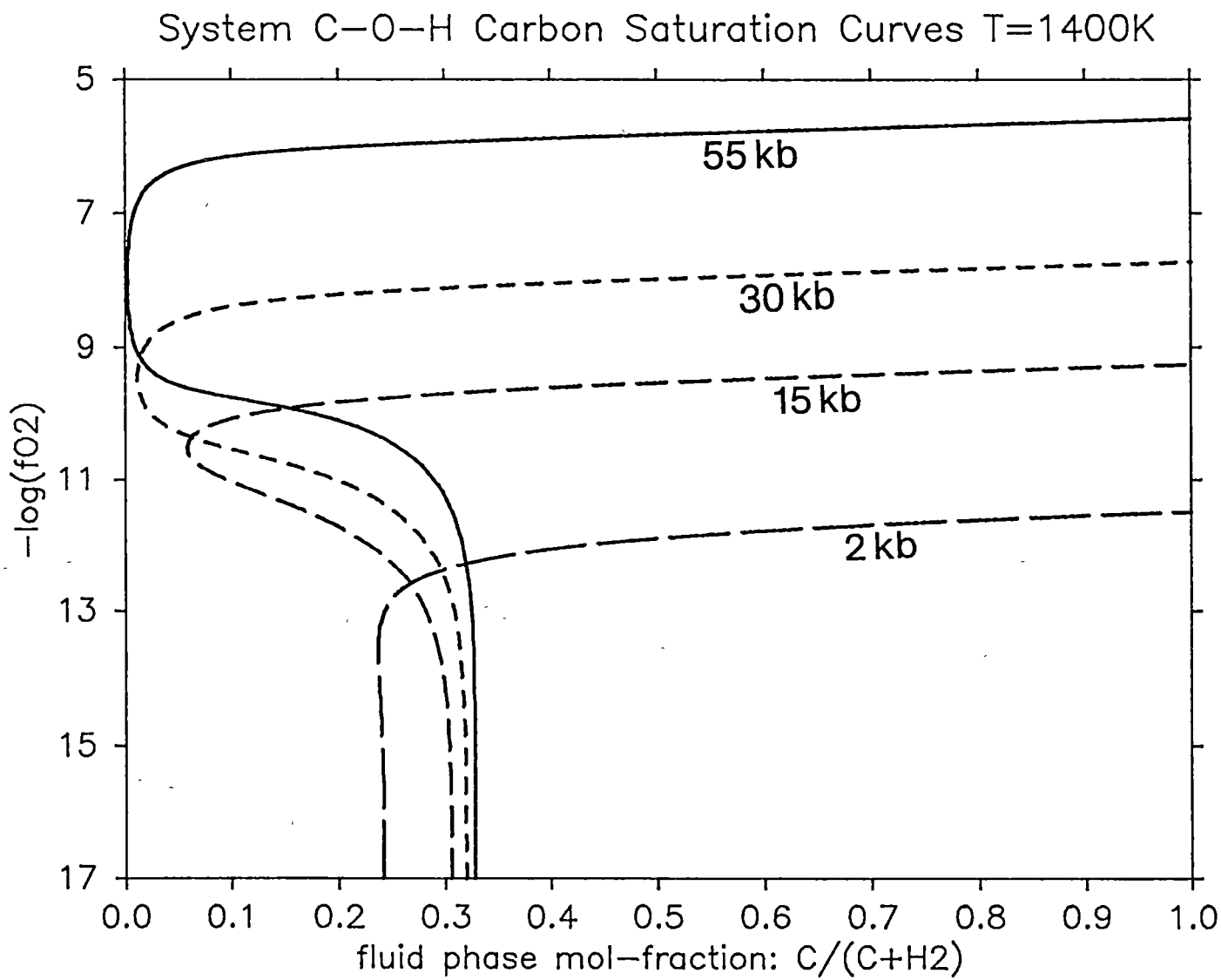
System C–O–H Carbon Saturation Curves T=1400K
5
7
9
11
13
15
17
−log(fO2)
55 kb
30 kb
15 kb
2 kb
0.0
0.1
0.2
0.3
0.4
0.5
0.6
0.7
0.8
0.9
1.0
fluid phase mol–fraction: C/(C+H2)

Fig. 2.6B Temperature variation of the graphite saturation surface for P = 30 kbar.

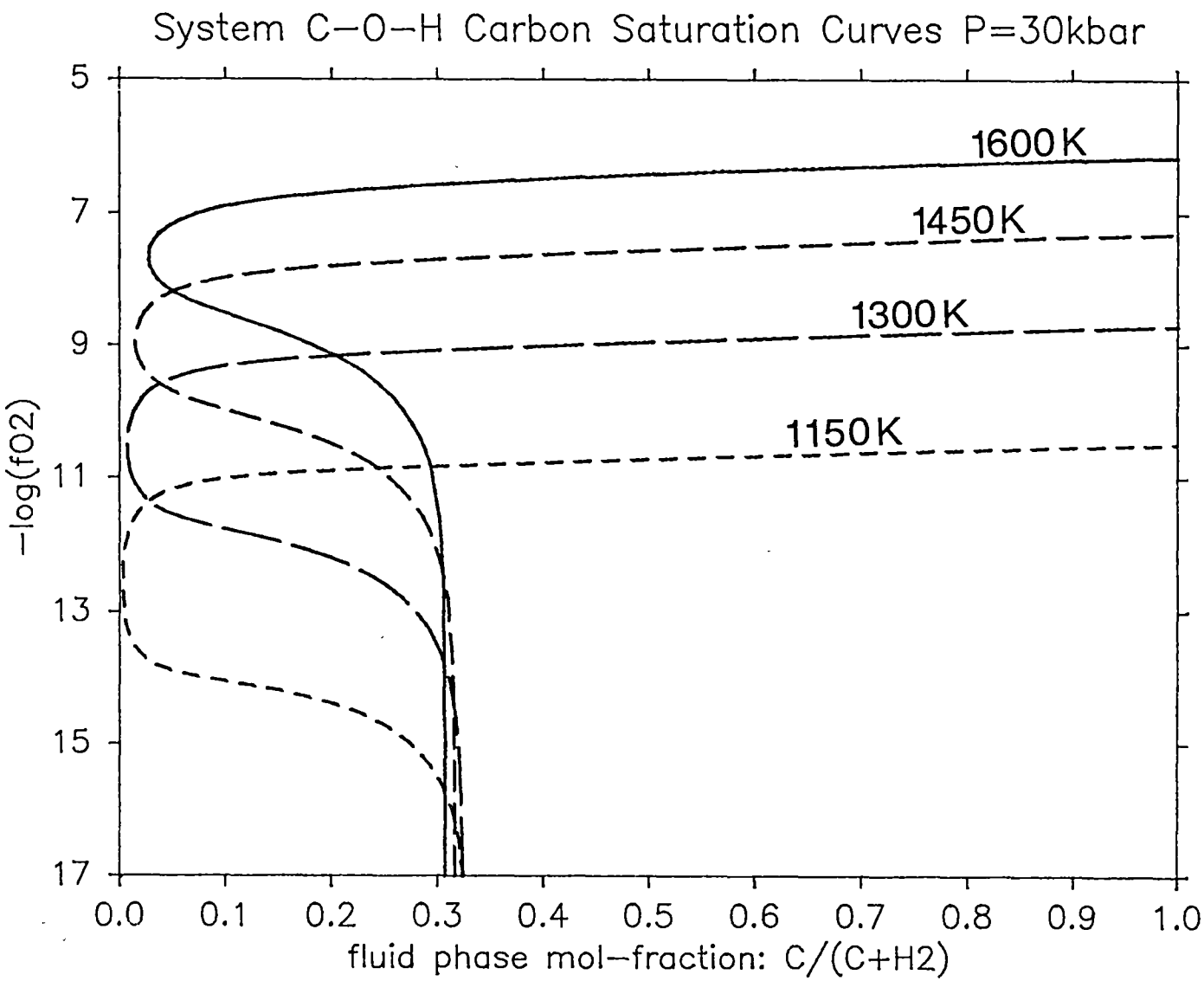
System C–O–H Carbon Saturation Curves P=30kbar
1600K
1450K
1300K
1150K
−log(fO2)
5
7
9
11
13
15
17
0.0
0.1
0.2
0.3
0.4
0.5
0.6
0.7
0.8
0.9
1.0
fluid phase mol–fraction: C/(C+H2)

Table 2.6B Composition of fluids at x_{H_2O} = maximum as a function of T , P = 30 kbar.

T/K	H_2O	CO_2	CO	H_2	CH_4	C_2H_6	log fO_2
1700	91.5	3.2	0.5	2.2	2.6	0	-6.7
1400	97.5	1.1	0	0.5	0.8	0	-9.2
1100	99.6	0.2	0	0.1	0.1	0	-13.1

2.7 Species Distribution along the Carbon Saturation Curve over the Range 2-50 kbar.

Diagrams at 1600 and 1400 K plotting log(x_i = mole fraction of species) vs pressure have been constructed over the pressure range 2-50 kbar at four fO_2's along the carbon saturation surface to illustrate the behaviour of the C-O-H volatiles as a function of P,T and fO_2. The diagrams are explained below.

(i) fO_2 = graphite-CO_2-CO (GCO) [Figs 2.7A and 2.7B]

Figs 2.7A and B correspond to the fluid composition at the X_C = 1 termination of the carbon saturation curve. Only the species CO_2 and CO are present and the governing equilibria are:

$$1.\quad C + O_2 = CO_2$$
$$2.\quad C + CO_2 = 2CO$$

Equilibrium (2) is dominant at low pressures and high temperatures as can be seen in Fig. 2.7B for 1600 K where x_{CO} exceeds x_{CO_2} at P < 3.5 kbar. At 1400 K x_{CO_2} is always larger than x_{CO}; CO reaches a level of ~30 mol% at 2 kbar. At pressures beyond ~30 kbar at 1400 K and ~45 kbar at 1600 K CO is not an important species (<1 mol%).

(ii) fO_2 = graphite-H_2O (maximum) [Figs 2.7C and 2.7D]

Fluid compositions correspond to those at the point on the carbon saturation curve where x_{H_2O} reaches a maximum. As discussed in Section 2.6 the dominant phase equilibria are:

$$C + H_2O = H_2 + CO \quad \text{(favoured by low P, high T)}$$
$$\text{and } 2C + 2H_2O = CO_2 + CH_4 \quad \text{(favoured by high P, low T)}$$

in addition two other equilibria can relate minor phases:

$$C + 2H_2O = CO_2 + 2H_2 \quad \text{(favoured by high P)}$$
$$\text{and } 7/2\ C + 3H_2O = 3/2\ CO_2 + C_2H_6 \quad \text{(favoured by high T, low P)}$$

Figs 2.7A to 2.7H Isothermal (T = 1400 K and T = 1600 K) log(x_i = mole fraction of species) versus pressure (range: 2-50 kbar) diagrams at various fO_2 conditions on the graphite saturation curve.

A, B fO_2 = GCO; C, D fO_2 = GW; E, F fO_2 = IW;
G,H fO_2 = MOEG

——— H_2O; —— —— CO_2; —·—·— CO;
— — — H_2; - - - - - CH_4; -·-·-·-·- C_2H_6.

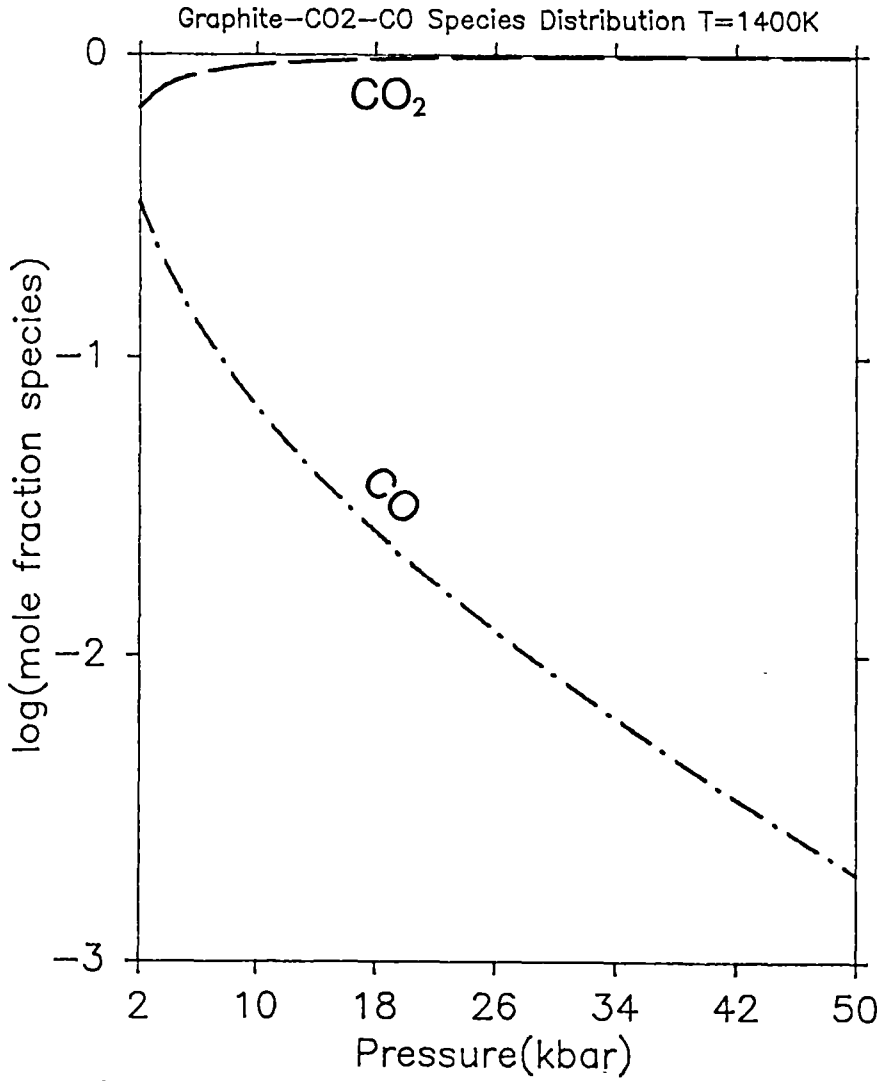
Graphite–CO2–CO Species Distribution T=1400K
0
−1
−2
−3
log(mole fraction species)
CO_2
CO
2
10
18
26
34
42
50
Pressure(kbar)

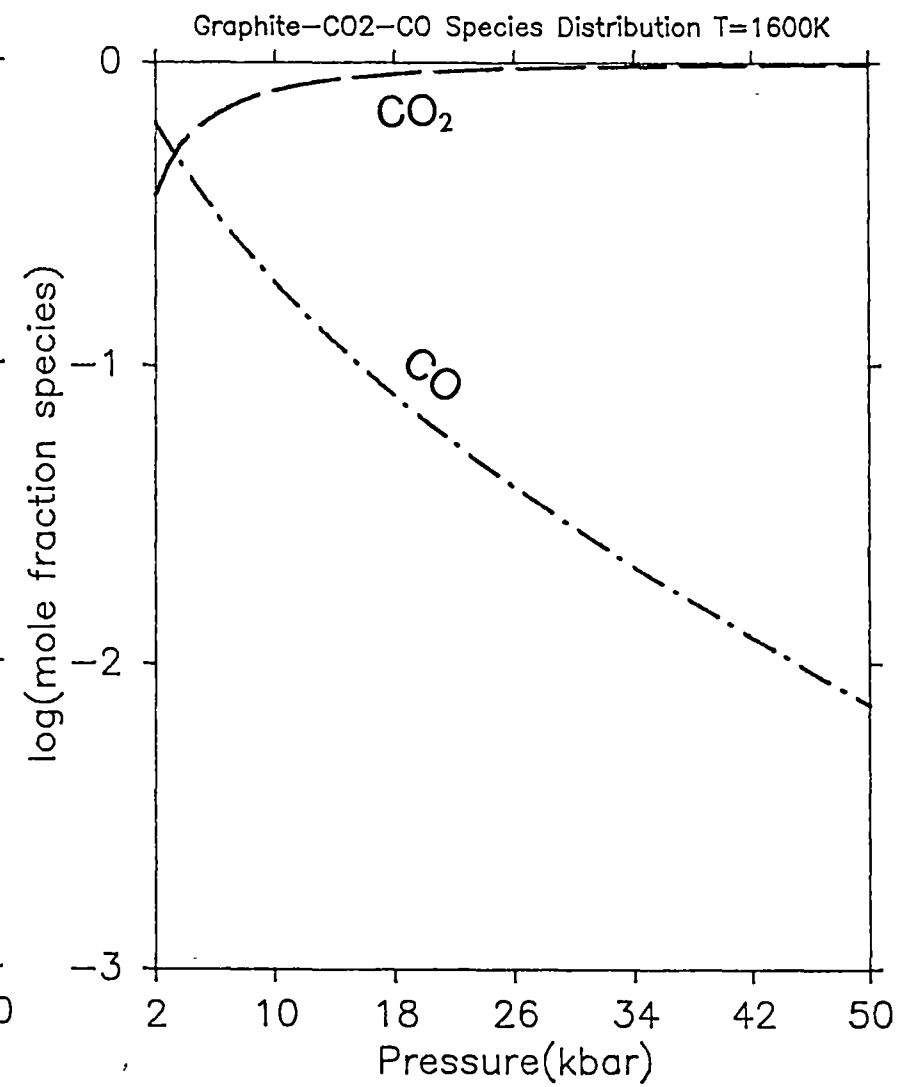
Graphite–CO2–CO Species Distribution T=1600K
0
−1
−2
−3
log(mole fraction species)
CO_2
CO
2
10
18
26
34
42
50
Pressure(kbar)

Figs 2.7A & B

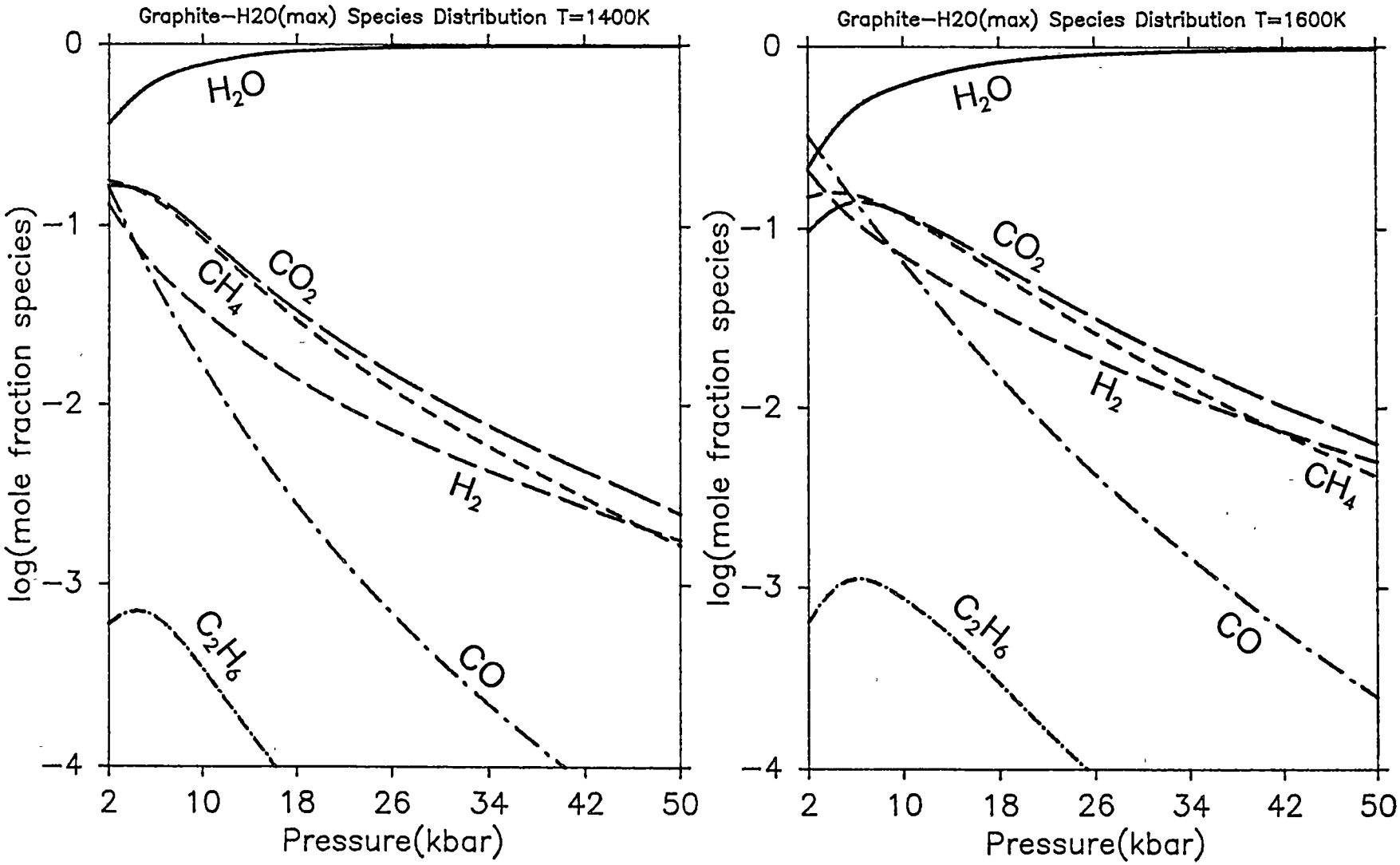
Graphite–H2O(max) Species Distribution T=1400K
log(mole fraction species)
0
−1
−2
−3
−4
H2O
CO2
CH4
H2
C2H6
CO
2
10
18
26
34
42
50
Pressure(kbar)
Graphite–H2O(max) Species Distribution T=1600K
log(mole fraction species)
0
−1
−2
−3
−4
H2O
CO2
H2
CH4
C2H6
CO
2
10
18
26
34
42
50
Pressure(kbar)

Figs 2.7C & D

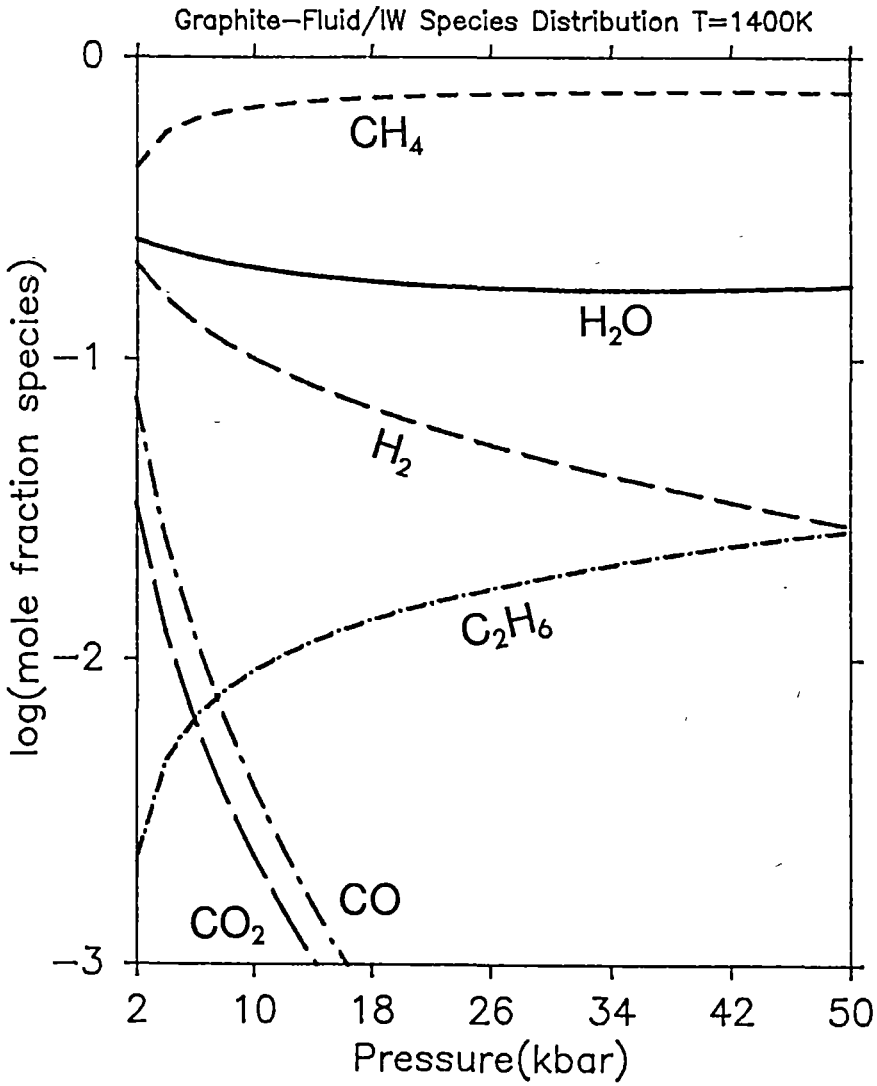
Graphite–Fluid/IW Species Distribution T=1400K
log(mole fraction species)
0
−1
−2
−3
CH4
H2O
H2
C2H6
CO
CO2
2
10
18
26
34
42
50
Pressure(kbar)

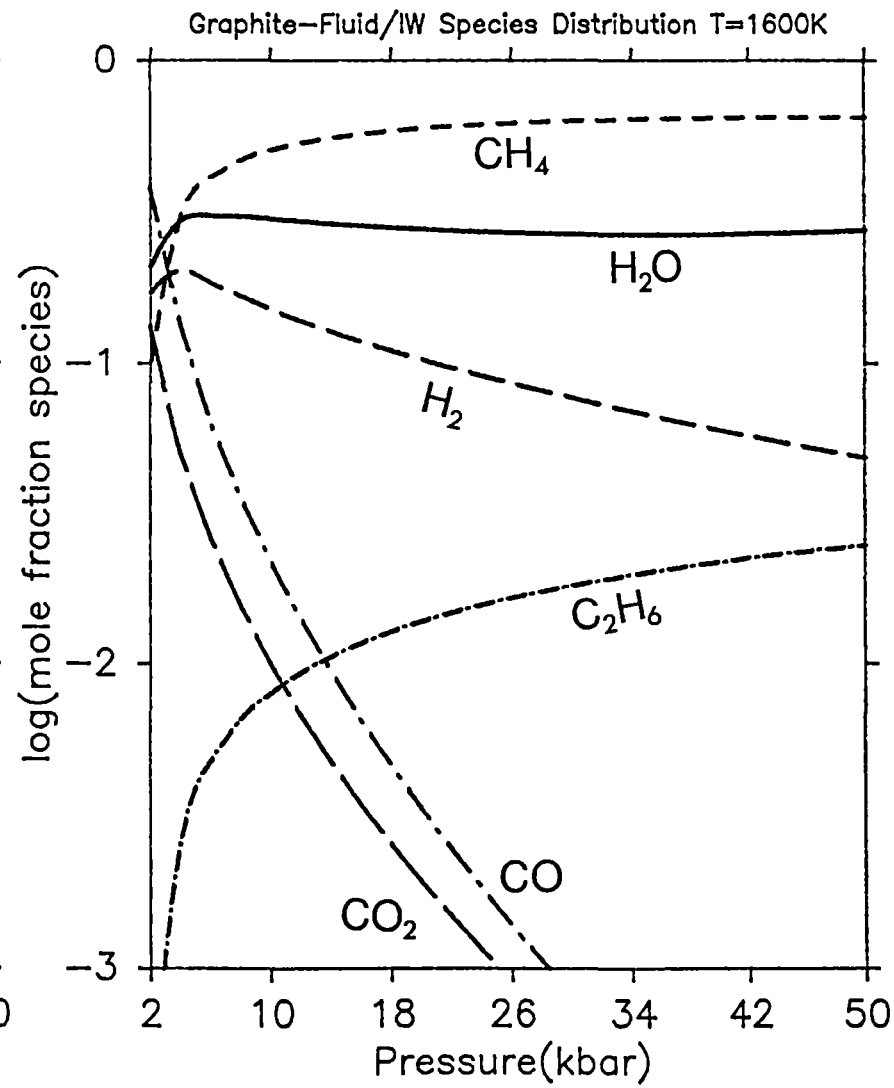
Graphite–Fluid/IW Species Distribution T=1600K
log(mole fraction species)
0
−1
−2
−3
CH4
H2O
H2
C2H6
CO
CO2
2
10
18
26
34
42
50
Pressure(kbar)

Figs 2.7E & F

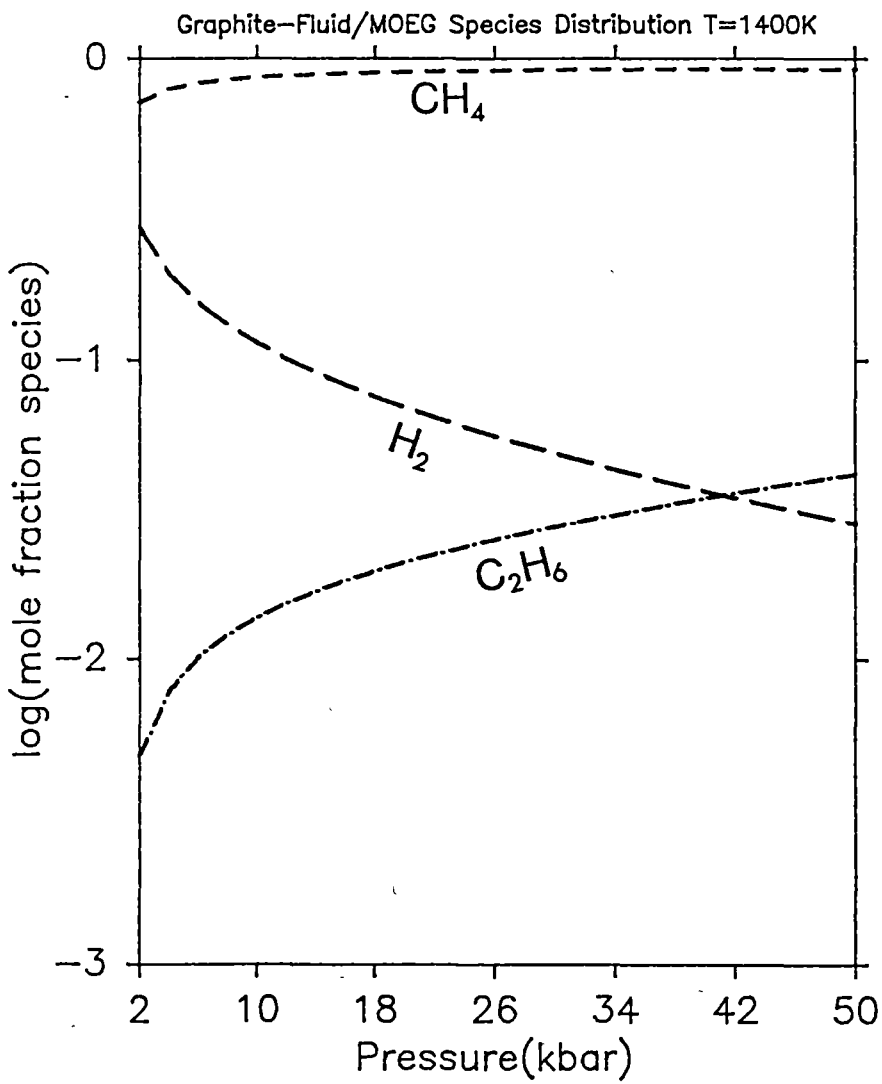
Graphite–Fluid/MOEG Species Distribution T=1400K
0
−1
−2
−3
log(mole fraction species)
CH_4
H_2
C_2H_6
2
10
18
26
34
42
50
Pressure(kbar)

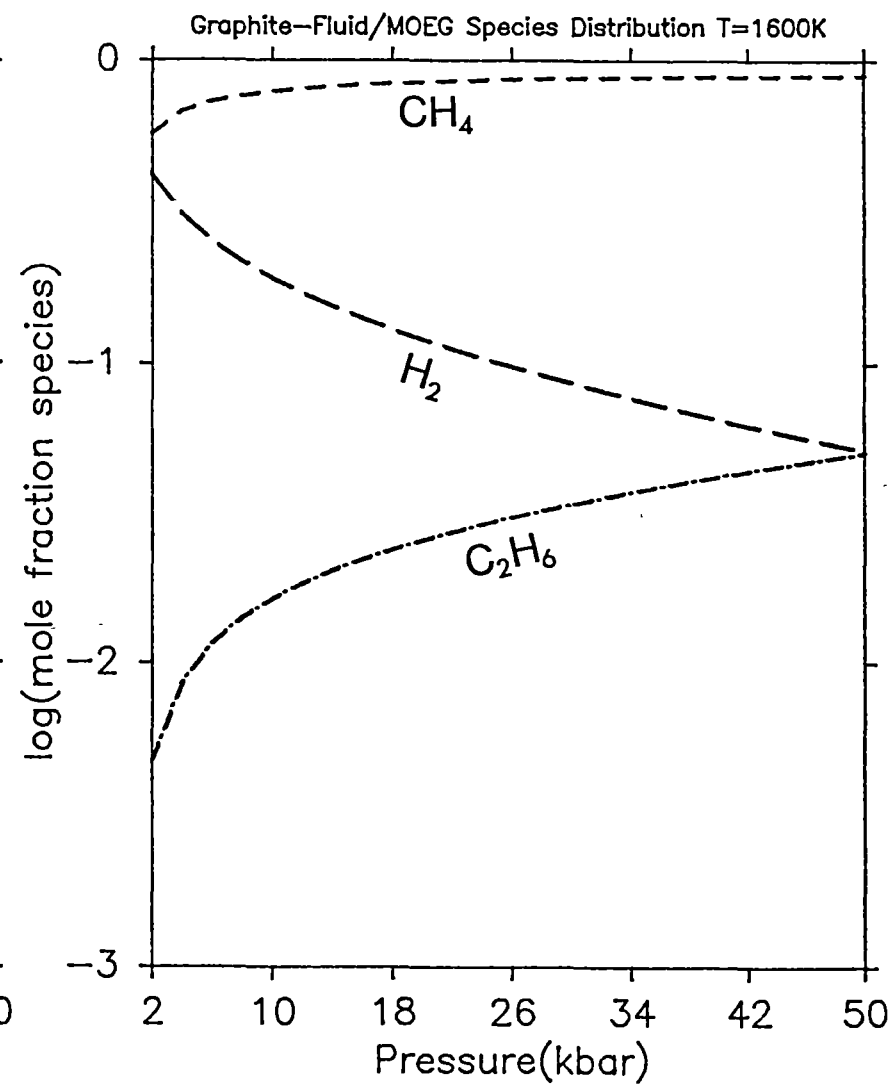
Graphite–Fluid/MOEG Species Distribution T=1600K
0
−1
−2
−3
log(mole fraction species)
CH_4
H_2
C_2H_6
2
10
18
26
34
42
50
Pressure(kbar)

Figs 2.7G & H

as indicated by the relative changes in slopes of the log x_i curves, with increasing pressure.

(iii) fO_2= iron-wustite (IW) [Figs 2.7E and 2.7F]

Fluid compositions correspond to those at the intersection of the carbon saturation curve and the synthetic IW buffer. Because oxide fO_2 buffers such as IW show much less variation with P than those involving graphite it is not appropriate in this case to relate the species distribution to governing internal equilibria. However the following features may be noted for C-O-H systems buffered at IW:

(a) At P < 3 kbar at 1600 K, CO is the dominant species. CO is replaced by H_2O then CH_4 as pressure increases. Above 15 kbar the proportion of CO drops to <1 mol%.

(b) At P > 10 kbar, T = 1600 K fluids are CH_4 > H_2O mixtures with H_2 and C_2H_6 as minor components. $x_{C_2H_6}$ increases with P at the expense of H_2.

(c) At 1400 K, CO or CO_2 are unimportant above 2 kbar and fluids are CH_4> H_2O mixtures over the full P range.

(iv) fO_2 = α-SiC-Mg_2SiO_4-$MgSiO_3$-C (MOEG) [Figs 2.7G and 2.7H]

Under the extremely reduced conditions of equilibration with α-SiC (fO_2 ~ 6-7 log units below IW at 1400-1600 K, 30 kbar) fluids are dominated by CH_4 with H_2 important at low pressures and C_2H_6 at high pressures. C_2H_6 reaches levels of ~5 mol% at 50 kbar, 1600 K.

2.8 Graphite-Fluid and Diamond-Fluid fO_2 Buffer Curves: their relation to oxide buffers and some experimental constraints.

Oxygen fugacity is buffered in the system C-O by the coexistence of graphite or diamond and a fluid phase containing CO_2 and CO. This buffer, commonly abbreviated CCO and here designated GCO for graphite-C-O and DCO for diamond-C-O, is often used in experimental studies. It has been calculated as a function of P,T and fO_2 by French & Eugster (1965) using values of $\phi^{\circ}_{CO_2}$ and ϕ°_{CO} from sources then available; ideal mixing between CO_2 and CO was assumed. The approximate equation of French & Eugster, based on the assumption that P_{CO_2} = fCO_2 = P_{fluid}, reproduces values of log fO_2 over the range 0.1-2 kbar, 500-1200 K that agree satisfactorily with their initial non-ideal treatment. Beyond 2 kbar the equation is untested. More recently, Woermann et al. (1977) have examined, experimentally, the

intersection of the FMQ (fayalite-magnetite-quartz) and MW (magnetite-wustite) buffers with GCO to 27 kbar:

FMQ-GCO $3SiO_2 + 2Fe_3O_4 + C = 3Fe_2SiO_4 + CO_2$ ...(2.8A)

MW-GCO $2Fe_3O_4 + C = 6\text{"}FeO\text{"} + CO_2$ ...(2.8B)

These curves represent univariant equilibria that plot as lines in P,T-space. From their experimental results Woermann et al. (1977) suggested that GCO lies between the ideal equation of French & Eugster (1965) and calculations employing MRK coefficients derived by Holloway (1977). However, few experimental details were given and equilibrium has not been demonstrated by run reversals. In addition, the assemblage Qtz+Fayalite is unstable with respect to ferrosilite ($FeSiO_3$) above about 16 kbar at 1000°C (Lindsley et al., 1968) making the determined FMQ-CCO curve to 27 kbar somewhat suspect.

As part of this study, the GCO curve was recalculated using 5PRMK fugacity coefficients; there was no assumption of ideal mixing. An equation of the form:

$$\log (fO_2/\text{bar}) = a + b \ln T + c/T + d(P/T) + e(P/T)^2 \quad \ldots (2.8C)$$

with P/bar and T/K

was found to provide a good fit to the calculated P-T-fO_2 data with a multiple regression coefficient exceeding 0.999. Oxygen fugacities generally reproduced those calculated to better than ± 0.1 log fO_2 units over the range 5-50 kbar, 800-1700 K. Fitted parameters and statistics are listed in Table 2.8. The water maximum point (x_{H_2O} = maximum) on the C-O-H carbon saturation curve also proved amenable to description in P-T-fO_2 space by equation (2.8C). This curve represents the fO_2 of graphite (or at higher pressures, diamond) in equilibrium with a water-rich fluid and as illustrated by Figs 2.6A and 2.6B lies below GCO (or DCO) by ~1-3 log fO_2 units. Just as CCO is an fO_2-buffer if carbon is equilibrated with an initial CO_2 vapour, so too is the system carbon + initial H_2O fluid which at equilibrium corresponds to the x_{H_2O} maximum on the carbon saturation curve. The locus of these points in P-T-fO_2 space defines the graphite- or diamond-water (maximum) buffers (abbreviated GW or DW respectively). GW was calculated by searching iteratively for the (P,T,fO_2) coordinates of maximum x_{H_2O} fluids along the carbon saturation surface using a modified version of program COH/GRAPHITE6. The resultant points were fitted to equation (2.8C) with program FUNFIT and both parameters and fit statistics are listed in Table 2.8.

Table 2.8 Equations for graphite buffer curves.*

	a	b	c	d	e
GCO	2.0815	0.25754	-21060	0.17112	-7.4268×10^{-4}
GW	5.0186	-6.5844×10^{-2}	-22674	0.12858	-6.6384×10^{-4}

Fit Statistics	R	MPD**
GCO	0.999710	0.82%
GW	0.999725	0.66%

* applicable over the range 5-50 kbar, 800-1700 K.

** MPD = mean percent deviation

$$= \sum \left[100 * \left| \log fO_{2\ calc} - \log fO_{2\ fit} \right| / \log fO_{2\ fit} \right] \Big/ n$$

where n = number of data points.

GW appears to be a useful approximation for the "furnace-buffered" fO_2 condition in solid-media high pressure apparatus employing talc + graphite sleeved assemblies. Talc undergoes dehydration at no more than 800°C for all pressures (Helgeson et al., 1978) and in the presence of graphite, fluids will always be close to the water maximum (see also Section 4.7). It must be emphasised that talc + graphite assemblies alone cannot buffer fO_2 within an encapsulated sample at GW since the system (assembly + encapsulated sample) is an open one and compositional gradients will exist particularly in H_2 which readily diffuses through Pt and other noble metals. Fig. 2.8A illustrates the T-fO_2 behaviour of graphite and other relevant fO_2 buffers at 30 kbar; T-fO_2 equations are taken largely from Schwab & Kustner (1981) and are tabulated together with appropriate pressure corrections in Appendix 9. Both GCO and GW have steeper dT/d(log fO_2) slopes at any one T than typical oxide or silicate buffers. GW lies between IW and MW at T > 1000°C and between EMOG (Eggler & Baker, 1982) and MW at lower T; GCO lies ~1.5 log fO_2 units higher. A feature of the diagram is the shallow angle intersection between the graphite buffers and MW or NNO (Ni-NiO). This may lead to a large uncertainty in the calculated position of the univariant intersection curve for only a small error in fO_2 of either participating fO_2-buffer reaction. This problem is well

Fig. 2.8A Oxygen buffer curves as a function of T and log fO_2 at 30 kbar.

MOEG Moissanite/forsterite/enstatite/graphite (stability limit of SiC in Fe-free peridotite)

OIE-2 Olivine/iron/enstatite, x_{Fe} = 0.1 (approx. T-fO_2 limit of metallic iron in peridotite assemblages)

IW Iron/wustite

MW Magnetite/wustite

GW Graphite-water (x_{H_2O} =maximum)

GCO Graphite-CO_2-CO

EMOG Enstatite/magnesite/forsterite/graphite [calculated termination at ~1240°C where intersection of enstatite/magnetite/forsterite/vapour equilibrium (EMOV) with GCO occurs].

NNO Nickel/nickel oxide

HM Hematite/magnetite.

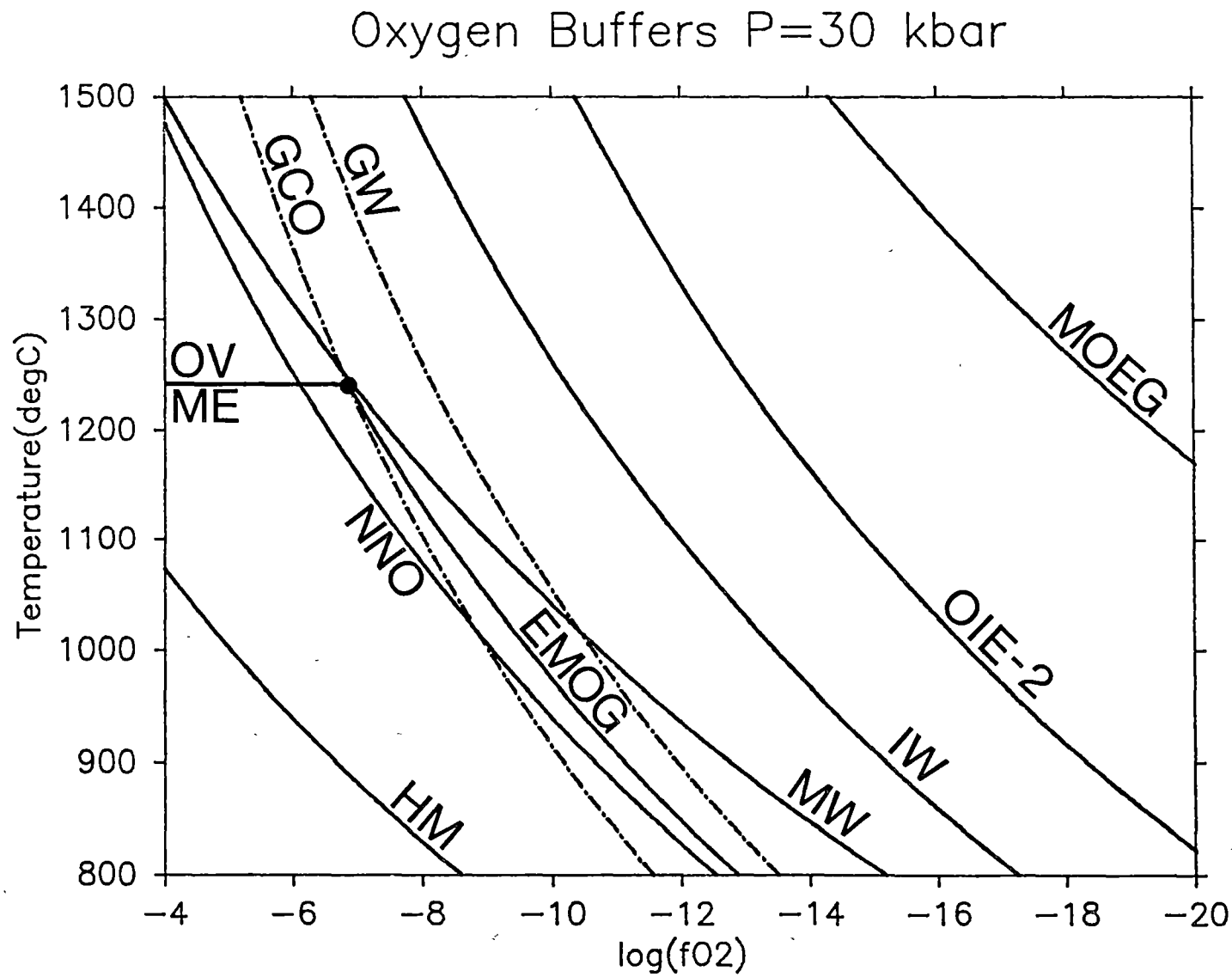
Oxygen Buffers P=30 kbar
Temperature(degC)
log(fO2)
1500
1400
1300
1200
1100
1000
900
800
−4
−6
−8
−10
−12
−14
−16
−18
−20
GCO
GW
OV
ME
NNO
EMOG
HM
MW
IW
OIE-2
MOEG

illustrated by Fig. 2.8B in which the univariant reactions GCO-MW and GCO-NNO ($2NiO + C = 2Ni + CO_2$) have been plotted assuming maximum errors of ± 0.2 log fO_2 units in both curves.

A series of high pressure experiments were carried out in piston cylinder apparatus to confirm the position of the GCO-MW intersection as given by Woermann et al. (1977) and to determine the accuracy of the calculated GCO curve which employs 5PMRK fugacity coefficients. Full experimental details are given in Appendix 10 and will be only briefly summarised here. Starting materials were either hematite + graphite or wustite + siderite + graphite mixtures. In the former case hematite reacts with graphite to give an initial product of magnetite + C-O vapour and in the latter case siderate acts as the source of CO_2/CO by a breakdown reaction occurring above ~740°C at 10 kbar and probably >800°C at 30 kbar (Weidner, 1972). Mixes were prepared with approximately equal volume fractions of components to ensure sufficient grain-to-grain contact for rapid reaction. These were loaded into graphite capsules, dried at 110°C then sealed in 3.56 mm O.D. Pt or $Ag_{50}Pd_{50}$ capsules. In order to minimise H_2 diffusion, run assemblies consisted of combination outer talc/inner pyrex sleeves. Run durations were typically 3-9.5 hours depending on temperature; two higher T runs were of 24 hours duration in an attempt to achieve complete reaction.

Results are presented diagramatically in Fig. 2.8B together with the results of Thompson & Kushiro (1972) and the invariant GCO-MW-EMOG intersection point of Eggler et al. (1980). (The latter data is presented in abstract form only with claimed reversals of experimental runs, however see later for problems.) The data points of Woermann et al. (1977) are omitted for clarity but their interpreted univariant line passes close to the wustite-in points of this study except at 30 kbar where their line passes some 50°C below. As is evident from the arrows indicating reaction direction (Fig. 2.8B, this study), the univariant reaction could not be reversed satisfactorily due to the persistence of the assemblage magnetite + wustite + graphite + vapour over a large T-range at all pressures. This feature was also noted by Thompson & Kushiro (1972) whose points are consistent with those determined here despite much shorter run times: 2 hours (950°C) to 15 min (1600°C). It is not clear whether the univariant curve should correspond to the set of wustite-in or the set of magnetite-out data points. In the former case, metastable persistence of magnetite, presumably due to sluggish reaction kinetics, is suggested. While in the latter case metastable growth of wustite would be required. Unfortunately

Fig. 2.8B Univariant MW-GCO and NNO-GCO fO_2 buffer intersections. Dashed lines = calculated P,T envelope of intersection using ± 0.2 log fO_2 unit error brackets on both oxide and GCO equilibria.

MW-GCO

This work:

- ● magnetite + graphite + V
- ◔ wustite + magnetite + graphite + V
- » wustite formation from initial hematite/graphite mix
- « magnetite formation from initial wustite/siderite/graphite mix.

Thompson & Kushiro (1972):

- □ wustite
- ◪ wustite + magnetite
- ■ magnetite

Eggler et al. (1980):

- ⊠ multiple intersection point MW-GCO-EMOG

NNO-GCO

Woermann et al. (1982):

- ○ Ni formation) a number of points omitted for
- ● Ni absent) clarity.

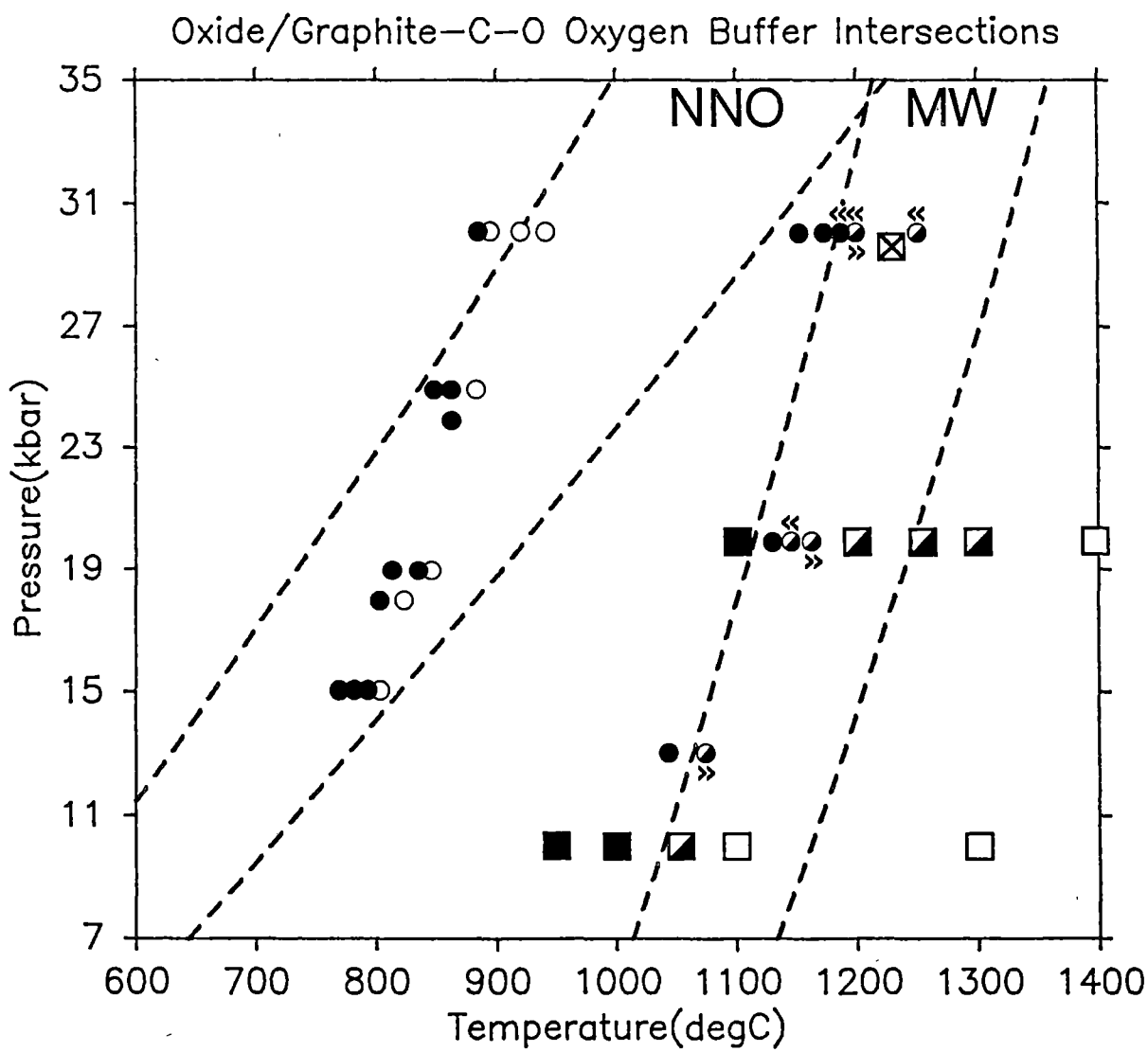
Oxide/Graphite–C–O Oxygen Buffer Intersections
NNO
MW
Pressure(kbar)
35
31
27
23
19
15
11
7
600
700
800
900
1000
1100
1200
1300
1400
Temperature(degC)

none of the processes by themselves agrees well with the experimental data. For example, at 30 kbar, 1200°C two experiments were performed of 3 hours and 24 hours duration respectively. Both gave coexisting wustite + magnetite assemblages. The greater proportion of wustite, however, was present in the shorter duration run which also started with an initial hematite/graphite mix whereas the reverse should apply for a kinetic argument. Choice of the magnetite-out curve based on the Kushiro & Thompson data results in a shallow dP/dT slope passing well beyond the invariant point as determined by Eggler et al. (1980) and in disagreement with the calculated slope of the MW-GCO intersection at any temperature.

There is an additional complication in interpretation of the experiments if H_2 diffusion into the capsule from breakdown of talc is significant. This may very well be a time dependent process and could result in dilution of or reaction with the vapour phase, e.g.

$$H_2 + CO_2 = H_2O + CO$$

which subsequently must re-equilibrate with graphite by reduction of magnetite; the GCO buffer in effect begins to migrate towards GW giving an apparent lower temperature intersection (cf. Fig. 2.8A). If this is an important process the true MW-GCO intersection will occur at temperatures ~50-100°C higher than the first appareance of wustite. The dP/dT slope of the wustite-in curve determined experimentally is similar to that of the calculated curve. However, the experimental data contains ambiguities and cannot in themselves define the curve for GCO-MW intersection; Fig. 2.8B is consistent with this suggestion.

Problems also arise in the calculation of MW since the stoichiometry of wustite changes markedly with P,T and fO_2 (Shen et al., 1983). In this study, wustite compositions determined by powder diffractometry along the MW-GCO intersection lie between $Fe_{0.91}O$ and $Fe_{0.93}O$ while wustites along the calibrated MW curve at 1 atm (taken from Schwab & Kustner, 1981) vary from $Fe_{0.88}O$ at 1000°C to $Fe_{0.85}O$ at 1300°C (Darken & Gurry, 1945). The MW T-fO_2 curve for observed wustite compositions at high pressures will thus be displaced to lower fO_2's for a given T and hence the MW-GCO intersection for the observed wustite compositions should theoretically lie at higher temperatures than the calculated curve (Figs 2.8A and 2.8B).

Despite the difficulties in the interpretation of the results, available experimental data (Thompson & Kushiro, 1972; Eggler et al., 1980; Woermann et al., 1977) are qualitatively consistent with the calculated MW-

GCO intersection envelope to $\pm$0.2 log fO_2 units. The shallow angle of MW-GCO intersection in T-fO_2 space combined with uncertainty in the position of the MW curve at high pressure does not allow calculation of the univariant reaction to better than a ~120°C range in temperature. In this regard, the conclusion of Woermann et al. (1977) that GCO lies at lower fO_2's than those calculated with MRK ϕ_{CO_2} and ϕ_{CO} values is not substantiated. The GCO equilibrium equation of Woermann et al. (1977) assumes that all the deviation lies with the non-ideality of the CO_2-CO phase. However, MW itself is not accurately known to high pressure. Woermann et al.'s GCO equation, as seen below, is lower by 0.5-1.0 log fO_2 units than the calculated GCO employing 5PMRK fugacity coefficients.

Table 2.8A Comparison of graphite-CO_2-CO fO_2 buffer equations.

	GCO (5PMRK coefficients)	CCO (Woermann et al.)
15 kbar 1400 K	-9.4	-9.8
1600 K	-7.6	-8.3
30 kbar 1400 K	-7.8	-8.4
1600 K	-6.2	-7.0

Recently, the NNO-GCO univariant intersection was determined by Woermann et al. (1982) using a solid electrolyte cell at high pressure as an oxygen specific membrane to separate the Ni-O and C-O subsystems. The calculated NNO-GCO intersection to $\pm$0.2 log fO_2 units is presented in Fig. 2.8B; the width of the envelope is much greater than MW-GCO (covering a range up to ~200°C) as is expected from the even shallower angle of intersection in T-fO_2 space (Fig. 2.8A). The data points in Fig. 2.8B that delineate the experimental univariant curve correspond to the incoming of Ni metal. As with MW-GCO complete reaction giving 100% reduced component near the boundary was not achieved and equilibrium has therefore not been demonstrated. Except for the 30 kbar point, the Ni-in curve falls within the $\pm$0.2 log unit uncertainty limits. The dP/dT slope however corresponds poorly with that calculated and unlike MW-GCO it appears there are either experimental difficulties with the solid electrolyte technique at high pressure or the position of NNO in P-T-fO_2 space is not known with sufficient accuracy. Since the MW-GCO dP/dT slope is close to that

predicted there is no evidence to suggest that the steep NNO-GCO gradient is a result of a significant error in the calculated position of GCO.

At this stage it appears that the experimental determination of univariant fO_2 buffer intersections involving graphite + C-O fluid is able to provide only qualitative or at best semi-quantitative comparisons. There are a number of experimental difficulties including the possibility of H_2 entry and sluggish reaction kinetics that have prevented the demonstration of reaction reversibility. For the theoretical calculations, any uncertainty in the T-fO_2 position of the buffer curves is magnified into large error brackets in the calculated univariant reaction P,T location. Unless there are improvements in experimental technique, there is little value in this type of experimentation to obtain quantitative thermodynamic information.

2.9 Species Distribution in the Pseudo-divariant and Metastable Regions over the Range 2-50 kbar.

A series of diagrams (Figs 2.9A to 2.9F) at 1400 K plotting log (x_i = mole fraction species) vs pressure have been constructed over the pressure range 2-50 kbar at fO_2's corresponding to the MW and IW synthetic buffers. Three sets of X_C values 0.1, 0.5 and 0.9 were chosen to cover a broad range of carbon contents spanning both stable and metastable pseudo-divariant fields. The diagrams illustrate C-O-H fluid species distribution as a function of P, X_C and fO_2:

(a) Low carbon contents, $X_C = 0.1$ [Fig. 2.9A, fO_2=MW; Fig. 2.9B, fO_2=IW]

At fO_2 = MW, H_2O is the dominant species over the full P-range and CO_2 is present at a level just below 10 mol%. H_2, CO and CH_4 are minor species. At fO_2 = IW, H_2O remains dominant while CH_4 replaces CO_2 as the principal C-bearing species. H_2 is an important component at low pressures reaching as much as 50 mol% at 2 kbar. CO_2, CO and C_2H_6 are all minor or trace species. From fO_2 = MW to fO_2 = IW, C-O-H species at X_C = 0.1 change from H_2O-CO_2 to H_2O-CH_4-H_2 mixtures.

(b) Intermediate carbon contents, $X_C = 0.5$ [Fig 2.9C, fO_2=MW; Fig. 2.9D, fO_2=IW]

At fO_2 = MW, fluids closely approximate 50-50 H_2O-CO_2 mixtures over the full P-range. CO, H_2 (at low P) and CH_4 (high P) are minor species.

Figs 2.9A to 2.9F Isothermal (T = 1400 K) log(x_i = mole fraction species) versus pressure (range: 2-50 kbar) diagrams at fO_2 = MW and fO_2 = IW for various fluid X_C values in the stable and metastable divariant fields.

A, B X_C = 0.1; C, D X_C = 0.5; E,F X_C = 0.9;

——— H_2O; — — CO_2; — · — · CO;

— — — H_2; - - - - - CH_4; —·—·—·— C_2H_6.

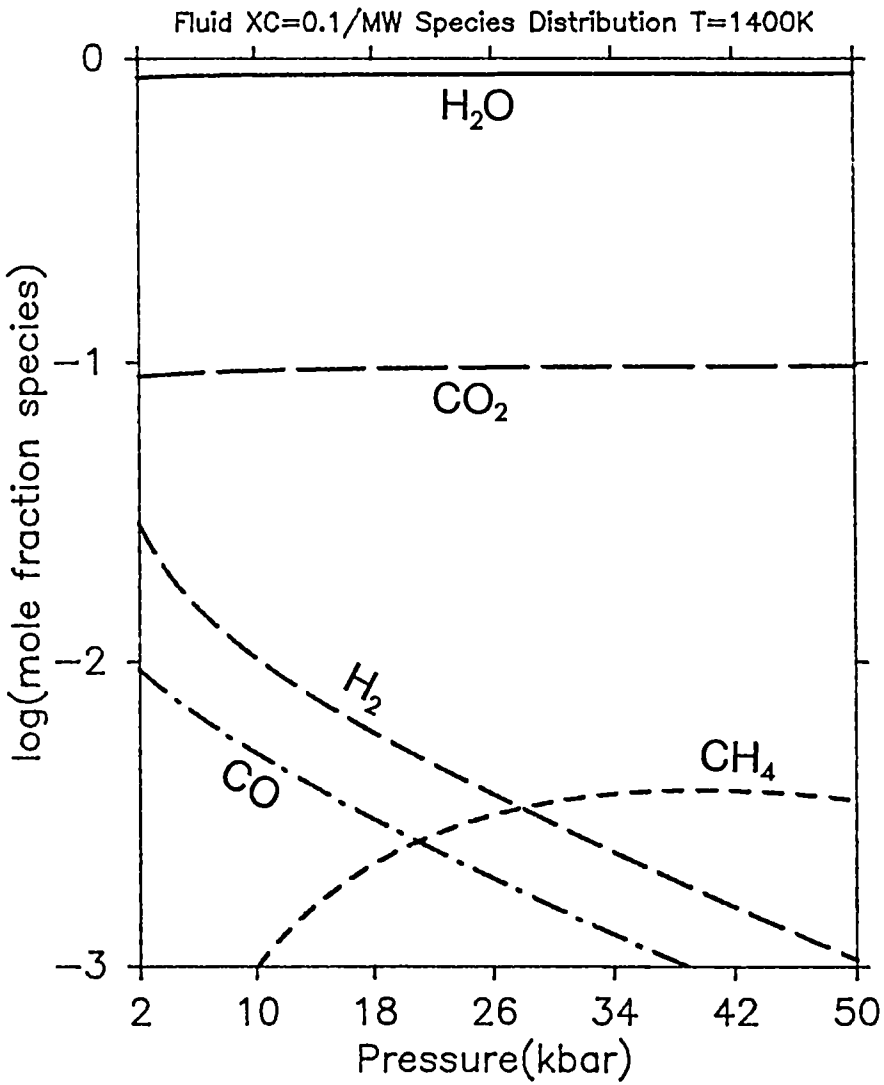
Fluid XC=0.1/MW Species Distribution T=1400K
log(mole fraction species)
0
−1
−2
−3
H_2O
CO_2
H_2
CH_4
CO
2
10
18
26
34
42
50
Pressure(kbar)

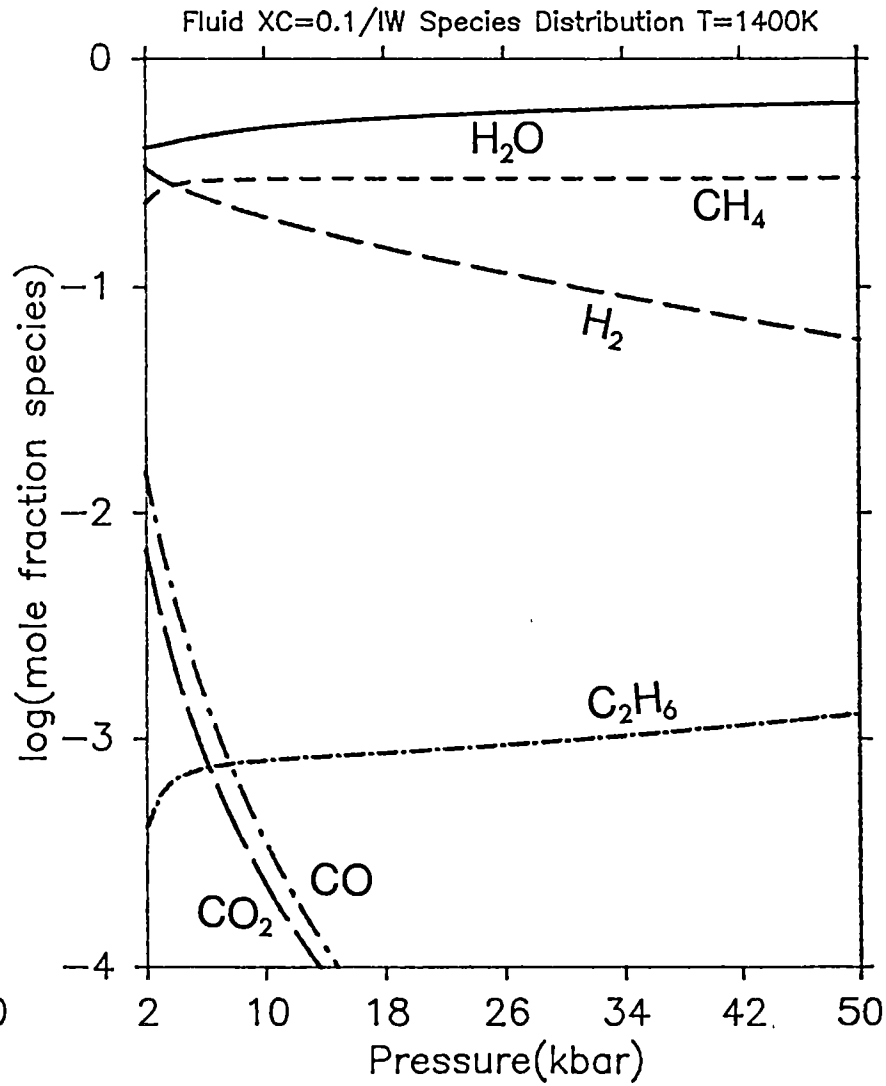
Fluid XC=0.1/IW Species Distribution T=1400K
log(mole fraction species)
0
−1
−2
−3
−4
H_2O
CH_4
H_2
C_2H_6
CO
CO_2
2
10
18
26
34
42
50
Pressure(kbar)

Figs 2.9A & B

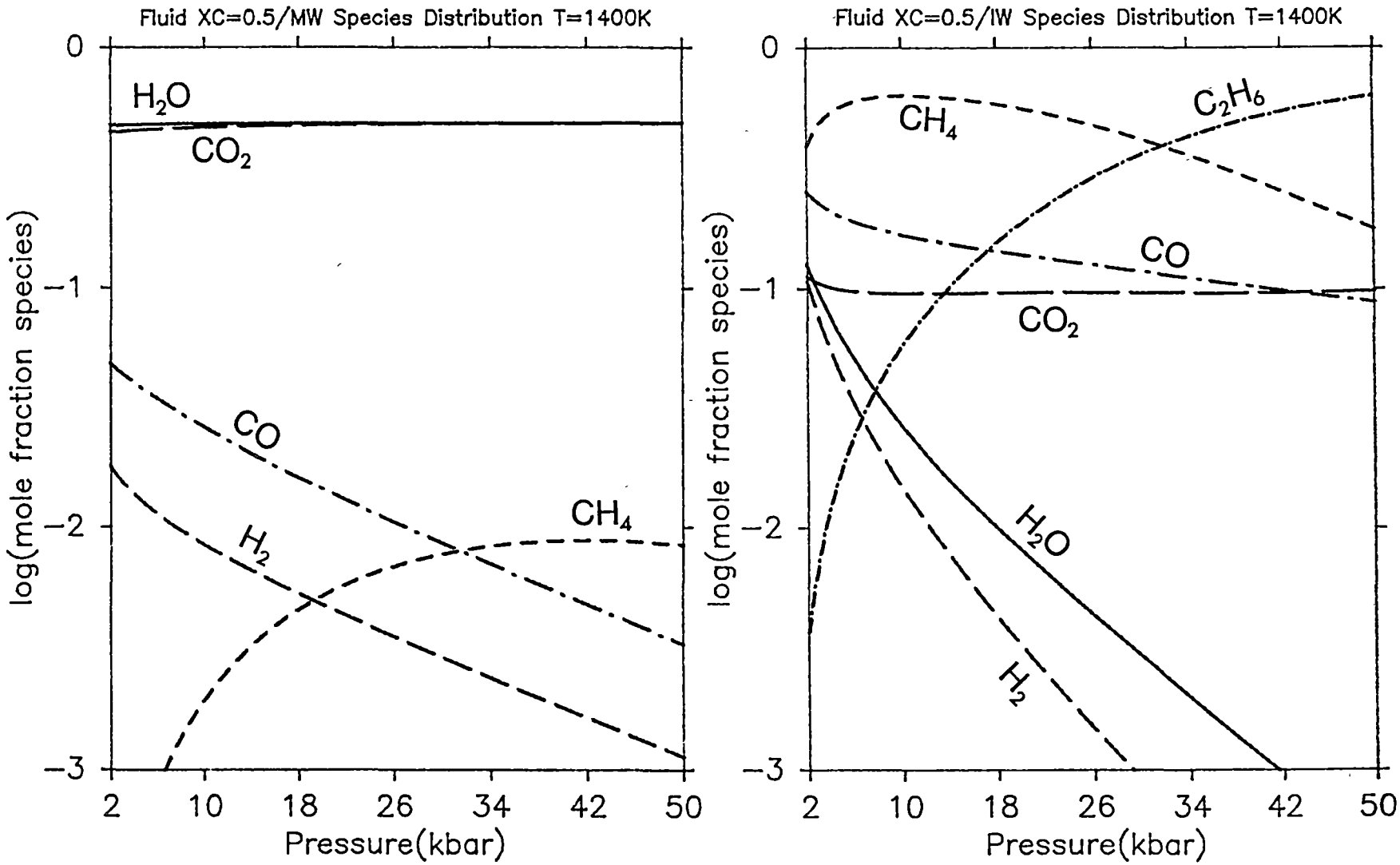
Fluid XC=0.5/MW Species Distribution T=1400K
log(mole fraction species)
0
−1
−2
−3
H_2O
CO_2
CO
CH_4
H_2
2
10
18
26
34
42
50
Pressure(kbar)
Fluid XC=0.5/IW Species Distribution T=1400K
log(mole fraction species)
0
−1
−2
−3
CH_4
C_2H_6
CO
CO_2
H_2O
H_2
2
10
18
26
34
42
50
Pressure(kbar)

Figs 2.9C & D

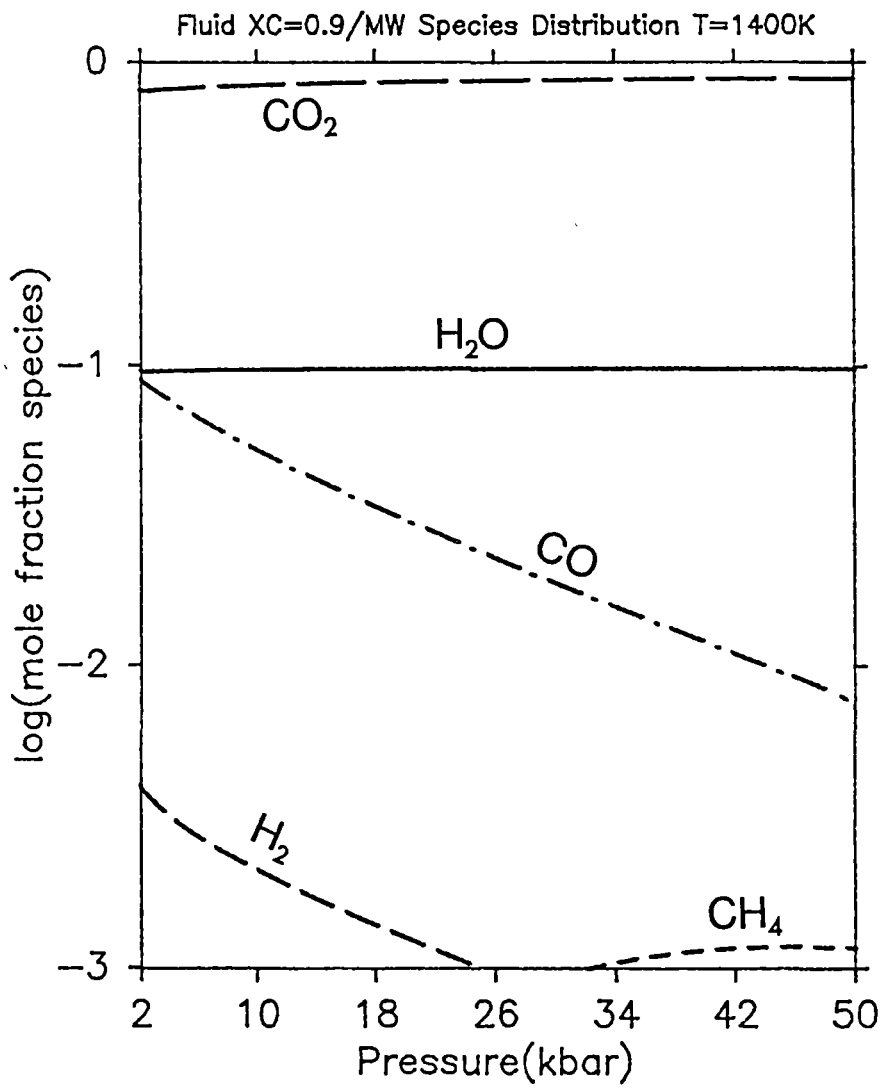
Fluid XC=0.9/MW Species Distribution T=1400K
log(mole fraction species)
0
−1
−2
−3
CO_2
H_2O
CO
H_2
CH_4
2
10
18
26
34
42
50
Pressure(kbar)

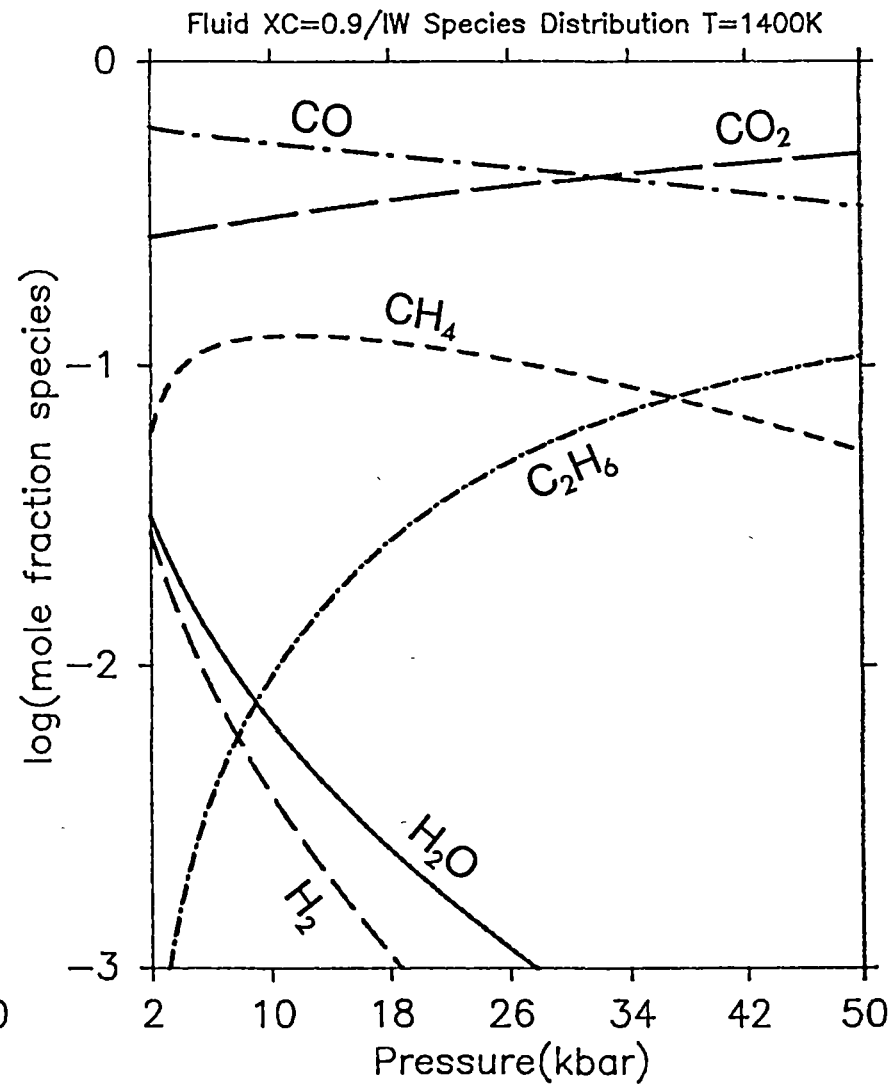
Fluid XC=0.9/IW Species Distribution T=1400K
log(mole fraction species)
0
−1
−2
−3
CO
CO_2
CH_4
C_2H_6
H_2O
H_2
2
10
18
26
34
42
50
Pressure(kbar)

Figs 2.9E & F

Under more reducing conditions (fO_2 = IW) there is a dramatic change in fluid composition due to carbon supersaturation. At P < 5 kbar CH_4, CO, H_2O, CO_2 and H_2 are all present at > 10 mol%. As pressure increases C_2H_6 begins to dominate exceeding x_{CH_4} at ~32 kbar and reaching >60 mol% by 50 kbar. Both CO and CO_2 are present at relatively constant levels of 10 mol% at P > 25 kbar while H_2 and H_2O are unimportant above ~20 kbar. From fO_2 = MW to fO_2 = IW, C-O-H species at X_C = 0.5 change from H_2O-CO_2 to CH_4-C_2H_6-CO-CO_2 mixtures; hydrocarbon-rich fluids dominate under high pressure, reduced conditions.

(c) <u>High carbon contents, X_C = 0.9</u> [Fig. 2.9E, fO_2=MW; Fig. 2.9D, fO_2=IW]

Carbon-rich fluids at fO_2 = MW are dominated by CO_2 with subordinate H_2O at ~10 mol%. CO is the only significant minor species. At lower fO_2's near IW, fluids lie in the metastable region below the carbon saturation curve for most of the P-range. Here CO > CO_2 > CH_4 mixtures are important at P < 30 kbar while at higher pressures CO_2 > CO > C_2H_6 > CH_4 is the order of abundance. As can be seen from the fO_2 = IW diagrams at intermediate to high carbon contents, CO and C_2H_6 (which are minor species in the stable pseudo-divariant region) now act as the major carbon carriers for supersaturated fluids.

2.10 Isoplething the Stable and Metastable Pseudo-divariant Region

Using program COH/FLUID6, values of (log fO_2, X_C, x_i) where i = H_2O, CO_2, CO, H_2, CH_4 or C_2H_6 may be obtained for any one P,T condition. A three-dimensional matrix containing 567 points was constructed for P = 30 kbar, T = 1600 K and the data contoured as lines of equal composition (isopleths) for each species on a log fO_2-X_C diagram. Contouring was performed with the program SURFACEII (Sampson, 1978) and is plotted in Figs 2.10A to 2.10F including the graphite saturation curve to delineate the metastable and stable fluid-only fields. Contours are drawn in the descending order 99, 97.5, 95 and thereafter in 5 mol% intervals to 5 mol% then 2.5, 1.0, 0.5 and 0.1 mol% levels. The latter four contours are less well constrained than the others due to their small spacings and wide distribution. A feature of all plots is that contours for each species radiate from a maximum point on the X_C axis closely corresponding to their position as located in Fig. 2.5. These diagrams illustrate compositional changes as a function of X_C and fO_2 and complement those presented in the

previous section. They are a useful reference for examining the path of C-O-H fluids undergoing oxidation or reduction in both closed and open systems.

(a) x_{H_2O} isopleths [Fig. 2.10A]

x_{H_2O} varies monotonously with X_C in the oxidised portion (fO_2 > GW) of the diagram. In the reduced portion of the stable region x_{H_2O} contours show much less variation with log fO_2 while in the metastable region H_2O abundance falls off rapidly at fO_2's below GW (log fO_2 < -8).

(b) x_{CO_2} isopleths [Fig. 2.10B]

At log fO_2 > -7.0, x_{CO_2} almost exactly mirrors x_{H_2O} contours attesting to the binary (CO_2-H_2O) nature of oxidised fluids under these conditions. CO_2 is not an important species in the stable region below the water maximum but is important in the carbon-rich, oxidised portion of the metastable region at log fO_2 > -10.

(c) x_{CO} isopleths [Fig. 2.10C]

CO is important only in the reduced portion (log fO_2 < -9) of the metastable region where fluids are carbon supersaturated.

(d) x_{H_2} isopleths [Fig. 2.10D]

x_{H_2} contours parallel the graphite saturation curve at fO_2's below the water maximum and in the stable region. Under carbon-poor and very reduced conditions H_2 reaches a maximum (>90 mol%). H_2 is unimportant in the metastable region.

(e) x_{CH_4} isopleths [Fig. 2.10E]

CH_4 is present at levels >5 mol% over much of the log fO_2-X_C diagram at log fO_2's below -7. Maximum CH_4 contents are achieved along the graphite-saturation curve.

(f) $x_{C_2H_6}$ isopleths [Fig. 2.10F]

C_2H_6 replaces CH_4 as the dominant hydrocarbon when X_C of the bulk fluid exceeds that of methane. In the reduced part of the metastable region between X_C = 0.35 and 0.55 C_2H_6 is the dominant species. It is likely that C_3H_8 (propane) and C_2H_4 (ethene), being relatively small molecules and having higher C/H ratios than ethane, will also be of some importance when fluids become carbon supersaturated. Calculations suggest C_2H_6/C_2H_4 ratios on the graphite saturation surface will lie at ~50-100 for P = 30 kbar, T = 1400-1600 K.

Figs 2.10A to 2.10F log fO_2-X_C diagrams at T = 1600 K, P = 30 kbar contoured in species mole fractions.

A: H_2O; B: CO_2; C: CO; D: H_2; E: CH_4; F: C_2H_6.

The graphite saturation curve separates stable from metastable fluid-only regions.

Fig. 2.10A

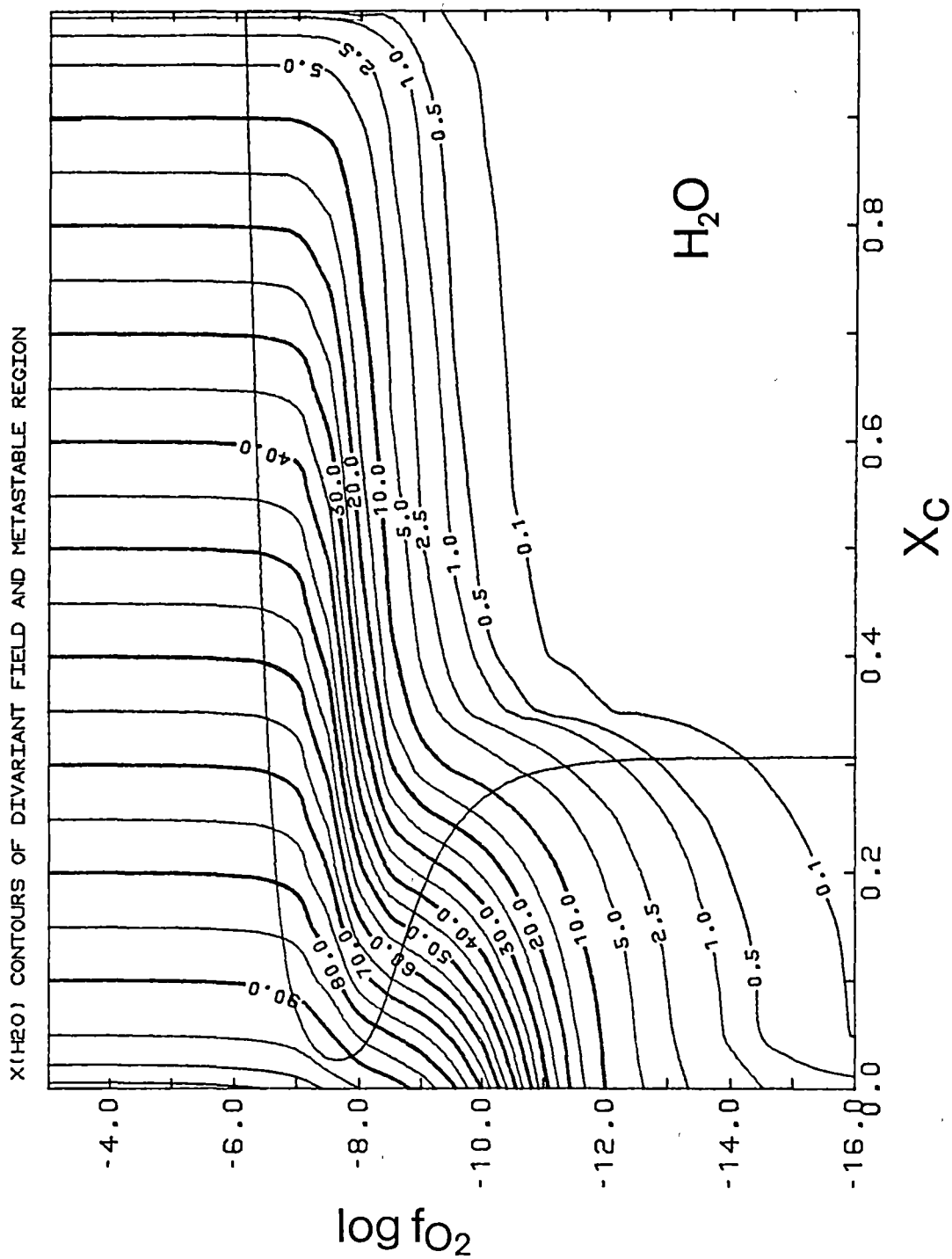
X(H2O) CONTOURS OF DIVARIANT FIELD AND METASTABLE REGION
H2O
log fO2
XC
-4.0
-6.0
-8.0
-10.0
-12.0
-14.0
-16.0
0.0
0.2
0.4
0.6
0.8
90.0
80.0
70.0
60.0
50.0
40.0
30.0
20.0
10.0
5.0
2.5
1.0
0.5
0.1

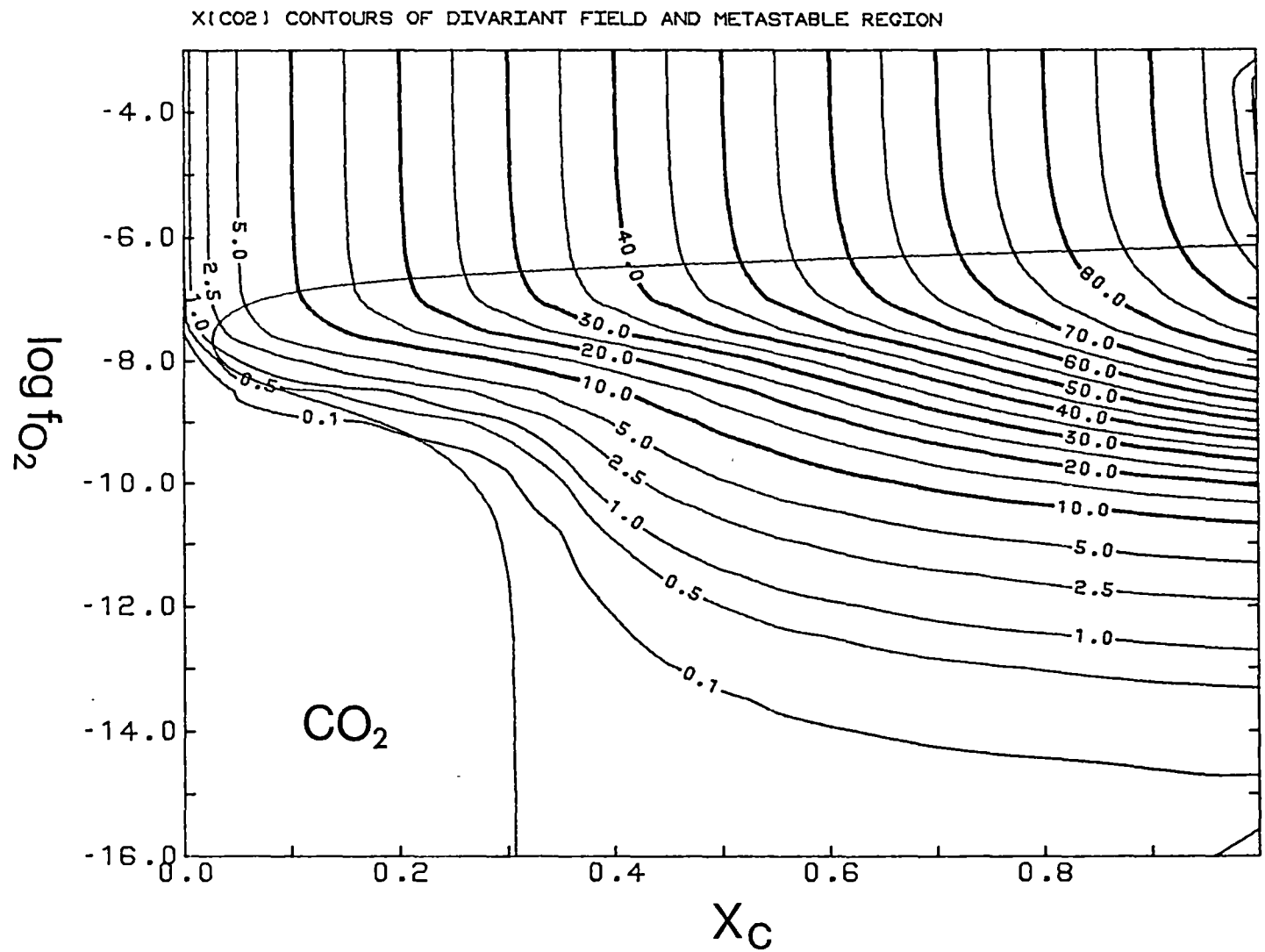
X(CO2) CONTOURS OF DIVARIANT FIELD AND METASTABLE REGION
log f_{O_2}
-4.0
-6.0
-8.0
-10.0
-12.0
-14.0
-16.0
0.0
0.2
0.4
0.6
0.8
X_C
CO_2
5.0
2.5
1.0
0.5
0.1
40.0
30.0
20.0
10.0
5.0
2.5
1.0
0.5
0.1
80.0
70.0
60.0
50.0
40.0
30.0
20.0
10.0
5.0
2.5
1.0
0.1

Fig. 2.10B

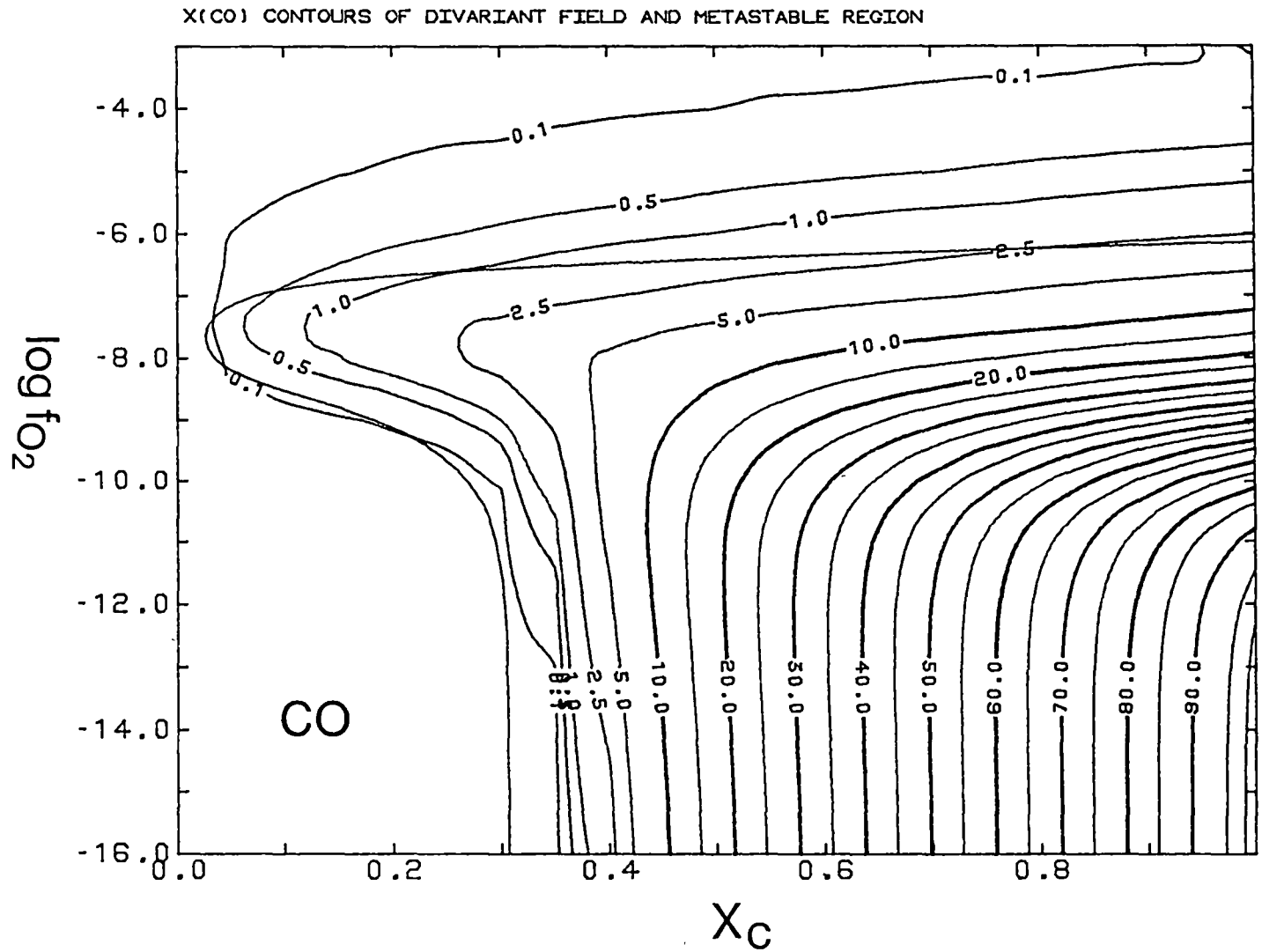
X(CO) CONTOURS OF DIVARIANT FIELD AND METASTABLE REGION
-4.0
-6.0
-8.0
-10.0
-12.0
-14.0
-16.0
log f_{O_2}
0.0
0.2
0.4
0.6
0.8
X_C
CO
0.1
0.5
1.0
2.5
5.0
10.0
20.0
30.0
40.0
50.0
0.09
0.07
0.08
0.06

Fig. 2.10C

Fig. 2.10D

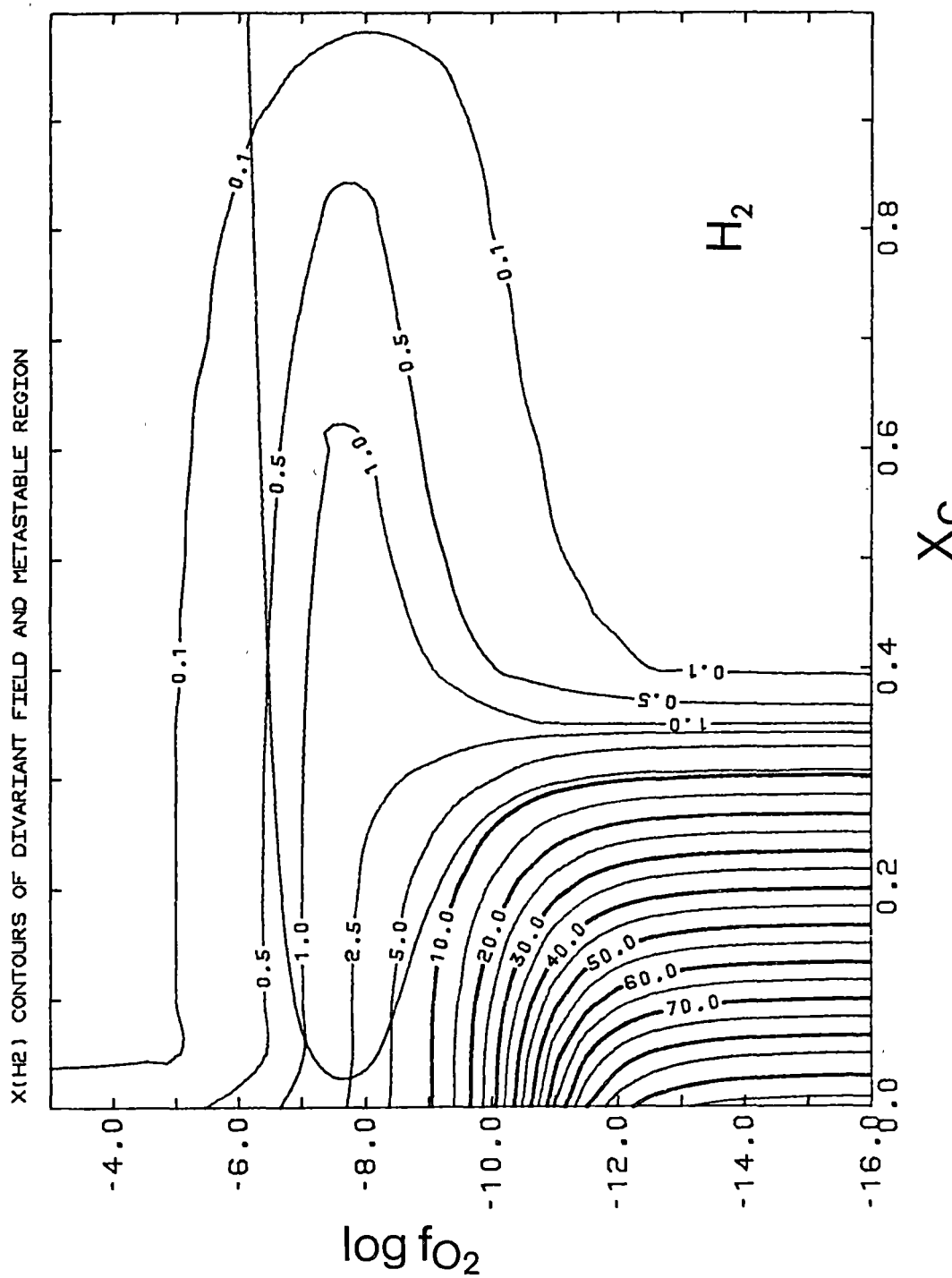
X(H2) CONTOURS OF DIVARIANT FIELD AND METASTABLE REGION
H2
0.1
0.5
1.0
2.5
5.0
10.0
20.0
30.0
40.0
50.0
60.0
70.0
-4.0
-6.0
-8.0
-10.0
-12.0
-14.0
-16.0
0.0
0.2
0.4
0.6
0.8
log fO2
XC

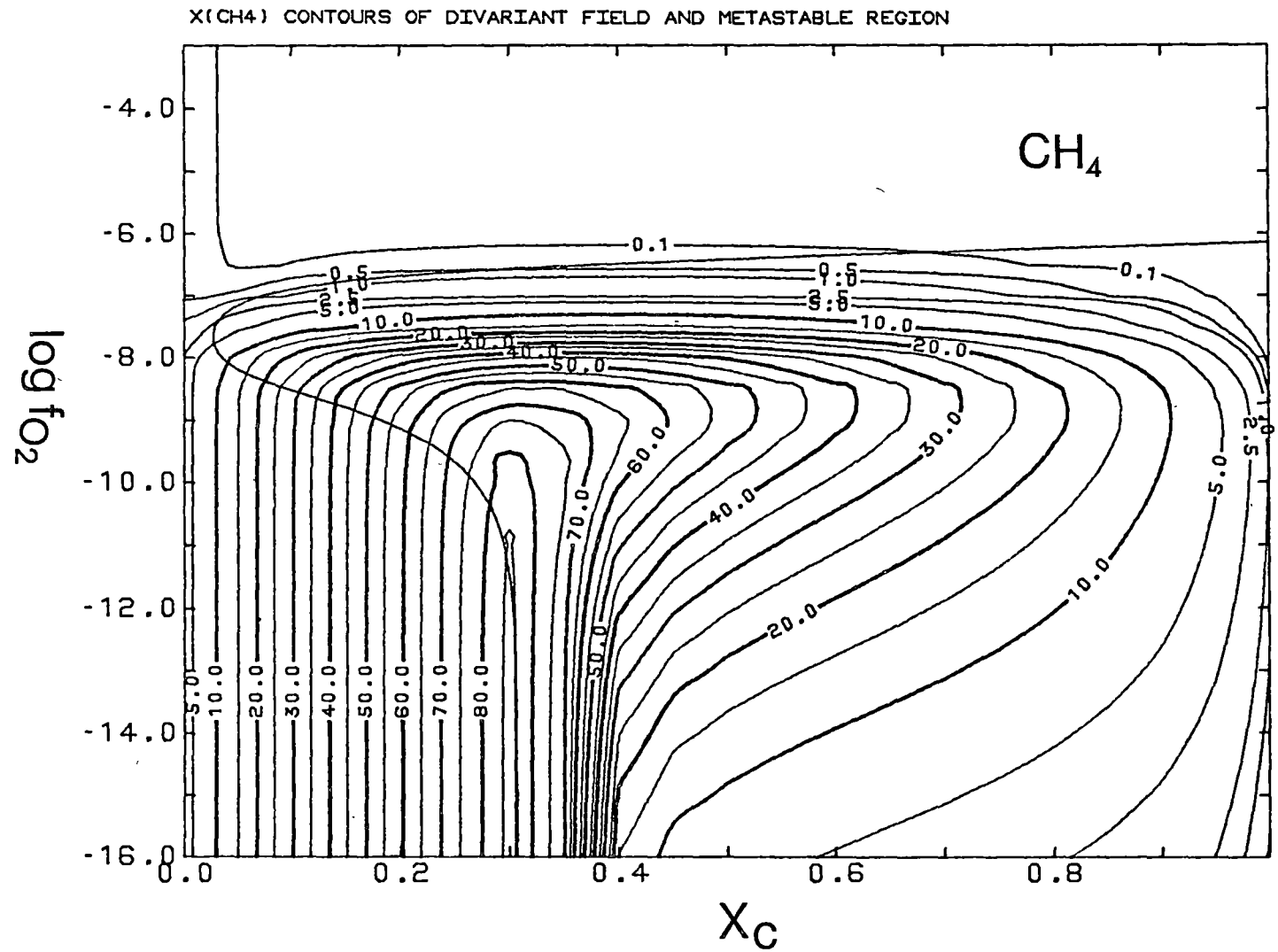
X(CH4) CONTOURS OF DIVARIANT FIELD AND METASTABLE REGION
CH4
log fO2
Xc
-4.0
-6.0
-8.0
-10.0
-12.0
-14.0
-16.0
0.0
0.2
0.4
0.6
0.8
0.1
0.5
1.0
2.5
5.0
10.0
20.0
30.0
40.0
50.0
60.0
70.0
80.0

Fig. 2.10E

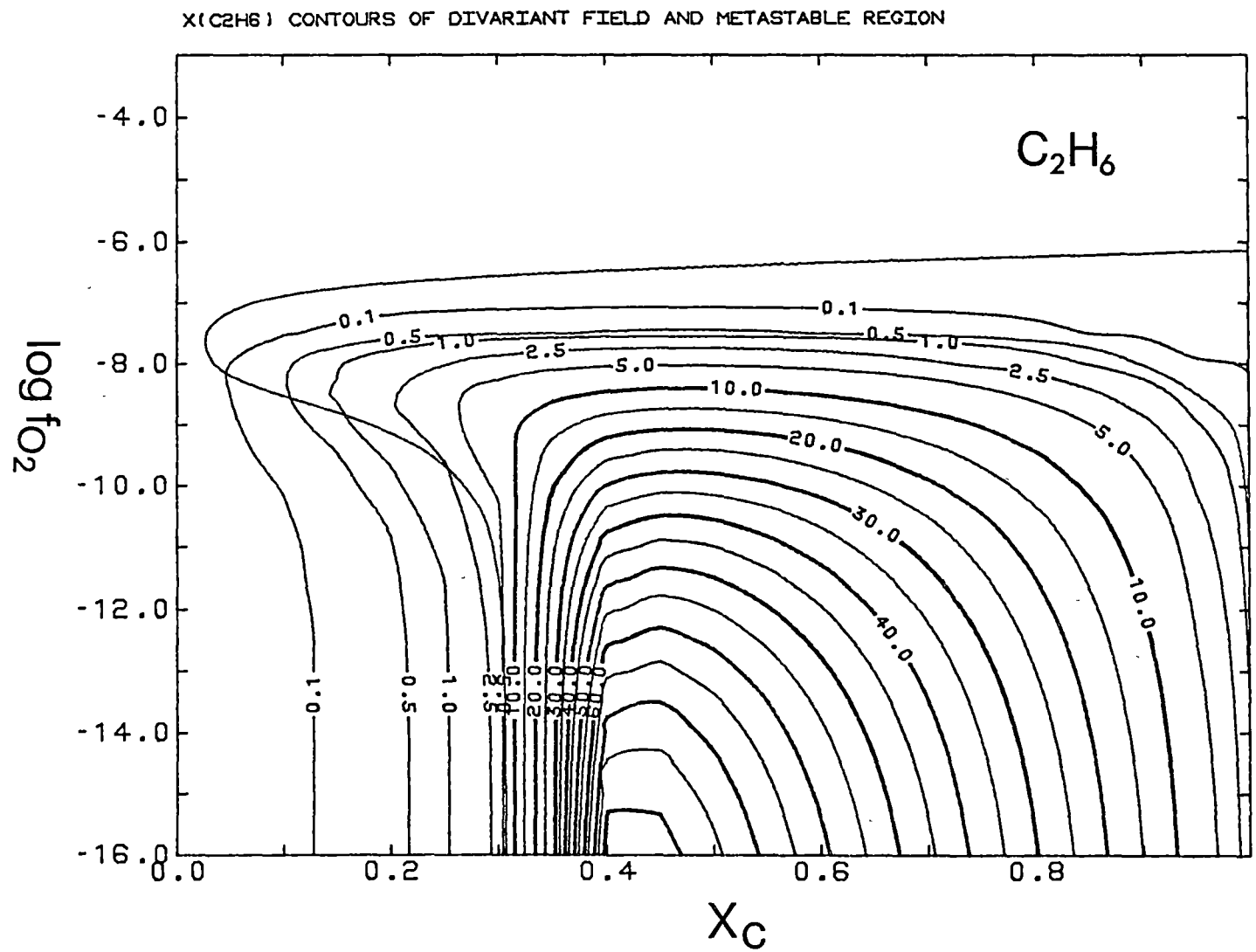
X(C2H6) CONTOURS OF DIVARIANT FIELD AND METASTABLE REGION
C2H6
log fO2
Xc
-4.0
-6.0
-8.0
-10.0
-12.0
-14.0
-16.0
0.0
0.2
0.4
0.6
0.8
0.1
0.5
1.0
2.5
5.0
10.0
20.0
30.0
40.0

Fig. 2.10F

2.11 Vapour Excess Mantle Melting under the influence of C-O-H Volatiles: a generalised model.

It is well known that silicate assemblages show large liquidus depressions when melted under conditions of high water activity. The olivine melilitite composition of Brey & Green (1976a), for example, shows a liquidus depression of ~450°C at 35 kbar with the liquid capable of dissolving as much as 40 wt% H_2O. Other volatiles such as CO_2 and CH_4 (Part 4) are much less soluble resulting in smaller liquidus depressions. Under CO_2-saturated conditions the olivine melilitite of Brey & Green (1976a) shows liquidus depressions of only ~100-150°C at 30-40 kbar dissolving between 9 and 11 wt% CO_2. It is therefore an acceptable approximation in silicate + C-O-H volatile systems to consider initiation of silicate melting to be largely a function of fH_2O provided the temperature is below the vapour excess liquidi of other volatiles.

The ability to contour the log fO_2-X_C diagram in terms of x_i or f_i readily allows projection of isothermal, isobaric vapour excess phase equilibria (Frost, 1979). In a generalised metal oxide-silica system carbon is capable of existing in three different forms in addition to vapour phase species; these are: carbonate, elemental carbon (graphite or diamond) and carbide (in a Fe-free system SiC will be the carbide stable at the highest fO_2). A hydrous phase (amphibole or mica in a natural system) will also be present where fH_2O is sufficient for hydrate stability.

Consider the simple system M-C-O-H where M = any divalent metal cation, e.g. Mg, where stable carbonate MCO_3, hydrate $M(OH)_2$ and carbide M_2C phases exist. The stability of the hydrate and hydrous melt will be constrained by contours in fH_2O while carbonate stability is a function of fCO_2 and carbide of fH_2^2/fCH_4 since $2M + CH_4 = M_2C + 2H_2$. Using the phase rule, schematic stability fields under vapour excess conditions may be delineated on a log fO_2-X_C diagram (Fig. 2.11A).

If the oxide phase is sufficiently soluble in the vapour phase, as may occur at very high fH_2O's, then a field of fluid-only, corresponding to complete solubility of the solid in the vapour, may occur. In this case it is assumed that entry of the solid phase does not significantly affect fugacity contours or the position of the graphite saturation curve. By

Fig. 2.11A Schematic isothermal, isobaric log fO_2-X_C diagram for the system M-C-O-H (M = divalent cation) under vapour excess conditions delineating phase fields for carbonate (MCO_3), oxide (MO), liquid (LIQ), supercritical fluid (F) and carbide (M_2C). V_1 = H_2O-CO_2 dominated volatile phase, V_2 = H_2O-CH_4-H_2 dominated volatile phase. Phase fields to the right of the carbon saturation curve include coexisting graphite (G). Note the limited fO_2 extent of the carbonate + G + V_1, hydrate + G + V_1 and oxide + G + V_1 fields which lie at fO_2's between point B and GCO. Invariant points A and B correspond to the first appearance of liquid as a function of increasing fH_2O as the x_{H_2O} maximum is approached.

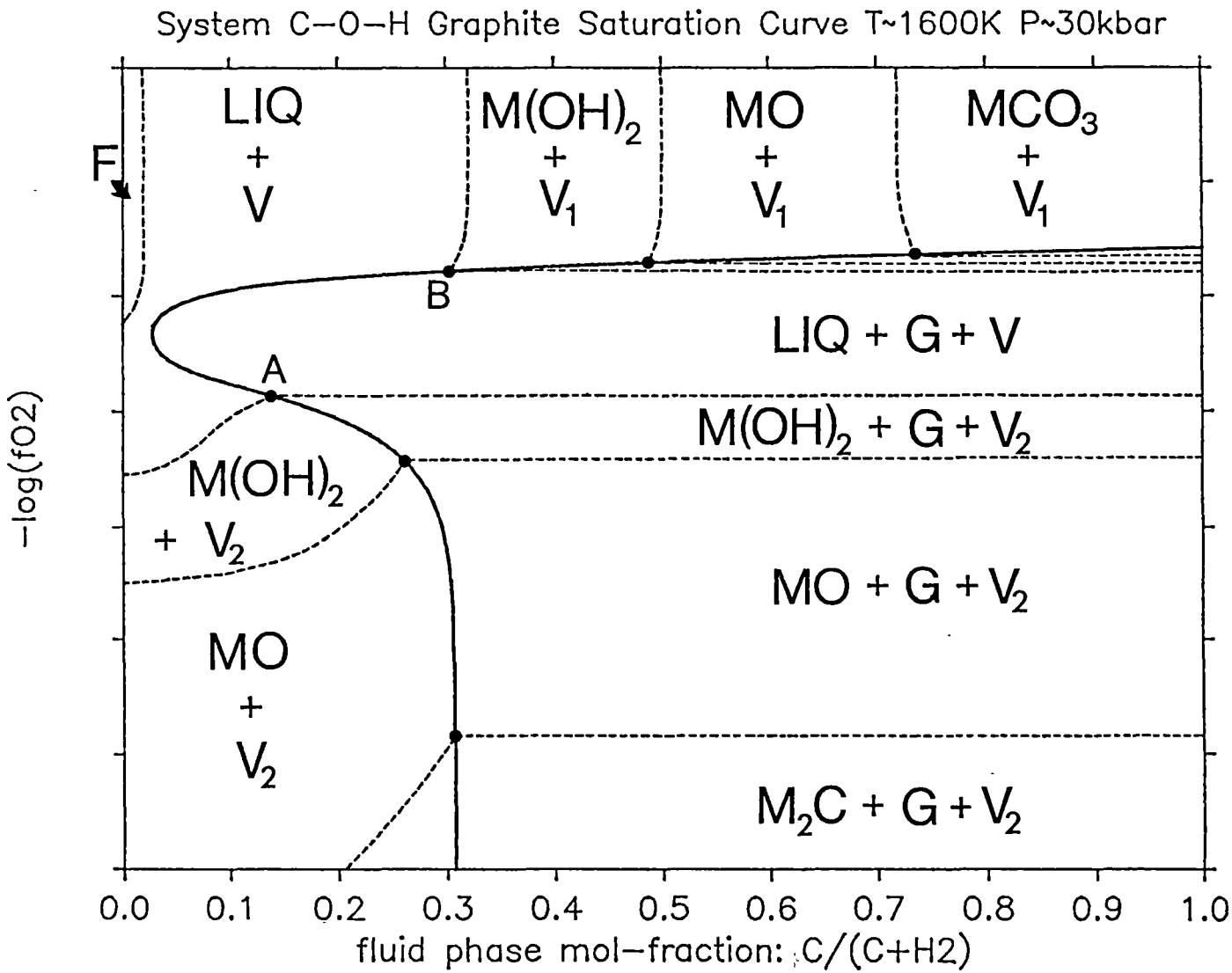
System C–O–H Graphite Saturation Curve T~1600K P~30kbar
LIQ + V
M(OH)2 + V1
MO + V1
MCO3 + V1
F
B
A
LIQ + G + V
M(OH)2 + G + V2
M(OH)2 + V2
MO + G + V2
MO + V2
M2C + G + V2
-log(fO2)
0.0
0.1
0.2
0.3
0.4
0.5
0.6
0.7
0.8
0.9
1.0
fluid phase mol–fraction: C/(C+H2)

analogy with this simple system, the phase stabilities of Fe-free graphite-bearing and graphite-free peridotites may be constructed in similar fashion (Fig. 2.11B).

Fig. 2.11B is intended only as a qualitative representation of phase stabilities and to illustrate likely mantle melting behaviour under vapour excess conditions. Phase field boundaries generally parallel the x_i contours of Section 2.10 since $f_i \propto x_i$ in the absence of large compositional dependancies in the ϕ_i's. As can be seen from both figures, isothermal, isobaric melting will be initiated in graphite-bearing systems at minimum fH_2O's corresponding either to a reduced condition (Point A) or an oxidised condition (Point B). The lines AY and BX correspond to the minimum fH_2O required for melting in the absence of graphite. At higher temperatures the field of liquid will expand at the expense of the hydrated peridotite fields. Vapour excess melting of silicate assemblages have been modelled (e.g. Wyllie, 1979) in the oxidised portion of the diagram where H_2O-CO_2 volatiles are important. Provided fO_2 remains above that of the GW buffer, vapour excess melting of graphite peridotites involving H_2O-CO_2 volatile mixtures will not differ greatly from the graphite-free system because fH_2O and fCO_2 contours extend in more or less parallel fashion from oxidised conditions towards the graphite saturation surface (Figs 2.10A and 2.10B). The same however cannot be said for conditions more reduced than GW. While the reduced portion of the diagram mirrors the oxidised part in terms of phase fields (with carbide rather than carbonate being the additional C-bearing phase), the nature of initial melts formed at "A", involving H_2O-CH_4 volatiles, are likely to be very different from melts formed at "B" where H_2O-CO_2 volatiles predominate. In view of the recent evidence suggesting that a significant proportion of the Earth's upper mantle may be as reduced as IW (Arculus & Delano, 1981; Arculus & Gust, 1981; Arculus et al., 1984) there is surprisingly little known of petrogenetic processes at low oxygen fugacities. Specifically, what is the nature of mantle melting under conditions more reduced than GW or DW? Is there evidence for the existence of mantle C-O-H fluids of reduced character? The first question is considered experimentally in Part 4 and the second question is amenable to investigation using the thermodynamic model for C-O-H fluids developed herein and is considered in the following Part.

Fig. 2.11B Schematic representation of possible phase relations in an Fe-free peridotite + excess C-O-H volatile system assuming the hydrous phase stability limit coincides with the solidus Y-A, B-X (as in the experimental work of Green, 1973).

CPer	carbonated peridotite
HPer	hydrated peridotite
HCPer	carbonated and hydrated peridotite
Liq(L)	liquid phase
Xal	anhydrous crystals (olv, opx, cpx, and/or gnt)
APer	anhydrous peridotite
SiCPer	SiC (moissanite)-bearing peridotite
V	volatile phase
Y-A,B-X	solidus trace.

Graphite peridotites occupy phase fields to the right of the carbon saturation curve. With increasing fH_2O, melting is initiated in graphite peridotites at either a reduced condition (point A) or an oxidised condition (point B).

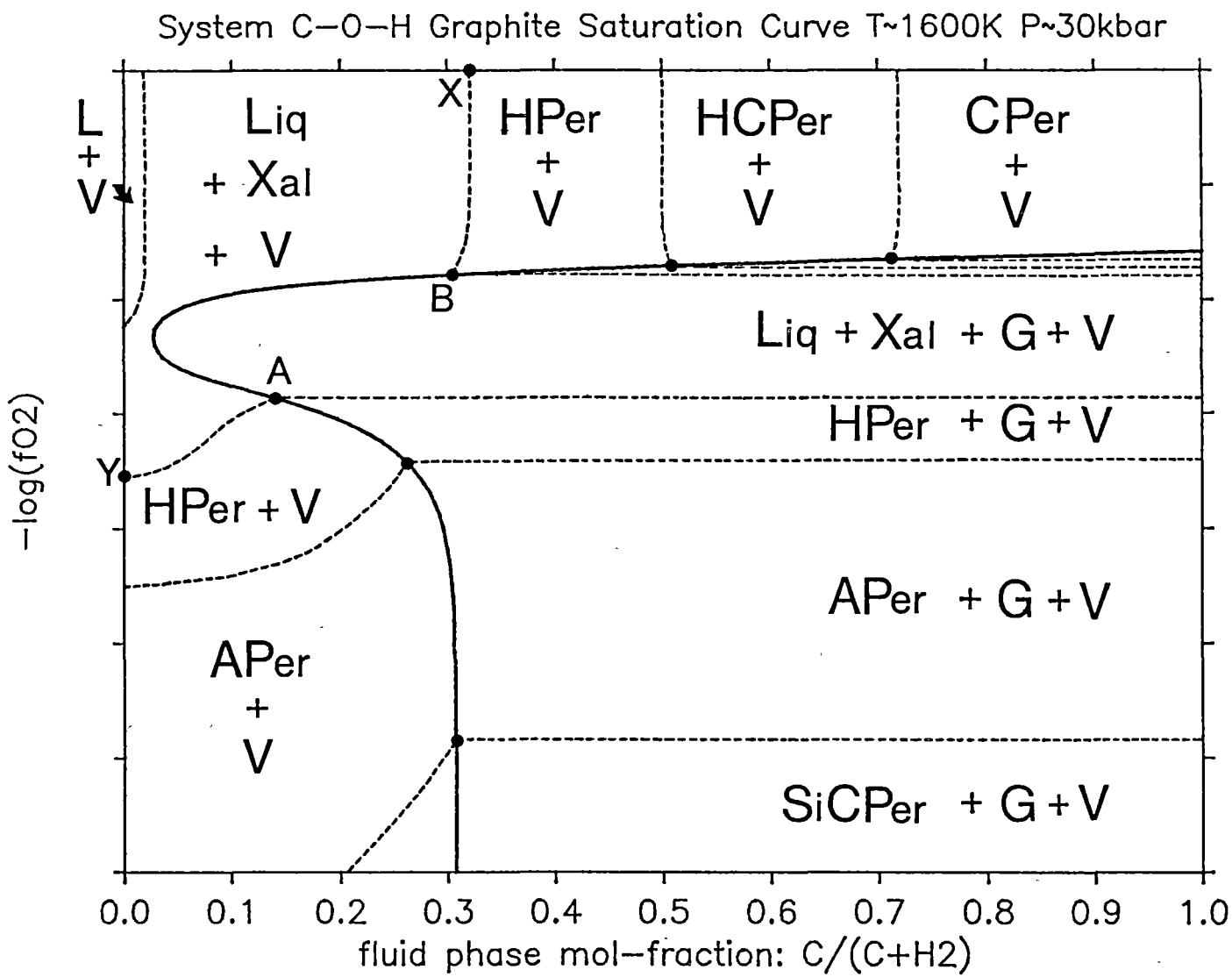
System C–O–H Graphite Saturation Curve T~1600K P~30kbar
L
+
V
Liq
+ Xal
+ V
X
HPer
+
V
HCPer
+
V
CPer
+
V
B
Liq + Xal + G + V
A
HPer + G + V
Y
HPer + V
APer + G + V
APer
+
V
SiCPer + G + V
-log(fO2)
0.0
0.1
0.2
0.3
0.4
0.5
0.6
0.7
0.8
0.9
1.0
fluid phase mol-fraction: C/(C+H2)

PART 3

A REAPPRAISAL OF THE NATURE OF FLUIDS INCLUDED IN DIAMOND: IMPLICATIONS FOR MANTLE REDOX CONDITIONS.

3.1 Introduction

Diamonds not formed by shock-induced processes are unequivocally samples of mantle material. Like other minerals, diamonds carry both solid and fluid impurities (in inclusions or other structural sites) that may provide information on the P,T and volatile activity conditions that prevailed during host mineral formation or during some later recrystallisation event. The significance of diamond is its potential as a "sampling device" for deep-seated mantle fluids (Roedder, 1984). Roedder considers that all other minerals would lack sufficient strength to contain high pressure mantle fluids. If this is so, then an investigation of fluids trapped in diamond is likely to place useful constraints on the upper mantle redox state and provide some insight into the mode of diamond formation.

In terms of depth of origin, diamond occurrence is constrained to a window in the Earth extending from ~140 km to ~200 km depth. This may, however, be a result of inadequate sampling and the lower limit could be as much as 670 km, as suggested by the recent discovery of magnesio-wustite inclusions in diamond (Scott-Smith et al., 1984). Noble gas isotopes (Ozima et al., 1983; Zashu & Ozima, 1984) together with Sm/Nd and Rb/Sr isotope systematics (Richardson et al., 1984) indicate largely Archaean formation ages for diamond with the further implication of a xenocrystic relation between diamond and much younger kimberlitic host rocks. One Mesozoic maximum K-Ar age obtained by Ozima et al. (1983), however, suggests that at least some diamonds may be of more recent origin. A significant result obtained by Richardson et al. (1984) is the indicated long (>3 Gyr) storage interval for diamond in enriched South African sub-cratonic lithosphere which developed within ~300 Myr after extraction of high partial melt fractions associated with komatiitic magmatism. This indicates a relatively rapid change in thermal regime with the early stabilisation of cool sub-cratonic mantle beneath southern Africa which has remained little changed for ~3 Gyr. Unsupported high $^{87}Sr/^{86}Sr$ ratios in garnet inclusions from these diamonds requires a precursory mantle

enrichment event. The authors suggest this may have occurred via "introduction and entrapment of asthenosphere-derived alkali, LREE and CO_2 enriched interstitial melt, which remained liquid until the time of diamond crystallisation" and further suggest the melt may have persisted through time. Since this model requires mantle fO_2 conditions to lie within the oxidised portion of the system C-O-H where CO_2 is stable (fO_2 > DW), this hypothesis is testable by examining the nature of fluids trapped within diamond. If it can be demonstrated that diamonds of South African and other origins have equilibrated with fluids of a character more reduced than DW, then models calling for the persistence of "CO_2-enriched" melts together with diamond in sub-cratonic mantle will not be tenable.

Unfortunately there are a number of analytical and interpretive problems that make evaluation of the nature of fluid impurities trapped in diamond far from straight-forward. In general, a number of assumptions will be required.

Problems and Assumptions

(a) <u>The nature of fluid inclusions in diamond.</u>

Conceivably, fluid impurities trapped in diamond may occur in sites ranging in size from microscopic fluid inclusions (tens of microns) to impurity aggregates located in crystallographic defect sites (of order hundreds to tens of angstroms). Roedder (1984) points out that optical methods have failed to unequivocally identify microscopic fluid-filled inclusions in diamond. The existence of such inclusions has, however, been inferred from SEM studies showing the presence of variously shaped cavaties (many of which appear to be interconnected) of ~1-30 μm size in "cloud-like" regions of diamond (Giardini & Melton, 1975). Similar cavaties are observed in polycrystalline diamond (Trueb & De Wys, 1969). Comparisons of cavity density and volume with estimates of the amount of fluid released in crushing experiments led Roedder (1984, p.510) to conclude that only a small proportion of the inclusions in diamonds studied by Giardini & Melton (1975) were likely to be filled with high pressure fluid. A possible implication of this result is that the larger size ranges of fluid inclusions have been eliminated by decrepitation processes during ascent to the surface. Presently analysed fluids may therefore originate largely from submicron sized inclusions. The first major assumption is that diamond-derived fluids released by crushing and other experiments,

represent a physically distinct fluid phase located in isolated inclusion sites.

By analogy with solid phase inclusions which are identifiable as either primary ("syngenetic") or secondary ("epigenetic") types (e.g. Meyer & Tsai, 1976) it might be expected that fluid inclusions, too, can be categorised in a similar manner. However, fluid inclusions can only be trapped by crystal growth within the physical and chemical conditions of diamond stability, greatly limiting the region in which secondary inclusions may form. Fluid types lying outside the region of diamond stability probably give rise to resorption and etching features commonly observed on diamond surfaces (Robinson, 1978, p.63). The second major assumption, therfore, is that fluids trapped by diamond are syngenetic or synmetamorphic in origin. For this to be true it is necessary to show that the strength of diamond is such that pressure differentials (i.e. internal fluid pressure minus external pressure) in excess of ~50 kbar can be withstood on transport of diamond from mantle depths to the Earth's surface.

(b) Equilibrium between fluid and host.

It is necessary to make the assumption that equilibrium was established between all coexisting phases during diamond crystallisation. Since consistent results are obtained for P,T-estimates in coexisting silicates included by diamond (Section 3.4) this assumption appears to be generally valid. However, examples of non-equilibrium can be found in some inclusion suites; for example, the compositionally different chromites of Gurney et al. (1984b) occurring in a single diamond. The problem of diamond crystallisation from fluids supersaturated in carbon and hence within the metastable phase field of the system C-O-H, must also be considered. It has been suggested that polycrystalline diamond aggregates (Gurney & Boyd, 1982) and growth twins or macles (Harris & Gurney, 1979) form under conditions of carbon supersaturation. In the former case there is clear textural evidence for rapid crystallisation from carbon enriched fluids.

(c) Analytical uncertainties.

The bulk of fluid analyses from diamond have been determined by crushing/mass spectrometry techniques (Melton & Giardini, 1974, 1975, 1981;

Giardini et al., 1982). In single crushing experiments, diamonds release fluid volumes ranging from as little as 10^{-8} cm^3(STP)/mg diamond up to around 10^{-5} cm^3(STP)/mg diamond. For diamonds of ~100 mg, the lowest measured gas volumes are at least 10 times the detection limit of modern mass spectrometers. For accurate quantitative work careful calibration procedures must be employed. Melton & Giardini (1974) estimate that their analyses have a maximum uncertainty of $\pm$5% in both volume and composition. Roedder (1984, p.509), however, criticises a number of aspects of Melton & Giardini's analytical technique - particularly spectrometer calibration, background correction and reproducibility [see Section 3.6(g)]. Unfortunately, without independant analyses it is not possible to evaluate the magnitude of any additional uncertainties. For the purposes of this study,mass spectrometric analyses of diamond-derived fluids by Melton, Giardini & co-workers have been taken directly from the literature with no other corrections applied. Further work will be necessary to confirm the accuracy of these results and to evaluate in more detail the analytical errors involved.

(d) Relation between fluid analyses and the composition of initially trapped volatiles.

Since diamond has most probably been subject to a complex history culminating in rapid transport to the Earth's surface, it is likely that the composition of originally trapped fluids will not represent those analysed today. The chief purpose of the present study is to determine the composition and species distribution of these original fluids under typical P,T equilibration conditions within the mantle by accounting for any later modifications. This requires as a basis a detailed thermodynamic model for C-O-H fluids at high pressures as discussed in Parts 1 and 2. Provided diamond and a fluid phase were in equilibrium or close to equilibrium (irrespective of the presence of a silicate melt or solid phases) then it should be possible to place constraints on mantle redox conditions and provide an insight into mantle fluid compositions. Further information would be required to place this within a time frame for mantle evolution.

Previous studies (Melton & Giardini, 1981; Giardini et al., 1982) have failed to account for many of the problems discussed above. The conclusions of these authors, based on the assumption that analysed fluid compositions reflect those present during diamond formation in the mantle,may not be correct.

3.2 Light Element Impurities in Diamond: Distribution

Volatile components may occur in a range of different structural sites in diamond (Bibby. 1982). The distribution and abundance of light elements (H to F) and other potential volatile phase constituents (S, halogens, noble gases) in sites other than fluid inclusions will have an important bearing on the interpretation of diamond-derived fluids. Bibby (1982) identifies four groups of impurities according to physical form:

(a) Substitutional Defects: elements that directly substitute for C in the diamond lattice. N is perhaps the best example of a substitutional impurity which may cause changes in many physical properties (e.g. absorption of radiation, thermal conductivity).

(b) Lattice Interstitials: elements that occupy voids in the diamond lattice.

(c) Mineral Inclusions: Microscopic or sub-microscopic particles, the latter identifiable by characteristic inter-element correlations (Sellschop, 1979). Data on the nature and occurrence of inclusions having a presumed syngenetic association with diamond have been summarised by Prinz et al. (1975), Meyer & Tsai (1976), Giardini et al. (1982), Harris & Gurney (1979), Scott-Smith et al. (1984), Haggerty & Tomkins (1983), Sharp (1966) and Seal (1966).

(d) Fluid Inclusions: Fluids analysed by crushing and graphitisation experiments (Melton & Giardini, 1974, 1975, 1981; Giardini et al., 1982) lie dominantly in the system C-O-H-N but also contain noble gases and rarely S-species. A number of relatively complex organic compounds (alkenes and alcohols) have been identified in addition to H_2O, CO_2, CO, CH_4, H_2 and N_2.

In terms of elemental abundances and distribution the impoprtant light elements N, H, O and C are considered in detail below.

(a) Nitrogen

N predominantly occurs as a substitutional impurity but may also be present in fluid inclusions. The various N-defect centres are the basis for diamond classification (Bibby, 1982):

Table 3.2A

Type/Subtype	Abundance in nature	Average N content*	Substitutional Defect
Ia IaA IaB	>90%	~800 ppm	Non-paramagnetic N-aggregate centres usually a mixture of two components A: (N pair) + B (larger even-N aggregate). Also commonly associated with N-platelets.
Ib	<2%	~100 ppm	Singly substituted paramagnetic N.
IIa	rare	~40 ppm	Contains a small amount of non-substitutional N.
IIb	rare	~40 ppm	Contains substitutional boron, p-type semiconductor.

* Sellschop et al. (1980)

(b) Hydrogen: H occurs in a variety of different impurity sites in diamond; as summarised in Table 3.2B, the H content of microscopic fluid inclusions may be exceeded by H present in substitutional and other defect sites. There is strong evidence to suggest the presence of submicron glass and/or fluid impurity aggregates ("melt droplets") in many diamonds.

(c) Oxygen: Table 3.2C; much of the 20-90 ppm O recorded in diamonds free of silicate and oxide impurities probably resides in microscopic and submicroscopic sized fluid inclusions and in interstitial/surface defect sites. Substitutional O has not been identified.

(d) Carbon: Impurity carbon may occur in a number of sites but the dominant locations are interstitial defects, N-platelets (Evans, 1973, cited by Bibby, 1982, p.6), fluid inclusions and graphitised regions of diamond. Both highly reduced carbon in the form of the carbide Fe_3C

Table 3.2B

Impurity Form	Identification Method	Amount H Reported	Reference	Comments
Substitutional, C-H (or N-H) bonding	IR 3107, 1405 cm^{-1} bands	~5 ppm*	Runciman & Carter (1971)	Confirmed by vacuum fusion experiments.
Surface Sites, H profile to ~4000Å depth in diamond	Ion beam analysis	200-2800 ppm Av. ~1500 ppm Annealing at 1200-1800°C results in surface enhancement from 200 ppm to ~1750 ppm.	Hudson & Tsong (1977) Sellschop et. al. (1980)	H is thought to be released into interstitial defect sites by destruction of nanometric sized glass or fluid impurity aggregates. H in this form is expected to diffuse rapidly to surface trapping sites.
Fluid Inclusions, H_2 or other H containing molecules	Crushing + mass spectrometry	~0.1 ppm	Melton & Giardini (1974, 1975, 1981)	Single crushing experiments probably represent incomplete volatile loss from inclusions.
Unidentified Inclusions, Hydroxyl and/or molecular water	IR	Not determined but variable.	Chrenko et al. (1967) Harris & Gurney (1979)	Submicron sized particles probably glass and/or fluid inclusions in diamond coat and "cloud-like" regions.
All Forms, Bulk analysis	Graphitisation + mass spectrometry	22 ppm	Melton & Giardini (1976) Bibby (1982, p.31)	Graphitisation to temperatures up to ~3000°C releases H in all sites. Comparison with ion-beam analyses suggests surface enhancements are ~10-100 x bulk H content.

* all ppm reported as µg/g

Table 3.2C

Impurity Form	Identification Method	Amount O Reported	Reference	Comments
Silicate and Oxide Inclusions	Visual, INAA	Variable, but up to 2000 ppm*	Sellschop (1979) Bibby (1982)	
Surface Sites, O depth profile	Ion beam analysis	Cleaned surface 77±15 ppm After annealing at 1200-1800°C 295±59 ppm	Sellschop et al. (1980)	As with hydrogen; O is interpreted as being derived from submicron sized impurity aggregates (glass and/or fluid).
Fluid Inclusions, O containing molecules	Crushing + mass spectrometry	~0.1-1.0 ppm	Melton & Giardini (1974, 1975, 1981)	Comments as for H apply.
Total O, diamonds without solid inclusions	INAA	~20-90 ppm	Bibby (1982) Sellschop (1979)	Many of the diamonds studied by Bibby have <1 ppm other impurities.
Total O, Bulk analysis	Graphitisation + mass spectrometry	1590 ppm	Melton & Giardini (1976) Bibby (1982, p.31)	High O presumably due to presence of solid inclusions reduced to CO by carbon.

* all ppm reported as µg/g

(Sharp, 1966) and oxidised carbon as carbonate (Chrenko et al., 1967) are known solid inclusions in diamond.

(e) Other Impurities: Chlorine has been reported at levels of 0.015-3.6 ppm, fluorine <5 ppm, sulphur 10-90 ppm and H_2S in trace proportions from crushing experiments (Bibby, 1982; Sellschop, 1979; Giardini et al., 1982). The noble gases are components of all fluid inclusions but are usually no more abundant than ~1 mol% in released fluids.

Inter-element correlations (Sellschop,. 1979; Fesq et al., 1975) particularly amongst lithophile elements suggest the presence of sub-microscopic melt, fluid and/or mineral inclusions. Attempts to estimate the major element chemistry of these trapped "magma droplets" give highly magnesian melts (Fesq et al., 1975). Sellschop (1979) believes sub-microscopic melt inclusions are essentially homogeneously distributed throughout all diamonds.

3.3 Light Element Impurities in Diamond: Results of Crushing, Graphitisation and Ion-Beam Studies

Twenty-one analyses of volatile light element impurities in diamond were selected from the literature. A complete list of sources and analyses are given in Appendix 11. The majority of the analyses were derived from crushing experiments but in three cases both crushing and graphitisation were performed on the same samples. In one case partial analysis in terms of H/O ratio was obtained from ion-beam studies. The primary rejection criteria was to discard any composition not having a dominance of C-O-H volatiles (>90 mol%); in practice nitrogen (as N_2) was the only other important component present at an average level of 1.6 atom% (with a standard deviation Sd = 1.6). Because nitrogen has not been incorporated into the theoretical model of species distribution, in the following discussion nitrogen is assumed to have no significant effect on C-O-H internal equilibria whether present originally as molecular N_2 or in some other form such as NH_3; this assumption is unlikely to be valid if nitrogen levels exceed about 10 atom%. Argon can be similarly considered since it is typically only a trace component of diamond fluids.

The data set under consideration (Appendix 11) is unfortunately, as with most diamond studies, a somewhat biased and restricted sample. More than a third of the analyses are derived from the relatively uncommon cubic diamond morphology of Zaire and Brazilian origin. These diamonds tend to release much larger gas volumes and be more easily crushed than the more common octahedral and dodecahedral forms of South African and Siberian production. Less than 10% of the sample comprises diamonds of South African origin and none are available from Siberia. Analyses from three Indian diamonds (Panna mine, central India) and six diamonds from Arkansas, North America comprise the balance of the data set.

The dominant C-O-H species in diamond derived fluids are in all cases H_2O, CO_2, CO, H_2 and CH_4. Components other than these five species were present at an average level of 4.1 vol% (S_d = 3.5). Other than N_2 and Ar, additional species comprise a series of alkenes (C_2H_4, C_3H_6, C_4H_8), alcohols (CH_3OH), C_2H_5OH), a higher alkane (C_4H_{10}) and surprisingly molecular oxygen (O_2); all were typically present at levels <2 vol%. An omission from this list are the lower alkanes ethane and propane, the former is predicted to be a minor component under reduced conditions (Section 2.7) while none of the other species are expected in fluids in equilibrium with diamond above trace proportions. However, in complex hydrocarbon mixtures the mass spectra of many species overlap and assignment to any one species may be somewhat arbitrary. Molecular oxygen cannot be a measurable component of fluids in equilibrium with diamond under any circumstances; the appearance of small amounts of O_2 here is possibly due to contamination or may occur via some catalytically induced post-diamond formation reaction.

3.4 Silicate Inclusions in Diamond and the Estimation of P,T Conditions of Formation.

Geothermobarometry studies on coexisting silicate mineral inclusions (both composite and isolated) in diamond places useful constraints on the P,T conditions of diamond crystallisation. The consistency in many cases between temperatures obtained from isolated inclusions and composite or touching types suggests retrograde re-equilibration was not important in either paragenesis and T estimates reflect the same condition for inclusion crystallisation and host or associated lherzolite crystallisation.

Summarised in Table 3.4 are a set of average P,T estimates for inclusion suites and diamond-bearing xenoliths.

Table 3.4

Reference	Rock/Inclusion type	T(est.)/^{o}C $\pm$ Sd/$\sqrt{n}$*	P(est.)/kbar $\pm$ Sd/$\sqrt{n}$
Boyd & Finnerty (1980)	Peridotite & dunite Gt$\pm$Olv$\pm$En$\pm$Di inclusions	1054 $\pm$ 64 1080 $\pm$ 67	56 $\pm$ 4 54 $\pm$ 3
Shee et al. (1982)	Peridotite Gt$\pm$Olv$\pm$En inclusions	1127 $\pm$ 9 1041 $\pm$ 16	55 $\pm$ 1 54 $\pm$ 1
Hervig et al. (1980)	Isolated and touching Gt$\pm$Olv$\pm$En$\pm$Di inclusions	1091 $\pm$ 43	53 $\pm$ 3
Gurney et al. (1984a)	Gt+Cpx pairs	1165 $\pm$ 7	50 - 60
Meyer & Tsai (1976)	Di+En$\pm$Gt Cpx+Gt	1075 $\pm$ 67 1015 $\pm$ 40	56 $\pm$ 4 -
Gurney et al. (1984b)	Gt+Cpx	1265	-
Harris et al. (1970)	Thermal expansion of garnet inclusions.	>1200	at 55 kb

*Sd = sample standard deviation, n = number of observations.

The above data indicate typical P,T crystallisation conditions for diamond that lie in the range 1000-1300^{o}C at between 50 and 60 kbar with most T estimates in the vicinity of 1100^{o}C. For the purposes of the following analysis a P,T condition of 1400K (1127^{o}C) and 55 kbar, very similar to that estimated for the diamond-bearing peridotite xenoliths of Shee et al. (1982) has been chosen for the bulk of the calculations and construction of diagrams in Sections 3.5 and 3.6. Perhaps somewhat fortuitously, this condition lies on the Clark & Ringwood (1964) shield

geotherm corresponding to a depth of 172 km (Dziewonski & Anderson, 1981). In addition, calculations were performed at two other points on the geotherm: 45 kbar (141 km depth), 1300 K and 70 kbar (215 km depth), 1500 K to test the applicability of the model over a range of conditions but still within or in the case of the 45 kbar point very close to the diamond stability field as defined by Kennedy & Kennedy (1976). The low temperature formation conditions for diamond indicated here are in accord with the suggestion of Boyd & Finnerty (1980) that most diamonds crystallise under sub-solidus conditions, however derivation from silicate melts saturated with water-rich volatiles is not precluded by these temperatures.

3.5 Fluid Compositions Co-existing with Diamond: The Stable Species Correction

Fig. 3.5 and Table 3.5 illustrate in log fO_2-X_C space the composition of C-O-H fluids in equilibrium with diamond at 55 kbar, 1400 K. Under these conditions H_2O, CO_2 and CH_4 are all present in significant amounts depending on fO_2. H_2 and C_2H_6 are expected minor species under reduced conditions (Section 2.7); the former always <3 mol% and the latter <5 mol%. CO is expected to be present in trace proportions only (<0.1 mol%). Reference to Appendix 11 and original data sources reveals that the species released by crushing experiments cannot have been in equilibrium with diamond under appropriate formation conditions. The large volumes of CO found (average 3.7 mol%, Sd = 4.4) are uncharacteristic of high pressure C-O-H fluids and suggest equilibration below 10 kbar. Similarly the high H_2 contents found in some diamonds suggest X_C-fO_2 conditions well removed from the diamond saturation curve, perhaps near composition "h" in Fig. 3.5. A feature of all analysed fluids is the high proportion of coexisting CO_2 (average 15.8 mol%, Sd = 7.2) and CH_4 (average 5.5 mol%, Sd = 2.6) in complete contrast to fluids lying on the diamond saturation curve where CH_4 and CO_2 are virtually mutually exclusive species. Again there is a suggestion that internal equilibration at $P < 10$ kbar and/or at $T >> 1400$ K has occurred (refer to Sections 2.7 and 2.10).

Fig. 3.5 log fO_2-X_C [= mole fraction $C/(C+H_2)$] diagram of the diamond saturation curve at P = 55 kbar, T = 1400 K. Points along the curve and in the stable divariant region (filled circles) together with a series in the metastable region (open circles) are identified by composition in Table 3.5. The synthetic oxide buffers MW and IW (from Schwab & Kustner, 1981 with P corrections) are indicated as heavy dashed lines. Hatched region delineates the stability of magnesite in the portion of the system $MgO-SiO_2-C-O-H$ relevant to mantle peridotites; the low fO_2 limit corresponds to the reaction:

$$Mag + Oen = Fo + G + O_2$$

which at this P and T coincides with the MW buffer. Magnesite may persist under these conditions to quite high mole fractions of H_2O before the limiting fCO_2 is reached, i.e. point "c" and its extension into the divariant field (dashed line) as:
Mag + Oen = Fo + V.

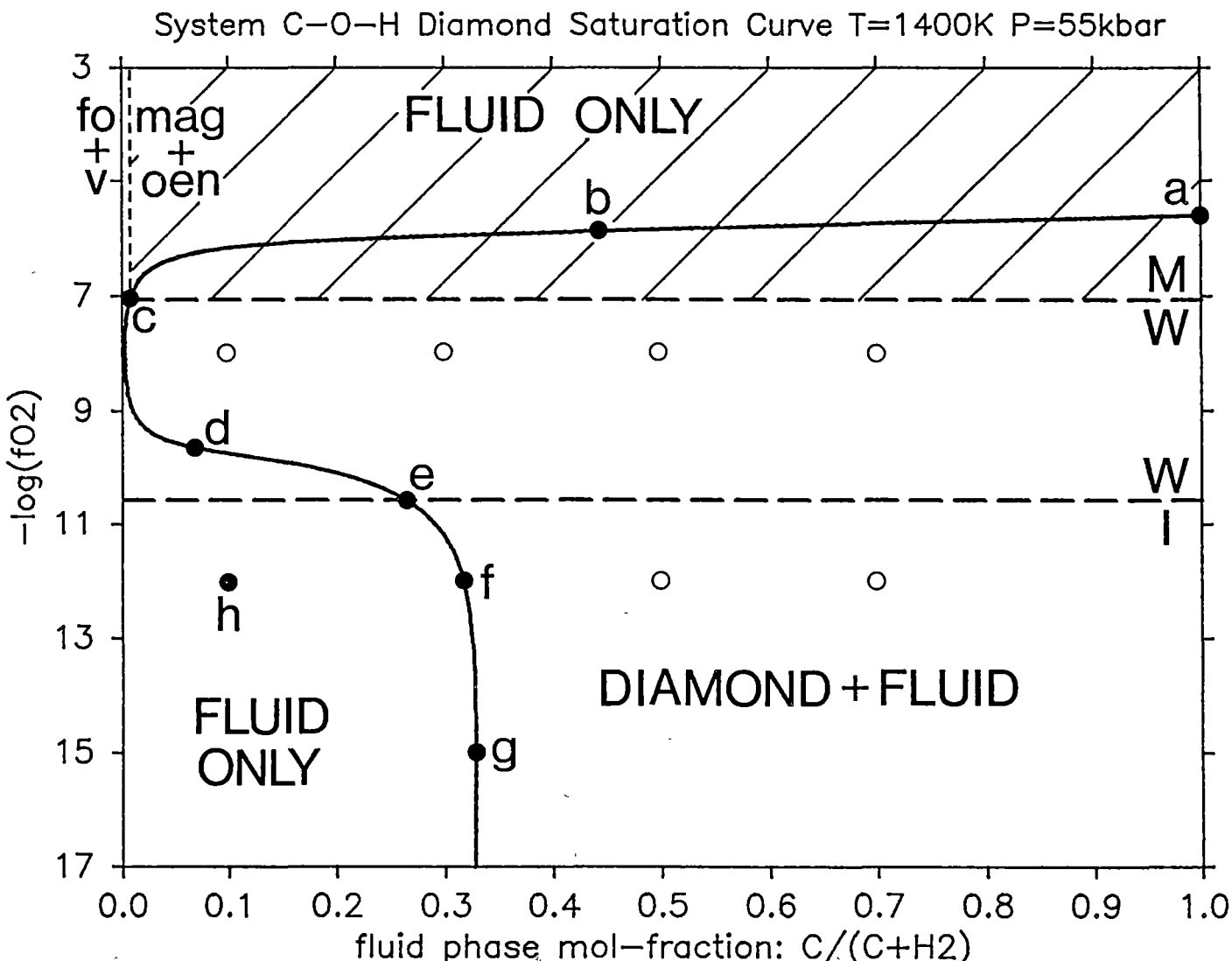
System C–O–H Diamond Saturation Curve T=1400K P=55kbar
fo + v
mag + oen
FLUID ONLY
a
b
c
d
e
f
g
h
M W
W I
FLUID ONLY
DIAMOND + FLUID
−log(fO2)
3
7
9
11
13
15
17
0.0
0.1
0.2
0.3
0.4
0.5
0.6
0.7
0.8
0.9
1.0
fluid phase mol–fraction: C/(C+H2)

Table 3.5 Fluid compositions at selected points in Fig. 3.5; T = 1400 K, P = 55 kbar.

1. EQUILIBRIUM FLUIDS

				mol% species*					
	$-\log fO_2$	X_C	X_O	H_2O	CO_2	CO	H_2	CH_4	C_2H_6	V^{mix} cm^3/mol
a	5.58	1.000	1.000	0	99.9	0.1	0	0	0	25.72
b	5.85	0.443	0.628	55.7	44.2	0.1	0	0	0	19.47
c[1]	7.07	0.007	0.337	99.3	0.6	0	0.1	0	0	14.26
c[2]	7.70	0.002	0.333	99.6	0.1	0	0.2	0.2	0	14.21
d	9.65	0.069	0.259	77.7	0	0	1.7	20.4	0.2	16.48
e[3]	10.58	0.263	0.064	19.1	0	0	2.6	75.6	2.7	22.71
f	12.00	0.316	0.011	3.3	0	0	2.7	89.9	4.1	24.40
g	15.00	0.327	0.000	0.1	0	0	2.7	92.8	4.4	24.75
h	12.00	0.100	0.155	46.5	0	0	23.5	30.0	0	16.96

1. fO_2 = MW 2. fO_2 = DW(max. x_{H_2O}) 3. fO_2 = IW

* Round-off error = $\pm$0.1 mol%.

2. METASTABLE FLUIDS (carbon supersaturated)

8.00	(	0.10	0.322	80.6	5.3	0.1	0.3	13.3	0.5	16.46
	(	0.30	0.339	46.9	17.8	0.4	0.3	30.8	3.7	20.59
	(	0.50	0.465	26.4	36.8	0.9	0.2	29.9	5.8	23.15
	(	0.70	0.681	16.0	61.3	1.4	0.1	18.0	3.2	24.11
12.00	(	0.50	0.174	0	3.2	14.2	0	7.0	75.5	33.57
	(	0.70	0.505	0	9.4	41.1	0	4.2	45.3	29.50

Irrespective of any re-equilibration amongst C-O-H species for whatever reason, it is immediately apparent that bulk H, O and C contents of the analysed fluids can be reconstituted into species stable under typical diamond crystallisation conditions. Let us assume for the moment that the system diamond-fluid is closed with respect to H, O and C and that no carbon is dissolved from or precipitated on the walls of fluid inclusions. The log fO_2-X_C diagram at 55 kbar, 1400 K neatly divides

oxidised H_2O-CO_2 fluids from reduced H_2O-CH_4-H_2-C_2H_6 fluids at the DW (diamond equivalent of GW) fO_2 buffer curve. This curve lies about 0.6 log units below both MW and the coincident EMOD buffer of Eggler & Baker (1982). The latter buffer defines the stability limit of carbonate ($MgCO_3$) coexisting with enstatite, forsterite, diamond and fluid at 55 kbar and extends to very water-rich fluid compositions (H_2O ~ 99 mol%) as indicated by point "c" in Fig. 3.5. Carbonate is stable only in the shaded portion of Fig. 3.5 at fO_2 > MW, EMOD.

Application of the stable species correction involves reconstituting the bulk fluid analyses in terms of the high pressure (>10 kbar) species H_2O, CH_4, H_2 and CO_2. Ethane must be neglected in order to obtain an unambiguous result and in any event is typically <1 mol% for the redox range considered here. The correction will be valid for all conditions in the range 30-70 kbar, 1300-1500 K. Where fluids do not contain excess H over O and C, a simultaneous equation is solved to distribute the elements amongst H_2O, CO_2 and CH_4; results are listed in column 2, Appendix 12. Program COH/FLUID6 was used to determine the (log fO_2,X_C) co-ordinates of the corrected fluids at 55 kbar, 1400 K and these points are plotted on log fO_2-X_C diagrams (Figs 3.6A to 3.6D) together with the diamond saturation curve.

It is immediately seen from the diagrams that none of the points plot on or even near the diamond saturation curve. These fluids thus could not have been in equilibrium with diamond under the chosen P,T conditions and as suggested previously most probably have been subject to some re-equilibration process to remove them from the saturation curve. Two groups of fluid compositions may be recognised from Figs 3.6A to 3.6D:

(a) Fluids super-saturated in carbon plotting at fO_2 ~ MW-1 log fO_2 unit. Compositions extend over a wide range of X_C values and contain substantial coexisting CO_2 and CH_4.

(b) Fluids plotting in the stable divariant region of the diagram at fO_2 ~ IW-1.4 log fO_2 units. Compositions are rich in H_2.

Both groups can only be explained by relaxing the assumption of closed system behaviour. The carbon super-saturation of group (a) may then be interpreted in terms of dissolution of carbon from the walls of the inclusion in response to some external change. Similarly group (b) fluids may have evolved by precipitating carbon on the inclusion walls. Carbon

dissolution/precipitation can be constrained adequately at high pressure with the aid of a few simple equilibria; if the system was also open to hydrogen then there are few constraints; some limits can however be placed on possible H loss/gain from the system.

3.6 Fluid Compositions Coexisting with Diamond: The Carbon Correction

Fluid compositions may be returned to the diamond saturation curve by assuming any deviations are the result of carbon precipitation or dissolution. For group (a) compositions plotting near the DW buffer, the principal governing equilibrium is:

$$CO_2 + CH_4 = 2C + 2H_2O \quad \ldots \quad (3.6A)$$

while for group (b) carbon precipitation may be described by the dominant equilibrium at lower fO_2's:

$$C + 2H_2 = CH_4 \quad \ldots \quad (3.6B)$$

the minor equilibrium:

$$2CH_4 = C_2H_6 + H_2 \quad \ldots \quad (3.6C)$$

can account for the small quantities of ethane and hydrogen found in high pressure fluids. Application of equation (3.6A) to group (a) fluids brings them all onto the diamond saturation curve by reversing the process of carbon dissolution; for group (b) fluids carbon is added via equation (3.6B). Minor species may be adjusted with equation (3.6C) for the particular P and T of interest with reference to a fluid composition vs fO_2 table generated by program COH/DIAMOND6 (Section 2.3). This has been investigated for the 55, 45 and 70 kbar conditions and the results presented in Appendix 12 and Figs 3.6A to 3.6D.

The following features may be noted:

(a) Estimated primary fluid compositions in equilibrium with diamond are all water-rich; no fluid has an X_C value above 0.33 [except the anomalous graphitisation experiment of Melton & Giardini (1976) discussed below].

(b) Fluids are divided into both oxidised (fO_2 > DW) and reduced (fO_2 <

Figs 3.6A to 3.6D Isothermal (T = 1400 K) log fO_2-X_C [= mole fraction $C/(C+H_2)$] diagrams constructed at 55 kbar showing diamond fluid inclusion compositions.

◇ stable species only correction applied

● stable species and carbon correction applied.

Dashed lines connect corrected analyses.

Analytical method: mass spectrometry unless otherwise indicated.

Fig. 3.6A	P1, P2, P3	Panna, Central India
	G	Average graphitisation result for P1 to P3.
	HNO-1	Ion-beam partial analysis (Sellschop et al., 1980) plotted on saturation curve. Unspecified South African origin.
Fig. 3.6B	K1, K2	Kimberley mine, South Africa.
	Pr	Premier mine, South Africa.

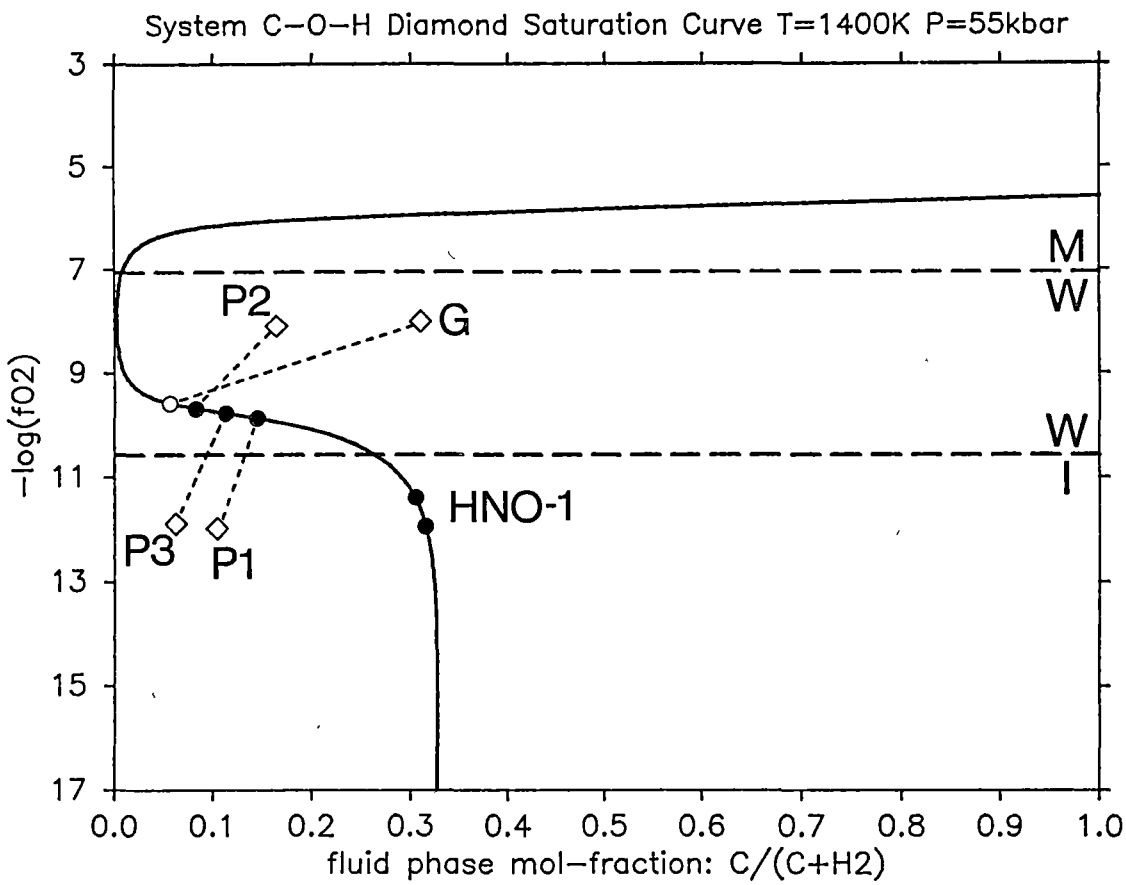
System C–O–H Diamond Saturation Curve T=1400K P=55kbar
3
5
7
9
11
13
15
17
−log(fO2)
M
W
W
I
P2
G
HNO-1
P3
P1
0.0
0.1
0.2
0.3
0.4
0.5
0.6
0.7
0.8
0.9
1.0
fluid phase mol–fraction: C/(C+H2)

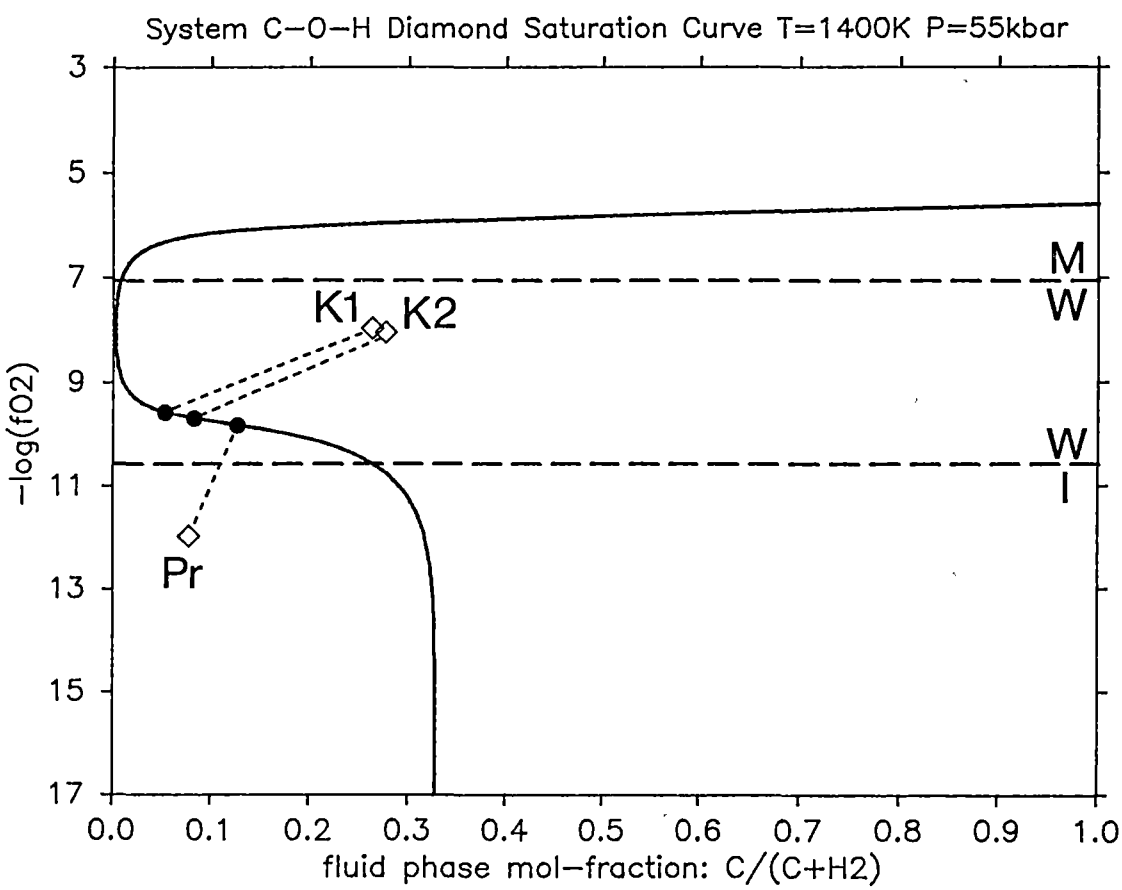
System C–O–H Diamond Saturation Curve T=1400K P=55kbar
3
5
7
9
11
13
15
17
−log(fO2)
M
W
W
I
K1
K2
Pr
0.0
0.1
0.2
0.3
0.4
0.5
0.6
0.7
0.8
0.9
1.0
fluid phase mol–fraction: C/(C+H2)

Fig. 3.6C A1-7 Arkansas, U.S.A.

G Graphitization result for single diamond.

* Point on saturation curve corresponding to complete H_2 loss from fluid A1 via the reaction:

$CH_4 + 2H_2O = CO_2 + 4H_2$.

Fig. 3.6D Z1-7 Zaire, cubic morphology.

B Brazil, cube showing translation of a small analytical error or inhomogeneity in fluid composition into a large fO_2 difference in the region close to the x_{H_2O} maximum.

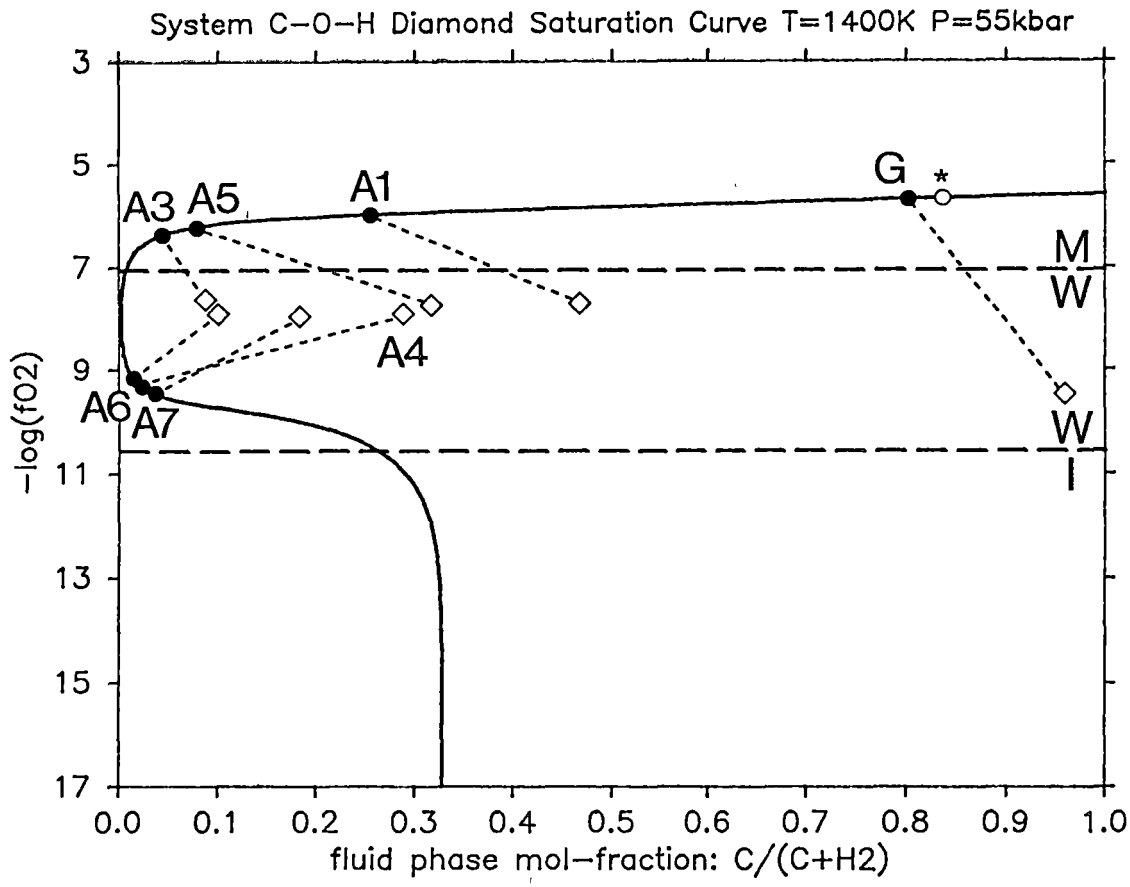
System C–O–H Diamond Saturation Curve T=1400K P=55kbar
-log(fO2)
3
5
7
9
11
13
15
17
A3
A5
A1
G
*
A4
A6
A7
M
W
W
I
0.0
0.1
0.2
0.3
0.4
0.5
0.6
0.7
0.8
0.9
1.0
fluid phase mol–fraction: C/(C+H2)

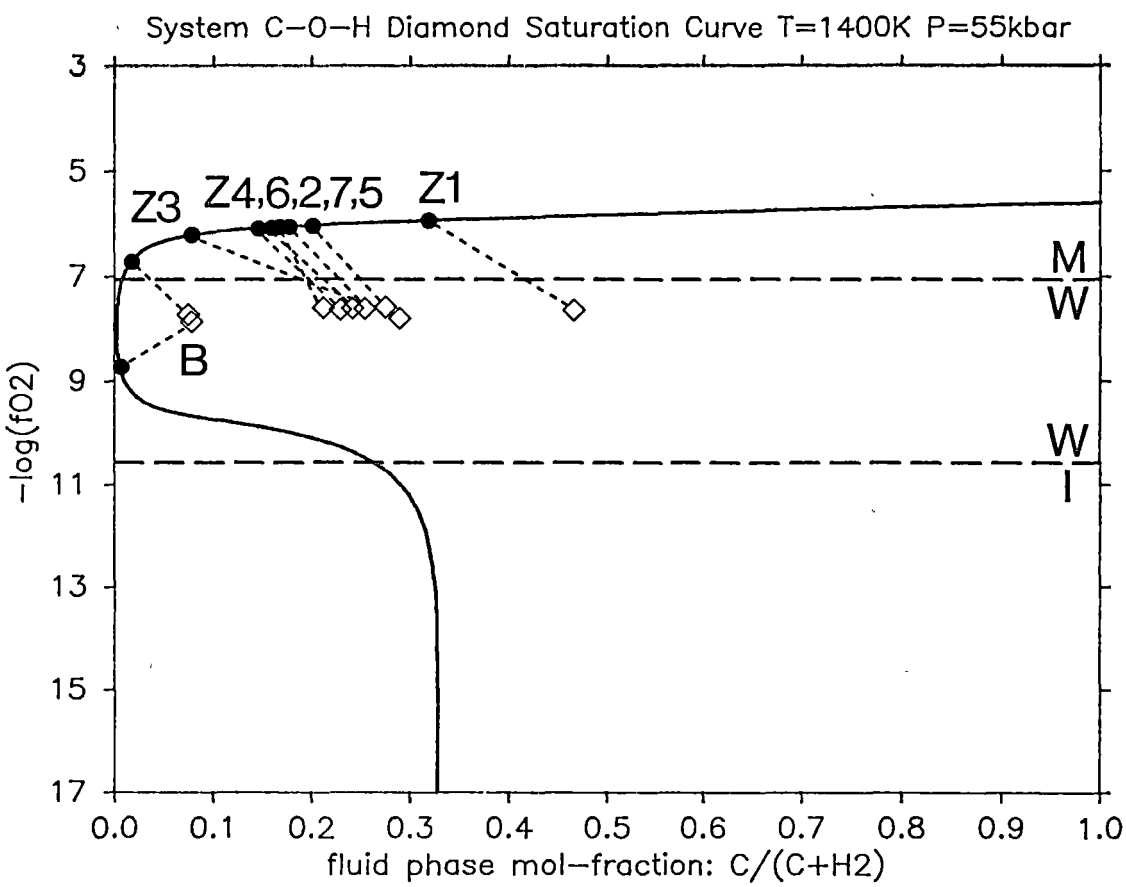
System C–O–H Diamond Saturation Curve T=1400K P=55kbar
-log(fO2)
3
5
7
9
11
13
15
17
Z3
Z4,6,2,7,5
Z1
B
M
W
W
I
0.0
0.1
0.2
0.3
0.4
0.5
0.6
0.7
0.8
0.9
1.0
fluid phase mol–fraction: C/(C+H2)

DW) groups. The former are H_2O-CO_2 mixtures and the latter H_2O-CH_4-H_2-C_2H_6 mixtures.

(c) The cubic diamond morphology exclusively contains fluids of the oxidised group. Diamonds from South Africa and India contain only reduced fluids while those from Arkansas are equally distributed between the two groups.

(d) There is no obvious correlation of fluid type with other diamond properties except morphology (Appendix 11).

(e) The average composition of graphitisation experiments on Panna diamonds gives a point plotting in log fO_2-X_C space that lies very close to the results obtained for crushing. Provided there has been no preferential H or O loss during graphitisation, the H/O ratio of fluid inclusions corrected for carbon approximates the bulk H/O of the diamond. This includes H and O residing in defect and other sites (Section 3.2) all of which are released by graphitisation but not by crushing. Since both experiments yield similar results there would seem to be little evidence for large scale diffusive H-loss from fluid inclusions or the volumetrically more significant defect sites.

(f) The graphitisation result obtained for an Arkansas diamond (Melton & Giardini, 1976) plots at a very carbon-rich composition well away from all other Arkansas diamond fluids. An uncorrected fluid such as A1 can only reach the point "G" in Fig. 3.6C by almost complete H_2 loss via a reaction of the type (indicated by the "*"):

$$2H_2O + CH_4 \text{ ----> } CO_2 + 4H_2\uparrow \qquad \ldots (3.6D)$$

Since there is no evidence for gross H-loss in other diamonds it appears unlikely that this experiment represents an accurate result, a conclusion also reached by Bibby (1982, p.31).

(g) Separate crushing experiments on samples of Brazilian cubic diamond "B" give similar compositions when only corrected for stable species but quite different (log fO_2,X_C) co-ordinates when the carbon correction is applied. This effect is accentuated by the large zone of diamond + water-rich fluid which extends over ~2 log fO_2 units. A small difference in measured H/O ratio will thus be transmitted as a large fO_2 difference on this portion of the diamond saturation curve. Fluids measured for diamond "B" suggest that small heterogeneities in inclusion chemistry may occur although such variations are within the range of analytical uncertainty.

(h) Ion beam studies by Sellschop et al. (1980) have provided analyses of H and O on cleaned diamond surfaces prior to and after annealing at high temperatures. Assuming H and O are present in surface sites with a ratio that is close to that of the bulk diamond (including fluid inclusions), a point on the diamond saturation curve, corresponding to a H/O compatible C-O-H fluid may be found. For diamond HNO-1 (of presumed South African origin) this occurs at fO_2 = IW-0.8 log fO_2 units for surface cleaned and fO_2 = IW-1.4 log fO_2 units after annealing. This diamond therefore belongs to the reduced group, having a similar H/O and hence fO_2 to Panna and Premier diamonds prior to carbon correction. Because no carbon analysis can be provided in this case, the X_C co-ordinate remains unlocated and no carbon correction is possible. It is likely though that HNO-1 follows a similar trend to other group (b) diamonds in which case primary fluids would be expected to be largely CH_4-H_2O mixtures.

(i) Results are applicable for both the 45 and 70 kbar conditions and by inference a large part of the diamond stability field as well.

3.7 Re-equilibration of Fluids Contained by Diamond: Evidence for Inclusion Volume Relaxation

Presently observed fluid compositions in diamond appear to be the result of a re-equilibration process occurring in response to external change. A secondary origin for these fluids is not required if it can be demonstrated that primary fluid inclusions with initial trapping pressures >50 kbar are able to survive decrepitation at lower confining pressures. The purpose of this Section is to determine whether any one re-equilibration process offers an adequate explanation for the observed fluids; the survivability of inclusions will be considered in Section 3.8 in the light of these results.

The most significant external change affecting diamond would obviously occur during transport from the mantle P,T regime to the Earth's surface. Reference to Figs 2.6A and 2.6B shows the effect of P and T variation on the position of the carbon saturation curve. To achieve fluid compositions near DW or GW with high X_C values (as found in most of the uncorrected diamond fluids) it would be necessary to decrease average internal fluid pressure from 55 kbar to less than ~10 kbar or alternatively to increase T to in excess of 1600 K. Two possible models can be imagined:

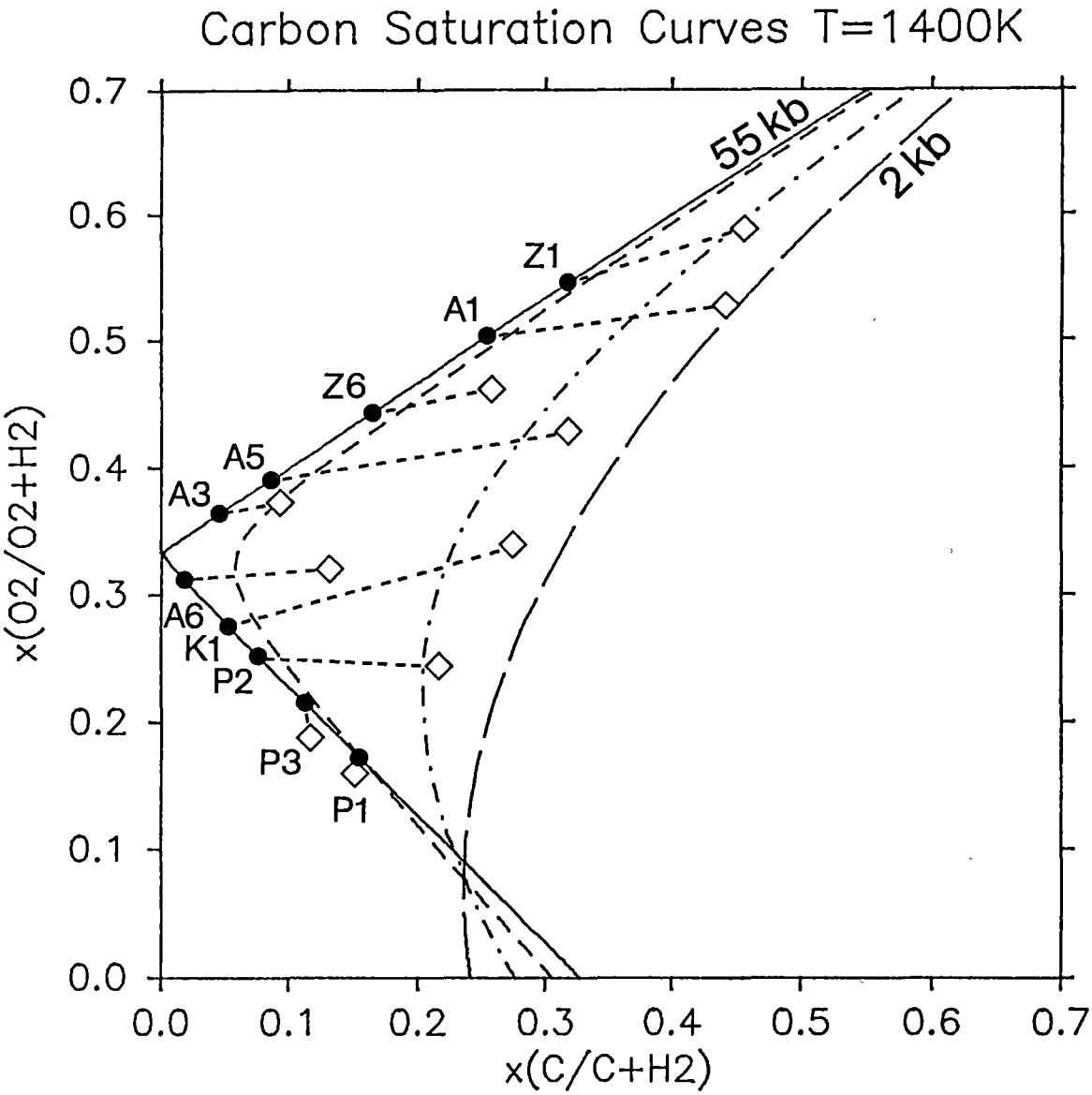

Fig. 3.7 X_C [C/(C+H_2)] versus X_O [O_2/(O_2+H_2)] diagram with diamond and graphite saturation curves indicated for 55 kbar (———); 15 kbar (-----); 5 kbar (—·—·—) and 2 kbar (— — —). Selected diamond derived fluid compositions are plotted:

◇ **uncorrected** fluids

● stable species and carbon corrections applied.

Uncorrected fluids show substantial low pressure character. Dashed lines connect low-P and 55 kbar corrected fluids.

(a) Relaxation in the volume occupied by fluid inclusions resulting in a decrease of apparent trapping pressures, e.g. as a result of fracture, elastic or plastic deformation, or chemical solution.

(b) Large increase in external temperature, e.g. a result of entrapment of diamond by host magma at pressures within the diamond stability field.

The latter model does not appear likely in view of the fact that external temperature increases of >500 K would be required to produce the observed high X_C^{fluid} contents at pressures >40 kbar. The required temperatures of >1600 K would be well beyond those necessary to generate volatile-rich kimberlite melts (Wyllie, 1980) and it is unlikely that diamond would survive transport to the surface along shallow dP/dT adiabatic gradients with such a high initial temperature (Anderson, 1979). In any event, the low pressure character of diamond-derived fluids (e.g. high CO contents) is difficult to explain by this mechanism.

If volume relaxation processes are important then they should be readily apparent on a $X_O(O_2/O_2+H_2)$ vs $X_C(C/C+H_2)$ diagram showing compositional variation in the position of carbon saturation curves as a function of pressure. Uncorrected fluid compositions (no stable species or carbon correction) are plotted on an isothermal X_O vs X_C diagram in Fig. 3.7 together with 55, 15, 5 and 2 kbar saturation curves. Uncorrected points are connected by dashed lines to the corrected fluids on the 55 kbar curve. In all cases except P1 and P3, uncorrected fluids plot below the 55 kbar saturation curve showing apparent average trapping pressures of between 15 and 2 kbar, clearly outside the diamond stability field. Thus if the fluids included in diamond can be shown to be consistent with a primary origin then inclusion volume relaxation due to fracture or some other mechanism is a significant process in the determination of final fluid composition. This result contrasts with most other crystal-fluid systems where Roedder (1981) believes constancy of inclusion volume has usually been maintained. Diamond is an exceptional case in this regard since the host phase and the fluid are capable of chemical interaction that can greatly alter the composition of the latter.

3.8 An Elastic Model for Crack Propagation about Fluid Inclusions in Diamond

The purpose of developing a model to describe the behaviour of fluids trapped in diamond in response to external pressure changes is two-fold. Firstly, what pressure differential (external confining pressure minus internal fluid pressure) can inclusions in diamond withstand without undergoing decrepitation, and is this sufficient to suggest a primary origin for fluids trapped in diamond? Secondly, is inclusion volume relaxation a likely physical process for producing observed fluid compositions? Can this be quantified in any way?

In reference to the first point, Roedder (1981, 1983) and Murck et al. (1978) have found moderate-sized (~5-20 μm) CO_2 inclusions in olivine that have withstood pressure differentials of as much as 7000 to 10,000 bars. In quartz 1 μm inclusions may survive ~6000 bar internal pressures but at ~12 μm this limit is near 1200 bars (Roedder, 1981). To investigate the decrepitation limits for diamond, we have chosen an isothermal elastic model to describe crack propagation about a spherical inclusion in diamond. The selection of isothermal behaviour is an approximation that considerably simplifies the problem. While the actual dP/dT path of diamond transport to the surface is likely to follow an adiabatic gradient resulting in temperature reductions of ~200 K at the surface (Anderson, 1979), the isothermal case represents the "worst possible" situation for the survivability of fluid inclusions.

Consider an ellipsoidal "penny-shaped" crack of radius c (Fig. 3.8A) initiated about a spherical fluid inclusion of radius R such that $c \gg R$ in a homogeneous, isotropic elastic body of overall dimensions very much larger than the crack radius c.

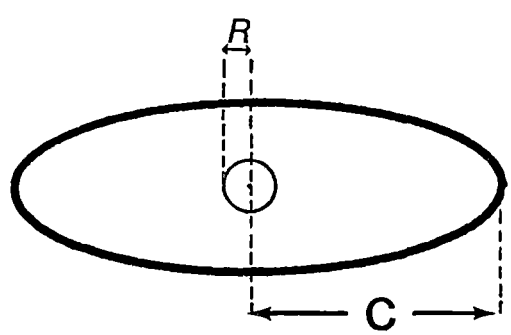

Fig. 3.8A Cross-section of ellipsoidal crack.

In reality there will be some departure from perfect elastic behaviour due to a small amount of plastic flow induced at the edges of the crack because of high stress concentrations. The strain energy will not however differ significantly from that derived by elastic equations (Sneddon, 1946).

Consider the work done by the system in generating the crack, there will be three contributions:

(a) Surface Energy, W_{sur}

Work must be done in creating the crack surface by C-C bond cleavage and may be expressed (Sneddon, 1946, p.260) by the equation:

$$W_{sur} = 2\pi c^2 \gamma \qquad \ldots \quad (3.8A)$$

where c = crack radius/m

γ = fracture surface energy/Jm^{-2}

Values of γ for diamond are summarised below:

Table 3.8A

	γ/Jm^{-2}	Medium
Theoretical calculation (Field, 1979, p.284)	5.3	Vacuum
Experimental (Field (1979, p.302)	6	Vacuum
Estimated	~4	Aqueous fluid

The fracture surface energy is typically reduced by amounts ~20-60% if the internal medium is a gas or fluid and not a vacuum (Field, 1979); choice of a value of ~4 Jm^{-2} is consistent with the difference in γ between silicate glass-vacuum and silicate glass-gas systems.

(b) Work of Compression, W_{com}

Work must be done in elastically compressing the atoms surrounding the ellipsoidal crack. An expression for W_{com} is derived by Sneddon (1946, p.244):

$$W_{com} = \frac{8(1-\sigma^2)}{3E} P_f^2 c^3 \qquad \ldots \quad (3.8B)$$

where σ = Poisson's ratio

E = Young's modulus/Nm^{-2}

P_f = final internal fluid pressure of inclusion + crack/Pa

For diamond the following values are applicable (Field, 1979, Appendix IIB):

$\sigma \sim 0.2$

$E = 10.5 \times 10^{11}\ Nm^{-2}$.

(c) Work of Fluid Expansion, W_{vol}

Work done by isothermal, reversible expansion of a C-O-H fluid into the growing crack.

$$W_{vol} = -\int_{P_i}^{P_f} P.dV \qquad \ldots \quad (3.8C)$$

where P_i = initial inclusion pressure, taken as 5.5×10^9 Pa or 55 kbar.

P_f = final inclusion + crack fluid pressure/Pa.

V = volume occupied by fluid/m^3.

A C-O-H fluid composition consisting of 80 mol% H_2O, 18 mol% CH_4 and 2 mol% H_2 was chosen for the model calculations; it is close to many of the reduced fluids derived from diamond (Figs 3.6A to 3.6D). Because of the similar volumetric properties of CH_4 and CO_2 (Section 1.5) this composition should also be generally applicable to oxidised fluids with ~20 mol% CO_2. 5PMRK molar volumes for T = 1400 K over a range of pressures from 1 to 60 kbar were calculated and fitted to a polynomial of the form:

$$V_m = \bar{a} + \bar{b}P^{-1} + \bar{c}P^{-2} + \bar{d}P^{-3} + \bar{e}P^{-4} \qquad \ldots \quad (3.8D)$$

using program FUNFIT (Veng Pedersen, 1977). The resultant fit gave a multiple correlation coefficient of 0.999921 and the following parameters:

$\bar{a} = 1.3431 \times 10^{-5}\ m^3 mol^{-1}$

$\bar{b} = 1.6876 \times 10^{4}\ m^3 Pa\ mol^{-1}$

$\bar{c} = -3.2534 \times 10^{12}\ m^3 Pa^2\ mol^{-1}$

$\bar{d} = 5.8163 \times 10^{20}\ m^3 Pa^3\ mol^{-1}$

$\bar{e} = -3.1409 \times 10^{28}\ m^3 Pa^4\ mol^{-1}$

Taking the derivative, dV, of equation (3.8D) with respect to P and substituting in equation (3.8C), an equation for W_{vol} is obtained in terms of P_f:

$$W_{vol} = \left[\bar{b} \ln P_f - \frac{2\bar{c}}{P_f} - \frac{3\bar{d}}{2P_f^2} - \frac{4\bar{e}}{3P_f^3}\right] + (\text{constant})$$

(d) Total work done by the system, W_{tot}

Total work done is the sum of the individial contributions:

$$W_{tot} = W_{sur} + W_{com} + W_{vol}$$

Spontaneous crack growth will occur when the condition $\partial W_{tot} / \partial c \leq 0$ applies; the minimum in the W_{tot} vs c curve corresponds to the equilibrium crack size (see Fig. 3.8B).

Using the constraint $V_{crack} = V_{fluid}$, i.e. the volume occupied by the fluid must equal that of the crack, W_{tot} may be obtained as a function of c. Integrating equation 3.3.2 of Sneddon (1946, p.242) to generate a volume of revolution, we get:

$$V_{crack} = \left[\frac{16(1-\sigma^2)}{3E}\right] c^3 P_f \qquad \ldots \quad (3.8E)$$

V_{fluid} (m^3) is obtained from equation (3.8D) by multiplying by the number of moles fluid present. The latter quantity follows directly from the initial specification of spherical inclusion size. Equating equations (3.8D) and (3.8E) and re-arranging in terms of c, we obtain:

$$c = \left[\left[\frac{3E.N}{16P_f(1-\sigma^2)}\right].(\bar{a}P_f^{-1} + \bar{b}P_f^{-2} + \bar{c}P_f^{-3} + \bar{d}P_f^{-4} + \bar{e}P_f^{-5})\right]^{1/3} \quad \ldots (3.8F)$$

where N = number of moles fluid occupying initial inclusion.

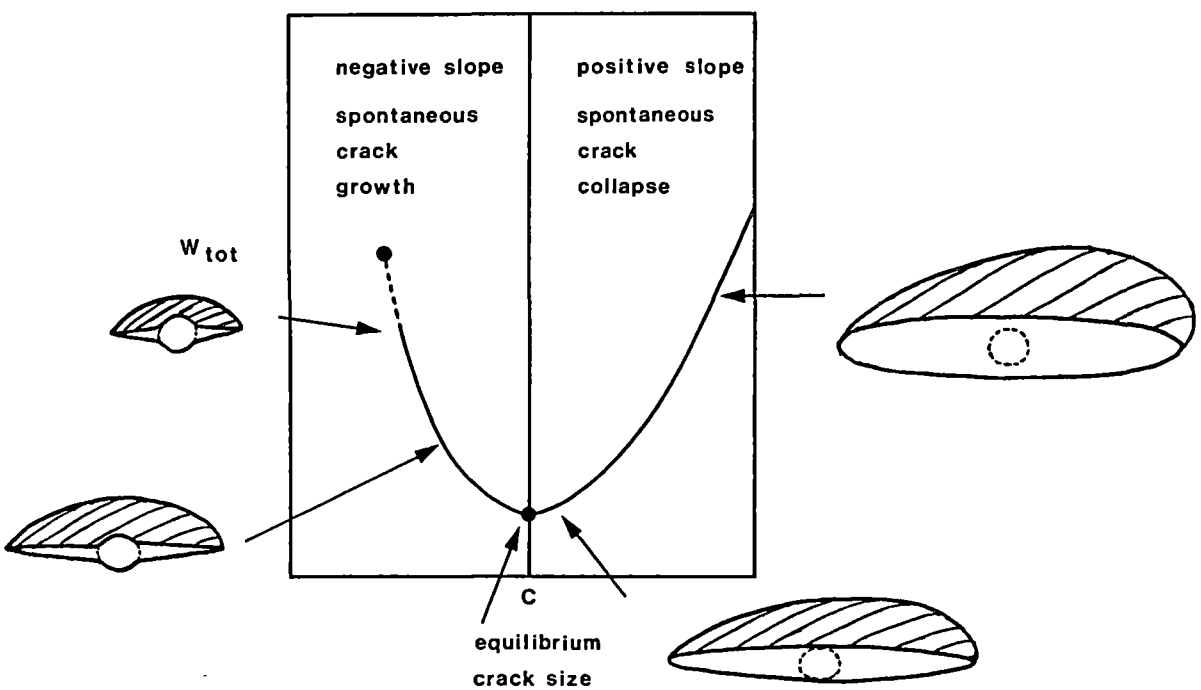

Fig. 3.8B W_{tot} vs c curve, schematic.

Using a simple numerical technique, equation (3.8F) may be solved for P_f at any crack radius c and hence W_{tot} determined. The W_{tot} vs c curve will terminate when c becomes so small that the initial spherical inclusion volume approaches V_{crack}. In this region the assumption that c be much larger than R (the initial inclusion radius) will not be valid and the surface area of the system can no longer be described entirely by the crack ellipsoid, i.e. there is a substantial initial spherical component. The W_{tot} vs c curve in the region where c approaches R will thus be an approximation only.

(e) Results

Program CRACKGEN, written in Algol, has been designed to perform the above calculations. Results and a sample output are presented in Fig. 3.8C and Table 3.8B below:

Table 3.8B Sample output: program CRACKGEN.

Pressure (initial) = 55 kbar (5.5×10^9 Pa)
Initial inclusion volume = 6.545×10^{-17} m^3 (65.5 μm^3)
Initial inclusion radius = 2.5 μm
Initial inclusion contents = 3.992×10^{12} mols fluid
$K = \{16(1-\sigma^2)/3E\} = 4.8762 \times 10^{-12}$ Pa^{-1}

Crack size: c	25 μm	50 μm	55 μm*	60 μm	100 μm
W_{sur}	1.571	6.283	7.603	9.048	25.13
W_{com}	7.083	5.066	5.101	5.186	6.670
W_{vol}	-9.565	-19.37	-20.85	-22.28	-32.63
W_{tot}	-0.911	-8.017	-8.150	-8.044	-0.829
P(final)/bar	13636	4077	3546	3138	1654
$V_{crack}/\mu m^3$	104	249	288	331	807

(W_{sur}, W_{com}, W_{vol}, W_{tot} in $\cdot 10^8$ J)

* minimum on c vs W_{tot} curve.

From the Table it is seen that the work done in creating the surface and compressing the C atoms surrounding the crack is offset by energy generated in reversible expansion of the trapped fluid. The final internal fluid pressure decreases very rapidly during the first stages of crack growth. Fig. 3.8C shows W_{tot} vs c curves for initial inclusion diameters of 1, 5, 10 and 20 μm. The corresponding equilibrium ellipsoidal crack radii (c) generated by expansion of a H_2O-CH_4-H_2 fluid in response to a reduction in external confining pressure are 6, 55, 170 and >300 μm with final internal fluid pressures of 9.6, 3.5, 2.0 and <1.5 kbars respectively. Selecting the arbitrary criterion that cracks will propagate to the diamond surface if radii exceed 0.3 mm (i.e., by assuming similarly sized inclusions are distributed <0.6 mm apart), it follows that initial primary inclusions of spherical or approximately spherical habit with diameters >10 μm are unlikely to survive and will decrepitate during transport from mantle depths to the surface.

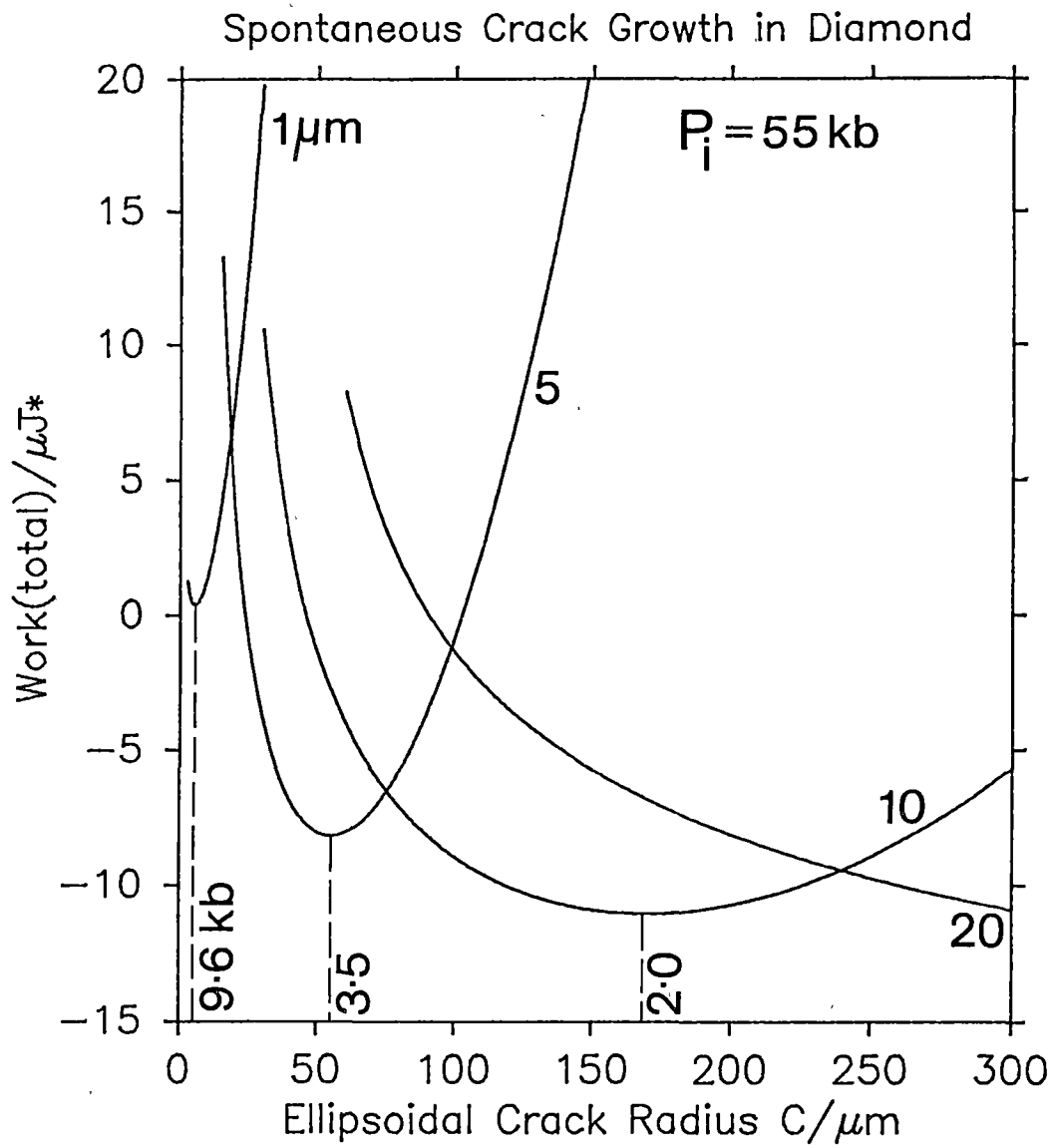

Fig. 3.8C Isothermal (T = 1400 K) curves showing total work done in elastically forming an ellipsoidal crack about an initially spherical fluid inclusion in diamond. Modelled on initial inclusions of 1, 5, 10 and 20 microns diameter containing a H_2O-CH_4-H_2 fluid at $P_{initial}$ = 55 kbar. Equilibrium crack radii occur at minima in the total work curves with corresponding internal fluid pressures indicated. Initial inclusions of >10 microns diameter are unlikely to survive transport to the Earth's surface.

* units of μJ refer only to the 20 μm curve; other curves as follows: 10 μm 10^{-7}.J; 5 μm 10^{-8}.J; 1 μm 10^{-9}.J

Those inclusions having diameters <10 um can probably survive decrepitation but may still develop large crack halos causing a significant decrease in internal fluid pressure and a corresponding shift in C-O-H equilibria towards a lower pressure regime during diamond transport. If these fluids are rapidly quenched at the Earth's surface or the cracks maintained by some non-elastic relaxation process (e.g. plastic deformation* or brittle failure) or if dissolution of the crack walls has occurred then evidence of low pressure fluid equilibration will be retained in diamond even though the model is strictly an elastic one.

Evidence for the operation of this type of process is found in SEM studies of high fluid inclusion density areas ("cloud-like" regions) in Arkansas diamonds (Giardini & Melton, 1975). The authors find that "relatively large flattened cavities" of 50-150 μm long dimension are common in both diamonds studied. One of these is sample A1 which contains average fluids of quite low pressure character (plotting near the 3 kbar carbon saturation curve in Fig. 3.7). Reference to Fig. 3.8C shows that fluids with an average internal pressure of ~3 kbar would correspond to an initial (i.e. at ~55 kbar) average inclusion size of between 5 and 10 microns. If crack halos form around such inclusions during ascent and volume relaxation is maintained by some non-elastic process, then cracks or voids of ~100 μm radius (see Fig. 3.8C) may be preserved in diamond. Some of the textures observed by Giardini & Melton (1975) can be explained by this type of process (e.g. the longtitudinal voids in their Figs 2 & 5). The implication here is that some of the large cavaties contain a low pressure (~2-3 kbar) fluid that may be released by crushing. Roedder (1984) noted that many of the larger cavities were interconnected with some actually intersecting the external surface. In these cases the distribution density of original fluid inclusions may have been high enough to allow connection of adjacent inclusions during volume relaxation. While these ideas are somewhat speculative at this stage, it is interesting to note in support of the volume relaxation model, that no uncorrected fluid

* A significant proportion of diamonds show evidence of post-deformation plastic deformation (Harris et al., 1984) and occurrence of non-elastic relaxation processes have been demonstrated for garnet inclusions in diamond (Harris et al., 1970).

compositions plot below 2 kbar in Fig. 3.7. This is exactly what is expected if fluid inclusions of size greater than about 10 microns diameter are unable to survive during ascent of diamond to the Earth's surface. The model thus appears consistent with both chemical and observational data.

In summary we find that:

(i) Primary fluid inclusions in diamond transported approximately isothermally to the Earth's surface are expected to withstand decrepitation provided original diameters do not exceed ~10 microns.

(ii) Crack propagation about fluid inclusions in diamond will occur spontaneously if initiated (e.g. by a high stress concentration in an imperfectly shaped inclusion) until an equilibrium crack size is reached. The criterion for spontaneous growth is that $\partial W_{tot} / \partial c \leq 0$ where W_{tot} = total work done in forming the new surface + compressing the atoms + expanding the fluid, and c = crack radius.

(iii) Processes of non-elastic relaxation (possibly plastic deformation and/or dissolution processes) may preserve the large cavities that are found in some diamonds.

(iv) Inclusion volume relaxation is a viable process for explaining the low pressure character of fluid compositions in diamond and should be amenable to quantitative modelling.

3.9 An Isothermal Model for the Pressure Relaxation Path of Diamond Fluids

The process of inclusion volume relaxation causes a reduction in internal fluid pressures. As indicated by fluid inclusion analyses this has the effect of shifting C-O-H fluid equilibria into a lower pressure regime. As a consequence, most analyses are enriched in carbon (high X_C^{fluid} values) indicating that the system was not closed and that dissolution of carbon from fluid inclusion walls has occurred. Some inclusion analyses suggest the reverse behaviour and may be related to carbon precipitation from the fluid. Can all these observations be reconciled in terms of a quantitative model plotting the path of fluid

composition as a function of pressure? This question has been investigated for four representative fluids: A5, Z1, K1 and P1.

The method is simply to take the 55 kbar corrected fluid compositions (Section 3.6) and follow at constant H/O ratio and temperature (in this case 1400 K) the compositional path at successively lower pressures to a limit of 2 kbar. This is done with a series of log fO_2 vs fluid composition tables generated by programs COH/DIAMOND6 and COH/GRAPHITE6. By using program COH/FLUID6 and an estimate of final inclusion pressure from Fig. 3.7, the (log fO_2,X_C) co-ordinates of the uncorrected fluids may also be determined. If the model correctly portrays the pressure relaxation process then these points should lie on or very close to the constant H/O curve.

Results are plotted in Fig. 3.9 on a log fO_2-X_C diagram and an example of the calculation for Z1 is given in Table 3.9 below.

Table 3.9 Constant H/O path for pressure relaxation in fluid Z1 at 1400 K.

	55 kbar	30 kbar	15 kbar	5 kbar	2 kbar	Z1*	best match P=4 kbar
H_2O	68.2	67.6	64.5	48.0	32.4	46.1	45.0
CO_2	31.8	31.8	32.1	32.8	29.1	30.4	32.0
CO	0	0.3	1.6	9.3	21.4	12.8	11.5
H_2	0	0.2	0.9	4.2	8.8	3.5	5.2
CH_4	0	0.1	0.9	5.7	8.3	7.2	6.3
log fO_2	-5.92	-8.09	-9.64	-11.06	-11.82	-	-11.25
X_C	0.318	0.321	0.340	0.440	0.533	0.456	0.456

* small amounts of ethanol and molecular oxygen present in original analysis recalculated as CH_4, H_2 and CO_2.

It is found from Fig. 3.9 that constant H/O curves for all four fluids overall tend toward higher X_C values, the largest increases occur for initial fluids that are rich in H_2O. Only for the most reduced fluid P1 does the carbon content actually decrease, reaching a minimum at ~30 kbar, then increases toward lower pressures. For Z1, A5 and K1 uncorrected

Fig. 3.9 Isothermal (T = 1400 K) log fO_2-X_C [= mole fraction $C/(C+H_2)$] diagram showing constant H/O re-equilibration paths (dashed lines) for four diamond derived fluids assuming a process of isothermal inclusion volume relaxation operates. Tick marks correspond to pressures of 30, 15 and 5 kbar going from 55 to 2 kbar along the constant H/O paths.

● 55 kbar corrected fluid compositions.

◇ best fit uncorrected fluid compositions.

Only fluid P1 (best fit at ~5 kbar) plots well off the modelled path suggesting departure from isothermal behaviour or operation of additional re-equilibration mechanisms.

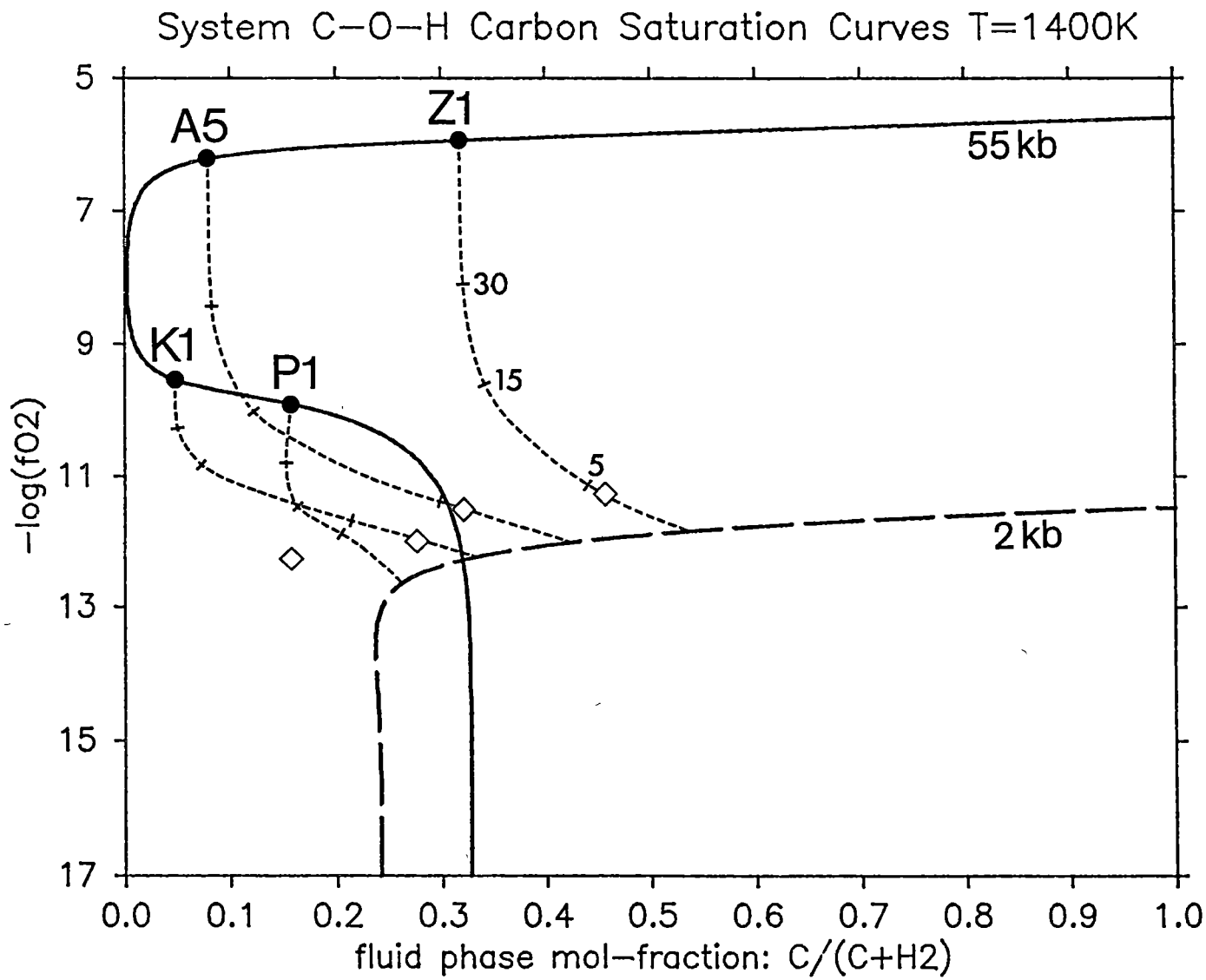
System C–O–H Carbon Saturation Curves T=1400K
A5
Z1
55 kb
30
15
5
K1
P1
2 kb
5
7
9
11
13
15
17
−log(fO2)
0.0
0.1
0.2
0.3
0.4
0.5
0.6
0.7
0.8
0.9
1.0
fluid phase mol–fraction: C/(C+H2)

fluids plot directly on the constant H/O curves, intersecting the graphite saturation curves at ~4 (Z1, A5) and ~3 (K1) kbar. Calculated species distributions at these pressures match reasonably well but not perfectly with actual compositions (see Table 3.9 for Z1). Bearing in mind that the uncorrected fluids are averages of a variety of differently equilibrated fluids depending on the inclusion and crack size distribution within the diamonds and that the model is only an isothermal approximation, agreement is well within allowable tolerances. Small amounts of alcohols and alkenes present in some diamonds cannot be modelled thermodynamically in a satisfactory manner at low pressures (Section 2.3). Their origin may be via some catalytic process on internal surfaces which are known to be chemically active (Thomas, 1979) (e.g. a Fischer-Tropsch type synthesis). This hypothesis is however speculative and the origin of these compounds remains open.

Fluid P1, and by analogy other H_2-rich fluids (P3, Pr) do not plot particularly close to the pressure relaxation curve despite the minimum in X_C near 30 kbar (indicating carbon loss from the fluid). This is supported by Fig. 3.7 where P1 and P3 uncorrected points plot in the stable divariant field and not on any of the carbon saturation curves. The high levels of H_2 in these fluids (>50 mol%) cannot be duplicated at 1400 K for any pressure between 0.5 and 55 kbar. These fluids may thus have been subject to a re-equilibration path that has deviated greatly from isothermal behaviour. It is also possible that some proportion of the H_2 reported analytically was derived as a result of defect site aggregation in response to external deformation processes. A process of vacancy enhanced aggregation of nitrogen has been proposed by Harris et al. (1984) in diamonds which show evidence of being plastically deformed. Evidence of deformation is found in diamonds P1-P3 from India which contain anomalous birefringent zones and have been descrined as being "intensely strained and brittle" by Giardini et al. (1982, p.184). Fortunately, if redistribution of H_2 has occurred from defect or other sites in Panna diamonds then this, as confirmed by graphitisation experiments, has not significantly affected the (log fO_2,X_C) co-ordinates of the corrected 55 kbar fluids.

It is of interest to calculate the magnitude of volume relaxation in fluid inclusions that would be solely due to dissolution of the inclusion walls. A calculation for fluid Z1 is given below assuming an initial spherical inclusion of 5 μm diameter.

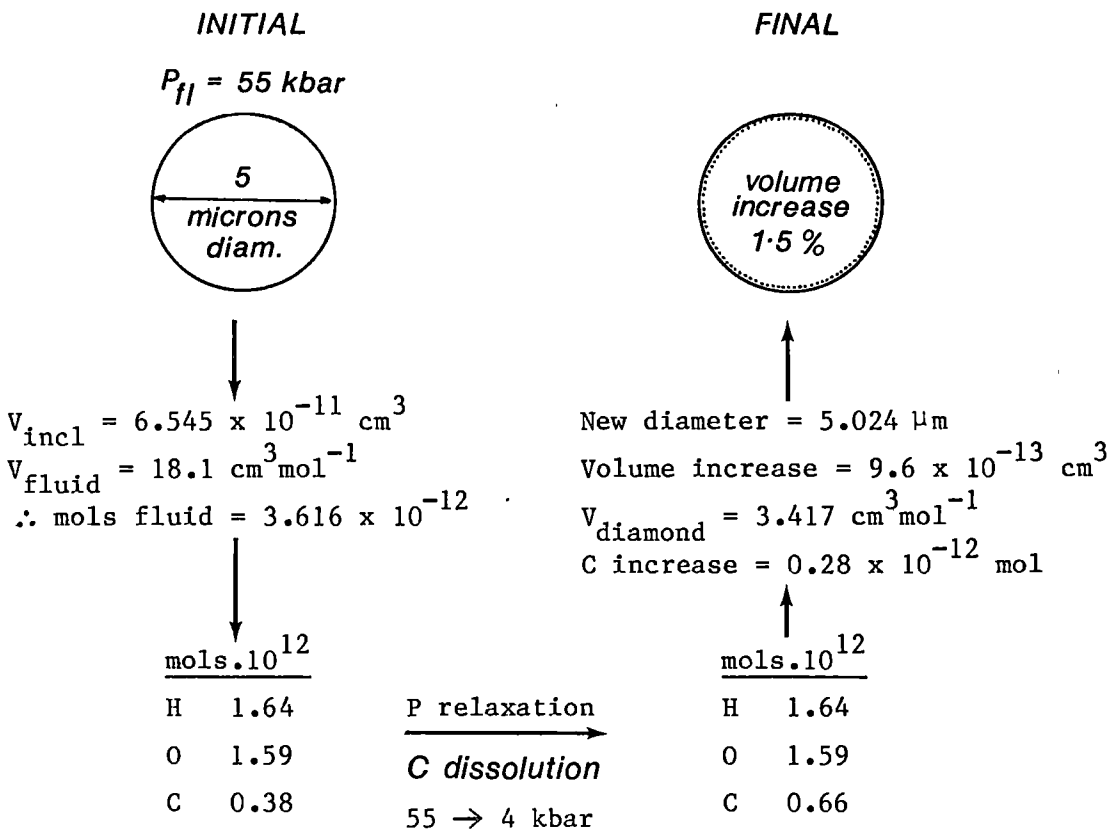

In this case there is a volume increase of 1.5% associated with removal of a rind of C atoms 0.012 μm thick from the inclusion walls. This amount in volumetric terms is not significant when considered against the potential effects of crack propagation, however even this small amount of dissolution leads to profound changes in fluid chemistry.

In summary we find:

(i) Modelling the pressure relaxation behaviour of fluids as paths of constant H/O ratio duplicates the chemical characteristics of most fluids trapped in diamond.

(ii) Agreement with observed species distribution is good considering the limitations of a simple isothermal model and the pressure averaged nature of analysed fluids.

(iii) High H_2 containing fluids are not consistent with the model suggesting departure from isothermal behaviour or some other process of internal hydrogen redistribution; this process does not affect corrected 55 kbar (log fO_2,X_C) co-ordinates.

(iv) The presence of small amounts of alkenes and alcohols in some analysed fluids cannot be explained by pressure relaxation proceses; their origin remains open.

3.10 Conclusions

It has been demonstrated that fluids trapped in diamond are consistent with a high pressure mantle origin that probably represents a syngenetic host-inclusion relationship. All fluids have been subject to a complex re-equilibration process that is well modelled by isothermal inclusion volume relaxation. Because the species found in analysed fluids do not represent those in equilibrium with diamond under formation conditions, the use of as-analysed species ratios such as H_2:H_2O and CO:CO_2 (e.g. Melton & Giardini, 1981) to infer conditions of diamond origin or the nature of mantle fluids (Giardini et al., 1982) cannot be valid. By employing appropriate correction procedures, diamond fluids may be returned to the carbon saturation curve. As it turns out, all fluids in equilibrium with diamond are water-rich, H_2O exceeding 50 mol% in all cases. As is evident from Figs 3.6A to 3.6D, a large group of diamonds have equilibrated with CH_4-H_2O fluids under conditions lying well outside the stability field of crystalline carbonate (Figs 3.5 and 3.6D). Diamonds belonging to this reduced group comprise all those of octahedral and dodecahedral morphology so far investigated as well as all those from South Africa, Central India and a proportion from Arkansas. Since the octahedral/dodecahedral morphology is volumetrically the most significant diamond class in most kimberlite provinces (e.g. Harris et al., 1984), it seems likely that the majority of diamonds belong to this group and thus have a genetic association with methane-bearing fluids. This contradicts the suggestion of Richardson et al. (1984) based on isotopic and other evidence that a residual "CO_2-enriched" asthenospheric interstitial melt has coexisted with South African diamonds perhaps over long time intervals. Diamond crystallisation in an environment of high H_2O and CH_4 activities at fO_2's slightly above IW instead point towards an enrichment event involving a CO_2-free largely aqueous fluid or melt phase.

Only those diamonds of cubic morphology and some from Arkansas of irregular habit are associated with oxidised H_2O-CO_2 fluids at fO_2's lying within the carbonate stability field. While cubic diamonds may be the most suitable for mass spectrometric analysis due to their relatively high fluid content, this diamond morphology is not particularly common. Most of the

samples analysed are from Zaire where even in the large Mbuji Mayi kimberlite field cubic diamonds make up only 10-15% of the population (Javoy et al., 1984). By contrast, cubic morphologies in the South African kimberlites comprise <1% of most size ranges (Harris et al., 1979, 1984). From synthetic studies (Muncke, 1979) cubic diamonds would appear to form under lower temperature and/or higher pressure conditions than those of octahedral habit. It appears that in the natural formation environment there also exists a fundamental difference in oxidation regimes between the two morphologies. A curious occurrence in some of the Zaire cubes is the inferred presence of solid hydrocarbon inclusions of ~100 μm diameter (Giardini et al., 1982). Fluids with a dominance of higher alkanes are only expected in the metastable divariant region under reduced conditions (Section 2.10); this is clearly not consistent with the presence of oxidised volatiles but could possibly be related to aqueous-hydrocarbon fluid-fluid immiscibility discussed in Section 1.6.

Recent isotopic evidence lends support to the hypothesis that reduced fluids and not oxidised are important in the genesis of most diamonds. The range and distribution of carbon isotopic values found by Deines (1980) in a large sample of diamonds of mainly South African and Siberian origin can only be explained satisfactorily by the involvement of methane-bearing fluids. Since the population studied was dominantly of octahedral/dodecahedral/macle morphology, this is consistent with the majority of diamonds belonging to the reduced group. It is not known whether cubic diamonds exhibit a characteristic isotopic signature as would be expected if, for example, a subduction related carbon source similar to that proposed for carbonado diamonds (Robinson, 1978) was involved. Non-cubic diamonds from Zaire, however, show typical $\delta^{13}C$ values in the range -4 to -10‰ (Javoy et al., 1984).

A number of conclusions and some important areas for further investigation arise from this study. Of great value in the future would be a systematic study of diamonds of known origin using a variety of analytical and isotopic techniques.

General conclusions:

(i) Mantle Fluid Compositions

The majority of diamonds are inferred to have equilibrated with mantle fluids of H_2O-CH_4 composition during growth and/or residence in the upper mantle. Corroborating evidence suggests a genetic link between methane-bearing fluids and diamond formation.

Diamonds of the rare cubic morphology have crystallised in an environment dominated by H_2O-CO_2 volatiles but no time or isotopic constraints on their origin are as yet available. This study confirms that C-O-H-N volatiles of mantle origin are not restricted to oxidised species. Petrogenetic models calling for the involvement of a fluid phase must therefore consider fO_2 as an important variable.

(ii) Mantle Redox State

Redox conditions appropriate to the formation of reduced group diamonds over the pressure interval 45-70 kbar and at 1300-1500 K lie in the range IW to IW + 1.5 log fO_2 units. This is consistent with recent intrinsic oxygen fugacity measurements on type"A" upper mantle spinel and peridotite samples of Arculus & Delano, 1981; Arculus & Gust, 1981; Arculus et al., 1984) which indicate fO_2's in the vicinity of IW. Since the conditions are well outside the stability range of crystalline carbonate, EMOD and similar carbonate-silicate-graphite or diamond fO_2 buffers (Eggler & Baker, 1982; Basaltic Volcanism Study Project, 1981) do not define appropriate fO_2 conditions for the crystallisation of diamond and therefore do not seem to be particularly useful reference buffers for regions of the mantle hosting elemental carbon and/or composed of type "A" material.

It is not possible, without a detailed systematic study, to place detailed time constraints on any upper mantle redox evolutionary path. The generally old, Archaean ages obtained for diamond however suggest persistence through time of relatively reduced regions of the mantle. The extent to which the redox state of upper mantle material can be modified by subduction processes or other interaction with the crust/hydrosphere/atmosphere is not known with any certainty; calculations by Arculus & Delano (1981) suggest that only small amounts of contamination with oxidised material are necessary for a drastic fO_2 increase.

(iii) Diamond Formation Mechanism

If diamond formation occurs largely by solid-fluid equilibria involving methane as a major fluid-phase component as suggested by Dienes (1980), then reference to Fig. 3.5 confirms that the methane decomposition reaction: $CH_4 = C + 2H_2$ would offer a viable mechanism for carbon precipitation. Oxidation of any precursor CH_4-H_2-H_2O fluid in the reduced divariant region of the system C-O-H (such as composition "h" in Fig. 3.5) either by diffusive H_2 loss to surroundings (Sato, 1978) or by direct oxidation reaction will follow a path of increasing fO_2 that eventually intersects the carbon saturation curve. At this point, no equilibrium fluid can pass from the reduced region into the oxidised without precipitating either diamond or graphite. Thus if a fluid of very reduced character, perhaps originating by degassing of mantle material with fO_2 characteristics approaching those of metal-silicate equilibrium (Arculus & Delano, 1981), passes into a more oxidised region or layer (e.g. as envisaged in the layered fO_2 mantle model of Haggerty & Tompkins, 1983) then diamond or graphite precipitation will be the result. Redox interactions of this type may also explain a number of other features of sub-cratonic mantle as sampled by kimberlitic magmatism. These ideas are developed further in Part 5.

One of the more interesting aspects of this study is the recognition of reduced species as important components in mantle-derived fluids. If volatile-rich magmatism occurs under fO_2 conditions as reduced as IW then the nature of petrogenetic processes is likely to be very different from systems based on oxidised CO_2-H_2O volatiles. The paucity of knowledge concerning silicate melt/reduced volatile interactions warrants a detailed experimental study - the subject of Part 4.

PART 4

AN EXPERIMENTAL AND SPECTROSCOPIC STUDY OF THE INTERACTION BETWEEN REDUCED C-O-H VOLATILES AND ALUMINOSILICATE MELTS.

4.1 Introduction and Previous Work

Current models of magma genesis in volatile-rich systems have usually assumed source-region fO_2 conditions some 3-4 orders of magnitude more oxidising than IW in support of the inferred petrogenetic role of CO_2-H_2O volatiles and carbonated peridotite (e.g. Wyllie, 1979, 1980). These ideas, however, cannot be relevant if magma genesis takes place in reduced regions of the upper mantle (fO_2 ~ IW) where C-O-H volatiles will be dominantly CH_4-H_2O mixtures and crystalline carbonates will not be stable (Part 2).

Little is known of how reduced volatiles interact with silicate melts. Eggler & Baker (1982) conducted a number of reconnaissance experiments determining the effect of C-H volatiles on the melting and liquidus phase relations of diopside and the composition $diopside_{35}pyrope_{65}$ at P > 20 kbar. Experimental fO_2 conditions were believed to be near the Si-SiO_2 buffer but could not be determined directly. No analysis of the C-H vapour phase generated by breakdown of $C_{14}H_{10}$ (anthracene) was presented. Eggler & Baker found liquidus depressions of ~100°C in diopside at 21 kbar and a large liquidus field of olivine plus garnet extending to at least 40 kbar in $Di_{35}Py_{65}$ coexisting with C-H fluid. In the latter case this differs from the effect of H_2O which does not bring garnet onto the liquidus and the effect of CO_2 which stabilises opx to high pressures. The presence of "depolymerised" phases such as olivine and garnet on the C-H volatile saturated liquidus led to the suggestion that reduced volatiles have a depolymerising effect on silicate melts. Quench problems did not allow spectroscopic investigation of the glasses produced in this study and a detailed solubility mechanism was therefore unable to be written. The only other available experimental data to date concerning reduced volatile interaction are that of Jakobsson & Holloway (1984). Experiments determining the albite liquidus from 10-30 kbar in the presence of graphite plus a C-O-H fluid phase were conducted at fO_2 = IW. Under these conditions fluids have substantial H_2O and CH_4 components (Part 2). Infrared spectra of quenched albite glasses contained much more H_2O than

predicted by Burnham's (1979) model and a lower molecular H_2O/hydroxyl group ratio than found by Stolper (1982a) for carbon-free systems. Calculations assuming all additional H_2O is present as hydroxyl in the glass gives an "excess OH" content of 2.7 wt% at 16 kbar, 1100°C. This amount was attributed to C-H volatile dissolution. Except for the identification of CO_3^{2-} ions in the glasses no quantitative data on carbon solubility were obtained due to graphite contamination.

Both the above studies found a substantial effect due to reduced C-H volatile interactions with silicate melts. This contrasts markedly with the earlier views of Holloway (1981) based on theoretical grounds that ... "neither CH_4 nor H_2 should be soluble enough to significantly affect melt properties." In the light of the above two studies it is of some importance to establish the detailed mechanism of reduced C-H volatile interaction with silicate systems. The dissolution process may involve either or all of the volatile species CH_4, H_2 and C_2H_6. Problems of graphite contamination, quench effects and uncertainty in the nature of the C-H fluids actually generated have limited previous studies. Resolution of these problems is essential for obtaining unambiguous spectroscopic and analytical results. The fO_2 conditions chosen for the present study are such that CH_4 is the dominant fluid species. At higher fO_2's where H_2O becomes important the effects of reduced C-H volatiles may not be clearly resolved from that of H_2O. Development of a suitable C-H fluid generation technique for sealed capsules in solid media piston cylinder apparatus represents an important part of this investigation as discussed in the following section.

4.2 Generation of C-H Fluids at High Pressure: Experimental Techniques

Development of C-H fluid generation techniques at high pressure requires careful consideration of a number of criteria: Run duration must be such that equilibrium is fully established between fluid and melt phases. Run times may not however be of excessive length due to potential fluid losses caused by H_2 diffusion from the noble metal capsules (in this case Pt) into the surrounding medium (see Shaw, 1967 and Section 4.7). This arises because reduced fluids (i.e. CH_4 and H_2) reach maximum mole fractions in the system C-O-H at fO_2's below about IW-2 log fO_2 units for P ~ 30 kbar, T ~ 1600 K. Under these conditions fH_2 inside the sample capsule will exceed that externally (which in this case is near the GW buffer, Section 4.7) and a gradient in fH_2 will thus exist. Any diffusive loss of hydrogen from a sealed capsule containing a C-H fluid phase will be counteracted by simultaneous graphite precipitation via the equilibrium:

$$CH_4 = 2H_2 + C \text{ (graphite)} \qquad \ldots\ldots 4.2A$$

which will proceed to the right until all fluid is consumed. Maintenance of fluid excess conditions thus requires minimisation of H_2 loss by employing run times as short as possible but still achieving fluid-melt equilibrium. For this reason it is essential that the method of fluid generation produces the thermodynamically stable C-H species distribution as rapidly as possible following attainment of final run P,T conditions. It is in this area that currently available methods relying on C-H fluid generation by pyrolysis of complex organic compounds (Holloway & Reese, 1974; Eggler & Baker, 1982) may not be appropriate. Thermal degradation of simple n-alkanes typically proceeds via C-C bond cracking to produce an array of smaller n-alkane and n-alkene fragments that eventually leads to a mixture of CH_4,H_2 and graphite on complete pyrolysis (Henderson et al., 1968). Cyclic and aromatic hydrocarbons are kinetically much more resistant to thermal degradation. Use of any of these compounds to generate an equilibrium C-H fluid runs the risk that partial degradation products may persist metastably. This problem is likely to be particularly acute with stable multinuclear aromatics such as anthracene (b.p. 340°C under pressure, CRC Handbook) which was used by Eggler & Baker (1982) as a source of C-H fluids in short duration (15 minutes) runs. A number of problems were found during evaluation of this compound as a potential source of C-H fluids: thermal degradation of anthracene sealed in 2.3 mm diameter (I.D.) $Ag_{50}Pd_{50}$ capsules and run at 30 kbar, 1100°C for times up

to 8 hours resulted in only partial decomposition. This was identifiable by the presence of birefringent areas amongst the black almost glassy pyrolysis product. XRD showed this material to consist chiefly of disordered graphite together with a broad 9Å feature probably indicating the presence of relict anthracene-like units. Support for this view was given by a loss of vapour always less than that expected for complete degradation. The use of aromatic hydrocarbons thus appears unsuited to the rapid generation and equilibration of a C-H fluid at high pressure. Better results might be expected with n-chain alkanes; however a technique that leads directly to a CH_4 dominated fluid without the necessity of re-equilibrating a variety of unknown pyrolysis fragments would be preferable.

Methane, together with a small amount of H_2, can be readily generated at 1 atm by the action of H_2O on Al_4C_3 (Wade & Banister, 1973). Since this reaction proceeds rapidly to completion and produces a C-H fluid with a species distribution close to that of high pressure equilibrium, it is an ideally suited generation reaction. By including $Al(OH)_3$ as the source of H_2O a convenient solid reactant can be prepared. At 30 kbar, $Al(OH)_3$ breaks down to corundum via the intermediate compound AlO(OH) (diaspore) so that fluid will be generated in two stages (at ~250°C and ~550°C; Kennedy, 1959) on work up to final P,T conditions. This mechanism may be important in preventing capsule rupture, more likely if all fluid is generated at only one point in the P,T path. Overall the methane generation reaction may be written:

$$4Al(OH)_3 + Al_4C_3 \longrightarrow 4Al_2O_3 + 3CH_4 \ (+ H_2, + C_2H_6) \qquad \ldots\ldots 4.2B$$

The possibility exists that under carbide excess conditions, a number of aluminium oxycarbide compounds may form by the above reaction (Foster et al., 1956); their pressure stability is, however, unknown.

An important constraint in generating any fluid under confining pressure is to assess the likely volume change that will occur during (i) quenching from high temperature (~ isobaric in piston cylinder apparatus) and (ii) release from pressure (~ isothermal). If the overall change exceeds the potential capsule free volume then rupture may occur. Density calculations for P,T relaxation from 1150°C, 30 kbar to 100°C, 0.5 kbar using the 5PMRK show that CH_4 is ~15 times more incompressible than H_2O and ~4 times that of CO_2 (Table 4.2).

Table 4.2 Volume changes (ΔV) for P,T relaxation during quenching and pressure release in piston-cylinder apparatus.

Species	ΔV (mm^3/mg of gas)	Weight of species required to achieve same volume expansion (mg).
CH_4	2.6	1.0
CO_2	0.6	4.3
H_2O	0.17	15.3

Experience has shown that capsules are unlikely to survive rupture if the internal fluid volume change exceeds about 5% of the capsule's empty volume. Thus a capsule of empty volume 50 mm^3 (corresponding to cylindrical dimensions of ~3 mm I.D. and ~7 mm length) should only be able to support 1 mg of CH_4 (see Table 4.2). This restriction requires dilution of fluid generating carbide/hydroxide mixtures with an inert component. In this case alumina was chosen as the dilutant and a carbide/hydroxide/alumina mixture, capable of generating 0.2 mg CH_4/10 mg mix, was prepared. To eliminate the possibility that adsorbed water or excess air in the capsule might lead to oxidation of methane and production of H_2O, a 1:1 molar ratio of $Al(OH)_3$ to Al_4C_3(three times carbide excess over reaction stoichiometry) was employed. Thus the presence of excess carbide after the run will indicate that the fO_2 of the system is effectively buffered by a reaction of the type:

$$Al_4C_3 + 3O_2 = 2Al_2O_3 + 3C \qquad \ldots\ldots 4.2C$$

All mixtures containing Al_4C_3 (98% purity, Goodfellows Metals #AL516010) were stored under vacuum desiccation (silica gel desiccant) to prevent reaction with atmospheric moisture. Aluminium hydroxide used in all mixes was A.R. grade; typical atmospheric water absorption was <0.05% with an observed ignition loss (1000°C, 14 hrs) of 34.56 wt% compared with 34.64 wt% expected for pure $Al(OH)_3$.

The high pressure capsule and assembly design employed in piston-cylinder apparatus experiments with C-H fluids is illustrated in Fig. 4.3 in the following Section (subsection 4.3B: experimental details). Talc rather than NaCl was chosen as the pressure transmitting medium to maximise the external fH_2 of the system and thus limit H_2 loss from the capsule.

Prior to experiments with silicates a "blank" run was performed at 30 kbar, 1300°C for 15 minutes with the aim of determining whether fluid-phase equilibrium is achievable in short run times by this technique.

Analysis of the fluid phase following the run was accomplished by mass spectrometry using a capsule piercing technique. The presence of a vapour phase is readily recognised by the puffed and distended nature of the capsule. The device used for capsule piercing consists of a modified regulating valve (Whitey #SS-1VS6, stainless steel) with a redesigned stem tip fashioned into a hardened needle point. A removable cradle serves to position and hold the capsule in place during piercing (Fig. 4.2).

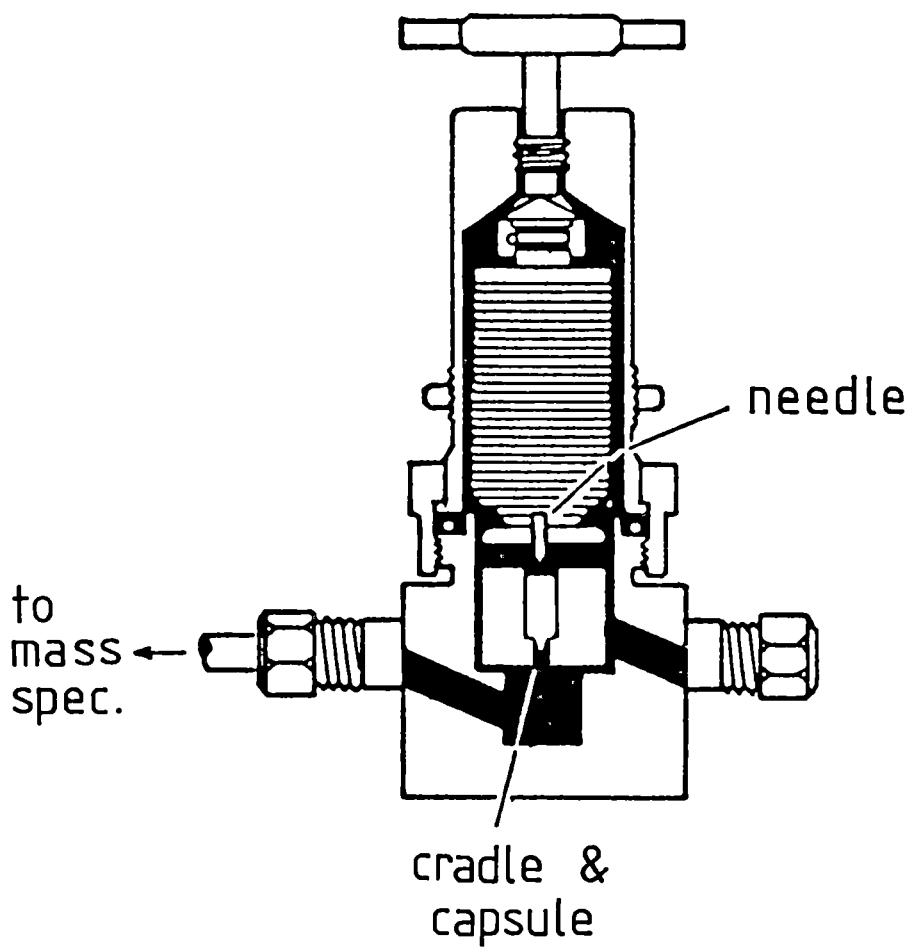

Fig. 4.2 Capsule piercing device (partly schematic).

Gases were released under vacuum (~10^{-6} torr) and directed into the ion-source of a VG-micromass 7070 double focusing mass spectrometer via a modified probe insertion technique. To achieve low background levels, particularly for H_2O caused chiefly by absorbed molecules on metal surfaces, it was found necessary to evacuate the whole system (probe plus piercer) for ~12 hours prior to taking measurements. After piercing, mass spectra were acquired by multiple scans of ~2 sec dura tion over the mass range 10-70 m/z. The total ion current was monitored during the piercing experiment and both background and sample spectra were recorded at various sensitivities. With the data acquisition system used by this instrument, H_2 was below the lower mass-range limit of recorded spectra. The presence of both H^+ and H_2^+ ions was however confirmed qualitatively by oscillographic traces down to low mass numbers. Results for the "blank" run are listed in Table 4.2B; values are normalised to zero background (mainly residual air and water vapour in the instrument, see Fig. 4.3C) by reference to the m/z 32 (O_2^+) peak (or, when off-scale, the m/z 40 (Ar^+) peak) assuming the sample capsule contains no trapped oxygen (unlikely at the fO_2's employed) or argon (confirmed by monitoring the O_2^+/Ar^+ ratio at lower sensitivity). XRD and optical examination of the solid product showed the presence of Al_2O_3, ordered graphite and excess Al_4C_3. The latter compound is readily identified by its characteristic straw-yellow colour and equigranular crystal habit. No oxycarbides were identified either optically or by XRD. The presence of abundant ordered graphite indicates that the fH_2 buffer reaction 4.2A has been operative during this experiment. Capsule piercing results are presented in Table 4.2B, next page. The form of the mass spectra for the blank run and for those runs with aluminosilicate melt present (see later in Section 4.3) are very similar. A typical methane spectrum is present in the range m/z 12-16 and ethane at m/z 24-30. The height of the m/z 29 peak ($C_2H_5^+$ fragment) compared with m/z 27 is slightly greater than that expected for pure ethane and a small proportion of another (unidentified) compound may be present as well (ethene, C_2H_4 cannot be a candidate however). Column 2 of Table 4.2 assumes all peaks in the range 24-30 belong to ethane. Trace amounts of C_{3-4} hydrocarbons are also present. Although the C_2H_6/CH_4 ratio of the fluid is higher than that calculated (perhaps due to quench effects),

Table 4.2B Capsule gases: blank run T-1278 (P = 30 kbar, T = 1300°C)

Species	m/z range	Total peak height at 10^{-6} sensitivity*	Mol% assuming H_2=8.1%**	Mol% calculated with 5PMRK***
CH_4	12-16	184,938	86.9	88.5
C_2H_6	24-30	10,436	4.9	3.4
C_{3-4}(total)	36-58	112	0.1	n.d.
H_2O	17-18	0	0	0
CO_2	44	0	0	0
H_2	1-2	n.d.	8.1	8.1

n.d. = not determined

* normalised to zero background

** theoretically calculated value (5PMRK) at 30 kbar, 1573 K

*** at log $fO_2 \leq -15$.

overall the agreement with theory is good. Derived fluids are thus believed to represent those at graphite-fluid equilibrium. Ethane is confirmed as a stable minor species at high pressure, as is the predicted low abundance of higher (>C_2) hydrocarbons. The absence of oxygen-containing volatiles (e.g. H_2O) puts an upper limit on the log fO_2 of the system at near -15 or ~IW-5 log fO_2 units (calculated with program COH/GRAPHITE6) under run conditions. The use of a carbide/hydroxide mixture thus proves to be a rapid and convenient method for preparing fluids dominated by CH_4 at high pressures.

4.3 Interaction between Aluminosilicate Melts and C-H Fluids

A. Choice of Compositions

Two aluminosilicate compositions were chosen for this investigation; these are jadeite ($NaAlSi_2O_6$) and sodamelilite ($NaCaAlSi_2O_7$) abbreviated Jd and Sm respectively hereafter. There are several reasons for this choice:

(i) From a structural point of view, Jd and Sm composition glasses (and by inference melts) have been intensively studied and are reasonably well characterised. Structural investigations have included x-ray diffraction studies (Jd: Taylor & Brown, 1979b) and Raman spectroscopic studies (Jd: Mysen et al., 1980a; Seifert et al., 1982; Sm: Mysen & Virgo, 1980a; Sharma & Yoder, 1979). In addition, oxidised volatile (CO_2, H_2O) interactions with both compositions at various pressures have been investigated and dissolution mechanisms proposed (Mysen & Virgo, 1980a, 1980b; Mysen et al., 1980b; Sharma, 1979).

(ii) Both Jd and Sm show good quenching behaviour in the presence of volatiles. Sm will retain up to ~6 wt% H_2O without precipitation of quench crystals or exsolution of vapour bubbles (Mysen & Virgo, 1980b). Furthermore, liquidus temperatures do not exceed 1400°C at 30 kbar pressure.

(iii) Sm is a simple four-component system analogue for basaltic compositions; with an NBO/T ratio of 0.667, this is within the range of most basaltic liquids (Mysen & Virgo, 1980b). Jd has a more polymerised melt structure with NBO/T ~ 0, similar to that of andesitic or granitic liquids.

Choice of chemically simple compositions that are well known structurally aids considerably in spectroscopic interpretation. This is especially important because as the system becomes more chemically complex, there are significant losses in spectroscopic resolution. Iron-bearing compositions have not been considered in this study primarily because fO_2 conditions in the presence of a C-H fluid will lie well within the Fe^0 stability field (fO_2 below QIE, refer to Appendix 9). The effect of reduced volatiles on these compositions must instead be investigated in the presence of mixed H_2O-CH_4-H_2 fluids at higher fO_2's (near the IW buffer for example). In this study we concentrate on identifying the mechanism of reduced C-H volatile dissolution free from interference by other species and thus provide the necessary basis for extension into natural systems.

B. Experimental Details

Two sets of experiments were performed, the first to determine the volatile-free liquidus of Sm at 30 kbar and the second set to equilibrate Jd and Sm compositions with a C-H fluid and, for Sm, to determine the liquidus temperature and liquidus phase or phases under C-H volatile saturation.

Jd and Sm starting materials were powdered glasses prepared from analytical reagent grade $CaCO_3$, Na_2CO_3, $Al(OH)_3$ and Na-free silicic acid. The latter two compounds were pre-fired at 1000°C to remove all hydroxyl and bound water. Mixes were ground twice to dryness under acetone (~1 hour), pelletised and sintered at 1000°C for 12 hours. The samples were then reground and melted in Pt crucibles at 1250°C and quenched in air to colourless glasses. Glass chips were retained for microprobe analysis and the remainder powdered. Probe analyses were within 1 mol% of theoretical values for all oxide components and homogeneity was established by comparison of broad-beam scan analyses over a range of magnifications (0.5 mm^2 to 50 um^2).

All high pressure experiments were carried out with 0.5" (1.27 cm) piston-cylinder apparatus (Boyd, 1962) using techniques similar to those of Green & Ringwood (1967). Temperatures were recorded with a $Pt/Pt_{90}Rh_{10}$ thermocouple automatically controlled to within ±5-7°C of the set value. Temperatures were monitored during the run with a Digical II model AN6520 (Analogic Corp.) digital thermometer accurate to ±1°C. Once stabilised, run durations of up to 1 hour seldom required any change of heating current.

All runs were carried out using the "piston-in" technique applying a -10% pressure correction to nominal load pressures. With talc sleeved assemblies quoted pressures are accurate to ±1 kbar (Green et al., 1966). Experiments with C-H volatiles were carried out in large capacity "buffer" assemblies as illustrated in Fig. 4.3A below. Volatile-absent runs with Sm were performed in "dry" assemblies (capsule dimensions: 2.3 mm O.D. x 3 mm length. BN parts replaced by fired pyrophillite and alumina).

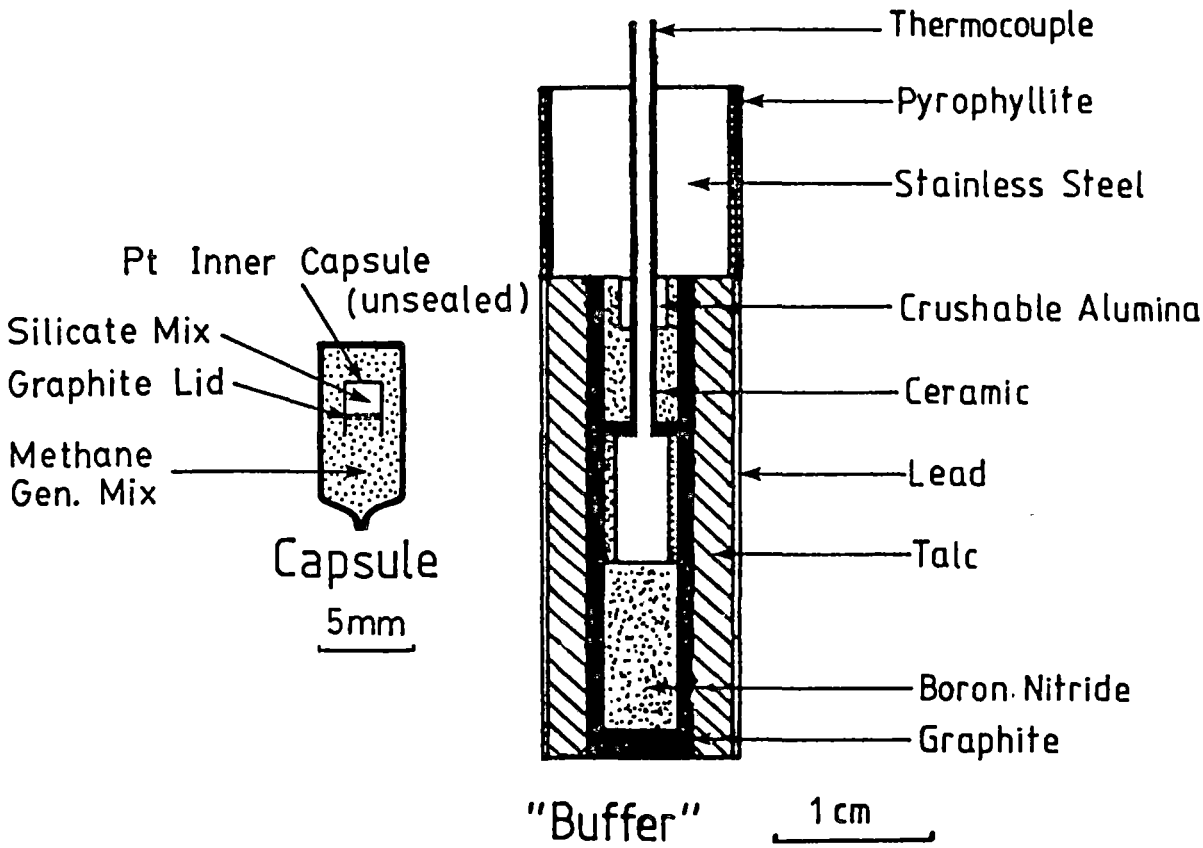

Fig. 4.3A Capsule and assembly design for high pressure, C-H volatile saturated runs in piston-cylinder apparatus (partly schematic).

C. Volatile-Absent Melting of Sm at 30 kbar.

The phase relations of Sm under volatile absent conditions have been determined by Yoder (1964) to 10 kbar. Crystalline Sm is stable above ~4-5 kbar and according to Yoder, melts over a solidus to liquidus T-interval of ~50°C. This behaviour was ascribed to formation of a melilite solid solution (presumably sodamelilite-gehlenite) in the presence of liquid. At 20 kbar, Kushiro (1964) found no evidence for the large solidus to liquidus range observed at lower pressures and determined that Sm melts congruently at 1350 ± 15°C.

Results of the melting experiments at 30 kbar are listed in Table 4.3A below. Special precautions were taken to ensure the runs remained H_2O-free. These included drying all assembly parts at 110°C for 24 hours and heating the sample Pt capsule plus Sm glass briefly to red heat prior to welding shut.

The rare glass encountered in run T-1159 indicates that at 30 kbar, like 20 kbar, the solidus and liquidus of Sm may be regarded as coincident within experimental precision. The crystalline material is therefore close to pure $NaCaAlSi_2O_7$ in composition. The melting point of Sm at 30 kbar is estimated at 1380 ± 10°C. Jadeite melts congruently to liquid at 1370 ± 10°C, 30 kbar (Bell, 1964).

Table 4.3A Sm melting at P = 30 kbar.

Run #	Duration (mins)	T (°C)	Product
T-1158	15	1420	All glass.
T-1159	15	1370	Interlocking equi-dimensional to prismatic Sm crystals (10-80 μm). Very rare interstitial glass.
T-1160	20	1395	All glass.

D. Interaction of C-H Fluids with Sm and Jd Composition Melts at P = 30 kbar.

Runs were performed with the capsule/assembly design shown in Fig. 4.3A and were of 30 minutes duration. All assembly parts were dried at 110°C, 24 hours prior to use to remove adsorbed H_2O. It has already been demonstrated that 15 minutes is sufficient time to achieve internal fluid equilibrium (Section 4.2) and 30 minutes was considered appropriate to establish equilibrium between melt and fluid phases while keeping any diffusive H_2 loss to a minimum (see subsection 4.5C). A successful run was indicated by the presence of a strongly puffed capsule and in each case analysis of the vapour phase was made by capsule piercing/mass spectrometry as described previously. Experimental results are outlined in Table 4.3B and selected microprobe analyses given in Table 4.3C.

Table 4.3B C-H fluid saturated runs at P = 30 kbar.

Run #	Composition	T(°C)	Theoretical wt CH_4 generated (mg)	Wt (mg) Jd or Sm	Product*
T-1296	Jd	1320	1.0	9.9	Clear glass, optical examination established the absence of microscopic crystalline, graphite or fluid inclusions.
T-1318	Sm	1320	1.0	11.7	Clear glass + euhedral grossular crystals. Glass contains an array of small <1 μm fluid inclusions.
T-1339	Sm	1350	1.0	11.6	Clear glass, no graphite inclusions. Large primary vapour bubble identified in T-1341; run T-1339 contains a few grossular crystals near top of capsule, i.e. away from hot-spot. Both glasses host an array of small fluid inclusions <1 μm in diameter.
T-1341	Sm	1350	0.9	12.0	

* Excess carbide confirmed in all runs.

The results of capsule piercing experiments for runs T-1296 and T-1341 are presented in Table 4.3D below; the mass spectrum for T-1341 is illustrated over a range of sensitivities in Fig. 4.3B and the instrumental background is illustrated in Fig. 4.3C. Results for other runs are closely similar to the data presented here.

4.3B

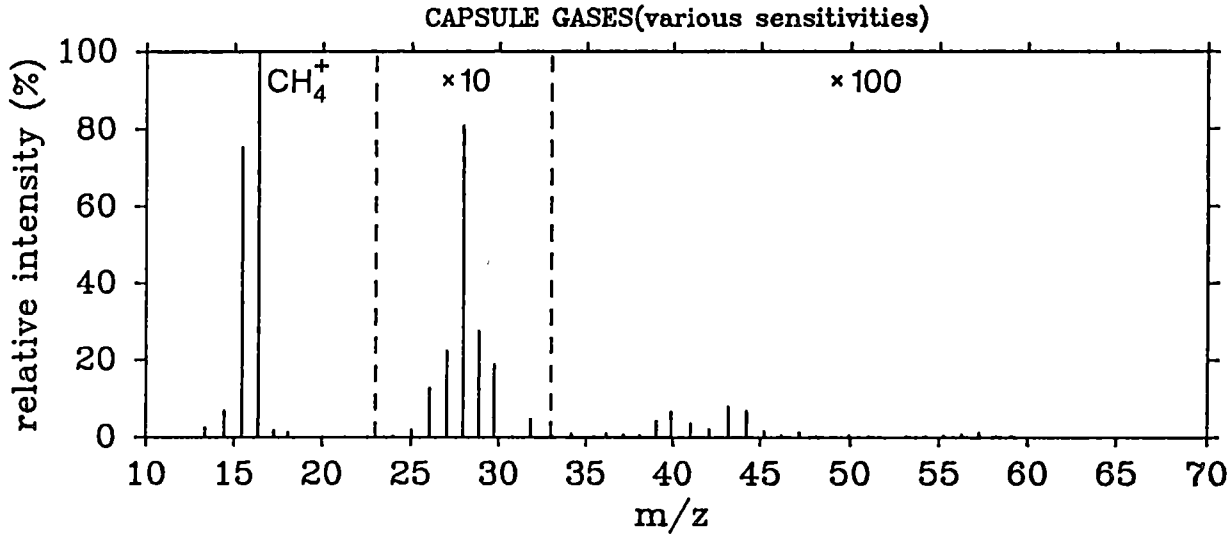

4.3C

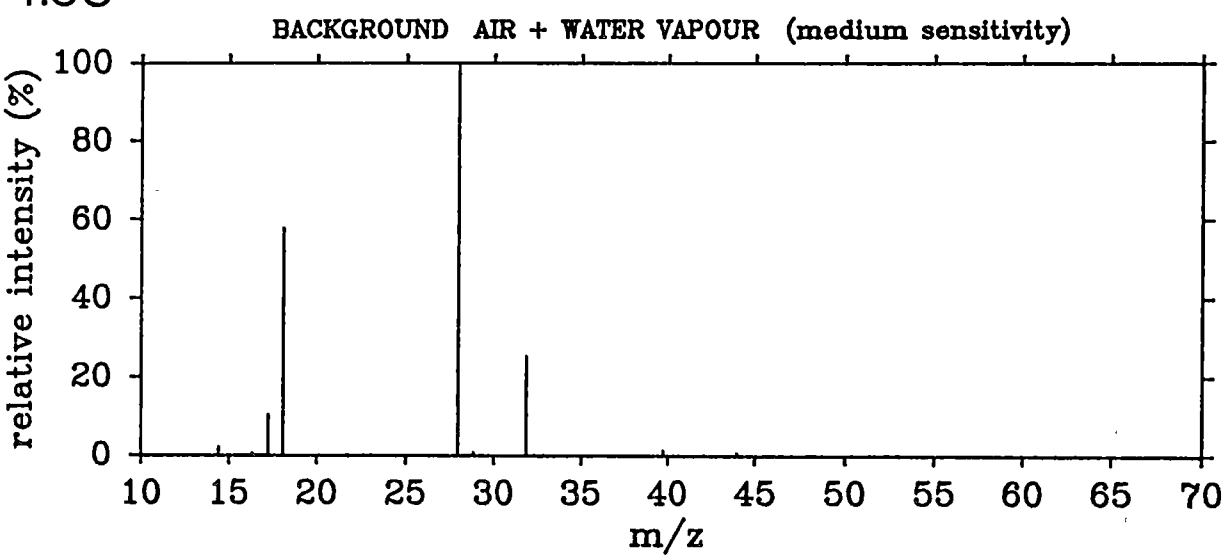

Fig. 4.3B Mass spectrum of capsule gases released from run T-1341 at low (m/z 10-23), medium (x10, m/z 23-33) and high (x100, m/z >33) sensitivities. Methane: m/z 13-17; ethane: m/z 25-30; C_{3-4} hydrocarbons m/z >36; background water vapour and air: m/z 17-18, 28, 32.

Fig. 4.3C Instrumental background at medium sensitivity.

	m/z
N^+	14
O^+, OH^+, H_2O^+	16-18
N_2^+	28 (full scale), 29
O_2^+	32
Ar^+	40
CO_2^+	44

Note suppression of background ion intensity in Fig. 4.3B due to input of capsule gases (ratios of individual gases, however, remain unchanged).

Table 4.3C Microprobe analyses.

	T-1296 Average Glass	T-1341 Average Glass	T-1339 Average Glass	T-1339 Grossular	Glass Adjacent Crystals
SiO_2	56.0 (0.6)*	44.2 (0.4)	44.0 (0.3)	39.48	43.1
Al_2O_3	23.6 (0.5)	18.6 (0.4)	18.6 (0.2)	22.56	17.7
CaO	-	20.9 (0.3)	21.1 (0.2)	37.56	20.4
Na_2O	14.7 (0.2)	11.8 (0.2)	12.1 (0.2)	0.00	13.4
Total	94.3	95.5	95.8	99.60	94.6
Cations:	O = 6	O = 7	O = 7	O = 12	O = 7
Si	2.000	1.995	1.984	2.978	1.980
Al	0.993	0.989	0.989	2.005	0.959
Ca	-	1.010	1.019	3.035	1.004
Na	1.018	1.032	1.058	0.000	1.194
total	4.011	5.026	5.050	8.018	5.137

* Figures in brackets are 1σ standard deviations.

Table 4.3D Capsule piercing/mass spectrometry results.

		T-1296 (Jd)			T-1341 (Sm)		
Range	m/z range	Sum of peak heights*	Mol% for H_2=8.5%	Calc.** (mol%)	Sum of peak heights*	Mol% for H_2=9.2%	Calc.** (mol%)
CH_4	12-16	133,610	87.2	88.0	153,039	85.7	87.1
C_2H_6	24-30	6,207	4.1	3.4	8,540	4.8	3.5
C_{3-4}	36-58	116	0.1	n.d.	151	0.1	n.d.
H_2O	17-18	213	0.1	0.1	322	0.2	0.2
CO_2	44	<10	0.0	0.0	0	0.0	0.0
H_2	1-2	n.d.	8.5	8.5	n.d.	9.2	9.2

* normalised to zero background against m/z 32(O_2^+) peak or m/z 40 (Ar^+) peak

** calculated with 5PMRK equation at appropriate P,T conditions

n.d. = not determined.

An important feature of Fig. 4.3B is the suppression of the background ion intensity noticeable on introduction of the large volume of capsule gases into the spectrometer (the ratios of background gases, e.g. m/z 28(N_2^+)/32(O_2^+) however remain unchanged). Since at the fO_2's considered here, the capsules will not contain any residual oxygen derived from trapped air (confirmed in each case by constancy of O_2^+/Ar^+ ratio between sample and background), the removal of background constituents can be readily achieved by normalising to zero O_2^+ (m/z 32) or Ar^+ (m/z 40) when oxygen is off-scale. By contrast with the blank experiment (Section 4.2) this procedure in the presence of aluminosilicate melt and at temperatures 20-50°C higher, results in a finite proportion of H_2O (0.1-0.2 mol%) in the fluid. Calculated log fO_2's in this case are in the range -13.5 to -14.0 or approximately IW-4.5 log fO_2 units under run conditions and only slightly more oxidised than the blank run.

The results outlined here indicate that interaction of C-H fluids and silicate melts leads to liquidus depressions of ~40°C in Sm and at least 50°C in Jd. This together with the consistently low microprobe totals reported in Table 4.3C implies a significant solubility of a reduced volatile component or components. All experiments retain excess carbide and mass spectra of quenched vapour indicates the presence of only trace quantities of bulk oxygen as H_2O. Thus the observed effects cannot be ascribed to absorbed H_2O or other external sources of oxidation. Under C-H fluid excess conditions the liquidus phase for the Sm composition is grossular ($Ca_3Al_2Si_3O_{12}$) and not crystalline sodamelilite as observed under volatile-absent conditions. The garnet structure may be described as depolymerised relative to crystalline sodamelilite, i.e. composed of isolated [SiO_4] tetrahedra and [$Al^{VI}O_6$] groups compared with the [$Al^{IV}Si_2O_7$] sheets of sodamelilite (Louisnathan, 1970). Insomuch as the structure of sodemelilite melt reflects that of the equilibrium liquidus phase these results suggest that C-H fluid dissolution leads to melt depolymerisation concomitant with AlO_4 --> AlO_6 conversion. Such a process is consistent with the appearance of garnet on the liquidus of the C-H volatile saturated $Di_{35}Py_{65}$ composition and the inferred expansion of the garnet phase volume in the system Di-Py-En relative to the volatile-absent and H_2O-saturated cases (Eggler & Baker, 1982). A more detailed understanding of the mechanism of C-H volatile interaction however requires detailed spectroscopic and analytical data.

4.4 FTIR Studies: Techniques and Instrumentation

The solubility mechanism of reduced C-H volatiles was investigated by Fourier Transform Infra-red (FTIR) spectroscopy using a Digilab model FTS-20E spectrometer with FTS-IMX interactive operating system and attendant software to perform a variety of tasks including automatic scaling, smoothing, plotting and spectrum subtraction. The Fourier transform IR technique offers significant advantages over conventional instrumentation. The spectrometer is based on the principle of the Michelson interferometer where the signal received by the detector represents the summation of all wavelength components (in the mid-IR region: 4000-400 cm^{-1}) interacting either constructively or destructively to produce an interferogram (Kagel & King, 1973). The interferogram is converted into the usual optical spectrum form (intensity vs frequency) by the cosine Fourier Transform; any missing wavelength components appear as absorption peaks. The chief advantages over conventional dispersive systems are in:

(i) increased signal-to-noise ratio; values >1000 can be achieved;

(ii) increased sensitivity due to high energy throughput;

(iii) availability of high spectral resolution;

(iv) short spectrum acquisition times even for signal averaging of up to 1000 scans over the full mid-IR region (<15 min. at 4 cm^{-1} resolution);

(v) all spectra are recorded in digital form allowing ready access to computer controlled spectral manipulation procedures such as scaling, band fitting, etc.

For the mid-IR region (4000-400 cm^{-1}) spectra of both glass and crystalline samples were obtained by the conventional KBr disc method. Approximately 2 mg (1 mg for crystalline compounds) of sample was ground together with 200 mg of IR-grade KBr in an agate mortar for 10 minutes. After drying the powder at 110°C, pellets were pressed between 1 cm diameter polished stainless steel dies; any cloudy discs were remade. Discs were then dried under P_2O_5 desiccant overnight to remove traces of adsorbed water.

Spectrum acquisition was performed by signal averaging 200 scans referenced against a blank KBr disc. A resolution of 4 cm^{-1} was employed, this being much lower than the intrinsic linewidth of glass phase samples and similar to that of crystalline silicates. In the case of condensed phases, and in particular glasses and amorphous compounds, instrumental resolution is usually insufficient to resolve broad overlapping bands; there is thus no advantage in obtaining spectra at very high resolutions

(<2 cm^{-1}) but some distinct time (acquisition and computing) disadvantages. A number of techniques exist for resolving multi-component band contours: the most popular of these deconvolution procedures include band-fitting (Jones & Pitha, 1976; Mysen et al., 1982b); difference spectroscopy including both real-time and spectral subtraction procedures (Painter & Coleman, 1980); and the recently developed technique of Fourier self-deconvolution (Kauppinen et al., 1981). Spectral subtraction is a powerful technique for investigating changes associated with addition of volatile or other solid components to a system. Subtraction of the component-bearing from the component-absent spectrum is conveniently and rapidly performed on spectra stored in digital form with the FTS-IMX package. Use of this technique, which has the advantage of being less subjective than band-fitting techniques, is made in interpreting the mechanism of C-H volatile dissolution.

Difficulties with the KBr disc technique rest largely with its reproducibility. Differences in sample preparation, reflected mainly in particle size distribution and orientation effects may lead to changes in bandwidths and relative intensities. Such changes are of critical importance in quantitative studies (Painter & Coleman, 1980; Fuller & Griffiths, 1978) but are of less importance in the interpretative work undertaken here. Nevertheless, reproducibility checks were performed by the preparation of duplicate discs, in all cases using identical preparative methods. Duplicates showed close similarity in spectral features. A sensitive test was to compare difference spectra of the same samples but prepared on different discs: identical gross features (to within ± 4 cm^{-1}) were observed in every case (these results are illustrated in the next section). It is believed that the reproducibility of the KBr disc method, provided sample preparation techniques remain consistent, is not a problem in the interpretation of the silicate glass and crystal spectra considered here.

After collection and computation of the spectrum, re-scaling, removal of linear sloping backgrounds (where necessary) and smoothing (glass spectra only) were performed. This latter procedure involves the fitting of an eleventh order polynomial to the spectral envelope to eliminate sharp spikes associated with atmospheric water vapour or CO_2 not completely purged from the instrument. The quality of the subtracted spectrum, which otherwise may contain variable narrow linewidth positive and/or negative features unrelated to the broader peaks of the silicate glass structure, is

greatly improved. Spectral subtraction performed on both smoothed and unsmoothed spectra in all cases result in identical broad-line (>2 cm^{-1} width) features.

In the far-IR region (in this case 500-100 cm^{-1}) samples were prepared by the standard nujol mull technique; slurries were mounted on high density polyethylene plates. Approximately 3 mg of glass sample was used. Because of the much lower energy radiation compared with the mid-IR region, averaging of 600-700 scans was generally required to achieve an acceptable signal-to-noise ratio. Samples had to be thoroughly dried and the instrument purged (with dry N_2) for ~5 minutes between sample changes to eliminate water vapour which in the far IR has a number of sharp rotation bands.

4.5 FTIR Studies: Introductory Remarks to Spectra Interpretation

The results presented in the following sections rely on careful interpretation of vibrational spectra. The assignment of IR and Raman absorption bands to structural features in silicate melts and glasses has been fully discussed in Appendix 13 with reference to the current spectroscopic literature. Many of the limitations and key assumptions in making spectroscopic assignments have been included there. In the following sections reference to Appendix 13 will be useful for the reader as knowledge of this background material is assumed in making band assignments; the accompanying discussion will therefore often be brief.

In the next section, FTIR spectra and their interpretation will be illustrated with examples relevant to both Jd and Sm compositions. Owing to the problem of non-uniqueness of structural interpretations, proposed mechanisms of volatile dissolution have always been made with reference to additional theoretical and analytical constraints.

4.6 Background, I: Interpretation of Volatile-Absent Glass and Crystal FTIR Spectra and the Discrimination of Al Co-ordination Environments

A. Systems Na_2O-SiO_2(NS) and Na_2O-Al_2O_3-SiO_2(NAS)

Selected spectra of 1 atm glasses in the systems NS and NAS were chosen to illustrate the gross features associated with polymerisation/depolymerisation of the silicate network and the effects of aluminium substitution. Preparative methods were identical to those for Sm and Jd glasses outlined in Section 4.3. Preparation of KBr discs for IR work was, however, carried out in a N_2 purged "dry box" with storage of glasses and discs under NaOH desiccation; this procedure was necessary to diminish the effects of atmospheric H_2O and CO_2 absorption to which these glasses are particularly susceptible.

FTIR spectra of the compositions NS_5 (pentasilicate, $Na_2Si_5O_{11}$), NS_3 (trisilicate, $Na_2Si_3O_7$) and NS_2 (disilicate, $Na_2Si_2O_5$) having NBO/Si ratios of 0.4, 0.667 and 1.0 respectively are shown in Fig. 4.6A. The effects of network depolymerisation as Na_2O/SiO_2 increases is clearly illustrated in the high frequency (1200-800 cm^{-1}) region. In NS_5 only one band envelope, centred at 1046 cm^{-1}, is resolved in this region. It arises largely from asymmetric stretching of Si-O-Si bridging groups and may be designated ν_{as}[Si-O-Si]. With increasing amounts of NBO the shoulder seen near 1000 cm^{-1} grows into a visually resolvable band envelope centred at 982 cm^{-1} in NS_3 and 941 cm^{-1} in NS_2. This causes the width of the high frequency envelopes to increase and extend below 800 cm^{-1}. The lower frequency band of the high frequency doublet may be assigned largely to asymmetric stretching of $Si\text{-}O^-$ non-bridging bonds (ν_{as}[$Si\text{-}O^-$] with some contribution arising from symmetric $Si\text{-}O^-$ stretching (the strongly Raman active ν_s[$Si\text{-}O^-$] bands) in the unresolved lowest frequency portion of the envelope. In the intermediate frequency range, 800-650 cm^{-1}, a medium strength envelope appears at 781, 768 and 760 cm^{-1} in the compositions NS_5, NS_3 and NS_2 respectively. Vibrations contributing to this band are quite delocalised and involve substantial motion of Si atoms situated in their oxygen co-ordination cage; additional contributions come from Si-O-Si in-plane bridge bending motions. Shoulders appearing near 660 cm^{-1} in NS_2 and other more depolymerised compositions accompany a decrease in intensity of the ~750 cm^{-1} band. These probably arise from symmetric stretching of the Si-O-Si bridge bond in pyrosilicate (Si_2O_7) and other units of similar NBO/Si that are likely to be present in these depolymerised glasses. A weak shoulder

Figs 4.6A to 4.6D FTIR absorbance versus wavenumber (cm^{-1}) spectra of silicate and aluminosilicate glasses and crystalline compounds. Sample preparation and spectrum acquisition as described in Section 4.4.

Fig. 4.6A FTIR spectra (1600-400 cm^{-1}) of the sodium silicate glasses NS_2, NS_3, NS_5 and the sodium aluminosilicate glasses N_5AS_{10} and N_3AS_4 ($N = Na_2O$, $A = Al_2O_3$, $S = SiO_2$).

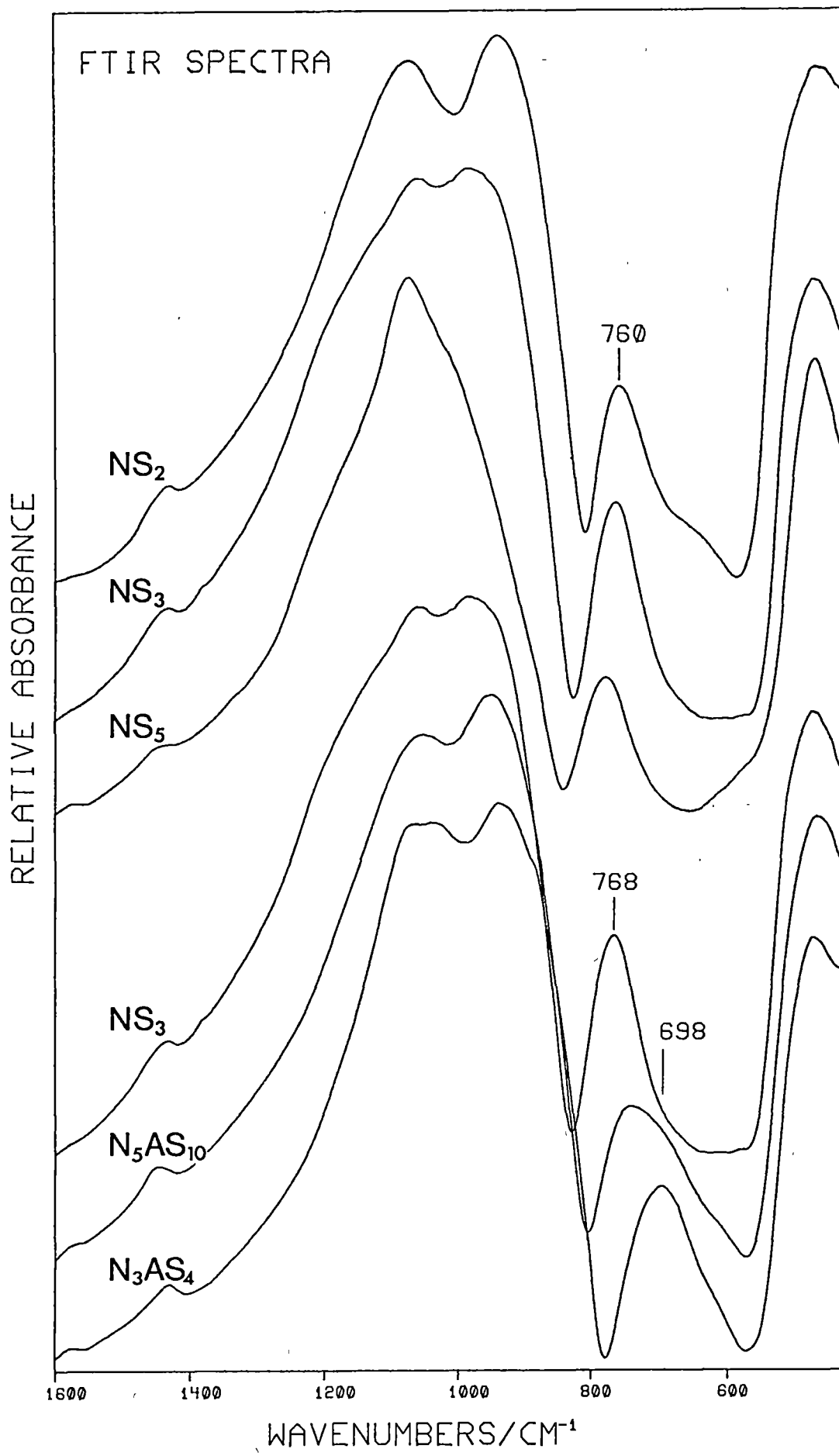
FTIR SPECTRA
760
768
698
NS2
NS3
NS5
NS3
N5AS10
N3AS4
RELATIVE ABSORBANCE
1600
1400
1200
1000
800
600
WAVENUMBERS/CM-1

at ~550 cm^{-1} in NS_5 also occurs in pure silica glass and is assignable to in-plane Si-O-Si bridge bending vibrations. The low frequency band envelope, 530-400 cm^{-1}, is due to stretching plus bending motions involving dominantly oxygen atom displacements. As predicted by Furukawa et al. (1980), the low frequency bandwidth increases with increasing degree of depolymerisation.

Bands present at ~1430 cm^{-1} in NS and NAS series glasses are due to small amounts of dissolved carbonate derived from absorbed atmospheric CO_2. The amount present is not significant (<1 wt% carbonate) in terms of its effect on the volatile-free glass structure and is very difficult to eliminate without performing all preparative steps under CO_2-free conditions.

B. Structure and Band Assignments in Melilite and Melilite Analogue Glasses.

The effects of Al substitution have been investigated in the system Na_2O-Al_2O_3-SiO_2 (NAS) by direct replacement of the charge balanced component $NaAlO_2$ for SiO_2 in the trisilicate (NS_3) composition. Half a mole replacement gives $Na_{2.5}[Al_{0.5}Si_{2.5}O_7]$ (N_5AS_{10}) and one mole gives $Na_3[AlSi_2O_7]$ (N_3AS_4). The latter composition is the sodic analogue of sodamelilite: $NaCa[AlSi_2O_7]$. FTIR spectra of the series NS_3, N_5AS_{10} and N_3AS_4 show systematic shifts towards lower frequencies for both high frequency ν_{as}[NBO] and ν_{as}[BO] bands and the mid-range envelope. These changes have been observed in studies of Al-substituted systems by Raman spectroscopy (Mysen et al., 1981; Seifert et al., 1982) and were associated with a coupling of Si-O and Al-O stretching vibrations by these authors. McMillan et al. (1982) have suggested a different interpretation whereby Al^{3+} acts only as a modifying cation in the manner of Ca^{2+} or Na^{+} and vibrations maintain a high degree of Si-O character. Since these two models can equally well describe the high frequency Raman spectra, there is at this stage little to favour either model. The spectra of melilite crystals and glasses however reveal some important features in the interpretation of the structural vs spectroscopic role of Al relevant to both models.

Compared with NS_3 glass, the N_3AS_4 composition has additional bands appearing in the FTIR spectrum at 1072 cm^{-1} and ~880 cm^{-1} (shoulder).

These may be compared with similar bands in the Raman spectra of gehlenite (Geh) and Ca-Tschermak's pyroxene (CaTs) composition glasses and crystals observed by Sharma et al. (1983). Their origin has been attributed by the authors to increased localisation of the high frequency stretching modes resulting from Al <---> Si substitution. On this basis, Sharma et al. asssigned the separate highest frequency bands to ν_{as}[Si-O-Si] and ν_{as}[Si-O-Al] vibrations (see Table 4.6B, C). A similar interpretation may be made for the 1072 cm^{-1} and 1034 cm^{-1} bands in N_3AS_4 glass. The new shoulder at ~880 cm^{-1} is best assigned to Al-O stretching vibrations (McMillan et al., 1982).

In the mid-frequency region there is a dramatic shift in the position of the mid-range band envelope from 768 cm^{-1} (NS_3) through 745 cm^{-1} (N_5AS_{10}) to 698 cm^{-1} (N_3AS_4). An IR mid-range envelope centred near 700 cm^{-1} is characteristic of $NaAlO_2$ or $Ca_{0.5}AlO_2$ substitution of the silicate network in numerous aluminosilicate glasses where Al/(Al+Si) exceeds about 0.25. For example, jadeite, sodamelilite (Fig. 4.6B), albite, nepheline and gehlenite (see Table 4.6C) glasses all have mid-range band envelopes located near 700 cm^{-1}. In Al-free systems the mid-range envelope is located at ~800-750 cm^{-1} and includes a substantial contribution from vibrations of Si atoms situated in their oxygen coordination cage (McMillan, 1984a). "Cage-like" motions of Al surrounded by a tetrahedral arrangement of oxygen give a calculated "reversal frequency" of 635 cm^{-1} in MD simulations (Soules & Busby, 1981). Because the mid-range absorption is strongly delocalised in behaviour (Ferraro & Manghnani, 1972), expected strong coupling between Si and Al vibrations is consistent with the observed frequency shift of the mid-range band to near 700 cm^{-1}, i.e. intermediate between pure Si and Al "cage-like" vibrations. A mid-range envelope of medium to strong intensity situated near 700 cm^{-1} in aluminosilicate glasses is thus a good indication for the presence of network substituted AlO_4 polyhedra. This view is consistent with the study of Tarte (1967) where frequencies characteristic of "isolated" AlO_4 tetrahedra were identified in the range 800-650 cm^{-1} for both crystalline and vitreous compounds.

The IR spectrum of N_3AS_4 glass is in many respects similar to that of crystalline sodamelilite (see Table 4.6B and Figs 4.6A, B) which is isostructural with the other melilite endmembers Ak (akermanite) and Geh (Louisnathan, 1970b). Based on x-ray determinations, the melilite structure is best considered as a sheet-like arrangement of $[MT_2O_7]^{4-}$

Fig. 4.6B FTIR spectra (1500-400 cm^{-1}):

A: Crystalline sodamelilite (prepared at 30 kbar).

B: Volatile-free sodamelilite glass (quenched at 30 kbar).

C: C-H fluid saturated sodamelilite glass (30 kbar, 1350°C, run T-1341).

D: Sodamelilite glass containing 5.5±0.2 wt% dissolved H_2O (prepared at 30 kbar, graphite inner capsule, run T-1250). Note trace of carbonate present; identifiable by absorptions at 1500-1400 cm^{-1}.

E: Crystalline jadeite (prepared at 25 kbar).

F: Volatile-free jadeite glass (quenched at 1 atm).

G: C-H fluid saturated jadeite glass (30 kbar, 1320°C, run T-1296).

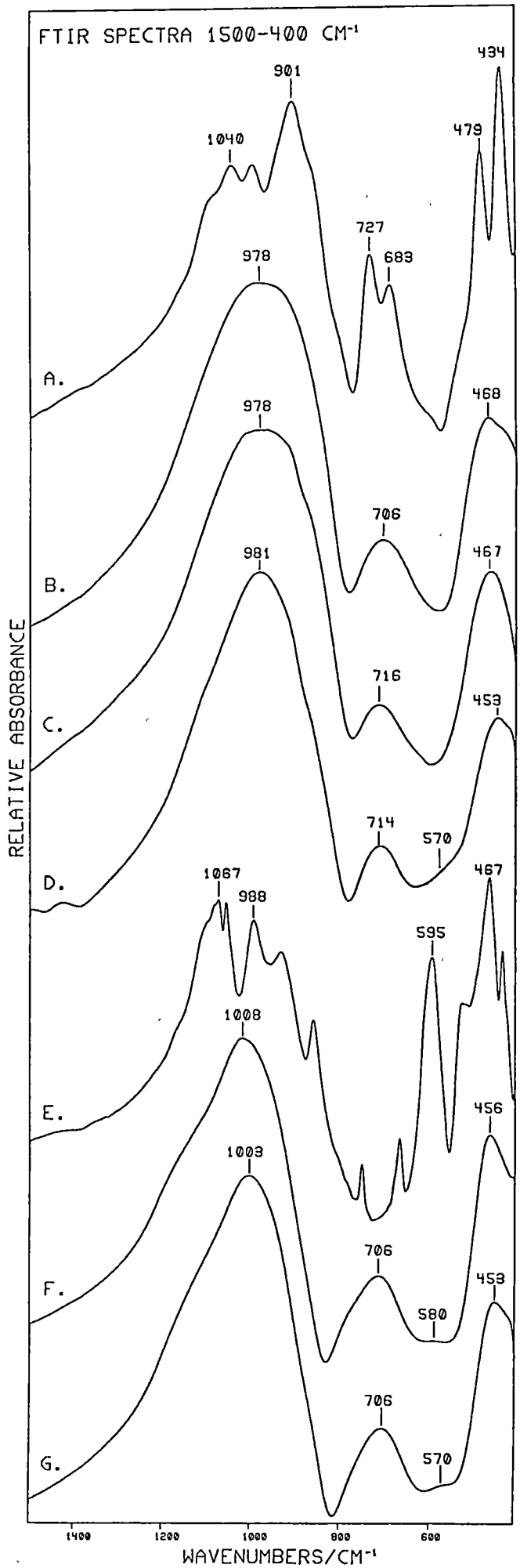
FTIR SPECTRA 1500-400 CM⁻¹
RELATIVE ABSORBANCE
WAVENUMBERS/CM⁻¹
1400
1200
1000
800
600
A.
1040
901
727
683
978
479
434
B.
978
706
468
C.
981
716
467
D.
714
570
453
E.
1067
988
595
467
F.
1008
706
580
456
G.
1003
706
570
453

Fig. 4.6C FTIR spectra (4000-400 cm^{-1}):

A: Volatile-free jadeite glass (quenched at 1 atm).

B: C-H fluid saturated jadeite glass (30 kbar, 1320°C, run T-1296).

C: Volatile-free sodamelilite glass (quenched at 30 kbar).

D: C-H fluid saturated sodamelilite glass (30 kbar, 1350°C, run T-1341).

E: Sodamelilite glass reduced by interaction with silicon carbide at 1500°C, 30 kbar (see text, Section 4.8).

F: Hydrous sodamelilite glass (5.5±0.2 wt% H_2O; same as Fig. 4.6B, spectrum D).

Note: weak positive or negative bands near 2350 cm^{-1} are due to atmospheric CO_2 vapour.

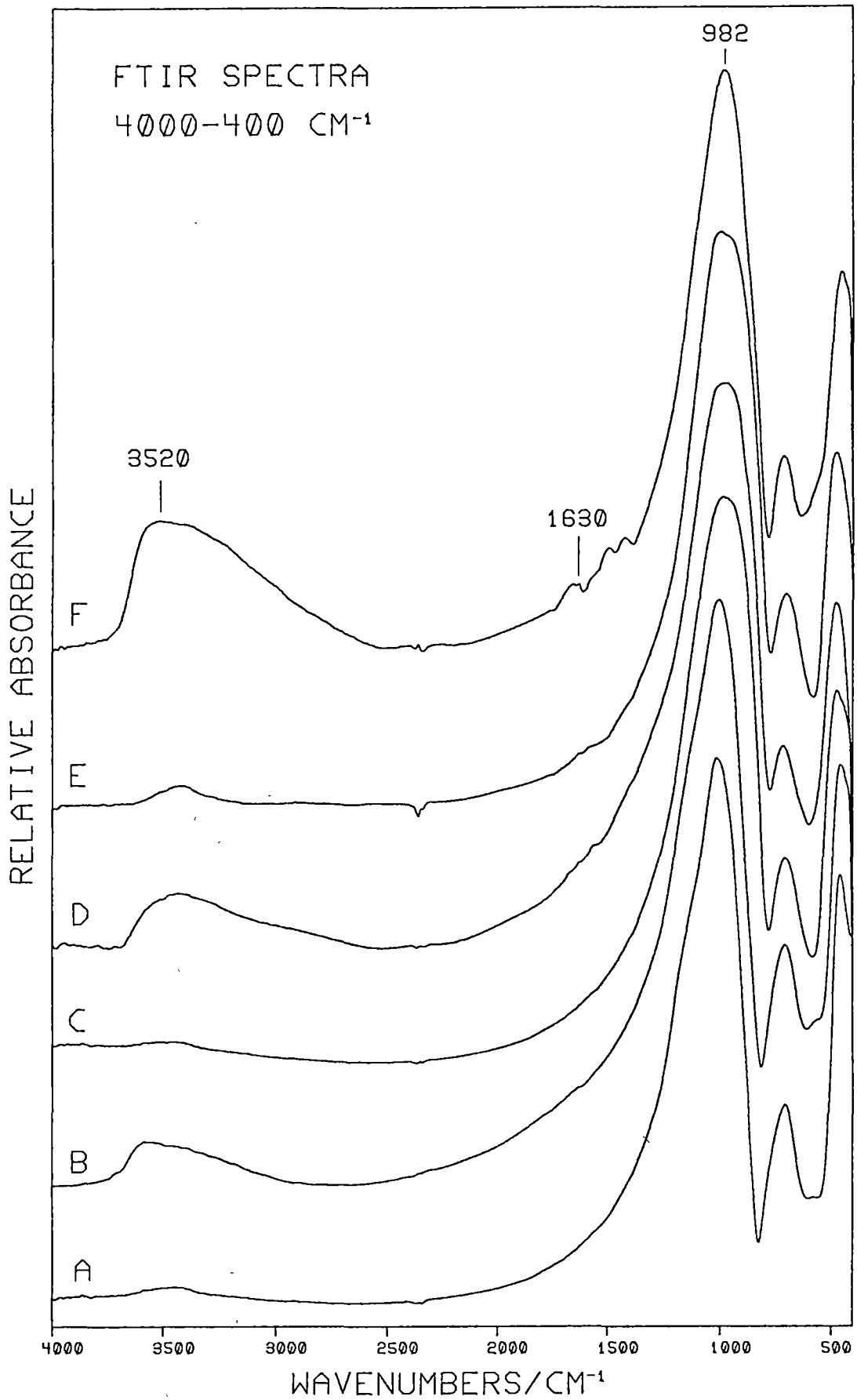
FTIR SPECTRA
4000-400 CM-1
982
3520
1630
F
E
D
C
B
A
RELATIVE ABSORBANCE
4000
3500
3000
2500
2000
1500
1000
500
WAVENUMBERS/CM-1

Fig. 4.6D Difference spectra (1500-400 cm^{-1}) (component-bearing) minus (component-absent):

A: (C-H fluid saturated jadeite glass) minus (1 atm volatile-free jadeite glass).

B: Same as A but duplicate KBr discs were used to record both component-bearing and component-absent spectra (reproducibility check).

C: (C-H fluid saturated sodamelilite glass) minus (30 kbar volatile-free sodamelilite glass).

D: (SiC reduced sodamelilite glass) minus (30 kbar volatile-free sodamelilite glass) [the "reduced component"].

E: (Hydrous sodamelilite glass) minus (30 kbar volatile-free sodamelilite glass) [the "oxidised component"].

A combination of spectra D and E well reproduces the difference spectrum of CH_4-H_2 fluid saturated sodamelilite glass [reduced + oxidised component].

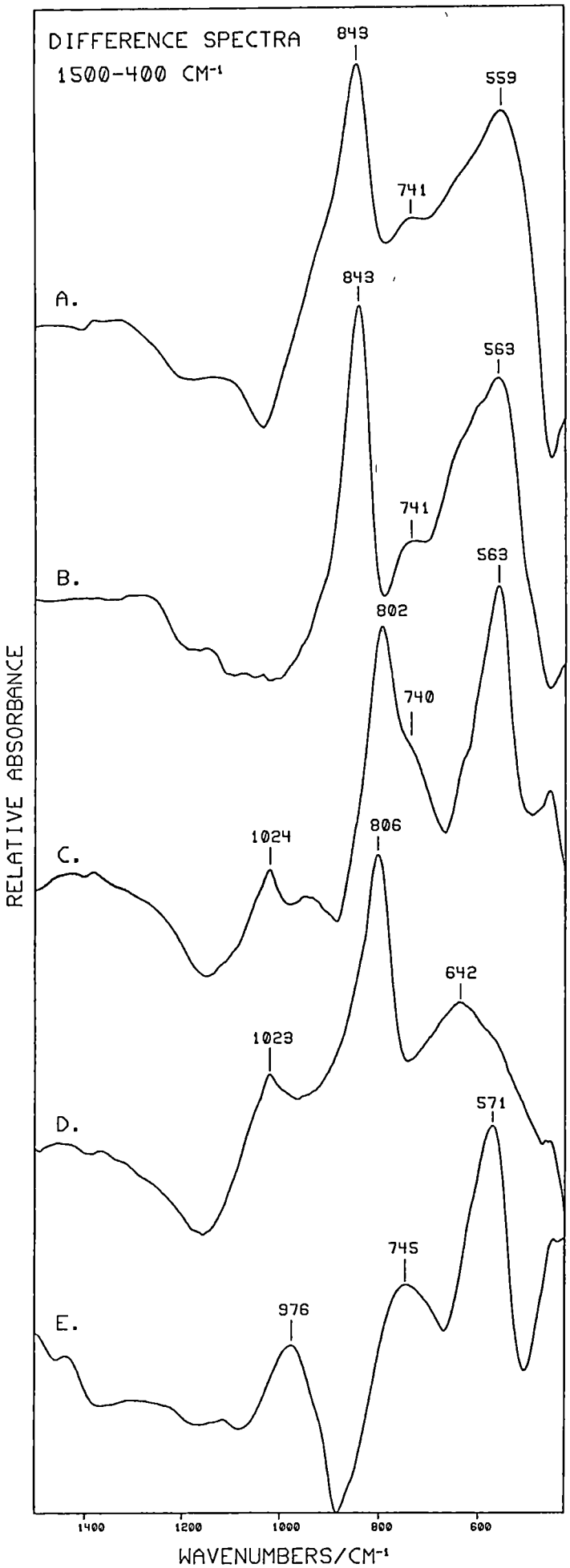
DIFFERENCE SPECTRA
1500-400 CM⁻¹
843
559
741
A.
843
563
741
B.
563
802
740
C.
1024
806
642
1023
D.
571
745
976
E.
RELATIVE ABSORBANCE
1400
1200
1000
800
600
WAVENUMBERS/CM⁻¹

Table 4.6A Akermanite $Ca_2MgSi_2O_7$

IR & R $Rb_2Pb_2Si_2O_7$ linear bridge pyrosilicate crystal (Tarte et al., 1973)	IR Hardystonite (Zn-Ak) crystal (Kimata, 1979)	IR Ak crystal (Kimata, 1979)	R Ak crystal (Sharma & Yoder, 1979)	Tentative Assignments	IR Ak glass (this work)	R Ak glass (Sharma & Yoder, 1979)
			1067 vw	...)		
		1044 sh		...)		
1026 ν_{as}[Si-O-Si]	1010 s	1010 s	1023 vw	...)ν_{as}[Si-O-Si]	)	
	970 s	973 s	986 w	...)	)	
					)964 vs	
913 ν_{as}[Si-O^-]	920 vs	935 vs		...)	) br	914 s
889Rν_s[Si-O^-]	885 sh	905 sh	904 s	...)ν_{as} and	)	
	838 s	851 s		...)ν_s[Si-O^-]	847 sh	858 sh
	682 w	685 w		$\nu[SiO_4]$?	...704 w sh	
668R ν_s[Si-O-Si]			661 m	ν_s[Si-O-Si]	?	683 m
		(642 m		...)		
	618 s	(623 sh		...)δ[Si-O-Si]		
		589 m	...598 w	..$\nu[MgO_4]$	..579 sh	
562 δ[Si-O^-]	549 sh	(559 w		...)		
		(520 sh		...)δ[Si-O^-]	517 s	533 w
	503 s			$\nu[ZnO_4]$?		
476)						
452R) δ[Si-O^-]	455 s	478 s	477 w	...)	482 sh	
407 δ[Si-O-Si]			447 w	...)δ[O]		

Band intensity:
- vs very strong
- s strong
- m medium
- w weak
- vw very weak
- br broad
- vbr very broad
- sh shoulder

Vibrational modes:
- ν_{as} asymmetric stretch
- ν_s symmetric stretch
- δ deformation

Probable band correlations indicated by .....
All glasses quenched from 1 atm unless otherwise stated.

R - Raman IR - Infrared

Table 4.6B Sodamelilite $NaCaAlSi_2O_7$

IR N_3AS_4 glass (this work)	IR Sm crystal (this work)	R Sm crystal (Sharma & Yoder, 1979)	Tentative Assignments	IR Sm glass (this work)*	R Sm glass (Sharma & Yoder, 1979)
1072 s	1070 sh,s		...) ν_{as}	)	
1034 s	1040 s		...) [Si-O-Si]	)	(1013)**
		1023 m	...) [Si-O-Al]	)	(990)**
				)978 s,vbr	980 m
	(986 s	972 sh	...) ν_{as} and ν_s	)	
937 vs,br	(	930 m	...) [(Si,Al)-O^-]	)	(907)**
	(901 vs	894 sh	...)	)	
870 sh	850 sh		...) ν[Al-O]	)	
	810 sh		...)	)	
	(727 m	724 sh,m	... $\nu[SiO_4]$?	)	
698 m	(			...)706 m,br	
	(683 m		... $\nu[AlO_4]$	)	
		665 sh	... δ[Si-O-Si]		
635 sh	640 sh,w	648 s	... ν_s[Si-O-Si]	?	648 sh
					562 sh
	(530 sh,w	539 m	... δ[Si-O-Al]	)	
	(	512 vw	)	)	
473 s,br	(479 s	485 w	)	)	
	(	460 w	) δ[O]	...)468 s,br	490 s
	(434 vs		)	)	
	(	412 w	)	)	

* Run T-1159 quenched from 30 kbar.
** Deconvolutions of 980 cm^{-1} band suggested by Mysen & Virgo (1980).
Band intensities as for Table 4.6A. Probable band correlations indicated by .....
All glasses quenched from 1 atm unless otherwise stated.

Table 4.6C Gehlenite $Ca_2Al_2SiO_7$

IR Gallium subst. Geh crystal (Kimata, 1979)	IR Geh crystal (Kimata, 1979)	R Geh crystal (Sharma et al., 1983)	Tentative Assignments	IR Geh glass (this work)	R Geh glass (Sharma et al., 1983)
1005 s	1022 s	1005 vw	...) ν_{as}		1004 w,sh
		998 w	...) [Si-O-Si]		
			) [Si-O-Al]	...984 s	
945 vs	970 s	977 m	...) ν_s & ν_{as}		
895 s	917 s	914 m	...) [Si,Al-O^-]	.. 918 s	896 s
870 s	887 s		...) [Si,Ga-O^-]		
	851 s	841 w,sh	...) ν[Al-O]	... 860 s	
	803 vs	796 m	...)	... 818 sh	
718 s	717 m		... $\nu[SiO_4]$?	...) 690 m,sh	
	685 m		... $\nu[AlO_4]$	)	
653 s	648 s	655 m,sh	... δ[Si-O-Si]		662 sh
		626 vs	... ν_s[Si-O-Si]		
583 m			...) ν[Ga-O]	?	
550 m			...) &		552 s
525 m			...) $\nu[GaO_4]$		
503 m	531 m	528 w	... δ[Si-O-Al]		
472 m	477 m	459 w	...) δ[O]	...) 457 m	
	414 s	425 vw	...)	)	

Band intensities as for Table 4.6A. Probable band correlations indicated by .....
All glasses quenched from 1 atm unless otherwise stated.

groups (where M = Al^{IV},Mg or Zn; T = Al^{IV} or Si) within which the nature of bonding is largely covalent; the adjacent sheets are held together by Ca^{2+} and Na^{+} ions with interlayer bonding being predominantly ionic (Louisnathan, 1969). The average Al-O distance in the M-site of gehlenite is 1.785 Å and in sodamelilite 1.762 Å, clearly consistent with the properties of a tetrahedron in a framework aluminosilicate (Louisnathan, 1970a, 1970b). In sodamelilite Al and Si are ordered on tetrahedral sites and Ca and Na are disordered over the larger, distorted 8-co-ordination site. Since N_3AS_4 glass is spectroscopically similar to crystalline Sm, it is likely that there is considerable Al and Si ordering on tetrahedral sites in this glass.

Raman and IR investigations of the melilite minerals have been carried out by Sharma et al. (1983), Sharma & Yoder (1979) and Kimata (1979). Results of these studies together with additional FTIR spectroscopic data on the melilite composition glasses (this work) have been summarised in Tables 4.6A, B and C. Tentative band assignments were made from band correlations with reference to Appendix 13.

Bands due to AlO_4 polyhedra are clearly identified for Geh by comparison with the gallium substituted analogue $Ca_2Ga_2SiO_7$. They occur at 851, 803 and 685 cm^{-1} and are also represented by bands at 850, 810 cm^{-1} (weak shoulders) and 683 cm^{-1} in Sm. The 850-800 cm^{-1} absorptions appear in the "characteristic frequency" range for condensed (i.e. interconnected) AlO_4 polyhedra as defined by Tarte (1967) and are due to stretching vibrations of Al-O-Al linkages as discussed by McMillan et al. (1982). The ~680 cm^{-1} band is probably a stretching vibration largely involving motion of Al with its tetrahedral co-ordination cage. An analogous motion for Si is tentatively proposed for the bands near 700 cm^{-1} in Geh, Sm and Ak. The presence of bands due to Al-O-Al linkages, albeit weak shoulders, in crystalline Sm must indicate some degree of Si,Al disorder amongst tetrahedral sites.

Despite the structural interpretations of Louisnathan (1969, 1970a, 1970b) all the crystalline melilites exhibit spectral features, associated with the silicon-oxygen stretch bands, that strongly resemble those of pyrosilicate minerals and compounds (i.e. those containing $[Si_2O_7]^{6-}$ groups), see example given in Table 4.6A. The $[Si_2O_7]$ dimer must therefore be considered as the basic vibrating unit of the melilite minerals rather than the aluminosilicate sheet of Louisnathan. This implies strong

localisation of Si-O and M-O (M = A,Mg or Zn) vibrations (i.e. negligible coupling) despite the fact that together they make up the integral $[MSi_2O_7]^{3-}$ structural unit of the melilite endmembers. Such an interpretation is similar to the model proposed by McMillan (1984a) that argues against significant Si,Al coupling of vibrational modes in aluminosilicate glasses.

As noted by Sharma & Yoder (1979), the IR and Raman spectra of Sm glass do not resemble the spectrum of the crystalline solid (which is similar to N_3AS_4 glass, however). The absence in the glass of an intense IR band or band component near 900 cm^{-1}, corresponding to the strong $\nu_{[NBO]}$ band at this frequency in the crystal, indicates that the vibrating unit in Sm glass cannot be regarded as an $[Si_2O_7]$ group but rather must represent a much more polymerised aluminosilicate network structure with little Al,Si ordering on tetrahedral sites (cf. N_3AS_4 and Sm glass spectra, Fig. 4.6A and B). This conclusion is supported by Sharma & Yoder (1979) and Mysen & Virgo (1980a); both studies suggest a structure dominated by network aluminosilicate units of the type $[NaAlSi_2O_7]^{2-}$ having NBO/T = 0.667. The Sm analogue glasses NS_3 and N_3AS_4 both have bulk NBO/T ratios of 0.667 but differ from Sm glass in that their spectra indicate the presence of substantial NBO (Fig. 4.6A, Table 4.6B). This may arise from:

(i) greater localisation of Al-O and Si-O stretching vibrations consistent with greater degree of Al,Si order in N_3AS_4 glass, and

(ii) much less uniform distribution of structural units than found in Sm glass, e.g. equilibria of the type: $2[\equiv Si\text{-}O^-] = [\equiv Si(O^-)_2] + [\equiv Si\equiv]$, as proposed by Mysen et al. (1982a), may be important.

For Ak glass, IR and Raman spectra (Table 4.6A) are similar to the crystalline phase suggesting that $[Si_2O_7]$ pyrosilicate groups are the dominant vibrating unit and in the absence of Al the melt structure is therefore relatively depolymerised as also proposed by Sharma & Yoder (1979).

The Raman spectra of gehlenite (Geh) glass and crystals are by contrast significantly different. Sharma et al. (1983) found the glass to consist of a 3-d aluminosilicate network together with a high proportion of $[SiO_4^{4-}]$ monomeric units identified by a strong band near 900 cm^{-1}. A bimodal "Q_0-Q_4" dispersion of tetrahedral environments is thus indicated (de Jong et al., 1981).

In summary the melilite endmember and analogue glasses exhibit a variety of different structural types ranging from those with significant NBO (Ak) to aluminosilicate network structures exhibiting limited (Sm) or substantial (N_3AS_4) Al,Si ordering or which contain a high proportion of other discrete units (Geh). The correlations between spectra developed in Tables 4.6A,B & C allow interpretation of the IR spectra of melilite and related glasses in terms of the basic vibrational units present. In the crystalline melilites and by analogy in the vitreous phase as well, these units may not always correspond directly with the basic structural units identified by x-ray diffraction methods. This is believed mainly due to the effects of increasing band localisation which may be correlated with the degree of tetrahedral site ordering. This suggestion has important implications for the structural role of Al as determined by vibrational spectroscopy since glasses of gross structural similarity may exhibit different degrees of Al,Si order and hence significantly different vibrational spectra. The results for melilite glasses and crystals suggest that in aluminosilicate glasses such as Sm, the high frequency bands are best described by the delocalised or Si,Al coupled vibrational model of Mysen and co-workers while in glass structures exhibiting more Al,Si order, such as N_3AS_4, the model of McMillan and co-workers may be more appropriate.

In all glasses studied, the mid-range envelope of moderate IR intensity can be shown to respond in a predictable fashion to $NaAlO_2$ or $Ca_{0.5}AlO_2$ substitution of the silicate network. This absorption arises from strongly delocalised vibrational modes associated mainly with the aluminosilicate framework cations Si and Al.

As seen above, the structural diversity of melilite and related glasses makes them useful subjects for illustrating the principles of applying vibrational spectroscopy to structural problems in aluminosilicate melts and glasses. This application will be important in elucidating the mechanism of C-H volatile solubility.

C. Structure and Band Assignments in Jadeite and Related Glasses

FTIR spectra of crystalline jadeite and Jd glass quenched at 1 atm are presented in Fig. 4.6B. That there are considerable structural differences between the crystal and glass is readily apparent from the

pronounced dissimilarity in the spectra. This difference is well known from x-ray diffraction (RDF), Raman spectroscopic and ^{27}Al MAS-NMR studies (Taylor & Brown, 1979b; Mysen et al., 1980a; de Jong et al., 1983). The glass can be approximated by a stuffed tridymite 3-d network structure based on six-membered rings with Al in four-fold co-ordination while the crystal has a monoclinic pyroxene structure based on $[Si_2O_6]_\infty$ chains and AlO_6 groups.

Structural differences involving AlO_6 --> AlO_4 co-ordination changes between crystal and glass and between crystalline polymorphs are found in numerous other systems. Examples include $LiAlSi_2O_6$ glass and the α, β and γ-spodumene polymorphs (Sharma & Simons, 1981) and vitreous and crystalline CaTs ($CaAl_2SiO_6$), Sharma et al. (1983). Both studies were Raman investigations, and although structural changes could be readily characterised, direct identification of bands due to AlO_4 and AlO_6 polyhedra was not possible with this technique. As discussed in Appendix 13, IR spectroscopy is expected to be sensitive to the nature of Al-O polyhedra particularly if vibrations can be regarded as largely independant of other modes (although this is not necessarily so, see below). Tarte (1967) has suggested frequency ranges for bands indicative of Al-O polyhedra:

	AlO_4	AlO_6
Isolated polyhedra	800-650	530-400
Condensed polyhedra (i.e. containing Al-O-Al linkages)	900-700	680-500

The ranges quoted are consistent with the presence of tetrahedrally co-ordinated Al in the aluminosilicate glasses investigated in this study even though the delocalised nature of the mid-range envelope is hardly consistent with an "independant" vibration. Vibrations of AlO_6 groups are probably better approximated as independant and this has been used by Farmer et al. (1979) and Serna et al. (1977, 1979) to distinguish octahedrally co-ordinated Al in aluminosilicate gels and Al-serpentine minerals. AlO_6 groups are identified by strong absorptions in the 500-600 cm^{-1} region in both studies. It is therefore tempting to suggest that the strong band at 595 cm^{-1} in crystalline jadeite (Fig. 4.6B) which is absent or weak in the glass spectrum, can be assigned to a dominant contribution

from AlO_6 vibrations. As expected, no band exists near 700 cm^{-1} in crystalline jadeite to indicate the presence of AlO_4 but such a band does exist in crystalline and vitreous Sm (Table 4.6B, Fig. 4.6B).

Reference to tabulated IR spectra for a variety of silicate minerals, including structurally related Al-containing and Al-free varieties, strongly support the hypothesis that **strong or very strong** bands in the 520-620 cm^{-1} range are indicative of octahedrally bound Al. While there are a few notable exceptions to the rule (such as the feldspar and scapolite series which have medium to strong IR bands in this region presumably related to their four-membered ring structures) there is good general agreement for a diverse range of mineral structures and compositions, as summarised in Table 4.6D below. The natural extension of this rule is to aluminosilicate glasses where direct identification of AlO_6 polyhedra has not been possible with other techniques. Bands in the 520-620 cm^{-1} region may thus indicate the presence of AlO_6 polyhedra. Other possibilities for IR bands in this region include an Si-O-Si bridge bending vibration as observed in pure silica and silica-rich glasses, bands associated with three- or four-membered ring structures (as in the feldspars and scapolites) and absorptions arising from defect centres (summarised in Appendix 13). The last mentioned case is somewhat controversial as the existence of defect centres in aluminosilicate glasses has been questioned by McMillan (1984a); in any event the IR band at ~600 cm^{-1} in silica glass is only weakly IR active and shows little change in intensity with neutron irradiation unlike that expected for an IR active defect band (Bates et al., 1974, fig. 6).

In 1 atm Jd and Ne (nepheline) composition glasses a weak band exists at ~580 cm^{-1} (Fig. 4.6B, Jd) and may indicate the presence of a small amount of non-network, octahedrally co-ordinated Al or alternatively four-membered ring structures may be present. Mysen et al. (1980a) have found that no changes occur in the silicate network of Jd glass from 1 atm to 38 kbar and thus find no evidence to suggest that an Al co-ordination change takes place with pressure as proposed by Kushiro (1976). These Raman results, however, do not preclude the presence of a small, constant proportion of octahedrally co-ordinated Al in Jd melt over the pressure

Table 4.6D Relationship between six-fold Al co-ordination and IR bands in the region 520-620 cm^{-1}.

Mineral	Al co-ordination number	vs or s bands 520-620 cm^{-1}
Jadeite	6	595
α -spodumene	6	590
Acmite	no Al	absent (505-502)*
Diopside	no Al	absent (513-510)*
Hedenbergite	no Al	absent (515-509)*
Kyanite	6	598-597
Sillimanite	6,4	545-544
Andalusite	6,5	535-520
Mullite	6,4	560-550
Topaz	6	609
Staurolite	6	595-586
Almandine**	6	570-569
Pyrope**	6	575-565
Grossular	6	540-538
Spessartine	6	565-562
Uvarovite	no Al	absent
Andradite	no Al	absent (512-510)*
Gibbsite	6	562-540
Kaolinite	6	545-535
Halloysite	6	545-550
Montmorillonite	6,4	520
Pyrophyllite	6	542-535
Talc	no Al	absent
Muscovite	6,4	540
Phlogopite	4	absent
Gehlenite	4	absent
Sodamelilite	4	absent
Zoisite	6	575

Data sources: Liese (1975) and Gadsden (1975).

* closest strong bands in the ~500-600 cm^{-1} region.

** Omori (1971) calculates the AlO_6 stretching frequency to be ~630 cm^{-1} for Alm-Pyr garnet in reasonable agreement with the observed strong band at ~570 cm^{-1}.

range investigated. Current techniques for the detection of Al co-ordination environments, including solid-state MAS-NMR (de Jong et al., 1983), do not appear sensitive enough to distinguish the Al co-ordination

in jadeite glass (but see Ohtani et al., 1985); the question of Al^{VI} existence in these glasses therefore remains open to further investigation.

4.7 Background, II: An FTIR study of the water dissolution mechanism in Sm glass at 30 kbar.

Two experiments at P = 30 kbar were performed in piston-cylinder apparatus to prepare hydrous Sm glasses containing ~6 wt% H_2O. The primary object of this study was to provide an IR spectroscopic analysis of the water solubility mechanism in Sm glass for the purposes of comparison with the spectroscopic effects of reduced C-H volatile dissolution. From the discussion in Appendix 13.5 it is unlikely that the parallel Raman investigation of Mysen & Virgo (1980) was able to establish full details of the H_2O solubility mechanism. A secondary objective of this study was to assess the effects of internal reduction/oxidation by H_2 migration to or from the sample capsule. Runs T-1238 and T-1250 were carried out at 1300°C for durations of 15 minutes and 75 minutes respectively using talc-sleeved assemblies with 2.3 mm O.D. Pt capsules and small graphite inner capsules containing ~5 mg of powdered Sm glass. Water was introduced in the form of an $Al(OH)_3$/graphite mixture capable of generating 25 wt% water by hydroxide breakdown. Internal capsule fO_2's using this arrangement are expected to be near GW (see Section 2.8). If external fO_2's are >GW then oxidation will proceed via the water decomposition equilibrium:

$$H_2O_{(melt)} \rightarrow H_2\uparrow + 1/2\ O_{2(melt)} \qquad \ldots\ 4.7A$$

allowing diffusive H_2 loss from the noble metal capsule. If external fO_2's are <GW then the internal reduction will take place by H_2 diffusion into the capsule. In the presence of graphite, the operation of the former process should be evident from the presence of dissolved carbonate in the product glasses via the oxidation reaction:

$$C(\text{graphite}) + O_2 + O^{2-}_{(melt)} = CO^{2-}_{3\ (melt)} \qquad \ldots\ 4.7B$$

Product glasses were clear with no vapour bubbles but many small graphite inclusions especially adjacent to the walls of the inner capsule. Both runs were vapour undersaturated. FTIR spectra were recorded on ~1 mg of sample dispersed in KBr matrices as discussed in Section 4.4. Analysis of sample T-1250 by pyrolysis/gas chromatography (see Section 4.8) gave a H_2O content of 5.5 $\pm$ 0.2 wt%.

FTIR spectra of the glasses show the presence of weak bands in the 1500-1400 cm^{-1} region assignable to the ν_3 absorption of dissolved carbonate anions. In the 15 minute run, carbonate is present only in negligible proportions. After 75 minutes the ν_3 carbonate band (a doublet; refer to Appendices 13.5 and 15) is readily apparent in the glass spectrum (Fig. 4.6B). This clearly indicates operation of an oxidation process, the progress of which can be monitored by observing the rate of growth of the carbonate ν_3 bands.

If it is assumed that H_2-diffusion through the outer Pt capsule is the rate limiting step in the oxidation process then using the diffusion equation of Shaw (1967) and noting the oxidation equilibria defined in equations 4.7A and 4.7B, an approximate value for the ratio P_{H_2}(internal)/P_{H_2}(external) may be obtained [P_{H_2}(internal) refers to the internal capsule environment, and P_{H_2}(external) refers to P_{H_2} in the surrounding assembly]. Estimating the maximum amount of dissolved carbonate at 0.5 wt% over 75 minutes (from comparison of ν_3 band areas with an Sm glass of known carbonate content, see Appendix 15) and knowing the proportions of starting materials and capsule dimensions, the average maximum H_2 flux at 1300°C, 30 kbar is estimated be to 1 x 10^{-7} g $min^{-1}cm^{-2}$. This gives P_{H_2}(internal)/P_{H_2}(external) ~ 2-10 according to equation (2) of Shaw (1967). Since the ratio of P_{H_2}(GW)/P_{H_2}(GCO), calculated with Program COH/GRAPHITE6 is ~80 at 1300°C, 30 kbar and assuming P_{H_2}(internal) can be approximated by P_{H_2} of the GW buffer during the initial stages of the run, then fO_2 of the talc/graphite/BN external environment must lie between GW and GCO at about GW+0.3 to GW+0.9 log fO_2 units. Thus in unbuffered hydrothermal experiments having initial fO_2's below this range, hydrogen will always diffuse out of unbuffered capsules leading to oxidation of the capsule contents.

These results may be applied to the problem of CH_4 decomposition discussed in Section 4.2 by again assuming rate limiting H_2 diffusion through the Pt capsule membrane. For a H_2 flux of 10^{-7} g $min^{-1}cm^{-2}$, complete H_2 loss via the equilibrium $CH_4 = 2H_2 + C$, from a capsule initially containing 1 mg of CH_4 should take ~42 hours. For a 30 minute duration experiment only about 1-2% of total available hydrogen on a molar basis would be lost by diffusion. This supports the choice of run times made in Section 4.2.

FTIR Spectra and the Mechanism of Water Dissolution in Sm Melt

For both hydrous Sm glasses, FTIR spectra in the region below 1400 cm^{-1} are identical and thus appear unaffected by the small amounts of carbonate present. Compared with the large proportion of dissolved H_2O (some 46 mol% in run T-1250), the structural role of carbonate at these low levels is expected to be insignificant. Graphite has negligible IR activity and no bands in the 4000-400 cm^{-1} region (confirmed on KBr discs containing 2 mg of dispersed graphite) and therefore will not contribute to the observed absorption bands in the hydrous glasses. Interpretation of the 1400-400 cm^{-1} spectra and difference spectra (hydrous minus volatile-absent glass) can thus be made entirely in terms of the effect of H_2O dissolution.

Hydrous (T-1250) and volatile-absent Sm glass spectra may be compared by reference to Fig 4.6B (spectra B and D) and Fig. 4.6C (spectra C and F). The principle differences of hydrous from volatile-absent Sm spectra are summarised below:

(i) presence of a broad O-H stretching absorption centred near 3520 cm^{-1}.
(ii) a band near 1630 cm^{-1} due to the presence of dissolved molecular water (see Appendix 13.5).
(iii) narrowing in the width of the high frequency envelope.
(iv) decrease in the intensity and shift to higher wavenumbers of the mid-range envelope.
(v) appearance of a new absorption near 570 cm^{-1}.
(vi) shift in the position of the low frequency envelope.

These changes are more clearly illustrated in the difference spectrum (hydrous Sm minus anhydrous Sm) presented in Fig. 4.6D (spectrum E).

Positive and negative features are summarised in Table 4.7A together with proposed assignments (see Appendix 13.5).

Table 4.7A Difference Spectrum: (Sm + H_2O, run T-1250) minus (Sm glass quenched from 1395°C, 30 kbar) - features and assignments.

Positive Features (cm^{-1})	Suggested Assignment*	References and Comments
976	ν [Si-OH]	Stolen & Walrafen (1976); Mysen et al. (1980b)
745	ν [Al-O-Al] associated with AlO_4 clusters.	Tarte (1967); similar bands found by Serna (1977) in disordered amesites.
571	ν [AlO_6]	Strongest positive feature; assigned as discussed in this Section and Section 4.6.
Negative Features (cm^{-1})	**Component Removed**	**References and Comments**
~1100	ν_{as}[Si-O-Al] (ν[(Si,Al)-O^-] (of Mysen & (co-workers.	Loss of bridging oxygen involving linkage with Al.
890	(OR (ν[$Si(OAl)_4$] (of McMillan & (co-workers.	Loss of NBO probably accompanying removal of Al.
680	ν[AlO_4]	Loss of tetrahedrally co-ordinated Al.
490	δ[Si-O^-]	Loss of NBO, refer to changes in low-frequency envelope width on polymerisation in NS_2-NS_5 series (Fig. 4.6A).

* ν = stretching modes

δ = deformation (stretching + bending) modes.

The results presented above strongly suggest that H_2O dissolution in Sm is accompanied by substantial structural re-organisation of Al, formation of Si-OH linkages and an apparent **decrease** in the proportion of NBO. These general conclusions are similar to those proposed by Mysen & Virgo's (1980b) Raman study of hydrous Sm melt but differ in detail. The IR difference spectra have bands at 745 and 571 cm^{-1} indicating the presence of both condensed AlO_4 polyhedra (AlO_4 "clusters") and AlO_6 groups. Alternative assignments of the 571 cm^{-1} band to three- or four-membered ring structures or defect sites are not consistent with the types of network structure identified in hydrous Sm melt by Raman spectroscopy (Mysen & Virgo, 1980b) nor with the effect of H_2O on the ~570 cm^{-1} "defect band" in aluminosilicate glasses (addition of H_2O actually causes a decrease in the intensity of this band, Appendix 13.5). Negative features in the difference spectra also support a major re-organisation of Al. The most prominent negative band occurs at 890 cm^{-1} and indicates a loss of NBO stretch modes. In the model of Mysen and co-workers and McMillan and co-workers (Appendix 13.4) removal of Al from the network will cause loss of the lowest frequency $\nu_{[NBO]}$ band components from the high frequency envelope just as observed here. The 490 cm^{-1} negative band results from decrease in the width of the low frequency envelopes; reference to Fig. 4.6A (NS_5 to NS_2 series) shows this may be related to a decrease in the proportion of $Si\text{-}O^-$ (NBO) bonds. An apparent decrease in the proportion of structural units containing NBO relative to 3-d network units was also obtained in the Raman studies of Mysen & Virgo (1980b) and was considered in later work (Mysen et al., 1982a) to result from the reaction:

$$Si\text{-}O^- + H_2O = Si\text{-}OH + OH^-$$

in combination with the formation of Al-depleted 3-d network units of NBO/T ~ 0.

The mechanism of H_2O dissolution in Sm melt as outlined by the FTIR data, is best written in the form of a series of related equilibria to take into account Al distribution between network AlO_4, AlO_4 clusters and non-network AlO_6. The mechanism must include molecular water <--> hydroxyl group equilibria since FTIR spectra indicate the presence of both species. Furthermore, it can be inferred that some form of alkali or alkaline earth-hydroxyl complexes are formed by H_2O interaction with the cations released from charge balancing positions in the network as a result of Al

redistribution. De Jong & Brown (1980a) have shown that Al-O-Si and Al-O-Al linkages in aluminosilicate networks are destabilised in the absence of charge compensating cations. It is quite possible, therefore, that OH^- complexation with Na^+ or Ca^{2+} is a major contributing factor in Al expulsion from the network. Direct spectroscopic evidence for the presence of hydroxyl complexes would lie in the far IR region below 400 cm^{-1} ("cage-like" vibrations of CaO_n and NaO_n polyhedra, e.g. Rao & Elliot, 1981) which at present has not been investigated for hydrous glasses. The Raman studies of Mysen & Virgo (1980b) also support the presence of metal-hydroxyl complexes in hydrous Sm melt. The proposed mechanism of H_2O dissolution in Sm is outlined below:

General equation forming AlO_6 groups

$$[NaAl^{IV}Si_2O_7]^{2-} + H_2O = [Al^{VI}O_2]^- + [Na(OH)]^o + [SiO_2(OH)]^- + [SiO_2]^o \quad ....4.7C$$

additional equilibria are required to relate observed spectroscopic features:

AlO_4 Cluster Formation

$$n[Al^{VI}O_2]^- = [Al^{IV}O_2]_n^{n-} \quad ....4.7D$$

Molecular H_2O

$$2[SiO_2(OH)]^- = [H_2O]_{molec} + [Si_2O_5]^{2-} \quad ....4.7E$$

Complex Formation

$$2[SiO_2(OH)]^- + Ca^{2+} = 2[SiO_2]^o + [Ca(OH)_2]^o \quad ....4.7F$$

Protonated Silicate Complex Formation

$$[SiO_2(OH)]^- + 2[SiO_2]^o = [Si_2O_5]^{2-} + [SiO(OH)]^+ \quad ....4.7G$$

The equations presented above show plausible locations for hydrogen on a number of different sites, i.e. as hydroxyl bound to silicon, in hydroxyl-metal complexes, as protonated silicate complexes or in the form of dissolved molecular H_2O. The last form mentioned contributes the dominant proportion of soluble H_2O at water contents exceeding about 4 wt% (Stolper,

1982a); this amount not being particularly composition sensitive. The H_2O solubility equation proposed for Sm melt by Mysen & Virgo (1980b) is very specific and does not include the effects of molecular H_2O or AlO_4 clustering (Raman spectroscopy is probably not sensitive enough to detect the vibrational modes of these species, see McMillan et al., 1983, for example). The more generalised set of equilibria presented in equations 4.7C to G probably gives a more physically realistic description of the H_2O solubility process in an aluminosilicate melt with NBO/T > 0.

Considering reaction 4.7C alone, there is an increase in network NBO/T of 0.33 units per mole H_2O dissolved if Si-OH bonds are considered as non-bridging. The overall change in NBO/T considering the additional equilibria is difficult to judge because the extent to which reactions 4.7E, F and G proceed is unknown. What is clear, however, is that H_2O dissolution results in a decrease in the proportion of network $Al\text{-}O^-$ and $Si\text{-}O^-$ bonds: a major feature recorded by the IR spectra. Clearly, the dissolution mechanism of H_2O in aluminosilicate melts containing initial NBO (on an anhydrous basis) of similar concentration to that found in basaltic compositions, cannot be interpreted as a simple depolymerisation reaction of the type $Si\text{-}O\text{-}Si + H_2O = 2Si\text{-}OH$ as envisaged by Mysen et al. (1980b, equation 4). Indeed there is no requirement for Si-O-Si bond cleavage in the solubility mechanism proposed here. It is instead cleavage of the energetically more reactive Al-O-Si linkage (de Jong & Brown, 1980a) that is central to the mechanism of H_2O solubility in Sm melt. Hydrogen ions are expected to participate significantly in the hydrolysis of Al-O-Si bonds as proposed by de Jong & Brown (1980b).

Since Mysen et al. (1982a) have found that, compared with Sm, more polymerised melts such as Jd or An where NBO/T (anhydrous basis) ~ 0 "... respond similarly to solution of H_2O at high pressures", it is possible to write H_2O solubility reactions analogous to those of equations 4.7C to G. Thus for a Jd melt unit:

$$[NaAl^{IV}Si_2O_6] + H_2O = [Al^{VI}O_2]^- + [SiO_2]^o + [SiO(OH)]^+ + [Na(OH)]^o \quad \text{....4.7H}$$

and additional equilibria of the type 4.7D to G can relate other features of the solubility mechanism; again their equilibrium positions are unknown for any P,T and fH_2O condition and may differ from those of Sm.

4.8 Dissolution Mechanism of Reduced C-H Volatiles in Sm and Jd Composition Melts.

The aim of this section is to evaluate the solubility mechanism of reduced C-H volatiles using both spectroscopic and analytical information. FTIR spectra of C-H fluid-saturated glasses (T-1341, Sm) and (T-1296, Jd) are presented in Fig. 4.6C (spectra D and B) and Fig. 4.6B (spectra C and G). Perhaps the most obvious feature of these spectra is the presence of a broad OH absorption band located near 3600 cm^{-1}. The mechanism of H_2O solubility as discussed in the previous section is therefore expected to be highly relevant to the reduced volatile solubility process. Detailed comparisons between the FTIR spectra of C-H volatile-saturated glasses and both volatile-absent and hydrous glasses are made in the following subsections.

FTIR Spectrum of Sm + C-H Fluid Equilibrated Glass 30 kbar, 1350°C: Major Features

(i) Presence of a broad, asymmetric O-H stretch band centred at ~3580 cm^{-1}. Comparison of O-H peak areas with hydrous Sm glass containing 5.5 $\pm$ 0.2 wt% H_2O (after normalising the 980 cm^{-1} envelope in both spectra to an absorbance of 1) gives an estimated dissolved hydrogen content equivalent to 2.7 $\pm$ 0.3 wt% H_2O (if all H is derived from CH_4 then this would correspond to a methane solubility of 1.2 $\pm$ 0.1 wt%).

(ii) No absorptions appear in the frequency range 2600-1700 cm^{-1}.

(iii) A weak band appears at ~1630 cm^{-1} (ν_2 H-O-H bending vibration) due to the presence of dissolved molecular H_2O. There is no evidence for dissolved carbonate which has a characteristic ν_3 absorption band or bands at ~1600-1380 cm^{-1} (Appendix 13.5).

(vi) The high frequency envelope is similar in shape to the volatile-absent glass except for the appearance of a weak shoulder at the low frequency limit.

(v) The shape, position and intensity of the mid-range envelope is unlike that of volatile-absent Sm glass but resembles the hydrous glass except for a stronger absorption near 650 cm^{-1}.

(vi) The minimum near 570 cm^{-1} in volatile-absent Sm has shifted to 590 cm^{-1} in the C-H volatile-saturated glass; this compares with 650 cm^{-1} in the hydrous glass. Such behaviour suggests that C-H dissolution is accompanied by appearance of a band near 570 cm^{-1}.

(vii) There is little change in the low frequency envelope except at <425 cm^{-1} where KBr background effects become noticeable.

FTIR Spectrum of Jd + C-H Fluid Equilibrated Glass 30 kbar, 1320°C: Major Features

In this subsection, comparisons have been made between C-H fluid-saturated Jd glass quenched from 30 kbar, 1320°C and the 1 atm volatile-absent Jd glass. Such comparisons are valid since the Raman spectroscopic study of Mysen et al. (1980a) has shown that the structure of quenched Jd melt "... remains essentially unaffected" by pressure up to at least 38 kbar.

(i) The FTIR spectrum of C-H volatile-saturated Jd glass is similar to that of Sm over the range 4000-1500 cm^{-1}. Estimated dissolved hydrogen is equivalent to 2.5 $\pm$ 0.3 wt% H_2O. This number is a guide only to the amount present since hydrous Sm glass and not Jd glass was used as the reference.

(ii) In the high frequency envelope changes in the highest frequency limb are noticeable as is a shift in the lowest frequency minimum from 840 to 810 cm^{-1}. There is a shift in the envelope maximum from 1008 cm^{-1} to 1003 cm^{-1}.

(iii) The mid-range envelope shows loss of a band component near 790 cm^{-1} but otherwise little obvious difference.

(iv) There is a marked change in the region near 570 cm^{-1} evident from both Figs 4.6C and 4.6B. C-H volatile dissolution causes growth of a band near 570 cm^{-1} suggesting an Al co-ordination change (cf. spectrum of hydrous Sm glass).

The features identified in the above comparisons show that C-H volatile dissolution in aluminosilicate melts results in the formation of O-H bonds both in the form of hydroxyl groups and a proportion of dissolved molecular water. Carbonate is not a product of C-H volatile dissolution at these fO_2's. To proceed further with this analysis it is necessary to examine plausible dissolution mechanisms and apply any necessary theoretical constraints.

Mechanisms for the dissolution of reduced volatiles in silicate melts have been suggested by very few authors. In a study that investigated the solubility behaviour of CO as a CO_2-CO volatile mixture, Eggler et al. (1979) suggested that CO dissolves by a carbonation reaction of the type:

$$CO + 2O^- = CO_3^{2-} \quad .... \ 4.8A$$

where "O^-" = non-bridging oxygen. Eggler & Baker (1982) proposed two mechanisms for CH_4 dissolution based on analogous reactions for H_2O, i.e.

$$4Si\text{-}O\text{-}Si + CH_4 = 4Si\text{-}OH + C \quad .... \ 4.8B$$

$$Si\text{-}O\text{-}Si + CH_4 = Si\text{-}CH_3 + Si\text{-}OH \quad .... \ 4.8C$$

and finally Jakobsson & Holloway (1984) suggested that CH_4 dissolution may result in the appearance of carbonate via the reaction:

$$CH_{4(fluid)} + O_{(melt)} = 4OH_{(melt)} + CO_{3(melt)} \quad .... \ 4.8D$$

The validity of three of the above mechanisms is, however, highly questionable. This arises from a failure to ensure that the reactions are correctly charge balanced and/or chemically realistic. For example, equation 4.8A while apparently charge balanced, actually assumes a novel oxidation state for oxygen (a one minus charge equivalent to a peroxide anion). How such a species can be equated with NBO is not clear. Reactions 4.8B & D have been conveniently simplified by dropping all anion charges! [in fact the reactions are impossible to balance]. Since electroneutrality should always be obeyed when balancing any chemical reaction, it is evident that if a reduced volatile dissolves in a silicate melt to give an "oxidised bond" such as O-H or O-C, then this must be balanced at equilibrium by concurrent production of a "reduced bond". Such a bond is one involving an element in a lower oxidation state and/or one excluding oxygen. Candidates in the case of a C-H fluid could include: Si-H, Si-C, C-H, Si-Si and analogous bonds involving Al and other metal cations. Any mechanism describing reduced volatile dissolution in silicate melts **must** incorporate this basic theoretical constraint.

Reference to the FTIR spectra of Sm and Jd C-H fluid-saturated glasses immediately eliminates metal-hydrogen or C-H bonds as candidates for the "reduced bond". This is because bonds of this type have

characteristic IR stretching frequencies in the range ~3000-1700 cm^{-1} where no absorption was noted, e.g. C-H bonds are expected at 3050-2850 cm^{-1} and Si-H bonds at 2250-2100 cm^{-1} (Pouchert, 1981). Thus reaction 4.8C suggested by Eggler & Baker (1982), while being properly charge balanced and involving Si-C and C-H as reduced bonds, is not consistent with observed spectroscopic results.

A strong indication that structural features not found in hydrous Sm melt are present in C-H fluid-saturated Sm glass is provided by the observed drop in liquidus temperatures of only ~40-50°C (Section 4.3). With the equivalent of ~2.7 wt% H_2O present the expected melting point depression is at least 150°C. For example, in the system albite-H_2O containing 2.9 wt% H_2O there is a drop in albite melting temperature of ~180°C at 20 kbar (Burnham, 1979); this value increases with increasing pressure. Even in a system containing substantial NBO (anhydrous basis), such as the olivine basanite composition of Green (1973), a liquidus depression of ~160°C is found for a water content of 2.5 wt% at 30 kbar. The effects observed here must be attributed to substantial differences in solubility mechanism between H_2O and C-H fluid implying the presence of a "reduced component" as required by charge balanced criteria. Spectroscopic identification of the component, which is probably masked by Si-O vibrations, is best achieved by analysis of the (volatile-bearing) minus (volatile-absent) glass difference spectra.

Difference spectra for Sm and Jd glasses are presented in Fig. 4.6D. Positive and negative features are listed in Table 4.8A and are entirely consistent with the changes deduced from comparisons of volatile-saturated and volatile-absent spectra discussed at the beginning of this section. In Table 4.8A, spectra A and B were obtained from duplicate KBr discs (both C-H saturated Jd and 1 atm Jd glasses prepared separately) and demonstrate the reproducibility of this technique; both spectra show identical features. From the Table 4.8A it is apparent that the difference spectra bands can be separated into features associated with OH dissolution and an unknown "reduced component" characterised by a prominent band appearing on the lower frequency limb of the high-frequency envelope at 843 cm^{-1} in Jd and 802 cm^{-1} in Sm. The difference of 41 cm^{-1} between the two bands may be equated with a similar difference in the range spanned by the high-frequency envelopes in the volatile-absent Jd and Sm composition glasses. This strongly suggests the "reduced component" is intimately bonded with the silicate network.

Table 4.8A Difference spectra for C-H volatile-saturated glasses 1500-400 cm^{-1}.

Positive Features (cm^{-1})		Proposed assignment and comments.
Spectra A & B*	Spectrum C	
843	802	Reduced component, strongest positive feature.
741	740	$[AlO_4]_n$ clusters associated with OH formation.
~640(sh)	~640(sh)	Reduced component.
559,563	563	ν $[AlO_6]$, non-network AlO_6 due to OH formation
-	1024	Reduced component.
-	~950	ν [Si-OH]
Negative Features (cm^{-1})		
~1170	~1150	Loss of ν[Si-O-Al] component.
~1050	-	Loss of ν[Si-O-Si] component.
~800	-	Loss of δ[Si-O-Si] (in plane) component?
-	~700	Loss of $\nu[AlO_4]$ component.

*Spectra A and B: (C-H volatile-saturated Jd glass, T-1296) minus (1 atm volatile-free Jd glass spectrum). In duplicate.

Spectrum C: (C-H volatile-saturated Sm glass, T-1341) minus (30 kbar volatile-free Sm glass spectrum).

ν = stretching mode δ = deformation mode sh = shoulder.

The theoretical and spectroscopic constraints discussed above, greatly limit the choice of a reduced component to such an extent that there are only two realistic possibilities:

I. A network unit containing Si-C bonds.

II. A non-stoichiometric network component containing units having an O/Si ratio less than 2; as found for example, in amorphous silicon monoxide (Yasaitis & Kaplow, 1972).

The former alternative implies that only hydrocarbon species (i.e. dominantly CH_4) are involved in the dissolution process while the latter alternative is a general reduction of the silicate network and could involve H_2 as well as CH_4. Support for I is given by the known range of IR active Si-C bond stretching frequencies for molecular compounds (see Table 4.8B). These span the range ~700 cm^{-1} to 1226 cm^{-1} encompassing the region that includes the strongest difference spectrum features at ~840 (Jd) and ~800 (Sm) cm^{-1}. However, these bands also appear to be consistent with the presence of silicon monoxide or related units. Compared with pure silica glass, the high frequency envelope in amorphous silicon monoxide is shifted down frequency by some 100 cm^{-1} (Pliskin & Lehman, 1965; Khanna et al., 1981). A similar shift in band components in aluminosilicate glasses would be sufficient to extend the high frequency envelope to lower wavenumbers and hence result in the observed ~840 and ~800 cm^{-1} positive difference features.

Table 4.8B Range of IR frequencies for Si-C bonds relevant to molecular or amorphous materials.

Compound	$\nu_{[Si-C]}$ (cm^{-1})	Reference
Organosilicon compounds: $Si-CH_3$ bonds.	740-680	Pouchert (1981)
Matrix isolated SiC_2 molecules.	835 (853 in electronic spectrum)	Weltner & McLeod (1964)
Matrix isolated SiC molecules.	1226	As above, calculated value using a force constant of 744 Nm^{-1}.

Process I and II may be described by the following balanced equations (for an Sm melt-unit):

Mechanism I: CH_4 volatile solubility

$$2[Al^{IV}Si_2O_7]^{3-} + CH_4 = 2[Al^{VI}O_2]^- + 4[OH]^- + \{Si\text{-}C\} + 3[SiO_2]^o \quad \ldots\ 4.8E$$

additional equilibria can relate spectroscopically observed and inferred species:

Molecular water

$$2[OH]^- = [H_2O]_{molec} + [O]^{2-} \quad \ldots\ 4.8F$$

Depolymerisation

$$[OH]^- + [SiO_2]^o = [SiO_2(OH)]^- \text{ etc.} \quad \ldots\ 4.8G$$

AlO_4 cluster and hydroxy complex formation

$$n[OH]^- + n[NaAl^{IV}O_2] = [Al^{IV}O_2]_n^{n-} + n[Na(OH)]^o \quad \ldots\ 4.8H$$

AlO_6 group and hydroxy complex formation

$$[OH]^- + [NaAl^{IV}O_2] = [Al^{VI}O_2]^- + [Na(OH)]^o \quad \ldots\ 4.8I$$

where {} = unidentified location in silicate network.
[] = melt unit or complex.

Mechanism II: Network reduction by CH_4 and/or H_2

$$[Al^{IV}Si_2O_7]^{3-} + H_2 \text{ (or } 1/2\ CH_4) = [Al^{VI}O_2]^- + 2[OH]^- + \{Si\text{-}O\} + [SiO_2]^o \text{ (+ } 1/2\ C^o) \quad \ldots\ 4.8J$$

plus additional equilibria as indicated for mechanism I.

The extent to which the additional equilibria proceed is unknown but probably differs from that of pure H_2O. Equilibrium 4.8I may be more important in reduced systems (cf. band intensities in Figs 4.6 D and C).

Mechanisms I and II are similarly constructed; both reactions produce 4 moles of O-H bonds per mole of dissolved methane. The solution process is accompanied by a redistribution of Al co-ordination environments as discussed for hydrous melts. The major difference is in the nature of the reduced bond formed. In mechanism I, a significant melt-phase solubility of reduced carbon as Si-C bonds is implied. This mechanism is directly analogous to the structural role of nitrogen in Na_2O-CaO-oxynitride glasses recently investigated by Brow & Pantano (1984). Based on FTIR and x-ray photoelectron spectroscopic results the authors concluded that nitrogen is present in the silicate network of oxynitride glasses in the form of Si-N bonds with N in three-fold (i.e. doubly bridged) and possibly two-fold (i.e. singly bridged) co-ordination sites. With increasing N content the principle changes in the FTIR spectra are seen in the high-frequency envelope which broadens and shifts to lower wavenumbers as the spectra take on features resembling that of pure silicon nitride (Si_3N_4). These changes would result in difference spectra similar to those observed for the C-H fluid saturated glasses. The maximum amount of nitrogen dissolved in the Na_2O-CaO-oxynitride glasses at 1 atm was ~2.2 wt% N (or 3.23 mol%) but the effects of N substitution on the network are clearly seen in the FTIR spectrum at much lower levels (~1 mol% N).

Mechanism II requires the presence of a silicate network unit with an O:Si ratio <2; this is represented in equation 4.8J by a {SiO} or "silicon monoxide" group. It is conceivable that such units might resemble those found in amorphous silicon monoxide. The RDF study of Yasaitis & Kaplow (1972) favours a structure for this compound based on puckered $(SiO)_n$ rings (perhaps with n=6) where the average co-ordination number about each Si atom does not deviate significantly from two. The ratio between first and second nearest neighbour distances is consistent with a Si-O-Si bond angle of 96.7°. Such a structure gives each Si atom a formal valancy of II. Other interpretations for the structure of amorphous SiO suggest a random arrangement of Si-Si and Si-O bonds or a mixture of amorphous Si and SiO_2 domains (Ching, 1982). These models are not favoured in the present case because Si-Si bonds have strong IR (and Raman) absorptions at ~500 cm^{-1} (e.g. $\nu_{[Si-Si]}$ organo-silicon compounds: 540-450 cm^{-1}; matrix isolated Si_2: 507 cm^{-1}; amorphous SiC_xO_y: 508 cm^{-1};

Nakamoto, 1978; Weltner & McLeod, 1964; Gorman & Solin, 1974) which are not observed in the difference spectra.

In order to decide which of the mechanisms I or II (or conceivably some combination) best represents the dissolution mechanism of reduced C-H volatiles, a two-fold approach was taken. Firstly, a high pressure experiment was conducted to verify the assignment of bands at 1024, 802 and ~640 cm^{-1} in the Sm difference spectrum to the required reduced melt component. Secondly, analyses for C and H were performed on ~mg-sized clear, inclusion-free glass chips by a pyrolysis/gas chromatography technique. Quantitative and semi-quantitative electron microprobe analyses for C were also undertaken.

Spectroscopic verification of the reduced component FTIR spectrum involved preparation of a substituted Sm glass containing a known amount (in this case 13.6 wt%) of the component "$NaCaAlSi_2O_3C_2$": a sintered $NaCaAlO_3$ oxide mixture plus finely ground α-SiC (SOFREM Arbina Black, high purity grade, 99.3 wt% SiC). This corresponds to an Sm glass in which oxygen has been substituted by 1.5 wt% carbon in the form of carbide ions, C^{4-}(equivalent to a methane solubility of 2 wt% via mechanism I). If α-SiC dissolves completely in the glass at high P,T and the resultant FTIR difference spectrum is identical to the reduced component spectrum identified in Table 4.8A then mechanism I will be confirmed. On the other hand, if α-SiC dissolves with production of graphite and the resultant FTIR difference spectrum is also identical to that of Table 4.8A then mechanism II will be confirmed (since $SiC + SiO_2$ --> 2{SiO} + C[graphite]). If the reduced component cannot be identified spectroscopically then both mechanisms will appear unlikely candidates for describing reduced volatile solubility. Operation of a combination of mechanisms I and II will have to be decided on the basis of analytical results.

The SiC dissolution experiment was performed in a talc/pyrex sleeved assembly with the sample mixture enclosed in an inner graphite capsule and sealed in an outer Pt capsule of 2.3 mm O.D. This arrangement was necessary to prevent formation of a low melting Si-Pt alloy via the reaction SiC + Pt --> SiPt-alloy + C. Run conditions were P = 30 kbar, T = 1500°C for a duration of 90 minutes. All assembly parts were dried at 110°C, 24 hours prior to use to eliminate traces of adsorbed water.

The product was examined optically and found to consist of clear glass plus disseminated graphite, some grains were larger and clearly pseudomorphs after original α -SiC. No relict α -SiC was detected and complete dissolution was achieved. FTIR spectra are recorded in Fig. 4.6C (spectrum E) and Fig. 4.6D (spectrum D). The 4000-400 cm^{-1} spectrum shows the presence of a trace of dissolved H_2O ($\lesssim$0.5 wt%) at ~3600 cm^{-1} presumably arising from H_2 diffusion into the experimental charge. Note that graphite is essentially IR inactive and does not contribute to the observed spectrum. The spectrum at wavenumbers <1500 cm^{-1} is similar to C-H fluid saturated Sm (Fig. 4.6C, spectrum D) except for the absence of features associated with the structural re-arrangement of Al, i.e. intensity of the ~700 cm^{-1} envelope and position of the ~570 cm^{-1} minimum remains close to that of the volatile-free glass. This is clearly revealed in the 1500-400 cm^{-1} difference spectrum (Fig. 4.6D, spectrum D) which contains all the expected reduced component features. In fact, a combination of spectrum E (hydrous Sm glass) and spectrum D (reduced component) **reproduces almost exactly** the spectrum of C-H fluid saturated Sm glass. In the far IR region (500-100 cm^{-1}) too, the spectra of C-H fluid saturated and SiC-substituted Sm glasses are closely similar with common bands appearing at 340, 290, 239, 160 and 145 cm^{-1} related to the presence of a common component.

The above results strongly favour mechanism II identifying the reduced component with silicon monoxide groups. The ~800 cm^{-1} band is possibly associated with ⟨Si-O⟩ stretching in the silicate network; the 640 cm^{-1} band would then be the accompanying stretching + bending vibration of ⟨Si-O-Si⟩ bridging bonds. The absorption is located in a position expected for small Si-O-Si bond angle ring structures (Galeenev & Geissberger, 1983; see also Appendix 13.3) consistent with the model of Yasaitis & Kaplow (1972) for amorphous SiO.

Analytical Data

Quantitative carbon and hydrogen analyses were performed with a Hewlett-Packard 185B CHN analyser at the Analytical Services Section, Research School of Chemistry, A.N.U. (Canberra). The method has been previously applied by Brey (1976) in the analysis of ~mg quantities of silicate glasses containing dissolved carbonate and water.

For glasses containing reduced components, ~0.5 to 1.5 mg of sample was intimately mixed with 85 mg of $MnO_2/WO_3/Cr_2O_3$ oxidant and combusted at 1080°C for 90 seconds following an initial heating at 70°C to remove atmospheric gases. To determine whether this method gives accurate results for the analysis of substances containing (or with the potential to form) Si-C bonds, three standard compounds consisting of mixtures of finely ground α-SiC and silica powder were analysed. Silicon carbide is known for its great chemical intertness and high thermal stability due mostly to the stability of the Si-C bond when favourably situated as in the hexagonal lattice of α-SiC (Rochow, 1973). It is possible that small crystallites of α-SiC might form in the reduced glasses during the combustion process and remain unreactive to oxidation. Results for unknowns and standards are listed in Table 4.8C. Standards were combusted for 90 seconds and 120 seconds (in the latter case there was a considerable loss in sensitivity).

It can be seen from the results in Table 4.8C that the analysed carbon contents of the standards are between half and one-third of the known amounts present. This suggests incomplete oxidation of SiC has indeed occurred with greatest descrepancy occurring at C contents >0.5 wt%. Carbon values for the glass unknowns must therefore be regarded as minimum quantities only; if α-SiC forms metastably in these samples then analyses may be out by as much as a factor of two for total C contents $\leq$0.5 wt%. Hydrogen analyses (converted to wt% H_2O) are in good agreement with those deduced spectroscopically.

Despite these difficulties it is clear that the C-H fluid equilibrated glasses contain a minimum of ~1000 ppm C and a maximum of ~2000 ppm C. These results are substantially confirmed by quantitative and semi-quantitative electron microprobe analyses for carbon performed at the Electron Optical Centre, University of Adelaide (JEOL 733 microprobe, B.J. Griffin analyst) and Central Science Laboratory, University of Tasmania (JEOL-JXA50A microprobe). Measurements were obtained with a light element (STE crystal) wavelength dispersive spectrometer using 15 kV accelerating voltage in the former case and 10 kV in the latter. The beam in both cases was defocussed to a 10-20 μm diameter spot with 50 nA beam current to minimise specimen damage.

Table 4.8C C,H analytical results for glasses and standards.*

Sample	C/wt%	H_2O/wt%	Combustion time (sec)
T-1296 Jd + C-H fluid all glass.	0.13±0.03	2.9±0.4	90
T-1341 Sm + C-H fluid all glass.	0.09±0.07	3.0±0.5	90
T-1318 Sm + C-H fluid glass+grossular crystals.	0.12±0.04	1.7±0.1	90
T-1250 Sm + H_2O all glass.	-	5.5±0.2	90

Standards ($SiC+SiO_2$)	Expected wt% C	Analysed wt% C	Combustion time (sec)
A	0.5	0.24±0.04	90
		0.18±0.02	120
B	1.0	0.32±0.03	90
		0.21±0.06	120
C	1.5	0.51±0.07	90

* all samples analysed in duplicate, averages and standard deviations quoted.

Detection limits: C 0.05 wt%
H 0.02 wt%
H as H_2O 0.18 wt%

Polished epoxy mounts containing the samples, blanks and an array of standards (graphite, SiC and various carbonates) were coated with aluminium following the method of Mathez & Delaney (1981). Analyses at E.O.C., Adelaide were performed by 60 second counts on the peak and 20 seconds on the backgrounds with the spectrometer positioned 10 mm either side of the peak position. Full ZAF corrections were applied. Surface carbon contamination, derived from cracking of vacuum pump oils under the beam, resulted in a detection limit for carbon of ~0.2 wt%. Analyses of standards, blanks and unknowns gave results of high consistency mainly due to the good precision obtainable with long counting times at reasonably high count rates. Absolute accuracy is difficult to judge due to the large matrix corrections used and the effects of surface contamination. These uncertainties could amount to errors of as much as ±30%. Results are presented in Table 4.8D.

Table 4.8D Microprobe analyses for Carbon.*

Sample	Expected wt%	Wt% analysed
Graphite (treated as unknown)	100.00	101.22
T-1178 Sm containing dissolved CO_2 (volatile undersaturated)	2.1±0.2	2.15
T-1296 Jd + C-H fluid	~0.1-0.2	<0.2**
T-1341 Sm + C-H fluid		
T-1339 Sm + C-H fluid		

* B.J. Griffin, analyst.
** limit of detection ≈0.2 wt%.

Semi-quantitative microprobe analyses carried out at the University of Tasmania confirm these results and are presented as wavelength versus intensity plots in Fig. 4.8. Both sets of microprobe data indicate carbon contents in the C-H fluid saturated glasses near or below the limit of detection (<2000 ppm) consistent with the gas chromatographic results.

Fig. 4.8 Plots of carbon K_α radiation intensity versus detector position obtained by electron microprobe analysis of samples using a light element wavelength dispersive spectrometer (STE crystal). A detector position of 125.71 mm corresponds to a wavelength of 44.0 Å.

A: Silicon carbide standard; for this sample intensity scale x0.3, all other samples x1.0.

B: Sodamelilite glass containing ~2 wt% C as dissolved carbonate (T-1178).

C: C-H fluid saturated sodamelilite glass (T-1341).

D: C-H fluid saturated jadeite glass (T-1296).

E: C-H fluid saturated sodamelilite glass (T-1339, run contains a few grossular crystals).

F: Background carbon levels measured on a volatile-free sodamelilite glass substrate.

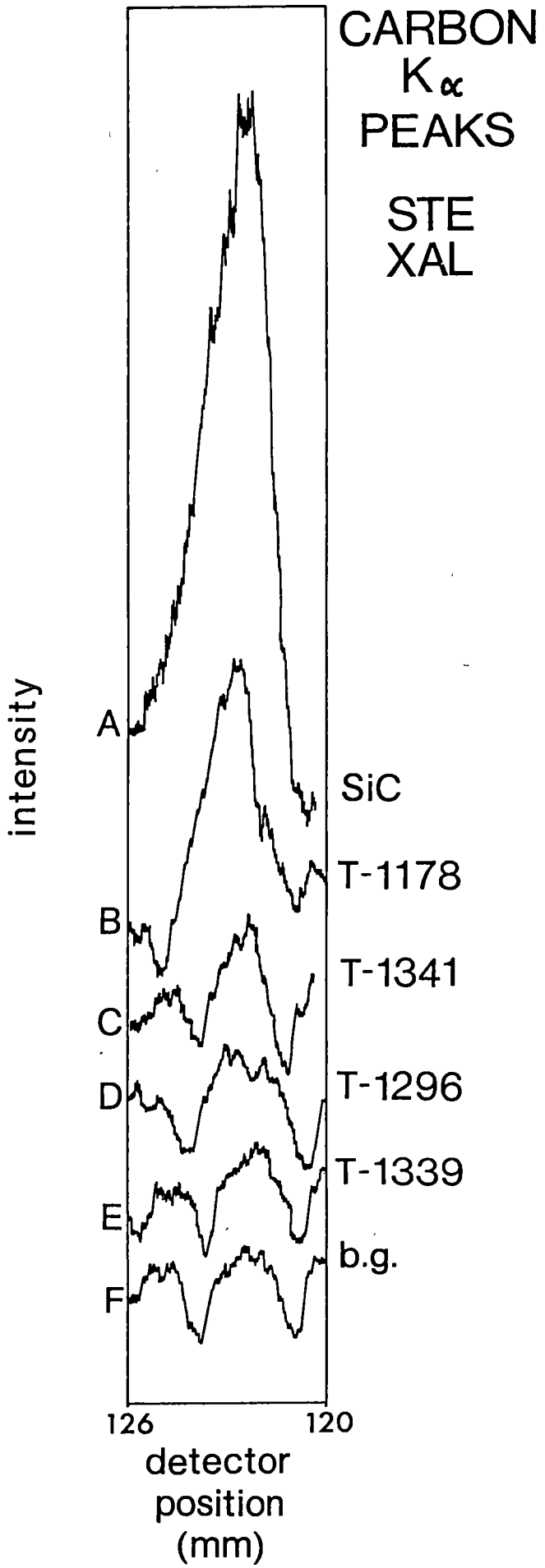
CARBON
Kα
PEAKS
STE
XAL
intensity
A
SiC
T-1178
B
T-1341
C
D
T-1296
T-1339
E
b.g.
F
126
120
detector
position
(mm)

For mechanism I to operate a reduced carbon solubility of 8000-12000 ppm is required. The above results therefore support mechanism II as the dominant process for reduced volatile interaction with aluminosilicate melts. The small amount of carbon detected could dissolve either by mechanism I or in the form of atomic carbon occupying interstitial sites or cation vacancies as found by Freund et al. (1980) in oxide and silicate lattices. For synthetically grown forsterite crystals Freund et al. (1980) determined C contents in the range ~40-170 ppm/wt (0.05 to 0.20 atom%) and for natural olivines from the Eifel district $\geq$800 ppm/wt (>1.0 atom%); similar or higher levels of carbon might be expected to dissolve in silicate melts in this manner and remain undetected by IR and Raman spectroscopic methods. These data do not rule out the possibility that ~1000-2000 ppm carbon is present as Si-C bonds via approximately 10% contribution to the overall reduced volatile solubility process by mechanism I.

The recognition of mechanism II as the dominant process of C-H volatile solubility does not discriminate between the particular reduced volatile species involved. Since the mechanism is a general reduction of the silicate network that may take place in the presence of any of the reduced volatiles H_2, CH_4 or C_2H_6, all are potential candidates for melt-soluble species, however, only for CH_4 (and C_2H_6) is the precipitation of graphite or diamond a necessary condition of the solubility process.

Limited data exist on the solubility behaviour of H_2 or its effects on liquidus relations. Nakamura (1974) believes only a small amount of H_2 is soluble in hydrous SiO_2 liquids at 15 kbar while Luth & Boettcher (1984) observe dramatic shifts in melting temperature of albite as a function of fH_2 in the system albite-H_2O-H_2; their results are difficult to relate to a simple lowering of fH_2O as a result of H_2 dilution.

In order to clarify the effect of reduced volatiles on liquidus phase relations at high pressure it will be of some importance to compare liquidus behaviour of C-H volatiles with that of their oxidised counterparts H_2O and CO_2, and the volatile-absent system. This topic is investigated in the following section.

4.9 Contrasting Effects of H_2O, CO_2 and CH_4 on Liquidus Phase Relations in the System Ne-Fo-Q.

A. Introduction

At pressures >25 kbar the system nepheline(Ne)-forsterite(Fo)-silica(Q) contains liquidus phase fields of forsterite (Fo), enstatite$_{ss}$ (En_{ss}) and jadeite$_{ss}$ (Jd_{ss}) analagous to the major minerals of upper mantle peridotite. The system forms the base of the simplified basaltic tetrahedron (Yoder & Tilley, 1962) and as such offers a useful model for investigating small degrees of partial melting of mantle peridotite. For these reasons, liquidus phase relationships in the system Ne-Fo-Q have been widely studied particularly as a function of pressure and activity of volatile species (Kushiro, 1968, 1972; Eggler, 1978; Windom & Boettcher, 1979). The position of the Fo-En_{ss} two-phase boundary is a sensitive indicator of melt-phase silica activity and hence the relative degree of silicate melt polymerisation/depolymerisation. As a general rule, the liquidus phase precipitated from a silicate melt at constant pressure will reflect the polymerisation state of that composition (there are a number of exceptions to this "rule", however, such as crystalline and vitreous Jd discussed in Section 4.6C). Thus a melt precipitating forsterite on the liquidus (forsterite has a structure based on isolated [SiO_4] tetrahedra, NBO/Si = 4) can be considered as less polymerised relative to a melt precipitating enstatite (structure based on [Si_2O_6] chains, NBO/Si = 2). Kushiro (1968, 1975) found that additions of oxide or volatile components to a variety of binary or ternary silica-metal oxide systems resulted in large shifts in the liquidus Fo-En_{ss} two-phase boundaries. This effect stems from the relative expansion of Fo or En_{ss} liquidus phase fields and is indicative of the changes in melt polymerisation that accompany addition of network forming or network modifying components. The magnitude and direction of the phase boundary shifts roughly parallel the order of oxide basicity (Kushiro, 1975; Fraser, 1977), i.e.

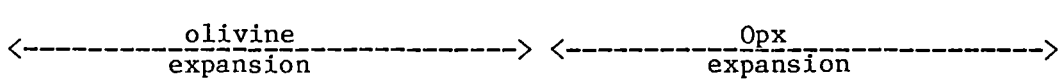

$K_2O, Na_2O > H_2O > CaO > MgO > FeO > Fe_2O_3, Al_2O_3 > TiO_2 > P_2O_5 > CO_2$

network modifying — network forming

In the system Ne-Fo-Q there is a large pressure effect on the position of the Fo-En_{ss} two-phase boundary; with increasing pressure the enstatite phase field increases markedly (Kushiro, 1968, fig. 4). This effect is thought to be largely due to volume and compressibility differences between the assemblage (En_{ss}+liquid) relative to (Fo+liquid) with increasing pressure (Kushiro, 1984); some contribution from pressure-sensitive structural changes in the silicate melt, however, cannot be ruled out.

The aim of the present study is to determine the location of the Fo-En_{ss} two-phase boundary in the system Ne-Fo-Q under conditions dominated by a CH_4-rich vapour phase. Comparisons can then be made with the boundary position under volatile-absent, H_2O-saturated and CO_2-saturated conditions. Intermediate positions would correspond to boundary estimates in the presence of a mixed volatile phase. The resultant phase diagrams can be used to predict the nature of mantle melting under conditions of saturation with different volatile species and hence over a range of fO_2's.

A pressure of 28 kbar was chosen for this investigation to allow incorporation of the volatile-absent experimental data of Windom & Boettcher (1979) along the joins Jd-En and Jd-Fo as well as duplicating pressure conditions near the top of the oceanic LVZ where $\lesssim$2% partial melt is believed to exist (Green & Liebermann, 1976). During the course of this study it was found necessary to considerably amend the preliminary phase diagrams of Windom & Boettcher (1979, figs 2 and 7) which are inconsistent with the earlier data of Kushiro (1968) and the present results. Parts of this work are not relevant to the current investigation and have been reported separately (Gupta et al., 1985).

B. Experimental Details

Experiments were conducted along the join $Ne_{55}Q_{45}$-$Ne_{55}Fo_{45}$ to provide good (i.e. approx. 90°) intersection with the two-phase boundary at liquidus temperatures that are not too refractory (i.e. <1500°C). Endmember mixes were prepared from A.R. grade Al_2O_3, SiO_2, Na_2CO_3 and MgO fired at 900°C after thorough mixing by repeated grinding under acetone. Intermediate compositions were then made up as required from the $Ne_{55}Q_{45}$ and $Ne_{55}Fo_{45}$ endmembers and compositions checked by microprobe analysis of glass beads prepared by fusion on an Ir-strip heater. Full details of run conditions and products are given in Appendix 14. Special precautions were

taken to avoid entry of water into volatile-absent, CO_2-saturated and C-H fluid saturated runs including drying of all assembly parts at 110°C, 24 hours prior to use and storage of mixes under vacuum desiccation. Mixes for volatile-absent and C-H fluid saturated runs once loaded into their capsules were heated briefly to red heat (torch flame) to remove all traces of adsorbed H_2O. Run times for CO_2 and volatile-absent experiments were kept to a minimum to avoid H_2 diffusion into the sample capsules and hence the risk of H_2O formation. C-H fluid saturated runs were conducted as described in Sections 4.2 and 4.3B; in all cases excess carbide was confirmed following the experiment. Vapour saturation was confirmed in each run by piercing the sample capsule and noting the weight loss at 25°C and 110°C. All water-saturated runs produced a fine white precipitate surrounding the fluid exit hole; this arises from the large solid-phase solubility in high P,T aqueous fluids as discussed by Ryabchikov et al. (1982). Since the major fluid soluble components in this system are likely to be Na_2O and SiO_2 (Ryabchikov et al., 1982), the composition of equilibrium liquid will lie off the ternary join and contain more of the lower solubility Mg_2SiO_4 component than the bulk starting material. The extent to which the liquidus phase fields are modified by this process is difficult to judge. It is possible that loss of network modifying Na_2O to the fluid phase will be compensated by increased Fo content in the liquid thus resulting in a Fo-En_{ss} two-phase boundary not too different from the hypothetical case of 0% dissolved solids.

Products were examined optically and by electron microprobe analysis; all showed quench effects of variable extent, mainly as $MgAl_2SiO_6$(MgTs)-rich (though sometimes extending to Jd-rich) pyroxene overgrowths and individual crystallites on and about $enstatite_{ss}$ (quench "feathers" or "beads"). Skeletal olivines are present in some runs. In selected runs, electron microprobe analyses established liquid and crystal compositions as recorded in Appendix 14. In practice, only for the volatile-absent runs, showing the least quench effects, were liquid compositions able to be obtained with only minor corrections for Na/Al ratio deviations from 1. This allowed the volatile-absent Fo-En_{ss} boundary to be well constrained with three experiments at $Ne_{55}Fo_{25}Q_{20}$. A liquid composition was estimated for CO_2-saturated run T-1227 by subtracting an average quench opx composition from analyses of a large glass patch formed by effective crystal/liquid separation. In both H_2O-saturated and C-H fluid-saturated

OH-containing glasses the combined effects of quench crystal growth and Na-volatilisation under the probe beam precluded any estimate of liquid composition.

C. Experimental Results

The experimentally determined Fo-En_{ss} two-phase boundaries for the Ne_{55} composition at P = 28 kbar are indicated below.

Table 4.9A

Volatile species	Fo(wt%)	Estimated Liquidus Temperature (^{o}C)
absent	24	1495±5
H_2O-saturated	18±1	1120±15
CH_4-H_2-saturated	21±1	1410±15
CO_2-saturated	34±1	1410±15

These data allow delineation of Fo and En_{ss} liquidus phase fields on the ternary Ne-Fo-Q digram (Fig. 4.9A); fields for Jd_{ss}, Sp ($MgAl_2O_4$ spinel) and Ne_{ss} ($nepheline_{ss}$) are from Gupta et al. (1985). At 28 kbar all liquid compositions in equilibrium with Fo and En_{ss} and derived from the compositions on the Ab-$Ne_{55}Fo_{45}$ join, whether H_2O- or CO_2-saturated, are Ne and Fo normative. The position of the volatile-absent two-phase boundary is consistent with the experimental results of Kushiro (1968) on the composition NFA-1 ($Ne_{62}Fo_{18}Q_{20}$) which has Fo on the liquidus up to 30 kbar. The intersection of the boundary with the Fo-Q binary system is estimated from the data of Chen & Presnall (1975) to occur near Fo_{24}. These constraints place the Fo-En_{ss} boundary at 28 kbar close to the composition $Jd_{32}Fo_{68}$ on the Jd-Fo join. This point is considerably different from $Jd_{50}Fo_{50}$ inferred by Windom & Boettcher (1979, fig. 2); their Fig. 3 (ternary liquidus diagram) is accordingly in error (Gupta et al., 1985). The latter diagram (Windom & Boettcher, 1979, fig. 3) suggests that the composition NFA-1 should have Jd_{ss} on the liquidus at 28 kbar and evidently has not been drawn with reference to the earlier data of Kushiro (1968). Fig. 4.9B presents the amended phase diagram for the Jd-Fo pseudobinary join. The main changes from Windom & Boettcher (1979) are the expansion of the Fo+L phase field to $Jd_{32}Fo_{68}$ and the correction of two erroneously plotted points, i.e. $Jd_{70}Fo_{30}$, 1340°C (Fo+En_{ss}+L **not** En_{ss}+L) and $Jd_{80}Fo_{20}$, 1300°C (Jd_{ss}+L **not** Jd_{ss}+Fo+L).

Fig. 4.9A Ternary liquidus phase diagram (wt%) for the system Ne-Fo-Q at 28 kbar showing the position of the Fo-En_{ss} two-phase boundary under volatile-absent and CO_2, H_2O and CH_4-H_2 volatile-saturated conditions. Volatile-absent phase boundaries in the sub-system Ne-Jd-Fo are from Gupta et al. (in press) and this work. Dashed phase boundaries are inferred. Studied compositions are indicted by the filled circles on the join $Ne_{55}Fo_{45}$-$Ne_{55}Q_{45}$, adjacent numbers indicate wt% Fo component. Composition NFA-1 is from Kushiro (1968) and the 20 kbar water-saturated Fo-En_{ss} boundary is from Kushiro (1972). Double circles are determined liquid compositions.

Fig. 4.9B Amended pseudobinary phase diagram for the join Jd-Fo at 28 kbar (after Windom & Boettcher, 1979, fig. 3). The Fo-En_{ss} two-phase boundary intersects this join near the composition $Jd_{32}Fo_{68}$.

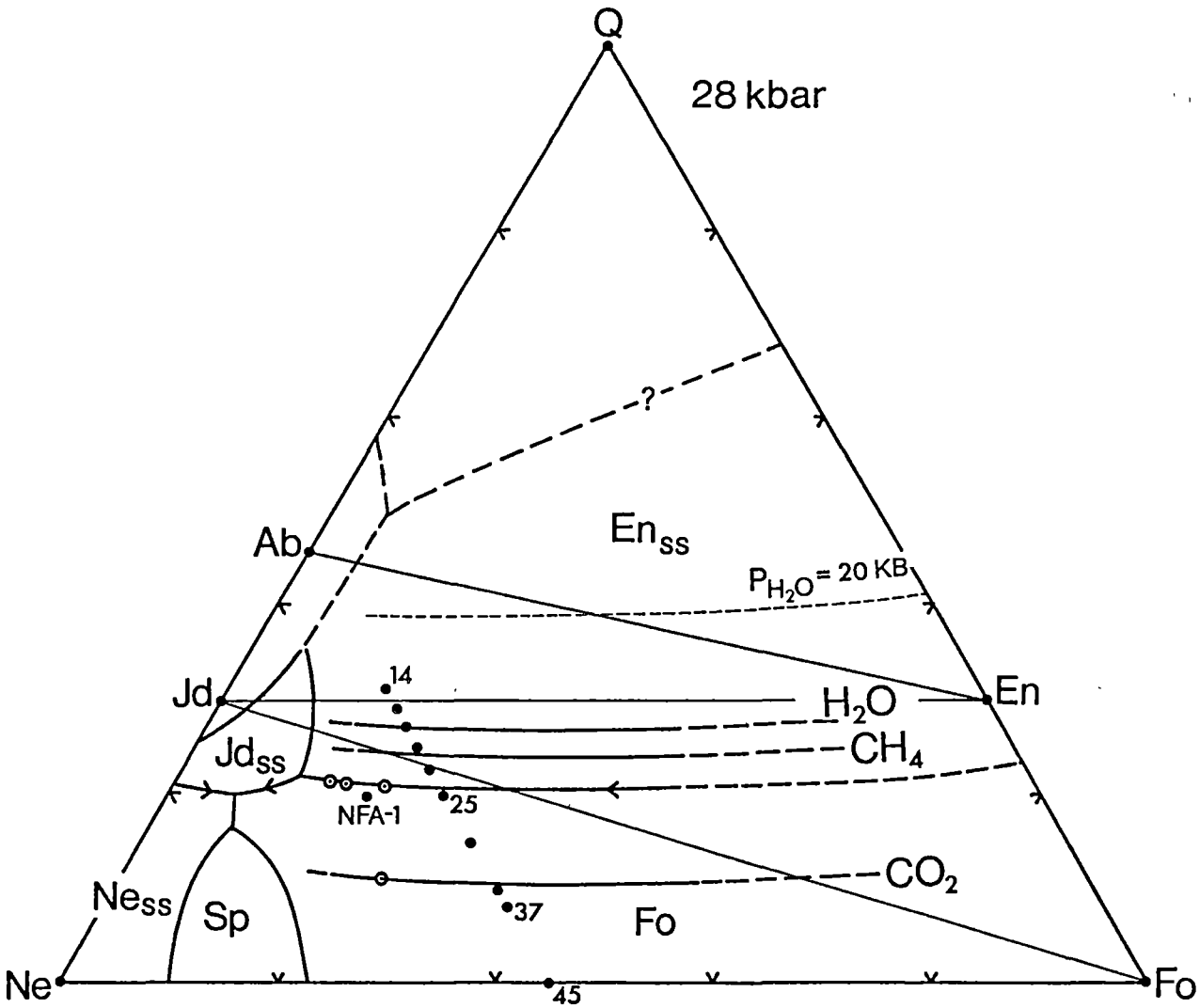
Q
28 kbar
Ab
En_{ss}
P_{H_2O}= 20 KB
Jd
14
H_2O
En
Jd_{ss}
CH_4
NFA-1
25
CO_2
Ne_{ss}
Sp
37
Fo
Ne
45
Fo

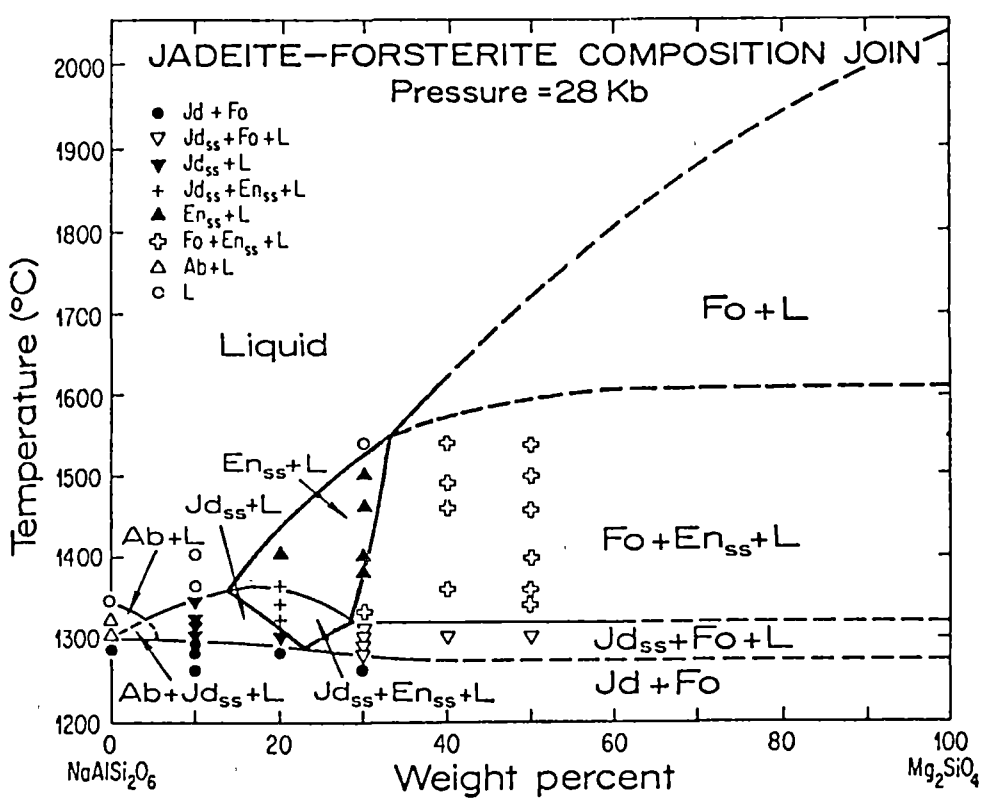
JADEITE–FORSTERITE COMPOSITION JOIN
Pressure =28 Kb
Jd + Fo
Jd_{ss} + Fo + L
Jd_{ss} + L
Jd_{ss} + En_{ss} + L
En_{ss} + L
Fo + En_{ss} + L
Ab + L
L
Liquid
Fo + L
En_{ss} + L
Jd_{ss} + L
Ab + L
Fo + En_{ss} + L
Jd_{ss} + Fo + L
Jd + Fo
Ab + Jd_{ss} + L
Jd_{ss} + En_{ss} + L
Temperature (°C)
2000
1900
1800
1700
1600
1500
1400
1300
1200
0
20
40
60
80
100
$NaAlSi_2O_6$
Weight percent
Mg_2SiO_4

The shift in position of the Fo-En_{ss} boundary relative to the volatile-absent system is greatest for CO_2-saturation (expansion of En_{ss} field from Fo_{24} to Fo_{34} at Ne_{55}). Equilibrium and quench En_{ss} compositions on this boundary are the richest in MgTs component of all systems studied (see Fig. 4.9C and Appendix 14). Equilibrium crystals contain ~15-17 wt% Al_2O_3. The composition of quench crystals presumably reflects liquid properties [largely chemical although both physical (e.g. melt+crystal densities) and kinetic (e.g. nucleation effects) may be important]. Quench crystal compositions are thus expected to provide a rough guide to activities of oxide components in the melt phase. In the CO_2-saturated system this is illustrated by the Na_2O-poor (i.e. Jd-poor) and MgTs-rich nature of quench pyroxene when compared with volatile-absent and C-H fluid saturated runs of similar temperature and silica activity [defined by co-existing equilibrium Fo and En_{ss} crystals which buffer $a(SiO_2)$ via the reaction:

$$Mg_2SiO_4(Fo) + SiO_2(melt) = 2MgSiO_3(En_{ss})].$$

These results are in accord with the mechanism of CO_2 dissolution discussed in Appendices 13.5 and 15 where $a(Na_2O)$ is expected to be drastically lowered by formation of stable sodium-carbonate complexes in the liquid; this process is then reflected in the Na-poor nature of equilibrium, and especially quench, pyroxenes (Figs 4.9C and D). The high proportion of MgTs component in both equilibrium and quench pyroxenes is also related to sodium-carbonate complex formation. Since carbonate is an efficient remover of Na^+ from charge balancing positions in the network, expulsion of Al from the network into six-fold co-ordination sites or $(AlO_4)_n$ clusters will be a direct result of CO_2-dissolution (Appendix 15). The increased activity of non-network Al_2O_3 is reflected in the compositions of both equilibrium and quench pyroxene as a significant MgTs component.

The above proceses can be illustrated by the following CO_2-solubility mechanism for the composition $Ne_{50}En_{50}$ (mol% basis) or $Ne_{58.6}Fo_{29.0}Q_{12.4}$ (wt% basis) analogous to that discussed in Appendix 15 for sodamelilite ($Ne_{50}Fo_{50}$ is the Mg-analogue of Sm).

Fig. 4.9C Plot of pyroxene compositions (mol%) coexisting with forsterite for selected runs in the system Ne-Fo-Q (see Table 14C, Appendix 14). Quench pyroxenes extend to very Jd-rich compositions in the CH_4-fluid saturated and volatile-absent systems.

C-H fluid (i.e. CH_4-H_2) saturated
volatile-absent
CO_2-saturated
H_2O-saturated.

Arrow indicates the approximate equilibrium crystal-quench rim-quench crystal compositional trend.

Fig. 4.9D Plot of Al occupying octahedral sites/ ΣAl versus Na_2O (wt%) for pyroxenes of Fig. 4.9C. Dotted areas indicate equilibrium pyroxenes. Note the trend toward higher $Al^{oct}/\Sigma Al$ and Na_2O in the order CH_4 > volatile absent > CO_2 (H_2O not directly comparable) reflecting different activities of melt components (see text).

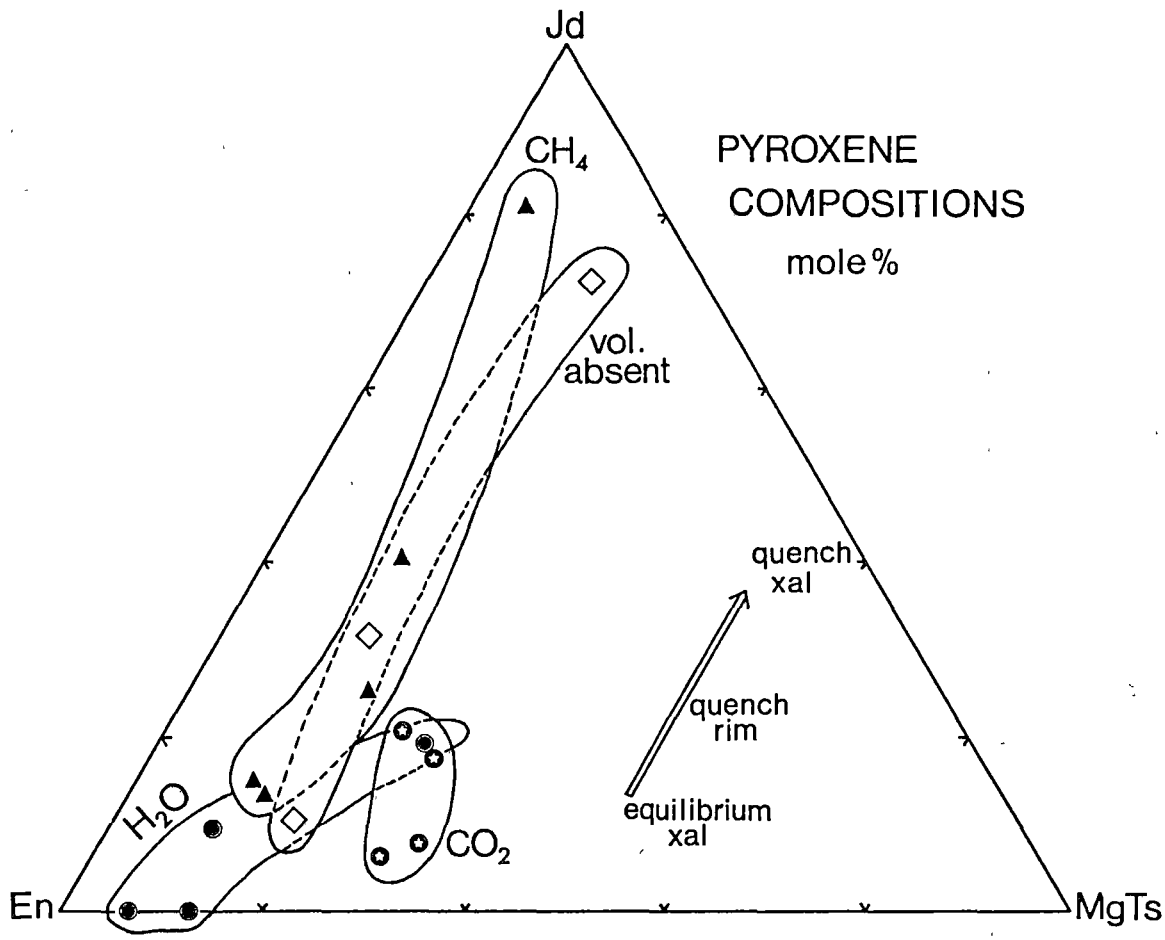
Jd
CH4
PYROXENE
COMPOSITIONS
mole %
vol.
absent
quench
xal
quench
rim
equilibrium
xal
H2O
CO2
En
MgTs

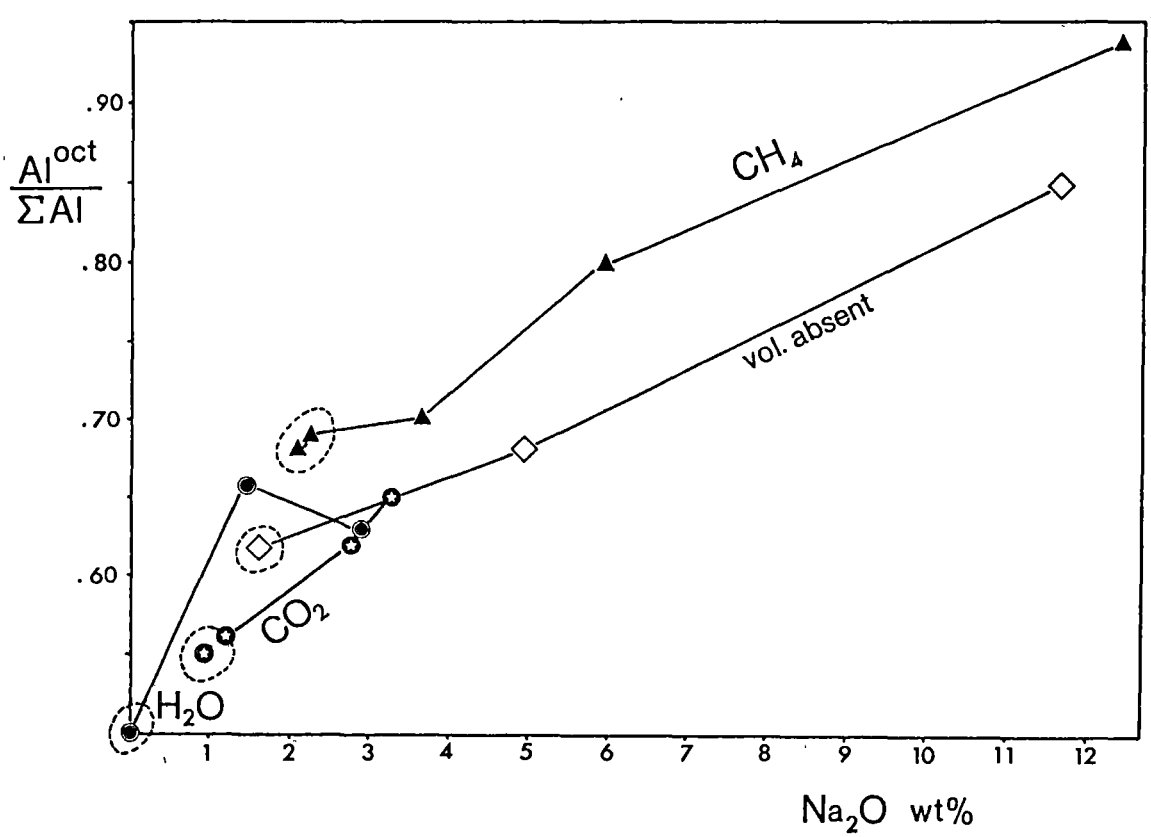
.90
.80
.70
.60
Al oct / ΣAl
CH4
vol. absent
CO2
H2O
1
2
3
4
5
6
7
8
9
10
11
12
Na2O wt%

CO_2 solubility mechanism (system Ne-Fo-Q)

$$2NaMgAl^{IV}Si_2O_7 + CO_2 = [Na_2CO_3]^o + 2[Al^{VI}O_2]^- + 2Mg^{2+} + 2[SiO_2]^o + [Si_2O_5]^{2-}$$

change in NBO/T = -0.167

Al-clustering can related by the additional equilibrium:

$$n[Al^{VI}O_2]^- = [Al^{IV}O_2]_n^{n-}$$

The reaction:

$$Mg^{2+}_{melt} + [Al^{VI}O_2]^-_{melt} + [Al^{IV}O_2]^-_{melt} + [SiO_2]^o_{melt} = \{MgAl^{VI}Al^{IV}SiO_6\}_{pyroxene}$$

describes precipitation of MgTs-rich pyroxene.

The depolymerising role of both H_2O and CH_4dominated fluids is clearly illustrated in Fig. 4.9B. Expansion of the Fo phase field at Ne_{55} relative to the volatile-absent system is from Fo_{24} ---> Fo_{18} for H_2O-saturation and from Fo_{24} ---> Fo_{21} for C-H fluid-saturation. This shift is not as large as that for CO_2 in the opposite direction, however there appears to be a substantial pressure effect associated with the H_2O-saturated boundary. At P_{H_2O} = 20 kbar this is found near $Ne_{55}Fo_7Q_{38}$ (Kushiro, 1972) a difference of Fo_{11} from the volatile-absent boundary at the same pressure (cf. the Fo_6 difference at 28 kbar). This effect may be ascribed to a diminishing ability of H_2O to depolymerise melts at higher pressures and could be due to a number of factors:

(i) changes in the solubility of solid components in co-existing aqueous fluid with pressure (similar proportions of water were added to the 28 kbar runs as those used by Kushiro, 1968; see Appendix 14).

(ii) dissolution of a higher proportion of H_2O in molecular form with increasing P_{H_2O} as shown by Stolper (1982a); since molecular water dissolves without Si-O-Si bond cleavage there will be no accompanying network depolymerisation.

(iii) change in behaviour of H_2O with pressure toward that of a network polymeriser by formation of a greater proportion of alkali cation-hydroxy complexes relative to Si-OH bonds in an analogous fashion to

CO_2 dissolution forming carbonate complexes; the two roles can be described by the following equilibria (for the Mg analogue of Sm):

Cation complexing role (polymeriser)

$$2NaMgAlSi_2O_7 + H_2O = 2[Na(OH)]^o + 2Mg^{2+} + 2[Al^{VI}O_2]^- + [Si_2O_5]^{2-} + 2[SiO_2]^o$$

change in NBO/T = -0.167

Depolymerising role

$$NaMgAlSi_2O_7 + H_2O = Na^+ + Mg^{2+} + [Al^{VI}O_2]^- + 2[SiO_2(OH)]^-$$

change in NBO/T* = +1.33

(* counting Si-OH groups as non-bridging).

The suggestion that the effect of H_2O becomes more polymerising with increasing pressure (depth) via any of the above mechanisms has important consequences for magma genesis in the upper mantle. While further work is required to support this hypothesis, the preliminary data outlined here indicate that the olivine-orthopyroxene two-phase liquidus boundaries in H_2O-saturated and volatile-free peridotite compositions may be almost coincident at pressures in the range 40-50 kbar. It has been commonly assumed in the literature, e.g. Eggler (1974, 1978) that the generation of primary silica under-saturated, nepheline-normative magmas (i.e. basanites, nephelinites and melilitites) at pressures of ~25-35 kbar requires CO_2 in the source region. However, in the model system Fo-Ne-Q at 28 kbar, all liquids in equilibrium with olivine, orthopyroxene and clinopyroxene, irrespective of the volatile phase present, are ne-normative and likely to remain so even on addition of calcic components to the system. Silica-undersaturated primary magmas could thus conceivably be produced by small degrees of melting under H_2O-saturated conditions at ~40 kbar or H_2O-undersaturated at lower pressures. Indeed, the experimental data of Green (1973), for an olivine-basanite composition, demonstrate that the phases of garnet peridotite are on the basanite liquidus at 25-35 kbar and moderate water contents (2-7 wt%) in the complete absence of CO_2.

The Fo-En_{ss} two-phase boundary for saturation with reduced C-H fluids falls between H_2O and the volatile-absent system. Such behaviour largely reflects the depolymerising role of OH released from dissolution of CH_4 and/or H_2. The FTIR spectrum and difference spectrum (Fig. 4.9E) recorded for the largely glass product of run T-1289 confirms the presence of all the spectral features identified with reduced volatile dissolution in Section 4.8; additional bands can be assigned to crystalline En_{ss} which makes up ~10% of the charge. Assignments have been made with reference to Section 4.8 and are listed in Table 4.9B. Some variation in the position of bands is expected due to compositional differences between the subtracted spectra arising from the presence of En_{ss} in the high pressure glass, however all reduced and oxidised component features are present.

Table 4.9B Difference spectrum (2000-400 cm^{-1}) run T-1289: ($Ne_{55}Fo_{20}Q_{25}$ + C-H fluid, ~90% glass) minus ($Ne_{55}Fo_{20}Q_{25}$ 1 atm glass).

Positive Features (cm^{-1})	Assignment
~1630 weak	ν_2[H-O-H] bend of dissolved molecular H_2O
~1404 very weak	ν[C-O], carbonate (?)
~1080 weak	enstatite*
1020 very weak	reduced component
937 weak	ν[Si-OH]
828 strong	reduced component
748 weak	$[AlO_4]_n$ clusters
696 weak	enstatite*
648 medium	reduced component
579 strong	$\nu[AlO_6]$ of melt and quench enstatite(?)
517 strong	enstatite*
Negative Features (cm^{-1})	
~1190	loss of ν[Si-O-Al]
~700	loss of νAlO_4

* identified from IR data for crystalline enstatite (Liese, 1975).

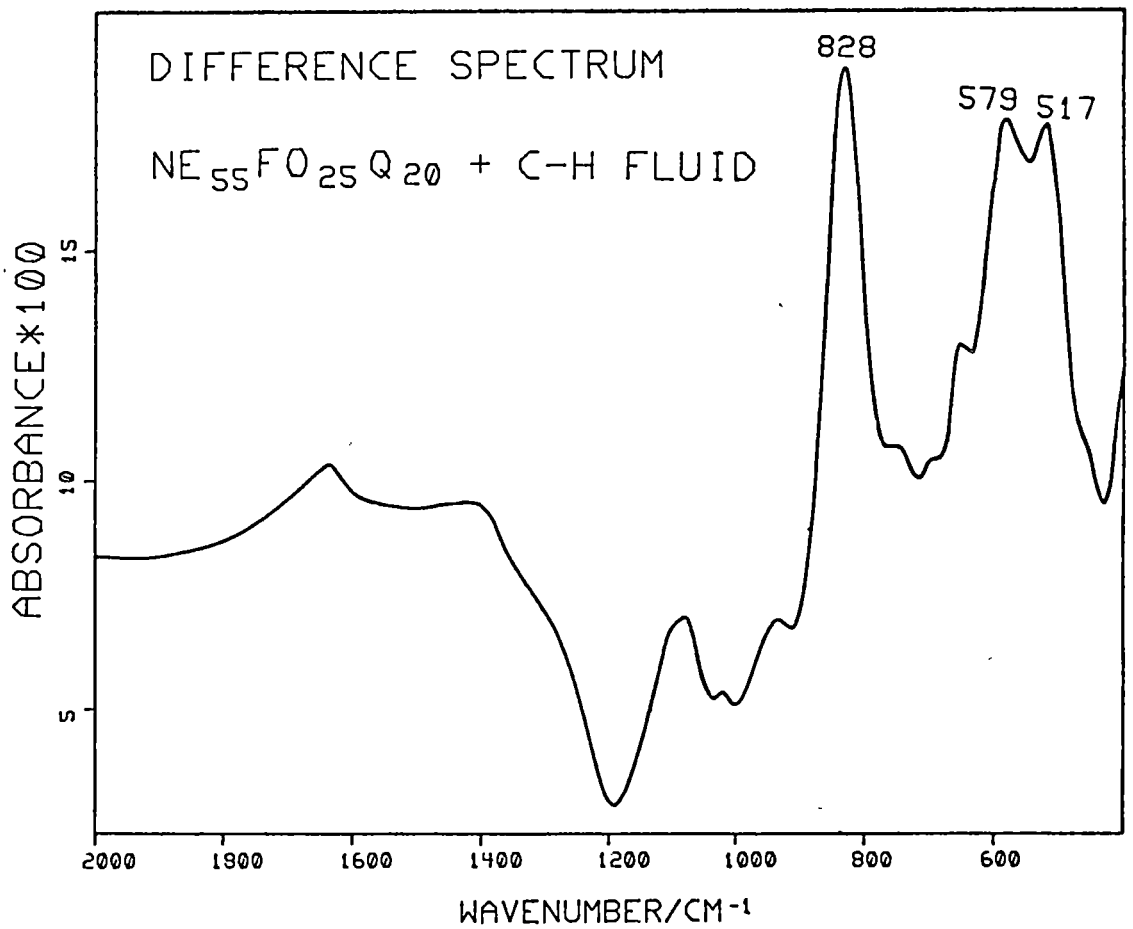

Fig. 4.9E FTIR difference spectrum (C-H fluid saturated $Ne_{55}FO_{25}O_{20}$ glass containing ~10% enstatite crystals, run T-1289) minus ($Ne_{55}Fo_{25}Q_{20}$ 1 atm glass):
Reduced component features appear at 1020, 828 and 648 cm^{-1}; the band at 579 cm^{-1} suggests the presence of AlO_6 groups and the band at 517 cm^{-1} is due to crystalline enstatite (cf. Fig. 4.6D).

The compositions of equilibrium, quench rim and quench crystal pyroxenes for volatile-absent, C-H fluid, H_2O and CO_2-saturated runs in which $a(SiO_2)$ is buffered by the presence of both Fo and En_{ss} primary (i.e. equilibrium) crystals has been compared in Figs 4.9C and D and Appendix 14. The proportion of octahedral Al relative to total pyroxene Al content ($Al^{oct}/\Sigma Al$) varies with volatile species in the order:

$$CH_4\text{-}H_2 \;>\; \text{volatile-absent} \;>\; CO_2 \;>\; H_2O$$

for the equilibrium pyroxenes (circled in Fig. 4.9D). With the exception of one point in the H_2O-saturated system, this order is retained for quench rims and quench crystals. Such behaviour may be correlated directly with melt-phase activity of both octahedrally co-ordinated aluminium (Al^{oct}) and Na_2O. For the volatile-absent, C-H volatile and CO_2-saturated runs which have similar temperatures (~1400°C) and hence $a(SiO_2)$'s, melt-phase activities of Al^{oct} and Na_2O are largely a function of the volatile solubility mechanism but for the H_2O-saturated runs a temperature effect probably dominates (since run temperatures are ~300°C lower). The high melt-phase activities of Al^{oct} and Na_2O in both C-H fluid-saturated and volatile-absent runs lead to extreme Jd component enrichments in quench pyroxenes (Figs 4.9C and D). The most Jd-rich (i.e. Al^{oct} rich) pyroxene is quenched from the C-H volatile-saturated run and has the composition $Jd_{80}En_{14}MgTs_5$ (mol% basis). The high activity of Al^{oct} under reduced volatile saturation rationalises the large expansion of the garnet liquidus phase-field found by Eggler & Baker (1982) for the composition $Di_{35}Py_{65}$ and the present observations of grossular as the high-P liquidus phase in C-H volatile-saturated Sm melts (rather than the crystalline Sm found under volatile-absent conditions). This arises because at high Al^{oct} activities the liquidus phase of **highest** $Al^{oct}/\Sigma Al$ will be strongly favoured (in garnet Al is exclusively in octahedral co-ordination, $Al^{oct}/\Sigma Al = 1$, by contrast with MgTs-rich pyroxene or crystalline Sm).

For mixed fluids, the position of the Fo-En_{ss} boundary in the system Ne-Fo-Q can be inferred to lie at positions intermediate between the respective endmember volatile boundaries. Thus for a reduced H_2O-CH_4-H_2 fluid the boundary at Ne_{55} will be between Fo_{18} and Fo_{21} and for oxidised H_2O-CO_2 fluid mixtures between Fo_{11} and Fo_{34} depending strongly on x_{CO_2}.

The increase in melt-phase Al^{oct} activity and the depolymerising role for C-H fluids found in the system Ne-Fo-Q investigation is consistent with the proposed mechanism of C-H fluid dissolution in aluminosilicate melts discussed in Section 4.8. The idea that carbon-rich eclogites could be the products of fractional crystallisation of mantle melts under conditions of CH_4-H_2O-H_2 volatile saturation as proposed by Eggler & Baker (1982) is supported by the data presented here. Kushiro & Yoder (1974) stated that "... in the presence of water ... it should be possible for eclogite to form from garnet lherzolite" at depths greater than the 26 kbar limit in the volatile-absent case, i.e. to within the stability field of diamond. Since both H_2O and CH_4-H_2 have similar melt depolymerising behaviour the findings of Kushiro & Yoder will apply equally well to CH_4-H_2O-H_2 volatile mixtures as to pure H_2O. The added advantage in the case of carbon-rich eclogites is that the precipitation of carbon either as diamond or graphite is intrinsic to the mechanism of CH_4-rich volatile dissolution (Section 4.8). This is in accord with the origins of graphite-diamond eclogite from the Roberts Victor kimberlite as discussed by Hatton & Gurney (1979). The authors propose an origin based on rapid crystallisation of melts produced by volatile-induced partial melting of garnet lherzolite where melt volumes are such that gravitational separation of diamond or graphite is ineffective. While the authors propose that carbon is a result of reduction of a CO_2-bearing vapour during cooling, an alternative mechanism involving CH_4-H_2O-H_2 fluid-induced partial melting with accompanying carbon precipitation (reaction 4.8J) can equally well explain the origin of these rocks.

4.10 Summary and Concluding Remarks

In this Part, the mechanism of C-H volatile solubility in aluminosilicate glasses has been deduced from the interpretation of FTIR spectra with careful consideration of both theoretical and analytical constraints. Because the mechanism depends greatly on correctly relating spectral features to structural units in the glass, a step-wise process of interpretation has been pursued. An important result of this study is the recognition that IR spectra are capable of directly discriminating between different Al co-ordination environments in a variety of aluminosilicate minerals and glasses. In the latter case, the presence of network AlO_4 groups is characterised by a mid-range envelope centred near 700 cm^{-1};

clustering of AlO_4 groups with the formation of Al-O-Al linkages is identified by bands at frequencies ~40-80 cm^{-1} higher. Cage-like vibrations of non-network Al identified with AlO_6 octahedra have a characteristic IR band near 570 cm^{-1}. To date, the discrimination of Al co-ordination environments with IR spectroscopy has been applied only in a few limited studies of geological interest (Serna, 1977, 1979; Farmer et al., 1979).

On spectroscopic and theoretical grounds reduced C-H volatile dissolution can be resolved into soluble oxidised and reduced components. The former is represented by O-H bonds (as hydroxyl groups and molecular water) and affects melt structure much in the manner of H_2O dissolution. The reduced component, however, is somewhat enigmatic. Combined analytical data together with a specifically designed experiment establish that the reduced component is consistent with a network silicon-oxygen unit where the formal valency on silicon is reduced from IV to II (O:Si stoichiometry of the system <2). At the fO_2 conditions of these experiments, i.e. ~IW-4.5 log fO_2 units, a general reduction of the silicate network is evidently favoured over formation of Si-C bonds (analogous to Si-N bond formation in oxynitride glasses) which is the only other plausible reduced component. Nevertheless, the reduced carbon solubility in these aluminosilicate melts is ~1000 ppm (minimum) possibly as Si-C bonds or in the form of atomic carbon, C^o.

Liquidus phase relations in the system Ne-Fo-Q have established that C-H fluid dissolution raises melt activities of network modifying Al relative to other volatile species and the volatile-absent condition. This is in accord with the proposed dissolution mechanism and the observed expansion of the garnet phase volume in other systems.

The finding that the network portion of silicate melts is quite susceptible to reduction via formation of groups with O/Si < 2, has not been demonstrated previously. Reduced systems such as the enstatite chondrite group of meteorites have intrinsic oxygen fugacities that lie below IW. Measured values for the equilibrated EL enstatite chondrite group give fO_2's in the range ~IW-3 to IW-4 log fO_2 units (Brett & Sato, 1984; Walter & Doan, 1969) near the redox conditions of the present C-H fluid experiments. In these rocks Si is distributed amongst:

metal (kamacite with ~1-4 wt% metallic Si),
silicate (mainly enstatite), and
silicon oxynitride (sinoite, $Si_2N_2O_2$) phases

with graphite and not silicon carbide as an important accessory (Sears et al., 1982). This solid phase distribution of Si redox environments (at least at relatively low pressures) is consistent with the interpretation of C-H fluid equilibrated aluminosilicate glasses where a reduced silicate network plus graphite is evidently more stable than the equivalent melt structure containing Si-C bonds. It is possible to express the relationship between solid phases and a corresponding melt at fO_2 ~ IW-4 log fO_2 units via a disproportionation equilibrium of the type:

$$2[Si^{II}O_x]_{\substack{silicate\\melt}} = (2-x)[Si^{o}]_{\substack{metallic\\phase}} + x[Si^{IV}O_2]_{\substack{solid\\silicate}}$$

where $1 < x < 2$.

In view of recent hypotheses supporting the early incorporation of large amounts of reduced enstatite chondritic components into the Earth's mantle (Smith, 1982; Javoy & Pineau, 1983; Ito et al., 1984; Sun, in press) such equilibria are expected to have an important bearing on the mantle-core segregation of Si.

There are numerous implications for magma genesis and evolution raised by the results presented in this Part. The purpose of the final Part is to examine the likely petrogenetic role of reduced C-H volatiles in the light of this information.

PART 5

MANTLE METHANE AND THE ROLE OF REDUCED VOLATILES IN "REDOX MELTING" OF THE MANTLE.

5.1 Scope

The purpose of this Part is to discuss the role played by reduced C-H volatiles (i.e. H_2, CH_4 and other hydrocarbons) in mantle processes. To assess this role it is necessary to pose a number of questions. Firstly, what evidence exists to suggest that reduced volatiles are currently being (or have been in the past) degassed from mantle sources? In this context it will be important to evaluate the role of "juvenile" hydrocarbons and hydrogen as the products of degassing of primary magmas. Evidence on the nature of volatiles transported by primary magmas provides important constraints on the extent and nature of mantle degassing.

The second question is somewhat more wide-ranging: what is the range and distribution of mantle redox environments? Is this consistent with the fO_2 stability of reduced volatiles?

The final section of this thesis will be aimed at bringing together some of the ideas from Parts 2 to 4 into a model of volatile induced mantle melting under reduced conditions. This hypothesis is necessarily speculative but offers a useful basis for understanding how magmas might originate in a mantle that is now known to be more reduced than fO_2=FMQ.

5.2 Reduced volatile degassing of the mantle: evidence for deep-seated methane.

A. Introduction

The idea that the Earth's mantle is, and has been in the past, a major source of abiogenic hydrocarbons contributing to petroleum, natural gas and associated carbonate deposits has been popularised as the "deep-Earth-gas" hypothesis by Gold (1979) and Gold & Soter (1980, 1982). The hypothesis proposes a flux of mantle-derived methane capable of reaching the near-surface environment by ascent through zones of crustal weakness;

the major portion of this fluid is then assumed to reach the surface via volcanic eruptions (following oxidation of most CH_4 to CO_2), slow seepage or during earthquakes. In the third case, seismic phenomena have been related to variations in deep gas pressure.

Not surprisingly, the hypothesis is somewhat controversial and has been the subject of much debate (North, 1982; Planetary Science Unit, 1982; Bell, 1983; Oremland, 1983; Gold & Soter, 1983; Roedder, 1984). Gold's theory however gains strong support from several areas. Of relevance to this study is the observed outgassing of methane-rich fluids in a diverse range of tectonic environments. There is compelling evidence to indicate that many of these fluids are of mantle origin or at least contain a mantle-derived component. In other cases the evidence is circumstantial and these cases must be critically assessed. What the criteria for distinguishing primordial or juvenile* reduced fluids and how this relates to concepts of mantle fO_2 will be discussed below and in the following section.

B. Mantle methane outgassing traced by ^3He and other isotopes.

Since noble gases are chemically unreactive and are strongly fractionated into a fluid or vapour phase relative to liquid and/or crystals, helium-3 and other noble gas isotopes can be used as sensitive indicators of primordial volatile components derived from the Earth's mantle. In the terrestrial environment, ^3He is purely a primordial isotope. ^4He is however only partly primordial, the majority of presently observed ^4He being radiogenically derived. Variations in $^3He/^4He$ of Earth materials largely depend on the $^3He/(Th+U)$ ratio of the bulk source material together with its time history. The geochemistry of helium isotopes has recently been reviewed by Lupton (1983) and Ozima & Podosek (1983) and therefore will only be briefly discussed here. In general,

* a primordial volatile is defined here as one that was incorporated in the Earth at its time of formation; by contrast a juvenile volatile is one of mantle or magmatic origin that may, for example, include primordial as well as recycled crustal components.

most terrestrial $^3He/^4He$ ratios can be explained in terms of three components, i.e. atmospheric ($^3He/^4He = R_A = 1.4 \times 10^{-6}$), radiogenic and mantle. As discussed later, mantle He can probably be divided into two separate sub-components. Closed-system evolution of He trapped in >3 Myr old diamonds suggests that initial primordial He was close to solar in composition (Ozima et al., 1983). He-isotope values are sensitive to tectonic setting reflecting different contributions from endmember components. Characteristic values are summarised below where the $^3He/^4He$ ratio (R) is referenced against that of air and quoted as R/R_A.

Table 5.2A Characteristic $^3He/^4He$ signatures.

Environment	R/R_A	Reference
Air	1	1
MORB	≃8-9	1
Subduction zones	≃5-7	1
"Hot spot" (e.g. oceanic islands, rift zones)	≃12-30	1
Continental rocks (crustal or radiogenic He)	0.01-0.1	1
Planetary (extraterrestrial/ meteoritic)	≃100	1
Solar	≃280	1
Diamonds	0.03-226	2
Initial primordial mantle	>200	3
present (degassed mantle	~9	4
day (undegassed mantle	~60	4

1. Lupton (1983) and Ozima & Podosek (1983)
2. Ozima et al. (1983)
3. Zashu & Ozima (1984)
4. Lupton (1983, fig. 7); see also Hart et al. (1979) and Allegre et al. (1983).

"Hot spots" such as Hawaii have the most primitive terrestrial He for igneous rocks (Rison & Craig, 1983). A value of $R/R_A \simeq 8$-9 is the signature of degassed and presumably depleted mantle identified with MORB's.

Oceanic Environments

An important application of He isotopes is in tracing localised degassing centres along mid-ocean ridges. Welhan & Craig (1979) first reported anomalous concentrations of CH_4, H_2, CO_2, CO and ^3He (up to 10^5 times excess over normal seawater values) associated with venting of high temperature (~350°C) hydrothermal fluids at 21°N on the East Pacific Rise (EPR). Endmember hydrothermal fluids, i.e. at 0% seawater dilution, contain ~1.3 cm^3kg^{-1} CH_4, 10-40 cm^3kg^{-1} H_2 and ~0.02 cm^3kg^{-1} He. Helium has a characteristic "depleted mantle" signature (R/R_A = 7.8) suggesting extraction of CH_4 and other gases directly from MORB by circulation of hydrothermal fluids (Welhan & Craig, 1983).

Welhan & Craig (1983) have ruled out a thermogenic* and/or biogenic* origin for CH_4 on the basis of $\delta^{13}C$ and other measurements. The variability of H_2 concentrations, however, may at least in part be due to microbial activity (Lilley et al., 1983). Methane $\delta^{13}C$ values are unusually heavy and range from -15 to -17.6 per mil unlike that of thermogenic or biogenic methane but very similar to Kamenskiy et al.'s (1976) predicted value for mantle methane (see Table 5.2B).

Table 5.2B Carbon-13 isotopic values for methane.

Source	$\delta^{13}C$(rel.PDB)per mil	Reference
Mantle methane	~ -15	Kamenskiy et al. (1976)
Crustal methane (thermogenic	~ -40 to -50	Claypool & Kvenvolden (1983)
(biogenic	~ -70 to -80	Claypool & Kvenvolden (1983)

A biogenic or thermogenic origin can be excluded on the basis of very low and uniform $CH_4/^3He$ ratios (~5 x 10^6) and low CH_4/C_2H_6 ratios (<500) (cf. Claypool & Kvenvolden, 1983). Welham & Craig (1983) have further demonstrated in crushing experiments on EPR MORB glasses that CH_4 and H_2 are present at a minimum level of 0.05-0.10 cm^3kg^{-1} and ~0.2 cm^3kg^{-1} respectively. Helium concentrations are 2-5 x 10^{-3} cm^3kg^{-1} with a ^3He excess of R/R_A = 8.0-8.2. Volatile extraction from MORB glasses via

*thermogenic methane = derived from thermal cracking or thermocatalysis of complex organically derived hydrocarbons.
biogenic methane = produced directly by biological processes e.g. by methanogenic bacteria.

abiogenic water-rock interactions could thus lead to observed anomalies in hydrothermal fluids; contributions from volatiles released by crystallisation or depressurisation of MORB liquids at depth are also likely. Lilley et al. (1983) have suggested that MOR hydrothermal fluids have a substantial biogenic input. However convincing evidence for this is only seen in low temperature (<20°C) MOR fluids and microbial activity beyond about 100°C has not been demonstrated (Baross et al., 1982).

Since the initial discoveries of Welham and Craig, CH_4, H_2 and ^3He-rich plumes have been identified at a number of hydrothermal centres on mid-ocean ridges. These are listed in Table 5.2C together with $CH_4/^3He$ ratios - a low value is characteristic of non-thermogenic/non-biogenic methane (after Kim, 1983).

Table 5.2C

CH_4-rich plumes	$(CH_4/^3He).10^6$
21°N East Pacific Rise (moderate rate spreading centre)	3-6
20°S East Pacific Rise (fast spreading centre)	7.0-20.6
Galapagos Spreading Centre* (GSC)	12.4-42
Marianas back-arc basin (axial volcano)	n.m.
Juan de Fuca Ridge	n.m.
Red Sea	0.8
Guaymas Basin, Gulf of California**	3100

n.m. = ^3He not measured

* reduced volatiles found by mass pyrolysis of GSC basaltic and andesitic glasses (Byers et al., 1983). CH_4: 0.01-0.03 wt% (bas.), 0.01-0.02 wt% (and.); CO: 0.03-0.05 wt% (bas.), $\leq$0.01 wt% (and.).

** CH_4 in this case is of thermogenic/biogenic origin due to large sediment accumulations cf. other values.

These results are supported by the work of Kim (1983) who obtained remarkable correlations between ^3He, CH_4 and temperature anomalies (the latter being an indicator of heat flux). Kim found that high CH_4

concentrations were invariably associated with a high concentration of primordial helium and a positive temperature anomaly. Such positive linear correlations are convincing evidence of a primordial origin for methane degassing at MOR vents. This is illustrated for the 20°S EPR centre in Fig. 5.2A where depth versus CH_4 conc. and depth versus $\delta^3He = [(R/R_A)-1].100$ plots record a section through the hydrothermal plume; note the close correspondence between CH_4 concentration and δ^3He. Fig. 5.2B shows the positive linear correlations between CH_4 and ^3He concentrations at EPR centres. It is evident from this figure that variations in slope of the lines, and hence $CH_4/^3He$ ratio, are dependant on vent site. Similar plots of temperature anomaly versus δ^3He are site independent suggesting that $CH_4/^3He$ ratio differences at any one hydrothermal centre are due to differences in the CH_4 concentrations of source basalts.

One particularly interesting discovery by Kim (1983), is a large CH_4 anomaly (comparable to 20°S EPR) and a linear CH_4 conc. versus heat flux relationship found over the summit of an axial volcano in the Marianas basin - a young back-arc spreading environment. Although no ^3He data are yet available it appears likely that venting of primordial CH_4 and other reduced gases occurs in both back-arc and MOR spreading environments. Future discoveries will probably indicate that this is a wide-spread process. Support for this contention, in the absence of direct measurement at hydrothermal vents, comes from the detection of non-biogenic hydrocarbons in MORB glasses. For example, Byers et al. (1983) have found CH_4 and CO in glasses from the Galapagos Rift (Table 5.2C) and Zolotarev et al. (1979a, 1979b) have reported gas contents in Atlantic MORB glasses (22°N, 37°N, 45°N and Reykjanes Ridge) that include ~0.06 cm^3kg^{-1} CH_4, 0.01 cm^3kg^{-1} C_2H_6 and ~1-2 cm^3kg^{-1} H_2 plus small quantities of condensed hydrocarbons ("bitumens") that coat grain boundaries and small cracks. Low CH_4/C_2H_6 ratios are consistent with a primordial origin.

Continental Environments

Elevated $^3He/^4He$ ratios have been found in geothermal gases at convergent plate margins (e.g. Japan, Kamchatka, New Zealand) and continental "hot spots" (e.g. Yellowstone, Ethiopian Rift) as recently summarised by Lupton (1983). At subduction zones essentially all ^3He must be derived from primary mantle sources since the subducted slab is expected to be largely outgassed and if composed largely of old oceanic crust will only contribute He of $R/R_A \sim 0.1$ (Lupton, 1983).

Fig. 5.2A Depth versus CH_4 concentration and depth versus $\delta^3He = [(R/R_A)-1]*100$ plots recording the cross-section of a hydrothermal plume at 20^oS on the East Pacific Rise. Note the close correspondence between CH_4 conc. and δ^3He indicating a primordial origin for CH_4 (after Kim, 1983, fig. 3.13).

Fig. 5.2B Linear correlations between CH_4 conc. and δ^3He at the same site as Fig. 5.2A provide further evidence for the primordial origin of CH_4. $CH_4/^3He$ ratios are dependant on vent site suggesting differences in the source concentration of CH_4 (after Kim, 1983, fig. 3.14).

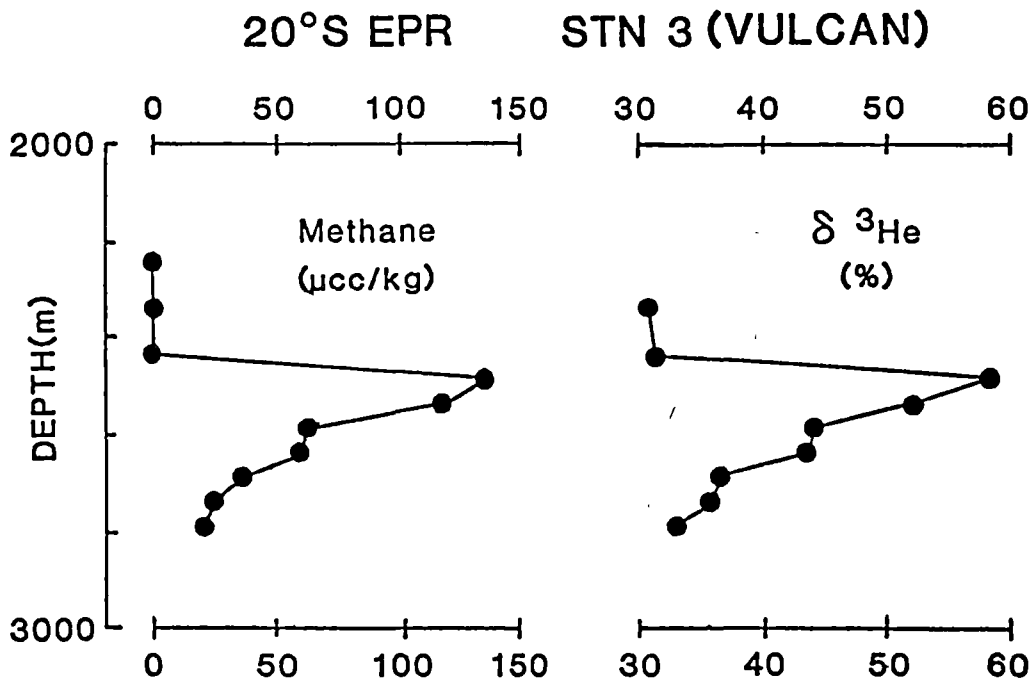
20°S EPR STN 3 (VULCAN)
0 50 100 150
30 40 50 60
2000
3000
DEPTH(m)
Methane
(µcc/kg)
δ 3He
(%)
0 50 100 150
30 40 50 60

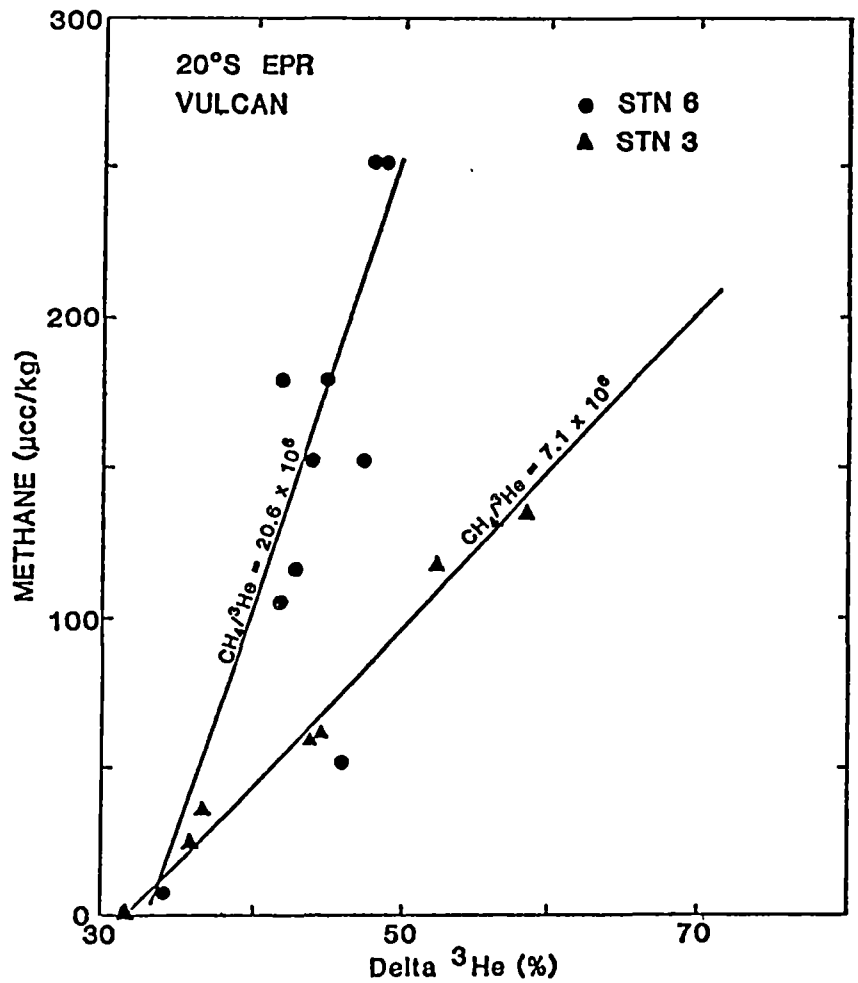
20°S EPR
VULCAN
STN 6
STN 3
CH4/3He = 20.6 x 10⁶
CH4/3He = 7.1 x 10⁶
METHANE (µcc/kg)
300
200
100
0
30
50
70
Delta 3He (%)

At convergent plate margins, geothermal gases having a mantle ^3He signature contain methane as a prominent component. For example, Kamenskiy et al. (1976) have clearly identified CH_4 consistent with primordial, as well as thermogenic and biogenic, origins in geothermal fluids from Kamchatka.

A similar study of CH_4-rich (mostly >80 vol% CH_4) natural gases from volcaniclastic reservoirs in Japan (Wakita & Sano, 1983) has established a primordial component amounting to at least 33%. The authors speculate that mantle-derived CH_4 and ^3He have been released from volcaniclastic reservoir rocks by diagenetic and hydrothermal activity.

Limited data on continental "hot spots" and rift areas indicate that $^3He/^4He$ ratios may extend to very high values similar to oceanic islands such as Hawaii. A high concentration of CH_4 in Lake Kivu (western African rift) is associated with a ^3He anomaly (Gold & Soter, 1982).

C. Methane Associated with Alkaline Intrusives

Hydrocarbon-rich fluid inclusions (typically containing ~70-90% CH_4) have been widely reported in nepheline syenite and related rocks from alkaline intrusive complexes, e.g. Petersilie & Sorensen (1970). Heavy $\delta^{13}C(CH_4)$ values and low CH_4/C_2H_6 ratios point to an abiogenic origin (Petersilie & Pripachkin, 1979). Gold & Soter (1982) have used this evidence to suggest that such fluids may be derived directly from a mantle source but such an interpretation requires a more thorough evaluation.

Detailed studies of fluid inclusions in minerals from the Ilimaussaq intrusion by Konnerup-Madsen et al. (1979) and Konnerup-Madsen & Rose-Hansen (1982) have established that the hydrocarbon-rich inclusions are largely of secondary origin. They are associated with all minerals of nepheline syenite (mainly confined to healed fractures) and with hydrothermal veins. Limited numbers of primary high salinity aqueous or mixed hydrocarbon-aqueous, and CO_2-N_2-aqueous inclusions occur in nepheline syenite; rare primary hydrocarbon-rich inclusions have also been identified. Highly saline and hydrocarbon-rich inclusions commonly coexist in hydrothermal veins.

Analysis of hydrocarbon-rich fluid inclusions trapped in nepheline have established extremely low bulk oxygen contents ($X_O \sim 0.01$) implying

very low fO_2 conditions during formation. Carbon contents ($X_C \sim 0.3$) suggest that the fluid phase was close to graphite saturation under estimated trapping conditions: 0.8-1.4 kbar, 500-800°C (Konnerup-Madsen et al., 1979). There appears, however, to be little evidence for the presence of graphite in these rocks (Roedder, 1984) although disseminated "bituminous substances" are commonly observed (Petersilie & Sorensen, 1970). This may be largely due to a kinetic phenomenon, i.e. failure of the fluids to nucleate graphite under low temperature (<800°C) conditions. Ziegenbein & Johannes (1980) report similar kinetic problems in experiments on C-O-H fluids at $T < 700°C$, $P = 2$ kbar.

Since most hydrocarbon-rich fluids have been shown to have a secondary origin and reveal low trapping temperatures, it is apparent that the presently observed fluid compositions are not representative of initial magmatic fluids. The extraordinarily low oxygen content and the distribution of inclusions in hydrothermal veins is consistent with an origin by aqueous-hydrocarbon fluid-fluid immiscibility from an evolved CH_4-rich fluid during the latter stages of magma crystallisation (see Section 1.6). Konnerup-Madsen & Rose-Hansen (1982) postulate that the aqueous phase is preferentially removed by dissolution in a melt phase that becomes progressively more alkaline and hence capable of dissolving excess water as the degree of crystallisation increases. However, hydrothermal veins retain both types of immiscible fluid. Immiscibility is likely to be enhanced by high salinities as discussed in Section 1.6.

According to Konnerup-Madsen & Rose-Hansen (1982) there are three main reasons why this type of process is unique to alkaline intrusive rocks:

(i) low solidus temperatures extending down to ~450°C at $P \sim 1$ kbar,
(ii) low oxygen fugacities during crystallisation, and
(iii) retention of volatiles.

Point (ii) is of critical importance in establishing the composition of initial magmatic fluids and in describing their evolutionary path in P-T-fO_2 space. Konnerup-Madsen & Rose-Hansen (1982) suggested that initial fO_2 conditions were near or slightly below MW progressing toward the "graphite-CH_4" buffer at lower temperatures. However to suggest $fO_2 \sim$ graphite-CH_4 is clearly a misinterpretation of the way in which this buffer is defined by Eugster & Skippen (1967; eqn.10). The graphite-CH_4 system buffers only fH_2; since no oxygen is present, fO_2 for this buffer must clearly be zero. The graphite-CH_4 buffer is of use in controlling fH_2 in high-pressure gas

apparatus where Pt membranes can separate different sub-systems but has no useful place in describing redox conditions in natural systems.

The method used by Konnerup-Madsen & Rose-Hansen (1982) to determine initial fO_2's is also subject to criticism since it is not clear whether all the phases, i.e. nepheline, albite, magnetite and olivine, are in equilibrium via the following reaction used to define fO_2:

$$6Fe_2SiO_4 + 3NaAlSiO_4 + 2O_2 = 4Fe_3O_4 + 3NaAlSi_3O_8$$

In any event, error brackets would be at least ± 1 log(fO_2) units. This uncertainty does not allow initial magmatic fluid compositions to be adequately constrained. Reference to Figs 2.7 and 2.9 (Part 2) gives some idea of the compositional range to be expected as a function of fO_2, X_C and P. If primary fluids are trapped in early crystallising minerals at pressures not less than ~4 kbar and T $\simeq$ 1000°C then at fO_2 ~ MW fluids near graphite saturation will be dominantly H_2O with minor CO_2, CH_4 and CO. At fO_2's between IW and MW fluids will be largely H_2O-CH_4-H_2 mixtures becoming CH_4 dominant near IW.

Within presently resolved fO_2 limits any of these compositions are suitable candidates for primary fluids. Sobolev et al. (1974) believe that the CO_2-N_2-CO-aqueous primary fluid inclusion set represent the initial magmatic fluids at Ilimaussaq and other alkaline intrusives thus putting fO_2 near MW. This would be consistent with the composition of volcanic gases issuing from the Mt Nyiragongo lava lake (a nephelinitic alkaline volcano of the western rift, East Africa) which are dominantly H_2O and CO_2 with minor CO, H_2 (Gerlach, 1980). Substantial CH_4 of presumed magmatic origin is also found dissolved in Lake Kivu on the southern flank of Nyiragongo and according to Gerlach may have an origin by low temperature equilibration of magmatic gases buffered by the rock. Such a process could also be responsible for the evolution of fluids prior to hydrocarbon-aqueous immiscibility in alkaline intrusions.

Despite the above suggestions, methane-rich primary inclusions have also been identified at Ilimaussaq and other intrusions. Thus in the absence of better constraints it is difficult to decide on the exact path of fluid evolution and whether initial CH_4-rich fluids were involved. Recently, Frost et al. (1984) have presented data indicating that quite reduced conditions prevailed during crystallisation of the Sybille pyroxene syenite, Wyoming. This intrusive contains primary graphite and nearly pure $FeTiO_3$ ilmenite constraining fO_2 to between IW+0.5 and MW-0.5 log fO_2 units

consistent with initial magmatic fluids at P = 3 kbar, T = 900°C containing substantial CH_4.

From the above discussion, the idea of Gold & Soter (1982) that the hydrocarbon-rich fluids in alkaline intrusives are of deep-seated mantle origin can only be substantiated insomuch as these fluids represent the last stage in a complex evolution involving initial magmatic fluids that were at least in some cases CH_4-bearing. Such fluids could very well have been of mantle origin but the link between them and presently observed compositions has not yet been established. Present evidence can not rule out the involvement of reduced mantle-derived fluids in the genesis of alkaline intrusives. Further investigations are therefore clearly warranted to better constrain fluid and fO_2 evolution in these systems.

D. Fluids Included by Diamond

This topic has been fully covered in Part 3. While the data set may not yet be of statistically significant size, it appears that most diamonds have equilibrated with mantle fluids of H_2O-CH_4 composition during growth and/or residence in the upper mantle. A genetic link between methane-bearing fluids and diamond is suggested.

E. Reduced Gases in Xenocrysts and Megacrysts of Mantle Origin

Reduced gases have been identified in a variety of xenocrysts and megacrysts from igneous environments. Matson et al. (1984) report CH_4 contents of 0.02-0.05 wt%, CO of 0.02-0.06 wt% and traces of higher hydrocarbons from mass pyrolysis experiments on amphibole megacrysts and glomerocrysts hosted by basanite. Matson et al. infer that such samples must have crystallised at depth under redox conditions less than FMQ.

Oberheuser et al. (1980, 1981) have found that substantial quantities of CH_4 and other hydrocarbons are released by in vacuo heating of olivine nodules from Eifel. Methane has also been reported in xenocrysts and xenoliths from kimberlite (see references quoted by Roedder, 1984, p.511). Finally, Pasteris (1981) inferred that the fluid coexisting with kimberlite during its subcrustal emplacement was probably CH_4-bearing judging by the nature of autoserpentinisation of kimberlite-hosted olivine.

F. Models for Mantle Degassing

In the previous sub-sections it has been shown that methane and other reduced volatiles of primordial mantle origin are currently being degassed at mid-ocean ridges. Using primordial ^3He to trace the origin of geothermal gases, a mantle contribution to methane in continental gas reservoirs and seepages has been confirmed. Association of mantle methane with the genesis of alkaline rocks is less certain but the low oxidation state of these intrusive bodies (near or below MW), compared with typical values near FMQ for other terrestrial magmas emplaced near the surface, suggests that initial CH_4-bearing magmatic fluids may have been involved in the genesis of these rocks. Xenocrysts and megacrysts of mantle origin, including diamonds have also been shown to contain methane and other reduced gases.

The above data indicate that reduced volatiles of mantle origin are associated with most igneous environments. Current estimates of CH_4 and H_2 fluxes at mid-ocean ridges are $\sim 2 \times 10^8$ $m^3 yr^{-1}$ and $\sim 10^9$ $m^3 yr^{-1}$ respectively (Welhan & Craig, 1979). The total amount of carbon degassed at mid-ocean ridges is not sufficiently well constrained to allow direct comparison with the calculated CH_4 flux. Using the model of Javoy et al. (1982), estimates of the total mid-ocean ridge carbon flux may be anywhere from 2 to 100 times the CH_4 flux. However, it is clear that reduced volatiles must be considered in any mantle degassing scheme although it is not known in what proportion reduced volatiles are degassed (or have been degassed in the past) relative to oxidised volatiles. While the latter are the dominant components in magmatic gases from active volcanic regions (e.g. A.T. Anderson, 1975) it is not at all clear whether they dominate at depth as this will depend very much on the mantle oxidation state as discussed in the next section. Gold & Soter (1982) argue that the reduced gases (CH_4, H_2) are the dominant mantle volatile species.

Since the nature of mantle degassing through time may have greatly changed the redox state of the mantle it is desirable to look at what constraints can be placed on the extent and distribution of this degassing process. In particular, is it possible to discriminate between source regions for reduced and oxidised volatiles?

For the reasons considered in Section 5.2A, the most useful constraints on mantle degassing are provided by isotopic studies of the

noble gases particularly He, Ar and Xe. Ozima & Podosek (1983) explain that individually, noble gas isotopes can only poorly constrain the extent of mantle degassing. In fact if ^{3}He has been degassing at the present rate accompanied by the other primordial gases in their nominal planetary ratios, then over 4.5 Gyr, ^{20}Ne, ^{36}Ar and ^{84}Kr isotopes suggest only 5-10% mantle degassing has occurred - presumably the rate was higher in the past but by how much? Fortunately more detailed answers can be obtained by considering the ratio of radiogenic to primordial isotopes. These are controlled by the concentration of involatile parent isotopes which for He, Ar and Xe decay over a useful range of half-lifes ($\sim 10^{7}$ to $\sim 10^{9}$ yr). Information about the extent of mantle degassing with time can thus be provided.

Ozima & Podosek (1983) have considered a simple three reservoir evolution model (mantle-crust-atmosphere) for He and Ar isotopes which suggests that there was an early catastrophic degassing event involving >70% loss of the mantle's volatile content. This was followed by continuous degassing up until the present where only a few percent of the original volatile inventory now remain. Consideration of Xe isotopic data suggests, however, that this model may be too simplistic. Because of the short half-life of the parent isotopes to ^{129}Xe ($\sim 10^{7}$yr), the discovery of significant $^{129}Xe/^{130}Xe$ anomalies amongst mantle-derived samples compared with air (Allegre et al., 1983) is strong evidence for the existence of an additional largely undegassed reservoir that has remained decoupled from the degassed mantle reservoir since early in the Earth's history. Other features of Ar and He isotopics also imply the existence of an undegassed reservoir (see Hart et al., 1979; Lupton, 1983, p.392-4).

Both Hart et al. (1979) and Allegre et al. (1983) using Sr and Nd isotopic data, have equated the degassed reservoir with a depleted upper mantle (source for both MORB and continental material) and similarly equated the undegassed reservoir with an undepleted lower mantle. This is consistent with current mantle two-layer convection models with a boundary layer located near 670 km (McKenzie & Richter, 1981; Lambert, 1981). Ozima & Podosek's three-reservoir model would then only apply to the upper mantle-crust-atmosphere system. Allegre et al. (1983) have pointed out that the relation between degassing and depletion may not necessarily be simple and more complex descriptions cannot be ruled out. The present model, however, provides the simplest interpretation of available data.

The existence of a largely undegassed lower mantle and a >90% degassed upper mantle has important consequences for the role of volatiles in mantle processes. If this approach is correct, then from the earlier discussion of ^{3}He anomalies (Section 5.2A), it is evident that at "hot spots" such as Hawaii (where $^{3}He/^{4}He$ ratios are up to four times larger than the MORB signature) there must be significant inputs of lower mantle volatiles.

Since there are major geophysical and probably geochemical contrasts between the upper and lower mantles, it is likely that such differences will also extend to redox environment. Gradual leakage of lower mantle volatiles into an upper mantle of contrasting fO_2 may therefore impose lower mantle redox conditions on regions of the upper mantle by direct redox interaction, particularly if unbuffered by solid-state equilibria (see Section 5.3B). This could have the effect of creating a somewhat heterogeneous distribution of oxidation states as will be discussed in the following Section.

5.3 The Oxidation State of the Upper Mantle and the Origin and Significance of Reduced Carbon

A. Redox Environments in the Upper Mantle

The redox conditions that prevail in the Earth's upper mantle have been the subject of much debate in the current literature (e.g. Sato, 1978; Haggerty, 1978; Ryabchikov et al., 1981; Arculus & Delano, 1981a; Eggler & Baker, 1982; Haggerty & Tompkins, 1983; Arculus et al., 1984). In terms of broad constraints, upper and lower limits can readily be placed on mantle fO_2's at least in regions of magma generation. Thus the trace element signature that characterises equilibrium with metallic Fe is not observed in terrestrial basalts (Kogarko & Arutyunyan, 1982) placing a lower limit on fO_2's at near OIE-2 (see Appendix 9) or about IW-3 log fO_2 units. Since terrestrial basalts at surface eruption seldom exhibit oxidation states above HM this probably represents a plausible upper limit to mantle fO_2's. The region IW-3 to HM, however, spans a large range of redox conditions and better constraints must rely on application of a number of different techniques:

(a) direct intrinsic fO_2 measurements on Fe-bearing samples using oxygen-ion specific electrolytes (e.g. Sato, 1972);

(b) thermodynamic calculation involving fO_2 sensitive mineral assemblages (e.g. olivine-opx-spinel; O'Neill & Wall, 1982);

(c) composition and speciation in fluids of mantle origin (e.g. fluids included in peridotite nodules or diamond (Bergman & Dubessy, 1984; Part 3, this work);

(d) inferences from the properties of magmas erupted at the surface, e.g. ilmenite-magnetite thermometry, Fe^{2+}/Fe^{3+} ratio of glasses, direct measurements of volcanic gas P_{O_2}.

Intrinsic Oxygen Fugacity Measurements

Intrinsic fO_2 measurements on mantle-derived samples have been performed at 1 atm in a number of laboratories. The data of Sato (1972) gave the first indication that magmatic fO_2's might extend to very reduced values near IW. Previously it had been assumed that fO_2's near FMQ were representative of the oxidation state of the mantle and erupted basalts (see Haggerty, 1978). Further measurements (Virgo et al., 1976; Sato, 1978; Arculus & Delano, 1981a; Arculus & Gust, 1981; Arculus, 1982; Arculus et al., 1984) have confirmed that redox conditions near IW are typical of many mantle-derived materials. Since other mantle samples record more oxidised values, Arculus et al. (1984) suggested that a uniform fO_2 for the mantle is not appropriate and provided the results can be adequately extrapolated to high pressures, a bimodal distribution of fO_2 environments is indicated. These correspond to:

(i) $fO_2 \simeq$ NNO to FMQ associated with "type B" (aluminous augite) peridotites and megacryst ilmenites.

(ii) $fO_2 \simeq$ IW to IW+1 associated with "type A" (chrome diopside) peridotites believed to make up the major portion of the shallower part of the upper mantle (Arculus, 1982).

Arculus et al. (1984) noted that "type A" material consistently has intrinsic fO_2's near IW irrespective of tectonic environment (i.e. continental, island-arc or oceanic island). The authors propose that more oxidised "type B" material is associated with an oxidising flux or "metasomatic event", a process that is thought to precede kimberlitic and related alkalic magmatism (e.g. Wass & Pooley, 1982).

Oxygen Barometry

Ilmenite-spinel (Haggerty & Tompkins, 1983), ilmenite-opx-olivine (Eggler, 1983) and spinel-opx-olivine (O'Neill & Wall, 1982) oxygen barometry on mantle-derived megacrysts and xenoliths do not lend support to

the bimodal distribution hypothesis of Arculus and co-workers. Calculated fO_2's from ilmenite-bearing assemblages lie mostly between FMQ and MW-1 log fO_2 units following pressure correction. Results from spinel lherzolites (sample size ~200) tend to cluster near MW with some samples being more oxidised and a few significantly more reduced.

To assess the validity of the above results, a number of factors must be considered: Firstly, large uncertainties may arise in this type of calculation from inadequate knowledge of silicate and oxide phase activity-composition relations. Secondly, assumptions of perfect stoichiometry in calculating Fe^{3+} contents of ilmenite or spinel from microprobe data will introduce error, particularly if Fe^{3+} contents are small as in mantle minerals. And thirdly, ilmenite-bearing assemblages are probably not representative of mantle material as a whole and may record conditions prevailing during a spatially and temporally restricted magmatic event. The present discrepancy between oxygen barometry and intrinsic fO_2 measurements is possibly due to these factors. In any event, use of this data to propose detailed models of fO_2 distribution in the upper mantle, such as the laterally zoned model of Haggerty & Tompkins (1983), must be regarded as premature at this stage. Two important points are brought out by such studies, however, i.e.

(i) a unique fO_2 value cannot be applied to the upper mantle, and

(ii) consistent with its geochemical heterogeneity (expressed in incompatible element abundances in particular) the upper mantle is also likely to be heterogeneous with respect to redox environments.

Fluid Inclusions in Mantle Samples

In theory, the composition and speciation of fluids trapped in mantle minerals should reflect the fO_2 conditions that prevailed during crystal growth or recrystallisation at depth. Unfortunately, fluid-filled inclusions in mantle ultramafic xenoliths are compositionally monotonous; they typically contain a nearly pure CO_2 fluid and are usually of small size (<15 microns diameter) creating difficulties in optical examination. Inclusions often show evidence of partial decrepitation and sometimes contain a glass-phase (e.g. Murck et al., 1978) or secondary minerals formed by fluid-host reactions (e.g. Andersen et al., 1984). Furthermore, CO_2 densities in olivine seldom indicate trapping pressures much above 10 kbar. This suggests that fluids trapped at higher pressures were most probably lost by full or partial decrepitation; the presently observed sample must therefore be somewhat biased. Roedder (1984) and Pasteris (in

press) have recently summarised many of the features of fluid inclusions in ultramafic xenoliths.

Most fluid inclusions from xenoliths appear to be of secondary origin and may have been through a number of recrystallisation and/or decrepitation/retrapping cycles or have been modified by reaction with the host phase, thus it is not clear what they can tell us about mantle fO_2. A pure CO_2-filled inclusion implies very high fO_2's (>FMQ) but over the range of fO_2 conditions identified for the mantle by other methods, i.e. ~FMQ to IW, a wide diversity of C-O-H fluid compositions, ranging over CO_2-CO, H_2O-CO_2 and CH_4-H_2O mixtures, is expected. The lack of observations of such volatile mixtures in inclusions has been explained by selective partitioning of H_2O into a melt phase (Mathez & Delaney, 1981), amphibole and secondary mineral formation (Andersen et al., 1984) and graphite precipitation or fractionation from the fluid (Bergman & Dubessy, 1984; Mathez & Delaney, 1981; Watanabe et al., 1983).

In some rare inclusion suites mixed fluids have been identified, for example: CO_2-H_2O fluid inclusions in spinel lherzolite from Ichinomegata, Japan which predate a later set of CO_2-glass inclusions (Trial et al., 1984), and CO_2-CO inclusions in a composite wehrlite xenolith (calculated fO_2 ~ FMQ; Bergman & Dubessy, 1984). Watanabe et al. (1983) have been able to reconstruct original CO_2-CO fluids from inclusions in Hawaiian dunite xenoliths by differential extraction of reduced and oxidised carbon. They obtained fO_2's near IW consistent with original intrinsic fO_2 measurements by Sato (1978).

Apart from the above few cases, however, the majority of fluid inclusions have compositions that cannot represent conditions of host/fluid equilibrium at depth (>10 kbar) in the mantle. Unlike the fluids included by diamond (Part 3), these fluids appear, at this stage, to be of little help in constraining the mantle redox state.

Oxygen Fugacities of Basaltic Magmas

Using the oxidation state of erupted basaltic magmas to infer redox conditions in the mantle is unlikely to be a useful approach due to redox modification processes occurring in the near-surface environment. This is well illustrated by the fO_2 evolution observed in large basic layered intrusions. Sato & Valenza (1980) have obtained intrinsic fO_2 data on rock samples and mineral separates from the lower, middle and upper layered

series at Skaergaard. They found fO_2's of first crystallised minerals from the lower and middle zones to be near IW but at higher stratigraphic levels fO_2 conditions are more oxidised and lie between MW and IW. Similar fO_2 variations with stratigraphic elevation have been observed for the Stillwater ($fO_2 \simeq$ IW to MW+1) and Bushveld ($fO_2 \simeq$ IW-1 to MW) layered intrusions (Elliot et al., 1982).

At Skaergaard, irreversible "self-reduction" behaviour in the intrinsic fO_2-T data led Sato & Valenza to suggest that reduced carbon controls fO_2 during the early stages of crystallisation of the Skaergaard magma. Graphite of magmatic origin has been shown to have a wide distribution in basic layered intrusions: Merkle & Hatton (1983); Ulmer (1983) and Volborth & Housley (1984). This fact in itself points to initial magmatic fO_2's being close to or less than MW since none of the more oxidising oxide buffers, which tend to parallel the P,T variation of fO_2 in basaltic systems, intersect the graphite saturation surface at magmatic temperatures. For example, a system buffered along FMQ will never precipitate magmatic graphite since intersections with the graphite saturation curve occur near 680°C at 10 kbar, 620°C at 5 kbar and <500°C at 1 bar, well below the basaltic solidus (see fO_2-T plots in Appendix 9).

A discrepancy in bulk rock versus oxide mineral intrinsic fO_2 trends at Skaergaard was attributed by Sato & Valenza to post-cumulus oxidation of the oxide phase. In the lower series of Skaergaard, magnetite is usually absent since at fO_2's below MW magnetite is no longer a stable component in Fe-Ti-spinels (see Fig.4 of Spencer & Lindsley, 1981). Both the above observations make Fe-Ti-oxide oxygen geobarometry of limited value in recording magmatic fO_2's during the early stages of crystallisation. As indicated by Mathez (1984) this also applies to fO_2 estimates in MORB's since by the time Fe-Ti-oxides appear significant fO_2-modification by crystallisation and degassing of H- and C-species has already occurred. The intrinsic fO_2 measurements on phenocrystic olivine by Sato (1972) and analogy with the early magmatic phase in layered intrusions suggest that undegassed oceanic basalts may be quite reduced in character ($fO_2 \simeq$ IW).

Mathez (1984) proposes that significant MORB oxidation, from fO_2 conditions near IW to those typical of erupted magmas, i.e. ~FMQ, takes place during degassing at shallow levels in the crust via redox equilibria involving melt and vapour phases. Mathez has modelled this in the simple system C-O by envisaging a process of "perfect fractional vaporisation" in

which a vapour of variable CO/CO_2 ratio is lost during degassing at P < 3 kbar. Oxidation proceeds by a reaction of the type:

$$CO_3^{2-}{}_{(melt)} \text{ ---> } CO_{(vap)} + O^{2-}_{(melt)} + 1/2\ O_{2(melt)}$$

A similar oxidative process involving diffusive H_2-loss was earlier proposed by Sato & Wright (1966) to explain oxidation phenomena in Hawaiian lava lakes. Sato (1978) later considered that H_2-loss is also likely to be an important process in the oxidation of hydrous magmas. Calculations by Mathez (1984) indicate that dissociation of only ~0.1 wt% H_2O is sufficient to oxidise a magma by approximately four orders of magnitude from IW to FMQ via the reaction

$$H_2O_{(melt)} \text{ ---> } H_2\uparrow + 1/2\ O_{2(melt)}$$

For oxidation beyond FMQ, the buffering influence of the

$$FeO_{(melt)} + 1/4\ O_2 = FeO_{1.5(melt)}$$

equilibrium tends to dominate and larger amounts of H_2O must be dissociated to achieve the same level of oxidation (see Mathez, 1983, Fig.2).

Other processes likely to be of importance are loss of reduced components, especially H_2, via the reverse of reaction 4.8J (Part 4) proposed for reduced volatile solubility. If dissolved carbonate can coexist with a silicate network of reduced stoichiometry (O:Si < 2) at fO_2's ~ IW and there is spectroscopic evidence to indicate this may occur in both the experimental work of Jakobsson & Holloway (1984) at fO_2=IW and in one high-pressure run from this study which was partially oxidised by loss of CH_4 vapour. In the latter case the FTIR spectrum of the glass revealed the presence of both dissolved carbonate and reduced network component; thus there is potential for release of hydrocarbons and CO with accompanying oxidation of the magma via the reactions of the type:

$$\{SiO\}_{(melt)} + CO_{3(melt)}^{2-} \text{ --> } CO\uparrow + [SiO_3^{2-}]_{(melt)} \qquad \text{....5.3A}$$

and

$$2\{SiO\}_{(melt)} + CO_{3(melt)}^{2-} + 4OH^-_{(melt)} + 4[FeO]_{(melt)} \;\text{-->}\; CH_4\uparrow + [Si_2O_7]^{6-}_{(melt)} + 4[FeO_{1.5}]_{(melt)} \quad \ldots.5.3B$$

where {SiO} = reduced network ("silicon monoxide") component
Reaction 5.3B, occurring during magma ascent, could be partly responsible for the primordial CH_4 observed at mid-ocean ridges.

B. Control of Upper Mantle fO_2 - Buffered or Unbuffered?

In Section 5.2 it was proposed that volatile influx can play a major role in modifying upper mantle fO_2 conditions by direct redox interaction provided the upper mantle is largely unbuffered. It is therefore important to assess the nature and likely distribution of fO_2 buffering assemblages.

In the absence of a fluid phase, there are only two types of solid state equilibria in mantle compositions that are likely to maintain fO_2, these are (i) ferric-ferrous equilibria involving spinel-pyroxene-olivine or ilmenite-pyroxene-olivine assemblages in which the oxide phase contains measurable Fe^{3+} and (ii) carbonate-elemental carbon-silicate equilibria proposed by Eggler & Baker (1982) as providing "typical" mantle fO_2 conditions.

Assemblages were spinel is stable are restricted to shallower portions of the upper mantle (this depends on bulk Cr/Cr+Al ratio but spinel may persist to at least 50 kbar in depleted peridotites; Nickel, 1983). Ilmenite-bearing assemblages are not particularly abundant in the upper mantle and their capacity to buffer fO_2 is therfore expected to be limited. As discussed in Part 3, carbonate-elemental carbon-silicate buffers are unlikely to be applicable in regions of the mantle hosting diamond. In view of the paucity of recorded primary crystalline carbonate from upper mantle assemblages (they appear largely restricted to unusual "metasomatic zones", e.g. Wass & Pooley, 1982; or to rare low-temperature peridotites, e.g. Smith, 1979) it is suggested here that such buffers would only apply in very restricted, localised regions. In most cases where buffers such as EMOG have been proposed e.g. for control of fO_2 in the Benfontein kimberlite sill of McMahon & Haggerty (1984), evidence that carbonate/elemental carbon/silicate assemblages actually coexist at depth is sparse. It is more likely in systems such as the Benfontein kimberlites that fO_2 is constrained along the oxidised portion of the carbon saturation surface (which spans a narrow range in fO_2 between GCO and ~GW, see Fig

2.5) by the presence of graphite coexisting with melt. There is no evidence to indicate that carbonate/elemental carbon/silicate buffers can be applied to the upper mantle as a whole.

In the remainder of the mantle, i.e. that not containing spinel or carbonate, silicate assemblages have insufficient Fe^{3+} content to maintain a viable buffering capacity and the system must remain essentially unbuffered. In such circumstances the fO_2 of the system is defined by the chemical potential of oxygen associated with the constituent solid phases (i.e. the intrinsic fO_2; see Sato, 1972). At any one P,T condition, the intrinsic fO_2 of a substance depends on small deviations from perfect stoichiometry and on the nature of impurity atoms occupying defect sites (see Freund et al., 1983 for a discussion of possible volatile impurities). Thus in an unbuffered, fluid-free area of the upper mantle intrinsic fO_2's will reflect a redox condition **imposed by some earlier event.** Such an event could have occurred:

(a) early in the Earth's history, e.g. core-mantle segregation, continental crust extraction, catastrophic degassing, or

(b) in some later process, e.g. magma extraction or passage, recycling of lithosphere, influx of volatiles from undegassed regions such as the lower mantle or metasomatic events.

In either case, to be observed today, fO_2-heterogeneous regions of the mantle would have had to remain effectively isolated over long time intervals. This certainly appears true of the mantle hosting diamond beneath South Africa (Richardson et al., 1984) and implies rather ineffective convective mixing and limited solid-state oxygen diffusion on a scale less than that of plate motions ($<10^3$ km). Small scale fO_2-heterogeneities may therefore have survived over long periods under fluid-absent or melt-absent conditions.

The proposal that volatile phase input, either pervasive or intense and localised, will be a plausible mechanism in creating fO_2-heterogeneous regions of the upper mantle is consistent with the inferred mantle fO_2-buffering regime outlined here.

C. Reduced Solid-State Carbon in the Upper Mantle

In the Earth's crust and mantle, reduced carbon in the solid-state may exist in several forms depending on pressure, temperature, oxidation state and kinetics of formation. The major forms are:

(a) The various polymorphs of crystalline elemental carbon: graphite, diamond and probably the carbynes (linear chain carbon polymorphs, see Whittaker, 1978; Hayatsu et al., 1980; Mathez & Delaney, 1981).
(b) Amorphous or partially ordered forms of carbon, some of which may be variably hydrogenated, i.e. "bituminous substances".
(c) Carbon in highly reduced form as the carbides cohenite (Fe_3C) and moissanite (α-SiC, various polytypes recorded).

Reduced carbon in categories (a) and (b) generally has a wide distribution in mantle materials, typically ~10-80 ppm (wt) in ultramafic nodules (Fuex & Baker, 1973; Mathez et al., 1982) and ranging up to ~150 ppm in submarine basaltic glasses (Pineau & Javoy, 1983). The latter value is probably an order of magnitude or more less than that required for reduced carbon saturation in silicate melts under pressure when compared to the carbon solubilities obtained in Section 4.8 as the limiting Fe-free system case. Degassing or oxidation processes at depth could account for low reduced carbon contents in surface erupted basaltic glasses. Elemental carbon of primary mantle origin may also be present in locally high concentrations. For example, macroscopic crystals of graphite and/or diamond are found in eclogite and peridotite nodules hosted by kimberlite (e.g. Hatton & Gurney, 1979; Shee et al., 1982; Dawson, 1980) and occur in association with ultramafic intrusives (e.g. Slodkevich, 1983).

Mathez & Delaney (1981) have discussed the nature and occurrence of dispersed primary carbonaceous material in basaltic glasses and ultramafic nodules. Attempts to characterise this material using carbon isotopes have resulted in a number of different interpretations, some controversial, e.g. Javoy et al. (1982), Pineau & Javoy (1983), Watanabe et al. (1983), Mattey et al. (1984), Poreda & Basu (1984), DesMarias & Moore (1984) and Sakai et al. (1984). Reduced carbon typically has light $\delta^{13}C$ values around -25 per mil while oxidised carbon has a so-called "mantle signature" near -5 per mil. Hypotheses for the origin of these two forms have included fractionation during degassing, separate mantle origins and unspecified organic contamination. However, a lack of adequate constraints on the nature of mantle carbon-13 reservoirs (it has now been recognised that some regions of the mantle are significantly ^{13}C depleted; Deines, 1984; Milledge et al. 1983) and the types of processes occurring during magmatic evolution make it difficult to unravel the detailed origin of dispersed reduced carbon in mantle-derived samples. A possible origin is suggested in the next section.

Hypothesis of Duba & Shankland

One of the more interesting possibilities associated with the presence of graphitic or amorphous carbon in the upper mantle has been discussed by Duba & Shankland (1982). The authors find that the presence of a layer containing only ~100 ppm of interconnected carbonaceous material would be sufficient to explain the high conductivity anomaly associated with the Low Velocity Zone.

Carbide in the Mantle

A curious and significant occurrence in mantle-derived samples is the presence of highly reduced carbon in the form of crystalline carbides. Cohenite (Fe_3C) is known only as an inclusion in diamond (Sharp, 1966) but moissanite (α-SiC) is much more widespread. Moissanite is an accessory mineral in kimberlites of the Aldan Shield, Siberian, and North China Platforms where it may reach amounts of up to 0.25% in the heavy mineral fraction (Frantsesson, 1970; He Quan-zhi, 1982). Since moissanite is also found as inclusions in porphyritic garnet lherzolite hosted by kimberlite, it is proposed by Dawson (1980) that SiC is largely a xenocrystic phase derived from mechanical disaggregation of xenoliths. Moissanite is not known directly from the South African kimberlites but has been reported together with detrital diamond in Witwatersrand conglomerates (Hallbauer et al., 1980) and a high Si-phase, probably moissanite, has been identified as an inclusion in graphite in a diamond-graphite eclogite from the Roberts Victor Mine (Hatton, 1978, p.32). In most occurrences in kimberlitic terrains moissanite is clearly an associate of diamond, in rare samples moissanite and diamond are actually intergrown (Varshavskiy & Shul'tyakov, 1967). Moissanite is also found in a wide range of non-kimberlitic volcanic rocks and placer deposits (Bauer et al., 1963; Kaminskiy et al., 1969; Lyakhovich, 1979) although some reported occurrences may have arisen from contamination by synthetic carborundum.

The clear association of moissanite with deep mantle-derived materials implies existence of extremely reduced conditions. For example, in the presence of forsterite, enstatite and carbon, SiC is stable at fO_2's near IW-8 log fO_2 units under upper mantle conditions (see MOEG buffer, Appendix 9). This is much more reducing than the fO_2 at which Fe-bearing silicates are reduced to metallic iron (or to Fe_3C in the presence of excess carbon). The occurrence of metallic Fe and even metallic Si

inclusions in moissanite (Frantsesson, 1970; Marshitsev et al., 1981) is evidence that such extreme conditions were achieved, at least transiently, during formation of the mineral. By virtue of the extreme reduction required to form SiC, this phase is incompatible at equilibrium with any known upper mantle mineral assemblage. Its persistence in the deep-mantle must therefore be a result of SiC's high chemical inertness and refractory nature (Rochow, 1973). Mantle moissanite may thus be a relict phase derived from either

(i) primordial carbides incorporated into the Earth from highly reduced source material, or

(ii) may be the product of highly reduced CH_4-H_2 fluid influx into a localised area of the upper mantle. Perhaps due to its kinetic inertness SiC is now the only remaining evidence of a reduction process that would have also involved the silicate minerals.

Process (ii) suggests a genetic link between CH_4-bearing fluids and moissanite formation as also proposed for the origin of diamond in Part 3. The close association between diamond and moissanite in nature supports the involvement of similar reduced fluids in their genesis.

5.4 Hypothesis of Redox Partial Melting Induced by Reduced Volatiles

In the previous two sections it has been demonstrated that the volumetrically most significant forms of basaltic magmatism are associated with initial oxidation states near or below MW. This is consistent with the presence of reduced carbon in submarine basaltic glasses and large basic layered intrusions, and with observed degassing of CH_4-bearing fluids at mid-ocean ridges. In the latter case, remarkable linear correlations between CH_4 and ^3He concentrations demonstrate the primordial origin of reduced volatiles. They may be released from MORB by near-surface water-rock interactions or by degassing at depth in response to crystallisation or internal redox reactions. These features accord with a dominance of upper mantle material having a redox signature lying between MW and IW although localised zones of higher oxidation, $fO_2 \sim$ FMQ, and of greater reduction, $fO_2 <$ IW, probably also occur.

Noble gas isotope systematics show that the upper mantle is largely degassed of primordial volatiles. The existence of a large, undegassed reservoir is however required to explain primordial/radiogenic noble gas isotope ratios. Other evidence correlates this undepleted reservoir with the lower mantle.

It was proposed in Section 5.2 that input of lower mantle volatiles into the upper mantle is an important process in modifying the redox state of the upper mantle particularly where fO_2 is not buffered by solid-state equilibria. Evidence of lower mantle degassing is provided by large ^3He anomalies (up to four times MORB values) in samples from Hawaii, Iceland, Samoa, Yellowstone "hot-spot" and the Ethiopian Rift (Lupton, 1983). This model for mantle degassing is most consistent with a two-layer convective mantle where an internal boundary layer at ~670 km depth effectively restricts exchange of solid material but allows fluid phase transport. Such models have been proposed recently by McKenzie & Richter (1981), Lambert (1981) and Smith (1982).

The chemical nature and oxidation state of the lower mantle is predicted to be a key factor in determining the redox evolution of the upper mantle. It was proposed in Section 5.3 that primary lower mantle fluids were likely to be CH_4-H_2 mixtures perhaps leaving evidence of their passage by extreme reduction of upper mantle material today recognised by the presence of unusually reduced phases such as moissanite. Reduced

volatiles, i.e. CH_4, C_2H_6 and H_2 have a distinct transport advantage over oxidised volatiles in that they form no known solid-state phase by interaction with mantle oxides over a wide fO_2 range (approx. IW-8 log fO_2 units to near MW where reduced volatiles become unimportant). The transport of free H_2O- or CO_2-rich fluid phases is strongly limited by carbonate or hydrate formation; the only way of transporting large amounts of C or H in oxidised form is probably via a silicate melt phase in which CO_3^{2-}, OH^- or H_2O (molecular) are dissolved. By contrast, CH_4 and H_2 will be readily transportable in a reduced fluid phase and hence have the potential to supply C and H to the upper mantle from the undegassed lower reservoir.

If CH_4-H_2 volatiles are to be degassed from lower mantle material then this implies quite reduced redox conditions, in fact well below IW. Thus there is a requirement for a fundamental fO_2 (and presumably chemical) difference between the upper and lower mantles. What evidence is there to suggest that the undegassed lower mantle is significantly reduced and chemically distinct? Answers to this question come from a number of sources:

Accretionary models of Earth formation, such as that of Smith (1982), place great emphasis on the highly reduced enstatite meteorites (chondrites and achondrites = aubrites) as source material for the accreting Earth. Intrinsic oxygen fugacity measurements on samples of equilibrated enstatite chondrites give fO_2's in the region IW-3 to IW-5 log fO_2 units (Brett & Sato, 1984; Walter & Doan, 1969). Enstatite chondrites are generally thought to form under conditions of elevated C/O ratio, near 1.0, compared with the solar value of 0.6 (Larimer & Bartholomey, 1979). Under these conditions a variety of unusual minerals are expected as early condenstates including carbides and nitrides. Smith's (1982) heterogeneous accretionary model proposes the incorporation of a significant proportion of enstatite chondritic material into the growing Earth. It is suggested that most of the enstatite chondritic silicate component is incorporated in the lower mantle while the metal-rich component (mainly Fe^o and sulphides) is segregated into the core. Enstatite chondrites also contain a few wt% carbon in reduced form, whether this is largely segregated into the core or retained in the silicate portion is unclear at present. Smith proposes that the upper mantle was accreted from more oxidised, volatile-rich material: perhaps an admixture of enstatite and carbonaceous chondritic components. Evidence is presented for the upper mantle alone being

involved in crust formation, the lower mantle is assumed to have remained effectively isolated during this process except for leakage of volatile constituents. The 670 km boundary then represents a major chemical subdivision of the Earth between a reduced, enstatitic lower mantle and a more oxidised, peridotitic upper mantle. Support for this idea comes from Ito et al's (1984) compositional constraints on lower mantle material. The authors find that lower mantle physical properties are consistent with a composition close to the bulk silicates of an enstatite chondrite. It is also highly significant that the **only** group of meteorites that lie on the same ^{17}O-^{16}O fractionation line as the Earth and Moon are the enstatite chondrites and achondrites (Clayton et al., 1984). All three bodies, i.e. Earth, Moon and enstatite meteorite parent, were therefore derived from a common oxygen reservoir.

Clayton et al. find that enstatite chondritic material with a few wt% of more volatile-rich C1 chondrite component is the best estimate for the primordial composition of the upper mantle. Most of the volatile component introduced with C1 chondrites was, however, probably lost from the upper mantle during early catastrophic degassing.

Other stable isotopic data are consistent with a terrestrial precursor of dominantly enstatite chondritic compositions (Javoy & Pineau, 1983), a view also supported by some estimates elemental abundances in the Earth (Sun, in press). In Brett's (1984) geochemical assessment of mantle-core equilibrium, it was found that upper mantle material has not been mixed very much with the remainder of the mantle following core formation. This finding is consistent with a two-layered mantle that was in-place early in the Earth's history. The concept that protomantle-protocore equilibrium was achieved during core formation is considered likely by Arculus & Delano (1981b) and possible by Brett (1984). If equilibrium did occur then core extraction is unlikely to have significantly affected original mantle redox states in the remaining silicate-rich portion since at equilibrium both silicate and metal phases would have had identical oxygen potentials. Undegassed lower mantle material should thus exhibit fO_2's similar to that found in intrinsic fO_2 measurements on enstatite chondrites, i.e. ~IW-4 log fO_2 units, although the effect of pressure on these results is not known with certainty. At lower mantle depths (>240 kbar) under fO_2 conditions near IW-4 log fO_2 units the stable carbon-bearing phase is possibly the carbide moissanite rather than diamond due to the large pressure dependance in fO_2 sensitive equilibria involving SiC

(see MOEG Appendix 9 for example). An equilibrium involving SiC, stishovite and fluid could be a potential fO_2 buffer reaction for lower mantle volatiles.

The evidence presented above although strongly model-dependant, supports the existence of an undegassed lower mantle reservoir of highly reduced character. It must be emphasised that this view is by no means universal and the opposite view, i.e. that the lower mantle is significantly oxidised in comparison with the upper mantle has been proposed (e.g. Arculus et al., 1984). Ringwood (1979, p.25) favours an identical mean composition for the upper and lower mantles. It remains to be seen whether the hypothesis presented above can be accommodated within the framework of homogeneous accretionary models of the type proposed by Ringwood(1979).

Consequences of Lower Mantle Degassing

Introduction of significant quantities of H- and C-bearing reduced volatiles into the more oxidised upper mantle will have an important role in modifying fO_2 and may even lead to partial melting accompanied by precipitation of reduced crystalline carbon. These phenomena will arise by direct redox interactions between solid mantle and a fluid of contrasting fO_2. This is illustrated in schematic fashion in Fig. 5.4A.

Initial lower mantle fluids are presumed to be highly reduced CH_4-H_2 mixtures with minor C_2H_6 and a primordial $^3He/^4He$ ratio; fO_2 may be near the stability limit of α-SiC defined by the equilibrium:

$$SiO_2(\text{stishovite}) + CH_4 = SiC + 2H_2 + O_2.$$

Influx of such a fluid into upper mantle material of higher fO_2 will cause fluid oxidation via direct redox interaction of the type:

$$H_{2(\text{fluid})} + O_{2(\text{u.mantle})} = H_2O_{(\text{fluid})}$$

or possibly by diffusive loss of H_2 to surrounding silicates where H_2 may have an appreciable solubility in lattice sites (see Freund et al., 1983). In regions of high reduced fluid flux where the fluid has not undergone significant oxidation, the adjacent mantle may exhibit locally extreme reduction with precipitation of α-SiC and reduction of Fe-bearing silicates to metallic iron (point A on Fig. 5.4A). During migration of the

Fig. 5.4A Diagram illustrating "redox melting" of the upper mantle resulting from interaction of reduced CH_4-H_2-C_2H_6 fluids of lower mantle derivation and upper mantle material of higher oxidation state. Reduced fluid influx may cause initial extreme reduction with precipitation of carbides (A). Fluid oxidation then proceeds by direct redox interaction with largely unbuffered upper mantle peridotite (B) until the carbon saturation surface is intersected and diamond or graphite precipitate (C). Continued oxidation will eventually raise fH_2O until the solidus is reached and partial melting begins (D). By this mechanism a "redox front", generated by lower mantle volatile outgassing, ascends into the upper mantle. Diagrams A to D are schematic log fO_2-X_C plots showing the evolution of the fluid phase as a function of depth (large filled circles). Lower dotted line is the upper stability limit of SiC, upper dotted line is the solidus under reduced conditions (first appearance of melt) - cf. Fig. 2.11B.

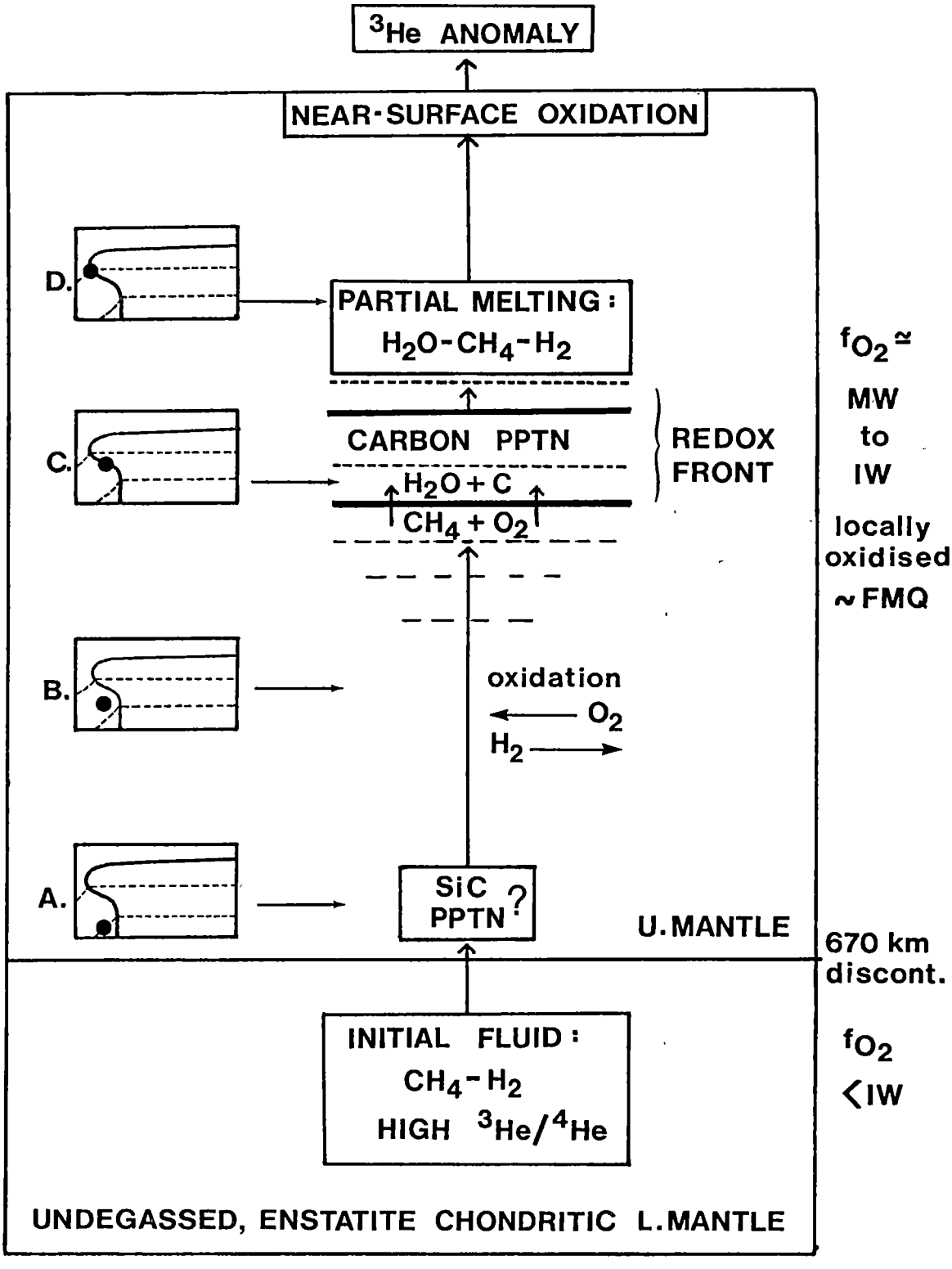
^{3}He ANOMALY
NEAR-SURFACE OXIDATION
D.
PARTIAL MELTING :
H_2O-CH_4-H_2
f_{O_2} ≃
MW
to
IW
C.
CARBON PPTN
$H_2O + C$
$CH_4 + O_2$
REDOX
FRONT
locally
oxidised
~FMQ
B.
oxidation
O_2
H_2
A.
SiC
PPTN ?
U.MANTLE
670 km
discont.
INITIAL FLUID :
CH_4-H_2
HIGH ^{3}He/^{4}He
f_{O_2}
<IW
UNDEGASSED, ENSTATITE CHONDRITIC L.MANTLE

fluid to higher levels in the upper mantle, fluid oxidation will proceed by the above processes (point B) until eventually the carbon saturation curve is intersected (point C). Here diamond or graphite will precipitate. The depth in the mantle at which this occurs will be dependant on the distribution of redox conditions as a function of depth. Thus if the ascending fluid intersects material of high oxidation state, say near MW, then oxidation will be more rapid and carbon precipitation will occur at greater depth than for material of average fO_2 near IW.

Carbon precipitation proceeds via the reaction:

$$CH_{4(fluid)} + O_{2(u.mantle)} = 2H_2O_{(fluid)} + C$$

and the fluid path will remain on the carbon saturation curve during continued oxidation. The precipitation of reduced carbon is significant for two main reasons: firstly, it marks a rapid increase in fH_2O of the fluid and secondly, on a time scale less than mechanical mixing by upper mantle convection, the zone of carbon precipitation will mark an advancing "redox front" where oxidised upper mantle is consumed, reduced carbon deposited and H_2O liberated. At the top of this front, fH_2O (and fCH_4) will reach values such that partial melting of mantle peridotite must occur (Point D, Fig. 5.4A). This corresponds to intersection with the reduced melting point "A" identified in Fig. 2.11B (Part 2). Depending on pressure and amount of fluid available a variety of melts are possible. In zones of high fluid flux, sufficient initial melting may occur to allow diapiric uprise of upper mantle material and hence more extensive melting at shallower depths. This idea is reminiscent of D.L. Anderson's (1975) deep-mantle "chemical plume" hypothesis in the sense that it represents an "upwelling of primitive material" however the "plume" in this case represents a flux of lower mantle-derived volatiles rather than a mass transfer of chemically undepleted silicate mantle. Spera (1981) has outlined some of the major properties of mantle fluids and has emphasised the importance of their heat transport capabilities particularly in localised zones of high fluid throughput. Thus local heating combined with raised fH_2O will both contribute to melting. "Hot spots" such as Hawaii that have undegassed reservoir ^3He anomalies could be products of this type of deep mantle volatile activity. More pervasive lower mantle degassing may be important, over time, in supplying the upper mantle with the volatile components C and H which may ultimately appear as components of basaltic magmas at mid-ocean ridge spreading centres.

In other areas of the mantle, perhaps subject to episodic fluid throughput, fluid-induced partial melts may be of small volume such that crystallisation and fractionation can occur at depth. Diamond and graphite-bearing eclogites are plausible products at ~40-50 kbar pressure. Diamonds hosted by harzburgites and other depleted peridotites may have a similar origin although more extensive partial melting on a regional scale is probably required. Boyd & Gurney (1982) consider that harzburgites and dunites strongly depleted in basaltic components and containing low-Ca, high-Cr pyropic garnets may be prominent constitutents in the roots of cratons. Since pyropes of low-Ca, high-Cr character are found as inclusions in diamond and as xenocrysts in kimberlites erupted within cratonic boundaries, Boyd & Gurney (1982) have suggested that depleted peridotites may be the major host for diamond crystallisation. Although a number of hypotheses to explain the diamond-low Ca pyrope association have been proposed by Boyd & Gurney (including ancient subduction and the presence of a carbonate-rich melt), the operation of a redox-melting process offers a viable alternative explanation. If the pre-cratonic South African mantle was subject to extensive flushing by deep-mantle derived CH_4-bearing fluids then large-scale melting accompanied by diamond precipitation may have taken place by the mechanisms discussed above. The passage of a redox front (or a series of redox fronts) would be effective in stripping the pre-cratonic mantle of its basaltic components leaving a highly refractory and diamondiferous harzburgitic residue. As a result, the sub-cratonic mantle would be expected, on average, to be quite reduced in character (fO_2 near IW) as expected from the composition of diamond-derived fluids discussed in Section 3.10.

An important consequence of raised fH_2O due to redox interaction is that the fluid-phase solubility of solids will increase dramatically. There is thus the potential for "mantle metasomatism" - but transport of a significant quantitity of solids can only be expected in the upper portion of the redox front (= lower portion of Low Velocity Zone?) where fH_2O is sufficiently high.

Beyond the redox front and associated partial melting zone, oxidation can proceed as far as about MW depending on the oxidation state of local mantle material. At fO_2 conditions between IW and GW silicate melts probably accommodate carbon as carbonate and perhaps as atomic carbon (a few thousand ppm/wt) which coexists with a silicate network of reduced O:Si stoichiometry (Section 4.8); Fe is presumably present dominantly or

exclusively in the divalent state. At fO_2 conditions near or above MW, methane is no longer a stable volatile species. Once methane is eliminated by oxidation reactions, a separate fluid phase can no longer exist in equilibrium with silicate melt. Carbon transport into the shallower portion of the upper mantle is thus predicted to occur largely as carbonate dissolved in a silicate melt phase. Plausible distributions of melt soluble species as a function of fO_2 are indicated in Fig. 5.4B.

In the near-surface environment degassing and other processes will result in oxidation as discussed previously. The best estimate of initial magma redox conditions for melts originating at the top of the redox front is GW to GW-1 log fO_2 units.

The above model is constructed for the passage of reduced fluids through upper mantle material of "normal" oxidation state, i.e. MW to IW. If reduced CH_4-bearing fluids interact with anomalously oxidised mantle (fO_2 ~ FMQ) then the result may be somewhat different. The large redox contrast between fluid and solid phases is likely to lead to very rapid fluid oxidation and associated carbon precipitation, H_2O production and partial melting. Provided the oxidation capacity of the anomalous zone is sufficiently large, the majority of the H- and C-components supplied by reduced fluids will enter the melt in oxidised form, i.e. as CO_3^{2-}, OH^- and H_2O (molecular). The partial melts resulting from this type of redox interaction may thus be melilititic or even kimberlitic (cf. Brey & Green, 1976a).

Final Statement and Future Work

While the above hypothesis of redox-induced partial melting is obviously speculative, the idea of deep mantle volatiles causing melting is not new (e.g. see Vollmer, 1983). The concept of redox interaction, however, has not been previously proposed. An important result of this section is the recognition that reduced volatiles (CH_4, H_2, C_2H_6) can act as a major transport medium for C and H from the undegassed deep mantle resevoir into the upper mantle.

It is proposed that evidence of fluid-solid redox reactions are preserved in the upper mantle as zones of high carbon concentration. Evidence of local partial melting may also persist in the form of carbonaceous eclogites. It is possible that in inactive areas of the

Fig. 5.4B Diagram showing the possible distribution of dissolved C-O-H volatile components in aluminosilicate melt as a function of oxygen fugacity for P ≃ 30-40 kbar, T ≃ 1500 K. Left-hand vertical axis shows the positions of various fO_2-buffers (see Appendix 9 for explanation of abbreviations). Right-hand vertical axis shows the major volatile-species in equilibrium with elemental carbon. Charge balance constraints require the presence of a reduced component (identifiable with reduction of the silicate network) at fO_2's less than approximately GW. More exotic components such as carbides and hydrides may be soluble in melts under conditions of extreme reduction.

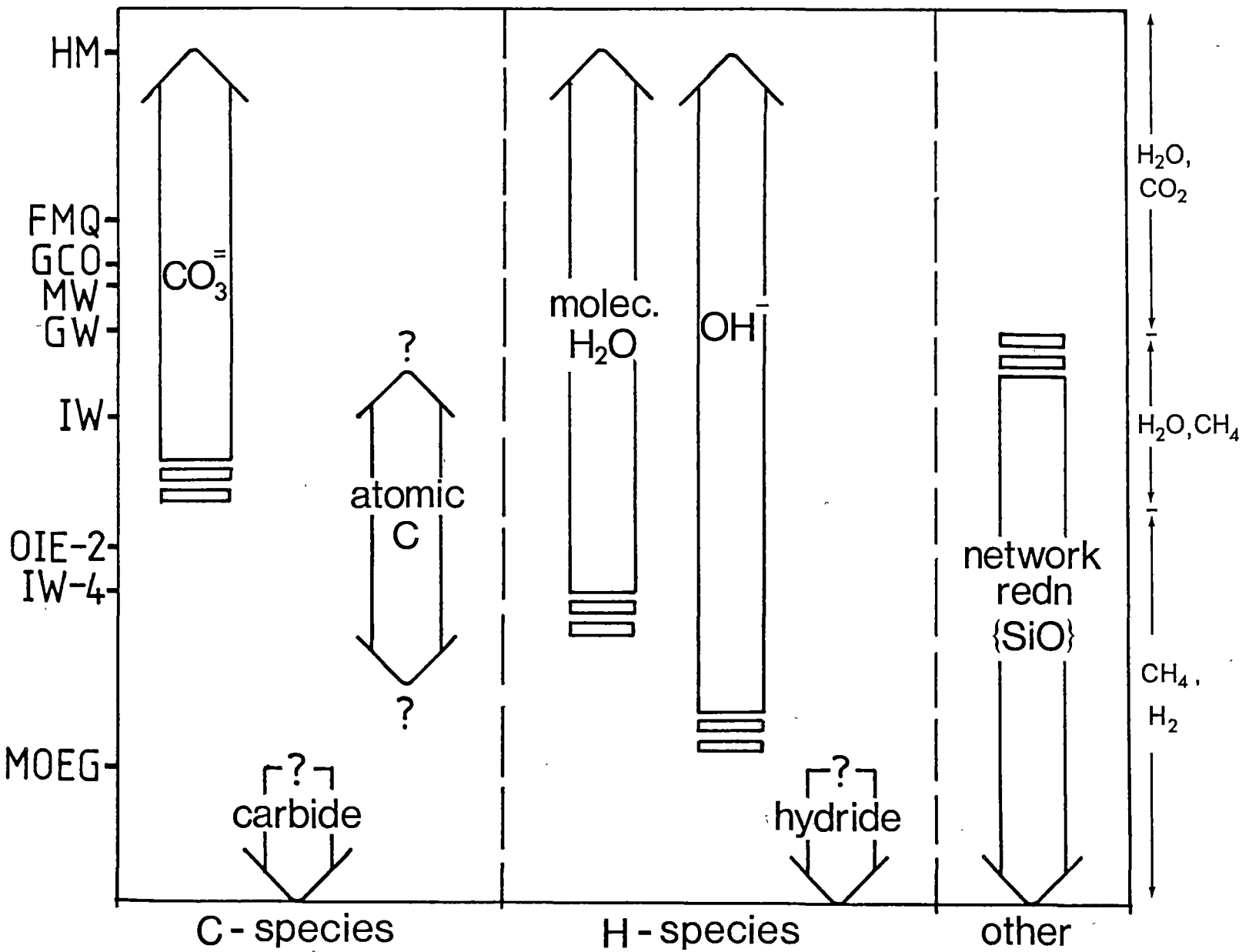
HM
FMQ
GCO
MW
GW
IW
OIE-2
IW-4
MOEG
$CO_3^=$
?
atomic
C
?
?
carbide
molec.
H_2O
OH^-
?
hydride
network
redn
{SiO}
H_2O,
CO_2
H_2O, CH_4
CH_4,
H_2
C - species
H - species
other

asthenosphere and at pressures <45 kbar "fossil redox fronts" consisting of inter-connected graphitic material may result in high conductivity anomalies exactly in the manner proposed by Duba & Shankland (1982).

Much more work is however required to substantiate these views. In particular more extensive and unbiased knowledge of the range and distribution of mantle redox environments is needed together with better constraints on mantle fluid compositions. On this latter point a detailed multi-disciplinary investigation of the nature of volatiles trapped in diamond would yield much useful information. In the area of reduced volatile interactions with silicate melts, the results presented here (Part 4) must be expanded to include transition-element-bearing aluminosilicate melts. These are probably best investigated under redox conditions near or slightly above IW where fH_2O is such that partial melting of peridotite will occur under upper mantle P,T conditions (i.e. corresponding to the reduced peridotite melting point "A" in the simple model presented in Section 2.11). The nature of the peridotite solidus under conditions more reduced than GW is completely unknown. Experimentation in these areas will be the next logical step in developing comprehensive knowledge of upper mantle melting behaviour under reduced conditions.

APPENDICES 1 TO 6

THERMOCHEMICAL, MOLAR VOLUME AND FUGACITY COEFFICIENT DATA FOR H_2O, CO_2, CO, H_2, CH_4 AND C_2H_6: EXPLANATION OF TABLES

TABLE 1: Thermochemical data at 1 bar

A Cp equation of the form

$$Cp/JK^{-1}mol^{-1} = a + bT + cT^{-2} + dT^{-1/2} + eT^{2}$$

is presented together with tabulated thermochemical functions in the style of Robie et al. (1978).

Cp	const. pressure heat capacity/$JK^{-1}mol^{-1}$
$S^{o}(T)$	std molar entropy/$JK^{-1}mol^{-1}$
$(H^{o}_{T}-H^{o}_{298})/T$	std molar enthalpy function/$JK^{-1}mol^{-1}$
$-F^{o}_{298}(T) = -(G^{o}_{T}-H^{o}_{298})/T$	std molar free energy function/$JK^{-1}mol^{-1}$
$G^{o}(T)$	std molar Gibbs free energy/$kJmol^{-1}$
$H^{o}(T)$	std molar enthalpy/$kJmol^{-1}$

The Gibbs free energy (chemical potential) of the pure species i at any pressure and temperature may be calculated using ln ϕ_i data from Table 7 and the equation:

$$\mu_{P,T} \equiv G_{P,T} = G^{o}_{1,T} + RT \ln \phi_{i(P,T)} + RT \ln (P/bar)$$

Tables 2 and 3: Plots of the P-V_m-T data-set used in regression analysis.

Plots show the distribution of data points in P-T and P-V_m space for each volatile species. The aim was to obtain an approximately uniform distribution of points from ~0.5 kbar to the maximum available pressure (typically ~10 kbar).

Units: P/bar, T/K, V_m/cm^3mol^{-1}

Scale: linear, maximum and minimum x and y values are indicated on the lower horizontal axis.

Table 4: (a) Regression statistics

Results of multiple non-linear regression fit (program FUNFIT, Veng-Pedersen, 1977) of volumetric data to the 5PMRK.

$$\text{Mean percent deviation in pressure (\%)} = \sum\left[\frac{|P_{calc}-P_{expt}|}{P_{calc}} \cdot 100\right] \Big/ n$$

n = number of sample points

where $$P_{calc} = \frac{RT(1+y+y^2-y^3)}{V_m(1-y)^3} - \frac{a_1+a_2/V+a_3/V^2}{T^{1/2}V_m(V_m+b)}$$

(b) Literature sources

Sources of experimental P-V_m-T data including P,T range of measurements and type of data smoothing and recalculation procedure employed.

Tables 5, 6, 7 and 8: Tables of molar volumes and fugacity coefficients derived from the 5PMRK.

Values are listed from 0.5-100 kbar over the ranges 400-1400°C (Tables 5 and 6) and 1000-1500 K (Tables 7 and 8).

Tables 9 and 10: Comparison of 5PMRK derived $\ln \phi_i^{pure}$ values with literature values.

Tabulations (except for ethane where comparative data is sparse) are for two temperatures (<1000 K and >1200 K). Difference values are tabulated as $\ln \phi_i$(literature) - $\ln \phi_i$(5PMRK).

Thermochemical Data for Gaseous Water(H2O) at P=1 bar.*

Cp Equation:
a= 7.3680E+00 b= 2.7468E-02 c=-2.2316E+05 d= 3.6174E+02 e=-4.8117E-06

Temp K	Cp J/mol.K	S(T) J/mol.K	(H-H298)/T J/mol.K	-F298(T) J/mol.K	G(T) kJ/mol	G(T) /RT	H(T) kJ/mol
298.15	33.57	188.83	0.000	188.83	-298.11	-120.260	-241.81
400	34.28	198.79	8.634	190.16	-317.88	-95.581	-238.36
500	35.18	206.53	13.850	192.68	-338.16	-81.343	-234.89
600	36.26	213.04	17.494	195.55	-359.14	-71.993	-231.32
700	37.45	218.72	20.259	198.46	-380.74	-65.418	-227.63
800	38.70	223.80	22.486	201.31	-402.87	-60.568	-223.82
900	39.97	228.43	24.359	204.07	-425.48	-56.861	-219.89
1000	41.24	232.71	25.984	206.73	-448.54	-53.948	-215.83
1100	42.48	236.70	27.427	209.27	-472.01	-51.610	-211.64
1200	43.69	240.45	28.733	211.72	-495.87	-49.701	-207.33
1300	44.85	243.99	29.928	214.06	-520.10	-48.119	-202.91
1400	45.95	247.36	31.033	216.32	-544.66	-46.792	-198.37
1500	46.98	250.56	32.062	218.50	-569.56	-45.669	-193.72
1600	47.96	253.62	33.026	220.60	-594.77	-44.710	-188.97
1700	48.85	256.56	33.931	222.63	-620.28	-43.885	-184.13
1800	49.68	259.38	34.783	224.59	-646.08	-43.171	-179.20

* Data Source= Robie, Hemingway & Fisher(1978).

WATER(H2O) P-V-T DATA SET
PLOT OF RESPONSE VERSUS INDEPENDENT VARIABLE X1 (ARB.UNITS)
Y= PRESSURE(BAR) X1= TEMPERATURE(K)

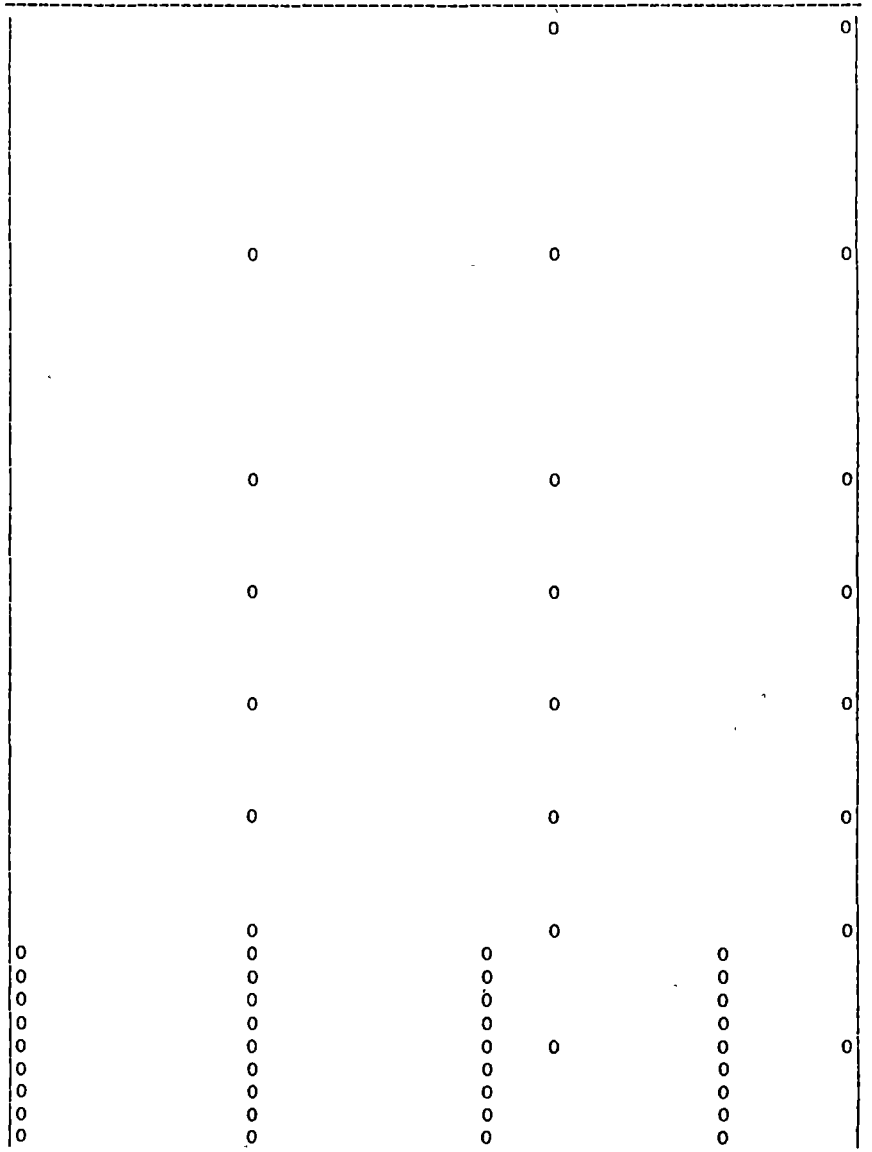

YMAX= .5000E+05 YMIN= .5690E+03 XMAX= .1273E+04 XMIN= .5730E+03

WATER(H2O) P-V-T DATA SET
PLOT OF RESPONSE VERSUS SECOND INDEPENDENT VARIABLE X2 (ARB.UNITS)
Y= PRESSURE(BAR) X2= MOLAR VOLUME(CM3/MOL)

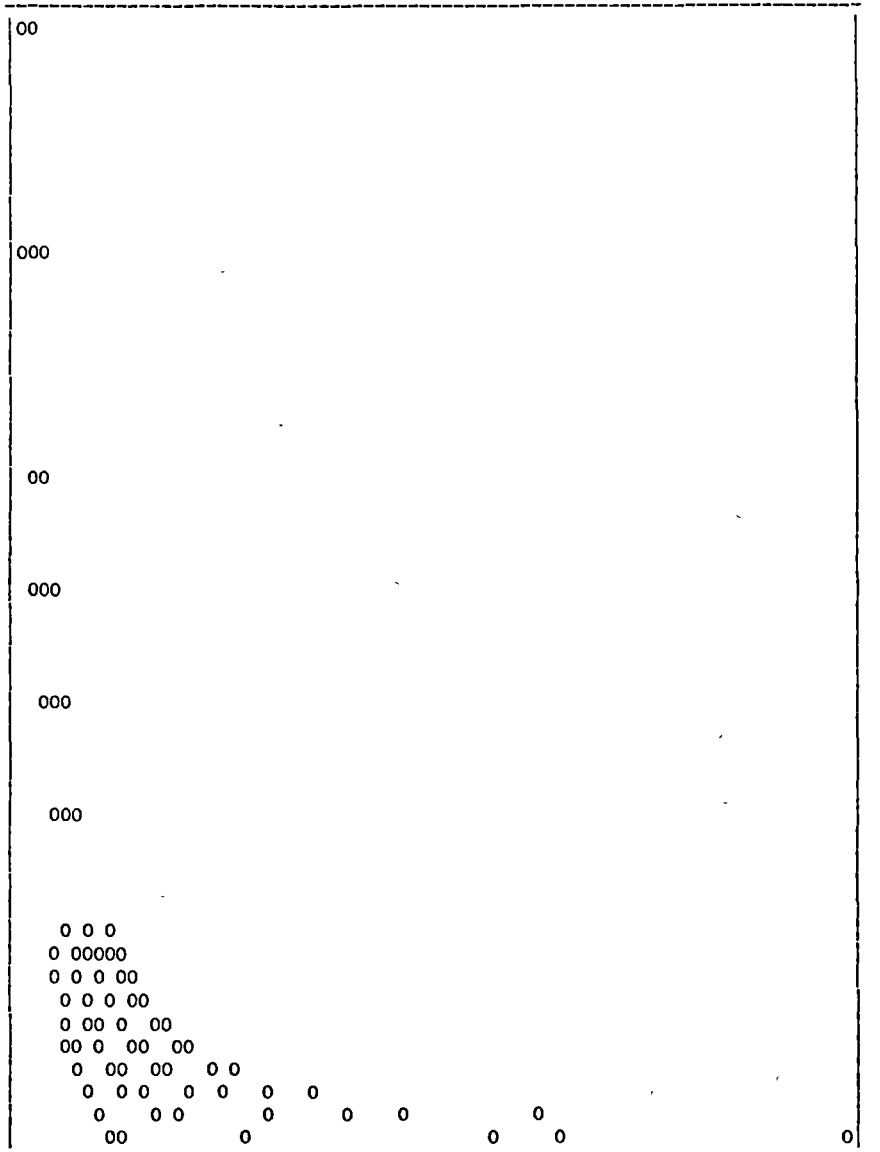

YMAX= .5000E+05 YMIN= .5690E+03 XMAX= .9117E+02 XMIN= .1349E+02

REGRESSION STATISTICS: 5-PARAMETER MRK EQN FIT TO WATER P-V-T DATA SET*

REGRESSION SUM OF SQUARES	1.04677E+10	(0.93104E+10)**
RESIDUALS SUM OF SQUARES	1.33296E+08	(1.29055E+08)
RESIDUALS MEAN SQUARE	1.40311E+06	(1.35847E+07)
MEAN OF RESIDUALS	-369.63	(-1419.3)
STD DEVIATION OF RESIDUALS	1184.53	(3685.75)
MULTIPLE CORRELATION COEFFICIENT R	0.995507	(0.997757)
MEAN PERCENT DEVIATION (ALL DATA)	4.65%	(6.61%)
MEAN PERCENT DEVIATION (DATA PTS >772K)	4.04%	(6.12%)

* Program FUNFIT, Veng-Pedersen(1977).
** Fit statistics for 10-parameter MRK eqn of Kerrick & Jacobs(1981) in brackets.

LITERATURE SOURCES AND RANGE OF WATER P-V-T DATA SET

	P Range/kbar	T Range/K
Tanishita et.al.(1976)*	0.5- 1.5	573- 773
Burnham, Holloway & Davis(1969a)**	1.0- 8.9	573-1173
Rice & Walsh(1957)***	5.0-50.0	773-1273

* unsmoothed experimental results.
** volumetric data smoothed by best fit to high order polynomials in P,T.
*** calculated values from shock-wave studies.

WATER(H2O) : TABLE OF MOLAR VOLUMES[cm3/mol] 5-PARAMETER MRK EQUATION

b1=2.134E+01 b2=5.420E+03 a1=1.329E+08 a2=2.541E+09 a3=1.915E+10

Pressure (kbar)	Temperature (K/degC): 673.15 400	873.15 600	1073.15 800	1273.15 1000	1473.15 1200	1673.15 1400
0.5	28.96	110.53	162.35	204.90	243.95	281.19
1.0	25.42	47.20	77.60	102.04	123.60	143.65
1.5	23.69	34.95	52.80	69.61	84.69	98.65
2.0	22.55	30.25	42.11	54.44	65.91	76.63
2.5	21.71	27.62	36.36	45.87	55.03	63.69
3.0	21.04	25.87	32.77	40.43	47.98	55.23
4.0	20.04	23.60	28.45	33.91	39.45	44.87
5.0	19.30	22.13	25.89	30.12	34.47	38.77
6.0	18.71	21.07	24.15	27.60	31.18	34.75
7.0	18.23	20.25	22.86	25.79	28.83	31.88
8.0	17.83	19.59	21.86	24.40	27.05	29.72
9.0	17.48	19.05	21.06	23.31	25.65	28.02
10.0	17.17	18.58	20.39	22.41	24.52	26.65
15.0	16.06	16.98	18.18	19.53	20.95	22.39
20.0	15.33	15.99	16.89	17.91	18.99	20.10
25.0	14.79	15.29	16.01	16.84	17.72	18.62
30.0	14.37	14.76	15.36	16.05	16.79	17.56
35.0	14.03	14.34	14.84	15.44	16.09	16.76
40.0	13.75	13.99	14.43	14.95	15.53	16.12
50.0	13.30	13.45	13.78	14.20	14.67	15.16
100.0	12.06	12.00	12.12	12.31	12.56	12.82

WATER(H2O) : TABLE OF ln(FUGACITY COEFFICIENTS) 5-PARAMETER MRK EQUATION

b1=2.134E+01 b2=5.420E+03 a1=1.329E+08 a2=2.541E+09 a3=1.915E+10

Pressure (kbar)	Temperature (K/degC): 673.15 400	873.15 600	1073.15 800	1273.15 1000	1473.15 1200	1673.15 1400
0.5	-0.836	-0.240	-0.099	-0.039	-0.009	0.008
1.0	-1.289	-0.454	-0.178	-0.064	-0.008	0.021
1.5	-1.476	-0.585	-0.229	-0.075	0.000	0.040
2.0	-1.557	-0.650	-0.254	-0.074	0.016	0.063
2.5	-1.583	-0.675	-0.259	-0.062	0.038	0.091
3.0	-1.574	-0.673	-0.248	-0.041	0.065	0.121
4.0	-1.495	-0.621	-0.195	0.019	0.131	0.189
5.0	-1.367	-0.530	-0.115	0.097	0.208	0.265
6.0	-1.210	-0.415	-0.017	0.187	0.292	0.346
7.0	-1.035	-0.285	0.092	0.284	0.383	0.431
8.0	-0.846	-0.144	0.209	0.388	0.477	0.519
9.0	-0.648	0.004	0.331	0.495	0.574	0.608
10.0	-0.444	0.158	0.458	0.606	0.673	0.699
15.0	0.631	0.972	1.127	1.183	1.187	1.165
20.0	1.743	1.817	1.819	1.776	1.712	1.638
25.0	2.864	2.669	2.516	2.373	2.236	2.109
30.0	3.984	3.521	3.212	2.966	2.757	2.576
35.0	5.098	4.368	3.903	3.555	3.274	3.038
40.0	6.206	5.210	4.590	4.139	3.785	3.495
50.0	8.397	6.875	5.945	5.291	4.793	4.394
100.0	18.949	14.868	12.433	10.787	9.584	8.657

WATER(H2O) : TABLE OF MOLAR VOLUMES[cm3/mol] 5-PARAMETER MRK EQUATION

b1=2.134E+01 b2=5.420E+03 a1=1.329E+08 a2=2.541E+09 a3=1.915E+10

Pressure (kbar)	Temperature (K/degC): 1000 727	1100 827	1200 927	1300 1027	1400 1127	1500 1227
0.5	145.12	168.38	189.89	210.29	229.93	249.03
1.0	67.36	81.14	93.55	105.06	115.94	126.36
1.5	46.17	55.18	63.70	71.72	79.33	86.61
2.0	37.54	43.80	50.02	56.03	61.82	67.39
2.5	32.96	37.63	42.41	47.13	51.74	56.22
3.0	30.08	33.78	37.61	41.46	45.25	48.98
4.0	26.57	29.17	31.89	34.66	37.43	40.19
5.0	24.44	26.44	28.54	30.70	32.88	35.05
6.0	22.96	24.59	26.31	28.08	29.86	31.66
7.0	21.86	23.24	24.69	26.19	27.71	29.24
8.0	20.99	22.19	23.46	24.75	26.08	27.41
9.0	20.29	21.35	22.47	23.62	24.79	25.97
10.0	19.70	20.65	21.65	22.69	23.74	24.80
15.0	17.72	18.36	19.03	19.72	20.43	21.14
20.0	16.54	17.02	17.53	18.06	18.60	19.14
25.0	15.73	16.12	16.53	16.95	17.39	17.84
30.0	15.12	15.44	15.79	16.15	16.52	16.90
35.0	14.64	14.92	15.22	15.53	15.85	16.18
40.0	14.25	14.49	14.75	15.03	15.31	15.61
50.0	13.65	13.83	14.04	14.27	14.50	14.74
100.0	12.06	12.14	12.23	12.34	12.46	12.59

WATER(H2O) : TABLE OF ln(FUGACITY COEFFICIENTS) 5-PARAMETER MRK EQUATION

b1=2.134E+01 b2=5.420E+03 a1=1.329E+08 a2=2.541E+09 a3=1.915E+10

Pressure (kbar)	Temperature (K/degC): 1000 727	1100 827	1200 927	1300 1027	1400 1127	1500 1227
0.5	-0.136	-0.088	-0.056	-0.034	-0.018	-0.006
1.0	-0.249	-0.157	-0.096	-0.054	-0.025	-0.003
1.5	-0.324	-0.201	-0.118	-0.062	-0.022	0.007
2.0	-0.363	-0.221	-0.125	-0.058	-0.010	0.024
2.5	-0.375	-0.223	-0.118	-0.044	0.009	0.047
3.0	-0.369	-0.211	-0.101	-0.022	0.034	0.075
4.0	-0.318	-0.157	-0.043	0.039	0.098	0.141
5.0	-0.235	-0.077	0.035	0.117	0.175	0.218
6.0	-0.133	0.019	0.127	0.205	0.262	0.302
7.0	-0.018	0.126	0.228	0.302	0.354	0.392
8.0	0.106	0.240	0.336	0.404	0.452	0.485
9.0	0.237	0.360	0.448	0.509	0.552	0.581
10.0	0.372	0.485	0.564	0.618	0.655	0.679
15.0	1.085	1.139	1.170	1.186	1.190	1.186
20.0	1.825	1.815	1.796	1.769	1.737	1.702
25.0	2.571	2.497	2.424	2.354	2.285	2.219
30.0	3.315	3.176	3.051	2.936	2.830	2.732
35.0	4.056	3.852	3.673	3.514	3.371	3.240
40.0	4.791	4.522	4.290	4.087	3.906	3.743
50.0	6.243	5.845	5.508	5.217	4.962	4.734
100.0	13.204	12.177	11.325	10.605	9.985	9.446

WATER(H2O) ln(FUGACITY COEFFICIENTS) : A COMPARISON OF 5-PARAMETER MRK EQN DERIVED COEFFICIENTS WITH LITERATURE VALUES. Temp= 873.15 K (600 degC).

Pressure (kbar)	ln(fugacity coefficient) (this work)	Difference (literature value*)minus(this work):				
		KJ	SHE	DH&HK	HC	BHD
0.5	-0.240	-0.004	0.043	-0.002	-0.002	-0.007
1.0	-0.454	0.002	0.089	0.001	-0.001	-0.005
1.5	-0.585	0.005	0.113			0.000
2.0	-0.650	0.008	0.125	0.009	0.008	0.002
2.5	-0.675	0.010	0.132			0.002
3.0	-0.673	0.011	0.135	0.013	0.012	0.004
4.0	-0.621	0.013	0.139	0.016	0.013	0.005
5.0	-0.530	0.017	0.142	0.019	0.013	0.009
6.0	-0.415	0.020	0.144	0.022	0.013	0.012
7.0	-0.285	0.023	0.147	0.025	0.012	0.015
8.0	-0.144	0.027	0.149	0.027	0.009	0.017
9.0	0.004	0.031	0.153	0.029	0.008	0.004
10.0	0.158	0.035	0.157	0.029	0.005	0.020
15.0	0.972	0.056	0.190	-0.026		
20.0	1.817	0.080	0.243	-0.046	-0.033	
25.0	2.669	0.105	0.313			
30.0	3.521	0.131	0.397	-0.077	-0.091	
40.0	5.210	0.184	0.602	-0.133	-0.168	
50.0	6.875	0.239	0.847	-0.207	-0.262	
100.0	14.868	0.529	2.488	-0.774	-0.921	

* KJ = Kerrick & Jacobs(1981).
SHE = Sykes, Holloway & Eichon(1978).
DH = Delany & Helgeson(1978) over P interval 10-100 kbar.
HK = Helgeson & Kirkham(1974) over P interval 0.5-9.0 kbar.
HC = Halbach & Chatterjee(1982) Appendix.B using G(f,T)H2O at 1 bar from Robie, Hemingway & Fisher(1978).
BHD = Burnham, Holloway & Davis(1969b).

WATER(H2O) ln(FUGACITY COEFFICIENTS) : A COMPARISON OF 5-PARAMETER MRK EQN DERIVED COEFFICIENTS WITH LITERATURE VALUES. Temp= 1273.15 K (1000 degC).

Pressure (kbar)	ln(fugacity coefficient) (this work)	Difference (literature value*)minus(this work):			
		KJ	SHE	HC	BHD
0.5	-0.039	0.003	0.015	0.006	
1.0	-0.064	0.006	0.027	0.008	0.002
1.5	-0.075	0.009	0.036		0.002
2.0	-0.074	0.011	0.043	0.011	0.004
2.5	-0.062	0.012	0.047		0.005
3.0	-0.041	0.012	0.049	0.010	0.004
4.0	0.019	0.012	0.052	0.008	0.001
5.0	0.097	0.011	0.052	0.005	-0.005
6.0	0.187	0.011	0.051	0.000	-0.011
7.0	0.284	0.013	0.051	-0.003	-0.010
8.0	0.388	0.014	0.050	-0.009	-0.010
9.0	0.495	0.017	0.050	-0.013	-0.006
10.0	0.606	0.019	0.050	-0.019	-0.004
15.0	1.183	0.040	0.061		
20.0	1.776	0.069	0.086	-0.071	
25.0	2.373	0.101	0.123		
30.0	2.966	0.138	0.172	-0.132	
40.0	4.139	0.216	0.299	-0.199	
50.0	5.291	0.300	0.457	-0.274	
100.0	10.787	0.755	1.569	-0.742	

* KJ = Kerrick & Jacobs(1981).
SHE = Sykes, Holloway & Eichon(1978).
HC = Halbach & Chatterjee(1982) Appendix.B using G(f,T)H2O at 1 bar from Robie, Hemingway & Fisher(1978).
BHD = Burnham, Holloway & Davis(1969b).

Thermochemical Data for Gaseous Carbon Dioxide(CO2) at P= 1 bar.*

Cp Equation:
a= 8.7820E+01 b=-2.6442E-03 c= 7.0641E+05 d=-9.9886E+02 e= 0.

Temp K	Cp J/mol.K	S(T) J/mol.K	(H-H298)/T J/mol.K	-F298(T) J/mol.K	G(T) kJ/mol	G(T) /RT	H(T) kJ/mol
298.15	37.13	213.79	0.000	213.79	-457.25	-184.457	-393.51
400	41.23	225.28	9.985	215.30	-479.63	-144.218	-389.52
500	44.65	234.87	16.589	218.28	-502.65	-120.912	-385.22
600	47.42	243.26	21.505	221.76	-526.56	-105.554	-380.61
700	49.66	250.74	25.372	225.37	-551.27	-94.720	-375.75
800	51.49	257.50	28.526	228.97	-576.69	-86.701	-370.69
900	53.02	263.65	31.165	232.49	-602.75	-80.551	-365.46
1000	54.30	269.31	33.416	235.89	-629.40	-75.701	-360.09
1100	55.38	274.54	35.365	239.17	-656.60	-71.793	-354.61
1200	56.30	279.39	37.072	242.32	-684.30	-68.586	-349.02
1300	57.10	283.93	38.583	245.35	-712.47	-65.917	-343.35
1400	57.78	288.19	39.930	248.26	-741.07	-63.666	-337.61
1500	58.38	292.20	41.141	251.06	-770.10	-61.749	-331.80
1600	58.89	295.98	42.234	253.75	-799.51	-60.100	-325.93
1700	59.34	299.57	43.228	256.34	-829.29	-58.672	-320.02
1800	59.74	302.97	44.134	258.84	-859.41	-57.425	-314.07

* Data Source= Robie, Hemingway & Fisher(1978)

CARBON DIOXIDE(CO2) P-V-T DATA SET
PLOT OF RESPONSE VERSUS INDEPENDENT VARIABLE X1 (ARB.UNITS)
Y= PRESSURE(BAR) X1= TEMPERATURE(K)

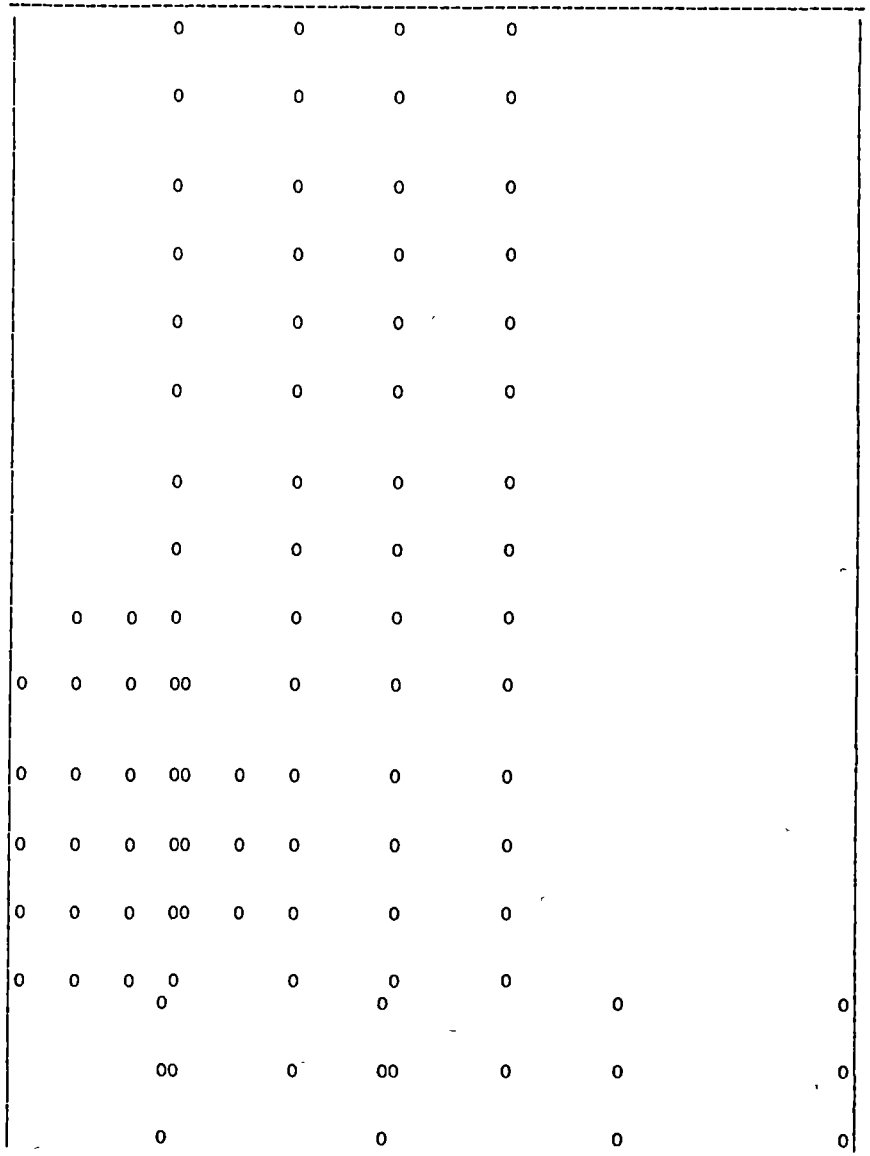

YMAX= .8000E+04 YMIN= .5000E+03 XMAX= .1273E+04 XMIN= .5480E+03

CARBON DIOXIDE(CO2) P-V-T DATA SET
PLOT OF RESPONSE VERSUS SECOND INDEPENDENT VARIABLE X2 (ARB.UNITS)
Y= PRESSURE(BAR) X2= MOLAR VOLUME(CM3/MOL)

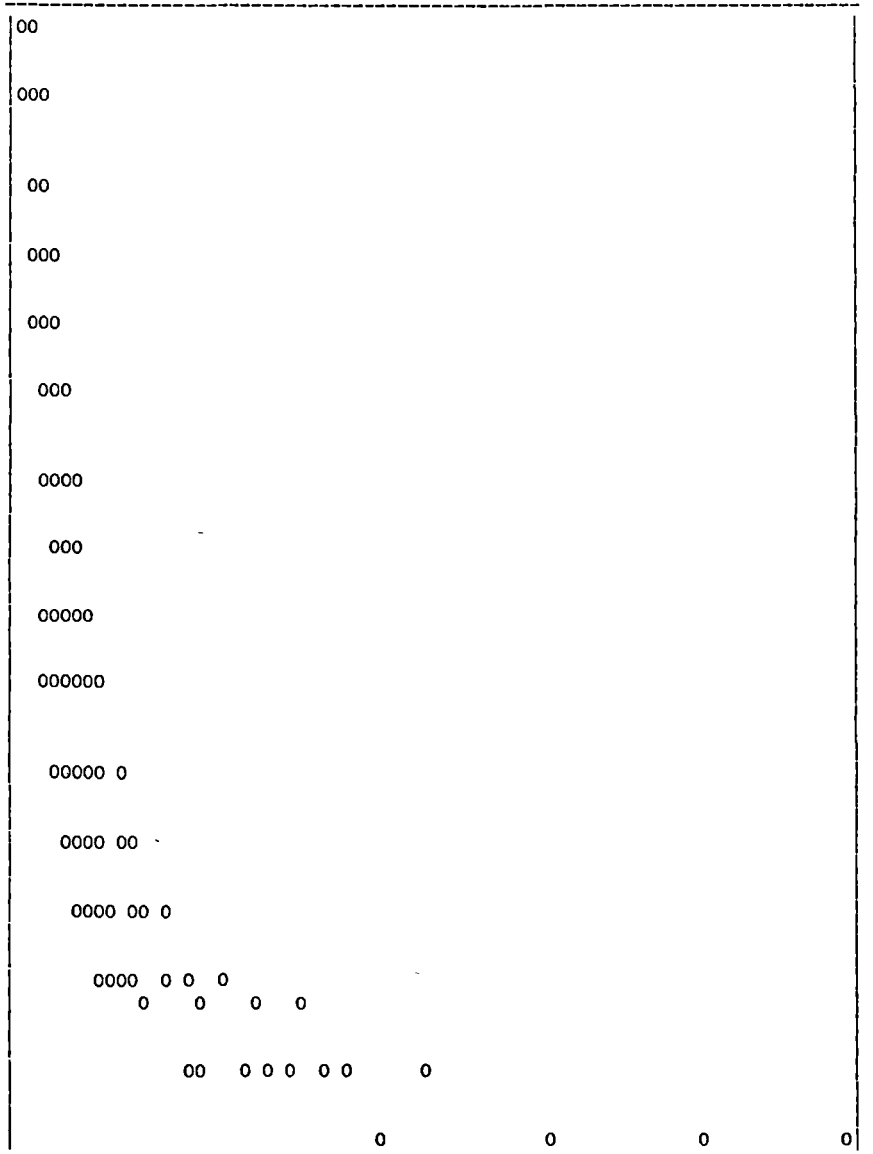

YMAX= .8000E+04 YMIN= .5000E+03 XMAX= .2356E+03 XMIN= .3407E+02

REGRESSION STATISTICS: 5-PARAMETER MRK EQN FIT TO CO2 P-V-T DATA SET*

REGRESSION SUM OF SQUARES	4.42666E+08	(4.42836E+08)**
RESIDUALS SUM OF SQUARES	5.01446E+06	(4.84426E+06)
RESIDUALS MEAN SQUARE	5.22339E+04	(5.04611E+04)
MEAN OF RESIDUALS	10.311	(43.861)
STD DEVIATION OF RESIDUALS	228.547	(224.635)
MULTIPLE CORRELATION COEFFICIENT R	0.995779	(0.996908)
MEAN PERCENT DEVIATION (ALL DATA)	3.42%	(2.55%)
MEAN PERCENT DEVIATION (DATA PTS >872K)	3.15%	(2.92%)

* Program FUNFIT, Veng-Pedersen(1977).

** Fit statistics for 10-parameter MRK eqn of Kerrick & Jacobs(1981) in brackets.

LITERATURE SOURCES AND RANGE OF CARBON DIOXIDE P-V-T DATA SET

	P Range/kbar	T Range/K
Kennedy & Holser(1966)*	0.5-1.4	673-1273
Juza, Kmonicek & Sifner(1965)*	1.5-4.0	548- 748
Shmonov & Shmulovich(1974)*	1.0-8.0	681- 981

* experimental volumetric measurements presented in smoothed form; smoothing procedure specified.

CARBON DIOXIDE(CO2) : TABLE OF MOLAR VOLUMES[cm3/mol] 5-PARAMETER MRK EQN

b1=4.553E+01 b2=1.073E+04 a1=1.287E+08 a2=1.122E+09 a3=4.443E+11

Pressure (kbar)	Temperature (K/degC): 673.15 400	873.15 600	1073.15 800	1273.15 1000	1473.15 1200	1673.15 1400
0.5	120.90	163.45	202.59	239.85	276.00	311.43
1.0	75.00	96.73	117.14	136.53	155.24	173.48
1.5	60.47	74.80	88.74	102.05	114.86	127.33
2.0	53.26	63.80	74.39	84.60	94.44	104.00
2.5	48.87	57.13	65.66	73.97	82.01	89.81
3.0	45.86	52.61	59.75	66.77	73.58	80.20
4.0	41.91	46.81	52.17	57.54	62.80	67.92
5.0	39.36	43.18	47.46	51.82	56.12	60.33
6.0	37.54	40.64	44.20	47.88	51.53	55.11
7.0	36.15	38.75	41.79	44.97	48.15	51.28
8.0	35.04	37.26	39.92	42.72	45.54	48.33
9.0	34.13	36.06	38.42	40.92	43.46	45.97
10.0	33.36	35.06	37.17	39.44	41.75	44.04
15.0	30.75	31.74	33.13	34.67	36.27	37.89
20.0	29.17	29.80	30.81	31.98	33.22	34.49
25.0	28.07	28.49	29.26	30.20	31.22	32.26
30.0	27.24	27.51	28.13	28.91	29.77	30.66
35.0	26.59	26.74	27.25	27.92	28.66	29.44
40.0	26.05	26.12	26.54	27.12	27.78	28.47
50.0	25.22	25.16	25.45	25.90	26.43	27.01
100.0	23.02	22.69	22.70	22.86	23.12	23.42

CARBON DIOXIDE(CO2) : TABLE OF ln(FUGACITY COEFFICIENTS) 5-PARAMETER MRK EQN

b1=4.553E+01 b2=1.073E+04 a1=1.287E+08 a2=1.122E+09 a3=4.443E+11

Pressure (kbar)	Temperature (K/degC): 673.15 400	873.15 600	1073.15 800	1273.15 1000	1473.15 1200	1673.15 1400
0.5	-0.048	0.070	0.107	0.117	0.117	0.114
1.0	0.085	0.220	0.255	0.257	0.248	0.236
1.5	0.276	0.395	0.416	0.404	0.383	0.360
2.0	0.493	0.581	0.581	0.554	0.519	0.484
2.5	0.725	0.772	0.749	0.703	0.654	0.607
3.0	0.965	0.967	0.917	0.852	0.788	0.729
4.0	1.458	1.361	1.252	1.148	1.053	0.970
5.0	1.960	1.756	1.586	1.440	1.314	1.206
6.0	2.463	2.150	1.916	1.727	1.570	1.437
7.0	2.967	2.542	2.243	2.011	1.822	1.665
8.0	3.469	2.931	2.567	2.291	2.071	1.889
9.0	3.969	3.318	2.888	2.568	2.316	2.110
10.0	4.467	3.702	3.206	2.842	2.558	2.328
15.0	6.913	5.585	4.758	4.174	3.732	3.382
20.0	9.297	7.412	6.257	5.456	4.858	4.390
25.0	11.627	9.194	7.714	6.699	5.948	5.364
30.0	13.914	10.938	9.139	7.911	7.009	6.311
35.0	16.163	12.652	10.535	9.098	8.046	7.236
40.0	18.380	14.338	11.908	10.264	9.064	8.143
50.0	22.733	17.644	14.595	12.542	11.051	9.911
100.0	43.433	33.294	27.266	23.245	20.355	18.168

CARBON DIOXIDE(CO2) : TABLE OF MOLAR VOLUMES[cm3/mol] 5-PARAMETER MRK EQN

b1=4.553E+01 b2=1.073E+04 a1=1.287E+08 a2=1.122E+09 a3=4.443E+11

Pressure (kbar)	Temperature (K/degC): 1000 727	1100 827	1200 927	1300 1027	1400 1127	1500 1227
0.5	188.55	207.68	226.38	244.76	262.88	280.79
1.0	109.82	119.80	129.54	139.08	148.46	157.71
1.5	83.72	90.56	97.25	103.79	110.22	116.56
2.0	70.56	75.79	80.91	85.94	90.88	95.74
2.5	62.56	66.79	70.96	75.06	79.10	83.07
3.0	57.14	60.70	64.22	67.69	71.11	74.48
4.0	50.19	52.89	55.59	58.25	60.89	63.50
5.0	45.87	48.04	50.23	52.40	54.56	56.69
6.0	42.88	44.69	46.53	48.37	50.20	52.01
7.0	40.65	42.22	43.80	45.40	46.99	48.57
8.0	38.92	40.29	41.69	43.10	44.51	45.92
9.0	37.53	38.75	40.00	41.26	42.53	43.80
10.0	36.37	37.47	38.60	39.75	40.90	42.06
15.0	32.59	33.33	34.09	34.88	35.68	36.49
20.0	30.42	30.96	31.54	32.15	32.77	33.39
25.0	28.95	29.38	29.85	30.34	30.84	31.36
30.0	27.88	28.23	28.61	29.02	29.45	29.89
35.0	27.04	27.33	27.66	28.01	28.38	28.76
40.0	26.36	26.61	26.89	27.20	27.53	27.87
50.0	25.32	25.51	25.73	25.97	26.23	26.51
100.0	22.67	22.71	22.79	22.89	23.02	23.15

CARBON DIOXIDE(CO2) : TABLE OF ln(FUGACITY COEFFICIENTS) 5-PARAMETER MRK EQN

b1=4.553E+01 b2=1.073E+04 a1=1.287E+08 a2=1.122E+09 a3=4.443E+11

Pressure (kbar)	Temperature (K/degC): 1000 727	1100 827	1200 927	1300 1027	1400 1127	1500 1227
0.5	0.098	0.109	0.115	0.118	0.118	0.117
1.0	0.248	0.256	0.258	0.256	0.252	0.247
1.5	0.414	0.415	0.410	0.402	0.392	0.380
2.0	0.586	0.578	0.565	0.549	0.532	0.514
2.5	0.762	0.743	0.721	0.697	0.672	0.648
3.0	0.938	0.909	0.876	0.844	0.811	0.780
4.0	1.292	1.238	1.185	1.135	1.087	1.042
5.0	1.645	1.565	1.490	1.421	1.358	1.298
6.0	1.995	1.889	1.792	1.704	1.624	1.551
7.0	2.343	2.209	2.090	1.983	1.887	1.799
8.0	2.688	2.526	2.384	2.259	2.146	2.044
9.0	3.029	2.840	2.676	2.531	2.402	2.286
10.0	3.368	3.151	2.964	2.800	2.655	2.524
15.0	5.024	4.668	4.367	4.108	3.881	3.681
20.0	6.626	6.133	5.720	5.366	5.059	4.789
25.0	8.186	7.557	7.032	6.585	6.199	5.861
30.0	9.711	8.948	8.313	7.775	7.310	6.905
35.0	11.207	10.312	9.568	8.939	8.397	7.926
40.0	12.678	11.652	10.801	10.082	9.464	8.927
50.0	15.560	14.275	13.212	12.315	11.547	10.880
100.0	29.167	26.636	24.552	22.804	21.314	20.028

C.DIOXIDE(CO2) ln(FUGACITY COEFFICIENTS) : A COMPARISON OF 5-PARAMETER MRK EQN DERIVED COEFFICIENTS WITH LITERATURE VALUES. Temp= 1300 K (1027 degC).

Pressure (kbar)	ln(fugacity coefficient) (this work)	Difference (literature value*)minus(this work):				
		SB	H	SS	BR	KJ
0.5	0.118	-0.020	0.003	-0.013	-0.014	-0.002
1.0	0.256	-0.049	-0.010	-0.017	-0.021	0.001
1.5	0.402	-0.079	-0.027	-0.022	-0.045	0.002
2.0	0.549	-0.105	-0.043	-0.024	-0.064	0.004
2.5	0.697	-0.129	-0.060	-0.025	-0.065	0.005
3.0	0.844	-0.149	-0.074	-0.023	-0.080	0.006
4.0	1.135	-0.182	-0.097	-0.013	-0.085	0.008
5.0	1.421	-0.205	-0.113	-0.002	-0.085	0.011
6.0	1.704	-0.222	-0.125	0.004	-0.088	0.014
7.0	1.983	-0.234	-0.133	0.004	-0.077	0.018
8.0	2.259	-0.241	-0.136	-0.003	-0.061	0.022
9.0	2.531	-0.244	-0.136	-0.018	-0.053	0.028
10.0	2.800	-0.242	-0.131	-0.040	-0.048	0.034
15.0	4.108	-0.190	-0.071		-0.031	0.069
20.0	5.366	-0.083	0.041		-0.032	0.112
25.0	6.585	0.066	0.187		-0.040	0.160
30.0	7.775	0.246	0.377		-0.043	0.209
35.0	8.939	0.453	0.585		-0.038	0.261
40.0	10.082	0.681	0.816		-0.047	0.315
50.0	12.315	1.191	1.329			0.426
100.0	22.804	4.427	4.577			1.003

* SB = Spera & Bergman(1980).
H = Holloway(1977).
SS = Shumlovich & Shmonov(1975).
BR = Bottinga & Richet(1981).
KJ = Kerrick & Jacobs(1981).

C.DIOXIDE(CO2) ln(FUGACITY COEFFICIENTS) : A COMPARISON OF 5-PARAMETER MRK EQN DERIVED COEFFICIENTS WITH LITERATURE VALUES. Temp= 1000 K (727 degC).

Pressure (kbar)	ln(fugacity coefficient) (this work)	Difference (literature value*)minus(this work):				
		SB	H	SS	BR	KJ
0.5	0.098	0.020	0.038	0.003	-0.010	0.011
1.0	0.248	0.008	0.039	-0.003	-0.011	0.015
1.5	0.414	-0.008	0.032	-0.009	-0.030	0.018
2.0	0.586	-0.022	0.024	-0.009	-0.044	0.021
2.5	0.762	-0.036	0.015	-0.009	-0.047	0.023
3.0	0.938	-0.046	0.009	-0.005	-0.056	0.025
4.0	1.292	-0.062	-0.002	0.007	-0.048	0.030
5.0	1.645	-0.071	-0.007	0.019	-0.035	0.035
6.0	1.995	-0.074	-0.007	0.027	-0.026	0.041
7.0	2.343	-0.073	-0.003	0.028	-0.011	0.046
8.0	2.688	-0.068	0.005	0.022	-0.009	0.052
9.0	3.029	-0.057	0.017	0.010	-0.010	0.059
10.0	3.368	-0.043	0.032	-0.010	-0.010	0.065
15.0	5.024	0.072	0.152		-0.014	0.099
20.0	6.626	0.247	0.331	OR 0.282	-0.040	0.133
25.0	8.186	0.467	0.554		-0.067	0.168
30.0	9.711	0.724	0.812		-0.078	0.203
35.0	11.207	1.011	1.101			0.239
40.0	12.678	1.323	1.415			0.275
50.0	15.560	2.008	2.103			0.345
100.0	29.167	6.246	6.353	OR -3.378		0.691

* SB = Spera & Bergman(1980).
H = Holloway(1977).
SS = Shumlovich & Shmonov(1975).
BR = Bottinga & Richet(1981).
KJ = Kerrick & Jacobs(1981).
OR = Ostrovsky & Ryzhenko(1978) values at 20 and 100 kbars.

Thermochemical Data for Gaseous Carbon Monoxide(CO) at P=1 bar.*

Cp Equation:
a= 4.5730E+01 b=-9.7115E-05 c= 6.6270E+05 d=-4.1469E+02 e= 0.

Temp K	Cp J/mol.K	S(T) J/mol.K	(H-H298)/T J/mol.K	-F298(T) J/mol.K	G(T) kJ/mol	G(T) /RT	H(T) kJ/mol
298.15	29.14	197.67	0.000	197.67	-169.47	-68.363	-110.53
400	29.10	206.19	7.384	198.81	-190.05	-57.146	-107.58
500	29.79	212.75	11.791	200.96	-211.01	-50.759	-104.63
600	30.58	218.25	14.857	203.40	-232.57	-46.620	-101.62
700	31.34	223.03	17.158	205.87	-254.64	-43.752	-98.52
800	32.03	227.26	18.975	208.28	-277.16	-41.669	-95.35
900	32.64	231.07	20.459	210.61	-300.08	-40.102	-92.12
1000	33.18	234.53	21.705	212.83	-323.36	-38.892	-88.83
1100	33.67	237.72	22.771	214.95	-346.97	-37.938	-85.48
1200	34.10	240.67	23.697	216.97	-370.89	-37.174	-82.09
1300	34.49	243.41	24.513	218.90	-395.10	-36.554	-78.66
1400	34.85	245.98	25.239	220.74	-419.57	-36.046	-75.20
1500	35.17	248.40	25.890	222.51	-444.29	-35.625	-71.69
1600	35.47	250.68	26.480	224.20	-469.25	-35.274	-68.16
1700	35.74	252.84	27.017	225.82	-494.42	-34.980	-64.60
1800	35.99	254.89	27.508	227.38	-519.81	-34.733	-61.02

* Data Source= Robie, Hemingway & Fisher(1978)

CARBON MONOXIDE(CO) P-V-T DATA SET
PLOT OF RESPONSE VERSUS INDEPENDENT VARIABLE X1 (ARB.UNITS)
Y= PRESSURE(BAR) X1= TEMPERATURE(K)

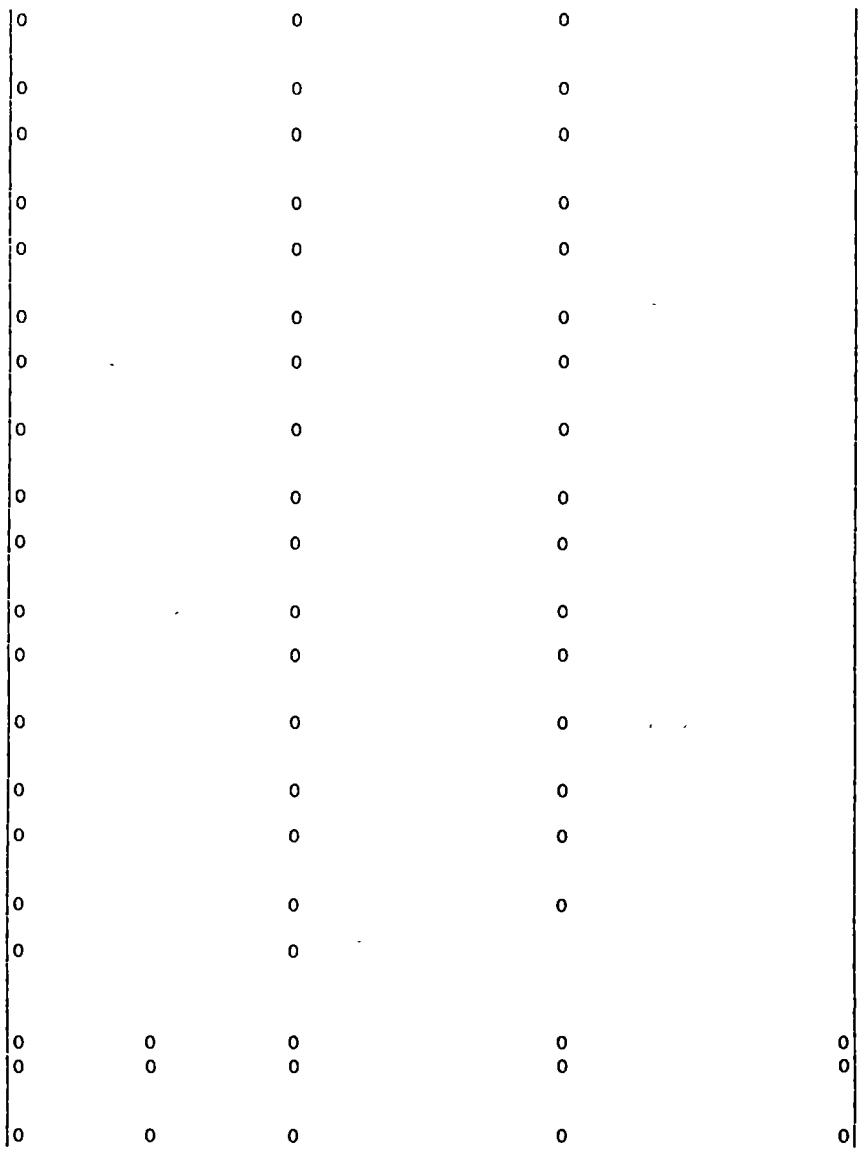

YMAX= .1000E+05 YMIN= .5070E+03 XMAX= .6730E+03 XMIN= .3730E+03

CARBON MONOXIDE(CO) P-V-T DATA SET
PLOT OF RESPONSE VERSUS SECOND INDEPENDENT VARIABLE X2 (ARB.UNITS)
Y= PRESSURE(BAR) X2= MOLAR VOLUME(CM3/MOL)

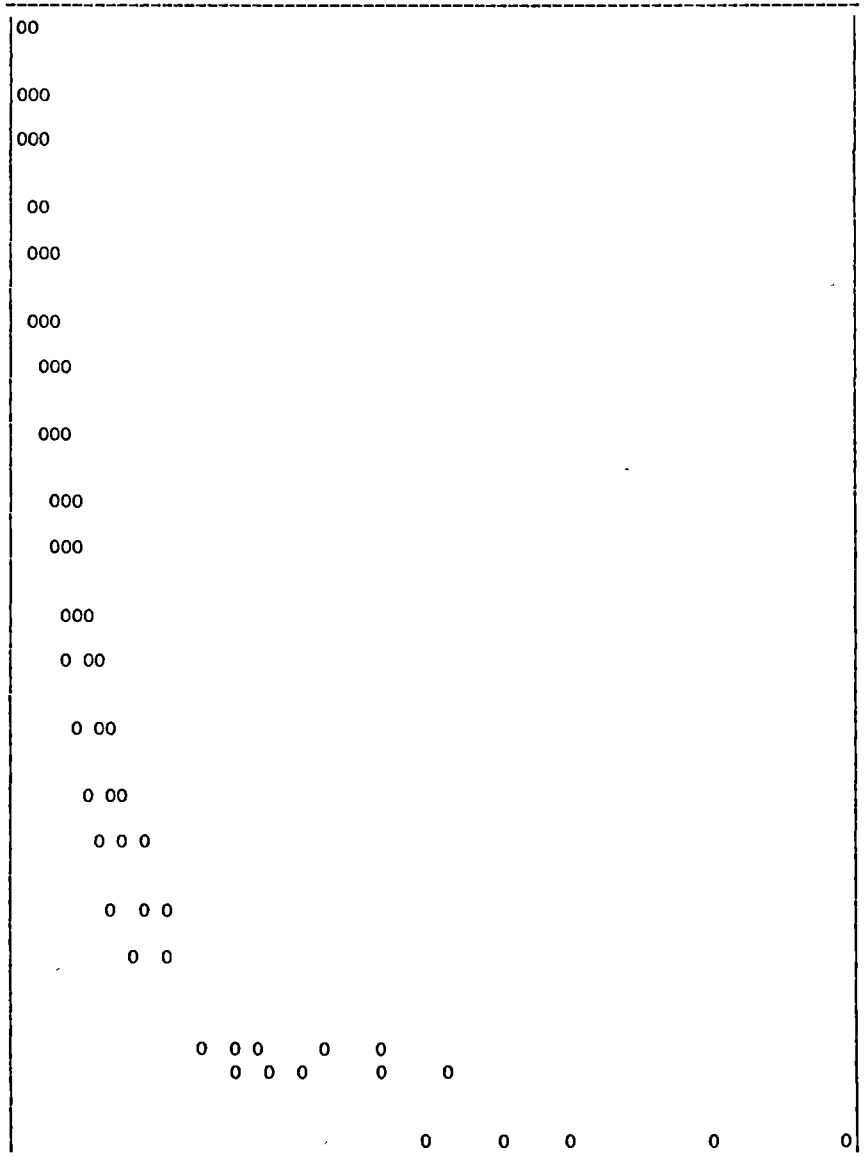

YMAX= .1000E+05 YMIN= .5070E+03 XMAX= .1394E+03 XMIN= .2690E+02

REGRESSION STATISTICS: 5-PARAMETER MRK EQN FIT TO CO P-V-T DATA SET*

REGRESSION SUM OF SQUARES	5.98980E+08
RESIDUALS SUM OF SQUARES	2.04680E+05
RESIDUALS MEAN SQUARE	3.41133E+03
MEAN OF RESIDUALS	8.29793
STD DEVIATION OF RESIDUALS	58.4066
MULTIPLE CORRELATION COEFFICIENT R	0.999834
MEAN PERCENT DEVIATION (ALL DATA)	0.97%
MEAN PERCENT DEVIATION (DATA PTS >572K)	0.68%

* Program FUNFIT, Veng-Pedersen(1977).

LITERATURE SOURCES AND RANGE OF CARBON MONOXIDE P-V-T DATA SET

	P Range/kbar	T Range/K
Smeeton-Leah(1962)*,**	0.5- 1.2	373-673
Robertson & Babb(1970)*	2.0-10.0	373-573

* volumetric data smoothed by best fit to derived equations in P,T and/or density.
** compilation of volumetric data from several different sources.

CARBON MONOXIDE(CO) : TABLE OF MOLAR VOLUMES[cm3/mol] 5-PARAMETER MRK EQN

b1=4.011E+01 b2=3.769E+03 a1=3.869E+07 a2=6.450E+08 a3=8.008E+09

Pressure (kbar)	Temperature (K/degC): 1000 727	1100 827	1200 927	1300 1027	1400 1127	1500 1227
0.5	197.80	215.28	232.63	249.87	267.03	284.11
1.0	115.00	123.92	132.77	141.56	150.29	158.98
1.5	87.04	93.09	99.10	105.06	110.97	116.86
2.0	72.75	77.38	81.96	86.50	91.01	95.50
2.5	63.97	67.73	71.46	75.16	78.82	82.47
3.0	57.95	61.14	64.30	67.44	70.54	73.62
4.0	50.14	52.62	55.07	57.50	59.90	62.28
5.0	45.21	47.26	49.28	51.28	53.26	55.23
6.0	41.77	43.53	45.26	46.98	48.67	50.35
7.0	39.20	40.75	42.28	43.79	45.28	46.76
8.0	37.19	38.58	39.95	41.31	42.65	43.97
9.0	35.57	36.84	38.08	39.32	40.54	41.74
10.0	34.23	35.39	36.54	37.68	38.80	39.90
15.0	29.85	30.70	31.54	32.37	33.19	34.00
20.0	27.35	28.04	28.72	29.39	30.06	30.71
25.0	25.69	26.27	26.85	27.43	27.99	28.55
30.0	24.48	25.00	25.50	26.01	26.51	27.00
35.0	23.55	24.01	24.47	24.92	25.37	25.81
40.0	22.81	23.23	23.64	24.06	24.46	24.87
50.0	21.68	22.04	22.39	22.75	23.10	23.45
100.0	18.90	19.12	19.34	19.56	19.78	20.00

CARBON MONOXIDE(CO) : TABLE OF ln(FUGACITY COEFFICIENTS) 5-PARAMETER MRK EQN

b1=4.011E+01 b2=3.769E+03 a1=3.869E+07 a2=6.450E+08 a3=8.008E+09

Pressure (kbar)	Temperature (K/degC): 1000 727	1100 827	1200 927	1300 1027	1400 1127	1500 1227
0.5	0.184	0.174	0.164	0.155	0.147	0.139
1.0	0.375	0.351	0.330	0.311	0.293	0.277
1.5	0.566	0.528	0.494	0.464	0.438	0.414
2.0	0.755	0.702	0.656	0.616	0.580	0.548
2.5	0.941	0.874	0.816	0.765	0.720	0.680
3.0	1.124	1.043	0.973	0.911	0.857	0.809
4.0	1.483	1.373	1.279	1.197	1.126	1.062
5.0	1.831	1.694	1.577	1.475	1.387	1.308
6.0	2.171	2.007	1.867	1.747	1.641	1.548
7.0	2.503	2.313	2.151	2.012	1.890	1.783
8.0	2.828	2.613	2.429	2.271	2.134	2.012
9.0	3.148	2.907	2.702	2.526	2.373	2.238
10.0	3.462	3.196	2.971	2.777	2.608	2.460
15.0	4.968	4.583	4.257	3.978	3.735	3.522
20.0	6.395	5.895	5.474	5.113	4.800	4.527
25.0	7.763	7.154	6.640	6.201	5.821	5.489
30.0	9.088	8.371	7.768	7.253	6.808	6.418
35.0	10.377	9.556	8.865	8.276	7.767	7.322
40.0	11.637	10.713	9.937	9.275	8.703	8.204
50.0	14.086	12.961	12.017	11.213	10.520	9.914
100.0	25.451	23.379	21.647	20.176	18.910	17.808

CARBON MONOXIDE(CO) : TABLE OF MOLAR VOLUMES[cm3/mol] 5-PARAMETER MRK EQN

b1=4.011E+01 b2=3.769E+03 a1=3.869E+07 a2=6.450E+08 a3=8.008E+09

Pressure (kbar)	Temperature (K/degC): 673.15 400	873.15 600	1073.15 800	1273.15 1000	1473.15 1200	1673.15 1400
0.5	139.24	175.39	210.60	245.25	279.53	313.57
1.0	85.16	103.56	121.53	139.20	156.65	173.94
1.5	66.81	79.27	91.47	103.46	115.28	126.98
2.0	57.31	66.82	76.14	85.29	94.29	103.20
2.5	51.38	59.13	66.72	74.17	81.49	88.72
3.0	47.27	53.85	60.29	66.60	72.80	78.91
4.0	41.85	46.96	51.96	56.85	61.65	66.36
5.0	38.37	42.58	46.71	50.75	54.70	58.58
6.0	35.89	39.51	43.06	46.52	49.90	53.22
7.0	34.03	37.21	40.33	43.38	46.36	49.28
8.0	32.55	35.41	38.21	40.95	43.62	46.23
9.0	31.35	33.94	36.50	38.99	41.42	43.79
10.0	30.35	32.73	35.08	37.37	39.61	41.79
15.0	27.02	28.75	30.47	32.15	33.79	35.38
20.0	25.09	26.47	27.85	29.21	30.54	31.83
25.0	23.78	24.94	26.12	27.27	28.40	29.50
30.0	22.82	23.83	24.86	25.87	26.87	27.83
35.0	22.08	22.97	23.89	24.80	25.69	26.56
40.0	21.48	22.28	23.12	23.95	24.76	25.55
50.0	20.56	21.23	21.94	22.65	23.35	24.04
100.0	18.27	18.63	19.06	19.50	19.94	20.37

CARBON MONOXIDE(CO) : TABLE OF ln(FUGACITY COEFFICIENTS) 5-PARAMETER MRK EQN

b1=4.011E+01 b2=3.769E+03 a1=3.869E+07 a2=6.450E+08 a3=8.008E+09

Pressure (kbar)	Temperature (K/degC): 673.15 400	873.15 600	1073.15 800	1273.15 1000	1473.15 1200	1673.15 1400
0.5	0.216	0.198	0.177	0.157	0.141	0.128
1.0	0.470	0.409	0.357	0.316	0.282	0.254
1.5	0.733	0.623	0.538	0.472	0.420	0.378
2.0	0.996	0.834	0.716	0.626	0.556	0.500
2.5	1.256	1.043	0.891	0.778	0.690	0.620
3.0	1.514	1.249	1.064	0.927	0.821	0.738
4.0	2.018	1.651	1.401	1.218	1.078	0.968
5.0	2.510	2.043	1.729	1.501	1.328	1.192
6.0	2.990	2.425	2.048	1.777	1.572	1.411
7.0	3.460	2.798	2.361	2.047	1.810	1.624
8.0	3.920	3.164	2.667	2.312	2.043	1.833
9.0	4.373	3.524	2.968	2.571	2.273	2.039
10.0	4.819	3.878	3.263	2.826	2.498	2.241
15.0	6.960	5.574	4.680	4.049	3.577	3.209
20.0	8.993	7.182	6.021	5.205	4.597	4.124
25.0	10.949	8.727	7.307	6.313	5.574	5.001
30.0	12.847	10.222	8.551	7.384	6.518	5.847
35.0	14.697	11.678	9.762	8.426	7.436	6.670
40.0	16.508	13.102	10.945	9.443	8.331	7.472
50.0	20.037	15.872	13.243	11.417	10.069	9.028
100.0	36.519	28.756	23.898	20.549	18.090	16.200

C.MONOXIDE(CO) ln(FUGACITY COEFFICIENTS) : A COMPARISON OF 5-PARAMETER MRK EQN DERIVED COEFFICIENTS WITH LITERATURE VALUES. Temp= 673.15 K (400 degC).

Pressure (kbar)	ln(fugacity coefficient) (this work)	Difference (literature value*)minus(this work):		
		RK	RV	M**
0.5	0.216	-0.051	0.006	0.006
1.0	0.470	-0.106	0.019	-0.004
1.5	0.733	-0.155	0.034	-0.012
2.0	0.996	-0.194	0.041	-0.015
2.5	1.256	-0.225	0.030	
3.0	1.514	-0.250	0.003	-0.019
4.0	2.018	-0.283	-0.091	-0.022
5.0	2.510	-0.297	-0.236	-0.023
6.0	2.990	-0.297	-0.417	-0.022
7.0	3.460	-0.284	-0.621	-0.021
8.0	3.920	-0.260	-0.847	-0.019
9.0	4.373	-0.229		-0.018
10.0	4.819	-0.189		-0.018
15.0	6.960	0.105		-0.016
20.0	8.993	0.512		
25.0	10.949	0.998		
30.0	12.847	1.544		

* RK = Redlich & Kwong(1949) with a=1.72124E+07 and b=27.3816 cm3/mol.
RV = Ryzhenko & Volkov(1971).
M = Mel'nik(1978).
** ln(fugacity coefficients) obtained by interpolation of tabulated values.

C.MONOXIDE(CO) ln(FUGACITY COEFFICIENTS) : A COMPARISON OF 5-PARAMETER MRK EQN DERIVED COEFFICIENTS WITH LITERATURE VALUES. Temp= 1273.15 K (1000 degC).

Pressure (kbar)	ln(fugacity coefficient) (this work)	Difference (literature value*)minus(this work):		
		RK	RV	M**
0.5	0.157	-0.046	-0.011	-0.024
1.0	0.316	-0.089	-0.024	-0.032
1.5	0.472	-0.125	-0.038	-0.045
2.0	0.626	-0.158	-0.053	-0.050
2.5	0.778	-0.187	-0.072	
3.0	0.927	-0.212	-0.094	-0.069
4.0	1.218	-0.252	-0.143	-0.081
5.0	1.501	-0.282	-0.206	-0.094
6.0	1.777	-0.304	-0.282	-0.103
7.0	2.047	-0.319	-0.366	-0.112
8.0	2.312	-0.329	-0.459	-0.122
9.0	2.571	-0.331	-0.559	-0.129
10.0	2.826	-0.330	-0.666	-0.137
15.0	4.049	-0.266		-0.169
20.0	5.205	-0.133		
25.0	6.313	-0.050		
30.0	7.384	0.271		
35.0	8.426	0.521		
40.0	9.443	0.796		

* RK = Redlich & Kwong(1949) with a=1.72124E+07 and b=27.3816 cm3/mol.
RV = Ryzhenko & Volkov(1971).
M = Mel'nik(1978).
** ln(fugacity coefficients) obtained by interpolation of tabulated values.

Thermochemical Data for Gaseous Hydrogen at P=1 bar.*

Cp Equation:
a= 7.4424E+00 b= 1.1707E-02 c=-5.1041E+05 d= 4.1017E+02 e=-1.3899E-06

Temp K	Cp J/mol.K	S(T) J/mol.K	(H-H298)/T J/mol.K	-F298(T) J/mol.K	G(T) kJ/mol	G(T) /RT	H(T) kJ/mol
298.15	28.82	130.68	0.000	130.68	-38.96	-15.717	0.00
400	29.22	139.23	7.407	131.82	-52.73	-15.854	2.96
500	29.25	145.75	11.774	133.98	-66.99	-16.114	5.89
600	29.29	151.09	14.689	136.40	-81.84	-16.405	8.81
700	29.42	155.61	16.784	138.83	-97.18	-16.697	11.75
800	29.62	159.55	18.375	141.18	-112.94	-16.980	14.70
900	29.90	163.06	19.639	143.42	-129.07	-17.249	17.68
1000	30.22	166.22	20.681	145.54	-145.54	-17.505	20.68
1100	30.58	169.12	21.564	147.55	-162.31	-17.747	23.72
1200	30.98	171.80	22.332	149.46	-179.36	-17.977	26.80
1300	31.39	174.29	23.013	151.28	-196.66	-18.195	29.92
1400	31.81	176.63	23.626	153.01	-214.21	-18.403	33.08
1500	32.24	178.84	24.186	154.66	-231.99	-18.601	36.28
1600	32.67	180.94	24.702	156.23	-249.98	-18.791	39.52
1700	33.10	182.93	25.184	157.75	-268.17	-18.973	42.81
1800	33.52	184.83	25.635	159.20	-286.56	-19.148	46.14

* Data Source= Robie, Hemingway & Fisher(1978).

HYDROGEN(H2) P-V-T DATA SET
PLOT OF RESPONSE VERSUS INDEPENDENT VARIABLE X1 (ARB.UNITS)
Y= PRESSURE(BAR) X1= TEMPERATURE(K)

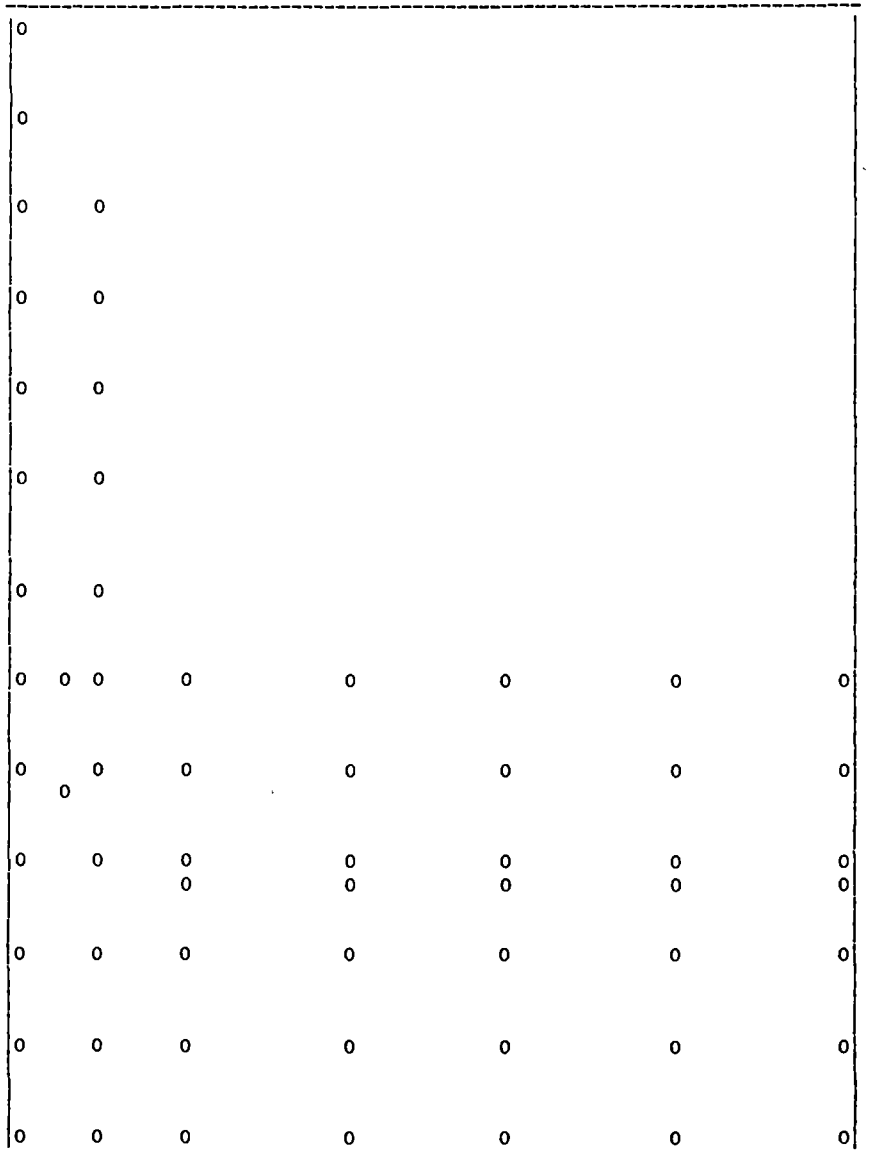

YMAX= .6500E+04 YMIN= .5000E+03 XMAX= .8730E+03 XMIN= .3730E+03

HYDROGEN(H2) P-V-T DATA SET
PLOT OF RESPONSE VERSUS SECOND INDEPENDENT VARIABLE X2 (ARB.UNITS)
Y= PRESSURE(BAR) X2= MOLAR VOLUME(CM3/MOL)

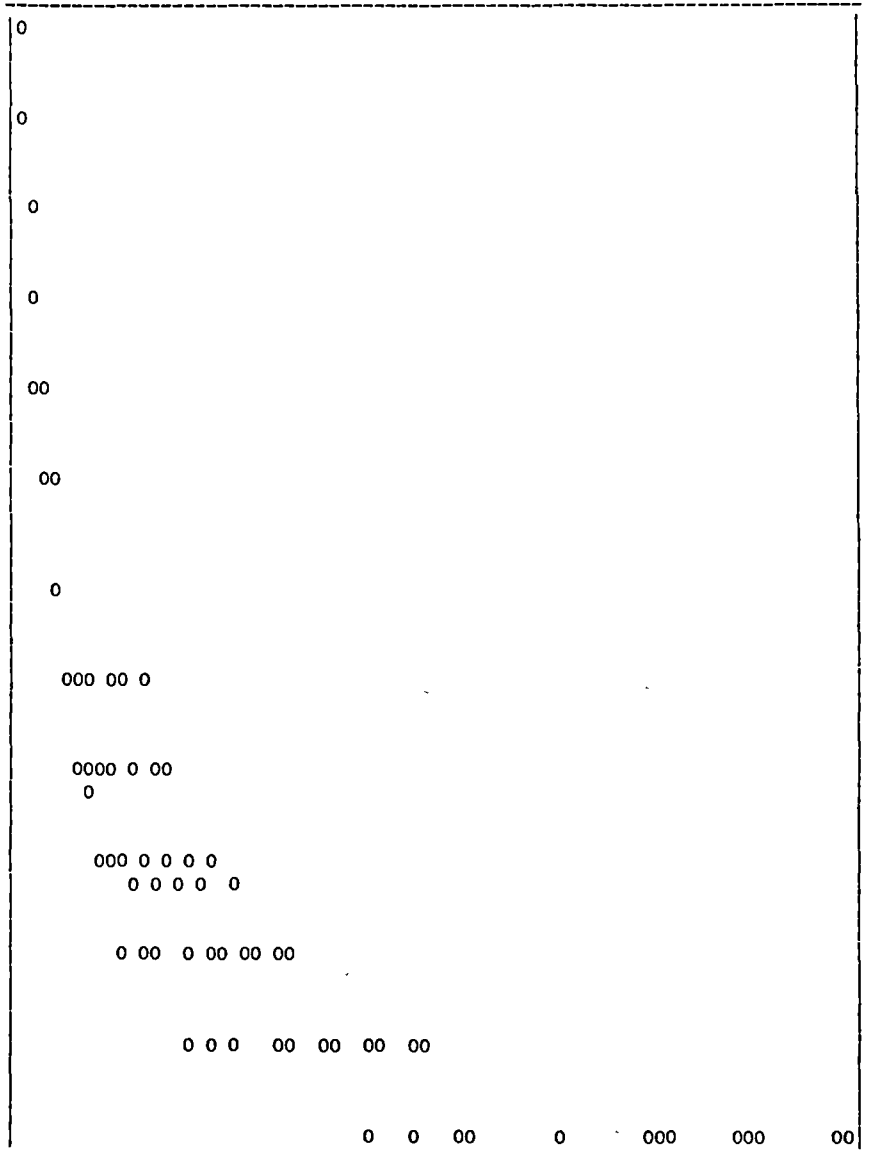

YMAX= .6500E+04 YMIN= .5000E+03 XMAX= .1609E+03 XMIN= .1840E+02

REGRESSION STATISTICS: 5-PARAMETER MRK EQN FIT TO HYDROGEN P-V-T DATA SET*

REGRESSION SUM OF SQUARES	1.69507E+08
RESIDUALS SUM OF SQUARES	1.89336E+04
RESIDUALS MEAN SQUARE	2.25400E+02
MEAN OF RESIDUALS	-3.95754
STD DEVIATION OF RESIDUALS	15.0133
MULTIPLE CORRELATION COEFFICIENT R	0.999949
MEAN PERCENT DEVIATION (ALL DATA)	0.66%
MEAN PERCENT DEVIATION (DATA PTS >772K)	0.75%

* Program FUNFIT, Veng-Pedersen(1977).

LITERATURE SOURCES AND RANGE OF HYDROGEN P-V-T DATA SET

	P Range/kbar	T Range/K
Tsiklis et.al.(1975)*	0.5-6.5	423-373
Michels et.al.(1959)**	2.5-3.0	398-423
Shaw & Wones(1964)**,***	0.5-3.0	473-873
Rhyzhenko & Volkov(1971)**,***	0.5-1.5	473-773
Presnall(1969)*	0.5-1.8	473-873

* unsmoothed experimental results.
** volumetric data smoothed by best fit to high order polynomials in P,T or density.
*** compilation of volumetric data from several different sources.

HYDROGEN(H2) : TABLE OF MOLAR VOLUMES[cm3/mol] 5-PARAMETER MRK EQUATION

b1=1.536E+01 b2=3.011E+03 a1=4.521E+06 a2=5.734E+07 a3=1.693E+09

Pressure (kbar)	Temperature (K/degC): 673.15 400	873.15 600	1073.15 800	1273.15 1000	1473.15 1200	1673.15 1400
0.5	128.38	161.54	194.72	227.90	261.10	294.31
1.0	72.03	88.57	105.15	121.74	138.33	154.93
1.5	52.99	64.03	75.09	86.17	97.24	108.32
2.0	43.32	51.61	59.93	68.26	76.59	84.91
2.5	37.41	44.06	50.74	57.43	64.11	70.79
3.0	33.40	38.96	44.55	50.15	55.74	61.32
4.0	28.25	32.45	36.69	40.92	45.15	49.38
5.0	25.04	28.43	31.86	35.28	38.70	42.11
6.0	22.83	25.68	28.57	31.45	34.33	37.20
7.0	21.20	23.67	26.16	28.66	31.15	33.64
8.0	19.94	22.11	24.32	26.53	28.73	30.93
9.0	18.94	20.88	22.86	24.84	26.82	28.79
10.0	18.11	19.86	21.66	23.47	25.27	27.05
15.0	15.45	16.65	17.90	19.16	20.41	21.66
20.0	13.98	14.89	15.85	16.83	17.81	18.78
25.0	13.01	13.74	14.53	15.34	16.16	16.96
30.0	12.31	12.93	13.60	14.29	14.99	15.68
35.0	11.78	12.31	12.90	13.50	14.12	14.73
40.0	11.36	11.82	12.34	12.88	13.43	13.98
50.0	10.73	11.09	11.51	11.96	12.42	12.88
100.0	9.19	9.33	9.55	9.80	10.06	10.33

HYDROGEN(H2) : TABLE OF ln(FUGACITY COEFFICIENTS) 5-PARAMETER MRK EQUATION

b1=1.536E+01 b2=3.011E+03 a1=4.521E+06 a2=5.734E+07 a3=1.693E+09

Pressure (kbar)	Temperature (K/degC): 673.15 400	873.15 600	1073.15 800	1273.15 1000	1473.15 1200	1673.15 1400
0.5	0.148	0.114	0.092	0.077	0.066	0.058
1.0	0.294	0.225	0.182	0.153	0.132	0.116
1.5	0.435	0.334	0.271	0.227	0.196	0.172
2.0	0.574	0.441	0.357	0.300	0.259	0.228
2.5	0.709	0.545	0.442	0.372	0.321	0.282
3.0	0.842	0.647	0.526	0.443	0.383	0.337
4.0	1.101	0.848	0.690	0.581	0.503	0.443
5.0	1.352	1.042	0.849	0.716	0.620	0.547
6.0	1.597	1.231	1.004	0.848	0.735	0.648
7.0	1.835	1.416	1.156	0.977	0.847	0.748
8.0	2.069	1.598	1.305	1.104	0.958	0.846
9.0	2.298	1.776	1.451	1.229	1.067	0.943
10.0	2.523	1.951	1.595	1.351	1.174	1.038
15.0	3.603	2.790	2.285	1.940	1.688	1.496
20.0	4.625	3.583	2.938	2.498	2.176	1.931
25.0	5.604	4.343	3.564	3.032	2.644	2.348
30.0	6.552	5.078	4.169	3.549	3.096	2.751
35.0	7.473	5.792	4.756	4.050	3.536	3.143
40.0	8.372	6.488	5.329	4.539	3.964	3.524
50.0	10.119	7.840	6.440	5.487	4.794	4.264
100.0	18.202	14.069	11.547	9.839	8.600	7.656

HYDROGEN(H2) : TABLE OF MOLAR VOLUMES[cm3/mol] 5-PARAMETER MRK EQUATION

b1=1.536E+01 b2=3.011E+03 a1=4.521E+06 a2=5.734E+07 a3=1.693E+09

Pressure (kbar)	Temperature (K/degC): 1000 727	1100 827	1200 927	1300 1027	1400 1127	1500 1227
0.5	182.58	199.17	215.77	232.36	248.96	265.56
1.0	99.09	107.38	115.67	123.97	132.26	140.56
1.5	71.04	76.58	82.11	87.65	93.19	98.73
2.0	56.88	61.05	65.21	69.38	73.54	77.70
2.5	48.30	51.64	54.98	58.33	61.67	65.01
3.0	42.50	45.30	48.10	50.90	53.69	56.49
4.0	35.14	37.26	39.38	41.49	43.61	45.72
5.0	30.61	32.32	34.03	35.74	37.45	39.16
6.0	27.51	28.95	30.40	31.84	33.28	34.71
7.0	25.25	26.50	27.75	29.00	30.24	31.49
8.0	23.51	24.62	25.72	26.83	27.93	29.03
9.0	22.13	23.12	24.12	25.11	26.10	27.08
10.0	21.00	21.91	22.81	23.71	24.61	25.51
15.0	17.44	18.07	18.70	19.33	19.95	20.58
20.0	15.50	15.98	16.47	16.96	17.45	17.94
25.0	14.24	14.64	15.05	15.45	15.86	16.26
30.0	13.35	13.69	14.04	14.39	14.74	15.08
35.0	12.68	12.98	13.28	13.59	13.89	14.20
40.0	12.15	12.41	12.68	12.96	13.23	13.51
50.0	11.35	11.57	11.80	12.02	12.25	12.48
100.0	9.46	9.58	9.70	9.83	9.96	10.09

HYDROGEN(H2) : TABLE OF ln(FUGACITY COEFFICIENTS) 5-PARAMETER MRK EQUATION

b1=1.536E+01 b2=3.011E+03 a1=4.521E+06 a2=5.734E+07 a3=1.693E+09

Pressure (kbar)	Temperature (K/degC): 1000 727	1100 827	1200 927	1300 1027	1400 1127	1500 1227
0.5	0.099	0.090	0.082	0.076	0.070	0.065
1.0	0.196	0.178	0.163	0.150	0.139	0.129
1.5	0.291	0.264	0.242	0.223	0.206	0.192
2.0	0.384	0.348	0.319	0.294	0.273	0.254
2.5	0.475	0.431	0.395	0.364	0.338	0.315
3.0	0.565	0.513	0.470	0.434	0.403	0.376
4.0	0.740	0.673	0.617	0.569	0.529	0.494
5.0	0.910	0.828	0.760	0.702	0.652	0.609
6.0	1.076	0.980	0.899	0.831	0.773	0.722
7.0	1.239	1.128	1.036	0.958	0.891	0.832
8.0	1.398	1.274	1.170	1.082	1.007	0.941
9.0	1.555	1.416	1.301	1.204	1.121	1.048
10.0	1.708	1.557	1.431	1.324	1.233	1.153
15.0	2.446	2.232	2.053	1.902	1.772	1.660
20.0	3.144	2.870	2.642	2.449	2.283	2.140
25.0	3.812	3.482	3.206	2.973	2.773	2.600
30.0	4.458	4.073	3.752	3.480	3.247	3.045
35.0	5.086	4.647	4.281	3.972	3.707	3.477
40.0	5.698	5.206	4.798	4.452	4.155	3.898
50.0	6.885	6.292	5.798	5.382	5.024	4.715
100.0	12.348	11.281	10.396	9.650	9.012	8.458

HYDROGEN(H2) ln(FUGACITY COEFFICIENTS) : A COMPARISON OF 5-PARAMETER MRK EQN DERIVED COEFFICIENTS WITH LITERATURE VALUES. Temp= 873.15 K (600 degC).

Pressure (kbar)	ln(fugacity coefficient) (this work)	Difference (literature value*)minus(this work):			
		RV	CP	SW	P**
0.5	0.114	0.003	0.011	-0.005	-0.016
1.0	0.225	0.013	0.026	-0.008	-0.023
1.5	0.334	0.030	0.043	-0.011	-0.028
2.0	0.441	0.047	0.063	-0.013	-0.034
2.5	0.545	0.066	0.087	-0.014	
3.0	0.647	0.085	0.112	-0.014	
4.0	0.848	0.115	0.167		
5.0	1.042	0.137	0.229		
6.0	1.231	0.148	0.296		
7.0	1.416	0.151	0.368		
8.0	1.598	0.139	0.442		
9.0	1.776	0.120	0.521		
10.0	1.951	0.095	0.603		
15.0	2.790		1.050		
20.0	3.583		1.542		
25.0	4.343		2.069		
30.0	5.078		2.620		

* RV = Ryzhenko & Volkov(1971).
CP = Chueh & Prausnitz(1967) using T(crit)=33.2 K & P(crit)=12.97 bar.
SW = Shaw & Wones(1964).
P = Presnall(1969).

** fugacity coefficients obtained by linear interpolation of tabulated values where appropriate.

HYDROGEN(H2) ln(FUGACITY COEFFICIENTS) : A COMPARISON OF 5-PARAMETER MRK EQN DERIVED COEFFICIENTS WITH LITERATURE VALUES. Temp= 1273.15 K (1000 degC).

Pressure (kbar)	ln(fugacity coefficient) (this work)	Difference (literature value*)minus(this work):		
		RV	CP	SW
0.5	0.077	-0.003	0.009	-0.007
1.0	0.153	-0.005	0.020	-0.012
1.5	0.227	-0.004	0.033	-0.017
2.0	0.300	-0.003	0.047	-0.020
2.5	0.372	-0.001	0.062	-0.024
3.0	0.443	0.001	0.078	-0.028
4.0	0.581	0.007	0.115	
5.0	0.716	0.007	0.155	
6.0	0.848	0.006	0.198	
7.0	0.977	0.005	0.245	
8.0	1.104	-0.002	0.293	
9.0	1.229	-0.026	0.344	
10.0	1.351	-0.024	0.397	
15.0	1.940		0.686	
20.0	2.498		1.007	
25.0	3.032		1.351	
30.0	3.549		1.713	

* RV = Ryzhenko & Volkov(1971).
CP = Chueh & Prausnitz(1967) using T(crit)=33.2 K & P(crit)=12.97 bar.
SW = Shaw & Wones(1964).

Thermochemical Data for Gaseous Methane(CH4) at P=1 bar.*

Cp Equation:
a= 7.8976E+01 b= 4.3186E-02 c= 1.8836E+06 d=-1.3202E+03 e=-1.0598E-05

Temp K	Cp J/mol.K	S(T) J/mol.K	(H-H298)/T J/mol.K	-F298(T) J/mol.K	G(T) kJ/mol	G(T) /RT	H(T) kJ/mol
298.15	35.64	186.26	0.000	186.26	-130.34	-52.581	-74.81
400	40.32	197.30	9.598	187.71	-149.89	-45.071	-70.97
500	46.41	206.95	16.347	190.60	-170.11	-40.920	-66.64
600	52.41	215.95	21.862	194.08	-191.26	-38.340	-61.69
700	57.96	224.45	26.628	197.82	-213.28	-36.647	-56.17
800	63.01	232.52	30.865	201.66	-236.14	-35.501	-50.12
900	67.58	240.21	34.695	205.52	-259.78	-34.716	-43.58
1000	71.70	247.55	38.193	209.36	-284.17	-34.178	-36.62
1100	75.41	254.56	41.411	213.15	-309.27	-33.816	-29.26
1200	78.74	261.27	44.385	216.88	-335.07	-33.584	-21.55
1300	81.71	267.69	47.144	220.55	-361.52	-33.447	-13.52
1400	84.34	273.84	49.708	224.13	-388.60	-33.385	-5.22
1500	86.66	279.74	52.096	227.65	-416.28	-33.379	3.33
1600	88.67	285.40	54.321	231.08	-444.54	-33.417	12.10
1700	90.40	290.83	56.394	234.44	-473.35	-33.490	21.06
1800	91.84	296.04	58.324	237.71	-502.70	-33.590	30.17

* Data Source= Robie, Hemingway & Fisher(1978).

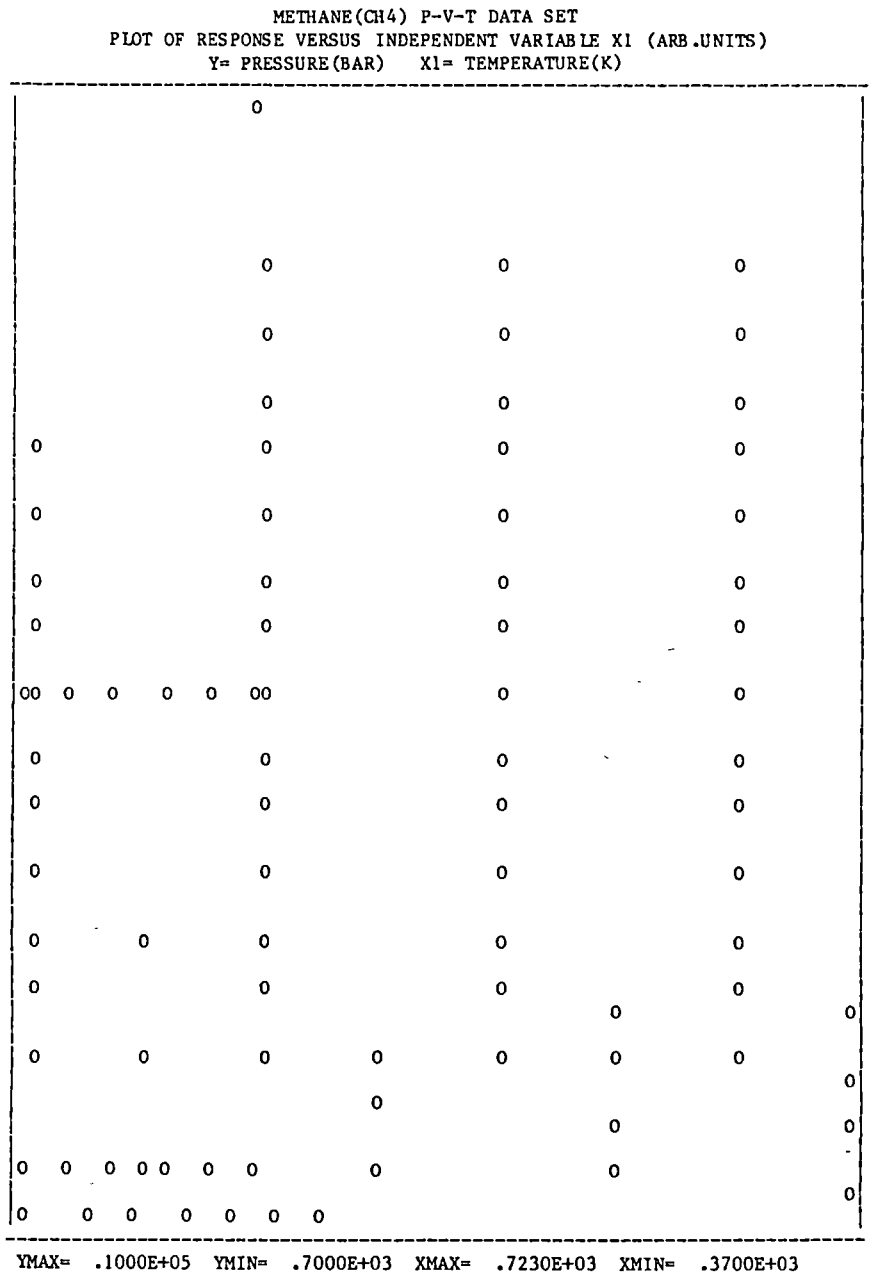
METHANE(CH4) P-V-T DATA SET
PLOT OF RESPONSE VERSUS INDEPENDENT VARIABLE X1 (ARB.UNITS)
Y= PRESSURE(BAR) X1= TEMPERATURE(K)
YMAX= .1000E+05 YMIN= .7000E+03 XMAX= .7230E+03 XMIN= .3700E+03

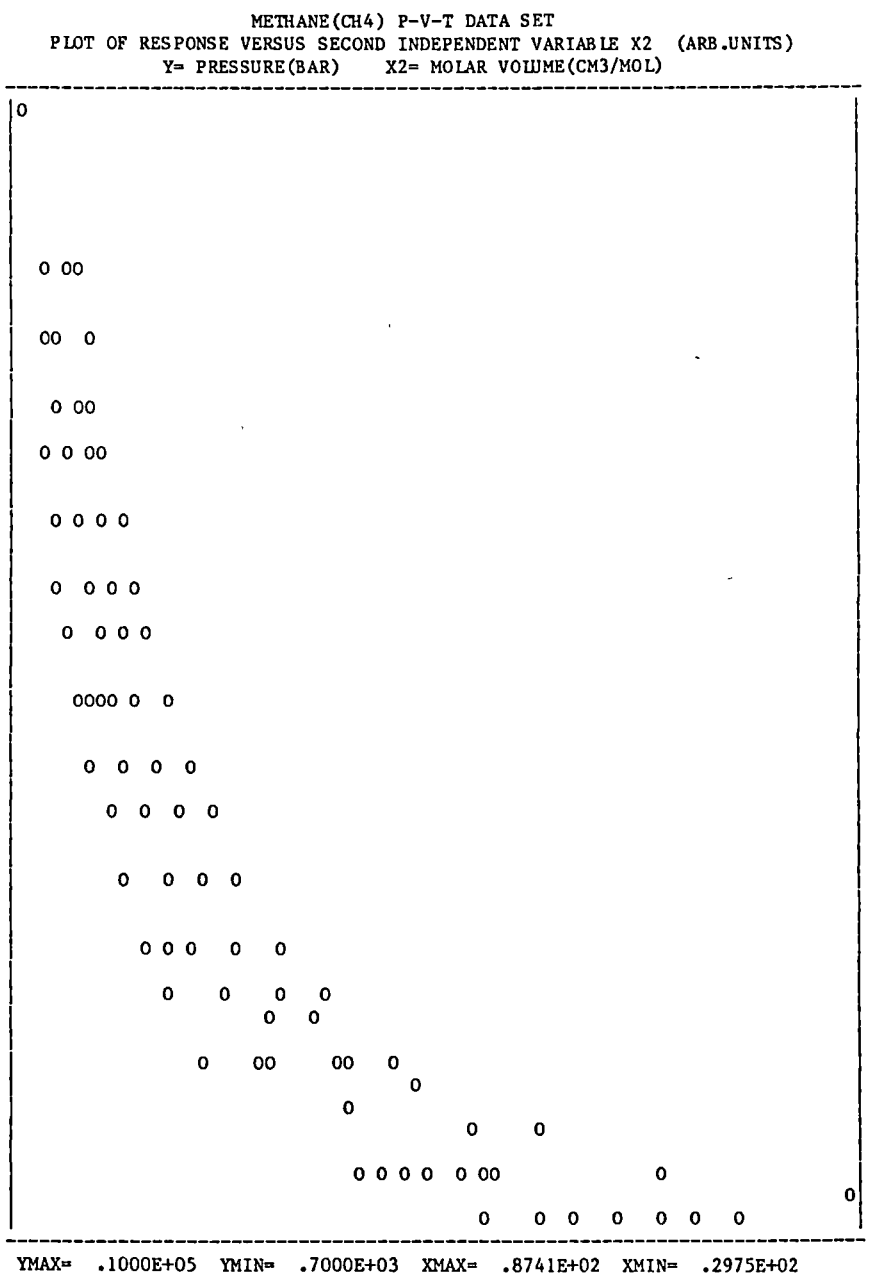
METHANE(CH4) P-V-T DATA SET
PLOT OF RESPONSE VERSUS SECOND INDEPENDENT VARIABLE X2 (ARB.UNITS)
Y= PRESSURE(BAR) X2= MOLAR VOLUME(CM3/MOL)
YMAX= .1000E+05 YMIN= .7000E+03 XMAX= .8741E+02 XMIN= .2975E+02

REGRESSION STATISTICS: 5-PARAMETER MRK EQN FIT TO METHANE P-V-T DATA SET*

REGRESSION SUM OF SQUARES	5.10184E+08	(5.15322E+08)**
RESIDUALS SUM OF SQUARES	1.85330E+07	(1.33946E+07)
RESIDUALS MEAN SQUARE	2.13023E+05	(1.53961E+05)
MEAN OF RESIDUALS	-218.245	(-171.994)
STD DEVIATION OF RESIDUALS	461.544	(392.379)
MULTIPLE CORRELATION COEFFICIENT R	0.991525	(0.995687)
MEAN PERCENT DEVIATION (ALL DATA)	5.42%	(3.82%)
MEAN PERCENT DEVIATION (DATA PTS >572K)	3.25%	(4.84%)

* Program FUNFIT, Veng-Pedersen(1977).
** Fit statistics for 10-parameter MRK eqn of Jacobs & Kerrick(1981a) in brackets.

LITERATURE SOURCES AND RANGE OF METHANE P-V-T DATA SET

	P Range/kbar	T Range/K
Goodwin(1974)*,***	0.7	370-500
Angus, Armstrong & DeReuck(1978)*,***	1.0-10.0	370-470
Ryzhenko & Volkov(1971)**,***	1.0- 3.0	370-500
Tsiklis, Linshits & Tsimmerman(1971)*	2.0- 8.6	373-673
Francesconi(1984)**	1.0- 2.5	523-723

* volumetric data smoothed by best fit to derived equations of state.
** volumetric data smoothed by best fit to polynomials in P,T.
*** compilation of volumetric data from several different sources.

METHANE(CH4) : TABLE OF MOLAR VOLUMES[cm3/mol] 5-PARAMETER MRK EQUATION

b1=4.338E+01 b2=7.409E+03 a1=6.742E+07 a2=2.893E+09 a3=9.749E+10

Pressure (kbar)	Temperature (K/degC): 673.15 400	873.15 600	1073.15 800	1273.15 1000	1473.15 1200	1673.15 1400
0.5	133.01	172.02	208.96	244.72	279.77	314.37
1.0	81.69	101.62	120.72	139.19	157.22	174.95
1.5	64.88	78.22	91.19	103.78	116.06	128.11
2.0	56.35	66.37	76.24	85.84	95.23	104.43
2.5	51.08	59.12	67.10	74.91	82.54	90.03
3.0	47.45	54.16	60.89	67.49	73.95	80.28
4.0	42.66	47.74	52.88	57.96	62.94	67.83
5.0	39.58	43.67	47.86	52.02	56.11	60.11
6.0	37.39	40.82	44.37	47.91	51.39	54.81
7.0	35.73	38.69	41.78	44.87	47.91	50.91
8.0	34.41	37.01	39.75	42.50	45.22	47.89
9.0	33.33	35.65	38.12	40.60	43.06	45.49
10.0	32.42	34.52	36.77	39.04	41.29	43.51
15.0	29.39	30.79	32.36	33.97	35.58	37.18
20.0	27.59	28.63	29.85	31.11	32.39	33.66
25.0	26.36	27.18	28.17	29.22	30.29	31.35
30.0	25.45	26.11	26.94	27.84	28.77	29.70
35.0	24.74	25.28	26.00	26.79	27.61	28.43
40.0	24.16	24.61	25.24	25.95	26.68	27.42
50.0	23.26	23.58	24.08	24.66	25.28	25.91
100.0	20.97	20.98	21.20	21.50	21.85	22.21

METHANE(CH4) : TABLE OF ln(FUGACITY COEFFICIENTS) 5-PARAMETER MRK EQUATION

b1=4.338E+01 b2=7.409E+03 a1=6.742E+07 a2=2.893E+09 a3=9.749E+10

Pressure (kbar)	Temperature (K/degC): 673.15 400	873.15 600	1073.15 800	1273.15 1000	1473.15 1200	1673.15 1400
0.5	0.140	0.167	0.164	0.153	0.141	0.130
1.0	0.352	0.360	0.338	0.310	0.283	0.259
1.5	0.591	0.563	0.515	0.467	0.424	0.387
2.0	0.842	0.770	0.693	0.623	0.564	0.514
2.5	1.097	0.977	0.869	0.778	0.702	0.638
3.0	1.354	1.184	1.045	0.931	0.838	0.761
4.0	1.867	1.594	1.391	1.232	1.105	1.001
5.0	2.377	1.999	1.730	1.526	1.366	1.236
6.0	2.882	2.398	2.064	1.815	1.621	1.466
7.0	3.380	2.790	2.392	2.098	1.872	1.691
8.0	3.873	3.178	2.714	2.377	2.118	1.912
9.0	4.360	3.560	3.033	2.652	2.360	2.130
10.0	4.842	3.938	3.347	2.922	2.599	2.344
15.0	7.183	5.768	4.865	4.227	3.749	3.375
20.0	9.435	7.521	6.314	5.472	4.844	4.356
25.0	11.619	9.217	7.714	6.671	5.898	5.298
30.0	13.749	10.868	9.074	7.835	6.919	6.212
35.0	15.835	12.482	10.402	8.970	7.915	7.101
40.0	17.885	14.066	11.704	10.081	8.889	7.971
50.0	21.894	17.157	14.241	12.245	10.783	9.661
100.0	40.789	31.661	26.097	22.326	19.587	17.500

METHANE(CH4) : TABLE OF MOLAR VOLUMES[cm3/mol] 5-PARAMETER MRK EQUATION

b1=4.338E+01 b2=7.409E+03 a1=6.742E+07 a2=2.893E+09 a3=9.749E+10

Pressure (kbar)	Temperature (K/degC): 1000 727	1100 827	1200 927	1300 1027	1400 1127	1500 1227
0.5	195.62	213.81	231.74	249.46	267.02	284.44
1.0	113.82	123.23	132.49	141.63	150.67	159.62
1.5	86.49	92.90	99.21	105.44	111.60	117.69
2.0	72.66	77.54	82.36	87.12	91.82	96.47
2.5	64.20	68.16	72.08	75.95	79.77	83.56
3.0	58.44	61.79	65.09	68.37	71.60	74.81
4.0	51.01	53.57	56.12	58.64	61.13	63.60
5.0	46.33	48.43	50.51	52.57	54.62	56.65
6.0	43.07	44.85	46.62	48.38	50.13	51.85
7.0	40.64	42.19	43.74	45.28	46.80	48.32
8.0	38.74	40.12	41.50	42.87	44.23	45.58
9.0	37.21	38.45	39.70	40.94	42.17	43.39
10.0	35.94	37.07	38.21	39.34	40.47	41.59
15.0	31.78	32.58	33.38	34.19	35.00	35.80
20.0	29.39	30.01	30.65	31.28	31.92	32.56
25.0	27.79	28.31	28.83	29.36	29.90	30.43
30.0	26.63	27.06	27.51	27.97	28.43	28.89
35.0	25.72	26.10	26.50	26.90	27.31	27.72
40.0	24.99	25.33	25.68	26.04	26.41	26.78
50.0	23.88	24.16	24.45	24.75	25.05	25.36
100.0	21.10	21.23	21.38	21.54	21.72	21.89

METHANE(CH4) : TABLE OF ln(FUGACITY COEFFICIENTS) 5-PARAMETER MRK EQUATION

b1=4.338E+01 b2=7.409E+03 a1=6.742E+07 a2=2.893E+09 a3=9.749E+10

Pressure (kbar)	Temperature (K/degC): 1000 727	1100 827	1200 927	1300 1027	1400 1127	1500 1227
0.5	0.166	0.162	0.157	0.151	0.145	0.139
1.0	0.347	0.334	0.320	0.306	0.293	0.280
1.5	0.533	0.508	0.484	0.461	0.439	0.419
2.0	0.720	0.683	0.648	0.615	0.585	0.557
2.5	0.907	0.856	0.810	0.767	0.728	0.693
3.0	1.092	1.028	0.970	0.917	0.870	0.827
4.0	1.459	1.367	1.286	1.213	1.148	1.090
5.0	1.819	1.700	1.595	1.503	1.420	1.347
6.0	2.174	2.026	1.898	1.786	1.687	1.598
7.0	2.522	2.347	2.196	2.065	1.949	1.845
8.0	2.866	2.663	2.490	2.338	2.206	2.088
9.0	3.204	2.975	2.778	2.608	2.459	2.326
10.0	3.539	3.282	3.063	2.874	2.708	2.562
15.0	5.156	4.767	4.438	4.156	3.910	3.694
20.0	6.702	6.185	5.749	5.377	5.054	4.772
25.0	8.195	7.553	7.014	6.554	6.156	5.809
30.0	9.648	8.882	8.242	7.696	7.225	6.814
35.0	11.067	10.180	9.440	8.810	8.267	7.794
40.0	12.457	11.452	10.613	9.900	9.287	8.752
50.0	15.170	13.931	12.898	12.023	11.271	10.616
100.0	27.863	25.509	23.557	21.909	20.498	19.275

METHANE(CH4) ln(FUGACITY COEFFICIENTS) : A COMPARISON OF 5-PARAMETER MRK EQN DERIVED COEFFICIENTS WITH LITERATURE VALUES. Temp= 673.15 K (400 degC).

Pressure (kbar)	ln(fugacity coefficient) (this work)	Difference (literature value*)minus(this work):				
		KJ	RK	TLT**	M**	RV
0.5	0.140	0.012	-0.021		0.033	0.041
1.0	0.352	0.018	-0.049		0.038	0.064
1.5	0.591	0.016	-0.073		0.037	0.078
2.0	0.842	0.011	-0.092	0.063	0.036	0.079
2.5	1.097	0.007	-0.106	0.058		0.065
3.0	1.354	0.004	-0.116	0.059	0.041	0.032
4.0	1.867	0.004	-0.124	0.059	0.047	-0.082
5.0	2.377	0.006	-0.120	0.060	0.054	-0.248
6.0	2.882	0.012	-0.105	0.066	0.058	-0.457
7.0	3.380	0.022	-0.081	0.070	0.060	-0.685
8.0	3.873	0.033	-0.049	0.070	0.060	-0.944
9.0	4.360	0.046	-0.009	0.067	0.058	
10.0	4.842	0.061	0.037	0.056	0.055	
15.0	7.183	0.153	0.345		0.023	
20.0	9.435	0.262	0.750			
25.0	11.619	0.381	1.228			
30.0	13.749	0.507	1.761			

* KJ = Jacobs & Kerrick(1981a)
RK = Redlich & Kwong(1949) with a=3.221E+07 and b=29.848 cm3/mol.
TLT = Tsiklis, Linshits & Tsimmerman(1971)
M = Mel'nik(1978)
RV = Ryzhenko & Volkov(1971)

** fugacity coefficients obtained by linear interpolation of tabulated values.

METHANE(CH4) ln(FUGACITY COEFFICIENTS) : A COMPARISON OF 5-PARAMETER MRK EQN DERIVED COEFFICIENTS WITH LITERATURE VALUES. Temp= 1273.15 K (1000 degC).

Pressure (kbar)	ln(fugacity coefficient) (this work)	Difference (literature value*)minus(this work):			
		KJ	RK	M**	RV
0.5	0.153	-0.017	-0.046	-0.002	-0.013
1.0	0.310	-0.025	-0.086	-0.026	-0.013
1.5	0.467	-0.032	-0.119	-0.041	-0.007
2.0	0.623	-0.040	-0.148	-0.058	0.002
2.5	0.778	-0.049	-0.173		0.010
3.0	0.931	-0.058	-0.194	-0.082	0.014
4.0	1.232	-0.075	-0.227	-0.103	0.009
5.0	1.526	-0.087	-0.249	-0.117	-0.017
6.0	1.815	-0.096	-0.263	-0.131	-0.064
7.0	2.098	-0.101	-0.270	-0.144	-0.125
8.0	2.377	-0.104	-0.272	-0.157	-0.203
9.0	2.652	-0.103	-0.269	-0.171	-0.291
10.0	2.922	-0.100	-0.260	-0.182	-0.396
15.0	4.227	-0.057	-0.166	-0.238	
20.0	5.472	0.015	-0.008		
25.0	6.671	0.106	0.199		
30.0	7.835	0.209	0.443		

* KJ = Jacobs & Kerrick(1981a)
RK = Redlich & Kwong(1949) with a=3.221E+07 and b=29.848 cm3/mol.
M = Mel'nik(1978)
RV = Ryzhenko & Volkov(1971)

** fugacity coefficients obtained by linear interpolation of tabulated values.

Thermochemical Data for Gaseous Ethane(C2H6) at P=1 bar.*

Cp Equation:
a= 2.0547E+02 b= 2.0345E-02 c= 3.1636E+06 d=-3.3575E+03 e= 0.

Temp K	Cp J/mol.K	S(T) J/mol.K	(H-H298)/T J/mol.K	-F298(T) J/mol.K	G(T) kJ/mol	G(T) /RT	H(T) kJ/mol
298.15	52.68	229.49	0.000	229.49	-153.11	-61.764	-84.68
400	65.51	246.71	15.001	231.71	-177.37	-53.332	-78.68
500	78.14	262.71	26.385	236.32	-202.84	-48.794	-71.49
600	89.40	277.97	35.970	242.00	-229.88	-46.082	-63.10
700	99.27	292.51	44.322	248.19	-258.41	-44.401	-53.66
800	107.98	306.34	51.746	254.60	-288.36	-43.353	-43.29
900	115.77	319.52	58.435	261.09	-319.66	-42.719	-32.09
1000	122.81	332.09	64.526	267.56	-352.25	-42.366	-20.16
1100	129.23	344.10	70.120	273.98	-386.06	-42.212	-7.55
1200	135.16	355.60	75.296	280.30	-421.05	-42.201	5.67
1300	140.67	366.64	80.115	286.52	-457.17	-42.296	19.47
1400	145.83	377.25	84.627	292.63	-494.36	-42.471	33.79
1500	150.70	387.48	88.871	298.61	-532.60	-42.706	48.62
1600	155.32	397.36	92.881	304.48	-571.85	-42.987	63.93
1700	159.72	406.91	96.685	310.22	-612.06	-43.303	79.68

* Data Source= Stull, Westrum & Sinke(1969).

ETHANE(C2H6) P-V-T DATA SET
PLOT OF RESPONSE VERSUS INDEPENDENT VARIABLE X1 (ARB.UNITS)
Y= PRESSURE(BAR) X1= TEMPERATURE(K)

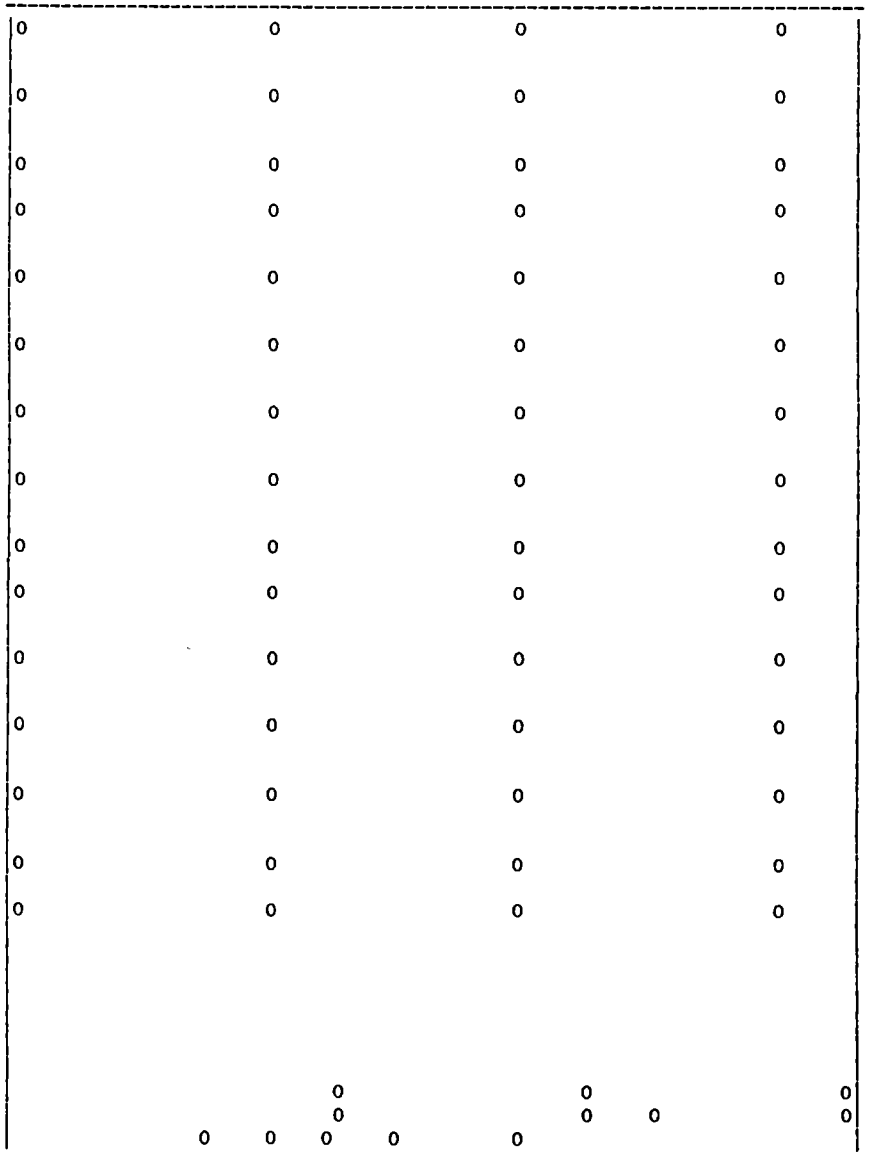

YMAX= .9000E+04 YMIN= .3040E+03 XMAX= .7000E+03 XMIN= .3730E+03

ETHANE(C2H6) P-V-T DATA SET
PLOT OF RESPONSE VERSUS SECOND INDEPENDENT VARIABLE X2 (ARB.UNITS)
Y= PRESSURE(BAR) X2= MOLAR VOLUME(CM3/MOL)

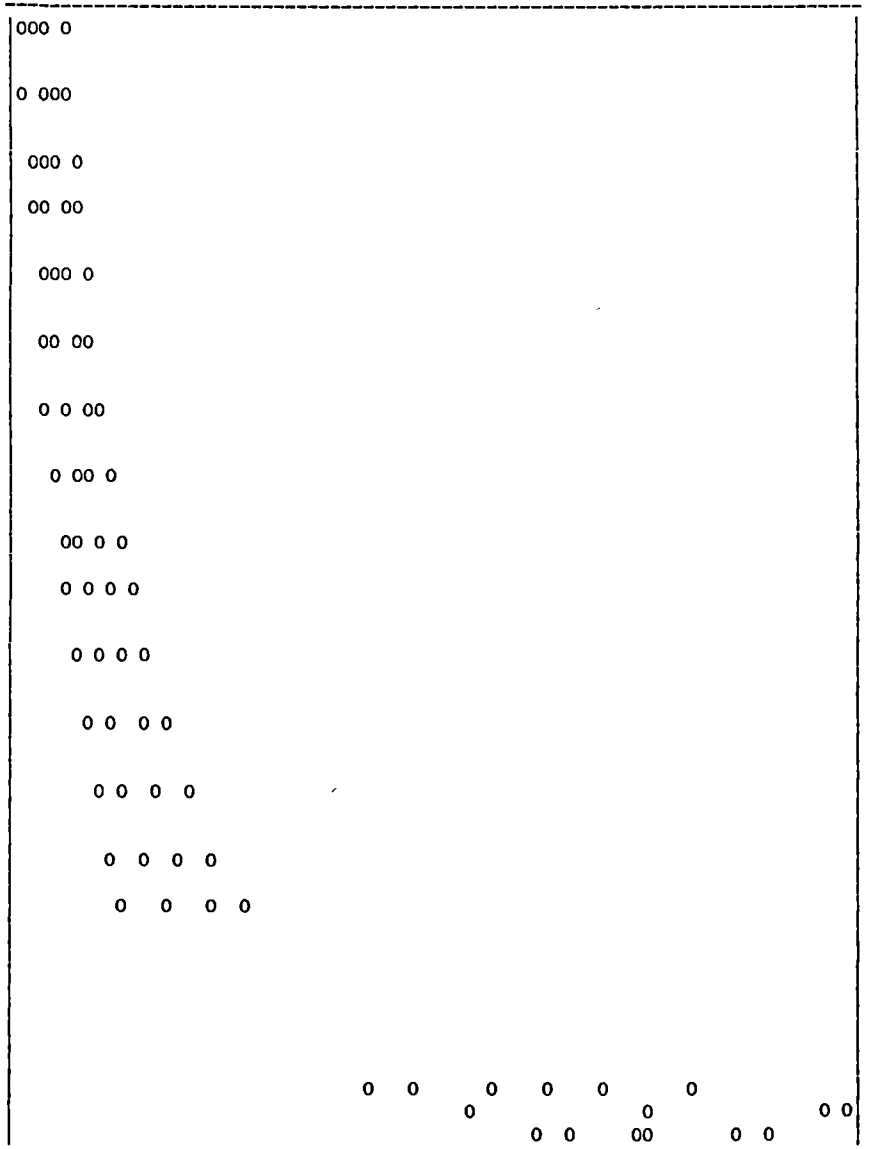

YMAX= .9000E+04 YMIN= .3040E+03 XMAX= .1428E+03 XMIN= .4210E+02

REGRESSION STATISTICS: 5-PARAMETER MRK EQN FIT TO C2H6 P-V-T DATA SET*

REGRESSION SUM OF SQUARES	5.96692E+08
RESIDUALS SUM OF SQUARES	6.08393E+05
RESIDUALS MEAN SQUARE	8.00516E+03
MEAN OF RESIDUALS	-40.4545
STD DEVIATION OF RESIDUALS	89.4716
MULTIPLE CORRELATION COEFFICIENT R	0.999613
MEAN PERCENT DEVIATION (ALL DATA)	2.53%
MEAN PERCENT DEVIATION (DATA PTS >572K)	2.64%

* Program FUNFIT, Veng-Pedersen(1977).

LITERATURE SOURCES AND RANGE OF ETHANE P-V-T DATA SET

	P Range/kbar	T Range/K
Uematsu et.al.(1975)**	0.3	448-498
Douslin & Harrison(1973)***	0.4	473-623
Goodwin et.al.(1976)*	0.7-0.5	500-700
Tsiklis et.al.(1972)**	9.0-2.0	373-673

* volumetric data smoothed by best fit to derived equations of state; data represents a compilation from several sources.
** experimental volumetric data presented in smoothed form; smoothing procedure specified.
*** experimental volumetric data presented in unsmoothed form.

ETHANE(C2H6) : TABLE OF MOLAR VOLUMES[cm3/mol] 5-PARAMETER MRK EQN

b1=7.637E+01 b2=5.605E+03 a1=1.826E+08 a2=5.332E+09 a3=1.417E+11

Pressure (kbar)	Temperature (K/degC): 673.15 400	873.15 600	1073.15 800	1273.15 1000	1473.15 1200	1673.15 1400
0.5	137.58	180.15	220.38	258.83	296.05	332.42
1.0	95.39	116.54	137.01	156.78	175.99	194.76
1.5	80.46	94.84	108.81	122.34	135.49	148.34
2.0	72.31	83.40	94.16	104.58	114.71	124.59
2.5	67.00	76.13	84.98	93.54	101.86	109.96
3.0	63.19	71.00	78.58	85.91	93.01	99.93
4.0	57.96	64.12	70.10	75.86	81.45	86.88
5.0	54.45	59.61	64.60	69.42	74.09	78.61
6.0	51.88	56.35	60.68	64.86	68.90	72.82
7.0	49.89	53.86	57.71	61.42	65.01	68.49
8.0	48.29	51.87	55.35	58.71	61.96	65.10
9.0	46.96	50.24	53.43	56.50	59.48	62.35
10.0	45.84	48.86	51.81	54.66	57.41	60.08
15.0	42.00	44.23	46.44	48.57	50.64	52.63
20.0	39.68	41.48	43.28	45.04	46.73	48.37
25.0	38.07	39.61	41.15	42.65	44.11	45.52
30.0	36.88	38.21	39.57	40.90	42.20	43.45
35.0	35.93	37.12	38.35	39.55	40.72	41.86
40.0	35.17	36.24	37.36	38.46	39.53	40.58
50.0	33.98	34.88	35.84	36.79	37.72	38.63
100.0	30.94	31.44	32.02	32.62	33.22	33.81

ETHANE(C2H6) : TABLE OF ln(FUGACITY COEFFICIENTS) 5-PARAMETER MRK EQN

b1=7.637E+01 b2=5.605E+03 a1=1.826E+08 a2=5.332E+09 a3=1.417E+11

Pressure (kbar)	Temperature (K/degC): 673.15 400	873.15 600	1073.15 800	1273.15 1000	1473.15 1200	1673.15 1400
0.5	-0.007	0.140	0.185	0.195	0.193	0.186
1.0	0.298	0.418	0.440	0.429	0.408	0.384
1.5	0.670	0.731	0.713	0.672	0.627	0.584
2.0	1.062	1.054	0.990	0.916	0.846	0.783
2.5	1.460	1.379	1.267	1.159	1.063	0.979
3.0	1.858	1.702	1.542	1.400	1.278	1.173
4.0	2.649	2.341	2.084	1.872	1.698	1.553
5.0	3.429	2.969	2.613	2.334	2.108	1.923
6.0	4.195	3.584	3.132	2.784	2.508	2.284
7.0	4.949	4.188	3.641	3.226	2.900	2.637
8.0	5.693	4.782	4.140	3.660	3.284	2.983
9.0	6.425	5.367	4.632	4.086	3.662	3.323
10.0	7.149	5.944	5.116	4.505	4.034	3.657
15.0	10.650	8.728	7.447	6.522	5.819	5.262
20.0	14.003	11.386	9.667	8.439	7.512	6.784
25.0	17.249	13.951	11.806	10.284	9.140	8.245
30.0	20.412	16.447	13.884	12.073	10.718	9.660
35.0	23.509	18.886	15.911	13.818	12.255	11.038
40.0	26.551	21.278	17.898	15.526	13.758	12.385
50.0	32.500	25.948	21.772	18.853	16.685	15.005
100.0	60.585	47.897	39.912	34.386	30.316	27.182

ETHANE(C2H6) : TABLE OF MOLAR VOLUMES[cm3/mol] 5-PARAMETER MRK EQN

b1=7.637E+01 b2=5.605E+03 a1=1.826E+08 a2=5.332E+09 a3=1.417E+11

Pressure (kbar)	Temperature (K/degC): 1000 727	1100 827	1200 927	1300 1027	1400 1127	1500 1227
0.5	205.90	225.63	244.93	263.89	282.55	300.98
1.0	129.61	139.70	149.62	159.39	169.02	178.54
1.5	103.75	110.65	117.43	124.12	130.72	137.23
2.0	90.26	95.58	100.81	105.96	111.04	116.05
2.5	81.77	86.14	90.44	94.67	98.84	102.96
3.0	75.84	79.58	83.25	86.87	90.44	93.95
4.0	67.94	70.88	73.78	76.62	79.43	82.19
5.0	62.80	65.26	67.68	70.06	72.40	74.70
6.0	59.12	61.25	63.35	65.41	67.44	69.43
7.0	56.32	58.21	60.08	61.91	63.71	65.48
8.0	54.09	55.81	57.50	59.15	60.78	62.38
9.0	52.27	53.85	55.39	56.91	58.40	59.87
10.0	50.74	52.20	53.63	55.04	56.42	57.78
15.0	45.64	46.73	47.80	48.85	49.89	50.91
20.0	42.63	43.52	44.40	45.27	46.12	46.95
25.0	40.59	41.35	42.11	42.85	43.58	44.30
30.0	39.08	39.75	40.42	41.08	41.73	42.37
35.0	37.90	38.51	39.11	39.71	40.30	40.87
40.0	36.95	37.50	38.06	38.60	39.14	39.67
50.0	35.49	35.97	36.44	36.92	37.38	37.85
100.0	31.80	32.10	32.40	32.70	33.00	33.30

ETHANE(C2H6) : TABLE OF ln(FUGACITY COEFFICIENTS) 5-PARAMETER MRK EQN

b1=7.637E+01 b2=5.605E+03 a1=1.826E+08 a2=5.332E+09 a3=1.417E+11

Pressure (kbar)	Temperature (K/degC): 1000 727	1100 827	1200 927	1300 1027	1400 1127	1500 1227
0.5	0.174	0.188	0.194	0.196	0.195	0.192
1.0	0.438	0.439	0.435	0.426	0.416	0.404
1.5	0.724	0.708	0.688	0.666	0.644	0.621
2.0	1.016	0.980	0.943	0.907	0.871	0.837
2.5	1.308	1.252	1.198	1.146	1.097	1.051
3.0	1.599	1.522	1.450	1.382	1.320	1.263
4.0	2.172	2.053	1.945	1.847	1.758	1.677
5.0	2.733	2.572	2.429	2.301	2.185	2.081
6.0	3.283	3.080	2.902	2.744	2.603	2.476
7.0	3.822	3.579	3.366	3.178	3.011	2.862
8.0	4.352	4.068	3.821	3.604	3.412	3.240
9.0	4.874	4.549	4.269	4.023	3.806	3.612
10.0	5.388	5.023	4.709	4.435	4.193	3.978
15.0	7.864	7.306	6.830	6.417	6.056	5.736
20.0	10.224	9.479	8.846	8.300	7.824	7.404
25.0	12.500	11.573	10.787	10.112	9.524	9.008
30.0	14.711	13.606	12.671	11.869	11.172	10.561
35.0	16.870	15.589	14.509	13.582	12.779	12.074
40.0	18.986	17.533	16.308	15.259	14.351	13.555
50.0	23.114	21.322	19.814	18.525	17.411	16.435
100.0	42.468	39.056	36.200	33.770	31.675	29.849

ETHANE(C2H6) ln(FUGACITY COEFFICIENTS) : A COMPARISON OF 5-PARAMETER MRK EQN DERIVED COEFFICIENTS WITH LITERATURE VALUES. Temp= 673.15 K (400 degC).

Pressure (kbar)	ln(fugacity coefficient) (this work)	Difference (literature value*)minus(this work):		
		RK	RJ	T
0.5	-0.007	-0.004	0.007	
1.0	0.298	-0.083	-0.094	
1.5	0.670	-0.147	-0.186	
2.0	1.062	-0.197	-0.265	
2.5	1.460	-0.234	-0.332	0.746
3.0	1.858	-0.260	-0.388	0.735
4.0	2.649	-0.288	-0.477	0.727
5.0	3.429	-0.291	-0.540	0.724
6.0	4.195	-0.271	-0.581	0.695
7.0	4.949	-0.234	-0.604	0.740
8.0	5.693	-0.184	-0.614	0.753
9.0	6.425	-0.119	-0.610	0.770
10.0	7.149	-0.044	-0.596	
15.0	10.650	0.463	-0.391	
20.0	14.003	1.130	-0.027	
25.0	17.249	1.910	0.450	
30.0	20.412	2.775	1.013	
35.0	23.509	3.707	1.643	

* RK = Redlich & Kwong(1949) with a=9.8892E+07 and b=45.1815 cm3/mol.
RJ = Robinson & Jacoby(1965).
T = Tsiklis et al.(1972).

APPENDICES 7 AND 8

LISTING OF COMPUTER PROGRAMS

COH/DIAMOND6

COH/FLUID6

```
$RESET LIST
COMMENT-----------------------------------------------------------------
                    PROGRAM "COH/DIAMOND6"
  A program that calculates the fugacity coefficients and molar volumes
  of fluid species in the system C-O-H under supercritical conditions
  using a 5-parameter MRK equation of state of the form:

                R*T*(1 + y + y2 - y3)        a1 + a2/V + a3/V2
        P   =   ---------------------    -   -----------------
                     V*(1-y)3                 sqrt(T)*V*(V+b)

  where y = b/4V and b = b1 + b2/T, cf. Kerrick & Jacobs(1981). Mole
  fractions of species in fluid mixtures in equilibrium with diamond
  are calculated at specified P,T & fO2.
  1= H2O(water)      2= CO2(carbon dioxide)  3= CO(carbon monoxide)
  4= H2(hydrogen)    5= CH4(methane)         6= C2H6(ethane)

     Program written in B6800 ALGOL by W.R.Taylor  10-APR-83
                                       modified  09-MAY-84
-----------------------------------------------------------------------;
BEGIN

FILE IN(KIND=DISK,FILETYPE=8,TITLE="COH/DIAMOND6/IN.");
FILE OUT1(KIND=PRINTER);
FILE OUT2(KIND=DISK,FILEKIND=DATA,TITLE="COH/DIAMOND6/OUT.");
FILE OUT3(KIND=DISK,FILEKIND=DATA,TITLE="COH/DIAMOND6/FUG.");

REAL ARRAY X,V,Z,Y,A,B,C,D,E,CSTAR,DSTAR,ESTAR,XOLD[1:6],
           CINT,DINT,EINT[1:6,1:6],F,LNOPURE,LNOMIX[1:6];
BOOLEAN ARRAY ERROR[1:3],DISKOUTPUT[1:2];
BOOLEAN CONVERGED,DIAMONDSTABLE;
REAL P,T,R,AMIX,BMIX,CMIX,DMIX,EMIX,YMIX,VMIX,ZMIX,FO2,LNFH2O,XOVAP,
     KCO2,KCO,KH2O,KCH4,KC2H6,XCVAP,LGFO2,LGFO2MIN,LGFO2MAX,STEPSZ;
INTEGER I,J,K,N,MAXN,ITERATION;
LABEL ERRORMESSAGE,DIAMONDLIMIT,NOCONVERGENCE,NEXTLOOP;
DEFINE FORR(S,U,W) = FOR S:=U STEP 1 UNTIL W #;

PROCEDURE ASSIGNPARAMETERS; BEGIN
  R:=83.143;
  COMMENT: MRK coefficients for H2O, CO2, CO, H2, CH4 & C2H6;
  B[1]:=21.34 + 5420/T;  C[1]:=1.329@8; D[1]:=2.541@9; E[1]:=1.915@10;
  B[2]:=45.53 + 10730/T; C[2]:=1.287@8; D[2]:=1.122@9; E[2]:=4.443@11;
  B[3]:=40.11 + 3769/T;  C[3]:=3.869@7; D[3]:=6.450@8; E[3]:=8.008@9;
  B[4]:=15.36 + 3011/T;  C[4]:=4.521@6; D[4]:=5.734@7; E[4]:=1.693@9;
  B[5]:=43.38 + 7409/T;  C[5]:=6.742@7; D[5]:=2.893@9; E[5]:=9.749@10;
  B[6]:=76.37 + 5605/T;  C[6]:=1.826@8; D[6]:=5.332@9; E[6]:=1.417@11;
END OF ASSIGNPARAMETERS;

PROCEDURE BMIXCALC(ELEMENT,PMIX);
 VALUE ELEMENT; INTEGER ELEMENT; REAL PMIX; BEGIN
  PMIX:=0;
  FORR(J,1,ELEMENT) DO PMIX:=PMIX + B[J]*X[J];
END OF BMIXCALC;

PROCEDURE PINTCALC(PARAMETER,ELEMENT,PINT);
 VALUE ELEMENT; INTEGER ELEMENT; REAL ARRAY PARAMETER[1],PINT[1,1];
 BEGIN
  FORR(I,1,ELEMENT) DO BEGIN
    FORR(J,1,ELEMENT) DO PINT[I,J]:=(PARAMETER[I]*PARAMETER[J])**0.5;
  END;
END OF PINTCALC;

PROCEDURE PMIXCALC(PINT,ELEMENT,PMIX);
 VALUE ELEMENT; INTEGER ELEMENT; REAL ARRAY PINT[1,1]; REAL PMIX;
 BEGIN
  PMIX:=0;
  FORR(I,1,ELEMENT) DO BEGIN
    FORR(J,1,ELEMENT) DO PMIX:=PMIX + PINT[I,J]*X[I]*X[J];
  END;
END OF PMIXCALC;

PROCEDURE PSTARCALC(K,PINT,ELEMENT,PMIX,TYPE,PSTAR);
 VALUE K,ELEMENT,PMIX,TYPE; INTEGER K,ELEMENT,TYPE; REAL PMIX,PSTAR;
 REAL ARRAY PINT[1,1]; BEGIN
  PSTAR:=0;
  FORR(J,1,ELEMENT) DO PSTAR:=PSTAR + 2*PINT[K,J]*X[J];
  PSTAR:=PSTAR + TYPE*PMIX;
END OF PSTARCALC;

PROCEDURE VOLUMECALC(VI,CI,DI,EI,BI,AOUT,VOUT,ZOUT,YOUT);
 VALUE VI,CI,DI,EI,BI; DOUBLE VI,CI,DI,EI,BI; REAL AOUT,VOUT,ZOUT,YOUT;
 BEGIN
  DOUBLE PES,AI,YI;
  PROCEDURE ASMBLV(G); VALUE G; DOUBLE G; BEGIN
    PROCEDURE CALCPES; BEGIN
      YI:=BI/(4*VI);
      AI:=CI + DI/VI + EI/VI**2;
      PES:=(R*T*(1+YI+(YI**2)-(YI**3)))/(VI*(1-YI)**3)
           -(AI/((T**0.5)*VI*(VI+BI)));
    END OF CALCPES;
    ERROR[1]:=FALSE;
    IF G=0 THEN CALCPES ELSE BEGIN
      WHILE PES>P DO BEGIN VI:=VI+G; CALCPES; END;
      IF PES<P THEN BEGIN
        VI:=VI-G; CALCPES;
        IF PES<P THEN BEGIN ERROR[1]:=TRUE; GO TO ERRORMESSAGE; END;
      END;
    END;
  END OF ASMBLV;
  ASMBLV(0);
  FORR(J,0,9) DO ASMBLV(10**(-J));
  AOUT:=AI; VOUT:=VI;
  YOUT:=BI/(4*VOUT);
  ZOUT:=(P*VOUT)/(R*T);
END OF VOLUMECALC;

PROCEDURE CALCFUGCOEFFPURE(BI,CI,DI,EI,VI,YI,ZI,LNO);
 VALUE BI,CI,DI,EI,VI,YI,ZI; REAL BI,CI,DI,EI,VI,YI,ZI,LNO;
  BEGIN
    REAL RT32; RT32:=R*(T**1.5);
    LNO:=((8*YI)-(9*YI**2)+(3*YI**3))/(1-YI)**3
         -LN(ZI)
         -CI/(RT32*(VI+BI))
         -DI/(RT32*VI*(VI+BI))
         -EI/(RT32*(VI**2)*(VI+BI))
         +(CI/(RT32*BI))*LN(VI/(VI+BI))
         -DI/(RT32*BI*VI)
```

```
          +(DI/(RT32*(BI**2)))*LN((VI+BI)/VI)
          -EI/(RT32*2*BI*(VI**2))
          +EI/(RT32*(BI**2)*VI)
          -(EI/(RT32*(BI**3)))*LN((VI+BI)/VI);
END OF CALCFUGCOEFFPURE;

PROCEDURE CALCFUGCOEFFMIX(K,BM,CM,DM,EM,VM,YM,ZM,BI,CS,DS,ES,LNO);
 VALUE K,BM,CM,DM,EM,VM,YM,ZM,BI,CS,DS,ES; INTEGER K;
 REAL BM,CM,DM,EM,VM,YM,ZM,BI,CS,DS,ES,LNO;
 BEGIN
   REAL RT32,VB; RT32:=R*(T**1.5); VB:=(VM+BM)/VM;
   LNO:= (4*YM-3*(YM**2))/(1-YM)**2
        +(B[K]/BM)*((4*YM-2*(YM**2))/(1-YM)**3)
        -(B[K]*CM)/(RT32*BM*(BM+VM))
        +((B[K]*CM)/(RT32*(BM**2)))*LN(VB)
        -(CS/(RT32*BM))*LN(VB)
        -DS/(RT32*BM*VM)
        +(DS/(RT32*(BM**2)))*LN(VB)
        +(B[K]*DM)/(RT32*VM*BM*(VM+BM))
        +(2*B[K]*DM)/(RT32*(BM**2)*(VM+BM))
        -((2*B[K]*DM)/(RT32*(BM**3)))*LN(VB)
        -ES/(RT32*2*BM*(VM**2))
        +ES/(RT32*(BM**2)*VM)
        -(ES/(RT32*(BM**3)))*LN(VB)
        +(B[K]*EM)/(RT32*2*BM*(VM**2)*(VM+BM))
        -(3*B[K]*EM)/(RT32*2*(BM**2)*VM*(VM+BM))
        +((3*B[K]*EM)/(RT32*(BM**4)))*LN(VB)
        -(3*B[K]*EM)/(RT32*(BM**3)*(VM+BM))
        -LN(ZM);
END OF CALCFUGCOEFFMIX;

PROCEDURE CALCEQCONST(DA,DB,DC,DD,DE,DVS,DAV,DBV,DSR,DGR,TR,EQK);
 VALUE DA,DB,DC,DD,DE,DVS,DAV,DBV,DSR,DGR,TR;
 REAL DA,DB,DC,DD,DE,DVS,DAV,DBV,DSR,DGR,TR,EQK;
 BEGIN
   REAL ENTHALINT,ENTROPINT,VOLUMEINT,DGRPT;
   ENTHALINT:=DA*(T-TR) + (DB/2)*(T**2-TR**2) - DC*(1/T-1/TR)
              + 2*DD*(T**0.5-TR**0.5) + (DE/3)*(T**3-TR**3);
   ENTROPINT:=DA*LN(T/TR) + DB*(T-TR) - (DC/2)*(1/T**2-1/TR**2)
              - 2*DD*(1/T**0.5-1/TR**0.5) + (DE/2)*(T**2-TR**2);
   VOLUMEINT:=(DVS + DAV*(T-TR))*P - 0.5*DBV*(P**2);
   DGRPT:=DGR - DSR*(T-TR) + ENTHALINT - T*ENTROPINT + VOLUMEINT;
   EQK:=EXP(-DGRPT/(8.3143*T));
END OF CALCEQCONST;

PROCEDURE SOLVEFORFH2O(LNO,LNFWATER);
 REAL ARRAY LNO[1]; REAL LNFWATER;
 BEGIN
   DOUBLE ARRAY Q[0:3]; DOUBLE PES,FH2O;
   PROCEDURE ASMBLF(G); VALUE G; DOUBLE G; BEGIN
     PROCEDURE CALCPES; BEGIN
       PES:=Q[0]*(FH2O**3) + Q[1]*(FH2O**2) + Q[2]*FH2O + Q[3];
     END OF CALCPES;
     ERROR[2]:=FALSE;
     IF G=0 THEN CALCPES ELSE BEGIN
       WHILE PES>P DO BEGIN
         FH2O:=DEXP(DLN(FH2O)-G); CALCPES;
       END;
       IF PES<P THEN BEGIN
         FH2O:=DEXP(DLN(FH2O)+G); CALCPES;
         IF PES<P THEN BEGIN ERROR[2]:=TRUE; GO TO ERRORMESSAGE; END;
       END;
     END;
   END OF ASMBLF;
   Q[0]:=(KC2H6*(KCH4**2))/((KH2O**3)*(FO2**1.5)*EXP(LNO[6]));
   Q[1]:=KCH4/(FO2*(KH2O**2)*EXP(LNO[5]));
   Q[2]:=1/(KH2O*(FO2**0.5)*EXP(LNO[4])) + 1/EXP(LNO[1]);
   Q[3]:=(KCO2*FO2)/EXP(LNO[2]) + (KCO*KCO2*FO2)**0.5/EXP(LNO[3]);
   IF (Q[3]<P) THEN BEGIN
     FH2O:=(P/Q[2]); ASMBLF(0); ERROR[3]:=FALSE;
   END ELSE BEGIN
     ERROR[3]:=TRUE; GO TO DIAMONDLIMIT;
   END;
   FORR(J,0,9) DO ASMBLF(10**(-J));
   LNFWATER:=DLN(FH2O);
END OF SOLVEFORFH2O;

PROCEDURE CALCMOLFRACTIONS(LNO,LNFWATER,FUG,XOUT);
 REAL ARRAY LNO,FUG,XOUT[1]; REAL LNFWATER;
 BEGIN
   FUG[1]:=EXP(LNFWATER);
   FUG[2]:=KCO2*FO2;
   FUG[3]:=(KCO*FUG[2])**0.5;
   FUG[4]:=FUG[1]/(KH2O*(FO2**0.5));
   FUG[5]:=KCH4*(FUG[4]**2);
   FUG[6]:=(KC2H6*FUG[5]**2)/FUG[4];
   FORR(J,1,6) DO XOUT[J]:=FUG[J]/(EXP(LNO[J])*P);
END OF CALCMOLFRACTIONS;

BEGIN
COMMENT-----------------------------------------------------------------
          INPUT FILE STRUCTURE(free-field format):
 line(1)  output to disk-file option (T or F)
          mole fraction & fugacity coefficient results,
          fugacities in bars of all species.
 line(2)  number of fO2 regions required,
          pressure(kbar),
          temperature(K).
 line(3)  fO2 region limits and step size parameter
          log(fO2)min, log(fO2)max, step size.
 example  T,F
          2,30.0,1400
          -18.0,-10.0,0.50
          -9.9,-6.0,0.10
-----------------------------------------------------------------------;
  READ(IN,/,FORR(J,1,2) DO DISKOUTPUT[J]);
  READ(IN,/,MAXN,P,T);
  IF P<(19.4 + (T-273.15)/40) THEN DIAMONDSTABLE:=FALSE
  ELSE DIAMONDSTABLE:=TRUE;
  P:=P*1000;
  WRITE(OUT1,<"*********** FLUID COMPOSITIONS IN THE SYSTEM C-O-H + ",
        "DIAMOND UNDER SUPERCRITICAL CONDITIONS ***********"/>);
  WRITE(OUT1,<"Pressure=",F5.1," kbar   Temp=",I5," K  (",I4," degC)"/>,
        P/1000,T,T-273);
  IF NOT DIAMONDSTABLE THEN WRITE(OUT1,<"** NOTE: Diamond is metastable"
    ," under these P,T conditions **"/>);
  ASSIGNPARAMETERS;
  PINTCALC(C,6,CINT);
  PINTCALC(D,6,DINT);
  PINTCALC(E,6,EINT);
```

```
COMMENT-----------------------------------------------------------------
     EQUILIBRIUM CONSTANTS:
     KCO2   :    C(diamond) + O2  =  CO2
     KCO    :    C(diamond) + CO2  =  2CO
     KH2O   :    H2 + (1/2)O2  =  H2O
     KCH4   :    C(diamond) + 2H2  =  CH4
     KC2H6  :    2CH4  =  C2H6 + H2
-----------------------------------------------------------------------;
CALCEQCONST(-58.943,3.460112@-2,-1.00942@6,1.0808@3,-1.0977@-5,
            -0.3417,-3.58785@-6,-6.8340@-8,
            6.26,-3.97275@5,298.15,KCO2);
CALCEQCONST(-94.805,3.900397@-2,-5.9761@5,1.82848@3,-1.0977@-5,
            -0.3417,-3.58785@-6,-6.8340@-8,
            179.17,1.17133@5,298.15,KCO);
CALCEQCONST(-2.42334@1,1.610666@-2,3.7635@4,1.619@2,-3.4218@-6,
             0.00,0.00,0.00,
            -4.4425@1,-2.28569@5,298.15,KH2O);
CALCEQCONST(-34.3538,5.6326@-2,1.68782@6,-4.8154@2,-1.87952@-5,
            -0.3417,-3.58785@-6,-6.8340@-8,
            -77.48,-5.3608@4,298.15,KCH4);
CALCEQCONST(54.9604,-5.432@-2,-1.11401@6,-3.0693@2,1.98061@-5,
            0.00,0.00,0.00,
            -12.42,6.8488@4,298.15,KC2H6);
WRITE(OUT1,<"K(CO2)=",E10.4," K(CO)=",E10.4," K(H2O)=",E10.4," ",
     "K(CH4)=",E10.4," K(C2H6)=",E10.4,/>,KCO2,KCO,KH2O,KCH4,KC2H6);
FORR(K,1,6) DO BEGIN
  VOLUMECALC((B[K]/4+1),C[K],D[K],E[K],B[K],A[K],V[K],Z[K],Y[K]);
  CALCFUGCOEFFPURE(B[K],C[K],D[K],E[K],V[K],Y[K],Z[K],LNOPURE[K]);
END;
WRITE(OUT1,<"**Pure Fluids**",X2,"Molar Volumes [cm3/mol]:",X16,
     "Ln(Fugacity Coefficients):">);
WRITE(OUT1,<X17,"H2O   CO2   CO    H2   CH4  C2H6 ",
     "       H2O    CO2    CO     H2     CH4   C2H6">);
WRITE(OUT1,<X15,6(F5.2,X1),X4,6(F6.3,X1)/>,FORR(K,1,6) DO V[K],
       FORR(K,1,6) DO LNOPURE[K]);
WRITE(OUT1,<"**Mixed Fluids**">);
WRITE(OUT1,<X26,"Mole Percent [100*X]:",X10,"Molar",X4,
     "Ln(Fugacity Coefficients):">);
WRITE(OUT1,<"log(fO2) C/C+H2 O2/O2+H2  H2O  CO2   CO   H2  CH4 C2H6 ",
     "  Volume   H2O    CO2    CO     H2     CH4   C2H6    NI">);
WRITE(OUT1,<111("-")>);
FORR(N,1,MAXN) DO BEGIN
  READ(IN,/,LGFO2MIN,LGFO2MAX,STEPSZ);
  FOR LGFO2:=LGFO2MIN STEP STEPSZ UNTIL LGFO2MAX DO BEGIN
    FO2:=10**(LGFO2);
    SOLVEFORFH2O(LNOPURE,LNFH2O);
    CALCMOLFRACTIONS(LNOPURE,LNFH2O,F,X);
    FORR(K,1,6) DO XOLD[K]:=X[K];
    CONVERGED:=FALSE; ITERATION:=0;
    WHILE NOT CONVERGED DO BEGIN
      BMIXCALC(6,BMIX);
      PMIXCALC(CINT,6,CMIX);
      PMIXCALC(DINT,6,DMIX);
      PMIXCALC(EINT,6,EMIX);
      FORR(K,1,6) DO BEGIN
        PSTARCALC(K,CINT,6,CMIX,0,CSTAR[K]);
        PSTARCALC(K,DINT,6,DMIX,1,DSTAR[K]);
        PSTARCALC(K,EINT,6,EMIX,2,ESTAR[K]);
      END;
      VOLUMECALC((BMIX/4+1),CMIX,DMIX,EMIX,BMIX,AMIX,VMIX,ZMIX,YMIX);
      FORR(K,1,6) DO BEGIN
        CALCFUGCOEFFMIX(K,BMIX,CMIX,DMIX,EMIX,VMIX,YMIX,ZMIX,B[K],
        CSTAR[K],DSTAR[K],ESTAR[K],LNOMIX[K]);
      END;
      SOLVEFORFH2O(LNOMIX,LNFH2O);
      CALCMOLFRACTIONS(LNOMIX,LNFH2O,F,X);
      FORR(K,1,6) DO IF ABS(XOLD[K]-X[K])>1@-9 THEN BEGIN
        CONVERGED:=FALSE; GO TO NEXTLOOP;
      END ELSE CONVERGED:=TRUE;
      NEXTLOOP:ITERATION:=ITERATION+1;
      IF ITERATION>30 THEN GO TO NOCONVERGENCE;
      FORR(K,1,6) DO XOLD[K]:=X[K];
    END;
    NOCONVERGENCE:IF NOT CONVERGED THEN WRITE(OUT1,<F8.3,X4,"***",
    "convergence was not achieved after 30 iterations*">,LOG(FO2));
    XCVAP:=X[2] + X[3] + (X[5]/3) + (2*X[6]/5);
    XOVAP:=(X[1]/3) + X[2] + X[3];
    WRITE(OUT1,<F7.3,2F8.3,X2,6(F4.1,X1),F7.2,X2,6(F6.3,X1),X1,"(",I2,
         ")"/>,LOG(FO2),XCVAP,XOVAP,FORR(K,1,6) DO 100*X[K],VMIX,
         FORR(K,1,6) DO LNOMIX[K],ITERATION);
    IF DISKOUTPUT[1] THEN WRITE(OUT2,<2F6.3,F8.3,6(F5.1),F9.3>,XCVAP,
      XOVAP,VMIX,FORR(K,1,6) DO 100*X[K],-LOG(FO2));
    IF DISKOUTPUT[2] THEN WRITE(OUT3,<F7.3,6E12.5>,-LOG(F02),
      FORR(K,1,6) DO (P*X[K]*EXP(LNOMIX[K])));
    ERRORMESSAGE:IF ERROR[1] OR ERROR[2] THEN WRITE(OUT1,<F8.3,X4,
    "*Error detected in PROC ASMBLX*"/>,LOG(FO2));
    DIAMONDLIMIT:IF ERROR[3] THEN WRITE(OUT1,<F8.3,X4,"*Diamond",
    " stability exceeded at this log(fO2)*"/>,LOG(FO2));
  END;
END;
WRITE(OUT1,<111("-")>);
CLOSE(OUT2,CRUNCH);
CLOSE(OUT3,CRUNCH);
END;

END OF PROGRAM.
```

```
$RESET LIST
COMMENT-----------------------------------------------------------------
                    PROGRAM "COH/FLUID6"
  A program that calculates the fugacity coefficients and molar volumes
  of fluid species in the system C-O-H under supercritical conditions
  using a 5-parameter MRK equation of state of the form:

                R*T*(1 + y + y2 - y3)        a1 + a2/V + a3/V2
        P   =   ---------------------    -   -----------------
                     V*(1-y)3                 sqrt(T)*V*(V+b)

  where y = b/4V and b = b1 + b2/T, cf. Kerrick & Jacobs(1981). Mole
  fractions of species in fluid mixtures in the absence of a crystal-
  line carbon phase are calculated at specified P,T,fO2 & X(C/C+H2)
  of the bulk fluid.
  1= H2O(water)      2= CO2(carbon dioxide)  3= CO(carbon monoxide)
  4= H2(hydrogen)    5= CH4(methane)         6= C2H6(ethane)

     Program written in B6800 ALGOL by W.R.Taylor  10-APR-83
                                       modified  30-MAY-84
-----------------------------------------------------------------------;
BEGIN

FILE IN(KIND=DISK,FILETYPE=8,TITLE="COH/FLUID6/IN.");
FILE OUT1(KIND=PRINTER);
FILE OUT2(KIND=DISK,FILEKIND=DATA,TITLE="COH/FLUID6/OUT.");
FILE OUT3(KIND=DISK,FILEKIND=DATA,TITLE="COH/FLUID6/LGX.");

REAL ARRAY X,V,Z,Y,A,B,C,D,E,CSTAR,DSTAR,ESTAR,XOLD[1:6],
           CINT,DINT,EINT[1:6,1:6],F,LNOPURE,LNOMIX[1:6];
BOOLEAN ARRAY ERROR[1:3],DISKOUTPUT[1:2]; BOOLEAN CONVERGED;
REAL P,T,R,AMIX,BMIX,CMIX,DMIX,EMIX,YMIX,VMIX,ZMIX,FO2,XO,XC,
     KCO,KH2O,KCH4,KC2H6;
DOUBLE FUGACITYH2,FUGACITYCO;
INTEGER I,J,K,N,MAXN,ITERATION;
LABEL ERRORMESSAGE,NOCONVERGENCE,NEXTLOOP;
DEFINE FORR(S,U,W) = FOR S:=U STEP 1 UNTIL W #;

PROCEDURE ASSIGNPARAMETERS; BEGIN
  R:=83.143;
  COMMENT: MRK coefficients for H2O, CO2, CO, H2, CH4 & C2H6;
  B[1]:=21.34 + 5420/T;  C[1]:=1.32@8; D[1]:=2.541@9; E[1]:=1.915@10;
  B[2]:=45.53 + 10730/T; C[2]:=1.287@8; D[2]:=1.122@9; E[2]:=4.443@11;
  B[3]:=40.11 + 3769/T;  C[3]:=3.869@7; D[3]:=6.450@8; E[3]:=8.008@9;
  B[4]:=15.36 + 3011/T;  C[4]:=4.521@6; D[4]:=5.734@7; E[4]:=1.693@9;
  B[5]:=43.38 + 7409/T;  C[5]:=6.742@7; D[5]:=2.893@9; E[5]:=9.749@10;
  B[6]:=76.37 + 5605/T;  C[6]:=1.826@8; D[6]:=5.332@9; E[6]:=1.417@11;
END OF ASSIGNPARAMETERS;

PROCEDURE BMIXCALC(ELEMENT,PMIX);
 VALUE ELEMENT; INTEGER ELEMENT; REAL PMIX; BEGIN
  PMIX:=0;
  FORR(J,1,ELEMENT) DO PMIX:=PMIX + B[J]*X[J];
END OF BMIXCALC;

PROCEDURE PINTCALC(PARAMETER,ELEMENT,PINT);
 VALUE ELEMENT; INTEGER ELEMENT; REAL ARRAY PARAMETER[1],PINT[1,1];
 BEGIN
  FORR(I,1,ELEMENT) DO BEGIN
    FORR(J,1,ELEMENT) DO PINT[I,J]:=(PARAMETER[I]*PARAMETER[J])**0.5;
  END;
END OF PINTCALC;

PROCEDURE PMIXCALC(PINT,ELEMENT,PMIX);
 VALUE ELEMENT; INTEGER ELEMENT; REAL ARRAY PINT[1,1]; REAL PMIX;
 BEGIN
  PMIX:=0;
  FORR(I,1,ELEMENT) DO BEGIN
    FORR(J,1,ELEMENT) DO PMIX:=PMIX + PINT[I,J]*X[I]*X[J];
  END;
END OF PMIXCALC;

PROCEDURE PSTARCALC(K,PINT,ELEMENT,PMIX,TYPE,PSTAR);
 VALUE K,ELEMENT,PMIX,TYPE; INTEGER K,ELEMENT,TYPE; REAL PMIX,PSTAR;
 REAL ARRAY PINT[1,1]; BEGIN
  PSTAR:=0;
  FORR(J,1,ELEMENT) DO PSTAR:=PSTAR + 2*PINT[K,J]*X[J];
  PSTAR:=PSTAR + TYPE*PMIX;
END OF PSTARCALC;

PROCEDURE VOLUMECALC(VI,CI,DI,EI,BI,AOUT,VOUT,ZOUT,YOUT);
 VALUE VI,CI,DI,EI,BI; REAL VI,CI,DI,EI,BI;
 REAL AOUT,VOUT,ZOUT,YOUT;
 BEGIN
  REAL PES,AI,YI;
  PROCEDURE ASMBLV(G); VALUE G; REAL G; BEGIN
    PROCEDURE CALCPES; BEGIN
      YI:=BI/(4*VI);
      AI:=CI + DI/VI + EI/VI**2;
      PES:=(R*T*(1+YI+(YI**2)-(YI**3)))/(VI*(1-YI)**3)
           -(AI/((T**0.5)*VI*(VI+BI)));
    END OF CALCPES;
    ERROR[1]:=FALSE;
    IF G=0 THEN CALCPES ELSE BEGIN
      WHILE PES>P DO BEGIN VI:=VI+G; CALCPES; END;
      IF PES<P THEN BEGIN
        VI:=VI-G; CALCPES;
        IF PES<P THEN BEGIN ERROR[1]:=TRUE; GO TO ERRORMESSAGE; END;
      END;
    END;
  END OF ASMBLV;
  ASMBLV(0);
  FORR(J,0,9) DO ASMBLV(10**(-J));
  AOUT:=AI; VOUT:=VI;
  YOUT:=BI/(4*VOUT);
  ZOUT:=(P*VOUT)/(R*T);
END OF VOLUMECALC;

PROCEDURE CALCFUGCOEFFPURE(BI,CI,DI,EI,VI,YI,ZI,LNO);
```

```
 VALUE BI,CI,DI,EI,VI,YI,ZI; REAL BI,CI,DI,EI,VI,YI,ZI,LNO;
  BEGIN
    REAL RT32; RT32:=R*(T**1.5);
    LNO:=((8*YI)-(9*YI**2)+(3*YI**3))/(1-YI)**3
          -LN(ZI)
          -CI/(RT32*(VI+BI))
          -DI/(RT32*VI*(VI+BI))
          -EI/(RT32*(VI**2)*(VI+BI))
          +(CI/(RT32*BI))*LN(VI/(VI+BI))
          -DI/(RT32*BI*VI)
          +(DI/(RT32*(BI**2)))*LN((VI+BI)/VI)
          -EI/(RT32*2*BI*(VI**2))
          +EI/(RT32*(BI**2)*VI)
          -(EI/(RT32*(BI**3)))*LN((VI+BI)/VI);
END OF CALCFUGCOEFFPURE;

PROCEDURE CALCFUGCOEFFMIX(K,BM,CM,DM,EM,VM,YM,ZM,BI,CS,DS,ES,LNO);
 VALUE K,BM,CM,DM,EM,VM,YM,ZM,BI,CS,DS,ES; INTEGER K;
 REAL BM,CM,DM,EM,VM,YM,ZM,BI,CS,DS,ES,LNO;
 BEGIN
   REAL RT32,VB; RT32:=R*(T**1.5); VB:=(VM+BM)/VM;
   LNO:= (4*YM-3*(YM**2))/(1-YM)**2
        +(B[K]/BM)*((4*YM-2*(YM**2))/(1-YM)**3)
        -(B[K]*CM)/(RT32*BM*(BM+VM))
        +((B[K]*CM)/(RT32*(BM**2)))*LN(VB)
        -(CS/(RT32*BM))*LN(VB)
        -DS/(RT32*BM*VM)
        +(DS/(RT32*(BM**2)))*LN(VB)
        +(B[K]*DM)/(RT32*VM*BM*(VM+BM))
        +(2*B[K]*DM)/(RT32*(BM**2)*(VM+BM))
        -((2*B[K]*DM)/(RT32*(BM**3)))*LN(VB)
        -ES/(RT32*2*BM*(VM**2))
        +ES/(RT32*(BM**2)*VM)
        -(ES/(RT32*(BM**3)))*LN(VB)
        +(B[K]*EM)/(RT32*2*BM*(VM**2)*(VM+BM))
        -(3*B[K]*EM)/(RT32*2*(BM**2)*VM*(VM+BM))
        +((3*B[K]*EM)/(RT32*(BM**4)))*LN(VB)
        -(3*B[K]*EM)/(RT32*(BM**3)*(VM+BM))
        -LN(ZM);
END OF CALCFUGCOEFFMIX;

PROCEDURE CALCEQCONST(DA,DB,DC,DD,DE,DVS,DAV,DBV,DSR,DGR,TR,EQK);
 VALUE DA,DB,DC,DD,DE,DVS,DAV,DBV,DSR,DGR,TR;
 REAL DA,DB,DC,DD,DE,DVS,DAV,DBV,DSR,DGR,TR,EQK;
 BEGIN
   REAL ENTHALINT,ENTROPINT,VOLUMEINT,DGRPT;
   ENTHALINT:=DA*(T-TR) + (DB/2)*(T**2-TR**2) - DC*(1/T-1/TR)
              + 2*DD*(T**0.5-TR**0.5) + (DE/3)*(T**3-TR**3);
   ENTROPINT:=DA*LN(T/TR) + DB*(T-TR) - (DC/2)*(1/T**2-1/TR**2)
              - 2*DD*(1/T**0.5-1/TR**0.5) + (DE/2)*(T**2-TR**2);
   VOLUMEINT:=(DVS + DAV*(T-TR))*P - 0.5*DBV*(P**2);
   DGRPT:=DGR - DSR*(T-TR) + ENTHALINT - T*ENTROPINT + VOLUMEINT;
   EQK:=EXP(-DGRPT/(8.3143*T));
END OF CALCEQCONST;
```

```
PROCEDURE SOLVEFORFH2(LNO,FHYDROGEN,FMONOXIDE);
 REAL ARRAY LNO[1];
 DOUBLE FHYDROGEN,FMONOXIDE;
 BEGIN
   DOUBLE PES,FH2,FCO; DOUBLE ARRAY Q[0:5];
   PROCEDURE ASMBLF(G); VALUE G; DOUBLE G; BEGIN
     PROCEDURE CALCPES; BEGIN
       DOUBLE ROOT1,ROOT2;
       ROOT1:=(-(Q[3]+Q[4]*FH2**2)+DSQRT((Q[3]+Q[4]*FH2**2)**2
              +(4*Q[5]*FH2**3*P)))/(2*Q[5]*FH2**3);
       ROOT2:=(-(Q[3]+Q[4]*FH2**2)-DSQRT((Q[3]+Q[4]*FH2**2)**2
              +(4*Q[5]*FH2**3*P)))/(2*Q[5]*FH2**3);
       IF ROOT1>ROOT2 THEN FCO:=ROOT1 ELSE FCO:=ROOT2;
       IF (ROOT1<0) AND (ROOT2<0) THEN BEGIN ERROR[3]:=TRUE;
       GO TO ERRORMESSAGE; END ELSE ERROR[3]:=FALSE;
       PES:=Q[1]*FH2 + Q[2]*FCO*(FH2**2) + Q[0]*(FCO**2)*(FH2**3);
     END OF CALCPES;
     ERROR[2]:=FALSE;
     IF G=0 THEN CALCPES ELSE BEGIN
       WHILE PES>P DO BEGIN
         FH2:=DEXP(DLN(FH2)-G); CALCPES;
       END;
       IF PES<P THEN BEGIN
         FH2:=DEXP(DLN(FH2)+G); CALCPES;
         IF PES<P THEN BEGIN ERROR[2]:=TRUE; GO TO ERRORMESSAGE; END;
       END;
     END;
   END OF ASMBLF;
   Q[0]:=(3*KC2H6)/(5*EXP(LNO[6])*(1-XC)*FO2);
   Q[1]:=(KH2O*FO2**0.5)/(EXP(LNO[1])*(1-XC))
         + 1/(EXP(LNO[4])*(1-XC));
   Q[2]:=(2*KCH4)/(3*EXP(LNO[5])*(1-XC)*(FO2**0.5));
   Q[3]:=(KCO*FO2**0.5)/(EXP(LNO[2])*XC) + 1/(EXP(LNO[3])*XC);
   Q[4]:=KCH4/(3*EXP(LNO[5])*XC*(FO2**0.5));
   Q[5]:=(2*KC2H6)/(5*EXP(LNO[6])*XC*FO2);
   FH2:=P/Q[1];
   FORR(J,0,9) DO ASMBLF(10**(-J));
   FHYDROGEN:=FH2;
   FMONOXIDE:=FCO;
END OF SOLVEFORFH2;

PROCEDURE CALCMOLFRACTIONS(LNO,FHYDROGEN,FMONOXIDE,FUG,XOUT);
 VALUE FHYDROGEN,FMONOXIDE; REAL ARRAY LNO,FUG,XOUT[1];
 DOUBLE FHYDROGEN,FMONOXIDE;
 BEGIN
   FUG[4]:=FHYDROGEN;
   FUG[3]:=FMONOXIDE;
   FUG[1]:=KH2O*FUG[4]*(FO2**0.5);
   FUG[2]:=KCO*FUG[3]*(FO2**0.5);
   FUG[5]:=(KCH4*(FUG[4]**2)*FUG[3])/(FO2**0.5);
   FUG[6]:=(KC2H6*(FUG[4]**3)*(FUG[3]**2))/FO2;
   FORR(J,1,6) DO XOUT[J]:=FUG[J]/(EXP(LNO[J])*P);
END OF CALCMOLFRACTIONS;
```

```
BEGIN
  READ(IN,/,MAXN,DISKOUTPUT[1],DISKOUTPUT[2]);
  READ(IN,/,P,T);
  P:=P*1000;
  WRITE(OUT1,<"********* FLUID COMPOSITIONS IN THE SYSTEM C-O-H ( ",
        "FLUID ONLY) UNDER SUPERCRITICAL CONDITIONS *********"/>);
  WRITE(OUT1,<"Pressure=",F5.1," kbar   Temp=",I5," K  (",I4," degC)"/>,
        P/1000,T,T-273);
  ASSIGNPARAMETERS;
  PINTCALC(C,6,CINT);
  PINTCALC(D,6,DINT);
  PINTCALC(E,6,EINT);
  COMMENT-----------------------------------------------------------------
       EQUILIBRIUM CONSTANTS:
       KCO    :    CO + (1/2)O2  =  CO2
       KH2O   :    H2 + (1/2)O2  =  H2O
       KCH4   :    CO + 2H2  =  CH4 + (1/2)O2
       KC2H6  :    2CO + 3H2  =  C2H6 + O2
  ------------------------------------------------------------------------;
  CALCEQCONST(1.7931@1,-2.201425@-3,-2.05905@5,-3.7384@2,0,
              0.00,0.00,0.00,
              -8.6455@1,-2.57204@5,298.15,KCO);
  CALCEQCONST(-2.42334@1,1.610666@-2,3.7635@4,1.619@2,-3.4218@-6,
              0.00,0.00,0.00,
              -4.4425@1,-2.28569@5,298.15,KH2O);
  CALCEQCONST(4.25202@1,1.9523455@-2,2.491335@6,-1.93618@3,-7.8182@-6,
              0.00,0.00,0.00,
              -1.70195@2,8.6463@4,298.15,KCH4);
  CALCEQCONST(1.40001@2,-1.527309@-2,3.86866@6,-4.17929@3,4.16970@-6,
              0.00,0.00,0.00,
              -3.5274@2,2.41414@5,298.15,KC2H6);
  WRITE(OUT1,<"K(H2O)=",E10.4,"   K(CO)=",E10.4,"   K(CH4)=",E10.4,
        "   K(C2H6)=",E10.4/>,KCO,KH2O,KCH4,KC2H6);
  FORR(K,1,6) DO BEGIN
    VOLUMECALC((B[K]/4+1),C[K],D[K],E[K],B[K],A[K],V[K],Z[K],Y[K]);
    CALCFUGCOEFFPURE(B[K],C[K],D[K],E[K],V[K],Y[K],Z[K],LNOPURE[K]);
  END;
  WRITE(OUT1,<"**Pure Fluids**",X2,"Molar Volumes [cm3/mol]:",X16,
       "Ln(Fugacity Coefficients):">);
  WRITE(OUT1,<X17,"H2O   CO2   CO    H2   CH4  C2H6 ",
        "       H2O    CO2    CO     H2     CH4   C2H6">);
  WRITE(OUT1,<X14,6F6.2,X4,6F7.3/>,FORR(K,1,6) DO V[K],
        FORR(K,1,6) DO LNOPURE[K]);
  WRITE(OUT1,<"**Mixed Fluids**">);
  WRITE(OUT1,<X26,"Mole Percent [100*X]:",X10,"Molar",X4,
       "Ln(Fugacity Coefficients):">);
  WRITE(OUT1,<"log(fO2) C/C+H2 O2/O2+H2  H2O  CO2   CO   H2  CH4 C2H6 ",
       "  Volume   H2O    CO2    CO     H2     CH4    C2H6    NI">);
  WRITE(OUT1,<111("-")>);
  FORR(N,1,MAXN) DO BEGIN
    READ(IN,/,FO2,XC);
    FO2:=10**(FO2);
    SOLVEFORFH2(LNOPURE,FUGACITYH2,FUGACITYCO);
    CALCMOLFRACTIONS(LNOPURE,FUGACITYH2,FUGACITYCO,F,X);
    FORR(K,1,6) DO XOLD[K]:=X[K];
    CONVERGED:=FALSE; ITERATION:=0;
    WHILE NOT CONVERGED DO BEGIN
      BMIXCALC(6,BMIX);
      PMIXCALC(CINT,6,CMIX);
      PMIXCALC(DINT,6,DMIX);
      PMIXCALC(EINT,6,EMIX);
      FORR(K,1,6) DO BEGIN
        PSTARCALC(K,CINT,6,CMIX,0,CSTAR[K]);
        PSTARCALC(K,DINT,6,DMIX,1,DSTAR[K]);
        PSTARCALC(K,EINT,6,EMIX,2,ESTAR[K]);
      END;
      VOLUMECALC((BMIX/4+1),CMIX,DMIX,EMIX,BMIX,AMIX,VMIX,ZMIX,YMIX);
      FORR(K,1,6) DO BEGIN
        CALCFUGCOEFFMIX(K,BMIX,CMIX,DMIX,EMIX,VMIX,YMIX,ZMIX,B[K],
        CSTAR[K],DSTAR[K],ESTAR[K],LNOMIX[K]);
      END;
      SOLVEFORFH2(LNOMIX,FUGACITYH2,FUGACITYCO);
      CALCMOLFRACTIONS(LNOMIX,FUGACITYH2,FUGACITYCO,F,X);
      FORR(K,1,6) DO IF ABS(XOLD[K]-X[K])>1@-9 THEN BEGIN
        CONVERGED:=FALSE; GO TO NEXTLOOP;
      END ELSE CONVERGED:=TRUE;
      NEXTLOOP:ITERATION:=ITERATION+1;
      IF ITERATION>30 THEN GO TO NOCONVERGENCE;
      FORR(K,1,6) DO XOLD[K]:=X[K];
    END;
    NOCONVERGENCE:IF NOT CONVERGED THEN WRITE(OUT1,<F7.3,X4,"*Warning",
    ", convergence was not achieved after 30 iterations*">,LOG(FO2));
    XO:=(X[1]/3) + X[2] + X[3];
    WRITE(OUT1,<F7.3,2F8.3,X2,6(F4.1,X1),F7.2,X2,6(F6.3,X1),X1,"(",I2,
          ")"/>,LOG(FO2),XC,XO,FORR(K,1,6) DO 100*X[K],VMIX,
          FORR(K,1,6) DO LNOMIX[K],ITERATION);
    IF DISKOUTPUT[1] THEN WRITE(OUT2,<2F8.3,6(F5.1),F9.3>,XC,
      VMIX,FORR(K,1,6) DO 100*X[K],-LOG(FO2));
    IF DISKOUTPUT[2] THEN WRITE(OUT3,<F7.3,6F8.3>,-LOG(FO2),
      FORR(K,1,6) DO LOG(X[K]));
    ERRORMESSAGE:IF ERROR[1] OR ERROR[2] THEN WRITE(OUT1,<F7.3,X4,
    "*Error detected in PROC ASMBLX*"/>,LOG(FO2));
    IF ERROR[3] THEN WRITE(OUT1,<F7.3,X4,"*Error in PROC CALCPES:",
    " both roots<0 *"/>,LOG(FO2));
  END;
  WRITE(OUT1,<111("-")>);
  CLOSE(OUT2,CRUNCH);
  CLOSE(OUT3,CRUNCH);
END;

END OF PROGRAM.
```

APPENDIX 9

OXIDE AND SILICATE OXYGEN BUFFERS

Equation*:

$$\log (fO_2/\text{bar}) = a + b/T + c(P/T) + dP + e(P^2/T)$$

where P(bar) and T(K).

Buffer**	a	b	c	$d.10^6$	$e.10^7$
IW	6.736	-27403	0.0532	3.0	0
MW	13.206	-32928	0.0841	-1.0	0
NNO	9.466	-25025	0.0451	2.4	0
FMQ	8.746	-25035	0.0944	-2.2	-1
HM	14.256	-24949	0.0200	-4.8	0
EMOG	7.830	-23781	0.0535	-0.8	0
MOEG	10.627	-45924	0.0607	-0.2	-1
OIE	7.203	-29479	0.0664	-0.2	-1

*Buffer equation in the form: $xA + O_2 = yB$ then

$a = [-\Delta S/2.303R]$

$b = [\Delta H/2.303R]$

$c = [(\Delta V - \Delta(\alpha V).298)]/2.303R$

$d = [\Delta(\alpha V)/2.303R]$

$e = [-0.5.\Delta(\beta V)]/2.303R$

where α = coefficient of thermal expansion.

β = coefficient of compressibility.

** IW = iron-wustite; MW = magnetite-wustite; NNO = nickel-nickel oxide; FMQ = fayalite-magnetite-quartz; HM = hematite-magnetite; EMOG = enstatite-magnesite-forsterite-graphite; MOEG = moissanite-forsterite-enstatite-graphite; OIE = forsterite-iron-enstatite, if $x_{Fe} = 0.1$ then $fO_2 \simeq$ OIE - 2 log fO_2 units.

Data sources:
Schwab & Kustner (1981): IW to HM
Eggler & Baker (1982): EMOG
Stull & Prophet (1971), Robie et al. (1978): MOEG, OIE (calculated from thermodynamic data).
Molar volume data from Robie et al. (1978) and Rochow (1973). Thermal expansion and compressibility data from Skinner (1966), Birch (1966) and Rochow (1973).

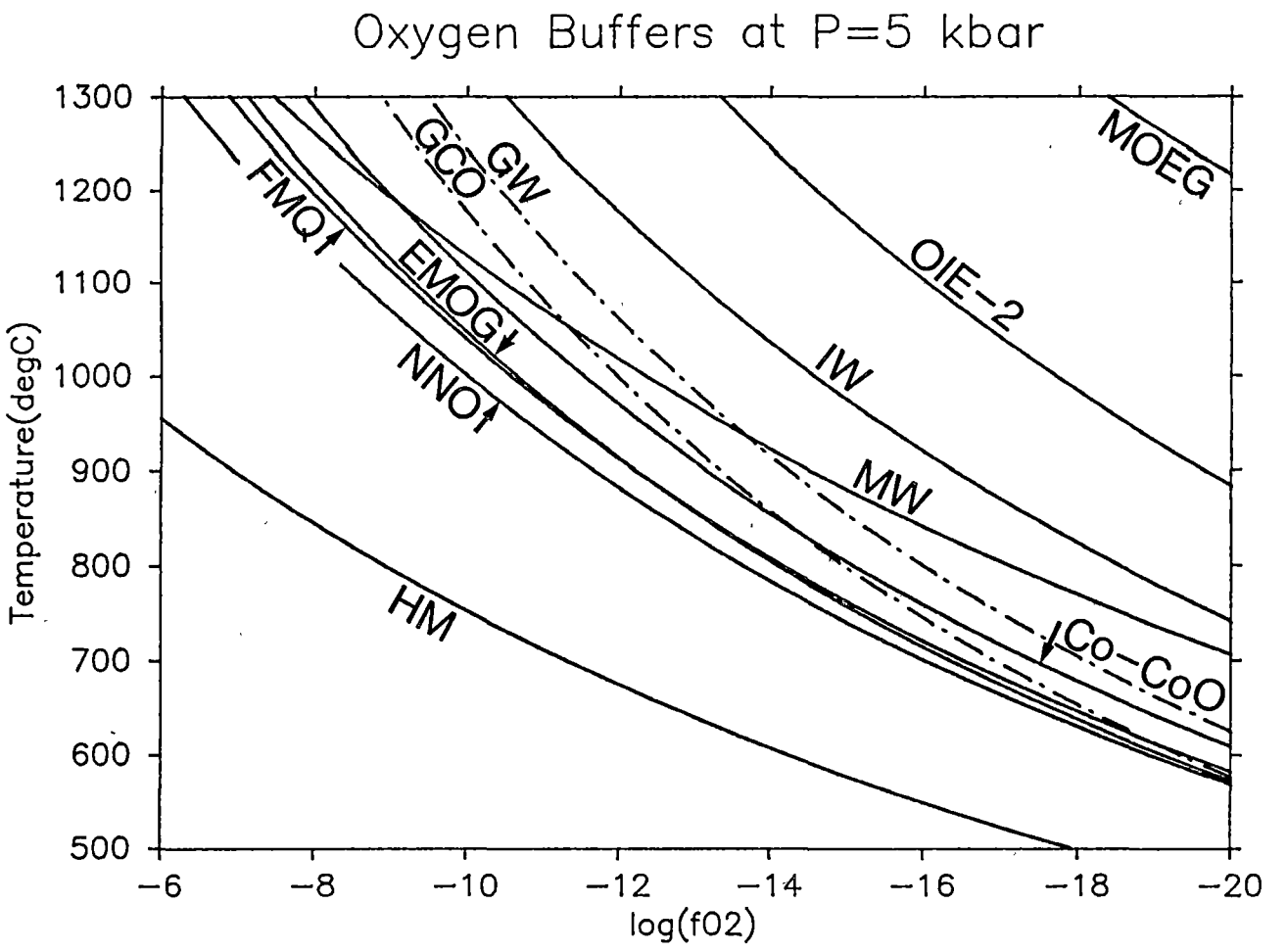
Oxygen Buffers at P=5 kbar
Temperature(degC)
log(fO2)
1300
1200
1100
1000
900
800
700
600
500
−6
−8
−10
−12
−14
−16
−18
−20
MOEG
OIE-2
IW
MW
Co-CoO
GW
GCO
EMOG↓
FMQ↑
NNO↑
HM

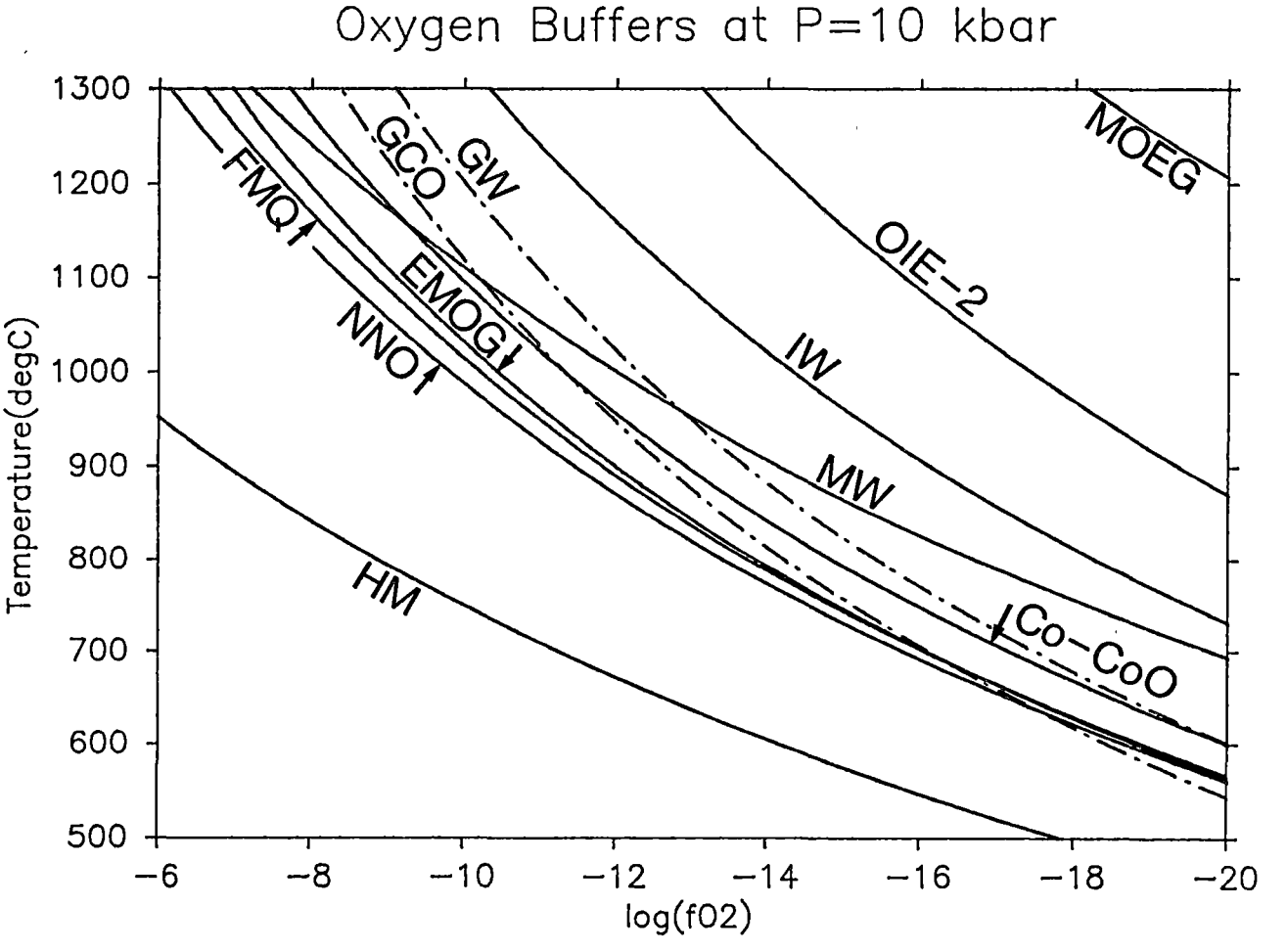
Oxygen Buffers at P=10 kbar
Temperature(degC)
log(fO2)
1300
1200
1100
1000
900
800
700
600
500
−6
−8
−10
−12
−14
−16
−18
−20
MOEG
OIE-2
IW
MW
Co-CoO
GW
GCO
EMOG↓
FMQ↑
NNO↑
HM

APPENDIX 10

EXPERIMENTAL DATA; MW-GCO UNIVARIANT INTERSECTION CURVE

Apparatus: Piston cylinder, solid-media.

Assembly: Talc outer + pyrex sleeve.

Capsule design: 3.56 mm O.D. Pt for T > 1160°C or $Ag_{50}Pd_{50}$ for T < 1160°C inner graphite capsule to separate oxide assemblage from noble metal outer.

Starting mixes: (1) Hematite + graphite, molar ratio 6:8.
(2) Wustite + siderite + graphite, molar ratio 2:1:1.2. Siderite was synthesized from Fe(II) oxalate at 6 kbar, 380°C for 26 hours (run T-983) giving a fine greyish-white powder confirmed optically and by XRD. Stored under vaccuum desiccation.

Product Identification: XRD and powder photographs with internal NaCl standard.

Run #	P/kbar	T/°C	Duration/ hrs	Starting Mix	Product	Cell Dimensions /Å
T-1005	30	1150	4	(1)	Magnetite	8.396
T-1007	30	1200	3	(1)	Magnetite+ wustite ~60:40*	8.398 4.282 ($Fe_{0.91}O$)
T-1011	30	1175	5	(1)	Magnetite	8.402
T-1014	30	1185	4.5	(2)	Magnetite	-
T-1022	30	1200	24	(2)	Magnetite+ wustite ~80:20	- 4.299 ($Fe_{0.93}O$)

Run #	P/kbar	T/°C	Duration/ hrs	Starting Mix	Product	Cell Dimensions /Å
T-1024	30	1250	24	(2)	Magnetite+ wustite ~40:60	8.393 4.290 ($Fe_{0.93}O$)
T-1028	20	1130	6	(1)	Magnetite	-
T-1029	20	1160	6	(1)	Magnetite+ wustite ~60:40	- 4.281 ($Fe_{0.91}O$)
T-1033	20	1140	33	(2)	Magnetite+ wustite ~40:60	
T-1042	13	1070	9.5	(1)	Magnetite+ wustite ~60:40	
T-1043	13	1040	9.5	(1)	Magnetite	

* determined from ratio of d_{100} peak heights for magnetite and wustite.

APPENDICES 11 AND 12

LITERATURE DATA ON DIAMOND CHARACTERISTICS AND FLUID COMPOSITIONS

APPLICATION OF STABLE SPECIES AND CARBON CORRECTION TO DIAMOND-DERIVED FLUIDS

Source	Ref.*	Symbol	Form/Size/Type	Volume Fluids Released on Crushing $10^5.cm^3$	Atom %			
					H	O	C	N
Panna, central India	MG81	P1	Rounded/tabular, 66 mg, type II	9.6	76.7	13.4	9.0	1.0
		P2	Spherical, 102 mg type I	29.0	68.2	21.0	10.1	0.7
		P3	Rounded/tabular, 175 mg, type I	18.5	75.6	18.2	6.1	0.0
Arkansas, U.S.A.	MG75	A1	412 mg, type I	3.4	42.0	35.5	16.2	6.3
		A3	177 mg, type II	27	58.8	32.2	3.4	5.7
		A4	152 mg, type I	7.7	59.8	26.0	13.0	1.2
		A5	108 mg, type I	4.4	54.3	31.8	12.8	1.1
		A6	85 mg, type I	102	65.3	29.1	5.5	0.0
		A7	73 mg, type II	7.7	62.6	25.3	9.2	2.8
South Africa, Kimberley, Premier	MG74	K1	Hexoctahedron,	0.48	62.4	22.4	12.7	2.5
		K2	~600 mg, type I	0.16	64.9	19.2	14.0	1.9
		Pr	rectangular, ~600 mg type II	0.18	76.3	16.6	7.2	0.0
Brazil (exact location unspecified)	MG74	B1	cubic	3.5	63.2	32.4	3.3	1.1
		B2		1.1	63.7	30.9	3.7	1.7
Zaire (exact location unspecified)	MG74	Z1	cubic	9.1	41.6	40.2	16.6	1.7
	GMM82	Z2	cubic	9.6	53.8	37.5	7.6	1.1
		Z3	cubic	4.0	54.9	32.1	11.7	1.4
		Z4	cubic, 38 mg	10	54.6	36.6	8.6	0.4
		Z5	cubic, 48 mg	12	50.7	38.1	10.0	1.3
		Z6	cubic	20	53.4	37.1	9.0	0.5
		Z7	13 cubic stones, total 288 mg	290	52.4	37.1	9.4	1.1
South Africa? HNO-1	SMA80	HNO-1	no details	Cleaned surface >1200°C (volatile release)	77 ppm/wt O 295 ppm/wt O		200 ppm/wt H 1750 ppm/wt H	

*References: MG74, MG75, MG81 Melton & Giardini (1974, 1975, 1981).
GMM82 Giardini et al. (1982)
SMA80 Sellschop et al. (1980).

Sample Number	Stable Species Correction (mol%)				Carbon Correction (mol%)					Oxygen Fugacity		
	H_2O	CO_2	CH_4	H_2	H_2O	CO_2	H_2	CH_4	C_2H_6	55 kb 1400K	45 kb 1300K	70 kb 1500K
P1	45.6	0.0	30.8	23.6	51.3	0.0	2.4	45.4	0.9	-9.9	-11.4	-8.5
P2	63.2	0.0	30.3	6.5	75.3	0.0	1.8	22.7	0.2	-9.7	-11.2	-8.2
P3	57.5	0.0	19.4	23.1	64.5	0.0	2.1	32.9	0.5	-9.8	-11.3	-8.4
Av. P (graphitised)	58.9	11.4	29.7	0.0	81.0	0.0	1.6	17.3	0.1	-9.6	-11.1	-8.2
A1	42.7	41.4	15.8	0.0	74.4	25.6	0.0	0.0	0.0	-6.0	-7.7	-4.1
A3	89.1	7.7	3.2	0.0	95.5	4.5	0.0	0.0	0.0	-6.4	-8.1	-4.5
A4	53.4	19.9	26.7	0.0	92.7	0.0	1.0	6.3	0.0	-9.3	-10.8	-7.9
A5	56.4	25.7	17.9	0.0	92.2	7.8	0.0	0.0	0.0	-6.2	-7.9	-4.4
A6	93.9	0.0	5.2	0.9	93.9	5.2	0.9	0.0	0.0	-9.2	-10.8	-7.8
A7	67.4	11.0	21.6	0.0	88.9	0.0	1.3	9.7	0.1	-9.5	-11.0	-8.0
K1	52.7	15.5	31.9	0.0	82.9	0.0	1.6	15.4	0.1	-9.6	-11.1	-8.1
K2	45.8	14.2	39.9	0.0	73.7	0.0	1.9	24.2	0.2	-9.7	-11.2	-8.3
Pr	53.5	0.0	23.2	23.3	60.1	0.0	2.2	37.2	0.6	-9.8	-11.3	-8.4
B1	89.9	5.8	4.4	0.0	98.7	1.4	0.0	0.0	0.0	-6.8	-8.5	-4.9
B2	88.2	5.2	6.6	0.0	98.3	0.0	0.5	1.2	0.0	-8.7	-10.2	-7.2
Z1	45.6	43.1	11.3	0.0	68.2	31.8	0.0	0.0	0.0	-5.9	-7.7	-4.1
Z2	76.4	20.0	3.6	0.0	83.6	16.5	0.0	0.0	0.0	-6.0	-7.8	-4.2
Z3	60.8	23.5	15.7	0.0	92.2	7.8	0.0	0.0	0.0	-6.2	-7.9	-4.4
Z4	73.0	20.8	6.2	0.0	85.4	14.6	0.0	0.0	0.0	-6.1	-7.8	-4.3
Z5	68.6	25.8	5.7	0.0	79.9	20.1	0.0	0.0	0.0	-6.0	-7.8	-4.2
Z6	71.9	22.2	5.9	0.0	83.6	16.4	0.0	0.0	0.0	-6.1	-7.8	-4.2
Z7	70.6	23.3	6.1	0.0	82.8	17.2	0.0	0.0	0.0	-6.0	-7.8	-4.2
HNO-1	Cleaned diamond surface									-11.4	-12.9	-9.9
	>1200°C (volatile release)									-12.0	-13.5	-10.6

APPENDIX 13

VIBRATIONAL SPECTROSCOPIC STUDIES OF SILICATE MELT STRUCTURE - A LITERATURE REVIEW AND CRITIQUE

A13.1 Introduction

Vibrational spectroscopy is a popular tool in experimental geochemistry. Both Raman scattering and infrared (IR) spectroscopy have been employed in the elucidation of silicate melt and glass structure. Much of this work has only recently yielded results of petrological significance with the development of a theoretical framework for the interpretation of vibrational spectra (e.g. Brawer, 1975; Brawer & White, 1975). An important prediction of the theory is that vibrational spectroscopy, and in particular the high frequency region of the Raman spectrum, is sensitive to small-scale structural features of the order 5-15Å which comprise units of several $[SiO_4]$ tetrahedra. Usual methods of structural analysis such as x-ray diffraction require the existence of order on a scale of hundreds of atomic spacings but in glasses no such order exists. The x-ray diffraction pattern in amorphous solids may, however, be analysed to yield a correlation function for atomic positions (e.g. radial distribution function or RDF) accurate to distances up to ~10Å (Wright & Leadbetter, 1976). Information is then provided on short range ordering and some overall picture of the glass structure may be obtained from a comparison of experimental and synthetic RDF's; the latter may be generated from known crystal structures (e.g. Taylor & Brown, 1979b: SiO_2-$NaAlSiO_4$ glass series; Okuno & Marumo, 1982: $NaAlSi_3O_8$ and $CaAl_2Si_2O_8$ glasses and melts) or hypothetical molecular arrangements (Taylor, 1979: the "quasi-crystalline" model). One of the major problems with this type of structural determination is that nearly identical RDF's can be obtained from quite different atomic models (Howitt & McElfresh, 1982) so that choice of any one model is unlikely to be unique. Despite these problems, x-ray studies provide a useful complementary technique to structural analysis by vibrational spectroscopy.

Models for the structure of silicate and silica-oxide glasses range over two extremes. The random network hypothesis, originally proposed by Zachariasen (1932), has no provision for the presence of short range order or crystal-like features. In silica glass, for example, the model assumes

an arrangement of inter-connected [SiO_4] tetrahedra completely lacking periodicity due to a random distribution of Si-O-Si bond angles. At the other extreme lies the crystallite theory (Randall et al., 1930; illustrated by Wright & Leadbetter, 1976) that proposes a glass structure based on highly ordered microcrystalline regions with dimensions of several tens of angstroms that strongly resemble the structure of the corresponding equilibrium solid. Much evidence exists to suggest the real structure of silicate glasses lies between these two models, which really only represent extremes in the degree of short range order present, as recently summarised by Bottinga et al. (1981). The existence of short range structures ("microheterogeneities") is clearly indicated from the data of Bottinga et al. (1981) although the dimensions of these features are probably quite small amounting to several [SiO_4] tetrahedra only. By proposing a model of glass structure represented by a collection of these structural units joined in one, two or three dimensions Brawer (1975) and Brawer & White (1975) have been able to successfully duplicate the vibrational spectra of a range of metal oxide-silica glasses. The structural unit concept has also been popular in the thermodynamic modelling of silicate melts (e.g. Fraser, 1977).

While this model is readily applicable in a number of areas, the extent to which the full bonding topology of the system can be defined in this way is debatable. As noted previously, the sensitivity of the commonly employed high frequency Raman bands (1200-800 cm^{-1}) and x-ray diffraction techniques does not appear to extend much beyond about 10Å, equivalent to only a few [SiO_4] tetrahedra (Wright & Leadbetter, 1976; McMillan, 1984a). Since it is at greater distances that distinction is made between alternative structural arrangements, e.g. "infinite" chains vs ring structures, information on the overall structure, i.e. the interconnection between smaller structural units, is not readily obtainable. Structural information of this type may in the future come indirectly from Monte Carlo (MC) simulations of melt and glass structure using appropriate pair potential functions to describe ionic interactions. The fixed lattice model developed by Borgianni & Granati (1979) gives a somewhat over-simplified picture of silicate melts (Nordin, 1984) and a more generalised approach is warranted. Modelling the dynamic properties of molten silicate systems, including analysis of the vibrational spectrum and determination of ionic diffusion coefficients may also be possible with molecular dynamics (MD) simulations as discussed by Woodcock et al. (1976). The application of both MD and MC computer simulation techniques to the

structure of silicate melts has been recently discussed by Matsui & Kawamura (1984).

In the geological literature much effort has been placed on correlating structural information on silicate melts and glasses with observed physical properties such as viscosity-pressure relationships and diffusion coefficients (e.g. Mysen et al. 1980a, 1982a). Considerable attention has also been devoted to understanding the effects of minor and volatile component additions to silicate liquids. It is well known that such components have an effect on natural and synthetic systems that is large in relation to their level of abundance (e.g. Kushiro, 1975). The mechanisms of TiO_2, P_2O_5 and oxidised volatile (H_2O, CO_2) dissolution have been investigated by Raman spectroscopy and the results summarised by Mysen et al. (1982a). More recent work on the H_2O solubility mechanism by Stolper (1982a, 1982b) and McMillan et al. (1983) using IR spectroscopic techniques have found, contrary to the Raman investigations, that a substantial fraction of the dissolved water is present in molecular form. This highlights the importance of the complementary nature of Raman and IR techniques since use of one technique by itself may provide only part of the answer sought. The differing activity of Raman and IR vibrational modes makes the former technique more powerful in investigations of the silicate glass network structure but indirect and often ambiguous in studies of volatile solubility (e.g. Mysen et al., 1980a) and cation co-ordination environments (e.g. Sharma & Simons, 1981; McMillan et al., 1982).

In Part 4 of this study, extensive use is made of IR spectroscopy mindful of published Raman data for the compositions investigated and the limitations and assumptions of vibrational spectroscopic techniques when applied to structural interpretations of silicate glasses; these problems are discussed and illustrated in the following sections.

A13.2 The Relationship between Glass and Melt Structure

Because of experimental difficulties and inconvenience little vibrational spectroscopic data have been obtained directly on silicate liquids. Most studies, including the work presented here, have been carried out on glasses quenched from high temperature liquids at pressures ranging from 1 atm to around 30 or 40 kbar.

While silicate liquids are known to be quite different from glasses in their thermodynamic and transport properties, it is usually assumed that below the glass transition temperature the system is kinetically "frozen" but still retains full vibrational freedom (Bottinga et al., 1981). Support for this conclusion comes from the similarity of vibrational spectra of liquids and their quenched glasses as recently summarised by Mysen et al. (1982a, 1983) and Seifert et al. (1981a). Two recent studies well illustrate this point: Domine and Piriou (1983) studied the IR reflectance spectrum of a glass and liquid in the system Na_2O-SiO_2. Only small differences were observed; these being attributed to the effects of thermal expansion and a small amount of extra disorder in the liquid. Domine & Piriou concluded that structural information may be validly extrapolated from the glassy to the liquid state. In the second example, Taylor et al. (1980) compared the RDF's for albite glass ($T < 763^{\circ}C$) and the corresponding super-cooled liquid ($T \sim 805^{\circ}C$). Except for small differences again attributable to thermal expansion no other significant changes were observed. These results were substantially confirmed by Okuno & Marumo (1982).

At high pressures no comparative studies of glass vs liquid structure have been undertaken. Mysen et al. (1982a, 1983) however present arguments for the retention of high pressure structures during quenching. Structural transformations with positive dT/dP slopes, e.g. Al(tet) -> Al(oct) conversions, were considered unlikely to back-react.

A note of caution has been put forward by Boettcher et al. (1982) for aluminosilicate glasses quenched from temperatures well above the solidus or melting point. In such glasses metastable high-enthalpy structures may persist rendering them unsuitable as models for liquids in equilibrium with a crystalline phase. Accordingly, in this study, glasses were quenched from temperatures no more than $50^{\circ}C$ above the relevant melting point or liquidus boundary.

A13.3 Form, Limitations and Assignment of Vibrational Spectra in Simple-System Silicate Glasses.

A. Introduction

In disordered solids such as glasses there is no long-range structural periodicity. Invariably, parameters that are to be determined must provide some description of the short range order present and may include nearest neighbour co-ordination numbers, average bond lengths and bond angles of co-ordinated atoms, rings and other polymeric structures. This description implies some statistical distribution about a mean structure that for disordered solids indicates a range of easily accessible configurations separated by only small energy barriers. In pure silica glass, for example, a broad distribution of Si-O-Si bond angles (ranging from 170^{o} to 130^{o}) is indicated by elastic scattering studies (Mossi & Warren, 1969), x-ray emission spectroscopy (Greaves et al., 1981) and by magic-angle spinning NMR (Dupree & Pettifer, 1984). The absence of long-range order and the degree of short-range variability in silica glass (and for that matter all multicomponent glasses) leads to vibrational spectra showing broad unresolved band envelopes. Bandwidths at half height may be as much as 50-300 cm^{-1}, more than ten times the width of comparable crystalline compounds. Thus elucidation of structural information normally requires the use of deconvolution procedures (as discussed in Section 4.3). Despite the application of statistical tests such techniques are unlikely to yield unique solutions - this is well illustrated by recent Raman spectroscopic investigations of vitreous silica. Seifert et al. (1982) selected Gaussian curves as band components and found that two bands were required to give an acceptable fit in both the highest frequency (~1100 cm^{-1}) and mid-range (~800 cm^{-1}) envelopes. The former band envelope has been assigned to asymmetric Si-O stretching vibrations of the 3-d network (Mysen et al. (1982a). This result, together with additional experimental evidence, led Seifert et al. (1982) to suggest the presence of at least two 3-d structural units in vitreous silica as proposed previously by Mysen et al. (1980a) but based on a different spectral interpretation. Seifert et al. (1982) believe these units differ in average Si-O-Si angle by only 5-10^{o}, this being sufficient to give rise to an asymmetric distribution of bond angles that are skewed toward lower angles. This interpretation and its extension to aluminosilicate systems has been criticised by McMillan et al. (1982) and McMillan & Piriou (1983) on the basis of the non-uniqueness of the deconvolution scheme of Seifert et al. The authors also point out

that a number of silica polymorphs have dual bands in the high frequency region and these certainly do not imply the presence of more than one structural unit in the crystalline solids.

The recent Si-O-Si bond angle distribution obtained by magic-angle spinning (MAS) NMR techniques (Dupree & Pettifer, 1984) shows a broad and nearly symmetrical peak with angles of roughly equal probability occurring over the range 140-155°. This distribution is much more consistent with the presence of only one structural unit than previous distributions, obtained by x-ray methods (Mossi & Warren, 1969) or derived theoretically (Soules, 1979), would indicate. These contrasting views highlight, even for the chemically simplest of glasses, the real limitations that exist in the assignment of vibrational bands to structural units and in the non-uniqueness of deconvolution procedures. Band assignments in general terms are usually made with reference to all available experimental and theoretical information. For Raman spectra the arguments leading to band assignments have been recently discussed by McMillan (1984a). No summary is as yet avilable for IR spectra although many bands are both IR and Raman active (though with differing intensities) and assignments will in many cases be applicable to both spectra.

In simple-system silicate and aluminosilicate glasses, IR and Raman spectra may be conveniently divided into high-frequency (1200-800 cm^{-1}), mid-range (800-650 cm^{-1}) and and low frequency (650-400 cm^{-1}) regions.

B. High-Frequency Raman Spectra

The high frequency portion of the Raman spectrum for glasses in the series SiO_2-MO or SiO_2-M_2O (where M = alkali or alkaline earth cation) are interpreted in terms of contributions from polarised bands identified with symmetric Si-O stretching motions of silicate units containing [SiO_4] tetrahedra with:

one (~1100-1050 cm^{-1}),
two (~1000-950 cm^{-1}),
three (~900 cm^{-1}) and
four (~850 cm^{-1})

non-bridging oxygens (NBO's), e.g. Mysen et al. (1982a); McMillan (1984a). In the notation of Engelhardt et al. (1975) these are designated Q_3, Q_2, Q_1 and Q_0 respectively to indicate the types of Si environments detectable by

x-ray emission spectroscopy and ^{29}Si MAS-NMR (Schramm et al., 1984). The silicate units are illustrated in Table 13.3A below:

Table 13.3A

NBO/Si	Q-species	unit*
4	Q_0	$Si(OM)_4$
3	Q_1	$(SiO)Si(OM)_3$
2	Q_2	$(SiO)_2Si(OM)_2$
1	Q_3	$(SiO)_3Si(OM)$
0	Q_4	$(SiO)_4Si$

* M = alkali cation

Band assignments are supported by the similarity of glass spectra to those of the corresponding crystalline orthosilicate, pyrosilicate, metasilicate and disilicate minerals. Mysen et al. (1980a) and Virgo et al. (1980) go somewhat further in their interpretation. They suggest from experimental evidence that silicate melts may be described in terms of a very limited number of anionic structural units, i.e.

$[Si_2O_4]^{0}$ 3-d networks,
$[Si_2O_5]^{2-}$ sheets,
$[Si_2O_6]^{4-}$ infinite chains,
$[Si_2O_7]^{6-}$ dimers, and
$[SiO_4]^{4-}$ monomers.

Moreover, many of the characteristic Raman spectral features may be successfully modelled by consideration of only a few silicate anions (Furukawa et al., 1981). For example, the strong similarity between Raman spectra of crystalline and vitreous diopside and other metasilicates was interpreted by Etchepare (1972) and Mysen et al. (1980a) to indicate a melt structure composed largely of $[Si_2O_6]_\infty$ infinite chains.

Seifert et al. (1981b) have attempted to quantify this model by using the relative area ratios of the symmetric stretch bands to calculate molar proportions of anionic units in the melt. The results indicate a pronounced sensitivity to the type of cation present as well as the expected shift in species distribution towards those of lower NBO/Si, i.e. sheets, 3-d networks with increasing silica content (Mysen et al., 1982a).

Contrary to the above "discrete anion speciation model" Brawer & White (1975) envisaged polymerisation/depolymerisation reactions, occurring on addition of silica or metal oxide components, to proceed via a **continuous mechanism** involving random cleavage or connection of Si-O-Si linkages. Mysen et al. (1982a) however consider that Raman and other data are inconsistent with the presence of any intermediate anionic units. This question has been taken up by McMillan (1984a) who presents strong evidence for the major high frequency bands being highly localised in character and as such unable to provide any information on the linkage of adjacent tetrahedral groups. If this is so, then molecular groups of different NBO/Si may be difficult to assign to any particular long-range (i.e. > 10Å) structure. Furthermore, McMillan (1984a) and McMillan & Piriou (1983) find that discrimination between infinite chains, $[Si_2O_6]_\infty$, and ring structures of equivalent NBO/Si ratio is not possible based solely on high frequency Raman bands. For example, the Raman spectra of vitreous diopside can be equally well compared with that of crystalline diopside (structure based on pyroxene chains), parawollastonite (pyroxenoid chains) or pseudowollastonite (Si_3O_9 rings), (see McMillan & Piriou, 1983). Other support for the stability of ring over linear chain structures comes from the chromatographic determination of polymer distribution in $PbO-SiO_2$ glasses in the range 50-10 mol% SiO_2 (Smart & Glasser, 1978). The authors find no evidence for the presence of linear chain structures beyond trimeric species. It appears that longer chains readily undergo intra- and inter-polymeric closure reactions forming more stable ring and cross-linked structures respectively.

Real silicate melts probably show behaviour intermediate between the two extremes of discrete and continuous polymerisation/depolymerisation discussed above. On theoretical grounds, support for this view is provided by Lacy's (1965) statistical model of silicate melts. The favoured structure of a melt or glass (noting the kinetic restrictions of the latter) is one of minimum Gibbs Free Energy. Lacey's calculations indicate this state is not necessarily correlated with a random dispersion of modifying cations and non-bridging oxygen. Instead, melts with NBO/Si between 0 and 2 are pictured in terms of a 3-d network structure with a proportion of terminal and side-chain structures enclosing polyvarietal discrete anionic groups. On probability grounds free anions and terminal structures are limited to <10 connected $[SiO_4]$ tetrahedra with a dominance of 4- and 6-membered ring, cross-linked or branched structures. It is envisaged that these units are associated with a significant proportion of

the modifying cations in a distribution reminiscent of the "micro-region" concept originally proposed by Florinskaya & Pechenkina (1963) and supported by more recent evidence (e.g. Urnes, 1969; Milberg & Peters, 1969).

The model takes a somewhat simplistic view of silicate melts in that it only considers the arrangement of silicate anionic units and disregards the role of the cation. As a result it best approximates glasses in which cation-cation interactions are moderately to strongly repulsive such as those glasses containing the higher molecular weight alkali atoms K, Rb and Cs (de Jong et al., 1981). The most probable (i.e. the ideal) dispersal of NBO and cations calculated by Lacey's model lies between the extremes of maximum dispersion (i.e. NBO and cations connected to the largest number of silicate tetrahedra within stoichiometric constraints) and minimum dispersion (i.e. NBO and cations connected to as few silicate tetrahedra as possible); the latter case results in a strongly bimodal Q_4-Q_0 distribution of Q-species as illustrated below for a $15M_2O$-$85SiO_2$ (mol%) composition melt (M = alkali cation) (after de Jong et al., 1981).

Table 13.3B Dispersal of Q-environments.

Dispersion	Q-species (%)					
	Q_4	Q_3	Q_2	Q_1	Q_0	Q_R^*/Q_4
maximum	65	35	0	0	0	0.54
most probable**	69.1	26.7	3.8	0.3	0	0.45
intermediate	82	0	18	0	0	0.22
intermediate	88	0	0	12	0	0.14
minimum	91	0	0	0	9	0.10

* $Q_R = Q_0+Q_1+Q_2+Q_3$
** Lacey's model

Lacey's model calculates, for the most probable NBO dispersal, that ~63% of $[SiO_4]$ tetrahedra in the metasilicate composition and ~17% in the disilicate composition will be present in the form of discrete anionic units. Polymerisation (e.g. as a result of SiO_2 addition) would occur in stages with the amount of discrete anionic units decreasing via linkage

with the network as terminal groups (attached by one Si-O-Si bridge) and finally as components indistinguishable from the network itself. Although somewhat idealised, the picture of dynamic equilibrium between 3-d network and other discrete structural elements is also provided by (i) Raman spectral observations of glasses in the systems $CaO-SiO_2$, $Ca_{0.5}Mg_{0.5}O-SiO_2$ and $MgO-SiO_2$ (Mysen et al. (1982a), (ii) ^{29}Si MAS-NMR studies of Li_2O-SiO_2 glasses (Schramm et al., 1984) and (iii) SiK_α x-ray emission spectroscopy of alkali and alkaline earth oxide-silica glasses (de Jong et al., 1981). In all three cases 3-d network and discrete anionic units are best resolved in silicate melts containing cations of high charge-radius (z/r ratio) where there is a tendency towards a minimum or bimodal dispersion of Q-environments. This tendency generally occurs in order of increasing cationic z/r:

$$Cs < K < Na < Li < Ba < Ca < Mg$$

<--- maximum dispersal ---- most probable ------/------- minimum (bimodal) dispersal --->

The results presented here rationalise the observation of Mysen et al. (1982a) who noted the instability of "sheet unit" or Q_3 species relative to Q_4 and $Q_{0,2}$ in $MgO-SiO_2$ melts. De Jong et al. (1981) have also been able to explain the apparent greater disorder found by Brawer & White (1975) in Raman spectra of Li_2O-SiO_2 glasses compared with K_2O-SiO_2 glasses in terms of a NBO distribution that is farther from ideal (i.e. the statistically most probable dispersal) the larger the z/r ratio of the constituent cation.

C. High-Frequency IR Region

Unlike the relatively simple Raman high frequency envelope which contains intense polarised bands assigned largely to symmetric Si-O stretching vibrations, the infrared spectrum in this region also includes bands arising from asymmetric stretches of non-bridging and bridging Si-O bonds; designated ν_{as}[Si-O-Si] and ν_{as}[Si-O-Si] respectively.

In heteropolar solids, an absorption will be infrared active when dissimilar atoms vibrate out-of-phase and Raman active when they vibrate in-phase (Laughlin & Joannopoulos, 1977). For example, strong negative correlations between silicon and oxygen displacements at 1080 cm^{-1}, 800

cm^{-1} and 450 cm^{-1} were found in the model of Laughlin & Joannopoulos (1977) for vitreous silica; all three values agree well with observed IR activity.

Infrared spectra of silicate glasses tend to be much more complex than their Raman counterparts, particularly in the high-frequency region. In simple binary metal oxide-silica systems of high NBO/Si two distinct envelopes, corresponding to bridging and non-bridging Si-O vibrations, may be resolved in this region (e.g. Ferraro & Manghnani, 1972; see Section 4.6A). For the same silica content, band shape is strongly influenced by the nature of the metal oxide present (Sanders et al., 1974) with ions of largest z/r (e.g. Mg^{2+}) disrupting the structural units present in vitreous silica the least (de Jong et al., 1981).

D. Mid-Range Region

The mid-range envelope (800-650 cm^{-1}) is of moderate strength in both T-corrected Raman (Seifert et al., 1982) and infrared spectra. It is composed of at least two and probably more band components (Seifert et al., 1982). McMillan et al. (1982) have suggested that the band near 800 cm^{-1} in silica glass is mainly associated with motions of Si atoms against their tetrahedral oxygen cage, with little associated oxygen displacement. This view is consistent with the large $^{30}Si/^{29}Si$ and small $^{18}O/^{16}O$ isotope shifts observed by Galeener & Geissberger (1983) and Galeener & Mikkelsen (1981) respectively. Further support for this assignment is provided by molecular dynamics calculations. Angell et al. (1982) found that displacements of Si atoms in a simulated melt of jadeite composition occur by a sequence of small and randomly directed motions that feature frequent reversals of trajectories. This implies an effective and rather high "rattling" frequency for an Si atom situated in its oxygen co-ordination "cage". Similar characteristics were found for both Al^{3+} and O^{2-} ion dynamics.

Calculations presented by Soules & Busbey (1981) give frequencies of trajectory reversal ("rattling" frequencies) near 890 cm^{-1} for Si and 634 cm^{-1} for Al^{IV} in MD runs on various silicate glass compositions. A similar MD study of vitreous silica by Giarofalini (1982) also placed the mid-range envelope near 900 cm^{-1}. In both cases this is ~100 cm^{-1} higher than that observed. By weakening the Si-Si repulsive term, however, Giarofalini (1982) substantially improved the agreement between the calculated and experimental frequency spectrum.

In the case of melts lacking a semi-rigid polymerised network (i.e. those with NBO/Si > 1) McMillan (1984a) suggests the mid-range vibrations might transform or couple to other modes having a greater degree of oxygen motion. This is evident in melts of NBO/Si approaching 4 where the mid-range band becomes progressively weaker with decreasing SiO_2 content; in vitreous fayalite, for example, the mid-range band is only present as a very weak shoulder (Kusabiraki & Shiraishi, 1981).

Bell & Dean (1972) and Laughlin & Joannopoulos (1977) also describe the mid-range band as a vibration involving substantial Si motion but include an additional contribution from Si-O-Si "bridge bending" (i.e. in-plane oxygen motion bisecting the Si-O-Si bond angle). Ferraro & Manghnani (1972) found both strong pressure and compositional dependancies for the 800-700 cm^{-1} envelope in the system Na_2O-SiO_2. The effect of pressure is to compress the inter-tetrahedral linkages effectively decreasing the volume of the [SiO_4] co-ordination polyhedra and thus raising the vibrational frequency. This behaviour together with the pronounced dependance of band position on NBO/Si led Ferraro & Manghnani (1977) to infer a strong degree of delocalisation and hence a "pseudo-lattice-like" character for this band.

E. Low Frequency Region

The low frequency region (650-400 cm^{-1}) in Al-free silicate glasses includes a series of strong to moderate intensity unresolved bands that in the IR appear mostly below 550 cm^{-1} and in the Raman spectrum generally in the range 650-450 cm^{-1}. In vitreous silica, the strong IR band near 470 cm^{-1} has been assigned largely to "rocking" motions of bridging oxygen where O vibrates in a direction perpendicular to the Si-O-Si plane (Laughlin & Joannopoulos, 1977). A weak shoulder near 550 cm^{-1} in the IR is probably associated with vibrations of predominantly "bending" character in which oxygen motion bisects the Si-O-Si bond angle. Two sharp bands appear at 604 cm^{-1} and 490 cm^{-1} in the Raman spectrum of vitreous silica; they are sensitive to neutron irradiation and have been attributed to localised modes associated with "broken bond" defects (Bates et al., 1974). The model requires only ~0.1 % of the Si-O-Si bridges in the structure to occur as ($Si\text{-}O^{-}\ ^{+}Si$) defect sites (Mysen et al., 1982a). This assignment is, however, by no means certain and both absorption bands have been ascribed, on isotopic evidence, to the presence of 3- and 4-membered ring structures (Galeener & Geissberger, 1983).

In the systems M_2O-SiO_2, MO-SiO_2 and in the fully polymerised $MAlO_2$-SiO_2, $M_{0.5}AlO_2$-SiO_2 aluminous systems, where M = monovalent or divalent alkali or alkaline earth cation, polarised bands of moderate to strong intensity appear in the Raman spectrum over the range 500-650 cm^{-1} (McMillan, 1984a; Seifert et al., 1982). These bands usually occur as an unresolved band envelope but in systems containing cations of low z/r, such as the K_2O-SiO_2 series glasses investigated by Verweij & Konijendijk (1976), they may be partly resolved. These absorptions are weakly active or inactive in the IR. Mysen et al. (1980a), Seifert et al. (1982) and Hass (1970) have suggested a correlation with the "defect" bands of silica glass. McMillan (1984a) does not agree with this view and ascribes the observed absorptions to new bands unable to be simply derived from those of vitreous silica. In the normal co-ordinate analysis of Furukawa et al. (1981) the 500-600 cm^{-1} Raman bands are modelled in terms of symmetric stretching plus bending vibrations of Si-O-Si bridge bonds with large displacements of bridging oxygen in the plane of the silicon-oxygen linkage. This motion is similar to that envisaged by Laughlin & Joannopoulos (1977) for the calculated strongly Raman active (but weakly IR active) band near 550 cm^{-1} in vitreous silica. Furukawa et al. (1981) find the frequency and intensity of the 500-600 cm^{-1} band to be strongly dependent on both the melt composition in terms of NBO/Si and the average Si-O-Si bond angle of constituent anionic units. The calculated band positions and intensities show the same trends as the experimental Raman spectra, i.e. increasing in intensity and frequency with decreasing Si-O-Si bond angle or addition of modifying cation.

McMillan (1984a) infers a high degree of vibrational localisation for the 500-600 cm^{-1} bands and correlates absorption frequency with the presence of units of differing NBO/Si. This is supported by the strong similarity of Raman spectra between vitreous $MSiO_3$ and $M_2Si_2O_5$ compositions (M = Li,Na,K) and the corresponding crystalline compounds which contain well defined units having NBO/Si of 2 and 1 respectively (Brawer & White, 1975). As expected for localised vibrations, the 500-600 cm^{-1} bands of intermediate glass compositions (bulk NBO/Si between 1 and 2) are readily described by the simple superposition of endmember spectra (Verweij & Konijendijk, 1976, Figs 1 and 2).

The most useful description of bands in the low frequency region judging by the analysis of Furukawa et al. (1981) is as bending plus stretching (deformation) modes involving a high degree of oxygen

displacement at Si-O-Si bridges. "Rocking" describes predominantly out-of-plane motions of oxygen and "bending" sensu stricto describes in-plane motions.

A13.4 Vibrational Spectra, Band Assignments and the Structure of Aluminosilicate Glasses and melts

Many recent publications in the geological literature have been devoted to understanding the structural role of aluminium in aluminosilicate melts and glasses. The ionic radius of aluminium is such that it is found in four-, five- and six-fold co-ordination to oxygen in aluminate and aluminosilicate minerals. This variability coupled with aluminium's known amphoteric behaviour, is good reason for presuming that Al^{3+} may adopt dual network-modifying and network-forming roles in the liquid or vitreous state. The usual interpretation (e.g. Mysen et al., 1982a) is that when sufficient alkali or alkaline earth cations are present to charge compensate Al^{3+}, as $NaAlO_2$ or $Ca_{0.5}AlO_2$ complexes for example, then Al will be present in tetrahedral co-ordination. This idea is borne out by x-ray diffraction, thermochemical and Raman spectroscopic studies of glasses in the system $NaAlSiO_4$-SiO_2 (Taylor & Brown, 1979b; Mysen et al., 1980a; Seifert et al., 1982; Navrotsky et al., 1982). Seifert et al. (1982) found from the Raman spectra of glasses in the series SiO_2-$Mg_{0.5}AlO_2$ that the 3-d network structure of vitreous silica is largely preserved with Al^{3+} incorporated in six-membered ring structures in the sodic system. In the calcic and magnesian systems the 3-d structure is interpreted in terms of a mixture of Al-free six-membered $[SiO_2]$ rings and four-membered interconnected $[Al_2Si_2O_8]^{2-}$ rings; the existence of aluminate ring structures with Al-O-Al linkages was also postulated. In all three systems, the effect of increasing bulk Al/(Al+Si) is to systematically shift the high frequency band envelopes (and in the sodic system, the individual deconvoluted band components as well) towards lower wavenumbers. This effect has been ascribed to strong coupling between Si-O and Al-O vibrational modes. The lack of any shift in the calcic and magnesian system band components was taken as indicative of a fixed Al:Si stoichiometry for structural units in these glasses. Sharma et al. (1983) in a Raman study of various CaO-Al_2O_3-SiO_2 glasses and crystals noted the close resemblance of short range structures in vitreous and crystalline anorthite ($CaAl_2Si_2O_8$). They also proposed a glass structure based largely

on four-membered "feldspar-like" rings with imperfect Al,Si ordering on the tetrahedral sites. RDF data for vitreous and liquid anorthite are consistent with this interpretation (Taylor & Brown, 1979a; Okuno & Marumo, 1982). The recent MD simulation of the anorthite melt structure at 2000 K by Matsui & Kawamura (1984) yields results consistent with the RDF data. Their model of melt structure is, however, somewhat different from other interpretations in that four-membered rings are found to become important only at higher pressures; there is a gradual decrease in 3-d ring size and increase in Al-O co-ordination numbers as pressure is raised. The model indicates that the degree of Al,Si ordering on tetrahedral sites in the glass is significantly less than in crystalline anorthite but is not completely random with Al-O-Si bonds being slightly preferred over both Si-O-Si and Al-O-Al linkages.

Using Raman spectroscopy to detect the presence of NBO, Mysen et al. (1981) find evidence for Al behaving as a network modifier (i.e. occupying sites of non-tetrahedral co-ordination) in melts where there is an insufficient proportion of alkali or alkaline-earth cations to charge compensate Al in the network. The distribution of Al^{IV} between the various network structural units in Na_2O and CaO aluminosilicate glasses has been investigated by Mysen et al. (1981). Tetrahedral Al was found to have a preference for the most polymerised (i.e. lower NBO/T, T = Si + Al^{IV}) units. In the calcic system this behaviour is the reverse of that found by Wood & Hess (1980) in Al_2O_3 partitioning experiments between immiscible alkali-free silicate melts. In these experiments $Ca_{0.5}AlO_2$ complexes were found to favour the low-SiO_2 melt (i.e. the least polymerised) fraction by a factor of about two. However, addition of the alkali cations Na^+ or K^+ resulted in strong concentration of Al_2O_3 in the more polymerised (high-SiO_2) melt consistent with the spectroscopic interpretation of Mysen et al. (1981) for sodic systems. The reason for the discrepancy in the calcic melts is not clear; Wood & Hess (1982) believe the non-uniqueness of the band deconvolution scheme proposed by Mysen et al. (1981) is the major cause.

McMillan et al. (1982) have studied the high-frequency Raman spectra of glasses in the series SiO_2-$Ca_{0.5}AlO_2$ and proposed a substantially different structural interpretation of the spectra compared with that of Mysen and co-workers. While still maintaining that the glasses in the series have structures based on a tetrahedral aluminosilicate framework, McMillan et al. (1982) proposed a deconvolution scheme that leads to band

components similar to those resolved in the system $CaMgSiO_4$-SiO_2 (McMillan, 1984b). They suggest the band components assigned to units with 4, 3, 2, 1 NBO/T (i.e. Q_0 to Q_3) in the latter system are analogous to the aluminosilicate units $Si(OAl)_4$, $-Si(OAl)_3$, $=Si(OAl)_2$ and $\equiv Si(OAl)$ respectively (where OAl represents a bridging Si-O-Al linkage and -Si, =Si, ≡Si represent one, two and three bridging Si-O-Si bonds respectively). On this basis the high frequency Raman envelope cannot involve coupled (Si,Al-O) vibrations as envisaged by Mysen et al. (1981) but rather must be dominantly of Si-O character modified by the Al^{3+} cation much in the manner of alkali or alkaline earth cations in simple binary glasses (e.g. McMillan, 1984b; Mysen et al., 1982a). McMillan & Piriou (1982) emphasize that their structural interpretation and that of Mysen & co-workers offers, at this stage, an equally valid description of aluminosilicate glass structure highlighting the fact that curve fitting or deconvolution techniques are unlikely to yield unique solutions.

Additional weak Raman bands occur near 790 cm^{-1} in the SiO_2-$Ca_{0.5}AlO_2$ glass series together with a band near 880 cm^{-1} observed by Mysen et al. (1981). These have been assigned by McMillan et al. (1982) to dominantly stretching vibrations of fully polymerised tetrahedral aluminate groups (aluminate "clusters" of Mysen & Virgo, 1980b). McMillan et al. (1982) believe ν_{Al-O} stretching vibrations will occur at frequencies 20-30% less than Si-O vibrations, the authors expect components of Al-O stretching and Al "cage" motions to appear in the 700-900 cm^{-1} region with a weak Raman intensity but a strong to moderate IR activity. In the low frequency region associated dominantly with bridging oxygen motions, McMillan et al. (1982) ascribe new bands at ~590 cm^{-1} and ~490 cm^{-1}, occurring over a wide compositional range in system $Ca_{0.5}AlO_2$-SiO_2 and $NaAlO_2$-SiO_2 glasses, to the presence of Al-O-Al and Al-O-Si linkages respectively. These results together with recent ^{27}Al solid state NMR work (de Jong et al., 1983) suggest that the "aluminium avoidance principle", i.e. instability of aluminate condensates or clusters, is not a strict rule in aluminosilicate glasses (cf. the MD model for anorthite melt; Matsui & Kawamura, 1984). Metal ions of high z/r such as Mg^{2+} or Li^+ may stabilise aluminate clusters and $=Si(OAl)_2$ groups via equilibria of the type:

$$\ddagger Si\ddagger + \ddagger Si(OAl)_2] \longleftarrow 2\ddagger Si(OAl)]$$

where -Si = Si-O-Si and Si(OAl) = Si-O-Al linkages

which lead to a departure from a perfect random Al dispersal and hence a greater tendency for liquid phase unmixing.

The purpose of a number of recent studies has been the elucidation of the Al co-ordination state in a variety of compositions. Sharma & Simons (1981) and Sharma et al. (1983) have compared the Raman spectra of crystalline aluminosilicates of known structure with the corrsponding glasses. Glasses of $LiAlSi_2O_6$ composition quenched from 1 atm, 10 kbar and 20 kbar show a strong similarity in their Raman spectra to the γ-spodumene polymorph which has a stuffed β-quartz type aluminosilicate framework structure in which Al is in four-fold co-ordination. This contrasts strongly with the spectrum of α-spodumene (pyroxene structure with Al in six-fold co-ordination) and suggests a strong preference for four-fold co-ordinated Al in aluminosilicate glasses with M/Al (M = Li,Na,K) near 1. Sharma & Simons (1981) point out that it is not possible with Raman spectroscopy to evaluate **directly** the effects of an AlO_4 --> AlO_6 co-ordination change due to weak band intensities and possible coupling effects. Instead this must be done indirectly by monitoring the intensity of bands associated with NBO. In a similar study, Sharma et al. (1983) have compared the Raman spectra of crystalline and vitreous anorthite, calcium Tschermak's (Cats) pyroxene and gehlenite. Only the anorthite spectrum resembles that of the crystalline phase. In Cats, Al is predominantly in four-fold co-ordination. The spectrum of gehlenite glass indicates a strong bimodal "Q_0-Q_4" dispersion of Si environments with Al charge balanced in the polymerised network by Ca^{2+}.

There has been considerable controversy in the geological literature concerning pressure-induced Al co-ordination changes in silicate liquids. Kushiro (1976, 1978, 1980) found significant viscosity and density changes in jadeite and albite melts with increasing pressure. This together with inflections in the melting curves of both compositions led Kushiro to suggest the occurrence of a pressure-induced structural change most probably involving an AlO_4 --> AlO_6 co-ordination change as is observed in the solid-state reaction: Ne + Ab --> 2Jd, for example. Mysen et al. (1980a, 1982a) have disputed this result on the basis of a lack of observable change in the Raman spectrum of jadeite glass to high pressure and the fact that many Al-free silicate melts exhibit comparable viscosity and density changes with pressure. Boettcher et al. (1982) by contrast consider that the glasses studied by Mysen et al. (1980a) are structurally unrepresentative of: (i) liquids from which they were quenched and/or (ii)

liquids that are in equilbrium with a crystalline phase. They consider the possibility that the fraction of Al in six-fold co-ordination may be below the limit of detection using Raman spectroscopy. However, Mysen et al. (1982a, 1983) consider that they can detect changes in the NBO content corresponding to conversion of ≈2% of Al^{3+} into non-tetrahedral co-ordination. Based on density differences Kushiro (1978) estimated that ~7% of the Al in high pressure albite melt could be non-tetrahedral. A change of this magnitude with pressure should therefore be detectable via Raman spectroscopy, however Mysen et al. (1980a) failed to detect the predicted Al co-ordination change in either Jd or Ab compositions to 38 kbar. More direct methods have also failed to detect co-ordination numbers for Al higher than 4 in aluminosilicate melts quenched at low pressures. Magic-angle spinning (MAS) ^{27}Al NMR experiments by de Jong et al. (1983) were unable to sample all the Al species in the glass as only a proportion of the Al gave rise to a narrow resonance. This contrasts with similar MAS-NMR measurements on $CaO-Al_2O_3-P_2O_5$ glasses in which three different Al environments were detected (Muller et al., 1984) i.e. AlO_6 and AlO_4 groups and Al-O-Al linkages. In the aluminosilicate NMR spectra of de Jong et al. (1983), a broad resonance underlies the narrow band making it impossible to partition all Al between four- and six-fold co-ordination sites. For albite, orthoclase, jadeite, nepheline and anorthite 1 atm glasses the narrow line feature corresponds to four-co-ordinate Al. X-ray AlK_a emission spectroscopy (summarised by Wong & Angell, 1976) also indicates that Al is confined mainly to four-fold co-ordination even in some glasses up to Al/Na = 1.5. However, Day & Rindone (1962) and Klonkowski (1983) in a series of 1 atm sodium aluminosilicate glasses with Al/Na > 1 and Velde & Kushiro (1978) in jadeite glass quenched from various pressures present AlK_α x-ray and other data that are consistent with the presence of Al^{VI}. In the latter study the results are interpreted in terms of a continuous, gradual Al^{IV} --> Al^{VI} change occurring in Jd melt with increasing pressure. The MD calculations of Matsui & Kawamura (1984) for compaction of An melt suggest that a gradual Al co-ordination change from AlO_4 ---> AlO_5 ---> AlO_6 is to be expected as pressure increases. However, the size distribution of aluminosilicate rings was also found to be strongly affected by pressure. Kushiro (1984) believes a decrease in average ring size occurring at moderate pressures, i.e. ~10-30 kbar, could account for the observed shift in AlK_α wavelength as well as explain viscosity and diffusion data. This does not exclude the possibility that Al co-ordination changes may take place at much higher pressures; Kushiro (1984) has suggested that a distinct inflection in the melting curve of pyrope at

~80 kbar which is accompanied by a change in quench phase from pyroxene to garnet (Ohtani et al., 1981) may be related to the expected Al^{IV} ---> Al^{VI} shift. Very recently Ohtani et al. (1985) have confirmed this hypothesis with a ^{27}Al-NMR study on vitreous albite quenched from a range of pressures. NMR spectra show that conversion of Al^{IV} to Al^{VI} in this composition begins at ~60 kbar and extends to pressures beyond 80 kbar. Significant conversion of $[SiO_4]$ to $[SiO_6]$ polyhedra are also expected at >20% compaction of silicate melt volumes (Matsui & Kawamura, 1980); this, however, would correspond to pressures in excess of 100 kbar.

Infrared spectroscopy has been suggested by Tarte (1965, 1967) as useful for directly characterising Al-O co-ordination polyhedra provided the vibrating unit remains largely independent of other groups. This appears valid, particularly for AlO_6 groups, in numerous crystalline aluminosilicates and the few glasses investigated by Tarte (1967). Many cations in the glass phase, including Al, can be identified from their characteristic MO_n (M = metal cation, n = co-ordination number) "cage" vibrations which appear to be quite localised in character (Rao & Elliott, 1981). The vibration frequency depends on the mass of the cation, the size of the oxygen polyhedron (both bond length and co-ordination number) and the nature of the co-ordinating oxygen ions (effective charge and type of network attachment). For Al, the approximation that these vibrations remain independent or localised breaks down for spinel minerals and other aluminate structures where substantial coupling with lattice modes is observed (e.g. the silicate spinels of Jeanloz, 1980).

IR techniques have already been successfully employed in distinguishing six-fold from four-fold co-ordinated Al in synthetic aluminosilicate gels (Farmer et al., 1979) and in aluminous serpentinites (Serna et al., 1977, 1979). The technique has not as yet been applied to silicate glasses in any systematic way. Because of difficulties experienced with other methods the ability of IR spectroscopy to distinguish tetrahedral/octahedral Al warrants further investigation. This topic has therefore been considered in some detail in Section 4.6.

In summary, at present the relationship between molecular structure and vibrational spectra for the aluminosilicate glasses is open to several interpretations. What is clear, however, is that in many melt compositions Al prefers to be bound as part of the silicate network in sites of tetrahedral co-ordination to oxygen and charge balanced by metal cations.

The order of Al-cation preference is K > Na > Ca > Fe^{2+} > Mg reflecting the relative stability of the appropriate $MAlO_2$ or $M_{0.5}AlO_2$ network complex (Hess & Wood, 1982). Evidence for the presence of Al-O co-ordination numbers higher than four is equivocal in 1 atm and moderate-pressure, volatile-free aluminosilicate melts. As yet, sufficient use has not been made of more direct methods for determining Al co-ordination. While Raman spectroscopy is unsuitable for this purpose both ^{27}Al MAS-NMR and IR spectroscopy offer future promise.

A13.5 Vibrational Spectra of Volatile (H_2O, CO_2)-bearing Silicate and Aluminosilicate Glasses and the Mechanism of Volatile Solubility

A. Water

Vibrational and NMR spectroscopic observations have firmly established that H_2O dissolves in silicate and aluminosilicate melts in the form of hydroxyl groups and molecular water (Bartholomew et al., 1980; Bartholomew & Schreurs, 1980; Bartholomew, 1983; Stolper, 1982a, 1982b; McMillan et al., 1983). Prior to these investigations, models of water solubility in silicate melts were based on the assumption that complete H_2O dissociation took place to produce two hydroxyl groups per H_2O group by interaction with oxygen ions of the melt:

$$H_2O_{(vapour)} + O^{2-}_{(melt)} = 2OH^-_{(melt)}$$

This model was believed to be applicable to melts at low total water content on the basis of observed linear relations between $f^{melt}_{H_2O}$ and $(x^{melt}_{H_2O})^2$. For example, Burnham & Davis (1974) established the relationship $f^{melt}_{H_2O} = k(x^{melt}_{H_2O})^2$, where k = Henry's Law contant, for melts in the system albite-H_2O at $x^{melt}_{H_2O} < 0.5$ (corresponding to total water contents $\lesssim$6 wt%) for pressures up to 10 kbar. This has been described by Eggler & Burnham (1984) as "Henrian-analogue" behaviour because of the resemblance to the Henry's Law relationship found in strong binary electrolytes. Since this implies complete ionic dissociation, Burnham & Davis (1974) described water dissolution in albite melts at $x^{melt}_{H_2O} < 0.5$ in terms of the cation exchange reaction:

$$H_2O_{(vapour)} + NaAlSi_3O_{8(melt)} = AlSi_3O_7(OH)_{(melt)} + NaOH_{(melt)} \quad \ldots\ldots 13.5A$$

At higher mole fractions of water where $f_{H_2O}^{melt}$ could not be related simply to $x_{H_2O}^{melt}$, the authors envisaged a direct interaction with briding oxygens:

$$H_2O_{(vapour)} + [O^o]_{(melt)} = 2[OH^o]_{(melt)} \quad \text{..... 13.5B}$$

The existence of dual H_2O solubility mechanisms has also been postulated by Oxtoby & Hamilton (1978a, 1978b) on the basis of a sharp change in slope of water solubility vs $f_{H_2O}^{1/2}$ curves determined for a variety of Na and K aluminosilicate melts. Hodges (1973) found a nearly identical solubility of water in high pressure (>10 kbar) forsterite, enstatite, diopside and anorthite melts when normalised to a per formula oxygen basis. The author suggested that this might be due to solution of water as discrete molecules. This view was later supported by a determination of the partial molar volume of water ($\bar{V}_{H_2O}^{melt}$) dissolved in diopside melt at 20 kbar (Hodges, 1974) which gave a value close to the molar volume of free water. By contrast, for low pressure albite melts, Burnham (1975) obtained partial molar volumes for H_2O much lower than that of free water and near $\bar{V}_{H_2O}$ calculated for a close-packed OH^- array suggesting a solution mechanism involving largely hydroxyl ions.

While dual H_2O solubility mechanisms are clearly indicated by these data, it appears doubtful that equations 13.5A and 13.5B adequately describe this process since recent studies have now established that molecular water is an important species in hydrous silicate melts even at low total water contents (TWC's). Stolper's (1982a) infrared study of a wide range of natural and synthetic glass compositions found a surprisingly consistent variation in molecular water/hydroxyl group ratio at any particular TWC. Molecular water was detected in all samples with TWC >0.5 wt%, the proportion of molecular water increasing continuously with increasing TWC. Hydroxyl groups are the dominant species below TWC ~ 4 wt%; beyond ~3.0 wt% TWC further water is added mostly in molecular form. IR bands specifically assignable to molecular water occur in the near-IR region at ~5230 cm^{-1} (combination bending + stretching) and mid-IR region at ~1630 cm^{-1} (ν_2 bending). That specific for OH groups (X-OH stretching + bending) appears near 4500 cm^{-1} (Stolper, 1982a). The broad peak centred near 3550 cm^{-1} in hydrous glasses is the fundamental O-H stretching vibration associated with both hydroxyl groups and molecular water. The asymmetry of this band has been attributed to the presence of an array of different H-bonding configurations (e.g. Serna et al., 1979; Nakamoto et al., 1955). The amount of molecular H_2O and hydroxyl groups may be

quantitatively determined in hydrous glasses from the absorbance values of the 5230 cm^{-1} and 4500 cm^{-1} bands by application of the Beer-Lambert Law (Bartholomew et al., 1980):

$$c = \frac{18.015 * \text{absorbance}}{\varepsilon * \rho * d}$$

where c = H_2O concentration (wt%)

ε = molar absorptivity ($\ell\, mol^{-1} cm^{-1}$)

d = specimen thickness (mm)

ρ = specimen density (gcm^{-3})

Strictly speaking ε will be a function of glass composition that must be determined in every case. Stolper (1982a) has shown, however, that the ratio $\varepsilon_{5230}/\varepsilon_{4500}$ is approximately constant (~2) for a wide range of glasses and may therefore be used to determine the ratio of molecular water to hydroxyl groups without a specific calibration.

A major consequence of the discovery of molecular water as a significant species is the invalidation of H_2O solubility mechanisms such as those proposed by Burnham & Davis (1974, eqns 13.5A and 13.5B) and Oxtoby & Hamilton (1978). Both models offer reasonable explanations for observed thermodynamic and thermophysical properties of hydrous melts but are not structurally realistic. This illustrates the great difficulty in attempting to derive a structural model indirectly from bulk thermodynamic data. Because bulk data are seldom sensitive on the level of individual species or units, a structural model obtained in this way is unlikely to represent a unique solution.

Stolper (1982b) has suggested an ideal quasi-chemical model for hydrous "acidic" melts based on the homogeneous equilibrium:

$$H_2O_{molec(melt)} + O^{o}_{(melt)} = 2OH^{o}_{(melt)} \quad \ldots\ldots \text{13.5C}$$

where O^{o} = bridging oxygen,

which may be combined with the heterogeneous equilibrium:

$$H_2O_{(vapour)} = H_2O_{molec(melt)} \quad \ldots\ldots \text{13.5D}$$

to describe melt-vapour equilibria.

Stolper (1982b) has successfully fitted this model to the data of Burnham & Davis (1974) for the system albite-water with some surprising results:

The observed linear relationship between $f_{H_2O}^{melt}$ and $(x_{H_2O}^{melt})^2$ at water contents $\lesssim$6 wt% is reproduced even though up to 50% of total water is present in molecular form. The interpretation of Burnham & Davis (1974) that linear f_{H_2O}-$(x_{H_2O})^2$ behaviour is compatible with dissolution of water exclusively as hydroxyl groups can thus no longer be considered as correct. Stolper finds the change from linear to non-linear f_{H_2O}-$(x_{H_2O})^2$ behaviour to be merely a consequence of equilibrium 13.5C shifting to the left with increasing pressure and not due to some arbitrary discontinuous change in solution mechanism at $x_{H_2O}^{melt} = 0.5$. The lack of compositional dependancy of water solubility at high pressures (Hodges, 1974) arises from the dominance of the molecular water component under these conditions. Only the hydroxyl component is predicted to have a substantial compositional dependance and this is observable at low total pressures (Uys & King, 1963), cf. $\bar{V}_{H_2O}$ values discussed earlier. A further important consequence of Stolper's model is that the observed large shifts in liquidus phase boundaries in hydrous systems (resulting from an increase in the phase volume of more depolymerised minerals) is a product of only the first 3-4 wt% of water dissolved. Stolper (1982b) believes it is this first amount that interacts with bridging oxygen to form hydroxyl groups; adding more water is likely to have only a small effect since most will dissolve in molecular form without undergoing any significant interaction with the silicate network components. Bartholomew (1983) finds the physical properties of hydrous silicate melts to be consistent with this view.

Eggler & Burnham (1984) have recently proposed a thermodynamic model for H_2O dissolution in diopside melt based on the assumption of structural similarities between "superhydrous" albite melt ($x_{H_2O}^{melt} > 0.5$) and anhydrous diopside melt, both of which contain a substantial proportion of NBO. By assuming a "Henrian-exponential" model: $a_{H_2O}^{melt} = k \exp(x_{H_2O}^{melt})$ and a limited number of constraints the H_2O-saturated diopside solidus could be well reproduced. There is, however, no structural basis for the model so that only limited interpretation of the solubility mechanism may be made. Eggler & Burnham suggest that H_2O is present in diopside melt largely in undissociated form or as "hydroxylation silicate complexes" associated with

NBO. The authors further speculate that the solubility mechanism of water is different for melts based largely on a 3-d aluminosilicate network (e.g. albite, jadeite) and those containing substantial NBO (e.g. diopside, enstatite, forsterite). A detailed spectroscopic investigation would be required to substantiate these views.

The effects of water solubility have been studied by Raman spectroscopy in a limited number of compositions: Mysen et al. (1980b): Ab, Jd and two Na-silicate glasses; Mysen & Virgo (1980b): sodamelilite (Sm) glass and McMillan et al. (1983): a re-investigation of hydrous albite glass.

Mysen et al. (1980b) found no evidence in the spectral region near 1600 cm^{-1} for the presence of molecular water in any of the compositions studied. The re-investigation by McMillan et al. (1983) however showed that the molecular water H-O-H ν_2 bending vibration is of very weak intensity in the Raman spectra of hydrous glasses and was evidently overlooked by Mysen et al. (1980b).

The aluminosilicate compositions Sm, Jd and Ab were found, according to Mysen et al. (1982a), to behave similarly to solution of water at high pressure. With increasing H_2O content Mysen et al. (1980b) and Mysen & Virgo (1980b) confirmed the depolymerising role of H_2O by finding that both $Si-O^-$ and Si-OH groups are produced; these were identified by new bands appearing near 870 cm^{-1} and 970 cm^{-1} respectively. Intensity shifts in the high frequency envelope suggested a decrease in Al/(Al+Si) of the 3-d network and by inference a co-ordination shift of some Al from four- to six-fold co-ordination. It has been proposed by Mysen et al. (1982a) that Al expulsion from the network occurs by removal of charge balancing Na on formation of hydroxy complexes of the type $Na(OH)_n^{n-1}$. Such complexes have been inferred but not actually shown to exist in hydrous aluminosilicate melts. Mysen et al. (1980b) find no evidence for the attachment of Al to hydroxyl groups - a conclusion also supported by the solubility studies of Oxtoby & Hamilton (1978).

McMillan et al. (1983) have suggested a different interpretation for some of the Raman bands in hydrous albite and other aluminosilicate glasses. The authors believe that the new band appearing at 850-900 cm^{-1} is best assigned to an Si-OH (and/or Al-OH) stretching vibration.

Deformation vibrations of Si-OH and Al-OH groups are expected near 1000-1100 cm^{-1} and would therefore overlap with network stretching vibrations perhaps resulting in the observed small changes associated with the high frequency envelope. A Raman band near 570 cm^{-1} in albite and other aluminosilicates shows a sharp **decrease** in intensity on H_2O addition; McMillan et al. (1983) have associated this change with break-up of Al-O-Al linkages but Mysen et al.'s (1980b) interpretation is in terms of a progressive elimination of "broken bond" defect sites by reaction with H_2O:

$$Si\overset{-}{O}\ \overset{+}{Si} + H_2O \longrightarrow 2Si\text{-}OH$$

(cf. Stolen & Walrafen, 1976; Bates et al., 1974).

The NBO-rich sodium di- and trisilicate glasses investigated by Mysen et al. (1980b) show substantially different behaviour on water addition compared with the aluminosilicates (cf. model of Eggler & Burnham, 1984). An apparent increase in the proportion of polymerised units with increasing H_2O content was interpreted by Mysen et al. (1982a) as due to a decrease in the proportion of NBO's as Si-OH groups are substituted for $Si\text{-}O^{-}Na^{+}$. A broad deconvoluted band at ~970 cm^{-1} was assigned to Si-OH stretching following Stolen & Walrafen (1976). The presence of $Na(OH)_n^{n-1}$ complexes, unable to be characterised by Raman spectroscopy, was inferred from mass balance considerations.

As indicated by the above results, Raman spectroscopy appears to have only limited use in identifying H_2O speciation in hydrous glasses. When combined with difficulties in band assignments and the non-uniqueness of band fitting procedures, the elucidation of the H_2O solubility mechanism, if based solely on Raman data, relies greatly on indirect evidence. IR spectroscopy has been used successfully by Stolper to distinguish dissolved H_2O species and may prove useful in the future for identifying metal-hydroxyl complexes (far-IR region) and distinguishing Al-O co-ordination environments. Further work is required to fully understand the H_2O solubility mechanism in silicate melts.

B. Carbon Dioxide

Because of the importance of CO_2 in the petrogenesis of silica-undersaturated alkaline rocks arising from its dramatic effect on liquidus mineral phase volumes at high pressure; extensive investigations of

solubility relations and mechanisms have been made (see recent summary by Holloway, 1981).

Solubility studies show that dissolution of CO_2 increases as a function of both pressure and melt basicity. The temperature dependence appears variable but this may in part be due to analytical problems (see Brey, 1976; and Brey & Green, 1976b). Efforts to elucidate the mechanism of CO_2 dissolution have centred around Raman and infrared spectroscopic measurements of quenched high pressure glasses mostly in simple systems:

albite-anorthite	Brey (1976); Mysen & Virgo (1980c)
diopside, sodamelilite	Sharma (1979); Mysen & Virgo (1980a); Rai et al. (1983)
akermanite	Sharma et al. (1979)
$NaAlO_2$-SiO_2	Mysen (1976)
K_2CO_3-$MgCO_3$-$CaCO_3$	Sharma & Simons (1980)
K_2O-SiO_2	Verweij et al. (1977)

A number of other studies have examined natural compositions but these will not be considered in any detail here due to poor spectroscopic resolution.

All studies have established that CO_2 dissolves in silicate melts dominantly, and in the majority of cases, exclusively as carbonate anions, CO_3^{2-}. Carbonate is readily identified by a number of characteristic bands that for molecular and site symmetry D_{3h} (i.e. planar with equal C-O bond distances and angles) will not be split by degeneracies of the vibrational modes (Alder & Kerr, 1963). For typical crystalline carbonates these are summarised below (after Liese, 1975 and Verweij et al., 1977):

Table 13.5A Internal vibrational modes of the carbonate anion.

Description*	Mode	D_{3h} Symmetry Class	Typical Range (cm^{-1})	Ideal Activity**	Typical Activity**	
					R	IR
sym. C-O stretch	ν_1	A_1'	1050-1090	R	s	w
CO_3 oopl defm.	ν_2	A_2''	860-880	IR	w	m
asym. C-O stretch	ν_3	E'	1600-1300	R & IR	w	s
CO_3 inpl. defm.	ν_4	E'	740-680	R & IR	m	m
overtone	$2\nu_2$	A_1'	1770-1740	R	w	vw

* sym. = symmetric, asym. = asymmetric, oopl. = out-of-plane, inpl. = in-plane, defm. = deformation.
** R = Raman active, IR = infrared active, s = strong, m = medium, w = weak, vw = very weak.

Departure of molecular symmetry (i.e. symmetry of the CO_3^{2-} anion only) and/or site symmetry (i.e. symmetry of anion plus arrangement of bonded cations) from D_{3h} will result in removal of E′ mode degeneracy and hence result in IR or Raman activation of D_{3h} symmetry disallowed modes. For example in aragonite, CO_3^{2-} has site symmetry C_s and probably also molecular symmetry C_s (Alder & Kerr, 1963) giving rise to a splitting of the ν_3 and ν_4 modes and appearance of the ν_1 band in the IR spectrum. In other minerals this may be caused by unidentate or bidentate CO_3^{2-} co-ordination involving a metal cation or hydrogen ion; bicarbonate, HCO_3^-, is an extreme example. Apparent splitting of bands can also arise from the presence of non-equivalent molecular sites; this may be distinguished from symmetry splitting by the observation of multiple bands for normally singly degenerate modes.

In the Raman spectra of CO_2-bearing diopside, sodamelilite and akermanite glasses quenched from high-pressure, Sharma (1979) and Sharma et al. (1979) found substantial splittings (~80-100 cm^{-1}) of the ν_3 bands. Similar splittings have been observed in the IR spectra of CO_2-bearing Ab-An and olivine melilitite glasses (Brey, 1976) and in K_2CO_3-$MgCO_3$-$CaCO_3$ system glasses (Sharma & Simons, 1980). In the latter case the ν_1 and ν_3

bands were resolvable into two components visually and three by curve fitting. This strongly suggests that CO_3^{2-} ions in this case occupy at least two and probably three non-equivalent sites each with molecular symmetries of at least C_3. Supporting evidence comes from a mass pyrogram of a K,Mg,Ca-carbonate glass showing three distinct CO_2 release peaks (Rai et al., 1983).

The Raman spectra of the CO_2 containing silicate glasses (Di,Ak,Sm) while showing the ν_3 splitting demonstrate no broadening or splitting of the sharp ν_1 band suggesting the presence of only one CO_3^{2-} site. The splitting may be reasonably interpreted as arising from unidentate or bidentate co-ordination of carbonate by a metal cation in a metallo-carbonate complex dissolved in the melt. Mass pyrograms of CO_2-bearing Di glasses do, however, show two release peaks suggesting the presence of more than one carbonate site (Rai et al., 1983). Further work is required to clarify the cationic environment of dissolved carbonate anions.

A number of studies have found spectroscopic evidence for the presence of molecular CO_2 in sodium-rich melts, e.g. Brey (1976): albite-rich compositions; Mysen (1976): albite, jadeite; Mysen & Virgo (1980c): albite. Molecular CO_2 may arise either from quench effects, e.g. decomposition of dissolved carbonate during quench as proposed by Brey (1976) or may represent true high pressure solution. Since neither possibility has been satisfactorily demonstrated or refuted to date, the question of molecular CO_2 speciation in silicate melts remains open.

Raman spectroscopy has been used to investigate changes in the silicate network following CO_2 dissolution. Sharma (1979) and Mysen & Virgo (1980a) speculated that in calcic systems CO_3^{2-} ions are most probably associated with Ca^{2+} as $[CaCO_3]^o$ complexes. In CO_2-bearing Ak glasses Sharma et al. (1979) established the polymerising role of CO_2 by both Raman spectroscopy and the gas chromatographic analysis of silicate anions released as trimethylsilyl derivatives.

Raman investigations of CO_2 dissolution in melts based on fully polymerised 3-d network structures were carried out by Mysen & Virgo (1980c) on the feldspar composition glasses An and Ab. The authors found evidence for a decrease in Al/(Al+Si) of the network on CO_2 addition and postulated formation of $[CaCO_3]^o$ or $[Na_2CO_3]^o$ complexes concomitant with Al^{3+} expulsion from the aluminosilicate network. However, no direct

spectroscopic evidence was given to indicate the presence of either metal-carbonate complexes or non-tetrahedral Al. Because of the importance of the questions raised by these recent Raman studies, two high pressure CO_2-bearing glasses (nepheline and sodamelilite compositions) were investigated by FTIR spectroscopy as part of this study. These results are presented in Appendix 15.

To summarise, in depolymerised melts, i.e. those with initially available NBO (basaltic melt analogues) the CO_2 dissolution mechanism may be simply represented by the equilibrium:

$$CO_{2(vapour)} + 2O^{-}[NBO]_{(melt)} = CO^{2-}_{3(melt)} + O^{o}[BO]_{(melt)} \quad \ldots\ldots 13.5E$$

The extent to which the reaction proceeds to the right will be very dependent on the nature of metal-carbonate complexes formed. In fully polymerised melts (granitic melt analogues) the CO_2 dissolution mechanism is more complex and may involve an Al^{IV} ---> Al^{VI} co-ordination change by removal of charge balancing alkali and alkaline earth ions from the network as carbonate complexes.

Spera & Bergman (1980) have combined spectroscopic information derived from these studies together with solubility data to develop a model for P-T-$x^{melt}_{CO_2}$ behaviour in a variety of bulk compositions. Relative CO_2 solubilities may be determined for binary and pseudobinary metal oxide-silica systems by reference to Gibbs Free Energy data for model carbonation/polymerisation reactions. For alkali- and alkaline-earth-silica systems, the predicted order of cation affinity for carbonate ions (i.e. Ca > K > Na > Li > Mg > Fe^{2+},Mn) is consistent with available CO_2 solubility data.

APPENDIX 14

EXPERIMENTAL RUNS ALONG THE JOIN $Ne_{55}Fo_{45}$-$Ne_{55}Q_{45}$ AT P = 28 KBAR: RESULTS AND MICROPROBE ANALYSES.

Table 14A

VOLATILE-ABSENT

Run Number	Fo (wt%)	Duration (min.)	T(°C)	Products**
T-1210*	25	15	1440	Fo+Opx+Liq+Qx (~40% xals)
T-1213*	25	10	1500	Liq+Qx
T-1215*	25	10	1475	Fo+Opx+Liq+Qx (~30% xals)
T-1218*	25	12	1490	Fo+Liq+Qx (~10% xals)
NFA-1 Kushiro (1968)	$Ne_{62}Fo_{18}Q_{20}$		1420	Fo+Liq+Qx
			1400	Fo+Opx+Liq

H_2O-SATURATED (~30 wt% H_2O added as liquid via microsyringe)

T-1175	18	60	1100	Fo+Opx (large primary xals)+Liq+Qx (5-10% xals)
T-1237	14	60	1040	Opx+Liq+Qx (~20% xals)
T-1304	20	60	1100	Fo+Liq+Qx (many vapour bubbles in glass, <5% xals)
T-1305	16	60	1060	Opx+Liq+Qx (many vapour bubbles in glass <10% xals)

CO_2-SATURATED (~15 WT% CO_2 generated from $Ag_2C_2O_4$)

T-1226	30	12	1390	Opx+Liq+Qx (large primary vapour bubbles + secondary bubbles, ~10% xals)
T-1227	35	12	1390	Fo+Opx+Liq+Qx (pronounced phase separation due to xal settling, primary and secondary vapour bubbles)
T-1334	37	12	1400	Fo+Liq+Qx+Qcarb (close to liquidus)

C-H FLUID SATURATED (~6-8 WT% CH_4 generated from $Al(OH)_3/Al_4C_3/Al_2O_3$ mixture)

T-1174	18	25	1280	Opx+Liq+Qx+Fo(tr)

				(~25% xals)
T-1208	25	20	1350	Fo+Opx+Liq+Qx (~30% xals)
T-1284	22	20	1380	Fo+Opx+Liq+Qx (quench feathers around opx evident, ~20% xals)
T-1289***	20	25	1380	Opx+Liq+Qx (~10% xals)
T-1291	20	25	1360	Opx+Fo+Liq+Qx (~20% xals)
T-1315	22	30	1395	Fo+Liq+Qx (~5% xals)

* Fo = forsterite; Opx = enstatite$_{ss}$; Liq = glass; Qx = quench silicates; Qcarb = quench carbonate; tr = trace; xal = crystal.

** Liquid composition obtained (see Table 14B).

*** FTIR spectrum and difference spectrum obtained.

Table 14B Liquid Compositions.

Oxide (wt%)	T-1213 Volatile-absent (all liquid)	T-1218 Volatile-absent (1490°C)	T-1215* Volatile-absent (1475°C)	T-1210* Volatile-absent (1440°C)	T-1227** CO_2-saturated (1390°C)
SiO_2	54.01	54.39	54.55	54.52	48.81
Al_2O_3	19.85	21.51	22.79	23.19	22.93
MgO	14.28	11.03	8.81	8.19	14.32
Na_2O	11.86	13.07	13.85	14.10	13.94
Fo	24.9(25)***	19.3	15.4	14.3	25.0
Ne	55.3(55)	59.9	63.5	68.6	63.9
Q	19.8(20)	20.8	21.1	21.1	11.1

* Liquids poorest in MgO and lying on the terminus of well defined liquid-bulk composition-equilibrium crystal tie lines. Slight deviation from Na/Al = 1 corrected by adding a small amount of $MgAl_2SiO_6$ (MgTs) component. Estimated equilibrium En_{ss} composition: $En_{85}MgTs_{15}$ (mol% basis, Al_2O_3 = 7.6 wt%).

** As above although deviation from Na/Al = 1 more extreme due to greater quench and higher proportion of Al_2O_3 in En_{ss}, liquid composition estimated by removing average "quench pyroxene" $En_{55}MgTs_{30}Jd_{15}$ (mol% basis) until Na/Al = 1.

*** Expected composition for $Ne_{55}Fo_{25}Q_{20}$ in brackets.

Table 14C Crystal Compositions

Oxides (wt%)	T-1210 (Vol-absent) En_{ss} core	T-1210 (Vol-absent) En_{ss} quench rim	T-1210 (Vol-absent) Quench Px	T-1175 (H_2O-sat.) En_{ss} core
SiO_2	55.46	54.72	56.74	58.36
Al_2O_3	11.27	15.58	23.39	3.38
MgO	31.68	24.79	8.20	38.26
Na_2O	1.59	4.91	11.67	0.00
Si	1.853	1.837	1.909	1.948
Al	0.444	0.617	0.928	0.133
Mg	1.578	1.241	0.411	1.904
Na	0.103	0.320	0.759	0.000
Total	3.978	4.015	4.007	3.985
Mol% endmembers*				
En	72.0	53.8	11.5	93.3
MgTs	17.4	14.6	16.1	6.8
Jd	10.5	31.5	72.4	0.0
$Al^{oct}/\Sigma Al$**	0.62	0.68	0.85	0.50

	T-1175 (H_2O-sat.) En_{ss} Rim #1	T-1175 (H_2O-sat.) En_{ss} Rim #2	T-1175 (H_2O-sat.) Forsterite	T-1175 (H_2O-sat.) En_{ss} quench xal
SiO_2	57.29	57.56	43.19	52.68
Al_2O_3	6.25	7.46	0.00	17.94
MgO	36.46	33.54	56.81	26.47
Na_2O	0.00	1.45	0.00	2.91
Si	1.910	1.922	1.010	1.762
Al	0.246	0.294	0.000	0.707
Mg	1.812	1.669	1.980	1.320
Na	0.000	0.094	0.000	0.189
Total	3.968	3.979	2.990	3.978
Mol% endmembers*				
En	87.3	80.2		54.2
MgTs	12.7	10.2		26.5
Jd	0.0	9.6		19.3
$Al^{oct}/\Sigma Al$**	0.50	0.66		0.63

Table 14C continued

	T-1227 (CO_2-sat.) En_{ss} core	T-1227 (CO_2-sat.) En_{ss} rim	T-1227 (CO_2-sat.) En_{ss} quench xal	T-1227 (CO_2-sat.) En_{ss} quench xal
SiO_2	51.98	50.26	50.56	50.62
Al_2O_3	15.74	17.98	18.90	17.81
MgO	31.32	30.55	27.76	28.24
Na_2O	0.95	1.20	2.78	3.33
Si	1.739	1.685	1.698	1.706
Al	0.621	0.710	0.748	0.707
Mg	1.561	1.526	1.390	1.419
Na	0.062	0.078	0.181	0.218
Total	3.983	3.999	4.017	4.050
Mol% endmembers*				
En	65.2	60.6	54.4	55.9
MgTs	28.5	31.6	27.9	23.2
Jd	6.3	7.8	17.8	20.8
$Al^{oct}/\Sigma Al$**	0.55	0.56	0.62	0.65

	T-1291 (CH_4-sat.) En_{ss} Core #1	T-1291 (CH_4-sat.) En_{ss} Core #2	T-1291 (CH_4-sat.) En_{ss} Rim #1	T-1291 (CH_4sat.) En_{ss} Rim #2
SiO_2	56.45	56.68	55.80	57.11
Al_2O_3	9.53	9.68	14.96	16.43
MgO	31.78	31.55	25.62	20.51
Na_2O	2.24	2.09	3.62	5.95
Si	1.889	1.894	1.863	1.908
Al	0.376	0.381	0.589	0.647
Mg	1.585	1.572	1.275	1.021
Na	0.145	0.135	0.235	0.386
Total	3.995	3.982	3.962	3.962
Mol% endmembers*				
En	73.8	73.7	57.1	46.3
MgTs	11.6	12.5	18.4	13.6
Jd	14.6	13.7	24.5	40.1
$Al^{oct}/\Sigma Al$**	0.69	0.68	0.70	0.80

Table 14C continued

Oxides (wt%)	T-1291 Forsterite	T-1291 Quench Px
SiO_2	43.12	57.52
Al_2O_3	0.00	23.37
MgO	56.88	6.68
Na_2O	0.00	12.43
Si	1.009	1.935
Al	0.000	0.926
Mg	1.983	0.335
Na	0.000	0.811
Total	2.992	4.007
Mol% endmembers*		
En		13.8
MgTs		5.7
Jd		80.5
$Al^{oct}/\Sigma Al$**		0.94

* Calculated by assigning Na to Jd, remaining Al to MgTs and remaining Mg to En.

** Al^{oct} = Jd + MgTs, Al = Jd + 2MgTs (mol% units).

APPENDIX 15

THE CO_2 DISSOLUTION MECHANISM IN NEPHELINE AND SODAMELILITE GLASSES: A RECONNAISSANCE FTIR STUDY IN THE FAR-IR AND MID-IR REGIONS.

This study is aimed chiefly at characterising the cationic environment of dissolved carbonate anions in two aluminosilicate glass compositions quenched from high pressure. Since direct spectroscopic evidence for the existence of dissolved metallocarbonate complexes in silicate glasses has not been presented to date, an important part of this investigation will be to record the far-IR spectra (<400 cm^{-1}) of carbonate-bearing glasses. It is in this region of the IR spectrum that absorptions characteristic of cation-oxyanion vibrations, such as those arising from cation-carbonate bonding in metallocarbonate complexes, appear (Rao & Elliot, 1981).

Glasses of nepheline (Ne) and sodamelilite (Sm) composition were chosen for this study to investigate the CO_2 solubility mechanism in both a fully polymerised aluminosilicate melt structure (Ne) and one containing available NBO (Sm). For comparative purposes IR spectra of the carbonate minerals dawsonite, $NaAl(OH)_2(CO_3)$, and shortite, $Na_2Ca_2(CO_3)$, were also recorded. While being broadly chemically analogous to the aluminosilicates Ne and Sm respectively, these carbonates have structures that make them of use in illustrating the spectroscopic effects of CO_3^{2-} anion symmetry and the presence of non-equivalent CO_3^{2-} sites.

Experimental Details

CO_2-saturated Ne glass was prepared at P = 30 kb in a piston-cylinder apparatus (run# T-1150) from a mixture of A.R. grade SiO_2, Al_2O_3 and Na_2CO_3 (available CO_2 = 13.4 wt%). To minimise possible H_2O or H_2 entry, assembly parts consisted of a fired pyrophyllite inner sleeve and an outer NaCl sleeve. The run duration was 5 min. at 1625°C and no external oxygen buffer was employed (identical run conditions were used by Mysen, 1976).

CO_2-bearing Sm glass (run# T-1178) was prepared at P = 30 kbar from a mixture of SiO_2, Al_2O_3, Na_2CO_3 and $CaSiO_3$ (available CO_2 = 7.9 wt%) using an outer talc/inner pyrex sleeved assembly. The run duration was 25 min at 1300°C. A hematite-magnetite external fO_2 buffer (double-capsule method) was employed to prevent graphite formation in the charge (this may arise from H_2 entry over the longer run times required at lower temperatures).

In both runs T-1178 and T-1150 all assembly parts and starting mixes were dried at 110°C for 24 hours prior to loading and run assembly.

Shortite, $Na_2Ca_2(CO_3)_3$, was prepared in piston-cylinder apparatus at P = 1.25 kbar, T = 390°C, run duration = 72 hours from a 1:2 molar mixture of Na_2CO_3:$CaCO_3$ to which 9 wt% H_2O was added as a flux. The product consisted of fine white crystals confirmed as shortite both optically and by XRD.

Dawsonite, $NaAl(OH)_2(CO_3)$, was provided courtesy of Dr F.L. Sutherland, Australian National Museum, Sydney. Sample # D42382.

Product Glasses

CO_2-bearing Sm glass is clear with no vapour bubbles. Negligible vapour loss on capsule puncture suggests that Sm melt was vapour undersaturated or just saturated at the run conditions employed. Microprobe analysis of C-content gives a value of 2.15 wt% (Section 4.8) identical to that expected for 7.9 wt% CO_2 dissolution. CO_2-bearing Ne glass is clear but has a greyish appearance due to a small amount of dispersed graphite presumably arising from CO_2 reduction. A puffed capsule and a vapour loss on puncture of ~60% of available CO_2 indicates vapour saturation of the melt. Estimated total C-content of the glass as CO_2 is 6 ± 1 wt%; Mysen (1976) obtained a CO_2 solubility of 5 wt% for Ne + CO_2 glass prepared under the same conditions.

FTIR spectroscopic examination of Ne and Sm CO_2-bearing glasses in the 4000-3000 cm^{-1} region reveals the presence of a small amount of H_2O (~0.5-1.0 wt%). Such an amount is invariably associated with experiments in piston-cylinder apparatus even when performed under "dry" conditions (Brey, 1976; Rai et al., 1983). It is assumed that this amount of H_2O dissolved in the glasses is not sufficient to affect the interpretation of IR spectra in terms of a CO_2 dissolution mechanism. Mid-range and far-IR spectra were recorded using the same techniques and instrumentation as discussed in Section 4.4.

Results: mid-IR region

Mid-range FTIR spectra of Ne and Sm CO_2-bearing glasses are presented in Figs 15A and B. The ν_3 carbonate absorptions appear as strong doublets centred near 1500 cm^{-1} and show large apparent splittings : 211 cm^{-1} for Ne + CO_2 and 83 cm^{-1} for Sm + CO_2. A splitting of ~100 cm^{-1} was observed

Figs 15A & 15B Mid-IR spectra of CO_2-bearing nepheline and sodamelilite glasses quenched at P = 30 kbar.

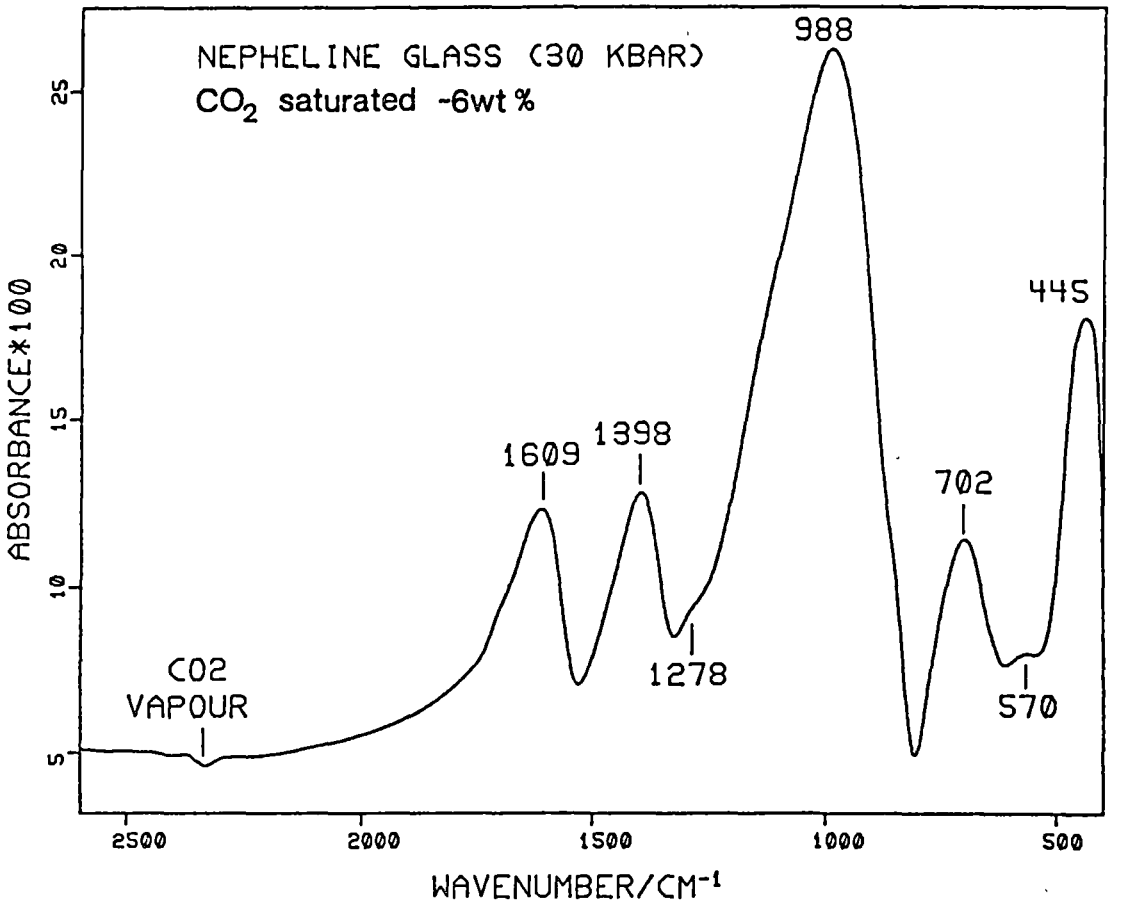
NEPHELINE GLASS (30 KBAR)
CO_2 saturated ~6wt %
988
445
1609
1398
702
1278
570
CO2
VAPOUR
ABSORBANCE*100
WAVENUMBER/CM^{-1}

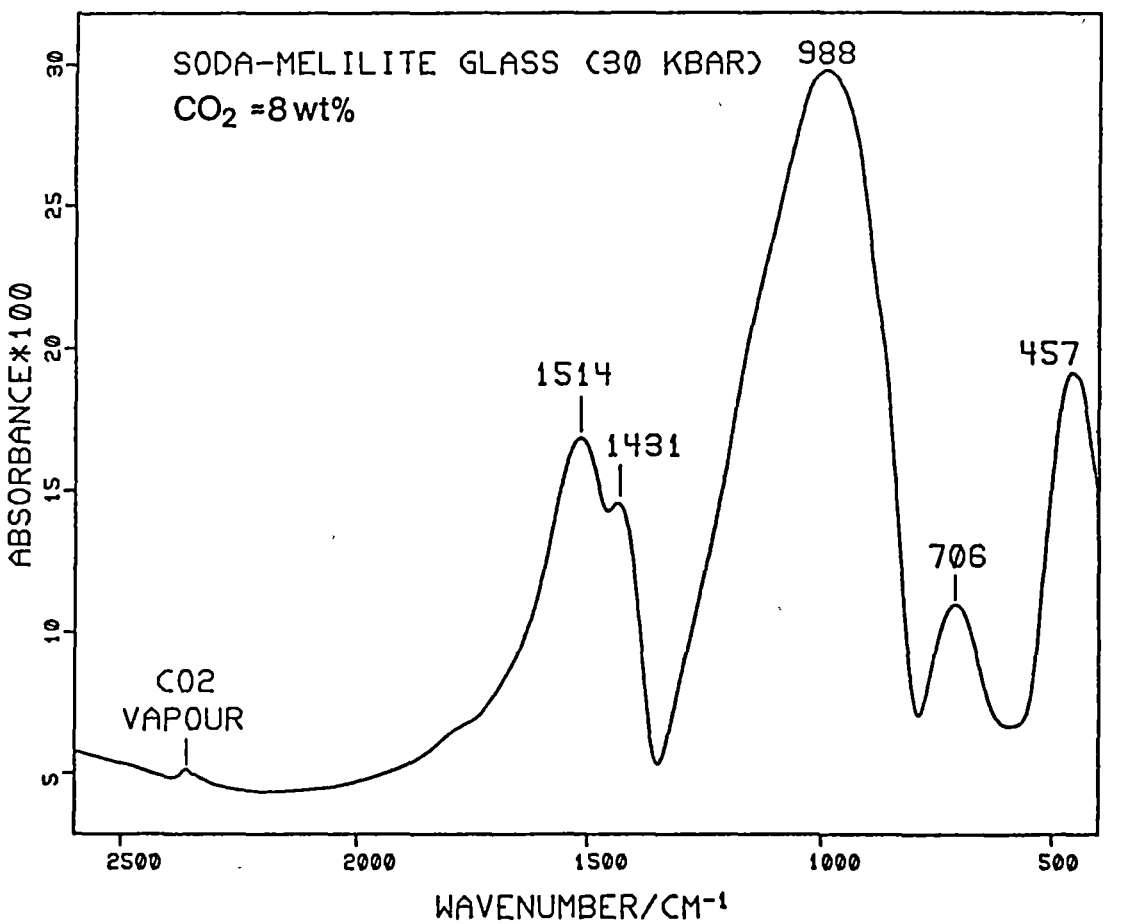
SODA-MELILITE GLASS (30 KBAR)
CO_2 ≈8 wt%
988
457
1514
1431
706
CO2
VAPOUR
ABSORBANCE*100
WAVENUMBER/CM^{-1}

for Sm + CO_2 at 20 kbar in the Raman spectroscopic investigation of Sharma (1979). A third absorption at 1278 cm^{-1} is present as a shoulder in Ne + CO_2 glass, this band is absent from volatile-free Ne glass and is presumably also a ν_3 band. Appearance of a prominent band at ~570 cm^{-1} accompanies CO_2 dissolution in Ne melt. There is no evidence in either spectrum for the presence of dissolved molecular CO_2; small fluctuations in atmospheric CO_2 in the instrument lead to weak positive or negative bands near 2350 cm^{-1}. The following positive features were recorded from the mid-IR difference spectra (volatile-bearing minus volatile-absent glass spectra):

Sm + CO_2	Ne + CO_2	Tentative Assignment
1524 s	1614 s	$\nu_3[CO_3^{2-}]$
1437 s	1402 s	
	1278 w	
1172 m	1138 m	ν[Si-O-Si]?
1022 m	1011 m	
977 m		
857 w	853 w	$\nu_2[CO_3^{2-}]$
769 m	768 m	$[AlO_4]_n$ clusters?
~690 sh	~700 sh	ν_4 $[CO_3^{2-}]$
~630 sh	~610 sh	?
564 s	540 s	$\nu[AlO_6]$

Both the ν_2 and ν_4 carbonate absorptions can be recognised although the bands are broad and reveal no fine structure. The most prominent change below 1200 cm^{-1} occurs in both Ne and Sm CO_2-bearing glasses and is due to appearance of a strong band at ~560-540 cm^{-1} assignable to Al in six-fold co-ordination (see Sections 4.6 and A13.4). This together with a band at ~770 cm^{-1}, possibly due to AlO_4 clusters, indicates that CO_2 dissolution, like that of H_2O, results in a redistribution of Al co-ordination environments in aluminosilicate melts. This view is consistent with Raman spectroscopic interpretations of the CO_2 solubility mechanism in feldspar composition glasses (Mysen & Virgo, 1980c).

The $\nu_3(CO_3^{2-})$ band: symmetry splitting, non-equivalent sites or both?

As discussed in Appendix 13.5 splitting of the ν_3 band may arise from a lowering of site or molecular symmetry of the carbonate anion. Apparent splitting can arise from the presence of non-equivalent carbonate sites. Conceivably, splitting due to both symmetry effects and non-equivalent sites may occur together and it may be difficult to distinguish the two. This is likely to be particularly so in broad line-width glass-phase spectra. As a general rule, however, it is proposed here that very large splittings of say ~200 cm^{-1}, as found in Ne + CO_2 glass, are most probably due to symmetry effects. This is illustrated in the mid-range spectra of dawsonite and shortite (Figs 15C and E).

In dawsonite, the CO_3^{2-} anion is bound by two of its oxygen atoms (O2,2') to metal cations, the remaining oxygen (O1) is the acceptor of two symmetrical hydrogen bonds. As a result, the O1-C bond is some 0.058Å shorter than the other two (Corazza et al., 1977). This gives rise to a large symmetry splitting (174 cm^{-1}) of the ν_3 band (labelled (B) in Fig. 15C) of similar magnitude to that observed in CO_2-bearing Ne glass.

In shortite two non-equivalent carbonate sites: C1 and C2, are present. They arise from two distinct Na,Ca-carbonate bonding topologies (Dickens et al., 1971). In addition, unequal C-O bond lengths (a difference of 0.013Å in C1 and 0.033Å in C2) and a slight non-planarity in C1 (0.012Å out of plane) result in symmetry splittings of the IR bands. Thus the ν_3 and ν_4 modes (labelled (B) and (E) in Fig. 15E) are split into four bands and the ν_1 and ν_2 modes are split into two bands. The frequency spread of ν_3 bands is some 113 cm^{-1}. On the basis of C-O bond distances the 1522, 1453 cm^{-1} pair and the 1481, 1409 cm^{-1} pair can probably be associated with C1 and C2 respectively. This suggests that symmetry splittings in shortite are ~70 cm^{-1} while non-equivalent site "splitting" probably amounts to half this value or less (taking mean band positions).

While it may not be strictly valid to extrapolate from crystalline compounds to glasses, the large ν_3 splittings observed in Ne and Sm CO_2-bearing glasses (211 cm^{-1} and 83 cm^{-1} respectively) combined with the overall broad similarity between Ne + CO_2 and dawsonite and Sm + CO_2 and shortite ν_3 bands is consistent with symmetry splitting being the primary cause of the visually resolvable ~1600-1300 cm^{-1} ν_3 features in the glass spectra. Because of poor band resolution, the existence of non-equivalent CO_3^{2-} sites cannot be decided with certainty from the IR spectra. The

Figs 15C & 15D Mid-IR and far-IR spectra of dawsonite, $NaAl(OH)_2(CO_3)$. Carbonate Bands: (A) combination and overtone bands; (B) ν_3; (C) ν_1; (D) ν_2; (E) ν_4.

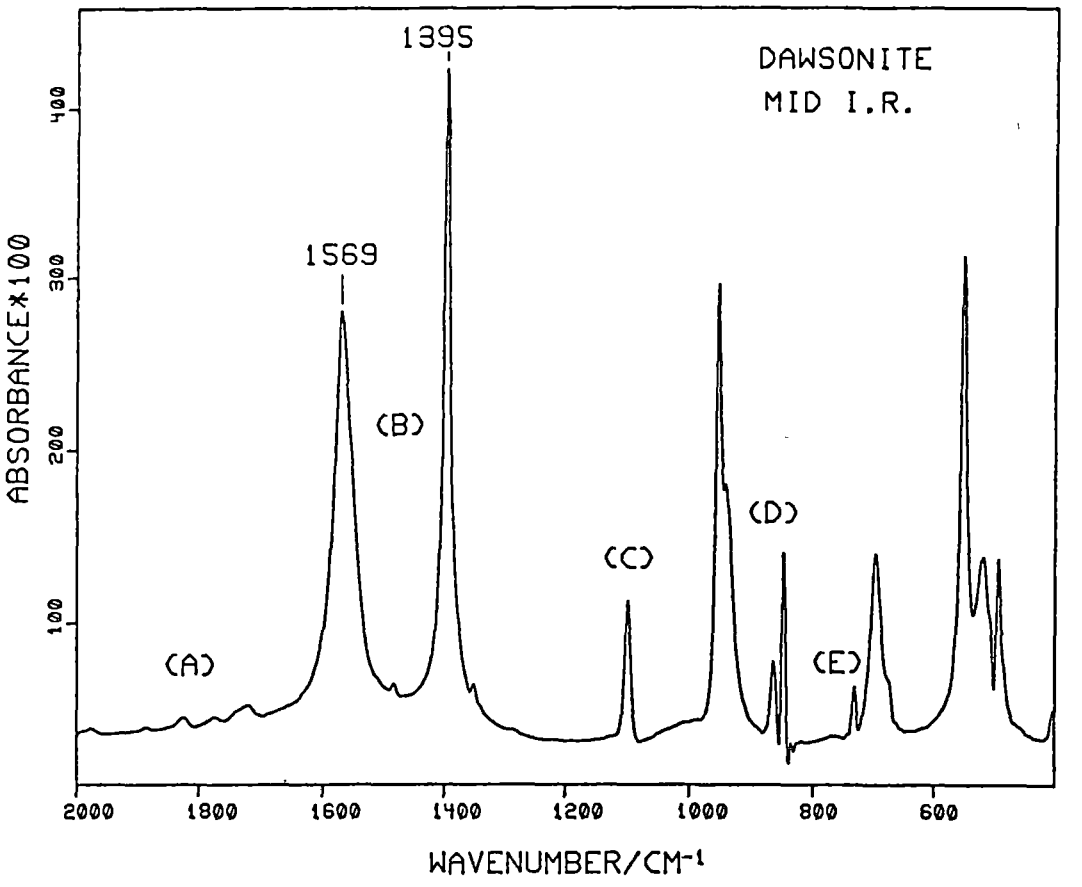
DAWSONITE
MID I.R.
1395
1569
(A)
(B)
(C)
(D)
(E)
ABSORBANCE*100
100
200
300
400
2000
1800
1600
1400
1200
1000
800
600
WAVENUMBER/CM-1

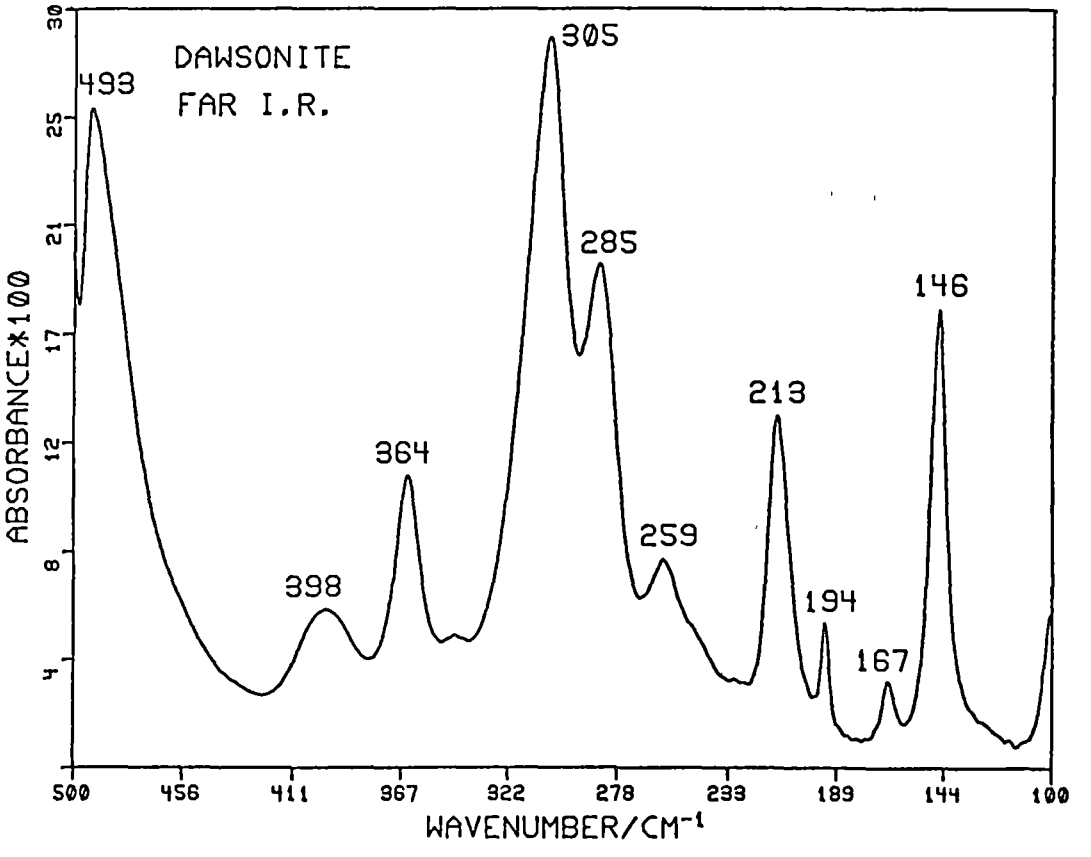
DAWSONITE
FAR I.R.
493
398
364
305
285
259
213
194
167
146
ABSORBANCE*100
4
8
12
17
21
25
30
500
456
411
367
322
278
233
189
144
100
WAVENUMBER/CM-1

Figs 15E & 15F Mid-IR and far-IR spectra of shortite, $Na_2Ca_2(CO_3)_3$. Carbonate bands: (A) combination and overtone bands; (B) ν_3; (C) ν_1; (D) ν_2; (E) ν_4.

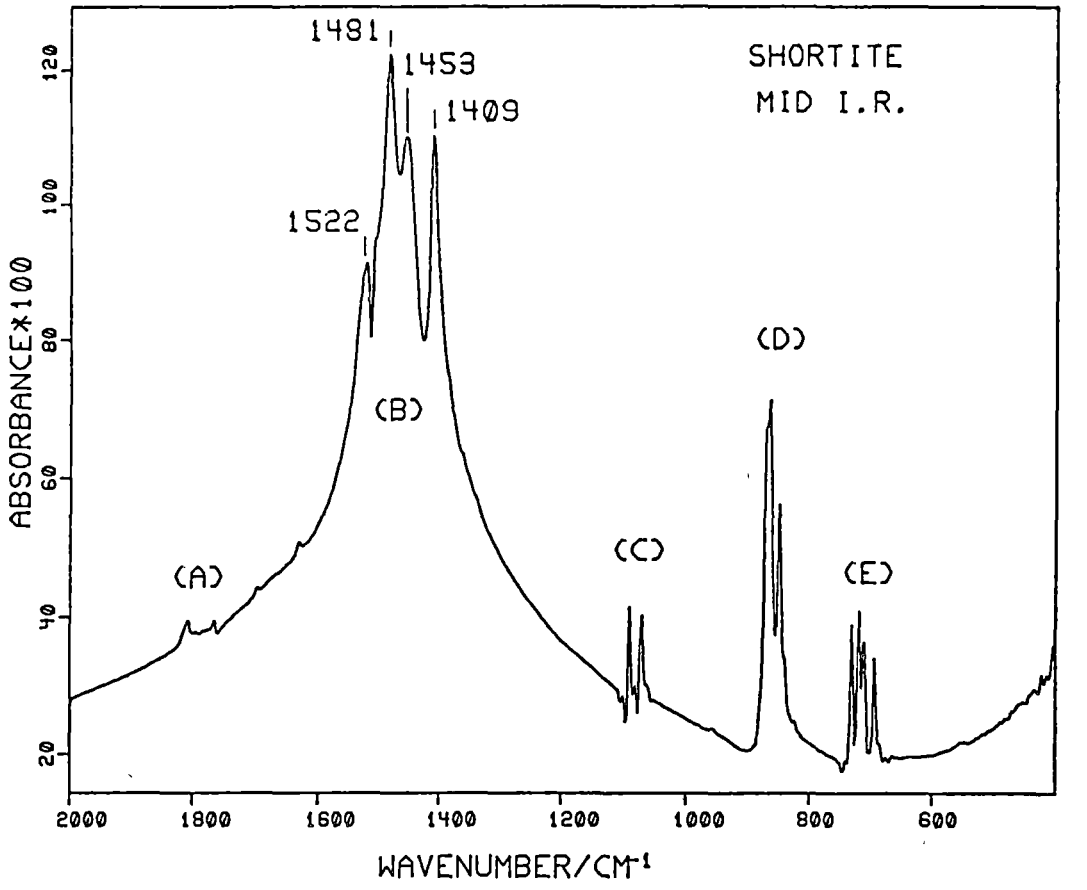
SHORTITE
MID I.R.
1481
1453
1409
1522
(A)
(B)
(C)
(D)
(E)
ABSORBANCE*100
120
100
80
60
40
20
2000
1800
1600
1400
1200
1000
800
600
WAVENUMBER/CM-1

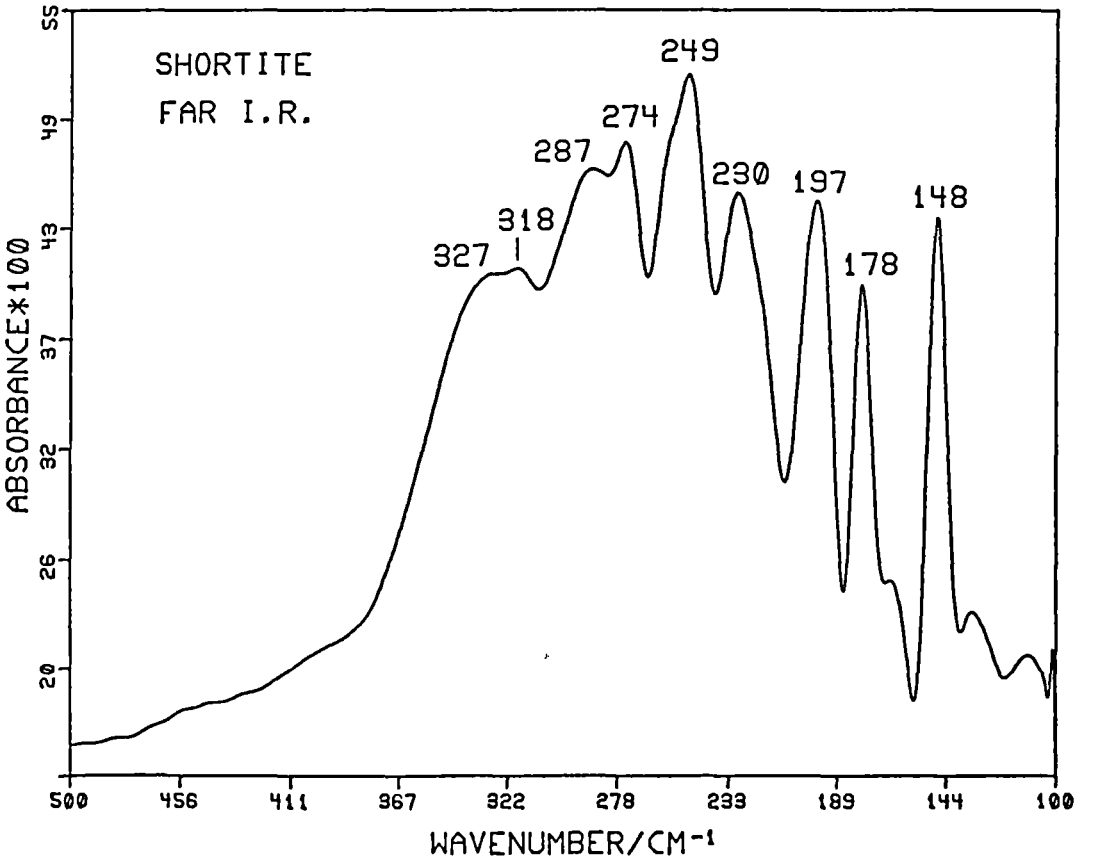
SHORTITE
FAR I.R.
249
274
287
230
197
148
178
318
327
ABSORBANCE*100
55
49
43
37
32
26
20
500
456
411
367
322
278
233
189
144
100
WAVENUMBER/CM-1

presence of a third ν_3 band in Ne + CO_2 at 1278 cm^{-1} does indicate, however, that more than one carbonate site may be present (the higher frequency band of the doublet is presumably masked under the 1398 cm^{-1} band).

The suggestion that symmetry splitting is the primary cause of ν_3 band shape differs from the view of Sharma & Simons (1980) who interpreted ν_3 splitting in CO_2-bearing Sm, Ak and Di glasses as due to the presence of non-equivalent CO_3^{2-} sites. While the presence of more than one ν_1 or ν_2 band is proof for the existence of non-equivalent CO_3^{2-} sites, the same cannot be said for the doubly degenerate ν_3 band. It is suggested here that (i) large ν_3 band splittings observed in the IR and Raman spectra of carbonate glasses and carbonate-bearing aluminosilicate glasses reflect CO_3^{2-} site-symmetry effects and (ii) that smaller apparent splittings arise from the presence of more than one carbonate site and are probably masked by broad band-widths of glass-phase spectra.

Evidence for metallocarbonate complex formation

Symmetry splittings of the ν_3 (CO_3^{2-}) band could conceivably arise by interactions between carbonate anions and the silicate network (as proposed by Sharma, 1979) or by metal cation-carbonate bonding interactions in metallocarbonate complexes (as proposed by Mysen & Virgo, 1980a, 1980c). Sharma & Simons (1980) rejected the latter idea on the grounds that bands due to cation-carbonate bonding could not be distinguished in the low frequency Raman spectra of carbonate-containing glasses.

To investigate the nature of cation-carbonate bonding, far-IR spectra (500-100 cm^{-1}) of CO_2-bearing Ne and Sm glasses (Figs 15G & 15H) were recorded. Rao & Elliot (1981) have shown that absorptions bands characteristics of "in-cage" vibrational motions of cations situated in oxygen co-ordination polyhedra appear in the far-IR spectra of oxide or anion containing glasses (e.g. silicate or carbonate). In crystalline solids, far-IR bands of a more delocalised nature (lattice vibrations) become important. These typically involve translation motions of metal cations relative to anions and may give rise to quite complex spectra as seen for shortite and dawsonite (Figs 15D & 15F). Sum and difference modes (combination bands) may also be of importance in the far-IR (Angino, 1967).

Far-IR spectra and difference spectra (carbonate-bearing glass spectrum minus volatile-free glass spectrum) reveal the presence of

Figs 15G and 15H Far-IR difference spectra of nepheline and sodamelilite glasses (CO_2-bearing minus volatile-absent spectra).

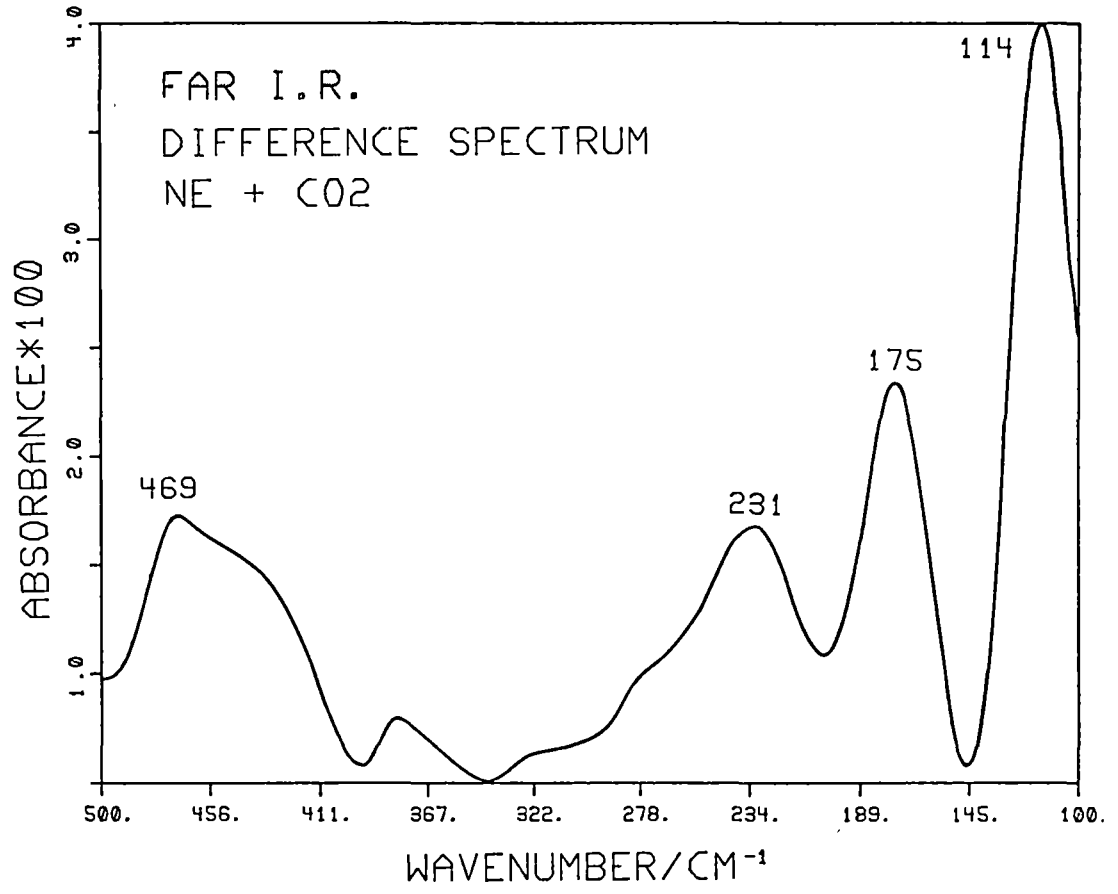
FAR I.R.
DIFFERENCE SPECTRUM
NE + CO2
114
175
231
469
ABSORBANCE*100
4.0
3.0
2.0
1.0
500.
456.
411.
367.
322.
278.
234.
189.
145.
100.
WAVENUMBER/CM-1

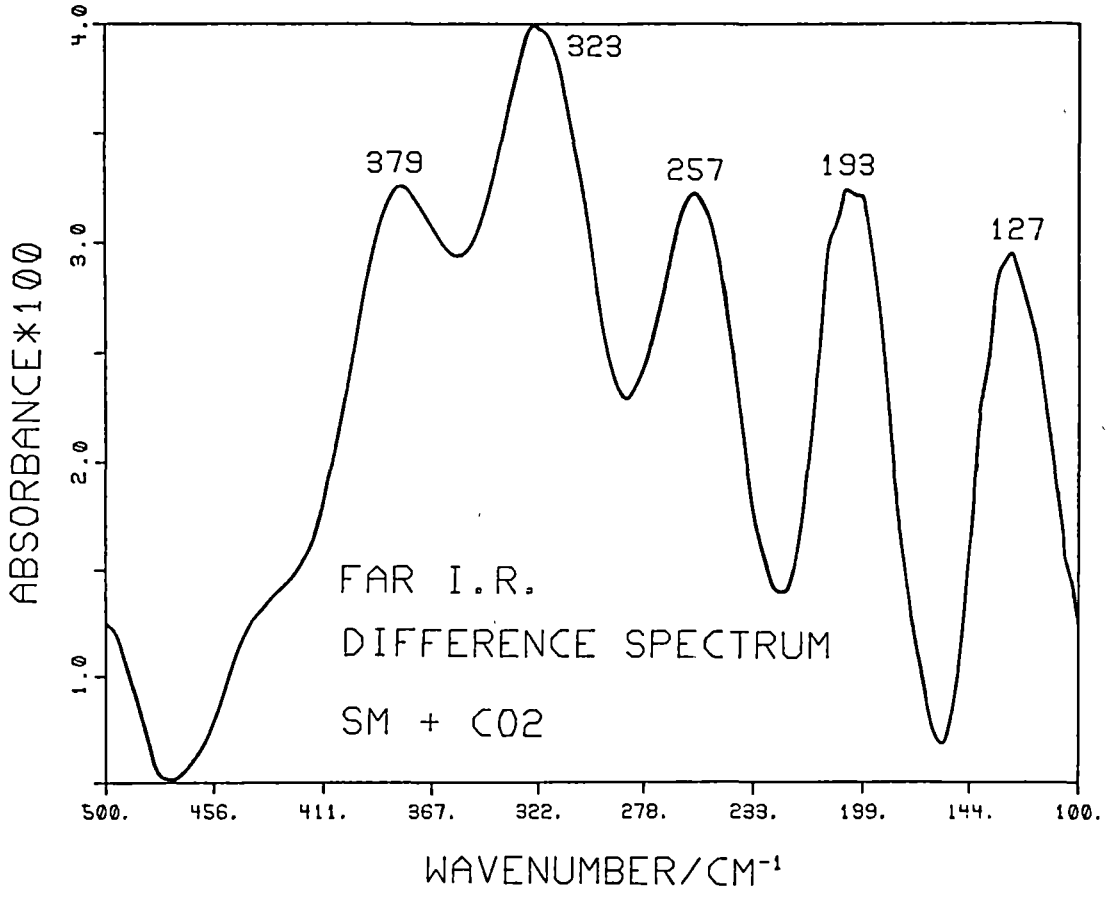
323
379
257
193
127
FAR I.R.
DIFFERENCE SPECTRUM
SM + CO2
ABSORBANCE*100
4.0
3.0
2.0
1.0
500.
456.
411.
367.
322.
278.
233.
189.
144.
100.
WAVENUMBER/CM-1

multiple absorption bands in both Ne and Sm CO_2-bearing glasses. For both glasses, three bands occur below 280 cm^{-1} and for Sm + CO_2, two bands occur between 380 and 280 cm^{-1} (Figs 15G & 15H).

These results confirm the existence of cation-carbonate bonding in CO_2-bearing glasses and provide direct evidence for the presence of metallocarbonate complexes. In CO_2-bearing Ne glass a wide range of sodium carbonate complexes can be proposed, i.e. $NaCO_3^-$, $Na_2CO_3^o$, $Na_3CO_3^+$ with Ne in unidentate and/or bidentate co-ordination. The presence of at least two of these possible complexes is required to explain the mid-IR spectra.

The far-IR difference spectrum of Sm + CO_2 has more bands than Ne + CO_2 presumably arising from the presence of both Ca-O and Na-O bonding associated with a mixed Ca-Na-carbonate complex. Such a bonding arrangement is present in shortite which has a superficially similar far-IR spectrum (Fig. 15F). It is possible that more than one carbonate complex is present in Sm + CO_2 glass giving rise to non-equivalent sites. However, good evidence for this (e.g. in ν_1 or ν_2 band splittings in the Raman spectrum) has not been obtained to date.

The results of the above mid-IR and far-IR investigations may be summarised by the following equations describing the dominant CO_2 solubility mechanism in Ne and Sm melts at pressure:
(a) nepheline melt (NBO/T = 0)

$$2[NaAl^{IV}SiO_4] + CO_2 = [Na_2CO_3]^o + 2[Al^{VI}O_{1.5}]^o + 2[SiO_2]^o$$

(assuming $Na_2CO_3^o$ is the dominant metallocarbonate complex).
(b) sodamelilite melt (NBO/T = 0.67)

$$NaCaAl^{IV}Si_2O_7 + CO_2 = [NaCaCO_3]^+ + [Al^{VI}O_2]^- + 2[SiO_2]^o$$

(assuming $NaCaCO_3^+$ is the dominant metallocarbonate complex).
In both cases, loss of charge compensating alkali cations from the network via metallocarbonate complex formation, results in a rearrangement of Al^{3+} co-ordination environments accompanying Al expulsion from the network.

REFERENCES

Alder, H.H. & Kerr, P.F., 1963. Infrared spectra, symmetry and structure relations of some carbonate minerals. Am. Min. 48: 839-853.

Allegre, C.J., Staudacher, T., Sarda, P. & Kurz, M., 1983. Constraints on evolution of Earth's mantle from rare gas systematics. Nature 303: 762-766.

Andersen, T., O'Reilly, S.Y. & Griffin, W.L., 1984. The trapped fluid phase in upper mantle xenoliths from Victoria, Australia: implications for mantle metasomatism. Contrib. Min. Petrol. 88: 72-85.

Anderson, A.T., 1975. Some basaltic and andesitic gases. Rev. Geophys. Space Phys. 13: 37-55.

Anderson, D.L., 1975. Chemical plumes in the mantle. Geol. Soc. Am. Bull. 86: 1593-1600.

Anderson, O.L., 1979. The role of fracture dynamics in kimberlite pipe formation. Proc. 2nd Int. Kimberlite Conf., Vol.1: 344-353.

Angell, C.A., Cheeseman, P.A. & Tamaddon, S., 1982. Tetrahedrally coordinated ionic liquids - anomalous transport properties and geophysical significance. In K-H. Bennemann, F. Brouers & D. Guitmann (Eds): IONIC LIQUIDS, MOLTEN SALTS AND POLYELECTROLYTES, Conf. Proc. Springer-Verlag, Berlin: 131-135.

Angino, E.F., 1967. Far infrared (500-30 cm^{-1}) spectra of some carbonate minerals. Am. Min. 52: 137-147.

Angus, S., Armstrong, B. & De Reuck, K.M., 1978. IUPAC INTERNATIONAL TABLES OF THE FLUID STATE, VOL.5: METHANE. Pergamon Press.

Arculus, R.J. & Delano, J.W., 1981a. Intrinsic oxygen fugacity measurements: techniques and results for spinels from upper mantle peridotites and megacryst assemblages. Geochim. Cosmochim. Acta 45: 899-913.

Arculus, R.J. & Delano, J.W., 1981b. Siderophile element abundances in the upper mantle: evidence for a sulfide signature and equilibrium with the core. Geochim. Cosmochim. Acta 45: 1331-1343.

Arculus, R.J. & Gust, D.A., 1981. The intrinsic oxygen fugacity of peridotites from Itinomegata, Japan, and megacryst ilmenite from the alnoitic breccia of Malaita, Solomon Islands. Res. Sch. Earth Sci., Aust. Natl Univ., Ann. Rep.: 132-135.

Arculus, R.J., 1982. Redox state evidence for the xenocryst status of diamond in kimberlite. Res. Sch. Earth Sci., Aust. Natl Univ., Ann. Rep.: 179-181.

Arculus, R.J., Dawson, J.B., Mitchell, R.H., Gust, D.A. & Holmes, R.D., 1984. Oxidation state of the upper mantle recorded by megacryst ilmenite in kimberlite and type A and B spinel lherzolite. Contrib. Min. Petrol. 85: 85-94.

Bartholomew, R.F. & Schreurs, J.W.H., 1980. Wide-line NMR study of the protons in hydrosilicate glasses of different water content. J. Non-Cryst. Solids 39: 679-684.

Bartholomew, R.F., Butler, B.L., Hoover, H.L. & Wu, C.K., 1980. Infrared spectra of a water-containing glass. J. Am Ceram. Soc. 63: 481-485.

Bartholomew, R.F., 1983. High-water containing glasses. J. Non-Cryst. Solids 56: 331-342.

Baross, J.A., Lilley, M.D. & Gordon, L.I., 1982. Is the CH_4, H_2 and CO venting from submarine hydrothermal systems produced by thermophilic bacteria? Nature 298: 366-368.

Basaltic Volcanism Study Project, 1981. BASALTIC VOLCANISM ON THE TERRESTRIAL PLANETS. Pergamon Press: 1286 pp.

Bates, J.B., Hendricks, R.W. & Shaffer, L.B., 1974. Neutron irradiation effects and structure of noncrystalline SiO_2. J. Chem. Phys. 61: 4163-4176.

Bauer, J., Fiala, J. & Hrichova, R., 1963. Natural alpha-silicon carbide. Am. Min. 48: 620-634.

Bell, P.M., 1964. High-pressure melting relations for jadeite composition. Rep. Geophys. Lab., Carnegie Inst. Ybk 63: 171-174.

Bell, P.M., 1983. Methane: mantle depths to crust. EOS Trans., Am. Geophys. Union, 64: 9.

Bell, R.J. & Dean, P., 1972. Localization of phonons in vitreous silica and related glasses. In R.W. Douglas & B. Ellis (Eds): PROC. 3rd INT. CONF. ON PHYSICS OF NON-CRYSTALLINE SOLIDS. Wiley-Interscience: 443-452.

Bergman, S.C. & Dubessy, J., 1984. CO_2-CO fluid inclusions in a composite peridotite xenolith: implications for upper mantle oxygen fugacity. Contrib. Min. Petrol. 85: 1-13.

Bibby, D.M., 1982. Impurities in natural diamond. Chem. Phys. Carbon 18: 1-91.

Birch, F., 1966. Compressibility; elastic constants. Geol. Soc. Am. Memoir 97: 97-173.

Bohlen, S.R., Boettcher, A.L. & Wall, V.J., 1982. The system albite-H_2O-CO_2: a model for melting and activities of water at high pressures. Am. Min. 67: 451-462.

Boettcher, A.L., Burnham, C.W., Windom, K.E. & Bohlen, S.R., 1982. Liquids, glasses and the melting of silicates to high pressures. Jour. Geol. 90: 127-138.

Borgianni, C. & Granati, P., 1979. Monte Carlo calculations of ionic structure in silicate and alumino-silicate melts. AIME Metall. Trans. 10B: 21-25.

Bottinga, Y. & Richet, P., 1981. High pressure and temperature equation of state and calculation of the thermodynamic properties of gaseous carbon dioxide. Am. J. Sci. 281: 615-660.

Bottinga, Y., Weill, D.F. & Richet, P., 1981. Thermodynamic modeling of silicate melts. Adv. Phys. Geochem. 1: 207-245.

Boyd, F.R., 1962. Phase equilibria in silicate systems at high pressures and temperatures. In R.H. Wentorf (Ed.): MODERN VERY HIGH PRESSURE TECHNIQUES. Butterworths, London: 151-162.

Boyd, F.R. & Finnerty, A.A., 1980. Condition of origin of natural diamonds of peridotite affinity. J. Geophys. Res. 85B: 6911-6918.

Boyd, F.R. & Gurney, J.J., 1982. Low-calcium garnets: keys to craton structure and diamond crystallization. Rep. Geophys. Lab., Carnegie Inst. Ybk 81: 261-267.

Brawer,S., 1975. Theory of the vibrational spectra of some network nd molecular glasses. Phys. Rev. B 11: 3173-3194.

Brawer, S.A. & White, W.B., 1974. Raman soectroscopic investigation of the structure of silicate glasses I. The binary alkali silicates. J. Chem. Phys. 63: 2421-2432.

Brett, R., 1984. Chemical equilibrium of the Earth's core and upper mantle. Geochim. Cosmochim. Acta 48: 1183-1188.

Brett, R. & Sato, M., 1984. Intrinsic oxygen fugacity measurements on seven chondrites, a pallasite, and a tektite and the redox state of meteorite parent bodies. Geochim. Cosmochim. Acta 48: 111-120.

Brey, G., 1976. CO_2 solubility and solubility mechanisms in silicate melts at high pressures. Contrib. Min. Petrol. 57: 215-221.

Brey, G.P. & Green, D.H., 1976a. Solubility of CO_2 in olivine melilitite at high pressures and role of CO_2 in the Earth's upper mantle. Contrib. Min. Petrol. 55: 217-230.

Brey, G.P. & Green, D.H., 1976b. Reply to Eggler and Mysen. Contrib. Min. Petrol. 55: 237-239.

Brow, R.K. & Pantano, C.G., 1984. Nitrogen co-ordination in oxynitride glasses. J. Am. Ceram. Soc. (Comm.) 67: C72-C74.

Brown,T.H., 1977. Introduction to non-ideal and complex solutions. Min. Assoc. Canada Short Course Handbk 2: 126-135.

Burnham, C.W., 1975. Water and magmas, a mixing model. Geochim. Cosmochim. Acta 39: 1077-1084.

Burnham, C.W., 1979. The importance of volatile constituents. In H.S. Yoder (Ed.): THE EVOLUTION OF THE IGNEOUS ROCKS, 50th Ann. Perspectives. Princeton Univ. Press: 439-482.

Burnham, C.W. & Davis, N.F., 1974. The role of H_2O in silicate melts: II. Thermodynamic and phase relations in the system $NaAlSi_3O_8$-H_2O to 10 kilobars, 700°C to 1100°C. Am. J. Sci., 274: 902-940.

Burnham, C.W., Holloway, J.R. & Davis, N.F., 1969a. The specific volume of water in the range 1000 to 8900 bars, 20° to 900°C. Am. J. Sci. 267A: 70-95.

Burnham, C.W., Holloway, J.R. & Davis, N.F., 1969b. Thermodynamic properties of water to 1000°C and 10,000 bars. Geol. Soc. Am., Spec. Paper 132.

Byers, C.D., Muenow, D.W. & Garcia, M.O., 1983. Volatiles in basalts and andesites from the Galapagos Spreading Center, 85° to 86°W. Geochim. Cosmochim. Acta 47: 1551-1558.

Carnahan, N.F. & Starling, K.E., 1969. Equation of state for non attracting rigid spheres. J. Chem. Phys. 51: 635-636.

Chen, C-H. & Presnall, D.C., 1975. The system Mg_2SiO_4-SiO_2 at pressures up to 25 kilobars. Am. Min. 60: 398-406.

Ching, W.Y., 1982. Theory of amorphous SiO_2 and SiO_x. I. Atomic structural models. Phys. Rev. B 26: 6610-6621.

Chou, I-M. & Williams, R.J., 1979. The activity of H_2O in supercritical fluids: H_2O-CO_2 at 600°C and 700°C at elevated pressures. Lunar Planet. Sci. (Abstracts) 10: 201-203.

Chrenko, R.M., McDonald, R.S. & Darrow, K.A., 1967. Infra-red spectra of diamond coat. Nature 213: 474-476.

Chueh,P.L. & Prausnitz, J.M., 1967. Vapor-liquid equilibria at high pressures. Vapor-phase fugacity coefficients in nonpolar and quantum-gas mixtures. Ind. Eng. Chem. Fundam. 6: 492-498.

Clark, S.P. & Ringwood, A.E., 1964. Density distribution and constitution of the mantle. Rev. Geophys. 2: 35-88.

Claypool, G.E. & Kvenvolden, K.A., 1983. Methane and other hydrocarbon gases in marine sediment. Ann. Rev. Earth Planet. Sci. 11: 299-327.

Clayton, R.N., Mayeda, T.K. & Rubin, A.E., 1984. Oxygen isotopic compositions of enstatite chondrites and aubrites. J. Geophys. Res. 89: C245-C249.

Corazza, E., Sabelli, C. & Vannucci, S., 1977. Dawsonite: new mineralogical data and structure refinement. Neues Jb. Miner. Mon. 9: 381-397.

Darken, L.S. & Gurry, R.W., 1945. The system iron-oxygen: I. The wustite field and related equilibria. J. Am. Chem. Soc. 67: 1398-1412.

Dawson, J.B., 1980. KIMBERLITES AND THEIR XENOLITHS. MINERALS AND ROCKS,VOL. 15. Springer-Verlag, Berlin: 252 pp.

Day, D.E. & Rindone, G.E., 1962. Properties of soda alumino-silicate glasses, III. Co-ordination of aluminium ions. J. Am. Ceram. Soc. 45: 579-581.

Deines, P., 1980. The carbon isotopic composition of diamonds: relationship to diamond shape, color, occurrence and vapor composition. Geochim. Cosmochim. Acta 44: 943-961.

Deines, P., 1984. Evidence for a systematic depletion in ^{13}C in parts of the mantle underlying the Orapa, Botawana, kimberlite. GSA Abstracts with Programs 16: 485.

De Jong, B.H.W.S. & Brown, G.E., 1980a. Polymerisation of silicate and aluminate tetrahedra in glasses, melts, and aqueous solutions - I. Electronic structure of $H_6Si_2O_7$, $H_6SiAlO_7^-$ and $H_6Al_2O_7^{2-}$. Geochim. Cosmochim. Acta 44: 491-511.

De Jong, B.H.W.S. & Brown, G.E., 1980b. Polymersiation of silicate and aluminate tetrahedra in glasses, melts and aqueous solutions - II. The network modifying effects of Mg^{2+}, K^+, Na^+, Li^+, H^+, OH^-, F^-, Cl^-, H_2O, CO_2 and H_3O^+ on silicate polymers. Geochim. Cosmochim. Acta 44: 1627-1642.

De Jong, B.H.W.S., Keefer, K.D., Brown, G.E. & Taylor, C.M., 1981. Polymerisation of silicate and aluminate tetrahedra in glasses, melts and aqueous solutions - III. Local silicon environments and internal nucleation in silicate glasses. Geochim. Cosmochim. Acta 45: 1291-1308.

De Jong, B.H.W.S., Schramm, C.M. & Parziale, V.E., 1983. Polymersiation of silicate and aluminate tetrahedra in glasses, melts and aqueous solutions - IV. Aluminium co-ordination in glasses and aqueous solutions and comments on the aluminium avoidance principle. Geochem. Cosmochim. Acta 47: 1223-1236.

Delany, J.M. & Helgeson, H.C., 1978. Calculation of the thermodynamic consequences of dehydration in subducting oceanic crust to 100 kb and >800°C. Am. J. Sci. 278: 638-686.

De Santis, R., Breedveld, G.L.F. & Prausnitz, J.M., 1974. Thermodynamic properties of aqueous gas mixtures at advanced pressures. Ind. Eng. Chem. Proc. Des. Dev. 13: 374-377.

Des Marais, D.J. & Moore, J.G., 1984. Carbon and its isotopes in mid-oceanic basaltic glasses. Earth Planet. Sci. Lett. 69: 43-57.

Dickens, B., Hyman, A. & Brown, W.E., 1971. Crystal structure of $Ca_2Na_2(CO_3)_3$ (shortite). Nat. Bur. Stds J. Res. 75A: 129-134.

Domine, F. & Piriou, B., 1983. Study of sodium silicate melt and glass by infra-red reflectance spectroscopy. J. Non-Cryst. Solids 55: 125-130.

Douslin, D.R. & Harrison, R.H., 1973. Pressure, volume, temperature relations of ethane. J. Chem. Thermodyn. 5: 491-512.

Duba, A.G. & Shankland, T.J., 1982. Free carbon and electrical conductivity in the Earth's mantle. Geophys. Res. Lett. 9: 1271-1274.

Dupree, E. & Pettifer, R.F., 1984. Determination of the Si-O-Si bond angle distribution in vitreous silica by magic angle spinning NMR. Nature 308: 523-525.

Dzialoszynski, L., Fabries J-F., Renon, H. & Thiebault, D., 1980. Comparison of analytical representations of thermodynamic properties of methane, ethane and ammonia. Ind. Eng. Chem. Fundam. 19: 329-337.

Dziewonski, A.M. & Anderson, D.L., 1981. Preliminary reference Earth model. Phys. Earth Planet. Int. 25: 297-356.

Eggler, D.H., 1974. Effect of CO_2 on the melting of peridotite. Rep. Geophys. Lab., Carnegie Inst. Ybk 73: 215-224.

Eggler, D.H., 1978. The effect of CO_2 upon partial melting of peridotite in the system Na_2O-CaO-Al_2O_3-MgO-SiO_2-CO_2 to 35 kb, with an analysis of melting in a peridotite-H_2O-CO_2 system. Am. J. Sci. 278: 305-343.

Eggler, D.H., 1983. Upper mantle oxidation state: evidence from olivine-orthopyroxene-ilmenite assemblages. Geophys. Res. Lett. 10: 365-368.

Eggler, D.H. & Baker, D.R., 1982. Reduced volatiles in the system C-O-H: Implications to mantle melting, fluid formation and diamond genesis. In S. Akimoto & M.H. Manghnani (Eds): HIGH PRESSURE RESEARCH IN GEOPHYSICS. Center for Acad. Publ., Tokyo: 237-250.

Eggler, D.H. & Burnham, C.W., 1984. Solution of H_2O in diopside melts: a thermodynamic model. Contrib. Min. Petrol. 85: 58-66.

Eggler, D.H. & Kadik, A.A., 1979. The system $NaAlSi_3O_8$-H_2O-CO_2 to 20 kbar pressure: I. Compositional and thermodynamic relations of liquids and vapors coexisting with albite. Am. Min. 64: 1036-1048.

Eggler, D.H., Mysen, B.O., Hoering, T.C. & Holloway, J.R., 1979. The solubility of carbon monoxide in silicate melts at high pressures and its effect on silicate phase relations. Earth Planet. Sci. Lett. 43: 321-330.

Eggler, D.H., Baker, D.R. & Wendlandt, R.F., 1980. fO_2 of the assemblage graphite-enstatite-forsterite-magnesite: experiment and application to mantle fO_2 and diamond formation. GSA Abstracts with Programs 12: 420.

Elliott, W.C., Grandstaff, D.E., Ulmer, G.C., Buntin, T. & Gold, D.P., 1982. An intrinsic oxygen fugacity study of platinum-carbon associations in layered intrusions. Econ. Geol. 77: 1493-1510.

Engelhardt, G., Zeigan, D., Jancke, H. & Hoebbel, D., 1975. Zur abhanigkeit der Struktur der Silicatanionen in Wassrigen Natrium-silicatlosungen vom Na:Si Verhaltnis. Z. Anorg. Allg. Chem. 418: 17-28.

Etchepare, J., 1969. Interpretation des spectres de diffusion Raman de verres de silice binaires. Spectrochim. Acta 26A: 2147-2154.

Etchepare, J., 1972. Study by Raman spectroscopy of crystalline and glassy diopside. In R.W. Douglas & B. Ellis (Eds): AMORPHOUS MATERIALS. John Wiley & Sons: 337-346.

Eugster, H.P. & Skippen, G.B., 1967. Igneous and metamorphic reactions involving gas equilibria. In P.H. Abelson (Ed.): RESEARCHES IN GEOCHEMISTRY, Vol.2. John Wiley & Sons: 492-520.

Farmer, V.C., Fraser, A.R. & Tait, J.M., 1979. Characterisation of the chemical structures of natural and synthetic aluminosilicate gels and sols by infrared spectroscopy. Geochim. Cosmochim. Acta 43: 1417-1420.

Ferraro, J.R. & Manghnani, M.H., 1972. Infrared absorption spectra of sodium silicate glasses at high pressure. J. Appl. Phys. 43: 4595-4599.

Fesq, H.W., Bibby, D.M., Erasmus, C.S., Kable, E.J.D. & Sellschop, J.P.F., 1975. A comparative trace element study of diamonds from Premier, Finsch and Jagersfontein mines, South Africa. Phys. Chem. Earth 9: 817-836.

Field, J.E., 1979. Strength and fracture properties of diamond. In J.E. Field (Ed.): THE PROPERTIES OF DIAMOND. Academic Press: 281-324.

Florinskaya, V.A. & Pechenkina, R.S., 1963. Infrared spectra of crystalline and glassy silicates of the Na_2O-SiO_2 system in the region up to 25 microns. Zh. Strukt. Khim. 4: 850-860.

Flowers, G.C., 1979. Correction of Holloway's (1977) adaptation of the modified Redlich-Kwong equation of state for calculation of the fugacities of molecular species in supercritical fluids of geologic interest. Contrib. Min. Petrol. 69: 315-318.

Foster, L.M., Long, G. & Hunter, M.S., 1956. Reactions between aluminium oxide and carbon: the Al_2O_3-Al_4C_3 phase diagram. J. Am. Ceram. Soc. 39: 1-11.

Francesconi, A.Z., 1984. Values of (p,V_m,T) for methane in the range 15 to 270 MPa and 323 to 723 K. J. Chem. Thermodyn. 16: 189-194.

Frantsesson, E.V., 1970. THE PETROLOGY OF THE KIMBERLITES. Translated from the Russian by D.A. Brown. Dept of Geology, Aust. Natl Univ., Canberra: 194 pp.

Fraser, D.G., 1977. Thermodynamic properties of silicate melts. In D.G. Fraser (Ed.): THERMODYNAMICS IN GEOLOGY. D. Reidel Publishing Co.: 301-325.

Fredericks, P.M., Osborn, P.R. & Swinkels, D.A.J., 1983. Materials characterisation by Fourier Transform infrared spectroscopy. B.H.P. Tech. Bull. 27: 26-32.

French, B.M., 1966. Some geological implications of equilibrium between graphite and a C-H-O gas phase at high temperatures and pressures. Rev. Geophys. 4: 223-253.

French, B.M. & Eugster, H.P., 1965. Experimental control of oxygen fugacities by graphite-gas equilibriums. J. Geophys. Res. 70: 1529-1539.

Freund, F., Kathrein, H., Wengeler, H., Knobel, R. & Heinen, H.J., 1980. Carbon in solid solution in forsterite - a key to the intractable nature of reduced carbon in terrestrial and cosmogenic rocks. Geochim. Cosmochim. Acta 44: 1319-1333.

Freund, F., Wengeler, H., Kathrein, H., Knobel, R., Oberheuser, G., Maiti, G.C., Reil, D., Knipping, U. & Kotz, J., 1983. Hydrogen and carbon derived from dissolved H_2O and CO_2 in minerals and melts. Bull. Mineral. 106: 185-200.

Frost, B.R., 1979. Mineral equilibria involving mixed-volatiles in a C-O-H fluid phase: the stabilities of graphite and siderite. Am. J. Sci. 279: 1033-1059.

Frost, B.R., Lindsley, D.H. & Fuhrman, M., 1984. Role of graphite in controlling the formation of hornblende, Sybille Syenite, Laramie Anorthosite Complex. GSA Abstracts with Programs 16: 513.

Fuex, A.N. & Baker, D.R., 1973. Stable carbon isotopes in selected granitic, mafic and ultramafic igneous rocks. Geochim. Cosmochim. Acta 37: 2509-2521.

Fuller, M.P. & Griffiths, P.R., 1978. Diffuse reflectance measurements by infrared Fourier Transform spectroscopy. Anal. Chem. 50: 1906-1910.

Furukawa, T., Fox, K.E. & White, W.B., 1981. Raman spectroscopic investigation of the structure of silicate glasses. III. Raman intensities and structural units in sodium silicate glasses. J. Chem. Phys. 75: 3226-3237.

Gadsden, J.A., 1975. INFRARED SPECTRA OF MINERALS AND RELATED INORGANIC COMPOUNDS. Butterworths, London: 277 pp.

Galeener, F.L. & Mikkelsen, J.C., 1981. Vibrational dynamics in ^{18}O-substituted vitreous SiO_2. Phys. Rev. B 23: 5527-5530.

Galeener, F.L. & Geissberger, A.E., 1983. Vibrational dynamics in ^{30}Si-substituted vitreous SiO_2. Phys. Rev. B 27: 6199-6203.

Garofalini, S.H., 1982. Molecular dynamics simulation of the frequency spectrum of amorphous silica. J. Chem. Phys. 76: 3189-3192.

Gerlach, T.M., 1980. Chemical characteristics of the volcanic gases from Nyiragongo Lava Lake and the generation of CH_4-rich fluid inclusions in alkaline rocks. J. Volc. Geotherm. Res. 8: 177-189.

Giardini, A.A. & Melton, C.E., 1975. The nature of cloud-like inclusions in two Arkansas diamonds. Am. Min. 60: 931-933.

Giardini, A.A., Melton, C.E. & Michell, R.S., 1982. The nature of the upper 400 km of the Earth and its potential as the source for non-biogenic petroleum. J. Petrol. Geol. 5: 173-190.

Gold, T., 1979. Terrestrial sources of carbon and earthquake outgassing. J. Petrol. Geol. 1: 3-19.

Gold, T. & Soter, S., 1980. The Deep-Earth-Gas hypothesis. Sci. Am. 242: 130-137.

Gold, T. & Soter, S., 1982. Abiogenic methane and the origin of petroleum. Energy Explor. Exploit. 1: 89-104.

Gold, T. & Soter, S., 1983. Methane and seismicity: a reply. EOS Trans., Am. Geophys. Union 64: 663.

Goodwin, R.D., 1974. The thermophysical properties of methane from 90-500 K at pressures to 700 bar. Nat. Bur. Stds, Tech. Note 653.

Goodwin, R.D., Roder, H.M. & Straty, G.C., 1976. Thermophysical properties of ethane from 90 to 600 K at pressures to 700 bar. Nat. Bur. Stds, Tech. Note 684.

Greaves, G.N., Fontaine, A., Lagarde, P., Raoux, D. & Gurman, S.J., 1981. Local structure of silicate glass. Nature 293: 611-616.

Green, D.H., 1973. Conditions of melting of basanite magma from garnet peridotite. Earth. Plan. Sci. Lett. 17: 456-465.

Green, D.H. & Ringwood, A.E., 1967. The genesis of basaltic magmas. Contrib. Min. Petrol. 15: 103-190.

Green, D.H. & Liebermann, R.C., 1976. Phase equilibria and elastic properties of the pyrolite model for the oceanic upper mantle. Tectonophysics 32: 61-92.

Green, T.H., Ringwood, A.E. & Major, A., 1966. Friction effects and pressure calibration in a piston-cylinder apparatus at high pressure and temperature. J. Geophys. Res. 71: 3589-3595.

Gupta, A.K., Taylor, W.R. & Green, D.H., 1985. Experimental study of the system forsterite-nepheline-jadeite at variable temperatures under 28 kb pressure. Am. Min. (submitted).

Gurney, J.J. & Boyd, F.R., 1982. Mineral intergrowths with polycrystalline diamonds from the Orapa Mine, Botswana. Rep. Geophys. Lab., Carnegie Inst. Ybk 81: 267-273.

Gurney, J.J., Harris, J.W. & Rickard, R.S., 1984a. Silicate and oxide inclusions in diamonds from the Orapa Mine, Botswana. Proc. 3rd Int. Kimberlite Conf., Vol. II: 3-9.

Gurney, J.J., Harris, J.W. & Rickard, R.S., 1984b. Minerals associated with diamonds from the Roberts Victor Mine. Proc. 3rd Int. Kimberlite Conf., Vol.II: 25-32.

Haggerty, S.E., 1978. The redox state of planetary basalts. Geophys. Res. Lett. 5: 443-446.

Haggerty, S.E. & Tompkins, L.A., 1983. Redox state of Earth's upper mantle from kimberlitic ilmenites. Nature 303: 295-300.

Halbach, H. & Chatterjee, N.D., 1982. An empirical Redlich-Kwong-type equation of state for water to 1000°C and 200 kbar. Contrib. Min. Petrol. 79: 337-345.

Hallbauer, D.K., Kable, E.J. & Robinson, D.N., 1980. The occurrence of detrital diamond and moissanite in the Proterozoic Witwatersrand conglomerates and their implications for crustal evolution. In U.F. Dornsiepen & V. Haak (Eds): INT. ALFRED WEGENER SYMPOSIUM, Summaries of Contributions. Dietrich Reimer, Berlin: 67-68.

Harris, J.W. & Gurney, J.J., 1979. Inclusions in diamond. In J.E. Field (Ed.): THE PROPERTIES OF DIAMOND. Academic Press: 555-591.

Harris, J.W., Milledge, H.J., Barron, T.H.K. & Munn, R.W., 1970. Thermal expansion of garnets included in diamond. J. Geophys. Res. 75: 5775-5792.

Harris, J.W., Hawthorne, J.B. & Oosterveld, M.M., 1979. Regional and local variations in the characteristics of diamonds from some southern African kimberlites. Proc. 2nd Int. Kimberlite Conf., Vol.1: 27-41.

Harris, J.W., Hawthorne, J.B. & Oosterveld, M.M., 1984. A comparison of diamond characteristics from the De Beers Pool Mines, Kimberley, South Africa. Ann. Sci. Univ. Clermont-Fd 74: 1-13.

Hart, R., Dymond, J. & Hogan, L., 1979. Preferential formation of the atmosphere-sialic crust system from the Earth. Nature 278: 156-159.

Hass, M., 1970. Raman spectra of vitreous silica, germania and sodium silicate glasses. J. Phys. Chem. Solids 31: 415-422.

Hatton, C.J., 1978. The geochemistry and origin of xenoliths from the Roberts Victor Mine. Unpubl. Ph.D. thesis, University of Cape Town: 179 pp.

Hatton, C.J. & Gurney, J.J., 1979. A diamond-graphite eclogite from the Roberts Victor Mine. Proc. 2nd Int. Kimberlite Conf., Vol.2: 29-36.

Hayatsu, R., Scott, R.G., Studier, M.H., Lewis, R.S. & Anders, E., 1980. Carbynes in meteorites: detection, low-temperature origin, and implications for interstellar molecules. Science 209: 1515-1518.

He Quan-Zhi, 1982. Kimberlites in China and their major components: a discussion on the physicochemical properties of the upper mantle. Terra Cognita 2: 245-246.

Helgeson, H.C. & Kirkham, D.H., 1974. Theoretical prediction of the thermodynamic behaviour of aqueous electrolytes at high pressures: I. Summary of the thermodynamic/electrostatic properties of the solvent. Am. J. Sci. 274: 1089-1198.

Helgeson, H.C., Delany, J.M., Nesbitt, H.W. & Bird, D.K., 1978. Summary and critique of the thermodynamic properties of rock-forming minerals. Am. J. Sci. 278A: 1-229.

Henderson, W., Eglinton, G., Simmonds, P. & Lovelock, J.E., 1968. Thermal alteration as a contributory process to the genesis of petroleum. Nature 219: 1012-1016.

Hervig, R.L., Smith, J.V., Steele, M., Gurney, J.J., Meyer, H.O.A. & Harris, J.W., 1980. Diamonds: minor elements in silicate inclusions: pressure-temperature implications. J. Geophys. Res. 85: 6919-6929.

Hess, P.C. & Wood, M.I., 1982. Aluminium co-ordination in meta-aluminous and peralkaline silicate melts. Contrib. Min. Petrol. 81: 103-112.

Hodges, F.N., 1973. Solubility of H_2O in forsterite melt at 20 kbar. Rep. Geophys. Lab., Carnegie Inst. Ybk 72: 495-497.

Hodges, F.N., 1974. The solubility of H_2O in silicate melts. Rep. Geophys. Lab., Carnegie Inst. Ybk 73: 251-255.

Holland, T.J.B., 1979. Experimental determination of the reaction paragonite = jadeite + kyanite + H_2O. Contrib. Min. Petrol. 68: 293-301.

Holland, T.J.B., 1981. Thermodynamic analysis of simple mineral systems. Adv. Phys. Geochem. 1: 19-34.

Holloway, J.R., 1977. Fugacity and activity of molecular species in supercritical fluids. In D.G. Fraser (Ed.): THERMODYNAMICS IN GEOLOGY. D. Reidel Publishing Co.: 161-181.

Holloway, J.R., 1981. Volatile interactions in magmas. Adv. Phys. Geochem. 1: 273-293.

Holloway, J.R. & Reese, R.L., 1974. The generation of N_2-CO_2-H_2O fluids for use in hydrothermal experimentation. I. Experimental method and equilibrium calculations in the C-O-H-N system. Am. Min. 59: 587-597.

Howitt, D.G. & McElfresh, D.K., 1982. A calculation of the free energies of some structural models for vitreous silica. Phys. Chem. Glasses 23: 107-109.

Hudson, P.R.W. & Tsong, I.S.T., 1977. Hydrogen impurity in natural gem diamond. Jour. Mat. Sci. 12: 2389-2395.

Ito, E., Takahashi, E. & Matsui, Y., 1984. The mineralogy and chemistry of the lower mantle: an implication of the ultrahigh-pressure phase relations in the system MgO-FeO-SiO_2. Earth Plan. Sci. Lett. 67: 238-248.

Jacobs, G.K. & Kerrick, D.M., 1981a. Methane: an equation of state with application to the ternary system H_2O-CO_2-CH_4. Geochim. Cosmochim. Acta 45: 607-614.

Jacobs, G.K. & Kerrick, D.M., 1981b. APL and Fortran programs for a new equation of state for H_2O, CO_2 and their mixtures at supercritical conditions. Comp. Geosci. 7: 131-143.

Jakobsson, S. & Holloway, J.R., 1984. Melting experiments with graphite-COH fluid-iron-wustite: a buffered system without iron-loss. Int. Workshop on Experimental Geochemistry, Abstracts. Monash University, Melbourne.

Javoy, M. & Pineau, F., 1983. Stable isotope contraints on a model Earth from a study of mantle nitrogen. Meteoritics 18: 320.

Javoy, M., Pineau, F. & Allegre, C.J., 1982. Carbon geodynamic cycle. Nature 300: 171-173.

Javoy, M., Pineau, F. & Demaiffe, D., 1984. Nitrogen and carbon isotopic composition in the diamonds of Mbuji Mayi (Zaire). Earth Plan. Sci. Lett. 68: 399-412.

Jeanloz, R., 1980. Infrared spectra of olivine polymorphs: alpha, beta phase and spinel. Phys. Chem. Min. 5: 327-341.

Jones, R.N. & Pitha, J., 1976. Computer programs for infrared spectrophotometry. Nat. Res. Coun. Canada Bull. 12 (2nd ed.).

Juza, J., Kmonicek, V. & Sifner, O., 1965. Measurements of the specific volume of carbon dioxide in the range 700 to 4000 bar and 50 to 475°C. Physica 31: 1735-1744.

Kagel, R.O. & King, S.T., 1973. Transforming IR spectroscopy. Industr. Res. 15: 54-59.

Kaminskiy, F.V., Bukin, V.I., Potapov, S.V., Arkus, N.G. & Ivanova, V.G., 1969. Discoveries of silicon carbide under natural conditions and their genetic importance. Int. Geology Rev. 11: 561-569.

Kamenskiy, I.L., Lobkov, V.A., Prasolov, E.M., Beskrovny, N.S., Kudryavtseva, E.I., Anufriev, G.S. & Pavlov, V.B., 1976. The components of the upper mantle of the Earth in gases of Kamchatka (according to He, Ne, Ar and C isotopy). Geochem. Int. 13: 35-48.

Kauppinen, J.K., Moffat, D.J., Mantsch, H.H. & Cameron, D.G., 1981. Fourier self-deconvolution: A method for resolving intrinsically overlapped bands. Appl. Spectrosc. 35: 271-276.

Kennedy, G.C., 1959. Phase relations in the system Al_2O_3-H_2O at high temperatures and pressures. Am. J. Sci. 257: 563-573.

Kennedy, G.C. & Holser, W.T., 1966. Pressure-volume-temperature and phase relations of water and carbon dioxide. Geol. Soc. Am. Memoir 97: 373-384.

Kennedy, C.S. & Kennedy, G.C., 1976. The equilibrium boundary between graphite and diamond. J. Geophys. Res. 81: 2467-2470.

Kerrick, D.M. & Jacobs, G.K., 1981. A modified Redlich-Kwong equation for H_2O, CO_2 and H_2O-CO_2 mixtures at elevated pressures and temperatures. Am. J. Sci. 281: 735-767.

Khanna, R.K., Stranz, D.D. & Donn, B., 1981. A spectroscopic study of intermediates in the condensation of refractory smokes: Matrix isolation experiments of SiO. J. Chem. Phys. 74: 2108-2115.

Kimata, M., 1980. Crystal chemistry of Ca-melilites on X-ray diffraction and infrared absorption properties. Neues Jb. Miner. Abh. 139: 43-58.

Kim, K-R., 1983. Methane and radioactive isotopes in submarine hydrothermal systems. Unpubl. Ph.D. dissertation, Scripps Institution of Oceanography, Univ. of California, San Diego: 206 pp.

Klonkowski, A., 1983. The structure of sodium alumino-silicate glass. Phys. Chem. Glasses 24: 166-171.

Kogarko, L.N. & Arutyunyan, L.A., 1982. Ni/Co ratios of basalt magmas as an indicator of mantle redox equilibria. Geochem. Int. 19: 114-123.

Konnerup-Madsen, J. & Rose-Hansen, J., 1982. Volatiles associated with alkaline igneous rift activity: fluid inclusions in the Ilimaussaq Intrusion and the Gardar Granitic Complexes (South Greenland). Chem. Geol. 37: 79-93.

Konnerup-Madsen, J., Larsen, E. & Rose-Hansen, J., 1979. Hydrocarbon-rich fluid inclusions in minerals from the alkaline Ilimaussaq intrusion, South Greenland. Bull. Mineral. 102: 642-653.

Kusabiraki, K. & Shiraishi, Y., 1981. The infra-red spectrum of vitreous fayalite. J. Non-Cryst. Solids 44: 365-368.

Kushiro, I., 1964. The join akermanite-soda melilite at 20 kilobars. Rep. Geophys. Lab., Carnegie Inst. Ybk 63: 90-92.

Kushiro, I., 1968. Compositions of magmas formed by partial zone melting of the Earth's upper mantle. J. Geophys. Res. 73: 619-634.

Kushiro, I., 1972. Effect of water on the composition of magmas formed at high pressures. J. Petrol. 13: 311-334.

Kushiro, I., 1975. On the nature of silicate melt and its significance in magma genesis: regularities in the shift of the liquidus boundaries involving olivine, pyroxene and silica minerals. Am. J. Sci. 275: 411-431.

Kushiro, I., 1976. Changes in viscosity and structure of melt of $NaAlSi_2O_6$ composition at high pressures. J. Geophys. Res. 81: 6347-6350.

Kushiro, I., 1978. Viscosity and structural changes of albite ($NaAlSi_3O_8$) melt at high pressures. Earth Plan. Sci. Lett. 41: 87-91.

Kushiro, I., 1980. Viscosity, density and structure of silicate melts at high pressures, and their petrological implications. In R.B. Hargreaves (Ed.): PHYSICS OF MAGMATIC PROCESSES. Princeton Univ. Press: 93-121.

Kushiro, I., 1984. Structures and some physical properties of silicate melts of geological interest. In I. Sunagawa (Ed.): MATERIALS SCIENCE OF THE EARTH'S INTERIOR. Terra Scientific Publ. Co., Tokyo: 39-60.

Kushiro, I. & Yoder, H.S., 1974. Formation of eclogite from garnet lherzolite: liquidus relations in a portion of the system $MgSiO_3$-$CaSiO_3$-Al_2O_3 at high pressures. Rep. Geophys. Lab., Carnegie Inst. Ybk 73: 266-269.

Lacy, E.D., 1965. A statistical model of polymerisation/depolymerisation relationships in silicate melts and glasses. Phys. Chem. Glasses 6: 171-180.

Lambert, R.StJ., 1981. A two-layer convective mantle with an internal boundary layer. In R.J. O'Connell & W.S. Fyfe (Eds): EVOLUTION OF THE EARTH, Geodynamics Series Vol.5. American Geophysical Union: 210-216.

Larimer, J.W. & Bartholomay, M., 1979. The role of carbon and oxygen in cosmic gases: some applications to the chemistry and mineralogy of enstatite chondrites. Geochim. Cosmochim. Acta 43: 1455-1466.

Laughlin, R.B. & Joannopoulos, J.D., 1977. Phonons in amorphous silica. Phys. Rev. B 16: 2942-2953.

Liese, H.C., 1975. Selected terrestrial minerals and their infrared absorption spectral data (4000-300 cm^{-1}). In C. Karr (Ed.): INFRARED AND RAMAN SPECTROSCOPY OF LUNAR AND TERRESTRIAL MINERALS. Academic Press, New York: 197-229.

Lilley, M.D., Baross, J.A. & Gordon, L.I., 1983. Reduced gases and bacteria in hydrothermal fluids: The Galapagos spreading center and 21°N East Pacific Rise. In P.A., Rona, K. Bostrom, L. Laubier & K.L. Smith (Eds): HYDROTHERMAL PROCESSES AT SEAFLOOR SPREADING CENTERS. Plenum Press, New York: 411-448.

Lindsley, D.H., Speidel, D.H. & Nafziger, R.H., 1968. P-T-fO_2 relations for the system Fe-O-SiO_2. Am. J. Sci. 266: 342-360.

Louisnathan, S.J., 1969. Refinement of the crystal structure of hardystonite, $Ca_2ZnSi_2O_7$. Z. Krist. 130: 427-437.

Louisnathan, S.J., 1970a. Refinement of the crystal structure of a natural gehlenite, $Ca_2Al(Al,Si)_2O_7$. Can. Mineral. 10: 822-837.

Louisnathan, S.J., 1970b. The crystal structure of synthetic soda melilite, $CaNaAlSi_2O_7$. Z. Krist. 131: 314-321.

Lupton, J.E., 1983. Terrestrial inert gases: isotope tracer studies and clues to primordial components in the mantle. Ann. Rev. Earth Planet. Sci. 11: 371-414.

Luth, R. & Boettcher, A., 1984. Hydrogen and the melting of silicates. GSA Abstracts with Programs 16: 580.

Lyakhovich, V.V., 1979. Origin of accessory moissanite. Int. Geology Rev. 22: 961-970.

Marshintsev, V.K., Zayakina, N.V. & Leskova, N.V., 1982. New find of cubic silicon carbide as inclusions in moissanite from kimberlitic rocks. Doklady ESS 262: 163-166.

Mathews, J.F., 1972. The critical constants of inorganic substances. Chem. Rev. 72: 71-100.

Mathez, E.A., 1984. Influence of degassing on oxidation states of basaltic magmas. Nature 310, 371-375.

Mathez, E.A. & Delaney, J.R., 1981. The nature and distribution of carbon in submarine basalts and peridotite nodules. Earth Plan. Sci. Lett 56: 217-232.

Mathez, E.A., Dietrich, V.J. & Irving, A.J., 1982. Abundances of carbon in mantle xenoliths from alkalic basalts. Terra Cognita 2: 199-200.

Matson, D.W., Muenow, D.W. & Garcia, M.O., 1984. Volatiles in amphiboles from xenoliths, Vulcan's Throne, Grand Canyon, Arizona, U.S.A. Geochim. Cosmochim. Acta 48: 1629-1636.

Matsui, Y. & Kawamura, K., 1980. Instantaneous structure of an $MgSiO_3$ melt simulated by molecular dynamics. Nature 285: 648-649.

Matsui, Y. & Kawamura, K., 1984. Computer simulation of structures of silicate melts and glasses. In I. Sunagawa (Ed.): MATERIALS SCIENCE OF THE EARTH'S INTERIOR. Terra Scientific Publ. Co., Tokyo: 3-23.

Mattey, D.P., Carr, R.H., Wright, I.P. & Pillinger, C.T., 1984. Carbon isotopes in submarine basalts. Earth Plan. Sci. Lett. 70: 196-206.

McKenzie, D. & Richter, F.M., 1981. Parameterized thermal convection in a layered region and the thermal history of the Earth. J. Geophys. Res. 86B: 11667-11680.

McMahon, B. & Haggerty, S.E., 1984. The Benfontein kimberlite sills: magmatic reactions and high intrusion temperatures. Am. J. Sci. 284: 893-941.

McMillan, P., 1984a. Structural studies of silicate glasses and melts - applications and limitations of Raman spectroscopy. Am. Min. 69: 622-644.

McMillan, P., 1984b. A Raman spectroscopic study of glasses in the system $CaO-MgO-SiO_2$. Am. Min. 69: 645-659.

McMillan, P. & Piriou, B., 1983. Raman spectroscopic studies of silicate and related glass structure - a review. Bull. Mineral. 106: 57-75.

McMillan, P., Piriou, B. & Navrotsky, A., 1982. A Raman spectroscopic study of glasses along the joins silica-calcium aluminate, silica-sodium aluminate, and silica-potassium aluminute. Geochim. Cosmochim. Acta 46: 2021-2037.

McMillan, P.F., Jakobsson, S., Holloway, J.R. & Silver, L.A., 1983. A note on the Raman spectra of water-bearing albite glasses. Geochim. Cosmochim. Acta 47: 1937-1943.

Mel'nik, Yu.P., 1978. Thermodynamic properties of carbon monoxide and methane at high temperatures and pressures - a new correlation based on the principle of corresponding states. Geochem. Int. 15: 49-62.

Melton, C.E. & Giardini, A.A., 1974. The composition and significance of gas released from natural diamonds from Africa and Brazil. Am. Min. 59: 775-782.

Melton, C.E. & Giardini, A.A., 1975. Experimental results and a theoretical interpretation of gaseous inclusions found in Arkansas natural diamonds. Am. Min. 60: 413-417.

Melton, C.E. & Giardini, A.A., 1976. Experimental evidence that oxygen is the principal impurity in natural diamonds. Nature 263: 309-310.

Melton, C.E. & Giardini, A.A., 1981. The nature and significance of occluded fluids in three Indian diamonds. Am. Min. 66: 746-750.

Merkle, R.K.W. & Hatton, C.J., 1983. Graphite in the Western Bushveld - primary magmatic or contamination? Symposium on the Bushveld Complex, Abstracts. Inst. Geol. Res. Bushveld Complex, Pretoria: 66-67.

Meyer, H.O.A. & Tsai, H-S., 1976. Mineral inclusions in natural diamonds: their nature and significance. Min. Sci. Eng. 8: 242-261.

Michels, A., De Graaf, W., Wassenaar, J.M., Levelt, J.M.H. & Louwerse, P., 1959. Compressibility isotherms of hydrogen and deuterium at temperatures between $-175^{o}C$ and $+150^{o}C$. Physica 25: 25-42.

Milberg, M.E. & Peters, C.R., 1969. Cation distribution in thallium silicate glasses. Phys. Chem. Glasses 10: 46-49.

Milledge, H.J., Mendelssohn, M.J., Seal, M., Rousee, J.E., Swart, P.K. & Pillinger, C.T., 1983. Carbon isotopic variation in spectral type II diamonds. Nature 303: 791-792.

Mozzi, R.L. & Warren, B.E., 1969. The structure of vitreous silica. J. Appl. Crystallogr. 2: 164-172.

Muller, D., Berger, G., Grunze I., Ladwig, G., Hallas E. & Haubenreisser, U., 1983. Solid-state high-resolution ^{27}Al nuclear magnetic resonance studies of the structure of $CaO-Al_2O_3-P_2O_5$ glasses. Phys. Chem. Glasses 24: 37-42.

Muncke, G., 1979. Physics of diamond growth. In J.E. Field (Ed.): THE PROPERTIES OF DIAMOND. Academic Press: 473-500.

Murck, B.W., Burrus, R.C. & Hollister, L.S., 1978. Phase equilibria in fluid inclusions in ultramafic xenoliths. Am. Min. 63: 40-46.

Mysen, B.O., 1976. The role of volatiles in silicate melts: solubility of carbon dioxide and water in feldspar, pyroxene and feldspathoid melts to 30 kbar and $1625^{o}C$. Am. J. Sci. 276: 969-996.

Mysen, B.O. & Virgo, D., 1980a. Solubility mechanisms of carbon dioxide in silicate melts: A Raman spectroscopic study. Am. Min. 65: 885-899.

Mysen, B.O. & Virgo, D., 1980b. Solubility mechanism of water in basalt melt at high pressures and temperatures: $NaCaAlSi_2O_7-H_2O$ as a model. Am. Min. 65: 1176-1184.

Mysen, B.O. & Virgo, D., 1980c. The solubility behaviour of CO_2 in melts on the join $NaAlSi_3O_8-CaAl_2Si_2O_8-CO_2$ at high pressures and temperatures: A Raman specroscopic study. Am. Min. 65: 1166-1175.

Mysen, B.O., Virgo, D. & Scarfe, C.M., 1980a. Relations between anionic structure and viscosity of silicate melts - a Raman spectroscopic study. Am. Min. 65: 690-710.

Mysen, B.O., Virgo, D., Harrison, W.J. & Scarfe, C.M., 1980b. Solubility mechanisms of H_2O in silicate melts at high pressures and temperatures: A Raman spectroscopic study. Am. Min. 65: 900-914.

Mysen, B.O., Virgo, D. & Kushiro, I., 1981. The structural role of aluminium in silicate melts - a Raman spectroscopic study at 1 atmosphere. Am. Min. 66: 678-701.

Mysen, B.O., Virgo, D. & Seifert, F.A., 1982a. The structure of silicate melts: implications for chemical and physical properties of natural magma. Rev. Geophys. Space Phys. 20: 353-383.

Mysen, B.O., Finger, L.W., Virgo, D. & Seifert, F.A., 1982b. Curve-fitting of Raman spectra of silicate glasses. Am. Min. 67: 686-695.

Mysen, B.O., Virgo, D., Danckwerth, P., Seifert, F.A. & Kushiro, I., 1983. Influence of pressure on the structure of melts on the joins $NaAlO_2$-SiO_2, $CaAl_2O_4$-SiO_2, and $MgAl_2O_4$-SiO_2. Neues Jb. Miner. Abh. 147: 281-303.

Nakamoto, K., 1978. INFRARED AND RAMAN SPECTRA OF INORGANIC AND COORDINATION COMPOUNDS. Wiley-Interscience, 3rd edition.

Nakamoto, K., Margoshes, M. & Rundle, R.E., 1955. Stretching frequencies as a function of distances in hydrogen bonds. J. Am. Chem. Soc. 77: 6480-6486.

Nakamura, Y., 1974. The system SiO_2-H_2O-H_2 at 15 kbar. Rep. Geophys. Lab., Carnegie Inst. Ybk 73: 259-263.

Navrotsky, A., Peraudeau, G., McMillan, P. & Coutures, J-P., 1982. A thermochemical study of glasses and crystals along the joins silica-calcium aluminate and silica-sodium aluminate. Geochim. Cosmochim. Acta 46: 2039-2047.

Nickel, K.G., 1983. Petrogenesis of garnet and spinel peridotites. Unpubl. Ph.D. thesis, University of Tasmania: 294 pp.

Nordin, M.R., 1984. Modelling of silicate melt systems. Unpubl. B.Sc.(Hons.) thesis, University of Tasmania: 74 pp.

North, F.K., 1982. Review of Thomas Gold's deep-Earth-gas hypothesis. Energy Explor. Exploit. 1: 105-110.

Oberheuser, G., Knobel, R., Wengeler, H., Maiti, G.C., Schaefer, R.G. & Freund, F., 1980. Solubility of gases in the solid phase: formation of C-H species from atomic C and H. Fortschr. Mineral. 58: 102-103. (in German)

Oberheuser, G., Knobel, R., Reil, D. & Freund, F., 1981. Metal transport in the gas phase: CO_2 and hydrocarbon evolution from olivine nodules, Eifel. Fortschr. Mineral. 59: 257. (in German)

Ohmoto, H. & Kerrick, D., 1977. Devolatilization equilibria in graphitic systems. Am. J. Sci. 277: 1013-1044.

Ohtani, F., Irifune, T. & Fujino, K., 1981. Fusion of pyrope at high pressures and rapid crystal growth from the pyrope melt. Nature 294: 62-64.

Ohtani, E., Taulelle, F. & Angell, C.A., 1985. Al^{3+} co-ordination changes in liquid aluminosilicates under pressure. Nature 314: 78-81.

Okuno, M. & Marumo, F., 1982. The structures of anorthite and albite melts. Min. Jour. Jap. 11: 180-196.

Olafsson, M. & Eggler, D.H., 1983. Phase relations of amphibole, amphibole-carbonate and phlogopite-carbonate peridotite: petrologic constraints on the asthenosphere. Earth Plan. Sci. Lett. 64: 305-315.

Omori, K., 1971. Analysis of the infrared absorption spectrum of almandine-pyrope garnet from Nijosan, Osaka Prefecture, Japan. Am. Min. 56: 841-849.

O'Neill, H.StC., & Wall, V.J., 1982. Oxygen fugacitites from the assemblage olivine-orthopyroxene-spinel. Res. Sch. Earth Sci., Aust. Natl Univ., Ann. Rep.: 177-179.

Oremland, R.S., 1983. Methane in association with seismic activity. EOS Trans., Am. Geophys. Union 64: 410.

Ostrovsky, I.A. & Ryzhenko, B.N., 1978. Fugacities of gases and some mineralogical reactions at very high pressures and temperatures (an extrapolation). Phys. Chem. Min. 2: 297-303.

Oxtoby, S., 1978. Physical properties of hydrous glasses. Progress in Experimental Petrology, NERC Report 1975-1978, 4: 32-40.

Oxtoby, S. & Hamilton, D.L., 1978. The discrete association of water with Na_2O and SiO_2 in NaAl silicate melts. Contrib. Min. Petrol. 66: 185-188.

Ozima, M. & Podosek, F.A., 1983. NOBLE GAS GEOCHEMISTRY. Cambridge University Press: 367 pp.

Ozima, M., Zashu, S. & Nitoh, O., 1983. $^{3}He/^{4}He$ ratio, noble gas abundance and K-Ar dating of diamonds - an attempt to search for the records of early terrestrial history. Geochim. Cosmochim. Acta 47: 2217-2224.

Painter, P.C. & Coleman, M.M., 1980. The application of FTIR to the determination of mineral matter in coal and oil shale. Digilab FTS/IR Notes #35. Digilab Div., Bio-rad Laboratories, Cambridge, Mass.

Pasteris, J.D., 1981. Occurrence of graphite in serpentinized olivines in kimberlite. Geology 9: 356-359.

Pasteris, J.D., in press. Fluid inclusions in mantle xenoliths. In P.H. Nixon (Ed.): MANTLE XENOLITHS. Wiley-Interscience 1985/86.

Petersilie, I.A. & Sorensen, H., 1970. Hydrocarbon gases and bituminous substances in rocks from the Ilimaussaq alkaline intrusion, South Greenland. Lithos 3: 59-76.

Petersilie, I.A. & Pripachkin, W.A., 1979. Hydrogen, carbon, nitrogen and helium in gases of igneous rocks. Phys. Chem. Earth 11: 541-545.

Pineau, F. & Javoy, M., 1983. Carbon isotopes and concentrations in mid-oceanic ridge basalts. Earth Planet. Sci. Lett. 62: 239-257.

Pitzer, K.S., Lippmann, D.Z., Curl, R.F., Huggins, C.M. & Petersen, D.E., 1955. The volumetric and thermodynamic properties of fluids II. Compressibility factor, vapor pressure and entropy of vaporization. J. Am. Chem. Soc. 77: 3433-3440.

Planetary Sciences Unit, University of Cambridge, 1982. Mantle methane - fool's gold? Nature 300: 312-313.

Pliskin, W.A. & Lehman, H.S., 1965. Structural evaluation of silicon oxide films. J. Electrochem. Soc. 112: 1013-1019.

Poreda, R.J. & Basu, A.R., 1984. Rare gases, water, and carbon in kaesutites. Earth Plan. Sci. Lett. 69: 58-68.

Pouchert, C.J., 1981. THE ALDRICH LIBRARY OF INFRARED SPECTRA. Aldrich Chemical Co., Wisconsin, 3rd edition.

Prausnitz, J.M., 1969. MOLECULAR THERMODYNAMICS OF FLUID-PHASE EQUILIBRIA. Prentice-Hall, New Jersey: 513 pp.

Presnall, D.C., 1969. Pressure-volume-temperature measurements on hydrogen from 200° to 600°C and up to 1800 atmospheres. J. Geophys. Res. 74: 6026-6033.

Prinz, M., Manson, D.V., Hlava, P.F. & Keil, K., 1975. Inclusions in diamonds: garnet lherzolite and eclogite assemblages. Phys. Chem. Earth 9: 797-815.

Rai, C.S., Sharma, S.K., Muenow, D.W., Matson, D.W. & Byers, C.D., 1983. Temperature dependence of CO_2 solubility in high-pressure quenched glasses of diopside composition. Geochim. Cosmochim. Acta 47: 953-958.

Randall, J.T., Rooksby, H.P. & Cooper, B.S., 1930. Structure of glasses: the evidence of x-ray diffraction. J. Soc. Glass Technol. 14: 219-229.

Rao, K.J. & Elliot, S.R., 1981. Characteristic vibrations of cations in glasses. J. Non-Cryst. Solids 46: 371-378.

Redlich, O. & Kwong, J.N.S., 1949. On the thermodynamics of solutions V. An equation of state. Fugacities of gaseous solutions. Chem. Rev. 44: 233-244.

Rice, M.H. & Walsh, J.M., 1957. Equation of state of water to 250 kilobars. J. Chem. Phys. 26: 824-830.

Richardson, S.H., Gurney, J.J., Erlank, A.J. & Harris, J.W., 1984. Origin of diamonds in old enriched mantle. Nature 310: 198-202.

Ringwood, A.E., 1979. ORIGIN OF THE EARTH AND MOON. Springer-Verlag: 295 pp.

Rison, W. & Craig, H., 1983. Helium isotopes and mantle volatiles in Loihi Seamount and Hawaiian Island basalts and xenoliths. Earth Plan. Sci. Lett. 66: 407-426.

Robie, R.A., Hemingway, B.S. & Fisher, J.R., 1978. Thermodynamic properties of minerals and related substances at 298.15 K and 1 bar (10^5 Pascals) pressure and at higher temperatures. U.S. Geol. Surv. Bull. 1452.

Robertson, S.L. & Babb, S.E., 1970. Isotherms of carbon monoxide to 10 kbar and 300°C. J. Chem. Phys. 53: 1094-1097.

Robinson, D.N., 1978. The characteristics of natural diamond and their interpretation. Min. Sci. Eng. 10: 55-72.

Robinson, R.L. & Jacoby, R.H., 1965. Better compressibility factors. Hydrocarbon Proc. 44: 141-144.

Rochow, E.G., 1973. The chemistry of silicon. In COMPREHENSIVE INORGANIC CHEMISTRY, Vol.9. Pergamon Press.

Roedder, E., 1981. Origin of fluid inclusions and changes that occur after trapping. Min. Assoc. Canada Short Course Handbk 6: 101-137.

Roedder, E., 1983. Geobarometry of ultramafic xenoliths from Loihi Seamount, Hawaii, on the basis of CO_2 inclusions in olivine. Earth Plan. Sci. Lett. 66: 369-379.

Roedder, E., 1984. FLUID INCLUSIONS. Reviews in Mineralogy 12. Mineralogical Society of America: 644 pp.

Ross, M., 1974. A theoretical analysis of the shock compression experiments of the liquid hydrogen isotopes and a prediction of their metallic transition. J. Chem. Phys. 60: 3634-3644.

Rovetta, M.R. & Mathez, E.A., 1982. Magnesite and other minerals in fluid inclusions in a lherzolite xenolith from an alkali basalt. Terra Cognita 2: 229.

Runciman, W.A. & Carter, T., 1971. High resolution infra-red spectra of diamond. Solid State Comm. 9: 315-317.

Ryabchikov, I.D., Green, D.H., Wall, V.J. & Brey, G.P., 1981. The oxidation state of carbon in the reduced-velocity zone. Geochem. Int. 18: 148-158.

Ryabchikov, I.D., Schreyer, W. & Abraham, K., 1982. Compositions of aqueous fluids in equilibrium with pyroxenes and olivines at mantle pressures and temperatures. Contrib. Min. Petrol. 79: 80-84.

Ryzhenko, B.N. & Volkov, V.P., 1971. Fugacity coefficients of some gases in a broad range of temperatures and pressures. Geochem. Int. 8: 468-479.

Sakai, H., Des Marias, D.J., Ueda, A. & Moore, J.G., 1984. Concentrations and isotope ratios of carbon, nitrogen and sulfur in ocean-floor basalts. Geochim. Cosmochim. Acta 48: 2433-2441.

Sampson, R.J., 1978. SURFACE II GRAPHICS SYSTEM, REVISION ONE. Kansas Geological Survey: 240 pp.

Sanders, D.M., Person, W.B. & Hench, L.L., 1974. Quantitative analysis of glass structure with the use of infrared reflection spectra. Appl. Spectrosc. 28: 247-255.

Sato, M., 1972. Intrinsic oxygen fugacities of iron-bearing oxide and silicate minerals under low total pressure. Geol. Soc. Am. Memoir 135: 289-307.

Sato, M., 1978. Oxygen fugacity of basaltic magmas and the role of gas-forming elements. Geophys. Res. Lett. 5: 447-449.

Sato, M. & Wright, T.L., 1966. Oxygen fugacities directly measured in magmatic gases. Science 153: 1103-1105.

Sato, M. & Valenza, M., 1980. Oxygen fugacities of the layered series of the Skaergaard Intrusion, East Greenland. Am. J. Sci. 280A: 134-158.

Schramm, C.M., De Jong, B.H.W.S. & Parziale, V.E., 1984. ^{29}Si magic angle spinning NMR study of local silicon environments in amorphous and crystalline lithium silicates. J. Am. Chem. Soc. 106: 4396-4402.

Schwab, R.G. & Kustner, D., 1981. The equilibrium fugacities of important oxygen buffers in technology and petrology. Neues Jb. Miner. Abh. 140: 111-142.

Scott-Smith, B.H., Danchin, R.V., Harris, J.W. & Stracke, K.J., 1984. Kimberlites near Orroroo, South Australia. Proc. 3rd Int. Kimberlite Conf., Vol.I: 121-142.

Seal, M., 1966. Nature of diamond coat. Phil. Mag. 13: 645-648.

Sears, D.W., Kallemeyn, G.W. & Wasson, J.T., 1982. The compositional classification of chondrites: II. The enstatite chondrite group. Geochim. Cosmochim. Acta 46: 597-608.

Seifert, F.A., Mysen, B.O. & Virgo, D., 1981a. Structural similarity of glasses and melts relevant to petrological processes. Geochim. Cosmochim. Acta 45: 1879-1884.

Seifert, F.A., Mysen, B.O. & Virgo, D., 1981b. Quantitative determination of proportions of anionic units in silicate melts. Rep. Geophys. Lab., Carnegie Inst. Ybk 80: 301-302.

Seifert, F., Mysen, B.O. & Virgo, D., 1982. Three-dimensional network structure of quenched melts (glass) in the systems SiO_2-$NaAlO_2$, SiO_2-$CaAl_2O_4$ and SiO_2-$MgAl_2O_4$. Am. Min. 67: 696-717.

Sellschop, J.P.F., 1979. Nuclear probes in physical and geochemical studies of natural diamonds. In J.E. Field (Ed.): THE PROPERTIES OF DIAMOND. Academic Press: 107-163.

Sellschop, J.P.F., Madiba, C.C.P. & Annegarn, H.J., 1980. Light volatiles in diamond: physical interpretation and genetic significance. Nucl. Inst. Meth. 168: 529-534.

Serna, C.J., Velde, B.D. & White, J.L., 1977. Infrared evidence of order-disorder in amesites. Am. Min. 62: 296-303.

Serna, C.J., White J.L. & Velde, B.D., 1979. The effect of aluminium on the infra-red spectra of 7Å trioctahedral minerals. Min. Mag. 43: 141-148.

Sharma, S.K., 1979. Structure and solubility of carbon dioxide in silicate glasses of diopside and sodium melilite composition at high pressures from Raman spectroscopic data. Rep. Geophys. Lab., Carnegie Inst. Ybk 78: 532-537.

Sharma, S.K. & Simons, B., 1980. Raman study of K_2CO_3-$MgCO_3$ glasses. Rep. Geophys. Lab., Carnegie Inst. Ybk 79: 322-326.

Sharma, S.K. & Simons, B., 1981. Raman study of crystalline polymorphs and glasses of spodumene composition quenched from various pressures. Am. Min. 66: 118-126.

Sharma. S.K. & Yoder, H.S., 1979. Structural study of glasses of akermanite, diopside and sodium melilite compositions by Raman spectroscopy. Rep. Geophys. Lab., Carnegie Inst. Ybk 78: 526-532.

Sharma, S.K., Hoering, T.C. & Yoder, H.S., 1979. Quenched melts of akermanite compositions with and without CO_2 - characterisation by Raman spectroscopy and gas chromatography. Rep. Geophys. Lab., Carnegie Inst. Ybk 78: 537-542.

Sharma, S.K., Simons, B. & Yoder, H.S., 1983. Raman study of anorthite, calcium Tschermak's pyroxene and gehlenite in crystalline and glassy states. Am. Min. 68: 1113-1125.

Sharp, W.E., 1966. Pyrrhotite: a common inclusion in South African diamonds. Nature 211: 402-403.

Shaw, H.R., 1967. Hydrogen osmosis in hydrothermal experiments. In P.H. Abelson (Ed.): RESEARCHES IN GEOCHEMISTRY, Volume 2. John Wiley & Sons: 521-541.

Shaw, H.R. & Wones, D.R., 1964. Fugacity coefficients for hydrogen gas between 0° and $1000^{\circ}C$ for pressures to 3000 atm. Am. J. Sci. 262: 918-929.

Shee, S.R., Gurney, J.J. & Robinson, D.N., 1982. Two diamond-bearing peridotite xenoliths from the Finsch Kimberlite, South Africa. Contrib. Min. Petrol. 81: 79-87.

Shen, P., Bassett, W.A. & Liu, L-G., 1983. Experimental determination of the effects of pressure and temperature on the stoichiometry and phase relations of wustite. Geochim. Cosmochim. Acta 47: 773-778.

Shmonov, V.M. & Shmulovich, K.I., 1974. Molal volumes and equation of state of CO_2 at temperatures from 100 to $1000^{\circ}C$ and pressures from 2000 to 10,000 bars. Doklady ESS 217: 206-209.

Shmulovich, K.I. & Shmonov, V.M., 1975. Fugacity coefficients for CO_2 from 1.0132 to 10,000 bar and 450-1300 K. Geochem. Int. 12: 202-206.

Shmulovich, K.I., Shmonov, V.M. & Zharikov, V.A., 1982. The thermodynamics of supercritical fluid systems. Adv. Phys. Geochem. 2: 173-190.

Skinner, B.J., 1966. Thermal expansion. Geol. Surv. Am. Memoir 97: 75-96.

Slodkevich, V.V., 1983. Graphite paramorphs after diamond. Int. Geol. Rev. 25: 497-514.

Smart, R.M. & Glasser, F.P., 1978. Silicate anion constitution of lead silicate glasses and crystals. Phys. Chem. Glasses 19: 95-102.

Smeeton-Leah, A., 1962. Carbon monoxide. In F. Din (Ed.): THERMODYNAMIC FUNCTIONS OF GASES, Vol.1. Butterworths: 135-175.

Smith, D., 1979. Hydrous minerals and carbonates in peridotite inclusions from Green Knobs and Buell Park kimberlitic diatremes on the Colorado Plateau. Proc. 2nd Int. Kimberlite Conf., Vol.2: 345-356.

Smith, J.V., 1982. Heterogeneous growth of meteorites and planets, especially the Earth and moon. J. Geology 90: 1-125.

Smith, W.R. & Missen, R.W., 1982. CHEMICAL REACTION EQUILIBRIUM ANALYSIS - THEORY AND ALGORITHMS. Wiley-Interscience: 364 pp.

Sneddon, I.N., 1946. The distribution of stress in the neighbourhood of a crack in an elastic solid. Proc. Roy. Soc. Lond. 187A: 229-260.

Sobolev, V.S., Bazarova, T.Yu. & Kostyuk, V.P., 1974. Inclusions in minerals of some types of alkaline rocks. In H. Sorenson (Ed.): THE ALKALINE ROCKS. John Wiley & Sons: 389-401.

Solin, S.A. & Gorman, M., 1974. Direct evidence for homonuclear bonds in amorphous SiC. Solid State Comm. 15: 761-765.

Soules, T.F., 1979. A molecular dynamic calculation of the structure of sodium silicate glasses. J. Chem. Phys. 71: 4570-4577.

Soules, T.F. & Busbey, R.F., 1981. Sodium diffusion in alkali silicate glass by molecular dynamics. J. Chem. Phys. 75: 969-975.

Spencer, K.J. & Lindsley, D.H., 1981. A solution model for coexisting iron-titanium oxides. Am. Min. 66: 1189-1201.

Spera, F.J., 1981. Carbon dioxide in igneous petrogenesis II. Fluid dynamics of mantle metasomatism. Contrib. Min. Petrol. 77: 56-65.

Spera, F.J. & Bergman, S.C., 1980. Carbon dioxide in igneous petrogenesis: I. Aspects of the dissolution of CO_2 in silicate liquids. Contrib. Min. Petrol. 74: 55-66.

Stolen, R.H. & Walrafen, G.E., 1976. Water and its relation to broken bond defects in fused silica. J. Chem. Phys. 64: 2623-2631.

Stolper, E., 1982a. Water in silicate glasses: an infrared spectroscopic study. Contrib. Min. Petrol. 81: 1-17.

Stolper, E., 1982b. The speciation of water in silicate melts. Geochim. Cosmochim. Acta 46: 2609-2620.

Stull, D.R. & Prophet, H., 1971. JANAF THERMOCHEMICAL TABLES, 2nd edition. Nat. Bur. Stds, Ref. Data Ser. 37.

Stull, D.R., Westrum, E.F. & Sinke, G.C., 1969. THE CHEMICAL THERMODYNAMICS OF ORGANIC COMPOUNDS. John Wiley & Son, New York: 865 pp.

Sun, S., in press. Earth's accretion and core formation. Nature (News & Views).

Sykes, M.L., Holloway, J.R. & Eichon, A.D., 1978. Self-consistent entropy from the modified Redlich-Kwong equation: H_2O. EOS Trans., Am. Geophys. Union 59: 1218.

Tanishita, I., Watanabe, K., Kijima, J., Ishii, H., Oguchi, K. & Uematsu, M., 1976. Experimental study of the P, V, T properties of water for temperatures in the range 323.15 K to 773.15 K and pressures up to 200 MPa. J. Chem. Thermodyn. 8: 1-20.

Tarakad, R.R., Spencer, C.F. & Adler, S.B., 1979. A comparison of eight equations of state to predict gas-phase density and fugacity. Ind. Eng. Chem. Proc. Des. Dev. 18: 726-739.

Tarte, P., 1965. The determination of cation co-ordination in glasses by infra-red spectroscopy. In J.A. Prinz (Ed.): PHYSICS OF NON-CRYSTALLINE SOLIDS. John Wiley & Sons, New York: 549-565.

Tarte, P., 1967. Infra-red spectra of inorganic aluminates and characteristic vibrational frequencies of AlO_4 tetrahedra and AlO_6 octahedra. Spectrochim. Acta 23A: 2127-2143.

Tarte, P., Pottier, M.J. & Proces, A.M., 1973. Vibrational studies of silicates and germanates - V. I.R. and Raman spectra of pyrosilicates and pyrogermanates with a linear bridge. Spectrochim. Acta 29A: 1017-1027.

Taylor, M., 1979. A quasi-crystalline model for interpretation of radial distribution functions: theory and experimental confirmation. J. Appl. Cryst. 12: 442-449.

Taylor, M. & Brown, G.E., 1979a. Structure of mineral glasses - I. The feldspar glasses $NaAlSi_3O_8$, $KAlSi_3O_8$, $CaAl_2Si_2O_8$. Geochim. Cosmochim. Acta 43: 61-75.

Taylor, M. & Brown, G.E., 1979b. Structure of mineral glasses - II. The SiO_2-$NaAlSiO_4$ join. Geochim. Cosmochim. Acta 43: 1467-1473.

Taylor, M., Brown, G.E. & Fenn, P.M., 1980. Structure of mineral glasses - III. $NaAlSi_3O_8$ supercooled liquid at 805°C and effects of thermal history. Geochim. Cosmochim. Acta 44: 109-117.

Thomas, J.M., 1979. Absorbability of diamond surfaces. In J.E. Field (Ed.): THE PROPERTIES OF DIAMOND. Academic Press: 211-244.

Thompson, R.N. & Kushiro, I., 1972. The oxygen fugacity within graphite capsules in piston-cylinder apparatus at high pressures. Rep. Geophys. Lab., Carnegie Inst. Ybk 71: 615-616.

Trial, A.F., Rudnick, R.L., Ashwal, L.D., Henry, D.J. & Bergman, S.C., 1984. Fluid inclusions in mantle xenoliths from Ichinomegata, Japan: evidence for subducted H_2O? EOS Trans., Am. Geophys. Union 65: 306.

Trueb, L.F. & De Wys, E.C., 1969. Carbonado: natural polycrystalline diamond. Science 165: 799-802.

Tsiklis, D.S. & Semenova, A.I., 1973. The molar volumes of aliphatic hydrocarbons at high pressures. Russ. J. Phys. Chem. 47: 1553-1554.

Tsiklis, D.S., Linshits, L.R. & Tsimmerman, S.S., 1971. Molar volumes and thermodynamic properties of methane at high pressures and temperatures. Dokl. Akad. Nauk SSSR 198: 384-386. (in Russian)

Tsiklis, D.S., Semenova, A.I., Tsimmerman, S.S. & Emel'yanova, E.A., 1972. Compressibility and thermodynamic properties of ethane at ultrahigh pressures and high temperatures. Russ. J. Phys. Chem. 46: 1677-1678.

Tsiklis, D.S., Linshits, L.R. & Tsimmerman, S.S., 1974. Measurement of the compressibility and calculation of molal volumes and thermodynamic properties of methane at superhigh pressures. Fluid Mech. Soviet Res. 3: 61-63.

Tsiklis, D.S., Maslennikova, V.Ya., Gavrilov, S.D., Egorov, A.N. & Timofeeva, G.V., 1975. Molar volumes and the equation of state for molecular hydrogen under high pressure. Dokl. Akad Nauk SSSR 220: 1384-1386. (in Russian)

Uematsu, M., Saegusa, S., Watanabe, K. & Tanishita, I., 1975. Thermodynamic properties of gaseous ethane and ethene. Rev. Phys. Chem. Jap. 45: 53-59.

Ulmer, G.C., 1983. Increasing evidence for graphite as a primary phase in many large mafic plutons. GSA, Abstracts with Programs 15: 709.

Urnes, S., 1969. Studies of the sodium distribution in sodium silicate glasses by the chemical difference method. Phys. Chem. Glasses 10: 69-71.

Uys, J.M. & King, T.B., 1963. The effect of basicity on the solubility of water in silicate melts. Trans. Metall. Soc. AIME 227: 492-500.

Van Thiel, M. & Alder, B.J., 1966. Shock compression of liquid hydrogen. Molec. Phys. 10: 427-435.

Varshavskiy, A.V. & Shul'tyakov, Yu.F., 1967. Oriented crystallisation of alpha-SiC on diamond. Dokl. Akad Nauk SSSR 173 (3): 571-574. (in Russian)

Velde, B. & Kushiro, I., 1978. Structure of sodium aluminosilicate melts quenched at high pressure; infrared and aluminium K-radiation data. Earth Plan. Sci. Lett. 40: 137-140.

Veng-Pedersen, P., 1977. Curve fitting and modeling in pharmacokinetics and some practical experiences with NONLIN and a new program FUNFIT. Jour. Pharmacokin. Biopharm. 5: 513-531.

Vera, J.H. & Prausnitz, J.M., 1972. Generalized Van der Waals theory for dense fluids. Chem. Eng. Jour. 3: 1-13.

Verweij, H. & Konijnendijk, W.L., 1976. Structural units in K_2O-PbO-SiO_2 glasses by Raman spectroscopy. J. Am. Ceram. Soc. 59: 517-521.

Verweij, H., Van den Boom, H. & Breemer, R.E., 1977. Raman scattering of carbonate ions dissolved in potassium silicate glasses. J. Am. Ceram. Soc. 60: 529-534.

Virgo, D., Huggins, F.E. & Rosenhauer, M., 1976. Petrologic implications of intrinsic oxygen fugacity measurements on titanium-containing silicate garnets. Rep. Geophys. Lab., Carnegie Inst. Ybk 75: 730-735.

Virgo, D., Mysen, B.O. & Kushiro, I., 1980. Anionic constitution of 1-atmosphere silicate melts: implications for the structure of igneous melts. Science 208: 1371-1373.

Volborth, A. & Housley, R.M., 1984. A preliminary description of complex graphite, sulphide, arsenide, and platinum group element mineralization in a pegmatoid pyroxenite of the Stillwater Complex, Montana, U.S.A. Tscher. Min. Petrol. Mitt. 33: 213-230.

Vollmer, R., 1983. Earth degassing, mantle metasomatism and isotopic evolution. Geology 11: 452-454.

Wade, K. & Banister, A.J., 1973. The chemistry of aluminium, gallium, indium and thallium. In COMPREHENSIVE INORGANIC CHEMISTRY, Vol.12. Pergamon Press.

Wakita, H. & Sano, Y., 1983. $^3He/^4He$ ratios in CH_4-rich natural gases suggest magmatic origin. Nature 305: 792-794.

Walker, D., Stolper, E.M. & Hays, J.F., 1978. A numerical treatment of melt/solid segregation: size of the eucrite parent body and stability of the terrestrial low-velocity zone. J. Geophys. Res. 83: 6005-6013.

Walter, L.S. & Doan, A.S., 1969. A determination of oxygen fugacities of chondritic meteorites. GSA Abstracts with Programs 1: 232-233.

Wass, S.Y. & Pooley, G.D., 1982. Fluid activity in the mantle - evidence from large lherzolite xenoliths. Terra Cognita 2: 229.

Watanabe, S., Mishima, K. & Matsuo, S., 1983. Isotopic ratios of carbonaceous materials incorporated in olivine crystals from the Hualalai Volcano, Hawaii - an approach to mantle carbon. Geochem. Jour. 17: 95-104.

Weidner, J.R., 1972. Equilibria in the system Fe-C-O. Part I: Siderite-magnetite-carbon-vapor equilibrium from 500 to 10,000 bars. Am. J. Sci. 272: 735-751.

Welhan, J.A. & Craig, H., 1979. Methane and hydrogen in East Pacific Rise hydrothermal fluids. Geophys. Res. Lett. 6: 829-831.

Welhan, J.A. & Craig, H., 1983. Methane, hydrogen and helium in hydrothermal fluids at 21°N on the East Pacific Rise. In P.A. Rona, K. Bostrom, L. Laubier & K.L. Smith (Eds): HYDROTHERMAL PROCESSES AT SEAFLOOR SPREADING CENTERS. Plenum Press, New York: 391-409.

Weltner, W. & McLeod, D., 1964. Spectroscopy of silicon carbide and silicon vapor trapped in neon and argon matrices at 4 K and 20 K. J. Chem. Phys. 41: 235-245.

Whittaker, A.G., 1978. Carbon: a new view of its high temperature behaviour. Science 200: 763-764.

Windom, K.E. & Boettcher, A.L., 1981. Phase relations for the joins jadeite-enstatite and jadeite-forsterite at 28 kb and their bearing on basalt genesis. Am. J. Sci. 281: 335-351.

Woermann, E.B., Knecht, B., Rosenhauer, M. & Ulmer, G.C., 1977. The stability of graphite in the system C-O. Extended Abstracts, 1st Int. Kimberlite Conf., Santa Fe.

Woermann, E., Stier, B. & Rosenhauer, M., 1982. The oxygen membrane cell - a device for controlling the oxygen fugacity in water-free high pressure systems. In W. Schreyer (Ed.): HIGH-PRESSURE RESEARCHES IN GEOSCIENCE. E. Schweiz. Verlag, Stuttgart: 519-528.

Wong, J. & Angell, C.A., 1976. GLASS STRUCTURE BY SPECTROSCOPY. Marcel Dekker, New York: 864 pp.

Wood, M.I. & Hess, P.C., 1980. The structural role of Al_2O_3 and TiO_2 in immiscible silicate liquids in the system SiO_2-MgO-CaO-FeO-TiO_2-Al_2O_3. Contrib. Min. Petrol. 72: 319-328.

Woodcock, L.V., Angell, C.A. & Cheeseman, P., 1976. Molecular dynamics studies of the vitreous state: simple ionic systems and silica. J. Chem. Phys. 65: 1565-1577.

Wright, A.C. & Leadbetter, A.J., 1976. Diffraction studies of glass structure. Phys. Chem. Glasses 17: 122-144.

Wyllie, P.J., 1979. Magmas and volatile components. Am. Min. 64: 469-500.

Wyllie, P.J., 1980. The origin of kimberlite. J. Geophys. Res. 85: 6902-6910.

Yasaitis, J.A. & Kaplow, R., 1972. Structure of amorphous silicon monoxide. J. Appl. Phys. 43: 995-1000.

Yoder, H.S., 1964. Soda melilite. Rep. Geophys. Lab., Carnegie Inst. Ybk 63: 86-89.

Yoder, H.S. & Tilley, C.E., 1962. Origin of basalt magma: an experimental study of natural and synthetic rock systems. J. Petrol. 3: 342-532.

Zachariasen, W.H., 1932. The atomic arrangement in glass. J. Am. Chem. Soc. 54: 3841-3851.

Zashu, S. & Ozima, M., 1984. $^{3}He/^{4}He$ ratio in diamonds and its implication on the early history of the Earth. EOS Trans., Am. Geophys. Union 65: 304.

Zharikov, V.A., Shmulovich, K.I. & Bulatov, V.K., 1977. Experimental studies in the system CMAS-CO_2-H_2O and conditions of high-temperature metamorphism. Tectonophysics 43: 145-162.

Ziegenbein, D. & Johannes, W., 1980. Graphite in C-H-O fluids: an unsuitable compound to buffer fluid composition at temperatures up to 700°C. Neues Jb. Miner. Mon. 7: 289-305.

Zolotarev, B.P., Voitov, G.I., Sarkisyan, I.S. & Cherevichnaya, L.F., 1979a. Distribution of gases and bitumens in basalts from holes 395 and 396, Leg 45. Initial Rep. DSDP, Vol.XLV: 647-651.

Zolotarev, B.P., Choporov, D.Y. & Voitov, G.I., 1979b. Petrochemistry of basalts and distribution of organic gases: holes 407, 408, 409, 410A, 411, 412, and 413, DSDP Leg 49. Initial Rep. DSDP, Vol XLIX: 727-744.